



**Mondragon
Unibertsitatea**

**Goi Eskola
Politeknikoa
Faculty of
Engineering**

MONDRAGON UNIBERTSITATEA
– FACULTY OF ENGINEERING –

**Thermal Distortion Effects on Cylindrical
Gear Teeth Contact**

by **Aitor Arana Ostolaza**

Division of Mechanical Design

Mechanical and Industrial Production Department

Supervised by:

Dr. Ibai Ulacia Garmendia

Dr. Jon Larrañaga Amilibia

*A Thesis submitted in partial fulfilment of the requirements for the degree of
Doctor of Philosophy in Engineering*

14th May 2019

Blanca, nire emazteari.
Amari eta aitari.
Maitasunez.

Laburpena

Engranajeen portaera termikoa arreta gutxien jaso duen arazo mekanikoetako bat izan da azken mendean. Sortutako beroaren jatorria dagoeneko ulertu arren, bere analisisia olioaren tenperatura egonkorraren iragarpenera mugatu da, engranajeen hutsegitean eragin zuzena baitu. Alabaina, literatura zientifikoaren berrikuspenak erakutsi du dilatazio termikoaren ondorioak ia ez direla aztertu. Bitartean, turbo-makinen industriako esperientziak frogatu du termikoki eragindako geometriaren distortsioak zeregin garrantzitsua duela karga banaketaren aldaketan hortzen haustura eragiten duelarik neurririk hartzen ez bada.

Doktorego tesi honen helburu nagusia termikoki eragindako engranaje zuzen eta helikoidalen geometriaren distortsioak sortutako portaera mekaniko irregularra aurreikustea, ebaluatzea eta zuzentzea da. Asmo horrekin, engranaje parean sortutako beroa kuantifikatu egin behar da eta tenperatura egonkorraren banaketa aurreikusi behar da aldez aurretik. Ondoren, hortzen deformazio termikoa zehazteko eredu bat garatu behar da karga banaketa kalkuluen ohiko fluxuan inplementatuz. Distortsio termiko mota eta zenbatekoa jakiteak, kargapean duen portaeraren ulermenarekin batera, hortzaren geometria zuzenketa ahalbidetuko du kontaktuaren portaera desegokia konpentsatuz.

Tesiaren lehen ataletan distortsio termikoaren jatorria deskribatzen da eta gaur egungo egoera berrikusten da. Ondoren, engranaje zuzen eta helikoidalen geometria eta zinematika aztertzen dira eta karga banaketa kalkulatzeko eredu analitiko bat garatzen da "thin slice" izeneko metodoa erabiliz. Segidan, engranaje pareen irristaketa marruskaduraren portaera aztertzen da, kontaktuan sortutako beroa kuantifikatzen da eta gurgil parearen tenperatura-banaketa aurreikusten da sare termikoen kontzeptuan oinarrituta. Kapitulu bakoitzean eredu berriak garatzen dira eta emaitzak literatura zientifikoko datu esperimentalekin baliozkotzen dira. Distortsio termikoa aurreikusteko eredu seigarren kapituluan aurkezten da, parametro ezberdinen analisisa egiten da eta adibide praktiko bat goitik behera aztertzen da, geometriaren distortsiotik abiatuta portaera termomekanikoa ikusi arte. Kapitulu honen amaieran, termikoki eragindako deformazioei aurre egiteko diseinu gomendioak biltzen dira eta hortzak zuzentzeko arauak proposatzen dira. Azkenean, transmisio errearen portaera termomekanikoa esperimentalki aztertzen da, ondorioak laburbiltzen dira eta etorkizuneko ildoak azpimarratzen dira. Emaitzen arabera, eta ohiko ustearen aurka, altzairuzko engranajeen distortsio termikoak karga banaketan eta transmisio errean eragina du eta, ondorioz, kontuan hartu behar da haien kontaktu analisian.

Resumen

El comportamiento térmico de engranajes es uno de los temas que menos atención ha recibido en el último siglo. Aunque el origen del calor generado es conocido, su estudio se ha limitado a la predicción de la temperatura estacionaria del lubricante ya que tiene una influencia directa en el fallo de los mismos. Sin embargo, la revisión de la literatura científica ha puesto en evidencia que los efectos de su expansión térmica apenas han sido analizados. Entretanto, la experiencia en turbo-máquinas indica que las distorsiones de geometría de origen térmico tienen un papel fundamental en la alteración de los patrones de contacto pudiendo incluso provocar la rotura del dentado si no se toman medidas.

El objetivo principal de esta tesis es predecir, evaluar y corregir el comportamiento mecánico no uniforme de parejas de engranajes rectos y helicoidales debido a la distorsión de la geometría inducida térmicamente. Para este fin, el calor generado por fricción debe ser cuantificado y la distribución de temperatura estacionaria debe ser predicha. Así mismo, debe desarrollarse un modelo de deformación térmica capaz de integrarse en los algoritmos de cálculo de distribución de carga habituales. La comprensión del tipo y magnitud de la distorsión térmica, junto a sus efectos en la distribución de carga, permitirán corregir la geometría del dentado y compensar comportamientos no deseados.

En los primeros capítulos de esta tesis se analiza el origen de la distorsión térmica y se revisa el estado del arte. Tras esto, se describen la geometría y cinemática de engranajes rectos y helicoidales y se desarrolla un modelo de distribución de carga analítico basado en el concepto de secciones delgadas. Posteriormente, se estudia el comportamiento del rozamiento en el engrane, se cuantifica el calor generado por el mismo y se predice la distribución de temperatura mediante el uso de redes térmicas. En cada uno de estos capítulos se desarrollan nuevos modelos que son validados con datos experimentales de la literatura científica. El modelo de distorsión térmica es introducido en el sexto capítulo, se desarrolla un estudio paramétrico y se analiza un caso práctico, desde la distorsión de la geometría hasta su comportamiento mecánico. Así mismo, se recogen recomendaciones de diseño para hacer frente a este fenómeno y se proponen directrices de modificación del dentado. Finalmente, se lleva a cabo un estudio experimental del error de transmisión termomecánico, se extraen conclusiones generales y se definen las líneas de trabajo a futuro. Los resultados presentados muestran que, contrariamente a la creencia común, la distorsión térmica en engranajes de acero sí afecta a la distribución de carga y el error de transmisión y, por lo tanto, debe ser considerado en el análisis de contacto.

Abstract

The thermal behaviour of geared transmissions has been one of the mechanical issues receiving the least amount of attention in the last century. Although the origins of heat generated in gearboxes is already understood, its analysis has been limited to the prediction of steady-state oil temperature, which has a direct influence in gear failure. However, scientific literature review has shown that the effects of thermal expansion have been hardly analysed. Meanwhile, field experience in turbo-machinery industry, proves that thermally-induced geometry distortion does play a significant role on contact pattern shift leading to tooth breakage if no counter-measures are provided.

The main objective of the present thesis is to predict, evaluate and correct uneven mechanical behaviour of spur and helical gears due to thermally-induced flank geometry distortion. For this purpose, heat generated in the gear mesh needs to be quantified and resulting steady-state temperature distribution must be predicted. Then, a model to determine thermal deformation of gear teeth must be developed and implemented on common load distribution calculation flowcharts. The understanding of the type and amount of thermal distortion, along with its effects on loaded behaviour, will allow to correct tooth geometry and compensate for undesired contact behaviour.

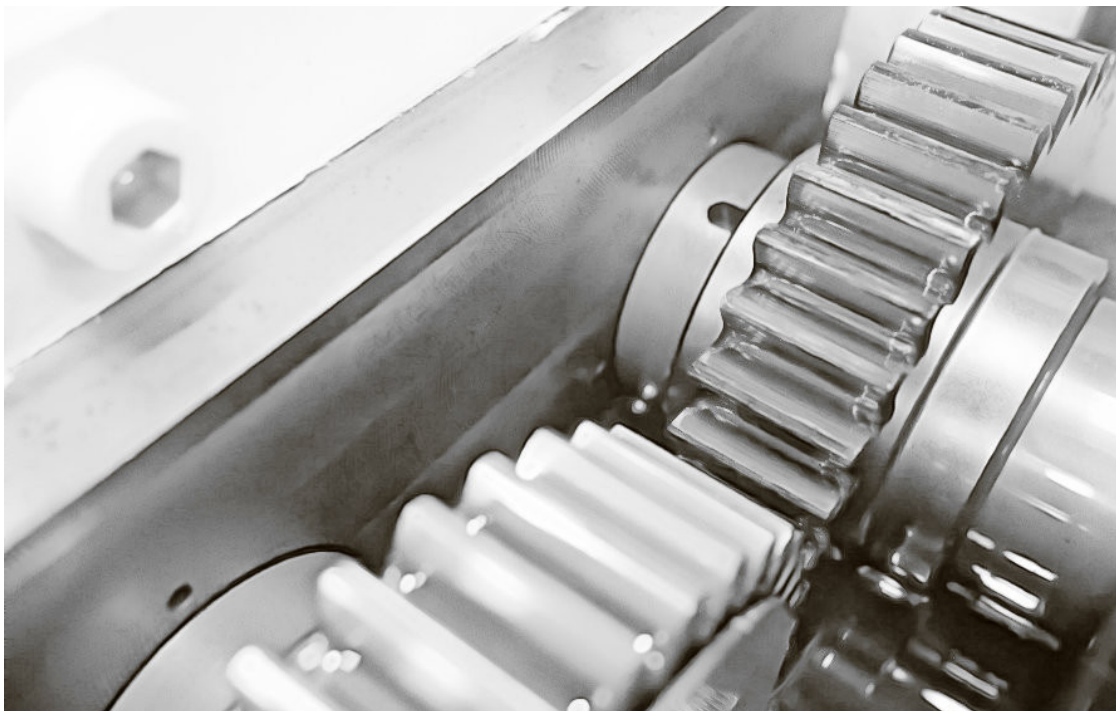
In the first chapters of the present thesis, a brief description of the origins of thermal distortion is presented and current state of art is reviewed. Then, spur and helical gear teeth geometry and kinematics are described and an analytical load distribution model following the so called “thin-slice” approach is developed. Next, sliding friction behaviour in meshing gears is analysed, the amount of heat generated in the mesh is quantified and temperature distribution is predicted based on the thermal-network concept. New models are developed within each of these chapters and results are validated with experimental measurements from literature. The thermal distortion model is introduced in chapter six, a parameter analysis is carried out and a test case is fully analysed, from geometry distortion to full thermo-mechanical behaviour. At the end of this chapter, design recommendations to cope with thermally-induced deformations are gathered and tooth modification rules are proposed. Finally, an experimental study on thermally-induced transmission error behaviour is carried out, conclusions are withdrawn and future work in the field is pointed out. Results show that, contrary to common belief, thermal distortion in steel gears does affect load distribution and transmission error and therefore it should be considered in gear tooth contact analysis.



**Mondragon
Unibertsitatea**

Goi Eskola
Politeknikoa
Faculty of
Engineering

Thermal Distortion Effects on Cylindrical Gear Teeth Contact



– Aitor Arana Ostolaza –

Mondragon Unibertsitatea, Faculty of Engineering
Mechanical and Industrial Production Department
Division of Mechanical Design

14th May 2019

Appreciation is a wonderful thing: It makes what is excellent in others belong to us as well.

— François Marie Arouet “Voltaire”, 1694 - 1778

Acknowledgements

Giving thanks is probably one of the simplest but most difficult acts at the same time, as one risks to take ownership of what has been given by others (often for free) if their work is not sufficiently acknowledged. That’s why I hope not to forget anybody in the following paragraphs, and if I do, I sincerely apologize beforehand.

First and foremost, I would like to thank my supervisors Dr. Ibai Ulacia and Dr. Jon Larrañaga for giving me the opportunity to develop this thesis, their guidance, friendship and trust through this period, especially in the last year of thesis. If this document has come to an end its because despite the many difficulties arising during these years, they have not given up supporting me and believing in this thesis project. I would also like to thank Mondragon Unibertsitatea, who provided the financial support as well as all the laboratories and testing equipment. In this regard, I would like to extend my deep appreciation to all the co-operative members of this institution who have aided to backup this thesis through the staff training program.

Son muchas las personas que han colaborado de una u otra manera en la culminación de este trabajo. Quiero agradecer especialmente el apoyo recibido por parte de todos los miembros del Departamento de Mecánica y Producción Industrial en general, y del área de Diseño Mecánico en particular, por permitir que pueda realizar esta tesis haciéndose cargo de las asignaturas, cursos y proyectos que no he podido impartir o desarrollar a lo largo de estos años. Espero poder devolver todo el apoyo recibido. A Ezpeleta, Izquierdo, Felix, Eraña, Garcia, Tena, Oyanguren y todos aquellos compañeros, actuales y pasados, que de una u otra manera habéis mostrado interés por mí y me habéis animado a seguir adelante. Como alguien me dijo una vez, “la tesis se acaba aunque no lo parezca” y no habría sido posible sin el apoyo de todas estas personas. Gracias a Julen Maskariano, por la paciencia y dedicación en el montaje y puesta a punto del banco de ensayos y el propio laboratorio (sin ti esos engranajes aún seguirían parados). Tampoco quisiera olvidarme de Iñaki Fernández de Bastida, Aitor Osa y Arkaitz Garate por vuestra disposición para ayudar cuando surgieron dificultades técnicas. A Jone, Paula y Duli, por su enorme ayuda a la hora de localizar artículos, tesis y demás documentos técnicos “raros” que os he pedido (¡no han sido pocos!), muchas gracias. Y como no podría ser de otra manera, no puedo dejar de agradecer a todos los alumnos, becarios y proyectos finales de carrera, sus aportaciones, diseños, simulaciones y ensayos. Especialmente a Jon German, Julen Elizegi, Aurea Iñurritegi, Andoni Gorostiza y Asier Dueñas; todos habéis puesto vuestro granito de arena en esta tesis.

Eta bukatzeko, eskerrik beroenak nire familiari eta lagunei. Bide luze honetan hor egotearren, zuen babesu sentitu dut une oro eta nigan nik neuk baino gehiago sinetsi duzuelako. Nire emazteari, Blanca, pazientzia izatearren, egunero irribarre bat eskaini baitidazu eta egun bakoitza bukatzeko egun bat gutxiago dela gogoratu didazu. Ama eta aitari, zuek gabe ez bainintzen honaino iritsiko, gogor lan egin duzue eta zuen ereduarekin irakatsi didazue. Ez ditut nahikoa hitz nigatik egin duzuen guztia eskertzeko. Aritz eta Itziarri, zuen alaitasuna transmititzearren eta nire kezkek partekatzearren. Bizitza tesia bakarrik ez dela gogoratu didazue. Eta nola ez, nire lagunei, Jonathan eta Alex, tesia dela eta elkar ikusi gabe denbora pasa arren beti hor egon zaretelako.

MILA ESKER BIHOTZEZ DENOI!

Declaration of originality

I hereby declare that this dissertation and the work described in it are the product of my own work and that, to the best of my knowledge, it contains no previously published material except where due acknowledgement has been made in the text as noted by citations. This PhD thesis has not been submitted for any other degree or diploma of Mondragon Unibertsitatea or other institute of higher education. The copyright of this document including data, figures, tables and text rests with the author and all the assistance received in preparing it have been acknowledged. Researchers are free to copy, distribute or transmit the thesis on the condition that they attribute it properly, that they do not use it for commercial purposes and that they do not alter, transform or build upon it.

A handwritten signature in black ink, appearing to read 'Aitor A.O.', with a large, sweeping underline that loops around the text.

Signed: *Aitor Arana Ostolaza*
Arrasate-Mondragon, 14th May 2019

Contents

List of Figures	xxi
List of Tables	xxvii
Nomenclature	xxix
1 Introduction	1
1.1 Background	2
1.2 Motivation	3
1.2.1 Thermal rating of gear drives	4
1.2.2 Thermal distortion of gear teeth	5
1.3 Hypothesis and research objectives	7
1.4 Dissertation outline	8
2 Literature Review	11
2.1 Heat generation and transfer in gears	12
2.1.1 Heat generation	12
2.1.2 Heat dissipation	21
2.2 Temperature distribution in cylindrical gears	26
2.2.1 Experimental observations	26
2.2.2 Analytical and numerical studies	32
2.3 Thermally induced teeth geometry distortion	34
2.3.1 Compensation of thermal distortion	43
2.4 Critical review of the state of the art	45
3 Gear Kinematics and Load Distribution Modelling	49
3.1 Involute teeth geometry description	50
3.1.1 Fundamental law of gearing and conditions of existence	50
3.1.2 Generation and modification of teeth geometry	56
3.2 Kinematic behaviour	63
3.2.1 Determination of kinematic relations	63
3.2.2 No-load transmission error behaviour	68
3.3 Load distribution and transmission error	71
3.3.1 Statement of the problem	71
3.3.2 Thin slice approach for 3D gear contact problems	76
3.3.3 Load capacity	81
3.4 Finite element validation	84
3.4.1 Description of the model and test cases	84
3.4.2 Results and discussion	87
3.5 Conclusions of Chapter 3	91

4	Prediction of Friction and Power Losses	93
4.1	Introduction	94
4.2	Sliding friction coefficient model	95
4.2.1	Friction coefficient model for full EHL contacts	95
4.2.2	Extension to partial EHL regime	102
4.2.3	Experimental validation	105
4.2.4	Discussion of results	108
4.3	Power loss prediction model	111
4.3.1	Teeth contact thermal behaviour	111
4.3.2	Thermally-coupled power loss prediction model	114
4.3.3	Experimental validation	118
4.3.4	Discussion of results	121
4.4	Conclusions of Chapter 4	122
5	Thermal Model for Cylindrical Gear Pairs	123
5.1	Introduction	124
5.2	Description of the thermal network model	125
5.2.1	Thermal network definition	126
5.3	Heat transfer in meshing gear pairs	132
5.3.1	Heat sources	132
5.3.2	Heat dissipation in dip-lubricated gears	138
5.4	Governing equations and solution method	144
5.4.1	Solution method	145
5.4.2	Thermo-mechanical coupling	147
5.5	Experimental validation	151
5.5.1	Discussion of results	154
5.6	Conclusions of Chapter 5	156
6	Thermal Distortion	159
6.1	Introduction	160
6.2	Thermally-induced geometry distortion	160
6.2.1	Profile distortion	161
6.2.2	Helix distortion	168
6.3	Thermal effects on mesh behaviour	172
6.3.1	No-load transmission error and backlash	173
6.3.2	Thermo-mechanical behaviour	177
6.4	Case study	184
6.4.1	Results	185
6.4.2	Compensation of thermal distortion	188
6.5	Design recommendations	190
6.5.1	Tooth modification guidelines	193
6.6	Conclusions of Chapter 6	195
7	Experimental Study	197
7.1	Back-to-back gear test bench design	198
7.2	Experimental methodology	202
7.2.1	Test specimens	202
7.2.2	Working conditions	204
7.2.3	Experimental setup and procedure	204

7.2.4	Transmission error measurement	206
7.3	Results	210
7.3.1	Backlash tests	210
7.3.2	Loaded transmission error measurements	212
7.3.3	Loaded and thermally affected transmission error tests	213
7.4	Discussion	215
7.5	Conclusions of Chapter 7	217
8	Conclusions and Future Work	219
8.1	Concluding remarks	220
8.2	Recommendations for future work	222
8.3	Scientific contributions	223
Appendices		
A	Bearing and Sealing Power Loss Models	227
B	Analytical - Numerical Distortion Comparison	231
C	Hertz Theory for Elliptical Contacts	235
D	Absolute to Incremental Angle Conversion Method	237
E	Manufactured Gear Inspection Data	239
E.1	Pinion and gear type A	240
E.2	Pinion type B	243
E.3	Gear type B	246
	References	249

List of Figures

1.1	Trend in EV/HEV traction motor speeds and power densities	2
1.2	High speed power loss breakdown according to ANSI/AGMA 6011	4
1.3	Gear failures related to high temperatures	5
1.4	Contact pattern shift due to thermal distortion in turbo-gears	6
1.5	Tooth end bending failure due to thermal instability	6
1.6	Research methodology	8
2.1	Sample torque loss breakdown from FZG gear test rig	12
2.2	Stribeck curve for a gear contact subject to common operating conditions	14
2.3	Simulated EHL pressure and film thickness distributions in a smooth contact	15
2.4	CFD simulations of no-load losses by Liu	17
2.5	Fundamental heat dissipation mechanisms in a gearbox	21
2.6	Gearbox external convection and radiation heat transfer coefficients . . .	22
2.7	Fling-off cooling effect in rotating spur gears	23
2.8	Axial oil pumping effect in rotating spur gears	24
2.9	Influence of speed, load and face width on flash temperatures	26
2.10	Transverse temperature distribution in spur gear tooth	27
2.11	Influence of oil jet flow rate and direction of rotation on temperature distribution of helical gear pairs according to Geiger	28
2.12	Effect of speed and torque in radial and axial oil fling-off temperatures . .	29
2.13	Temperature field of a high speed helical gear	30
2.14	Temperature distribution relative to PLV and torque	30
2.15	Temperature difference in “mesh-in” and “mesh-out” situations	31
2.16	Transverse temperature distribution in spur gear body and tooth	32
2.17	Influence of speed and torque on 3D temperature distribution of spur gears	33
2.18	Magnitude of radial tooth expansion with constant temperature increase .	34
2.19	Effect of temperature on mesh stiffness and load sharing ratio of Nylon gears	35
2.20	Involute profile deviation with temperature increase	36
2.21	Sensitivity of TE harmonics to temperature increase and correlation to transverse contact ratio according to Hensel et al.	37
2.22	Relative helical teeth distortion according to Henriot	38
2.23	Relationship between temperature and tooth root stress in large face width helical gears subject to high pitch line velocities	38
2.24	Barrelling of high-speed double helical gear set	39
2.25	Effect of temperature difference on load distribution of double helical gears	39
2.26	Thermal distortion of high speed gears due to material transformation . .	40
2.27	Displacements of internal components due to housing thermal growth . .	41
2.28	Shaft dilatation effect on bearing preload and bevel gear apex displacement	42
2.29	Double helical gear mesh axial bound due to shaft thermal growth	42
2.30	Profile correction recommendations to compensate thermal effects	43

2.31	Flank line correction to compensate thermal expansion	44
2.32	Lead modification guidelines to compensate thermo-mechanical deviations	44
3.1	Graphical description of involute curve generation	50
3.2	Generation processes for gear manufacturing	52
3.3	Basic rack dimensions according to ISO 53	53
3.4	Local system of coordinates and dimensions of the basic rack counterpart	56
3.5	Graphical description of tooth profile generation method	57
3.6	Different types of profile modification	59
3.7	Different types of flank line modification	60
3.8	Profile modifications relative to theoretical and generated tooth geometry	61
3.9	Generalized tooth profile and longitudinal modification scheme	61
3.10	Base tangent plane geometrical boundaries and systems of coordinates . .	64
3.11	Position and velocity parameters in the gear mesh	66
3.12	Kinematic behaviour of FZG type C spur gear set at $V_t = 8.3$ m/s	68
3.13	Separating distance of theoretical FZG type C spur gear set	69
3.14	Sample calculation of <i>NLTE</i> in modified FZG type C gear	70
3.15	Discretization of the base tangent plane for numerical integration	74
3.16	Thin slice compliance model representation	77
3.17	Dimensions and local coordinates for tooth slice compliance calculation .	78
3.18	Tooth transverse and longitudinal compliance	80
3.19	Bending and contact stresses for generated and modified FZG type C gear	83
3.20	Gear pair finite element mesh and boundary conditions	85
3.21	Influence of torque and face width on load distribution and <i>TE</i>	87
3.22	Contact ratio increase with load and face width	88
3.23	Influence of load and face width on mean level and <i>PTP TE</i>	88
3.24	Influence of shaft diameter on load distribution and <i>TE</i>	89
3.25	Influence of profile modifications applied on pinion	90
3.26	Influence of profile modifications applied on pinion	91
4.1	Comparison of instantaneous friction coefficients and power losses predicted by classical models and thermal EHL simulations on FZG gear type C . .	95
4.2	Representation of the smooth EHL line contact	96
4.3	Characteristic traction curve of rolling-sliding contacts	97
4.4	Non-dimensional shear stress model comparison	97
4.5	Density plot of the Deborah number along the path of contact for PAO oil	99
4.6	Probability density of Deborah numbers below one in gear conditions . . .	100
4.7	Comparison of predicted Eyring stress by Bair and Jacod as a function of temperature and pressure for sample ISO VG 100 mineral oil	101
4.8	Representation of asperities in contact in mixed lubrication	103
4.9	Generalized Stribeck curve sample width transitions	105
4.10	Numerical-experimental correlation of the VPT behaviour of M100 oil . .	106
4.11	Eyring stress as a function of temperature and pressure for M100 oil . . .	107
4.12	Numerical-experimental correlation of traction curves for different oils . .	107
4.13	Measured and predicted friction coefficients according to proposed model	108
4.14	Influence of Eyring stress on traction coefficient	110
4.15	Representation of a smooth thermal EHL line contact	111
4.16	Thermal network scheme of the EHL line contact	112
4.17	Thermally-coupled friction coefficient and power loss prediction flow chart	115

4.18	Comparison of computed film temperatures and thermal FE simulations	117
4.19	Influence of thermal coupling in local friction coefficients and power losses	118
4.20	Analytical-experimental correlation of power loss predictions as a function of speed and torque for mineral and PAO oils at constant temperature	119
4.21	Analytical-experimental correlation of power loss predictions as a function of oil temperature and surface roughness at constant torque	120
4.22	Overview of predicted power losses and experimental measurements	120
4.23	Influence of boundary friction coefficient on predicted average power loss and friction coefficient for C_{mod} gears at constant torque and temperature	121
5.1	Cylindrical control volume and thermal resistance simplification	125
5.2	Thermal network of the shaft-gear assembly	127
5.3	Thermal network of the gear pair and housing	129
5.4	Constriction resistance along the path of contact in FZG type C gears	131
5.5	Heat generated by FZG type C gears due to oil churning and windage	135
5.6	Influence of non-uniform load distribution on mesh frictional heat	136
5.7	Longitudinal gear teeth discretization for axial heat input modelling	136
5.8	Heat partitioning coefficient effect in FZG type C gear pair heat flux	137
5.9	Oil and air flow patterns around dip lubricated gear pair and housing	139
5.10	Oil-air mixture properties as a function of the fraction of oil in air	140
5.11	Biot number as a function of speed and tooth size	144
5.12	Thermo-mechanical temperature distribution prediction flowchart	147
5.13	Computed steady-state temperature distribution of FZG type C gears	148
5.14	Detail of predicted pinion and gear steady-state temperature distributions	149
5.15	Radial and axial temperature distributions for the simulated case	150
5.16	Computed transient temperatures of FZG type C pinion and gear, oil sump and interior air at constant speed and torque	151
5.17	Comparison of measured and predicted power losses	152
5.18	Comparison of temperature measurements and thermal network predictions for variable speeds, torques and immersion depths on FZG type C gears	153
5.19	Overview of predicted and measured bulk temperatures	154
5.20	Power losses as a function of oil level and operating speed	155
5.21	Influence of dynamic oil level on tooth temperatures	156
6.1	Representation of thermally-induced involute geometry distortion	161
6.2	Thermal distortion of FZG type C_{mod} gears at constant temperature	163
6.3	Parameter influence on FZG type C_{mod} gear flank distortion	164
6.4	Thermally-induced pitch and pressure angle deviations	165
6.5	Influence of module and number of teeth on thermally-induced pitch error	166
6.6	Influence of temperature and accuracy grade on relative pitch deviations	166
6.7	Total profile deviations as a function of initial design parameters	167
6.8	Thermally-induced lead and form deviations in the base tangent plane	169
6.9	Temperature, helix angle and face width influence on helix deviations	170
6.10	Definition of helix form deviation according to ISO 1328-1	171
6.11	Temperature, helix angle and face width influence on form deviations	171
6.12	Thermally-induced clearance decrease	173
6.13	Influence of temperature and manufacturing allowances on mesh jamming	174
6.14	Influence of thermal gradients on <i>NLTE</i> and normal deviations in LOA	175
6.15	Influence of temperature on separating distance	176

6.16	Influence of thermal state on load distribution at constant torque	178
6.17	Influence of temperature and load on relative contact length increase	178
6.18	Influence of longitudinal thermal gradients on load distribution	179
6.19	Influence of the composite effect of longitudinal and radial thermal gradients on load distribution at constant torque	180
6.20	Influence of bulk temperature increase and gradients on TE	180
6.21	Influence of temperature and load on mean level and peak-to-peak TE	181
6.22	Influence of longitudinal temperature gradient on TE at constant torque	182
6.23	Influence of temperature difference on stresses at constant torque	183
6.24	Influence of thermal gradients on stress behaviour at constant torque	183
6.25	Temperature distribution of pinion and gear in case study	185
6.26	Helical gear thermally-induced deviations and behaviour under load	186
6.27	Thermally-induced bending stress distribution and relative increase	187
6.28	Thermally-induced contact stress distribution and relative increase	188
6.29	Compensated load distribution relative to initial and distorted cases	189
6.30	Influence of distorted and compensated geometries on loaded TE	190
6.31	Derivation of profile slope error for tooth modification	193
6.32	Profile and helix slope modification proposal for the helical gear pair	194
7.1	Designed back-to-back test rig for external cylindrical gears	198
7.2	Overall view of designed test rig	200
7.3	Oil sump heating system and oil level inside gearbox	200
7.4	Thermocouple inserted in small module tooth	201
7.5	Position encoder assembly and bearing independent lubrication system	201
7.6	Spur gear sets A and B for quasi-static TE measurements	203
7.7	Experimental setup for thermo-mechanical TE measurement	205
7.8	Sample TE measurement in gear set A at 60 rpm and 100 Nm	207
7.9	FFT amplitude repeatability at mesh frequency as a function of torque	208
7.10	Repeatability of transmission error in gear sets A and B	209
7.11	TE mean level and PTP behaviour with increasing rotational speed	209
7.12	Influence of temperature on backlash reduction	211
7.13	Experimental loaded TE results for gear sets A and B	212
7.14	Experimental loaded TE results for gear sets A and B at 200 Nm torque	214
7.15	Summary of experimental and analytical TE mean level and PTP results	215
7.16	Gearbox temperature distribution relative to preset temperature	216
7.17	Influence of pinion and gear temperature differences on peak to peak TE	217
A.1	Speed, load and temperature effect on sealing and bearing power losses	230
B.1	FE modelling of gear expansion subject to a radial thermal gradient	231
B.2	Influence of thermal stresses on analytical predictions and comparison to numerical results for the case of small module gear	232
B.3	Influence of thermal gradient and tooth size on computed distortion error	233
C.1	Schematic representation of non-conformal solids in contact	235
D.1	Experimental transmission error measurement algorithm	238
E.1	Drawing of pinion and gear type A for manufacturing	240
E.2	Pinion and gear type A profile measurements	241

E.3	Pinion and gear type A flank line measurements	242
E.4	Drawing of pinion type B for manufacturing	243
E.5	Pinion type B profile measurements	244
E.6	Pinion type B flank line measurements	245
E.7	Drawing of gear type B for manufacturing	246
E.8	Gear type B profile measurements	247
E.9	Gear type B flank line measurements	248

List of Tables

2.1	Common sliding friction coefficient models in gear literature	16
2.2	Common rolling friction force equations in gear literature	17
2.3	Common churning power loss models in gear literature	18
2.4	Common windage power loss models in gear literature	19
2.5	Severity of thermal problems in helical gears according to Dudley	26
2.6	Common bulk temperature rise equations in gear literature	27
3.1	Basic rack coefficients for standard profiles according to ISO 53	53
3.2	Boundaries of regions in basic rack counterpart	57
3.3	Gear teeth generating functions per segment	58
3.4	Reference spur gear geometry for finite element validation	84
3.5	Material properties of case hardened 16MnCr5 steel for FE simulation	85
3.6	Test cases for finite element validation	86
4.1	Common shear stress models in EHL literature	97
4.2	Test matrix to identify Deborah number range in gear contacts	99
4.3	Asperity load sharing functions in gear literature	104
4.4	Selected lubricant properties	105
4.5	Regression coefficients for the selected lubricants	106
4.6	Coefficients for steady-state thermal resistance according to Terekhov	114
4.7	Spur gear geometry used by Zielgltrum for TEHL simulations	117
5.1	Heat partition coefficients in thermal network model	138
5.2	Forced convection heat transfer correlations for rotating gears and shafts	141
5.3	Characteristic lengths and mean fluid velocities in housing plates	142
5.4	Forced and natural convection heat transfer correlations for housing plates	143
5.5	Test conditions in Otto's experiments	151
6.1	Sample EV helical gear stage for thermal distortion case study	184
6.2	Summary of the influence of temperature distribution parameters on geometry, mesh behaviour, load distribution, transmission error and stress	191
7.1	Heidenhain RCN 2510 optical encoder characteristics	202
7.2	Spur gear sets A and B for experimental measurements	203
7.3	Operating conditions for experimental transmission error tests	204
B.1	Spur gear geometries for finite element simulation of thermal distortion	232
C.1	Summary of Hertzian parameters for elliptical contacts	236
E.1	Additional data for experimental spur gear sets A and B	239

Nomenclature

List of symbols¹

Sign	Unit	Description
a_w	[m]	Working centre distance
a_H	[m]	Semi-major axis of Hertzian contact region
b	[m]	Tooth face width
b_H	[m]	Semi-minor axis of Hertzian contact region
b_G	[m]	Distance between front and rear housing walls
c	[m]	Tip clearance
c_p	[m]	Specific heat capacity
c_y	[m]	Separating distance
d	[m]	Pitch diameter
d_a	[m]	Tip diameter
d_b	[m]	Base diameter
d_f	[m]	Root diameter
d_{Na}	[m]	Active tip diameter
d_{Nf}	[m]	Active root diameter
d_{sh}	[m]	Shaft diameter
d_w	[m]	Working pitch diameter
d_y	[m]	Y-circle diameter
e	[m]	Thermal effusivity
f	[Hz]	Frequency
f_c	[Hz]	Cut-off frequency
f_m	[Hz]	Mesh frequency
f_{pt}	[m]	Pitch error
f_s	[Hz]	Shaft rotation frequency
g_α	[m]	Length of path of contact
h	[m]	Tooth height
h	[-]	Convection heat transfer coefficient
h_a	[m]	Tooth addendum height
h_c	[m]	Central oil film thickness
h_f	[m]	Tooth dedendum height
h_k	[m]	Amount of gear tip chamfer or rounding
h_{min}	[m]	Minimum oil film thickness
h_G	[m]	Housing interior height
h_W	[m]	Shaft centreline height from oil sump bottom
j_{bn}	[m]	Normal backlash
j_{wt}	[m]	Working circumferential backlash
k	[W/m·K]	Thermal conductivity.
k	[m ⁻¹]	Curvature

¹For derivative parameters or additional meanings look for detailed explanations in each chapter.

Sign	Unit	Description
l	[m]	Tooth slice thickness
l_G	[m]	Housing interior width
m	[kg]	Mass
\dot{m}	[kg/s]	Mass flow rate
m_n	[m]	Normal module
p	[Pa]	Pressure
p_m	[Pa]	Mean contact pressure
p_H	[Pa]	Maximum Hertz contact pressure
p_{bt}	[m]	Transverse base pitch on the base cylinder
p_{et}	[m]	Transverse base pitch on the path of contact
p_{yt}	[m]	Transverse pitch on any diameter
\dot{q}	[W/m ²]	Heat flux
r	[m]	Pitch radius
r_a	[m]	Tip radius
r_b	[m]	Base circle radius
r_y	[m]	Y-circle radius
r_{Na}	[m]	Active tip radius
r_{Nf}	[m]	Active root radius
s_c	[m]	Chordal tooth thickness
t	[s]	Time
u	[m/s]	Rolling velocity of contact point relative to pinion or gear.
u	[-]	Gear ratio
w	[N/m]	Normal load per unit length
x	[-]	Profile shift coefficient
x_E	[-]	Manufacturing profile shift coefficient
z	[-]	Number of teeth
A	[m ²]	Surface area
A_{TE}	[rad]	Amplitude of transmission error
C	[m/N]	Compliance
C	[J/K]	Heat capacity
C_α	[μ m]	Amount of profile crowning (barrelling)
C_β	[μ m]	Amount of flank line crowning
C_m	[-]	Dimensionless churning drag torque
C_t	[-]	Dimensionless windage drag torque
D_e	[-]	Deborah number
E	[Pa]	Modulus of elasticity
E	[m]	Distance from shaft centreline to oil sump
E_s	[m]	Tooth thickness tolerance
F_{bt}	[N]	Nominal transverse load in the base tangent plane
F_r	[N]	Rolling friction force
F_s	[N]	Sliding friction force
G	[-]	Materials parameter associated to film thickness
G	[W/K]	Thermal conductance
H	[m]	Immersion depth of gear
H_v	[-]	Power loss factor
H_{vL}	[-]	Power loss factor considering stiffness
K	[N/m]	Stiffness
N	[rpm]	Rotation speed

Sign	Unit	Description
$NLTE$	[m]	No-load transmission error
L	[m]	Characteristic dimension in Reynolds number
PTP	[m]	Peak-to-peak transmission error
P_A	[W]	Input power
P_V	[W]	Total gearbox power loss
P_{VD}	[W]	No-load sealing power loss
P_{VL}	[W]	Total bearing power loss
P_{VL0}	[W]	No-load bearing power loss
P_{VLP}	[W]	Load-dependent bearing power loss
P_{VX}	[W]	No-load auxiliary power loss
P_{VZP}	[W]	Load-dependent gear mesh power loss
$P_{VZ0,C}$	[W]	No-load churning power loss
$P_{VZ0,W}$	[W]	No-load windage power loss
Q	[-]	Gear manufacturing quality
Q	[W]	Heat
Q_G	[W]	Heat input in gearbox housing
Q_{VD}	[W]	Heat input from sealing power loss
Q_{VL}	[W]	Heat input from bearing power loss
$Q_{VZ0,C}$	[W]	Heat input from gear churning power loss
$Q_{VZ0,W}$	[W]	Heat input from gear windage power loss
Q_{VZP}	[W]	Heat input from gear mesh power loss
U	[W/m ³]	Power density
U	[J]	Elastic potential energy
U	[m/s]	Relative velocity of fluid in Reynolds number
U	[-]	Speed parameter associated to film thickness
R	[K/W]	Thermal resistance
R_c	[K/W]	Thermal resistance of contact associated to flash temperature rise
R_f	[K/W]	Thermal resistance of fluid film
R_{fo}	[K/W]	Thermal resistance of fling-off
R_h	[K/W]	Thermal resistance of convection
R_p	[K/W]	Thermal resistance of contact associated to part assembly
R_r	[K/W]	Radial thermal resistance
R_{rd}	[K/W]	Thermal resistance of radiation
R_s	[K/W]	Thermal resistance of constriction
R_z	[K/W]	Planar wall (axial) thermal resistance
R_a	[m]	Average surface roughness
R_q	[m]	Root mean square surface roughness
R_z	[m]	Average roughness depth
S	[-]	Slip ratio
S_m	[m ²]	Immersed surface area of gear
S_r	[m ²]	Heat conduction surface in the radial direction
S_z	[m ²]	Heat conduction surface in the axial direction
SRR	[-]	Slide-to-roll ratio
T	[Nm]	Torque
TE	[m]	Transmission error
T_{drag}	[N·m]	Oil drag torque loss in bearings
T_{rr}	[N·m]	Rolling torque loss in bearings
T_{seal}	[N·m]	Sealing torque loss in bearings

Sign	Unit	Description
T_{sl}	[N·m]	Sliding torque loss in bearings
T_V	[N·m]	Total gearbox torque loss
T_{VD}	[N·m]	No-load sealing torque loss
T_{VL}	[N·m]	Total bearing torque loss
T_{VLO}	[N·m]	No-load bearing torque loss
T_{VLP}	[N·m]	Load-dependent bearing torque loss
T_{VX}	[N·m]	No-load auxiliary torque loss
T_{VZO}	[N·m]	No-load torque loss associated to gears
T_{VZP}	[N·m]	Load-dependent gear mesh torque loss
V	[m ³]	Volume
V_a	[m/s]	Axial meshing velocity
V_e	[m/s]	Oil entrainment velocity in the contact
V_m	[m/s]	Mean velocity of oil flowing down the walls of the casing
V_r	[m/s]	Sum of rolling velocities in the contact
V_s	[m/s]	Sliding velocity in the contact
V_t	[m/s]	Tangential velocity at pitch circle
V_a	[m ³]	Casing interior air volume
V_o	[m ³]	Oil sump volume
W	[N]	Total normal load
W	[-]	Load parameter associated to film thickness
X_L	[-]	Lubricant factor associated to friction coefficient
g	[m/s ²]	Acceleration of gravity
Fr	[-]	Froude number
Nu	[-]	Nusselt number
Pr	[-]	Prandtl number
Ra	[-]	Reyleigh number
Re	[-]	Reynolds number
Re_c	[-]	Critical Reynolds number
A	[-]	Theoretical start of meshing
B	[-]	Theoretical start of single tooth contact region on driving gear
C	[-]	Pitch point
D	[-]	Theoretical end of single tooth contact region on driving gear
E	[-]	Theoretical end of meshing
Y	[-]	Any point on base tangent plane
α	[Pa ⁻¹]	Pressure viscosity coefficient
α_i	[-]	Heat partitioning coefficient
α_n	[rad]	Normal pressure angle
α_y	[rad]	Pressure angle at Y-circle radius
α_t	[rad]	Transverse pressure angle
α_{wt}	[rad]	Transverse working pressure angle
α_{Fy}	[rad]	Local attack angle
α_L	[K ⁻¹]	Coefficient of linear thermal expansion
β	[rad]	Helix angle
β	[K ⁻¹]	Coefficient of volume expansion for fluids
β_b	[rad]	Base helix angle
γ	[s ⁻¹]	Shear rate
δ	[m]	Deflection under load
ϵ_α	[-]	Transverse contact ratio

Sign	Unit	Description
ϵ_a	[-]	Approach contact ratio
ϵ_f	[-]	Recess contact ratio
ϵ	[-]	Surface emissivity associated to radiation
ϵ	[m]	Total flank normal deviation
η	[Pa·s]	Dynamic viscosity
η_0	[Pa·s]	Dynamic viscosity at ambient pressure
θ	[°]	Absolute rotation angle in encoders
θ	[°]	Available angle for fling-off
θ	[rad]	Half the chord angle defined by oil level
κ	[-]	Ellipticity ratio
λ	[-]	Specific film thickness
μ	[-]	Friction coefficient
μ_s	[-]	Sliding friction coefficient
μ_r	[-]	Rolling friction coefficient
ν	[-]	Poisson's ratio
ν_k	[m ² /s]	Kinematic viscosity
ξ	[-]	Asperity-load sharing factor
ξ	[-]	Oil fraction in air
ξ_y	[K]	Roll angle at Y-cylinder
ρ	[m]	Curvature radius if referred to geometry
ρ	[kg/m ³]	Density if referred to material
ρ_a	[kg/m ³]	Air density
ρ_o	[kg/m ³]	Oil density
σ_F	[Pa]	Tooth root bending stress
σ_H	[Pa]	Contact stress
σ_{rr}	[Pa]	Radial stress
$\sigma_{\phi\phi}$	[Pa]	Circumferential stress
τ	[rad]	Angular pitch
τ_E	[Pa]	Eyring stress
τ_L	[Pa]	Limiting stress
ϕ_j	[rad]	Backlash angle
$\phi_{1,2}$	[rad]	Relative angular position of gear teeth
χ	[m ² /s]	Thermal diffusivity
ψ	[rad]	Inclination angle
$\psi_{1,2,\dots}$	[-]	Regression coefficients
ω	[rad/s]	Angular velocity
Θ	[K]	Temperature
Θ_b	[K]	Gear bulk temperature
Θ_a	[K]	Air temperature
Θ_c	[K]	Contact temperature
Θ_f	[K]	Oil film temperature in the contact
Θ_o	[K]	Oil temperature
Θ_{sh}	[K]	Shaft temperature
Θ_y	[K]	Y-cylinder temperature
Λ	[-]	Limiting stress pressure coefficient
Φ_T	[-]	Film thickness reduction factor for shear heating

Subscript	Description
i, j	Grid points. Counters in loops.
i, o	Inner and outer respectively when referred to diameters
f, s	Fluid and solid respectively when referred to friction coefficient
n, t	Normal and transverse directions respectively
o, a	Oil and air when referred to fluid thermophysical properties
r, s	Rolling and sliding respectively when referred to kinematics
r, ϕ , z	Cylindrical principal directions
x, y, z	Cartesian principal direction
y	Indicates Y-cylinder, associated to gear dimensions
H	Indicates Hertzian parameter
I,II	Engagement and exit sides in gear teeth face width
P0	For quantities associated to basick rack
1,2	Pinion and gear respectively
Acronym	Description
AGMA	American Gear Manufacturers Association
ANSI	American National Standards Institute
API	American Petroleum Institute
BL	Boundary lubrication (regime)
CFD	Computational Fluid Dynamics
CMM	Coordinate Measuring Machine
COF	Coefficient Of Friction
DIN	<i>Deutsches Institut für Normung</i> , German Institute for Standardization
DRIVE	Driving Research and Innovation for Vehicle efficiency and Energy sustainability
EAP	End of Active Profile
EHL	Elasto-Hydrodynamic Lubrication
FEM	Finite Element Method
FFT	Fast Fourier Transform
FVA	<i>Forschungsvereinigung Antriebstechnik</i> , Drive Technology Research Association
FZG	<i>Forschungsstelle für Zahnräder und Getriebebau</i> , Gear Research Centre
HEV	Hybrid-Electric Vehicle
ISO	International Organization for Standardization
KS	<i>Kraftstufe</i> , Load stage
ML	Mixed lubrication (regime)
LCP	Linear Complementarity Problem
LOA	Line Of Action
LTCA	Loaded Tooth Contact Analysis
NVH	Noise, Vibration and Harshness
ODE	Ordinary Differential Equations
PAO	Polyalphaolefin (oil)
PID	Proportional-Integral-Derivative (controller)
PLC	Programmable logic controller
PLV	Pitch Line Velocity
PVC	Pressure-Viscosity Coefficient
SAP	Start of Active Profile
TEHL	Thermo-Elasto-Hydrodynamic Lubrication
TVC	Temperature-Viscosity Coefficient
VG	Viscosity Grade
VPT	Vicosity-Pressure-Temperature

*A good traveler has no fixed plans
and is not intent upon arriving.
A good artist lets his intuition
lead him wherever it wants.
A good scientist has freed himself of concepts
and keeps his mind open to what is.*

—Lao Tzu's *Tao Te Ching*, poem 27, 4th century BC

1

Introduction

Contents

1.1	Background	2
1.2	Motivation	3
1.2.1	Thermal rating of gear drives	4
1.2.2	Thermal distortion of gear teeth	5
1.3	Hypothesis and research objectives	7
1.4	Dissertation outline	8

This chapter describes the framework of the present PhD thesis, briefly depicts thermal distortion effects in gear teeth and finally defines the fundamental hypothesis and objectives that have led the development of this research work. Background and motivation are described first. It will be shown that current environmental concerns are pushing the electrification of automotive and aeronautical vehicles where gearboxes are forced to work at high speed due to power density requirements. In such conditions, thermal issues are dominant and, as a consequence, machine element failure probability increases and thermal expansion becomes noticeable. Then, thermal distortion of gear teeth is briefly described, geometry expansion effects are identified and the main consequences are highlighted based on field experience from turbomachinery industry. It will be shown that scientific literature review has long pointed towards this direction but little analytical or numerical effort has been carried out on the topic. Finally, based on the research opportunities identified in the literature review, which is developed in the next chapter, an hypothesis is established, work objectives are defined and the outline of this dissertation is described.

1.1 Background

In the past decade, environmental concerns have driven most of the research effort in gear transmissions towards energy economy and fuel saving. The maximization of overall efficiency and the increase of power density have received a considerable amount of attention lately, and the number of research publications on the topic is a good indicator of such interest. In particular, automotive transmissions, promoted by the development of the electric vehicle (EV), search for a reduction in component size and mass along with lubricating oil volume; where dip lubricated gearboxes are designed with low oil levels to minimize churning power losses and increase power-to-weight ratios [1].

Moreover, the enhancement of power density is followed by an increase in rotational speed. According to the U.S. Department of Energy's Vehicle Technologies Office, electric and hybrid vehicle's traction motor speeds progressed from 6000 rpm in 2004 to 17000 rpm in 2017 [2]. Figure 1.1 shows this trend where the power density and speed targets for 2020 and 2025 are highlighted. As it can be seen, some EV models in the market have gone beyond the power density requirements for 2020 and others are very close to the speed limits for 2025. Actually, the 2017 roadmap from the U.S. Driving Research and Innovation for Vehicle efficiency and Energy sustainability office (DRIVE) expects 90% of volume reduction for 2025 which would translate into a 50 kW/l power density requirement at the expected 20000 rpm output speed [3].

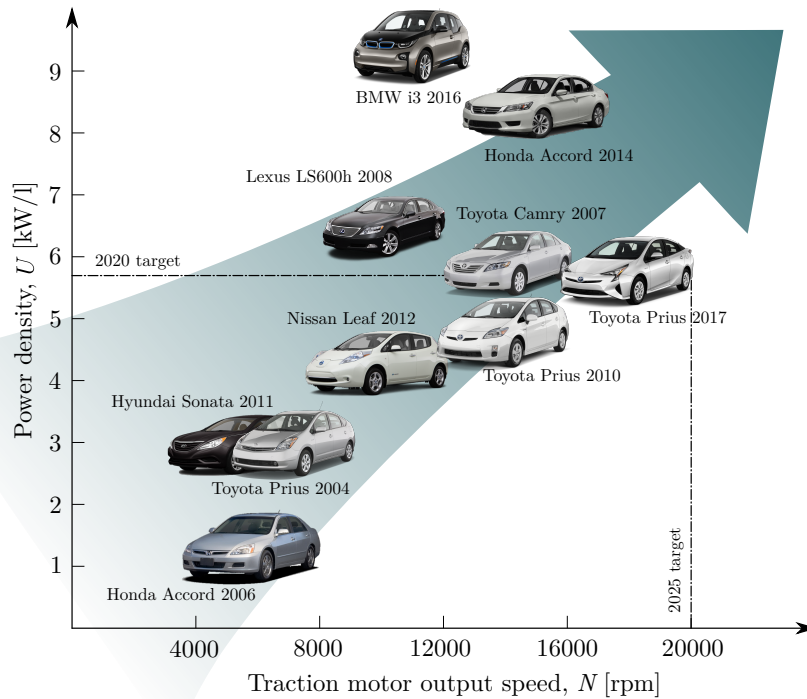


Figure 1.1: Trend in electric and hybrid-electric vehicle traction motor speeds and power densities

In order to accommodate electric traction motor speed to on-road car velocity, single-speed gearboxes are usually designed with high gear ratios and just one or two stages [4]. Some of the newest powertrain prototypes have been conceived to be driven by permanent magnet synchronous machines with output speeds close to 30000 rpm [5]; and new research projects are on the way in the German Research Association for Drive Technology (FVA) to even higher speeds, up to 50000 rpm [6]. According to Ayers [7], at such conditions thermo-mechanical problems are expected, not only in the electric traction motor but also in the gear transmission system, as bearings and gears are close to their thermal limits. At this point, automotive industry seems to meet requirements from aeronautical industry, and hence it may adopt its issues.

1.2 Motivation

In general, two different kinds of technical difficulties are inherent in a high speed gear unit. The first difficulty is a matter of a high rotational speed which may be found in the aerospace and aeronautical fields. The second difficulty is a matter of a high tangential velocity which is typical in the oil and gas industry.

High Pitch Line Velocities (PLV) may be found in transmissions located at the output of multi-megawatt turbo-machineries, like compressors and steam or gas turbines, where a high reduction ratio is needed to accommodate power. The gear units for these machineries become large in their size and consequently, the peripheral velocities of both the gear and the journal bearings become high to the extent that special mechanical and thermal considerations are necessary [8].

In high rotational speed gearboxes from the aeronautical industry (and soon expected in the automotive as well), the required power to be transmitted by the gears is rather small which allows the gears to be smaller and consequently not so high in pitch-line velocities. However, tangential speeds up to 120 m/s may be reached [9] which means that the number of tooth engagements per second is high and therefore the generated heat can be significant. Taking into account the smaller size of such gears, not only their mass is significantly reduced but their external surface too, which results in high bulk temperatures due to poor convective heat transfer. Furthermore, considering that these gears are often light-weighted, their thermal capacity is low and therefore, temperature increases rapidly which may produce thermal stresses.

In both cases, the most important and usually the first calculations that are performed account for mechanical loads such as bending and contact stresses. This may be done using standards developed by AGMA [10] or ISO [11], using the finite element method or a combination of analytical methods and experimental validation. However, if thermo-mechanical behaviour of the gears needs to be considered as well, no information is available through the open literature and the gear designer is faced with trying to improve the operational behaviour as the prototype system is under development; by continuously checking tooth contact patterns under load and applying modifications as recommended by current standards [12], or turning to manufacturer's field experience if available [13].

The thermal behaviour of a system is known to turn a successful gear set from the bending and contact stress point of view into a sudden failure from the resultant thermal operational characteristics [14]: tempering of case carburized material, gear tooth scoring, uneven load distribution, etc. Therefore, it is necessary to understand heat generation, temperature distribution and related tribological/mechanical consequences in gears to minimize risk of failure in these applications.

1.2.1 Thermal rating of gear drives

Heat generation in high speed gear sets can be broken down into the contributions of friction between the teeth (sliding and rolling friction), lubrication losses (oil churning or jet lubrication), the trapping and pumping of the air-lubricant mixture during the meshing and the losses associated to air windage. If power losses in the gearbox system are considered, then additional sources may appear such as those coming from bearings, sealings and shaft driven accessories. A sample breakdown of how energy is dissipated in high speed gears is found in Figure 1.2.

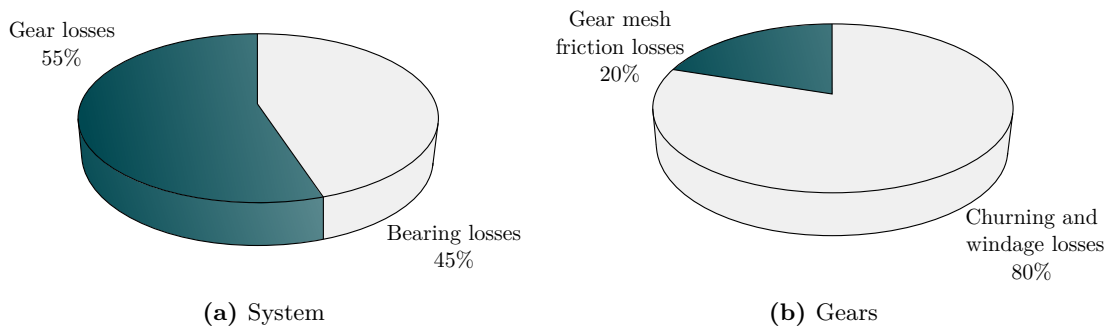


Figure 1.2: High speed gearbox power loss breakdown according to ANSI/AGMA 6011 [12]

In order to reach the thermal balance of the gearbox avoiding excessive temperature increase, the total heat generated by each of the power loss sources needs to be dissipated through the casing, the lubrication system or the cooling system. Current practice in calculating thermal rating is based on finding the maximum power that a unit can carry for 3 hours without the sump temperature exceeding 95°C when the ambient air temperature is not over 25°C [15, 16]. The prime variables in determining thermal capacity are the gearbox size, the input pinion speed and the gear ratio. According to Dudley [14] if a gear unit is built twice as large, the mechanical rating increases almost 8 to 1 and the thermal rating increases only about 3 to 1. This predicts that large gear units will be short of thermal capacity. The same happens when speed level is considered; literature review in Chapter 2 will show that temperature increases with speed and therefore, high speed gear units need further thermal analysis than common transmissions.

Gearbox life rating is closely related to operating temperatures and therefore it is important to predict and control its thermal behaviour. According to Höhn and Michaelis [17] typical gear failures like wear, scuffing, micropitting and pitting are influenced by oil sump and teeth temperature, as high contact temperatures lead to low viscosities and thus thin lubricant films increasing failure probability. Figure 1.3 shows some of the visible consequences of high temperatures on gear teeth.

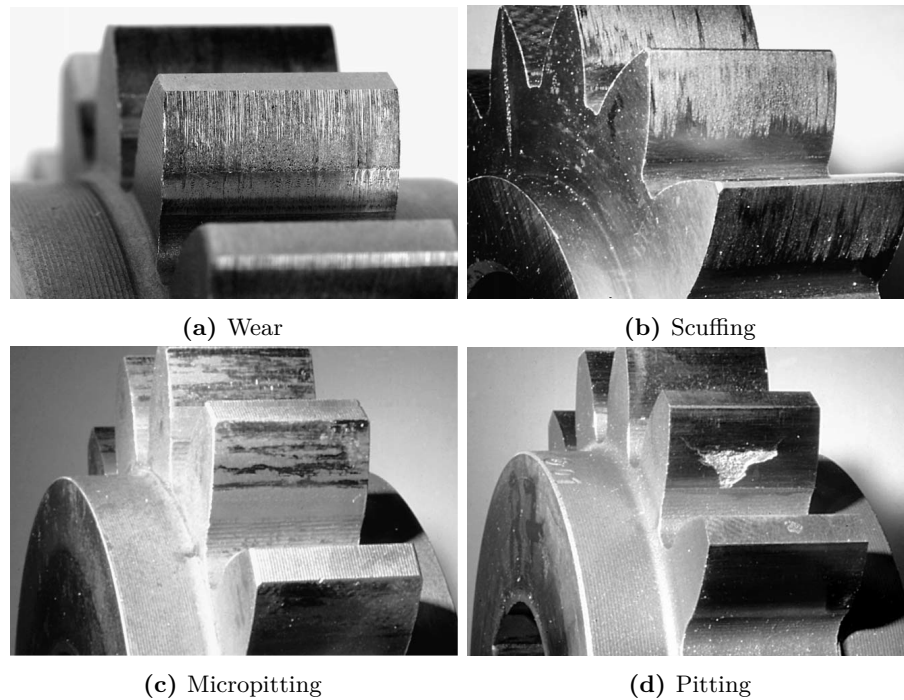


Figure 1.3: Gear failures related to high temperatures [17]

Moreover, an excessive local temperature increase may also give rise to metallurgical changes [14] because case carburized gear teeth are overheated enough to soften; leading to gear failure as a consequence. And finally, temperature increase is always followed by thermal expansion, and if the order of magnitude of the latter is large enough, tooth contact behaviour is altered and teeth fail as the result of uneven load distribution [18].

1.2.2 Thermal distortion of gear teeth

In turbo-machinery industry it is well known that in high speed helical gear drives of relatively large face width, the temperature of the teeth rises non-uniformly across the face width at pitch line velocities of about 100 m/s [19]. Temperature gradients are originated from the axial pumping of the oil-air mixture, which travels from the engagement side to the exit side where the fluid is expelled between the teeth. The maximum temperature is located approximately at 2/3 of the face width [20]. As a result of the non-uniform temperature distribution, non-uniform thermal distortion occurs; which is experimentally observed inspecting tooth contact pattern records like the one presented in Figure 1.4.

At higher pitch line velocities, from 120 m/s onward, depending on the face width to diameter ratio, it is no longer possible to achieve a uniform load bearing diagram [21]. Furthermore, in such conditions thermal deformation is much higher in magnitude than mechanical deflections and it is practically impossible to obtain uniform temperature distributions [22]. Welch and Boron [18] described this phenomena as “regenerative thermal instability”: a local increase in tooth load increases the heat generated in the mesh in this section, thus raising the temperature, increasing the expansion and hence the load and the heat generated. Meanwhile, unit loads in other areas are being slightly decreased and, as a consequence, these other areas are slightly contracting. This process can be thermally unstable (or regenerative), until tooth failure occurs (see Figure 1.5).

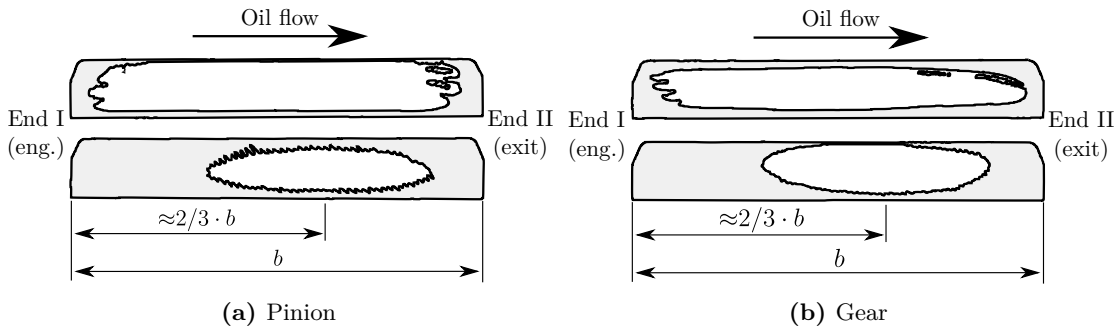


Figure 1.4: Contact pattern shift due to thermal distortion in turbo-gears (adapted from [21])

Taking into account that the current trends in automotive and aeronautical industries search for higher speeds, similar thermal phenomena can be expected even when the face width to diameter ratio is not as large as in the oil and gas industry. The increase in the number of engagements per second and in the transmitted power results in high power losses while, at the same time, the reduction in volume and mass leads to a reduction in heat transfer capacity. Such an increase in power-to-weight ratio will modify thermal balance and as a consequence a higher steady-state temperature will be reached. Under these conditions, thermal distortion could be significant.

Moreover, in these applications, significant temperature gradients are found between pinion and gear. The reduction of the oil level to minimize churning losses increases temperature difference between the driver and driven wheels, reaching 20°C to 30°C as shown by Höhn et al. [23], because the small size of the pinion results in a lower convection heat transfer due to the reduced oil-lubricated area. Such temperature difference leads to relative pitch deviations [24] that affect load distribution in a similar manner to manufacturing deviations [25].

Furthermore, temperature increase not only affects transverse pitch; Henriot [26] showed that pinion and gear teeth profile and lead are also influenced by temperature differences. Involute geometry is distorted by a radial thermal expansion that increases the base pitch while decreasing the pressure and helix angles at the same time, the order of magnitude being close to that of profile modifications [26]. Besides, radial expansion of both, pinion and gear, reduces backlash and mesh jamming may occur if insufficient allowance is provided. Thus, relative pitch deviations, backlash reduction and profile and helix angle errors coexist and may compensate each other or cause an even higher mismatch between meshing wheels than individual deviations. If thermally-induced geometry distortions are not compensated for, they may cause overloads in the tooth flanks, increasing contact and root bending stresses that endanger gear operation as shown by Welch and Boron [18] (see Figure 1.5).

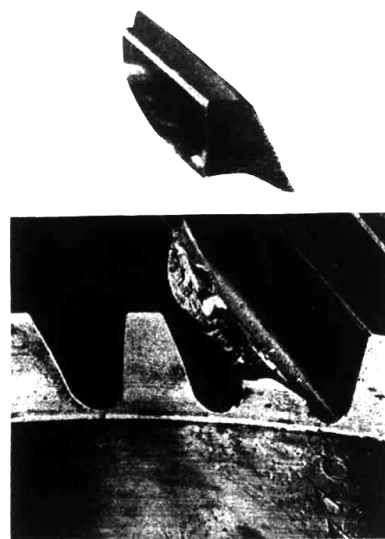


Figure 1.5: Tooth bending failure due to thermal instability [18]

Profile and lead deviations between pinion and gear under load can be corrected properly applying tooth modifications in the design stage, provided that manufacturing deviation tolerances are known and mechanical deflections have been calculated. However, thermal distortion in gears is not currently predictable and experimental measurements (i.e. fully loaded contact pattern checks) are required to define tooth modifications [8]. Moreover, AGMA 927-A01 standard [27] for load distribution calculation recognizes the existence and negative influence of thermal deformations but it does not provide a method to calculate and compensate them. With this background, it seems necessary to fully understand heat generation and heat transfer mechanisms in gears and to develop tools to predict operating temperatures and thermal distortions.

1.3 Hypothesis and research objectives

In view of the research opportunities presented in the critical review of the state of art in Chapter 2, the following research hypothesis is formulated:

Hypothesis

“Thermal gradients in cylindrical gear sets distort involute flanks in the same order of magnitude of manufacturing deviations, thus causing a load distribution mismatch that can be predicted and compensated by means of analytical methods.”

Therefore, in order to verify this hypothesis, the main objective of the present PhD thesis is to **predict, evaluate and correct uneven mechanical behaviour of spur and helical gears due to thermally-induced flank geometry distortion**, specially oriented to high speed/high power external cylindrical gears. To this aim, the following secondary objectives are defined:

- **O.1:** To analytically compute gear mesh kinematics, load distribution and transmission error of cylindrical gear pairs with tooth modifications, subject to variable torques and speeds.
- **O.2:** To predict heat flux and heat partition in the gear mesh as a function of instantaneous load, sliding speed and friction coefficient along the line of action.
- **O.3:** To develop a comprehensive thermal model to predict temperature distribution of cylindrical gear pairs as a function of geometry, running conditions and lubrication method.
- **O.4:** To analytically predict the amount of tooth flank normal deviation due to thermally induced geometry distortion and quantify the fluctuation of load distribution and transmission error with respect to ambient temperature.
- **O.5:** To set design guidelines, rules or strategies to deal with uneven load distribution due to combined elastic deflections and thermal distortion by defining the type and amount of profile and/or flank line modifications.
- **O.6:** To design, manufacture and assemble a back-to-back gear test rig and experimentally observe thermal distortion effects on mesh behaviour.

1.4 Dissertation outline

The following dissertation is divided in eight chapters and four appendices organised in a continuous manner as shown in Figure 1.6.

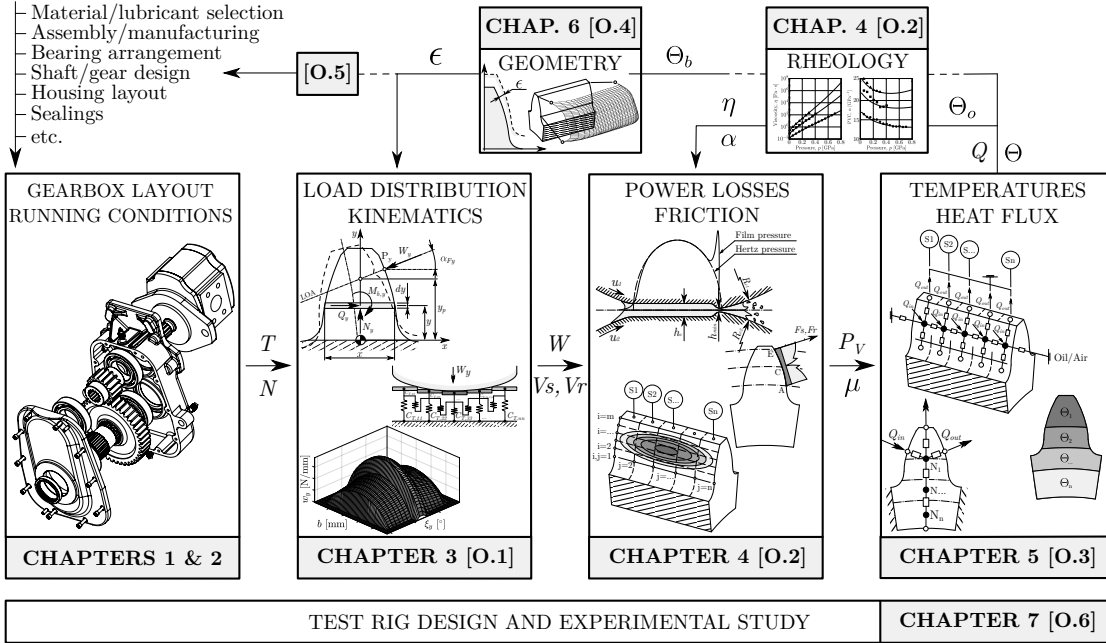


Figure 1.6: Research methodology

Chapter 1 introduces the background and motivation of this thesis, supported by up-to-date data on automotive gear transmissions and its relation with power density, high speeds and thermal issues. Then, a brief description of the thermally induced geometry distortion is provided which is followed by the definition of the research hypothesis and the formulation of the main objectives of this thesis.

Chapter 2 presents the literature review on the topic which has been separated from the introductory chapter for clarity. The main analytical, numerical and experimental research works on heat generation, temperature distribution and thermal distortion of gears are described here. A critical review of the state of the art is presented and research opportunities are identified at the end of this chapter.

Chapter 3 meets the demands of objective O.1 in Section 1.3. The main concepts, procedures and equations to compute gear geometry, kinematic behaviour and load distribution of external cylindrical gears are presented. The parameters directly related to thermal distortion are highlighted and the solution method is described in detail. Finally, a finite element validation of the model is carried out.

Chapter 4 responds to objective O.2 in Section 1.3. First, the computation of power losses and heat partitioning coefficient is presented. It will be shown that sliding friction coefficient plays a decisive role in the precise calculation of the heat flux from the gear mesh. Then, a new friction coefficient model and power loss prediction methodology are introduced and both are validated with experimental measurements from literature.

Chapter 5 addresses objective O.3 in Section 1.3. A novel thermal network model is developed for dip lubricated gear pairs that produces radial and longitudinal temperature distributions for thermal distortion modelling in the next chapter. Different heat sources are analysed, heat transfer mechanisms are discussed and the solution method for steady-state and transient regimes are introduced in this chapter. Finally, thermal lumped parameter predictions are compared to experimental results from literature.

Chapter 6 focuses on objectives O.4 and O.5 in Section 1.3. Thermally induced geometry distortion is predicted analytically for the first time and the latter is compared to manufacturing deviations. The influence of gear size, temperature increase or gradient type is discussed among other parameters and the effect on load distribution and transmission error is evaluated. Then, a case study from the automotive sector is fully analysed and the effect of thermal distortion on tooth contact behaviour is discussed. It is shown that, contrary to common belief, thermal expansion does affect mesh behaviour in medium-size cylindrical steel gears. At the end of the chapter, design guidelines are compiled as required by objective O.5.

Chapter 7 meets the demands of objective O.6 in Section 1.3. First, the developed back-to-back gear test rig is described and then, test methodology is presented. Thermo-mechanical transmission error behaviour of two gear sets is measured and results are compiled in terms of available normal backlash, transmission error mean level and peak to peak values, all of which are presented as a function of torque and temperature. At the end of the chapter, experimental results are discussed and some of the analytical predictions made in the previous chapter are validated. To the author's knowledge, none of the experimental results presented in this chapter (or similar ones), have been previously published in scientific literature.

Chapter 8 summarizes the major conclusions of the thesis classified per objective, fundamental contributions are highlighted and future research areas are defined. Finally, scientific contributions made during the PhD thesis period are also gathered.

Appendices present additional resources to understand the document, such as the analytical - finite element comparison of thermal distortions, Hertz theory for elliptical contacts, transmission error computation algorithm for absolute encoders and inspection data of the experimental gear sets.

Finally, to enhance readability of the document and with the purpose of ensuring the continuity of the different calculations, FZG gear type C-PT geometry [28] and its derivatives [29] are used as reference gears in all chapters and new ones are introduced in some of them to analyse specific mechanical/thermal behaviour. Similarly, standard FZG gearbox dimensions are used unless otherwise stated [30], reference lubricant is FVA-3 mineral oil [31] and operating conditions are defined by DIN 51354 standard [32].

*Two roads diverged in a wood, and I —
I took the one less traveled by,
And that has made all the difference.*

—Robert Lee Frost’s *The Road Not Taken*, 1916

2

Literature Review

Contents

2.1 Heat generation and transfer in gears	12
2.1.1 Heat generation	12
2.1.2 Heat dissipation	21
2.2 Temperature distribution in cylindrical gears	26
2.2.1 Experimental observations	26
2.2.2 Analytical and numerical studies	32
2.3 Thermally induced teeth geometry distortion	34
2.3.1 Compensation of thermal distortion	43
2.4 Critical review of the state of the art	45

This chapter presents the current state of the art relative to the thermal distortion phenomena in external cylindrical gears and in geared transmissions in general. The purpose of this literature review is identifying research opportunities on the aforementioned topic, such that a general thesis objective can be defined and the underlying hypothesis can be formulated. First of all, heat generation process and relevant heat transfer mechanisms are presented. The former is classified as a function of the load dependency of the heat source and the latter is grouped into radial and axial heat transfer processes. Then, overall temperature distribution in gears is presented. The key parameters in the development of the steady-state temperature field are described and the main research works on the prediction of bulk temperature of cylindrical gears are identified. In this section, special attention is paid to the mechanisms that allow for noticeable temperature gradients. Subsequently, the thermally-induced geometry distortion phenomena is described in detail. Different types of distortion are presented and compensation techniques to provide uniform bearing patterns are reviewed. Finally, conclusions are inferred and a critical review is developed in order to identify research opportunities on this field of study.

2.1 Heat generation and transfer in gears

2.1.1 Heat generation

Power losses lie at the origin of the heat flux to the pinion and gear, and therefore, they are responsible for the resulting temperature distribution. Sources of power losses in a gear drive are usually classified into two groups: i) load-dependent mechanical power losses due to friction in loaded contacts of bearings and gears and ii) load-independent losses (also known as “spin losses”) caused by viscous friction coming from oil churning and windage. The latter results from oil-air mixture drag on the face and sides of such machine elements, as well as pocketing/squeezing of lubricant in the in the surroundings of the contact zone. Niemann and Winter [33] computed total power loss as the sum of the individual contributions of gear, bearings, sealings and shaft driven accessories as shown in Figure 2.1. It can be observed that while load-dependent and spin power losses are comparable in magnitude under low speed conditions (below 7 m/s), spin losses clearly dominate at the highest operating speeds.

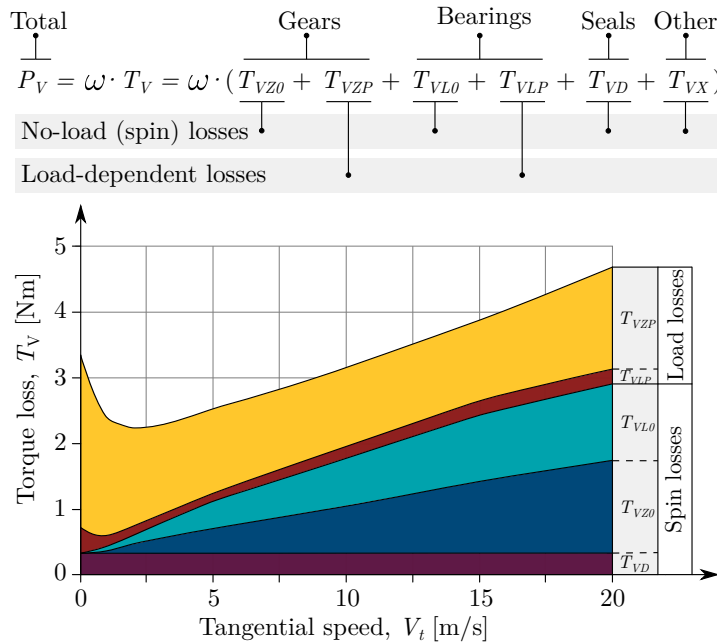


Figure 2.1: Sample torque loss breakdown from FZG gear test rig (adapted from [29])

Gear teeth steady-state temperature is mainly influenced by mesh-related losses, as well as heat coming from oil churning and windage; while the temperature of the supporting shaft and the gear hub is also affected by the heat coming from bearings and sealings.

Load dependent power losses

Power losses in the gear mesh, P_{VZP} , are the result of sliding and rolling friction forces and velocities. The difference in instantaneous rolling velocities, u_1 and u_2 , of the contact points of the pinion and the gear respectively, generates sliding of the mating surfaces. The product of the relative velocity, V_s , and the sliding friction force, F_s , created by the transmitted normal load, W , results in power loss along the entire length of

contact. Besides, the elastic deformation of the mating surfaces in the contact point and the drag force generated by the continuously squeezing lubricant film creates an additional source of power loss known as rolling force, F_r . Thus, the instantaneous power loss in any point $Y(x, z)$ on the base tangent plane can be expressed as the sum of a sliding and a rolling term [34]:

$$P_{VZP}(x, z) = P_{VZP,s} + P_{VZP,r} = [F_s \cdot V_s] + [F_r \cdot V_r] \quad (2.1)$$

where $V_s(x, z) = |u_1 - u_2|$ is the instantaneous sliding velocity and $V_r(x, z) = |u_1 + u_2|$ is the sum of rolling velocities at any point of the path of contact.

On the other hand, sliding friction force, F_s , is the product of normal load, W , and sliding friction coefficient, μ , while the rolling friction force, F_r , is proportional to the elastic deformation of the bodies and the lubricant film thickness between them [35]. Considering these relationships Equation 2.1 can be re-written as follows:

$$P_{VZP}(x, z) = [\mu \cdot W \cdot |u_1 - u_2|] + [F_r \cdot |u_1 + u_2|] \quad (2.2)$$

From the previous equation it is deduced that the accurate prediction of load-dependent power losses in a gear pair, and thus the prediction of generated heat, depends on the friction coefficient model, the instantaneous load, surface velocities and the equations for the rolling friction force. In Chapter 3 it is shown that kinematic behaviour and load distribution can be predicted from gear geometry and operating conditions. However, there is a significant scatter in predicted friction coefficients [36] as different lubrication regimes can be encountered in the gear mesh (see Figure 2.2) and there is no general method available that copes with the large range of operating conditions and gear geometries found in gear transmissions. As a consequence, large deviations can be found in the predicted heat flux leading to unreal temperature distributions. Therefore, sliding and rolling friction coefficient models are reviewed next.

a) Sliding friction coefficient The contact between gear teeth is non-conformal and it is characterized by a small area, significant body deformation and a high contact pressure. Besides, there is a thin lubricant film between the mating surfaces which gives rise to different situations depending on the degree of interaction between surface asperities: i) boundary lubrication (BL), ii) mixed lubrication (ML) or iii) elastohydrodynamic lubrication (EHL). Figure 2.2 depicts these regimes on a Stribeck curve for a line contact subject to typical gear operating conditions where the shaded region indicates the range of variation of loads (0.5 GPa to 2.5 GPa) and bulk temperatures (60°C to 140°C) for a given lubricant and surface roughness. As it can be seen, depending on the operating conditions, friction coefficient doubles or triples its value, and so does the generated heat. Considering that gear teeth are subject to variable loads, temperatures and speeds along the line of action, the friction coefficient changes proportionally and may even shift from full to partial EHL regime. The prediction of such complex behaviour has received a large amount of attention in the last decades.

Literature review stands out three main approaches of increasing complexity to predict friction coefficient and power losses in gears: i) experimental methods based on power loss factors, H_v , ii) empirical equations from twin disc measurements and iii) physics-based models. The first group of models (see [38–40] for classical models or more recently [41, 42]) are based on Ohlendorf’s approach [43] who proposed the power loss equation $P_{VZP} = P_A \cdot \bar{\mu} \cdot H_v$ for standard spur gears depending exclusively on gear geometry, H_v , the mean coefficient of friction, $\bar{\mu}$, and the input power, P_A . Experimentally measured power loss from FZG tests is used to calculate the mean coefficient of friction for different oils,

gear geometries, surface roughness and operating conditions. Then, the friction coefficient model is developed from regression analysis. However, the power loss factor, H_v , was not originally developed to account for the influence of helix angle, high contact ratio or tooth modifications. In addition, Wimmer [36] found that these models largely simplify load sharing between teeth and substantial deviations were predicted when mesh stiffness was considered. Although several corrections are proposed for these variables, and similar power loss factor models have been developed to prevent these shortcomings [44, 45], the accuracy of the majority of these friction coefficient models is still limited to simple gear geometries and specific operating conditions. Furthermore, power loss predictions following Ohlendorf’s approach neglect the variation of lubrication regime in the path of contact which may lead to significant errors when gears operate at high speeds and torques.

The second group of models (see [46–48] or more recently [49–51]) are based on regression analysis of tribometer measurements (e.g twin disc or ball on disc machines). Such tests allow to easily control the curvature radius, the contact width, disc/ball materials, lubricant type, oil jet temperature and slide to roll ratio. Therefore, friction behaviour is directly characterized under real contact pressures, velocities and temperatures [52]. When these models are used in the prediction of power losses in gears, the contact path must be discretized to compute instantaneous kinematic and load parameters which serve as inputs for the empirical friction models. The method accounts for the variation of friction coefficient along the line of action but some authors [50, 53, 54], point out that these models cannot be directly applied to gears due to differences in surface topography and roughness, large values of friction coefficient at the low slide-to-roll ratios found near the pitch point and varying lubrication regimes along the line of action. Although these authors have proposed different solutions to cope with these issues, all empirical models are developed for specific lubricants and therefore they cannot be directly used to predict friction with a different oil without loss of accuracy.

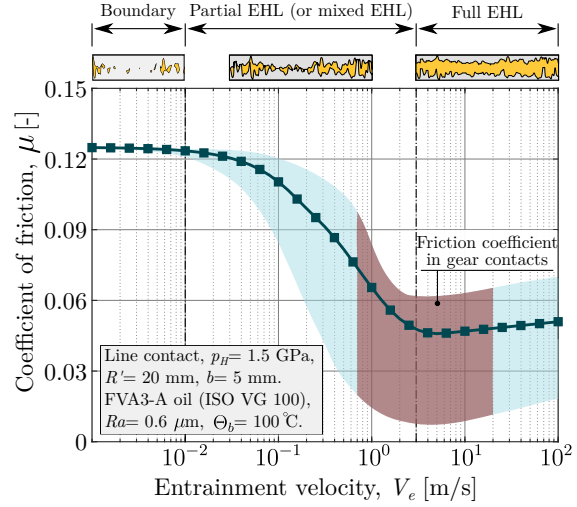


Figure 2.2: Simulated Stribeck curve for an equivalent gear contact subject to common operating conditions (calculated following ref. [37])

Finally, the third group of models is based on a pure tribological-rheological approach. Partial or full EHL friction coefficients are computed numerically following different techniques; provided that contact geometry, normal load and rolling velocities are known. The pioneering works by Oh [55], Okamura [56], Goglia [57] and Lubrecht [58], set the foundations of different approaches to the solution of the elastohydrodynamic contact problem: the differential deflection method [56], the iterative Newton-Raphson procedure applied to finite difference scheme [57], the finite element method [55] and the multigrid technique [58] are some of the most common in scientific literature.

In general, these methods discretize thoroughly the contact region (assumed paraboloid) and the lubricant film thickness and pressure distributions are computed by solving the Reynold's equation together with the energy, elasticity and force balance equations across the contact and taking into account the dependence of lubricant viscosity on temperature and pressure. Then, sliding traction is typically computed from Eyring or limiting shear stress models [59] and finally, instantaneous power losses are predicted. Figure 2.3 depicts pressure and film thickness distributions for two different oils computed following the differential deflection method. Although the pressure distribution at high load is approximately equal to the Hertz solution in both cases, the film thickness shape is very different as it depends on lubricant rheology. Therefore, sliding traction, and hence power loss, for each oil will be different as well. The third group of models can be applied either to smooth or rough surfaces with very accurate results and, since both the pressure distribution and the film thickness shape are known, rolling traction can also be computed as shown later in this section.

Recently, [34, 60, 61] have applied these numerical methods to the prediction of friction coefficient in cylindrical gear contacts. Although the results are accurate over a wide range of operating conditions, lubricants and lubrication regimes, the required computational time to compute the full length of the path of contact is high, even when efficient algorithms such as the multigrid method [60] are used. To solve this problem Xu et al. [34], and later Li and Kahraman [62], developed simple full and partial EHL friction coefficient models from the linear regression of thousands of numerical EHL simulations covering typical gear contact parameter ranges (i.e. pressure, temperature, slide-to-roll ratio, roughness, etc.). However, once again, both friction coefficient models were developed for specific lubricants and therefore they cannot be extended to other oils.

Table 2.1 summarizes some of the most common friction coefficient models in gear literature each of them representing a group of models respectively. As it can be observed, these friction coefficients rely on five sets of parameters representing contact conditions: i) geometry (b, ρ, R'), ii) kinematics (V_s, V_r, SRR), iii) load (w, F_{bt}, p_H), iv) lubricant (η_0, X_L) and v) surface roughness (Rq, Ra).

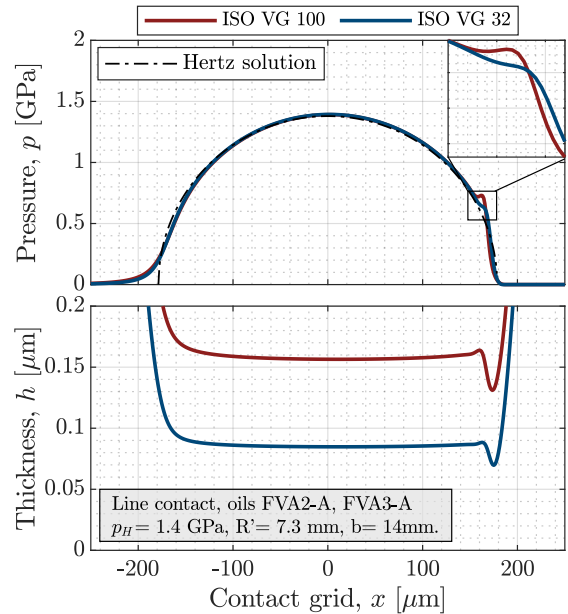


Figure 2.3: Simulated EHL pressure and film thickness distributions in a smooth contact computed following the differential deflection method

Table 2.1: Common sliding friction coefficient models in gear literature

Author	Equation
Schlenk [63]	$\bar{\mu} = 0.048 \cdot \left(\frac{F_{bt}/b}{V_{r,C} \cdot \rho_C} \right)^{0.2} \cdot \eta_0^{-0.05} \cdot Ra^{0.25} \cdot X_L \quad (2.3)$
Benedict & Kelley [46]	$\mu = 0.0127 \cdot \left(\frac{50}{50 - Rq} \right) \cdot \log \left(\frac{3.17 \cdot 10^8 \cdot w}{\eta_0 \cdot V_s \cdot V_r^2} \right) \quad (2.4)$
Xu [34]	$\mu = e^f \cdot p_H^{\psi_2} \cdot SRR ^{\psi_3} \cdot V_e^{\psi_6} \cdot \eta_0^{\psi_7} \cdot R'^{\psi_8} \quad (2.5)$
	$f = \psi_1 + \psi_4 SRR p_H \log(\eta_0) + \psi_5 e^{- SRR p_H \log(\eta_0)} + \psi_9 e^{Rq} \quad (2.6)$

b) Rolling friction force Rolling traction is the resistance to movement between two surfaces rolling without sliding as the result of the non-symmetrical pressure distribution under the EHL contact (see Figure 2.3). Crook [64] showed that in the full EHL regime the rolling friction force is proportional to the lubricant film thickness and independent of load. The total rolling traction force exerted on one body can be computed following Equation 2.7:

$$F_r = \frac{1}{2} \cdot \int_{-\infty}^{+\infty} h(x) \cdot \frac{\partial p(x)}{\partial x} dx \quad (2.7)$$

Contrary to sliding friction, the number of analytical models to calculate rolling traction is scarce and, to the author's knowledge, there is no empirical equation. Anderson and Loewenthal [65] applied a modified version of Crook's [64] EHL rolling traction formula for point contacts (see Table 2.2) to predict the efficiency of a spur gear system. In a similar manner, Wu and Cheng [35], and later on Xu [34], used the equation developed by Goksem and Hargreaves for full EHL line contacts [66] to evaluate power loss in spur gears. In both cases, the order of magnitude of the rolling term was negligible compared to the sliding one and hence, it is usually overlooked in similar research works.

However, Michlyn and Myunster [67] proved that near the pitch point, rolling friction force prevails causing surface wear, which means that energy is being dissipated and, therefore, it may be underestimated. Recently, Li and Kahraman [62] showed that the conventional way to compute rolling power losses is inappropriate and proposed a new method to derive such losses integrating the product of the local fluid shear stress and the sliding velocity across the film thickness. They proved that in case of mixed lubricated contacts, due to the extreme pressure gradients, rolling losses were underestimated. This approach requires solving the Reynold's equation for each contact point along the line of action, in the same way as the sliding friction coefficient models in the third group, which leads to time-consuming calculations.

Table 2.2 summarizes some of the most common rolling friction force models in gear literature. All models have been developed considering isothermal isoviscous regime and therefore, they may show errors at the highly loaded contacts of gear transmissions. To solve this issue, Archard and Baglin [68] presented a modified version of their equation to account for heavily loaded contacts but the calculation requires additional effort. Finally, these equations are usually presented in terms of non-dimensional groups, U , G and W , similarly to film thickness equations, where each of them accounts for the effect of speed, materials and load respectively.

Table 2.2: Common rolling friction force equations in gear literature

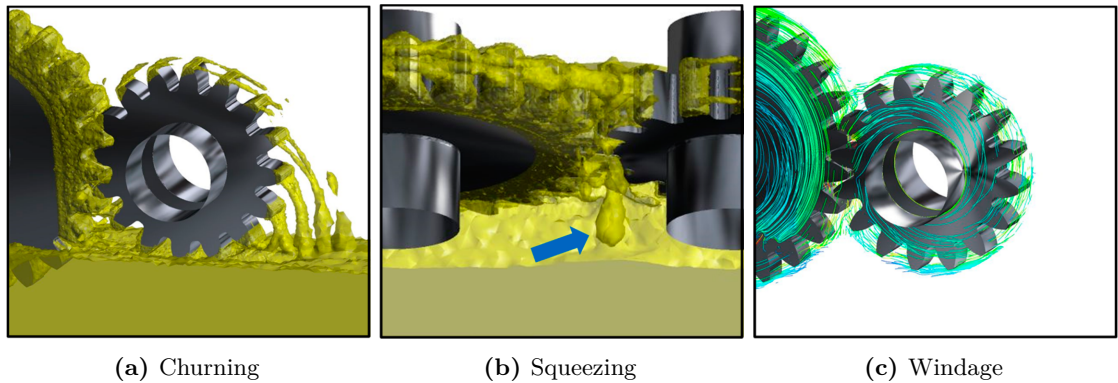
Author	Equation
Archard & Baglin [68]	$F_r = 2.08 \cdot (\eta_0 \cdot V_e \cdot w)^{0.5}$ (2.8)
Goksem & Hargreaves [66]	$F_r = 4.318 \cdot (G \cdot U)^{0.658} \cdot W^{0.0126} \cdot R'_x \cdot \alpha^{-1}$ (2.9)
Anderson & Loewenthal [65]	$F_r = 9 \cdot 10^7 \cdot [2.69 \cdot U^{0.67} \cdot G^{0.53} \cdot W^{-0.067}] \cdot R'_x \cdot b$ (2.10)

Load independent power losses

Load independent power losses, also known as “spin losses”, are of primary importance in high speed gears [69] and they are caused by a host of factors from the viscous dissipation of gear oil churning to the squeezing of lubricant in the meshing zone. According to [70] load independent losses can be classified in the following types:

1. Oil churning losses, defined as drag losses taking place on the periphery and faces of a gears partially immersed in lubricant.
2. Root filling losses, defined as the energy losses due to the swirling motion of lubricant in the cavity between adjacent teeth.
3. Oil pocketing/squeezing losses, caused by lubricant being squeezed out of the gear mesh due to the pumping action of gear pairs.
4. Windage losses, resulting from the oil-air mixture drag force on the face and sides of the gears as they rotate in free air.
5. Air pumping losses, due to the squeezing and pumping of compressible air from the meshing zone towards the tooth ends.

However, literature review, has shown that load independent losses are usually categorized in two principal contributions: churning and windage; while the rest of the terms are considered secondary and they are usually grouped together. In this sense, current CFD simulations [71] are helping understand the complex fluid flows inside the gearbox and thus help to separate the different power loss contributions as shown in Figure 2.4.

**Figure 2.4:** CFD simulations of no-load losses by Liu [71]

In the following paragraphs, churning and windage power losses are described in depth and other contributions are briefly introduced.

a) Oil churning Churning power losses appear when gears are running in an oil bath that generates a drag force on the face and sides of the gear. When gear teeth in rotation enter the static oil bath they face a drag force due to the pressure of the lubricant on the face of the teeth. Once the teeth exit the oil bath they throw the lubricant away by centrifugal fling-off (see Figure 2.4a). The rotational movement of the gear pair partially immersed in lubricant requires additional torque to overcome such drag forces.

There are several experimental studies on the churning drag torque, $T_{VZ0,C}$, of rotating disks and bladed rotors, but only a few of them are devoted to the gear oil churning phenomena. Table 2.3 gathers some of the most recurring empirical models in gear literature.

Table 2.3: Common churning power loss models in gear literature

Author	Equation
Terekhov [72]	$T_{VZ0,C} = \rho_o \cdot \omega^2 \cdot r^4 \cdot b \cdot C_m \quad (2.11)$
	$C_m = \psi_1 \cdot \left(\frac{H}{r}\right)^{\psi_2} \cdot \left(\frac{b}{r}\right)^{\psi_3} \cdot \left(\frac{V}{V_o}\right)^{\psi_4} \cdot \text{Re}^{\psi_6} \cdot \text{Fr}^{\psi_7} \quad (2.12)$
	$T_{VZ0,C} = C_{sp} \cdot C_1 \cdot e^{C_2 \cdot \left(\frac{V_t}{V_{t0}}\right)} \quad (2.13)$
	$C_{sp} = \left(\frac{4 \cdot h_{e,\max}}{3 \cdot h_c}\right)^{1.5} \cdot \left(\frac{2 \cdot h_c}{l_h}\right) \quad (2.14)$
Mauz [63]	$C_1 = 0.063 \cdot \left(\frac{h_{e1} + h_{e2}}{h_{e0}}\right) + 0.0128 \cdot \left(\frac{b}{b_0}\right)^3 \quad (2.15)$
	$C_2 = \frac{h_{e1} + h_{e2}}{80 \cdot h_{e0}} + 0.2 \quad (2.16)$
Changenet [73]	$T_{VZ0,C} = \frac{1}{2} \cdot \rho_o \cdot \omega^2 \cdot r^3 \cdot S_m \cdot C_m \quad (2.17)$
	$C_m = \psi_1 \cdot \left(\frac{m_n}{d}\right)^{\psi_2} \cdot \left(\frac{b}{d}\right)^{\psi_3} \cdot \left(\frac{H}{d}\right)^{\psi_4} \cdot \left(\frac{V_o}{d^3}\right)^{\psi_5} \cdot \text{Re}^{\psi_6} \cdot \text{Fr}^{\psi_7} \quad (2.18)$

In this table, $T_{VZ0,C}$ is the churning torque, ρ_o is the lubricant density, ω is the rotational speed, r is the gear pitch radius, S_m is the surface area of contact between the gear and the lubricant, C_m is the dimensionless drag torque, m_n is the module, d is the pitch diameter, H is the immersion depth, V_o is the oil volume, Re is the Reynolds number and Fr is the Froude number. Other parameters are of secondary importance and their meanings can be found in the original publications.

Terekhov [72] carried out several experiments with high viscosity oils, different modules and low rotational speeds and he derived an empirical equation for the drag torque from dimensionless analysis. Lauster and Boos [74] arrived to a similar expression from a different set of experimental data. Later on, Boness [75] experimented with two spur gears with small module immersed in water and obtained a different expression for the drag torque where the parameter for the immersed area was also included. In [76] Luke and Olver performed a number of experiments to determine churning loss in spur gear pairs in mesh. They compared their experimental observations on spin power losses with the previous formulations and found that, contrary to what Boness had predicted, the spin power losses were not strongly affected by the viscosity of the lubricant.

Furthermore, Luke and Olver's observations [76] called into question the attempt used to characterize spin power loss based on a Reynolds number dependent on lubricant viscosity. More recently, Changenet and Vexex [73] have presented a new model for the prediction of churning losses in automotive transmissions which accounts for the influence module, diameter, face width, speed, immersion depth and lubricant viscosity (see Table 2.3); what's more the proposed model accounts for the pinion and the gear in mesh and the sense of rotation. Although the proposed equation initially included the effect of the flow regime through the Reynolds' number (see Equation 2.18), the authors confirmed Luke and Olver's claim on the latter in a second publication [77], thus confirming that at high speeds the lubricant viscosity influence is negligible.

The models presented in the above paragraph have been developed from experimental results and therefore they do not account for all gear types, geometries and gearbox architectures. A deeper understanding of the physical phenomena responsible for viscous losses is still needed in order to improve the existing models. In this sense, Seetharaman [70] proposed a different approach for the computation of spin power losses. The author developed a physics-based model to predict power losses of gear pairs due to oil churning and windage that included individual formulations for evaluating drag and pumping components. Besides, with the improvement of computational capabilities CFD models are being used to better understand the fluid flows in both, oil churning and windage phenomena [78].

b) Windage Windage power loss can be defined as the power required to rotate a gear in free air when there is no frictional or viscous power loss in the gear mesh or the bearings. When pitch-line velocity is above 120 m/s, windage losses can be half or more of the total losses from the drive system [79]. However, windage power loss assessment is the weakest of the analytical tools available for predicting gearbox losses. Table 2.4 presents some of the regular empirical models in scientific literature.

Table 2.4: Common windage power loss models in gear literature

Author	Equation
Matsumoto [69]	$P_{VZ0,W} = 3.8 \cdot 10^{-22} \cdot N^3 \cdot d^5 \cdot \rho_a \cdot \left[0.006 + 0.02 \cdot \left(\frac{b}{d} \right)^{0.8} + \left(\frac{h}{d} \right) \right]$ (2.19)
Dawson [80]	$P_{VZ0,W} = N^{2.9} \cdot \left(0.16 \cdot d_f^{3.9} + d_f^{2.9} \cdot b^{0.75} \cdot m_n^{1.15} \right) \cdot 10^{-20}$ (2.20)
	$P_{VZ0,W} = \frac{1}{2} \cdot \rho_a \cdot \omega^3 \cdot r^5 \cdot C_t$ (2.21)
Diab [81]	$C_t = 60 \cdot \text{Re}^{-0.25} \cdot \left(\frac{b}{r} \right)^{0.8} \cdot z^{-0.4} \cdot \left[\left(\frac{h_1}{r} \right)^{0.56} + \left(\frac{h_2}{r} \right)^{0.56} \right]$ (2.22)

Several research works quantify windage power loss in disks rotating in motionless fluid but very few consider the energy dissipation in gears as the latter is a complex phenomena that depends on many parameters as shown in Table 2.4 namely, face width, b , gear blank diameter (represented by r , d or d_f), number of teeth, z , module, m_n , speed (ω or N) and air density, ρ_a .

Anderson and Loewenthal [65] developed an equation to quantify windage power loss from work done on turbine rotor wheels. The authors modified the density and viscosity of the surrounding fluid to account for the air-oil mixture environment inside the gearbox. Matsumoto et al. presented a similar equation in [69] based on the same groups of parameters and the influence of specific density. Later on, Dawson [80] carried out an extensive experimental work with rough/smooth discs and gears with variable pitch diameters, modules and face widths. The formula assumed that the side plates and the toothed periphery could be treated separately and it also accounted for the effective density of the fluid and the degree of enclosure. The author also found that, although the power loss in spur and helical gears was similar in magnitude, the flow behaviour was significantly different. Townsend and Dudley [82] presented an equation that included the effect of helix angle in the fraction of total power loss corresponding to the toothed periphery; however, the influence of effective density and degree of enclosure were not taken into account. A more recent study by Diab [81] further developed analytically Dawson and Townsend's formulae considering the behaviour of fluid flow in rotating teeth. In addition, the author developed a second approach for the windage phenomena based on dimensional analysis. Both methods presented a good correlation with experimental results. And finally, as in the case of churning losses, Seetharaman [70] also developed a physics based windage model that accounted for air pocketing/pumping and drag forces on the lateral surfaces.

Finally, CFD models [83–85] are also used to better understand the fluid flow in enclosed drives, the interaction between pinion and gear and the effect of helix angle. CFD method is specially helpful in designing shrouding configuration, which helps reduce total power loss significantly [86].

c) Oil and air trapping/squeezing/pumping According to the spin power loss classification presented by Seetharaman [70] at the beginning of section 2.1.1, viscous drag losses due to oil churning and windage are followed by secondary power loss sources such as the power required to fill the tooth root with the oil-air mixture, the energy needed to trap and deform the oil film between the meshing gear teeth and the power required to pump the mixture towards the tooth ends.

Mizutani et al. [87] carried out an interesting research work on the significance of different power loss sources in jet lubricated gears. The authors conducted various tests with long addendum spur gears at high speeds (maximum rotational speed 12000 rpm and pitch line velocities up to 75 m/s), loaded at different torque levels and subject to variable oil pressures. They concluded that gear power loss was proportional to tooth load and rate of oil flow at all gear speeds. However, at higher speeds the main sources of energy dissipation were windage and churning phenomena where the pumping and mixing of oil-air mist in the meshing teeth was found to be the main source of power loss. Such contribution to the total power loss is explained by the short time duration of a mesh period in high speed gears: the mixture of air and lubricant is successively accelerated, compressed and expanded in the inter-tooth spaces giving rise to a significant power loss and heating.

Another study by Ariura et al. [88] in jet lubricated gears concluded that the trapping of the oil in the tooth spaces dominates in the low speed range while in the high speed range the acceleration of the oil is predominant. The oil captured in the tooth clearances

is accelerated to the gear speed momentarily in two directions: rotating direction and axial direction. Matsumoto [69] included both sources in the prediction of high speed and high power helical gear power losses and the errors of the calculated values were less than 10% of the measured gear loss. A more recent study by Diab [89] included the air pumping action in the prediction of power losses in high speed gears. In this study the contribution of gas trapping seems to be of secondary importance as it represents only 3% of the total power loss, however, it plays a significant role in the thermal distortion of the gear flank causing a temperature difference of more than 30°C between the tooth engagement side and points situated about two-thirds of the width towards the exit [90]. This phenomena will be discussed later.

The physics based model by Seetharaman [70] also proved analytically that, among all the contributors to total spin power loss, oil-air squeezing is the major component, followed by drag forces on the faces and periphery and finally root filling losses. As in the previous viscous power loss sources, CFD numerical models are helping understand these phenomena. In this sense the computational model by Concli [91] showed that squeezing power loss increase with rotational speed and decrease with temperature, that is, viscosity.

2.1.2 Heat dissipation

In general-purpose transmissions, the heat generated in the pinion-gear contact is conducted away from the mesh area towards the room, through the body of the gear, shaft, bearings, housing and foundation, as shown in Figure 2.5. Besides, nearby bearings and sealings generate heat as well which is removed together with that coming from gear mesh by forced convection with the oil sump and the turbulent air flows inside the gear case. Meanwhile, the radiation effect is usually assumed to be a small percentage of the whole due to the relatively low temperatures of the considered machine elements [92]. The process of heat generation and transfer continues until the steady-state temperature is reached. However, in transmissions with moderately high pitch line velocities, the number of tooth engagements per second is high and the heat generated at the mesh must be conducted away from the tooth flank at a sufficiently high rate to avoid sudden temperature increases leading to gear scuffing. Thus, to avoid tooth failure, heat dissipation by convection must be enhanced introducing oil jets or increasing the relative immersion depth. In any case, high or low speeds, final temperature distribution depends on two main factors: i) the geometry and ii) the relation between heat generation and dissipation rates. In this section the latter is reviewed, focusing on heat transfer mechanisms typical from gear applications: i) the fling-off cooling effect and ii) the axial oil-air mixture pumping.

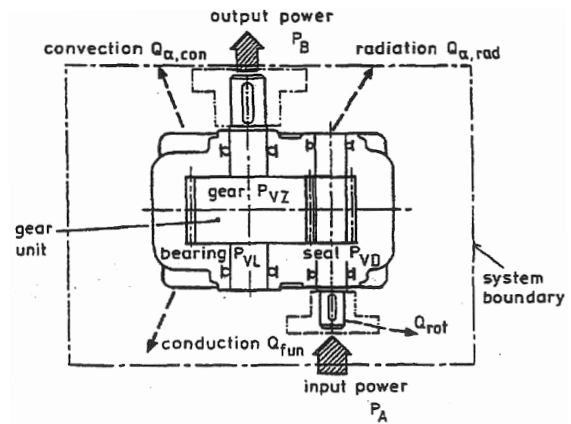


Figure 2.5: Fundamental heat dissipation mechanisms in a gear transmission [28]

One of the most exhaustive scientific studies on heat dissipation processes in gear transmissions was carried out by Funck [93], who analysed overall heat transfer mechanisms in the gearbox. Funck measured heat transfer coefficients of the different parts of the housing under composite effect of radiation and free/forced convection and found that, in most geared transmissions, the governing heat transfer method was that due to external convection because the heat exchange surface area of the gearbox is usually large and radiation term is half its value in comparison, as shown by Figure 2.6a. Moreover, it was experimentally proved that in real applications it is very unlikely to have free convection due to the rotation of shafts, couplings and cooling fan of the motor; as a consequence, 2 to 3 W/m²K differences arise between values measured in laboratory and workshop. Radiation effect was also analysed in this work by comparison of different surface finishing methods with a reference varnished surface with known emissivity and it was found that, for common gearboxes, surface emissivity could be considered constant an equal to 0.91. From this work, several convection and radiation empirical heat transfer coefficients were derived which are currently part of the ISO 14179-2 standard [16]. Similarly, Phillips [94] proposed years later an overall heat dissipation coefficient for gear casings located in a large indoor space and provided additional values for other conditions. This work is the reference document for the American radiation proposal of ISO 14179-1 standard [16].

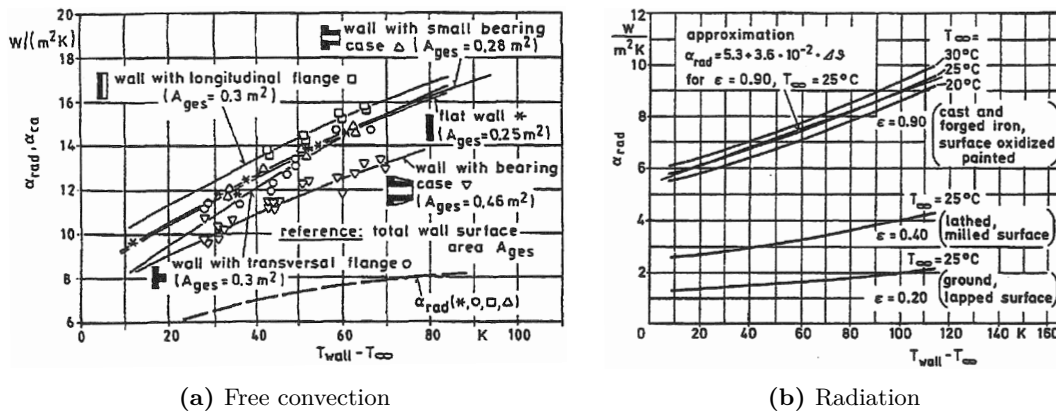


Figure 2.6: Gearbox external free convection and radiation heat transfer coefficients [63]

In a subsequent publication by Winter, Michaelis and Funck [95] it was shown that splash lubricated gearbox temperature is almost constant within $\pm 5^\circ\text{C}$ provided that immersion depth of the gears is adequate. However, if the oil level in the sump is too low, the heat generated in the gear mesh cannot be evenly distributed to the inner walls of the casing and dissipated to the room; as a consequence, gear temperature increases inevitably [63]. This point is specially important in the current PhD thesis as immersion depth is assumed to affect temperature distribution.

Similar publications can be found on specific heat dissipation processes in gear transmissions. For instance, Winter and Michaelis [92, 96] experimentally analysed heat transfer by conduction to the foundation; Funck [93] also studied the effect of casing fins and gearbox exposure to the sun; Lossl [97] analysed heat dissipation by forced convection on rotating shafts and couplings; and finally, Terauchi [98] experimentally studied the amount of heat flowing from bearings to the shaft.

Literature review has shown that almost all publications on gearbox heat dissipation are experimental and most of them were carried out in the mid-eighties. Furthermore, very few analytical or numerical works exist on the topic. In this sense, Joule et al. [99] analysed steady state temperature distribution of a gearbox using the finite element method and discussed the difficulties associated to calculating the thermal boundary conditions. It was found that evaluating the internal heat transfer coefficients for an oil-mist environment was questionable and experimentally measured surface heat fluxes were used instead. To solve this issue, Yazdani et al. [100] have recently applied a numerical multi-physics approach to the thermal mapping of dip-lubricated gear pairs including the influence of gear teeth and shafts in fluid flow behaviour. Numerical predictions were compared to experimental measurements with satisfactory results demonstrating that the method can provide a valuable physical insight into the thermal behaviour of gearboxes. Similarly, Christodoulis [101] has made an attempt to apply a numerical full multi-physics approach to analyse composite effect of fluid flows and heat transfer in the two-phase oil-air mixture inside the gearbox and also including heat transfer with the room. Despite the gear geometry was largely simplified, the model resulted extremely complex and computationally demanding and no conclusive results were obtained.

Meanwhile, analytical attempts to study heat dissipation processes in gears have been focused on the teeth region, where heat dissipation mechanisms are mainly ruled by centrifugal fling-off and axial oil pumping effects. Both mechanisms are briefly reviewed here.

Fling-off cooling

Generally, the oil supplied to the tooth face, either by jet lubrication or oil bath, flows along the profile due to the action of centrifugal force, generating an oil film that absorbs heat from the tooth surface with which it is in contact. Due to the action of centrifugal force, the oil is flung-off progressively dissipating heat from teeth as shown in Figure 2.7. Most gear drives are characterized by intermittent fling-off cooling which means that the oil is supplied to each tooth face once per revolution (when teeth enter the oil bath or pass under the oil jets). Besides, in dip lubricated gearboxes, if the oil level is increased, the available angle for fling-off cooling is reduced and so is the heat dissipated with this method.

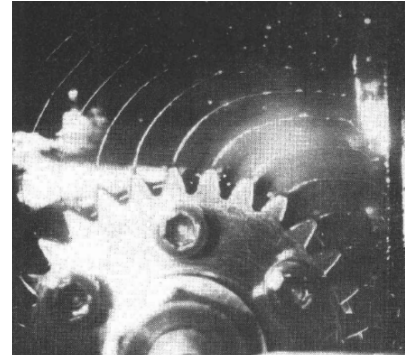


Figure 2.7: Fling-off cooling in rotating spur gears [102]

Literature on the fling-off cooling of gear teeth is scarce. DeWinter and Blok [103] analysed intermittent fling-off cooling and calculated the theoretical temperature distribution of the oil film on the flank. They showed that even with an abundant supply of oil and when the available rotation angle is largest, there is an upper limit to the heat withdrawable from the tooth surface of a spur gear when there is a centrifugal force. The maximum amount of heat, Q , removed from both flanks of all gear teeth during rotation can be calculated as follows.

$$Q = \left[\frac{5.6}{\pi} \cdot m_n \cdot z \cdot b \cdot \omega^{1/2} \cdot e \right] \cdot \Delta\Theta \quad (2.23)$$

where m_n is the module, z is the number of teeth, b is the tooth face width, ω is the rotational speed, $e = \sqrt{k_o \cdot \rho_o \cdot c_{p,o}}$ is the thermal effusivity and $\Delta\Theta$ is the temperature difference between teeth surface and oil.

In a previous publication, Blok [104] reported a similar expression including the effect of available rotation angle in dip lubricated gears and an equivalent equation for jet lubricated systems was also proposed. Moreover, years later, Van Heijningen [102] extended Blok's analysis to include continuous fling-off cooling method. These equations are specially useful in thermal lumped parameter models, as the term in brackets in Equation 2.23 can be considered a thermal resistance of convection between the oil sump and the teeth.

Equations by Blok, DeWinter and Van Heijningen were developed under the assumption that the quantity of lubricant is infinite at the start of the fling-off process which results in large cooling capacities. Akin and Mross [105] further developed Blok's approach and included the effect of side windage in the oil atomization process taking place in the space between adjacent teeth. Although their results highlighted the influence of the depth of impingement in the heat removal by intermittent fling off, the proposed method was not straightforward. Similarly, the study by Terauchi et al. [106] filled in this gap by calculating the initial oil film thickness, and showed that this parameter has a strong influence on the cooling effect. The authors also measured the average heat transfer coefficient on the tooth face based on the temperature difference between the tooth and the oil in experimental tests and they concluded that heat transfer coefficient increases with speed and viscosity while it decreases with the number of teeth. All these models give a qualitative measure of the parameters affecting heat dissipation in cylindrical gears.

Axial oil pumping

During the time period in which a tooth first crosses the addendum cylinder and proceeds to fill up most of the volume between the teeth, a fraction of the oil and the lubricant in the tooth space is expelled out of the gear. In the case of spur gears, the oil gets into the tooth space from both ends and the flow collides at the middle of tooth width, being expelled towards both ends as a consequence. Meanwhile, in helical gears the oil flow is unidirectional (from engagement to exit side), thus producing an axial oil pumping action that delivers oil to the flank surface dissipating heat on the way.

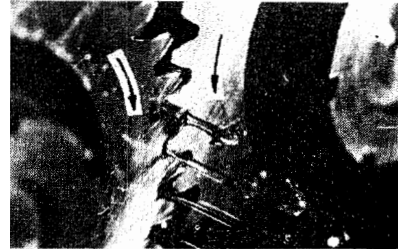


Figure 2.8: Axial oil pumping in rotating spur gears [88]

Contrary to fling-off cooling effect, the determination of the heat dissipation rates due to axial oil-air pumping is not easy as the compression of the fluid due to the action of meshing gear teeth generates heat as well. In the case of spur gears, Ariura et al. [88] experimentally measured the power required to pump the oil trapped between mating teeth and they proposed a simple analytical model to explain the oil trapping phenomena. Pechersky and Wittbrodt [107] analytically studied fluid flows in meshing spur gear pairs to assess the order of magnitude of fluid velocity, pressure and temperature. They found that fluid velocities were high and that significant temperature peaks arise when pressure reached its maximum value. More recent works on the squeezing action of meshing spur gear teeth can be found in power loss related literature, such as the analytical work by Seetharaman [70] or the CFD simulations by Concli [91], however, none of them studies heat transfer due to the oil pumping action.

In the case of helical gears, a few references on the topic can be found. Matsumoto et al. [69] analysed the pumping action effect of the oil trapped in tooth mesh clearances and provided a power loss model for oil acceleration in the radial and axial directions. In their work, the maximum quantity of oil trapped in the inter-tooth space was defined based on a simplified representation of the gear mesh, and the velocity along the tooth trace of the lubricating oil was assumed to be $V_a = V_t / \tan(\beta)$. Thus, with this information, it is possible to model heat transfer in the longitudinal direction as an advective transport of energy following Equation 2.24.

$$Q = [\dot{m} \cdot c_{p,o}] \cdot \Delta\Theta = [(\rho_o \cdot V_a \cdot A) \cdot c_{p,o}] \cdot \Delta\Theta \quad (2.24)$$

$$A = C \cdot [2 \cdot m_n \cdot j_{bn} + 0.5 \cdot (s_{ca,1} + s_{ca,2} + j_{bn}) \cdot (c_1 + c_2)] \quad (2.25)$$

where m_n is the normal module, j_{bn} is the normal backlash, s_{ca} is the chordal tooth thickness at the tip, c is the tip clearance, ρ_o is the oil density, $c_{p,o}$ is the specific heat capacity of oil and $\Delta\Theta$ is the temperature difference between teeth surface and oil. Subscripts 1 and 2 indicate parameters relative to pinion and gear respectively and finally, variable C was defined by Matsumoto et al. [69] as an empirical factor depending on the oil jet flow rate which takes into account the reduction of the amount of oil trapped in the mesh clearances at high speeds.

In the same way, Diab [89] developed an original one-dimensional semi-analytical model to simulate the air-lubricant pumping between gear teeth. The proposed approach sliced the spaces between the gear teeth into a number of finite volumes (connected by radial or axial flow exchange surfaces) and applied the continuity equation assuming a perfect gas submitted to isentropic compression-expansion cycles. Once critical conditions are reached, the exit flows are bounded and the gas in the control volume is compressed and heated. This model allows calculating fluid velocity, pressure and temperature variations along the tooth face and predicts that the pumping of the fluid between the teeth leads to over heating the gear face close to the trailing edge. The theoretical predictions were compared with the experimental evidence from two turbo-gear sets and it was found that the simulated temperature variations agreed reasonably well with measured data [90]. Moreover, a different set of experimental results by Houjoh et al. [108] confirm Diab's conclusions on pressure distribution in the tooth spaces, and their results also show that there is a exceptionally strong pressure at a point located at about 2/3 of the face-width; where maximum temperatures are known to occur and thermal distortion is maximum (see Figure 1.4).

Therefore, it seems that the uneven temperature distribution caused by the axial oil pumping lies at the origin of the thermal distortion of the tooth face width. Recommendations from practical experience gathered by Dudley in reference [14], suggest not using spur gear teeth when the pitch line velocity exceeds 50 m/s because the oil trapping problem becomes too troublesome; and in the case of helical gears, the severity of the oil trapping problem is evaluated with the axial meshing velocity, V_a , following recommendations on Table 2.5. According to Dudley [14], in a bad thermal situation, the gear teeth may turn blue and the paint on the gear casing may be burned by the casing hot spot. Furthermore, not only thermal problems arise when axial velocity is high, it must be taken into account that an axial velocity of 700 m/s is equivalent to around Mach 2 which also creates aerodynamic sound, as experimentally shown in [109].

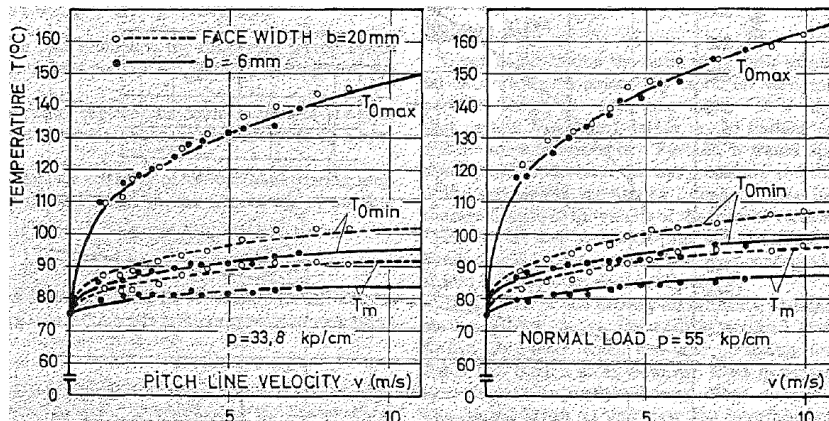
Table 2.5: Severity of thermal problems in helical gears according to Dudley [14]

V_a [m/s]	Severity
400	No trouble except in very large units where thermal distortion may be enough to require correction. (Need good oil-jet system and generous size casing).
500	Probably no serious trouble. (Need very good oil-jet system and generous size casing for gear sizes).
700	Probably have some trouble. May be manageable if gears are not too large and thermal distortions are handled by compensations in tooth fit.
850	Usually difficult to handle. Much skill in tooth compensations needed plus special quality of lubricant.
1000	Probably impractical to handle even with utmost design skill.

2.2 Temperature distribution in cylindrical gears

2.2.1 Experimental observations

Temperature distribution in gears has long been subject to study as gear scuffing failure is known to be affected by the high temperature levels reached in the tooth flank. Seminal experimental works by Teruchi and Miyao [110] or Niemann and Lechner [111] measured flash temperatures in gear teeth in an attempt to explain gear teeth scoring. The former analysed the relation between flank temperature rise and the contact position and showed that Blok's theory [112] for flash temperature increase correlates to local temperature increases. Moreover, it was found that load distribution is an important factor on surface temperatures and therefore, non-uniform contact patterns should be avoided as they produce local pressure increases. Meanwhile, Niemann and Lechner [111] carried out an extensive experimental work and additionally analysed the effects of gear geometry, surface roughness and oil type. It was found that tooth surface temperature is proportional to load and pitch line velocity, that is input power. Moreover, face width and longitudinal crowning were also found to affect surface temperature as well through the contact pressure increase. Figure 2.9 summarizes the influence of these parameters, where the difference between the maximum and minimum flash temperatures on the gear surface is highlighted. At the highest tangential speeds such difference reaches more than 50°C ; in any case, flash temperature is always above the steady-state average tooth temperature.

**Figure 2.9:** Influence of speed, load and face width on flash temperature increase [111]

Additional experiments conducted by Terauchi and Mori [113] on the influence of dynamic effects on temperature rise, highlighted the importance of friction coefficient and confirmed that maximum contact temperature is equal to the steady-state surface temperature of the gear plus Blok's flash temperature rise. This observation has defined current practice for the calculation of contact temperatures in standards (e.g. [114]). In this work, the authors considered surface temperature to be equal to oil temperature, however, it was later shown by Deng et al. [115] that surface temperature is quite different from that of oil, introducing an equation to compute the average temperature rise in the centre of the gear, which is commonly referred to as bulk temperature increase, $\Delta\Theta_b = \Theta_b - \Theta_o$.

Similar equations can be found in scientific literature for the evaluation of the steady-state gear temperature rise and Table 2.6 gathers some of the most common.

Table 2.6: Common bulk temperature rise equations in gear literature

Author	Equation
Deng et al. [115]	$\Delta\Theta_b = C_v \cdot C_x \cdot C_q \cdot b^{-1} \cdot P_{VZP}$ (2.26)
Oster [116]	$\Delta\Theta_b = 7400 \cdot \left(\frac{P_{VZP}}{a_w \cdot b}\right)^{0.72} \cdot \frac{X_S}{1.2 \cdot X_{C_a}}$ (2.27)
Terekhov [117]	$\Delta\Theta_b = \frac{C \cdot P_V \cdot \text{Re}^{\Psi_1} \cdot \text{Pr}^{\Psi_2}}{V_t \cdot H \cdot b \cdot c_{p,o} \cdot \rho_o} \cdot \left(\frac{H}{r}\right)^{\Psi_3} \cdot \left(\frac{V}{V_o}\right)^{\Psi_4} \cdot \left(\frac{h}{r}\right)^{\Psi_5} \cdot \left(\frac{h}{b}\right)^{\Psi_6}$ (2.28)

In this table parameter P_{VZP} , indicates mesh frictional power loss, b is the gear face width, h the tooth height, r the pitch radius and a_w is the operating centre distance. Variables C_v , C_x and C_q in Equation 2.26 are coefficients accounting for the influence of rotating speed, meshing position and oil supply rate respectively; while X_S and X_{C_a} in Equation 2.27 are the lubricant and tip relief factors. Finally, Equation 2.28 by Terekhov is the result of non-dimensional analysis of several experiments accounting for the influence of immersion depth, H , the ratio of gear volume, V , to the oil sump volume, V_o , the tangential speed, V_t , and the properties of oil, namely, its specific heat capacity, $c_{p,o}$ and its density, ρ_o . Finally, parameter C accounts for the influence of rotating direction.

These equations usually assume that pinion and gear are subject to the same temperature increase, however, when multiplication or reduction gear ratios are used, pinion and gear temperatures are usually different. Moreover, gear teeth temperature is not constant, specially in large module gears where significant gradients may arise between the loaded and unloaded flanks as shown by Knauer [118] (see Figure 2.10). Therefore, an additional temperature drop exists between the mating surface and the tooth centre. Experiments by Knauer also showed that temperature gradients between both flanks increase with speed and that temperature difference between tooth centre and unloaded flank is almost negligible. As a consequence, it is concluded that temperature gradients concentrate near the loaded flank.

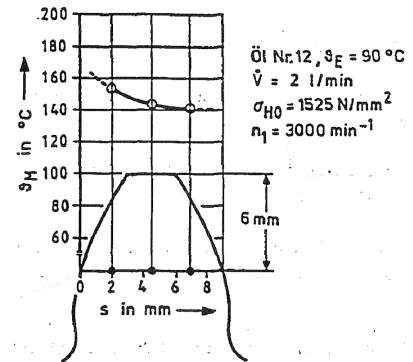


Figure 2.10: Transverse thermal gradient in spur gear tooth [118]

On the other hand, temperature differences between pinion and gear pairs have long been observed [24] but few experimental measurements can be found in literature, specially when middle size spur and helical gears are considered. In this sense, Mizutani [87] measured high speed spur gear pair temperatures as a function of jet oil flow rate and pressure for pinion and gears with 3 mm module and pitch diameters 120 mm and 231 mm respectively. Although measurements included pinion and gear teeth bulk temperatures along with those of the shafts and the oil mist, very few results were reported and the steady-state values were not published. At the same time, Greiner [119] analysed similar size helical gear teeth thermal behaviour subject to different jet lubrication conditions and showed that appreciable temperature differences exist between pinion and gear. Moreover, radial temperature gradients may become noticeable in some lubrication conditions as shown in Figure 2.11. Temperature differences between pinion and gear may reach 30°C; with the pinion always hotter than the gear due to its smaller size. Moreover, radial temperature gradients up to 20°C are observed with variable shape depending on direction of rotation.

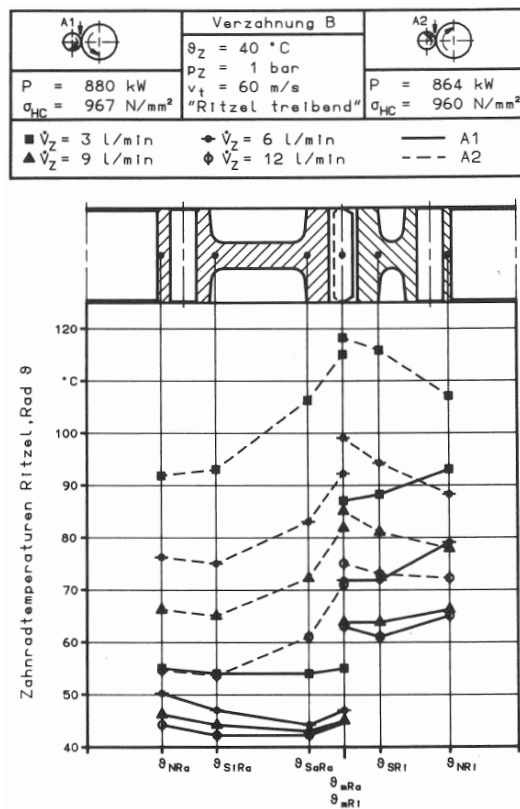


Figure 2.11: Influence of oil flow rate and rotating sense on helical gear thermal behaviour [119]

More recently, Otto [28] has measured thermal behaviour of dip-lubricated spur gear types FZG A and C-PT and the author has found that temperature increase depends on relative immersion depth, with the highest temperatures reaching the tempering region (above 170°C). Furthermore, temperature differences between pinion and gear almost reached 30°C in these experiments. Following this work, Geiger [120] has recently measured temperature distribution in the radial direction of FZG type C-PT gear pair

with variable rotating speeds and load stages. From his experimental results, the author has found that temperature differences between pinion and gear are negligible when relative immersion depth is $H/D = 0.5$, with steady-state bulk temperature levels close to that of the oil sump. However, temperature differences between tooth centre and shaft may reach 8°C even with favourable immersion depths.

Experiments conducted by Handschuh and Kilmain [9, 86] in high speed helical gears from the aeronautical industry have confirmed the existence of additional heat dissipation sources as previously described in Section 2.1.2. Temperature measurements of radially and axially flung-off lubricant near the teeth were carried out for variable operating conditions. Figure 2.12 shows non-dimensional experimental trends. At low speeds the axial and radial flung-off oil temperature measurements are nearly the same but as the rotational speed increases, the difference between the two locations becomes greater; which confirms the additional heat source due to axial oil pumping described by Diab [89].

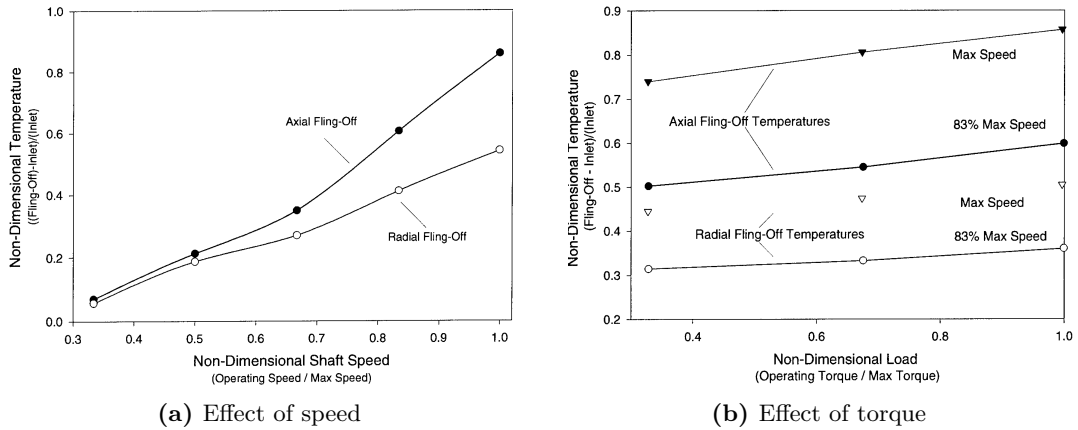


Figure 2.12: Effect of speed and torque in radial and axial oil fling-off temperatures [9]

This effect has long been known to affect temperature distribution in large size helical gear teeth from turbo-machinery industry. Preliminary investigations by Martinaglia [21], Akazawa [121] and Matsumoto et al. [20] have shown that only a small part of the heat taken up by the gear body is radiated out through the gear faces to dissipate in the air/oil mist atmosphere, the remainder is given off via the tooth surface. As a consequence, appreciable temperature gradients arise between gear teeth and shaft as shown in Figure 2.13a.

In contrast to the gear, the temperature difference between pinion teeth and shaft is much smaller. Akazawa [121] found that the latter was approximately 5°C at pitch line velocity of 120 m/s, and it became smaller as its PLV increased. It was assumed that this phenomenon was attributable to small heat mass of pinion, increasing of heat flow into the pinion due to the greater number of engagements per second and also to the fact that a large amount of heat was being transferred from the bearing to the pinion [121]. Because of these reasons the temperature of the pinion is usually higher than that of the gear and therefore an important temperature gradient exists between both.

Furthermore, due to the pumping action of the oil-air mixture trapped in the gear mesh, temperature distribution across the face width of such helical gears show a characteristic shape (see Figure 2.13b) with almost constant temperatures over the first half of the face-width and a steep rise up to a maximum temperature located at a point about $2/3$ of the face width towards the exit side.

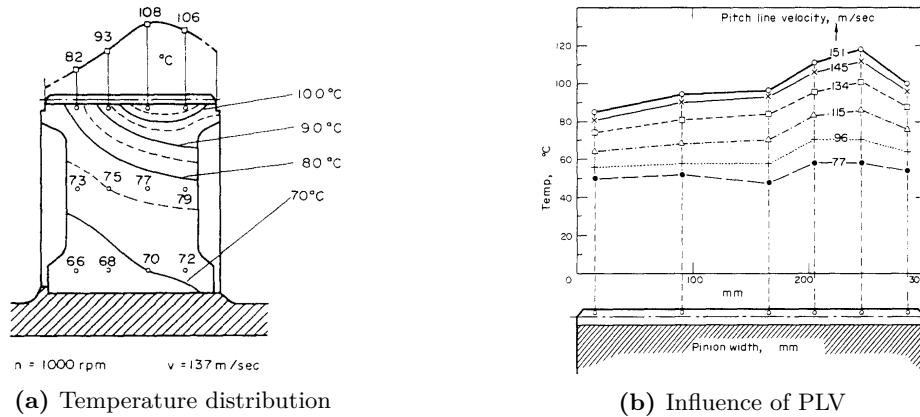


Figure 2.13: Temperature field of a high speed helical gear [21]

The most important research work on the temperature distribution of high speed gears was carried out by Matsumoto et al. [20]. In this work, the authors investigated the temperature field of high speed helical gears at PLV up to 150 m/s and output power of 1100 kW. The authors found that the thermal disturbance is a function of the square of PLV (see Figure 2.14), while the influence of torque on temperature can be small; which is also supported by the experimental evidence by Handschuh and Kilmain already shown in Figure 2.12b.

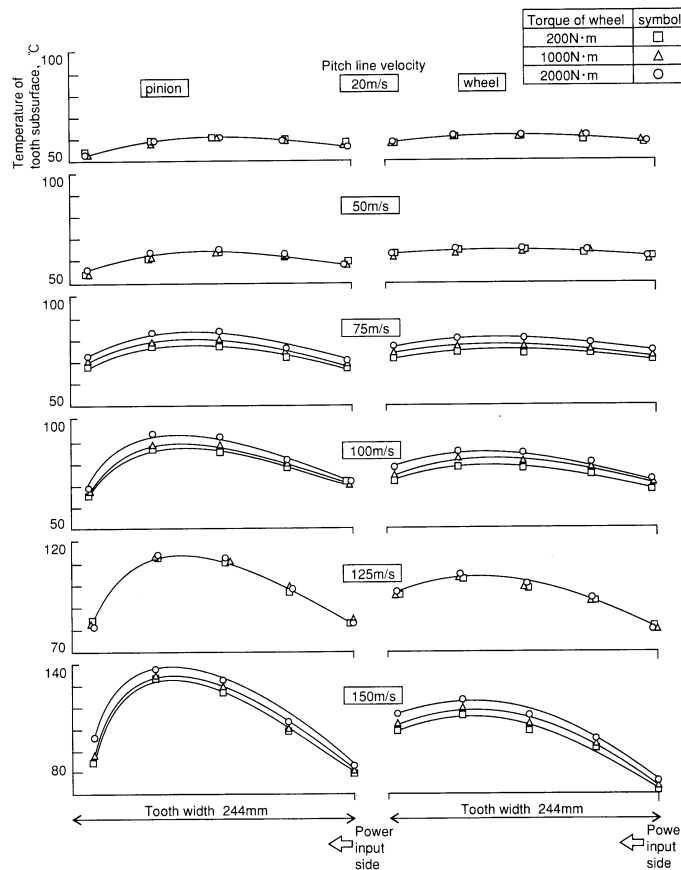


Figure 2.14: Temperature distribution relative to PLV and torque [20]

However, in a previous study by Akazawa et al. [121], the authors did not observe such temperature difference along the tooth trace. In this work the influence of the position of oil spraying nozzles in helical gear temperature distribution was experimentally studied, with a very similar test setup to that used by Matsumoto et al. in [20]. Nevertheless, their results didn't show an uneven temperature distribution along the face width, even at the highest PLV (160 m/s). After analysis of both configurations the only difference turns out to be the sense of the rotation and the teeth helix direction; which suggests that the non-uniform temperature distribution is closely related to these parameters. Yet, the author has not found additional experimental evidence on these variables except in double helical gears, where the temperature distribution is somewhat different.

Several authors [18, 90, 122] showed that in double helical gears, some combinations of rotating sense and helix direction could result in unfavourable temperature distribution. One combination results in “mesh in” engagement, by which the contact line of the gear mesh moves from both edges towards the gap. Opposite to “mesh in”, if the gear mesh starts at the gap and meshes out towards the edges of the face width, the combination is known as “mesh out”. In the first condition, the stream of the fluid flow is pumped from both sides of the gear towards the gap; producing a temperature increase in the middle of the gear while the ends are cooler due to increased forced convection heat transfer on the side faces. Contrarily, in the second condition, fluid is pumped away from the gap towards the tooth ends and therefore heat in the middle of the gear is dissipated rapidly. Both temperature distributions are presented in Figure 2.15.

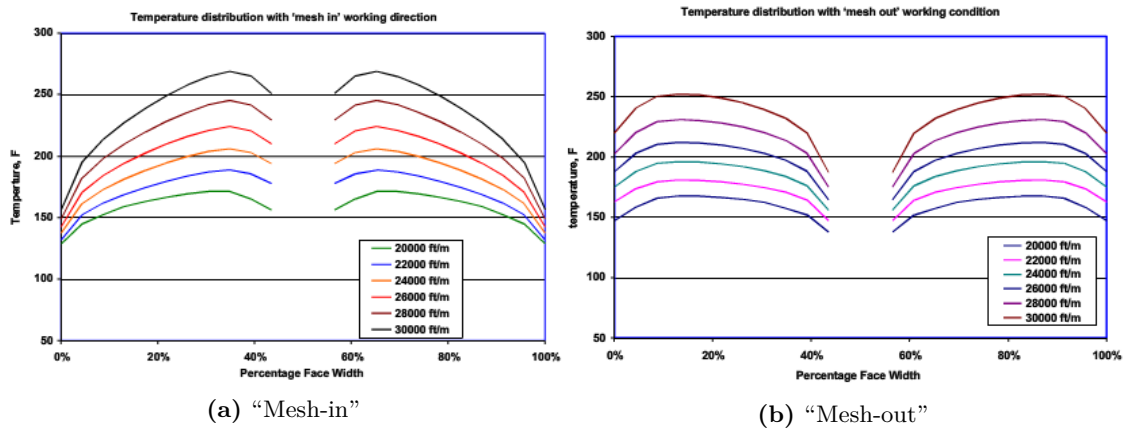


Figure 2.15: Temperature difference in “mesh-in” and “mesh-out” situations [122]

More recently, Handschuh et al. [123] conducted experiments in double helical gear sets with both oil pumping directions, inward and outward. Their study confirmed that the outward pumping arrangement had the lowest temperature at the gap locations while the inward pumping configuration had an increase in temperature towards the tooth gap. Moreover, in Handschuh et al.'s work a comparison between double helical and single helical gear temperatures and performance can also be found. Results showed that double helical gears with outward pumping arrangement, give the highest performance and lowest temperatures than its single-helical counterpart.

2.2.2 Analytical and numerical studies

Analytical or numerical studies on gear temperature distribution have usually been focused on either the prediction of the accurate surface temperature distribution or the overall bulk temperature rise. Finite element models are commonly used for the former (e.g. [124]) while thermal lumped parameter models prevail for the latter (e.g. [125]).

Up to date, very few numerical models have been developed for the analysis of temperature distribution in gears. Fundamental finite element simulations by Patir and Cheng [126] and El-Bayoumi [127] on steady-state and transient temperature distributions respectively, analysed radial thermal gradients in spur gear teeth. Authors found that, contrary to the popular assumption that the bulk temperature is constant along the tooth, appreciable temperature gradients may exist. At high cooling rates, mesh frictional heat is dissipated by convection from the tooth face rather than by conduction towards the body. As a consequence high temperatures are confined to a thin layer below the loaded flank which is consistent with experimental findings by Knauer [118]. If on the contrary, cooling rates are reduced, the shape of the gradient is relaxed (see Figure 2.16) and temperatures are almost constant. This conclusions were later validated experimentally by Townsend and Akin [128] who analysed the influence of jet impingement depth on temperature distribution.

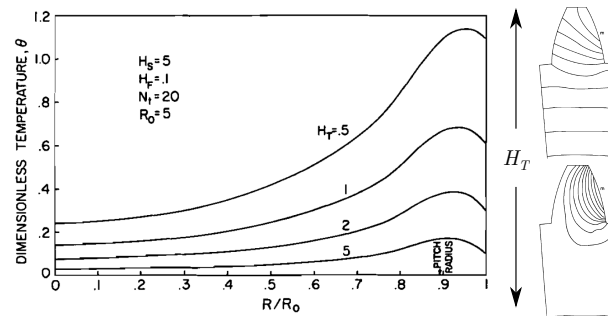


Figure 2.16: Transverse temperature distribution in gear body and tooth (adapted from [126])

Grekoussis and Retzepis [129] further developed Patir and Cheng's model to analyse the temperature distribution on the flank surface of pinion and gear, while Mihailidis and Bakolas [130] analysed the steady state temperature fields in gear pairs including the influence of adjacent teeth. Years later, Long et al. [131] presented one of the most interesting works on the topic. The authors analysed the influence of operating conditions and tooth geometry on frictional heat flux, average heat transfer coefficients and temperature distribution of narrow high speed spur gears. It was found that increasing the face width by a factor of three, increases the maximum surface temperature as much as 35% because the generated heat concentrates in the middle of the face width and it is not dissipated by the cooling oil. Similarly, it was shown that surface temperature increases with the normal module but so does the heat transfer coefficient; as a consequence, maximum temperature may increase or decrease depending on the composite effect. Finally, Long et al. stressed the influence of precise calculation of frictional heat flux (i.e. friction coefficient), while the effect of deviations on surface heat transfer coefficient were not as important.

Figure 2.17 summarizes some of the results of the simulations by Long et al. [131]. It is interesting to remark that, effectively, thermal gradients increase with speed due to the effect of the enhanced cooling rate as shown by Patir and Cheng [126]. Furthermore, the differences between the maximum and minimum surface temperatures also increase with speed, which is consistent with experimental findings by Niemann and Lechner [111].

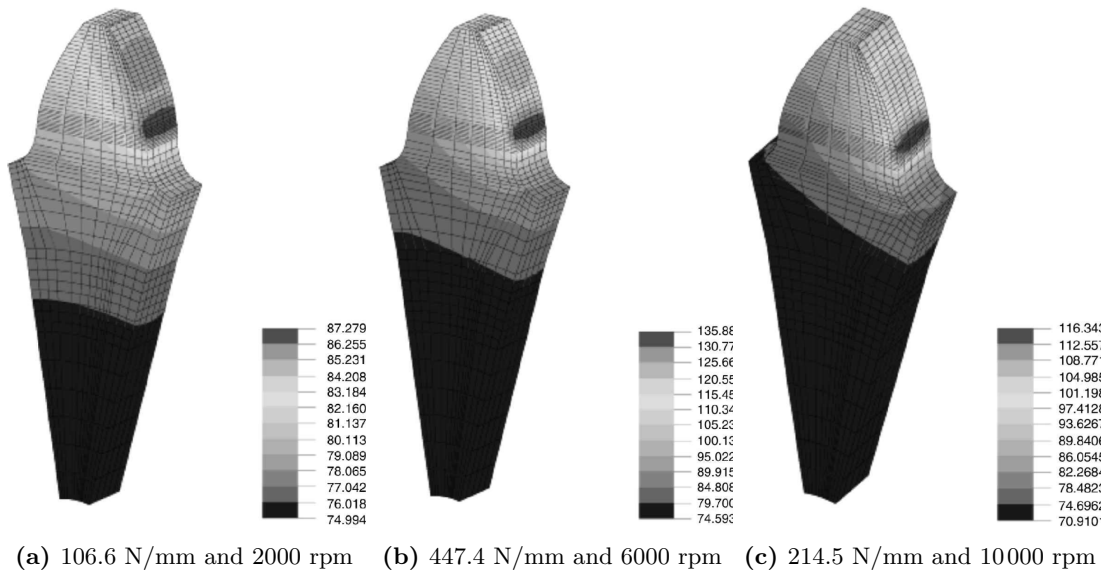


Figure 2.17: Influence of speed and torque on 3D temperature distribution of spur gears [131]

Recently, Luo and Li [132] studied the influence of pressure angle, profile shift coefficient and tooth modifications in the mesh frictional heat flux and the resulting temperature distribution. Furthermore, in a second publication, Tian and Li [133] pointed out that longitudinal temperature distribution on the pitch cylinder is not constant but rather parabolic, with the maximum temperature located in the middle of the face width and minimum symmetric values on both edges provided that load distribution is uniform. This point was also discussed by Patir and Cheng [126] and Long et al. [131].

Subsequent publications by Li dig into the conditions that produce non-symmetrical temperature distributions. For instance, it has been shown that in helical gears, temperature distribution is no more symmetric in the tooth trace direction due to local heat flux differences [134]. Similarly, manufacturing or assembly errors produce local pressure increases that affect heat flux patterns and temperature distributions [135].

Finally, it must be outlined that although the use of finite element models for the prediction of temperature field in gears is customary, other methods have also been proposed in scientific literature such as the finite difference method (e.g. [136]), the thermal network method (e.g. [137]) or purely analytical methods (e.g. [138]). However, the degree of accuracy of these models with respect to the finite element method is usually reduced in favour of the enhancement of computational time. In this sense, thermal lumped parameter models are a good compromise between accuracy and performance and the number of publications on the method is a good indicator of its interest (e.g. [120, 125, 137]).

2.3 Thermally induced teeth geometry distortion

According to Henriot [26] temperature increase modifies involute geometry of gear teeth due to base diameter expansion, leading to a base pitch error and a pressure angle deviation of the flank with respect to that initially manufactured. Moreover, if a temperature mismatch between pinion and gear exists, a relative profile slope and tooth pitch deviation arises and as a consequence, tooth contact behaviour is no longer uniform as shown by Sigg [24]. Depending on the temperature distribution of the gear pair, additional effects may superimpose on the latter (e.g. housing expansion) and lead to transmission failure as shown in Figure 1.5. In order to analyse the effects of the different types of thermally-induced geometry distortion, the following classification is proposed for this section:

1. Transverse profile distortion
2. Thermally-induced longitudinal deviations
3. Other sources of thermal distortion

Furthermore, it is to be noted that these deformations are added to those caused by purely mechanical strain and therefore, their composite effect must be closely observed.

a) Transverse profile distortion

Temperature increase of the gear produces a thermal expansion of both, gear body and teeth. If thermal gradients are neglected, such expansion is purely radial; and if gear size is sufficiently large, the order of magnitude of the dilatations is comparable to that of manufacturing deviations or tooth modifications. From the close analysis of Figure 2.18 it is concluded that the tip of the pinion distorts more than the root due to the greater radius and therefore, premature contact should be expected in meshing gear pairs. In effect, according to Welch and Boron [18] and Akazawa [121], the observation of tooth contact pattern records after full power operation on gears known to have excessively warm pinions, clearly show a strong root heavy marking on the teeth of the mating gear wheel in spite of being profile-corrected, which is explained by gear tip premature contact.

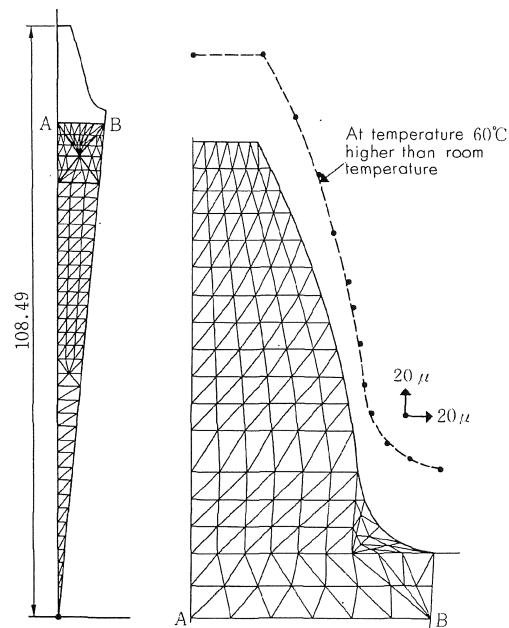


Figure 2.18: Order of magnitude of thermal growth with constant temperature increase [121]

Thermal growth at constant temperature increase is ruled either by gear size or by material's linear expansion coefficient. Therefore, one would expect thermal distortion in steel gears to become noticeable only in large wheels, typical from turbo-machinery industry, or in plastic gears, where not only thermal expansion coefficient is large but also mechanical properties are ruled by temperature.

Literature review has shown that metallic gear teeth thermal expansion has not received much attention, although there are some references to thermal distortion in plastic gear teeth. One of the most detailed analysis of the influence of temperature in plastic gears is the research work developed by Wang [139]. Wang carried out a finite element study of non-metallic spur gears in mesh and concluded that in plastic gears, the static transmission error, composite torsional mesh stiffness and load sharing ratio, depend strongly on both input load and temperature. He concluded that as a consequence of temperature increase, tooth load sharing can be widely expanded covering more than a complete mesh cycle with more teeth coming into the contact zone (triple contact) so that the gears will be running smoother (relative to transmission error and load share). The influence of temperature in mesh stiffness and load sharing ratio in Nylon PA6 gears is shown in Figure 2.19.

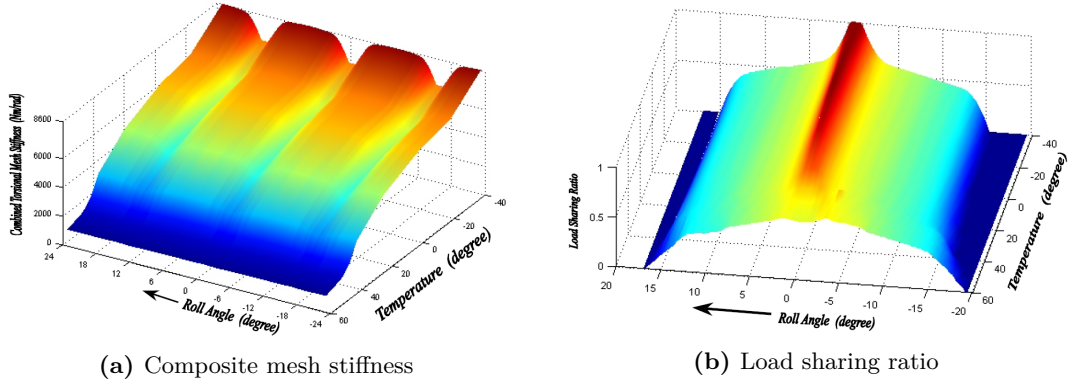


Figure 2.19: Effect of temperature on composite torsional mesh stiffness and load sharing ratio in Nylon PA6 gears under 50Nm torque [139]

Similarly, in a recent study Kashyap et al. [140] analysed experimentally the thermal expansion of Acetal spur gear teeth by heating them up and measuring their profile with a coordinate measuring machine (CMM). The authors found that geometry change is mainly due to local pressure angle deviations as shown in Figure 2.20, and they proposed two analytical methods to compute the distorted geometry. Unloaded transmission error behaviour of such gears was analysed following the latter and the authors concluded that *PTP* transmission error at elevated temperatures is significant in plastic gears; in the order of 3.2 μm for the considered gear geometries.

According to one of the analytical methods proposed by Kashyap et al. [140] the outside diameter, tooth thickness and pressure angle slope increases with temperature in a linear manner (see Figure 2.20) and therefore, the new pitch diameter, d' , normal module, m'_n and tooth thickness, s'_c , resulting after thermal expansion, can be calculated as follows.

$$m'_n = d'/z \quad (2.29)$$

$$d' = d \cdot (1 + \alpha_L \cdot \Delta\Theta_b) \quad (2.30)$$

$$s'_c = s_c \cdot (1 + \alpha_L \cdot \Delta\Theta_b) \quad (2.31)$$

Where α_L is the coefficient of linear thermal expansion and $\Delta\Theta_b$ is the bulk temperature increase with respect to ambient temperature.

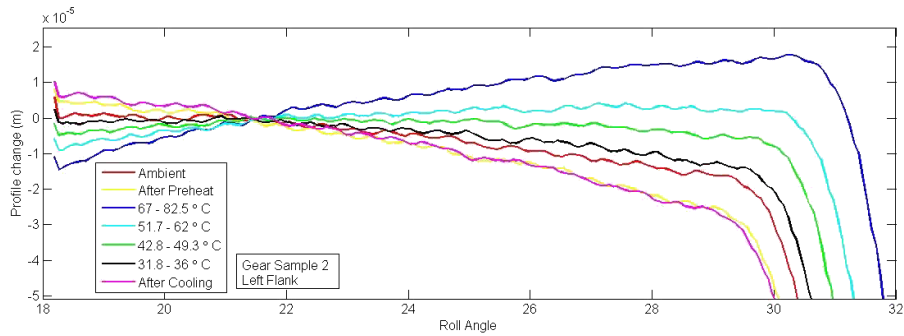


Figure 2.20: Involute profile deviation with temperature increase [140]

Although, the thermal properties of plastics are different from metals' (higher coefficient of expansion, smaller conductivity, etc.) the same trends are expected in steel gears which are usually subject to higher temperatures than its plastic counterparts. Furthermore, similar equations to those presented above were already introduced by Henriot [26] for steel gears three decades before. Henriot additionally related temperature increase to base diameter expansion, pressure angle reduction and pitch error. From his equations it is possible to estimate the order of magnitude of thermal distortion in steel gears. For instance, for a 100 mm pitch diameter gear subject to a 100°C temperature increase, flank normal deviation at the tooth tip is approximately 32 μm which is not negligible.

Similarly, Sigg [24] described years before the thermal effects on large size speed increasing/decreasing transmissions and related temperature differences between pinion and gear teeth to relative pitch deviations. He noticed that temperature increase produces a profile slope deviation and base pitch error which increases engagement shock. Although Sigg did not provide any equation relating errors, his comments on profile distortion are consistent with equations from Henriot [26]. What's more, Sigg [24] highlighted the composite effect of tooth deflections under load and thermal dilatations, and he concluded that in a reduction gear unit both effects tend to compensate each other while in a speed increasing one these two effects are additive.

Years later, Akazawa [121] measured a maximum temperature difference between pinion and gear of 40°C in turbo-gears running at PLV of 200 m/s and concluded that such thermal gradient also brings about a difference in the normal pitch between the pinion and the wheel that affects the smooth running of the gear set. His conclusions are consistent with previous findings by Sigg and Henriot, and additionally, Akazawa related temperature differences with gear ratio, thus indicating that transmissions with large gear ratios are sensitive to pitch errors.

Even though, references on thermally-induced geometry distortion of middle-size steel gears is scarce, recently Hensel et al. [141] have shown that temperature increase can also affect gears from automotive industry when design contact ratios are close to an integer value. In this study, transmission error harmonics were calculated for several gear designs, torque and temperature levels; where thermally-induced profile distortion was calculated following Equations 2.29 to 2.31 by Kashyap et al. [140]. The authors found that some gear sets were sensitive to temperature increase; and further analysis of results, showed a clear correlation between transverse contact ratio and temperature on transmission error harmonic behaviour as shown in Figure 2.21.

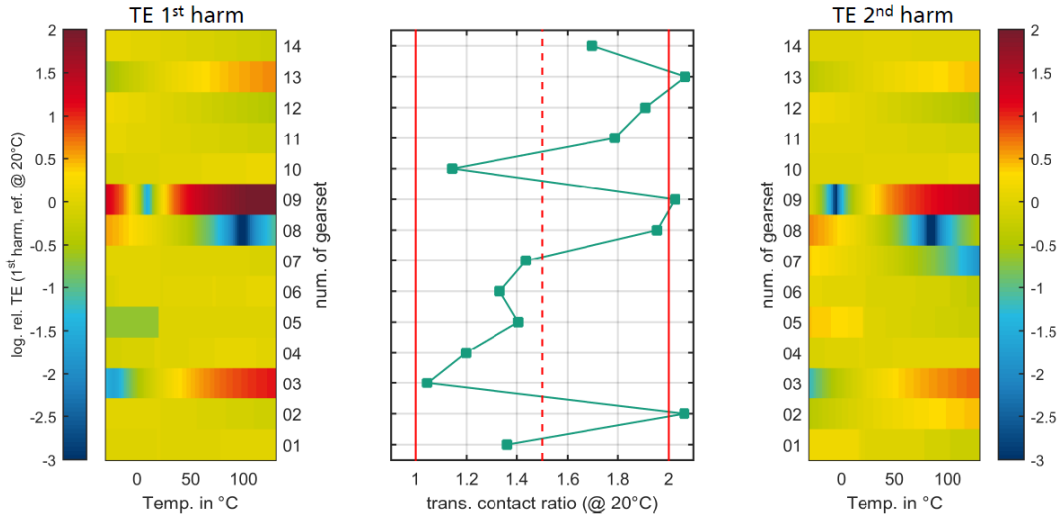


Figure 2.21: Sensitivity of TE harmonics to temperature increase and correlation to transverse contact ratio according to Hensel et al. [141]

Hensel et al. [141] did not provide a clear explanation for this behaviour and it was attributed to backlash reduction. However, it is possible that tip diameter expansion caused by temperature increase extends the length of the path of contact and thus, affects real contact ratio. If the latter is already in the vicinity of an integer value, composite effect of load and thermal growth produce a shift over the closest integer thus influencing transmission error harmonic behaviour.

In the same direction, a very recent experimental study by Luo and Li [142] on FZG type C-PT gears has shown that temperature affects vibration amplitude of the system through thermally-induced profile deviations; with temperature increases yielding larger vibration amplitudes. Furthermore, the authors state that the resonance frequency of the system is also affected by temperature as it changes meshing stiffness as well. Similarly, a series of studies [143–150] have also related gear teeth profile thermal distortion to transmission error behaviour, backlash reduction and even contact stresses. Although some of the ideas described in these articles are interesting, the hypotheses are not clearly stated and the results need further experimental or numerical validation.

b) Thermally-induced longitudinal deviations

In high speed transmissions with gear ratios other than unit, the pinion will have a higher average temperature than the mating gear. In these applications, helical gears are usually designed and therefore, profile slope deviations are followed by helix angle distortion.

Sigg [24] and Henriot [26] described the effect of a constant temperature increase on helix angle and showed that in large face width helical gear teeth, contact patterns are shifted towards the leading edge due to the composite effect of load and temperature. However, the thermal distortion of the helix is not clearly understood. Sigg [24] concluded that thermal gradient between pinion and gear causes a difference in base pitch, while helix angle remains unchanged. On the contrary, Henriot [26] claims that the relative thermal expansion in the axial direction produces a change in helix angle leading to an

helix mismatch. In both cases, the result is the same; with heavier tooth contact towards one of the ends. In the case of single helical gears, the relative thermal distortion can compensate gear teeth and body bending and torsion deflections; but in double helical gear sets, the effect can be more complex as shown in Figure 2.22.

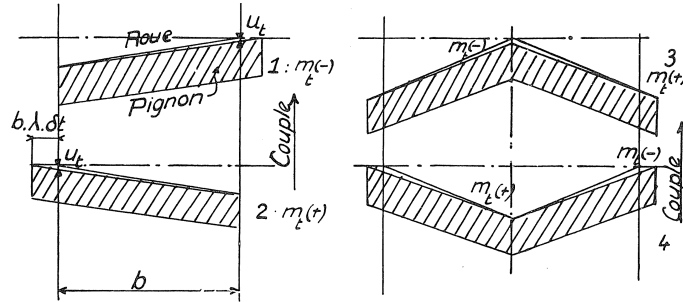


Figure 2.22: Relative helical teeth distortion according to Henriot[26]

Besides, Henriot [26] proposed to evaluate the severity of this load concentration with the “thermal distortion factor”, which is the ratio of the relative thermal distortion, u_t , to the total teeth deformation under load. The former is measured in the base tangent plane as shown in Figure 2.22 and it can be calculated following Equation 2.32, while the latter is computed as usual, by considering gear teeth stiffness and local loads [27].

$$u_t = (b \cdot \lambda \cdot \delta_t) \cdot \tan(\beta) \tag{2.32}$$

where, following the nomenclature in Figure 2.22, b is the face width, β is the helix angle, λ is the coefficient of linear thermal expansion and δ_t is the temperature difference.

However, as shown in Section 2.2 temperature increase in large face width helical gears is not uniform and longitudinal thermal gradients exist. Matsumoto et al. [20] found that the tooth root bending stress correlates to PLV, as an increase of the latter produces higher strain as shown in Figure 2.23. This behaviour was attributed to non-uniform temperature increase with bending stresses affected by thermal deformation. The contact pattern shift presented in Figure 1.4 is a physical evidence of this conclusion.

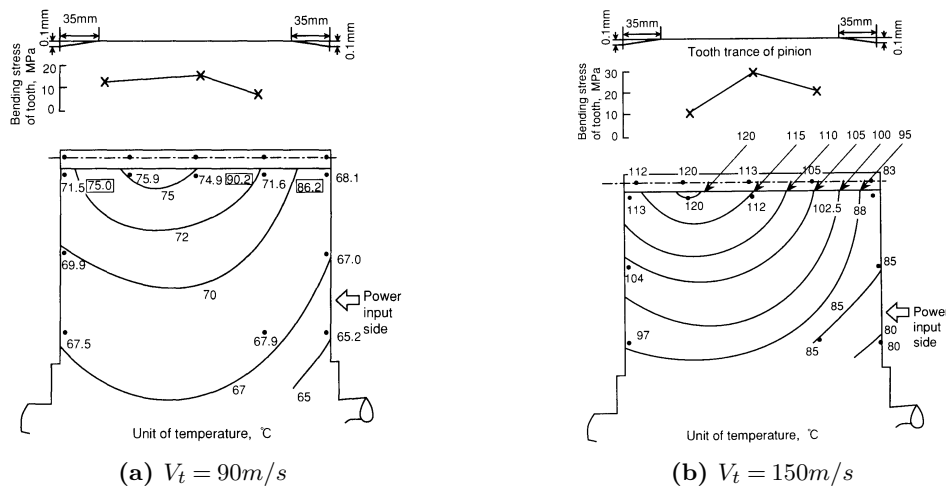


Figure 2.23: Relationship between temperature and tooth root stress in large face width helical gears subject to high pitch line velocities [20]

In a second report, Tozaki and Matsumoto [151] developed a calculation model for the load distribution in high speed helical gears by adding the temperature distribution and the thermal distortion to a conventional gear tooth contact calculation model which only took into account mechanical deflections. The results of this study confirmed that including the acceleration of the lubricating oil, along with the frictional losses and the thermal distortions in gear and shaft, predicted temperature distribution and tooth root stresses favourably.

In double helical gear sets, additional effects take place in the longitudinal direction. Temperature distribution in these gears is ruled by the engagement direction as shown by Wang [122]. In the “mesh-in” condition, the gap is usually hotter than the ends thus giving rise to a differential thermal expansion of the centre of the gear and producing the “barrel” shaped pitch cylinder depicted in Figure 2.24. Such thermal distortion may lead to a higher load per unit of length of face-width near the gap and a reduced unit load near the ends. This behaviour is consistent with experimental findings by Welch and Boron[18] who analysed the effect of tooth loading direction and temperature differentials on double helical gears by measuring tooth root strains. Results showed that longitudinal thermal gradients in these gears tends to affect tooth stresses in a triangular shape, with increasing values towards the gap or the ends, and leading to a heavy marking of the teeth in these regions.

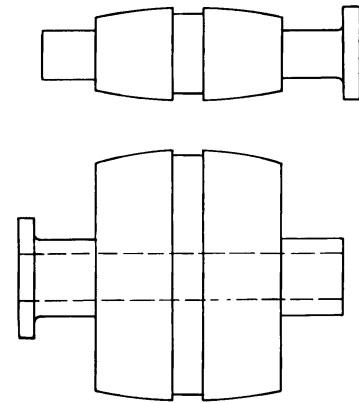


Figure 2.24: Barrelling of high speed double helical gear set [18]

Longitudinal load distribution in double helical gears is very sensitive to thermal gradients. Hayashi and Sayama [152] simulated the influence of a 5°C temperature difference between pinion and gear on longitudinal load distribution. Analytical results, depicted in Figure 2.25, predicted a considerable unit load variation at the helix ends. This effect, is superimposed to that caused by longitudinal thermal distortion and therefore, tooth root bending stresses can either be compensated or considerably increased.

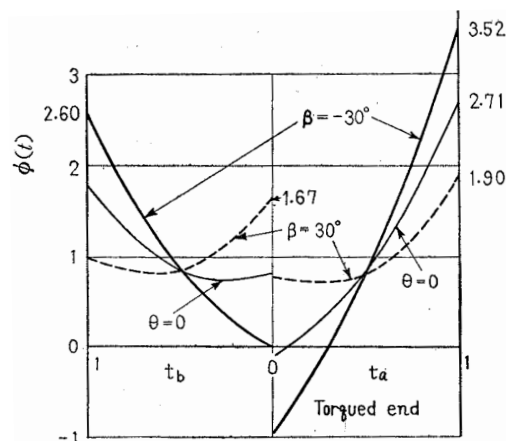


Figure 2.25: Effect of 5°C temperature difference between pinion and gear on longitudinal load distribution of double helical gears [152]

Finally a different theory for thermally-induced geometry distortion was proposed recently by Amendola [8]. The author suggests that localized temperatures across the tooth flank can reach levels that cause metallurgical transformation wherein entrained austenite transforms to martensite. This transformation results in an expansion of the case material thereby affecting the tooth thickness which results in a contact pattern change on both the loaded and non-loaded flanks. The mechanism of expansion is the result of the density difference between austenite and martensite; and it does not occur in a uniform manner since the temperature rise is asymmetrical over the tooth length. This theory is interesting as it helps to understand why thermally-induced geometry distortion in these gears does not disappear at ambient temperature after full power operation as shown in Figure 2.26.

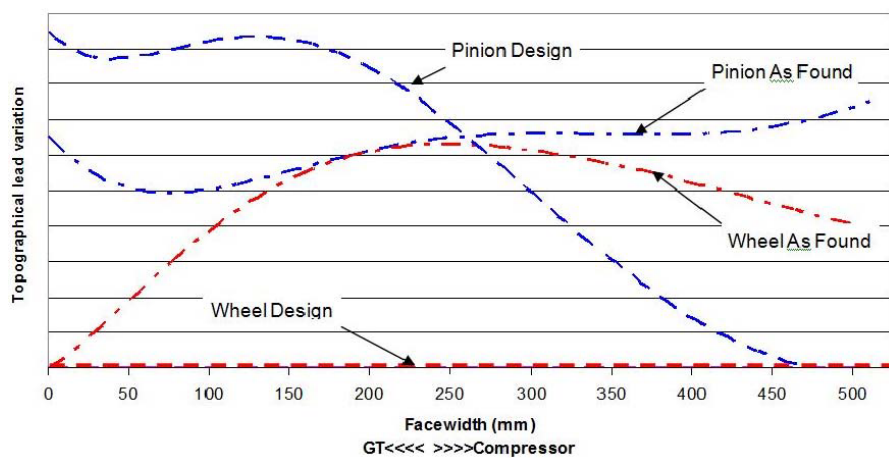


Figure 2.26: Thermal distortion of high speed helical gears due to material transformation [8]

It has been observed in this section that the great majority of research works on helical gear teeth thermal distortion are experimental and almost all of them date back to the past century. Very few recent work exist on the topic. In this sense, Wang [153] has lately provided a transformation matrix to calculate the position of the active tooth surface after thermal distortion. The author performed a sample calculation of the thermally-distorted geometry in a high speed helical gear application subject to a predefined temperature field. Although the concept is very interesting from the analytical/numerical simulation point of view, the study needs further refinement as the effect of helix angle is not clearly stated and the influence of temperature gradients and thermal stresses is not discussed. Similarly, a recent publication by Wang et al. [154] claims that the composite effect of thermal and mechanical strains influences contacts stresses significantly. However, there is no information on the temperature field, the finite element modelling assumptions are not described and the influence of radial and longitudinal gradients is not discussed.

c) Other sources of thermal distortion

The finite element study by Howells and Sciarra [155] proved that housing thermal expansion plays an important role in tooth contact when casing material is different from that of gears. The Vertol CH-47C helicopter transmission casing used in their study is made of magnesium, whose coefficient of thermal expansion doubles that of steel. The bearing outer races which are press-fitted into the housing result in a "floating" fit at operating temperatures due to the differential thermal expansion between the magnesium case and the bearing's steel outer races. Besides, housing thermal distortion produces gear mesh misalignment which has a detrimental effect on gear teeth contact, specially when bevel gears are considered due to the displacement of their cone centres. The composite effect of bearing clearances and gear centre distance expansion for this application is depicted in Figure 2.27 where the order of magnitude of the thermal distortion is also indicated. Furthermore, according to Dudley [14], in jet lubricated high speed helical gears, the oil-air mixture that is being pumped towards the exit of the mesh strikes the inner wall of the casing overheating it. The temperature difference between front and rear walls additionally misaligns gears and modifies load distribution as well.

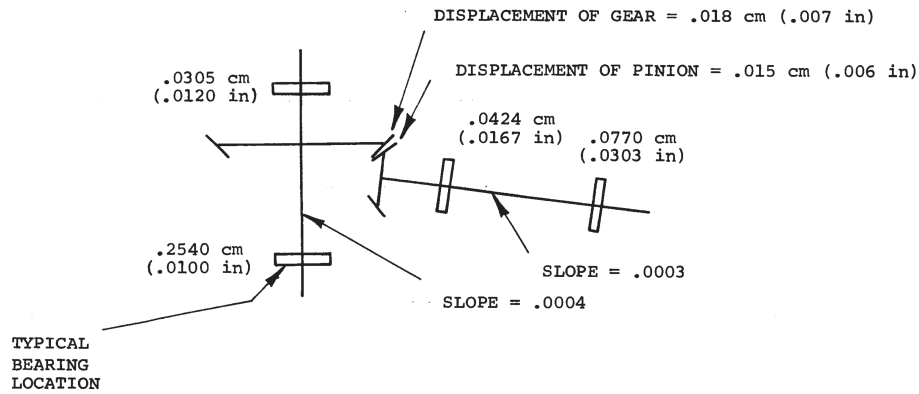


Figure 2.27: Displacements of internal components due to housing thermal growth [155]

The expansion of the housing, in combination with gear thermal growth, is also known to affect available backlash. DIN 3967 standard [156] calculates working backlash for a constant temperature increase taking into account that the expansion of the housing is different from that of the gears. The amount of backlash modification due to temperature rise can be calculated following Equation 2.33:

$$\Delta j_{wt} = a_w \cdot (\Delta\Theta_H \cdot \alpha_{L,H} - \Delta\Theta_G \cdot \alpha_{L,G}) \cdot 2 \cdot \frac{\tan(\alpha_n)}{\cos(\beta)} \quad (2.33)$$

where Δj_{wt} is the amount of working circumferential backlash modification due to temperature rise, $\Delta\Theta_H$ and $\Delta\Theta_G$ are the temperature increase of housing and gear respectively, α_H and α_G are the linear coefficients of thermal expansion for both and α_n and β are the normal pressure angle and helix angle respectively.

Similarly to the helicopter housing dilatation effect on bevel gear contact, shaft thermal growth can also influence bevel gear mesh behaviour. The experiments conducted by Terauchi et al. [157] proved that the thermal expansion of the shaft affects tooth contact pattern, gear tooth fillet stress and bearing preload in such gears. The tests were conducted at constant tooth load of 400 Kgf and variable speeds from 225 rpm to 1875 rpm. Displacements of the gear in the three directions were measured and bearing preload variation was recorded. Results, depicted in Figure 2.28, showed that preload increases with operating time and that axial displacements were significant in the direction of the apex, while the displacements in the horizontal and vertical directions did not vary.

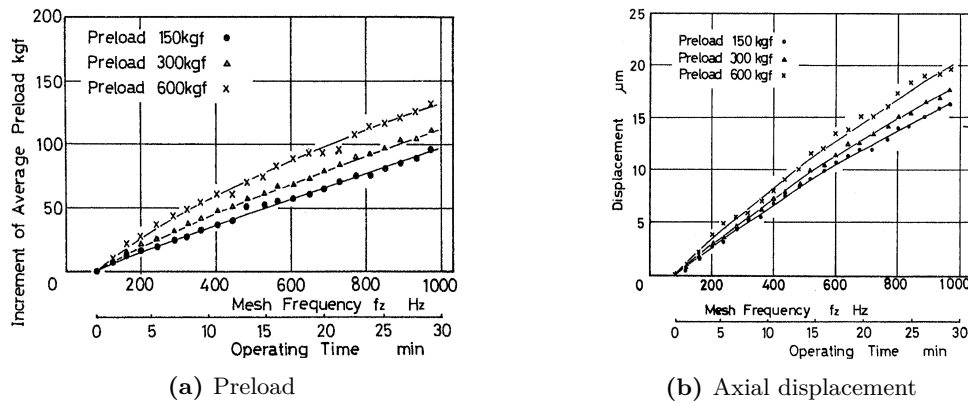


Figure 2.28: Effect of shaft dilatation on bearing preload and bevel gear apex displacement [157]

Shaft thermal expansion does not only affect bevel gears. Eldridge et al. [158] presented a series of examples in double helical gears showing that shaft transient thermal expansion can consume the axial clearance in the gearset and bind the mesh; which results in a gear set running without backlash. In the first example, depicted in Figure 2.29, the pinion undergoes a substantial axial displacement, as much as 0.43 mm. The comparison of pinion and gear positions reveals that the former moves considerably further axially than the latter due to transient thermal growth, leading to gear jamming if axial dilatation is large enough. The mechanical coupling of torsional and lateral motion results in the torsional vibration producing a lateral response; and depending on the stiffness of the bearings varying levels of lateral response were measured.

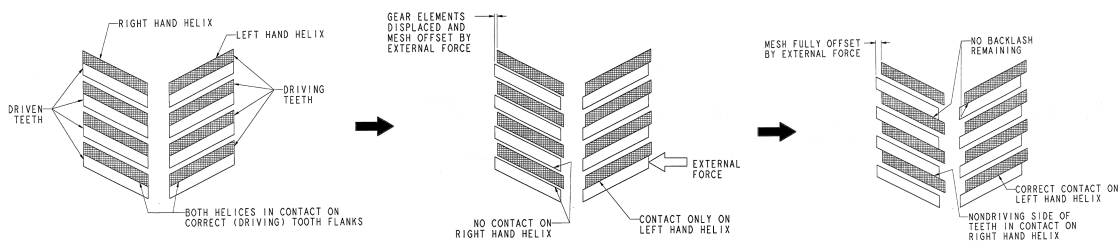


Figure 2.29: Double helical gear mesh axial bound due to shaft thermal growth [158]

2.3.1 Compensation of thermal distortion

As it has been described at the very beginning of this chapter, under normal circumstances gear teeth profile and helix are assumed to be deflected only under the effects of load. However, it has been shown that temperature differences do exist in gear pairs which cause pitch errors, profile slope deviations and helix angle mismatch, leading to non-uniform load distributions. In some cases, specially in helical gears running at the highest speeds, uneven temperature distributions exist across the face with as well and contact conditions are even more detrimental, with bearing patterns localized towards the tooth ends accelerating tooth failure. To ensure a uniform tooth contact under these conditions, profile and longitudinal corrections must be applied to pinion and gear teeth.

Literature review shows that currently there is no analytical or numerical method to predict load distribution due to thermal distortions and hence tooth modifications can't be designed beforehand. Although some standards such as AGMA 927 [27] consider including thermal effects in the future, current standards suggest in-site full speed and full load dynamic tests to observe the cumulative effect of gear tooth deviations, deflections under load and temperature on contact pattern before applying tooth modifications [12].

Much of the field knowledge is not available in the open literature and therefore, it is not possible to fully understand the effects of uneven temperature distribution on load distribution. Among the few published studies reference [24] by Sigg from Maag Gear Company gives some valuable guidelines to cope with the thermal distortion phenomena. In this AGMA fall technical meeting report, the author suggests calculating the base pitch deviation of the pinion relative to the gear due to temperature differences between both. Corresponding profile corrections are made by changing the inclination of the tolerance zone as shown in Figure 2.30, that is by modifying profile slope.

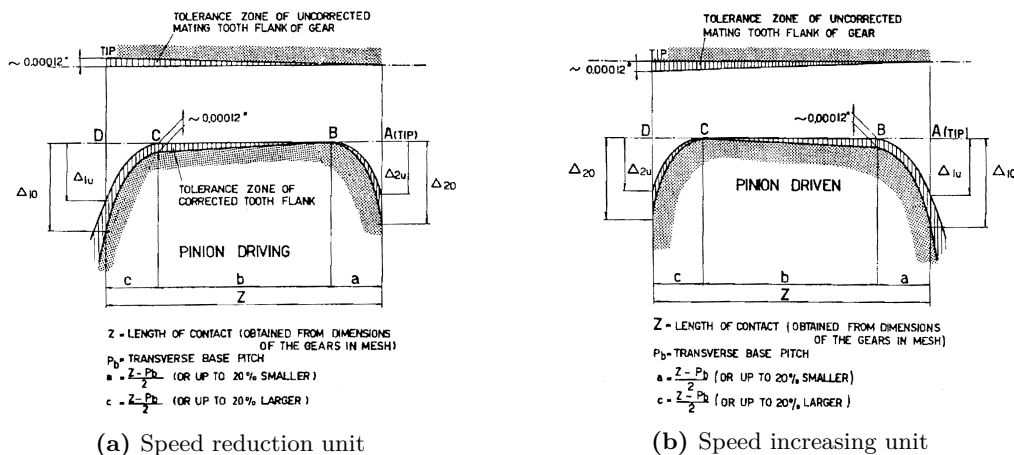


Figure 2.30: Profile correction recommendations to compensate temperature increase effects [24]

According to the author, in the case of speed reduction units the higher temperature of the pinion produces a larger base pitch and this effect helps in reducing tooth engagement shock because the effects of temperature difference and tooth deflection tend to compensate each other. On the contrary, in speed increasing units the situation is reversed, increasing tooth engagement shock because the effect of deflections under load and temperature are additive. In order to compensate thermal distortion effects in both cases Sigg [24] suggested the profile correction guidelines presented in Figure 2.30.

Furthermore, Maag Gear Company [159] also points out that the unequal heating of the gear pair influences mesh alignment in service as the pinion tooth assumes a slightly smaller helix angle due to larger temperature increase than its mating gear. Thus, to compensate this effect, the pinion is designed with a steeper helix angle. However, no recommendation is provided on the amount of modification and therefore, field experience is required to design such tooth corrections.

In the study by Martinaglia [21], the author considers that the thermal distortion of the pinion is large but also irregular so that the desired even load distribution must be ascertained by means of special concave/convex longitudinal flank corrections. Figure 2.31 presents the layout of the flank line correction for high PLV gears with cumulative thermal distortion problems. The degree of correction of these gears is in the order of 40 μm .

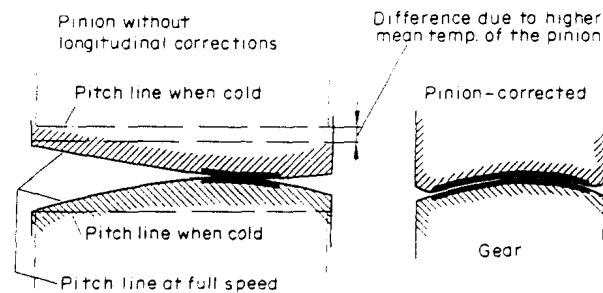


Figure 2.31: Flank line correction to compensate for thermal expansion [21]

Nageli [22] also points out that in these gears thermal distortion is higher in magnitude than mechanical deflections and therefore tooth modification is mandatory. Furthermore, if composite effect of mechanical loads and thermal effects is considered in Figure 2.32, the shape of lead modifications is very different compared to those designed to compensate purely mechanical loads. Moreover, Nageli performed a sample safety calculation of a turbo gear set including and neglecting lead modifications. Results showed that tooth corrections reduced face load factor from 1.7 to 1.1 increasing contact stress and bending safety factors from 1.9 to 2.4 and from 2.2 to 3.4 respectively.

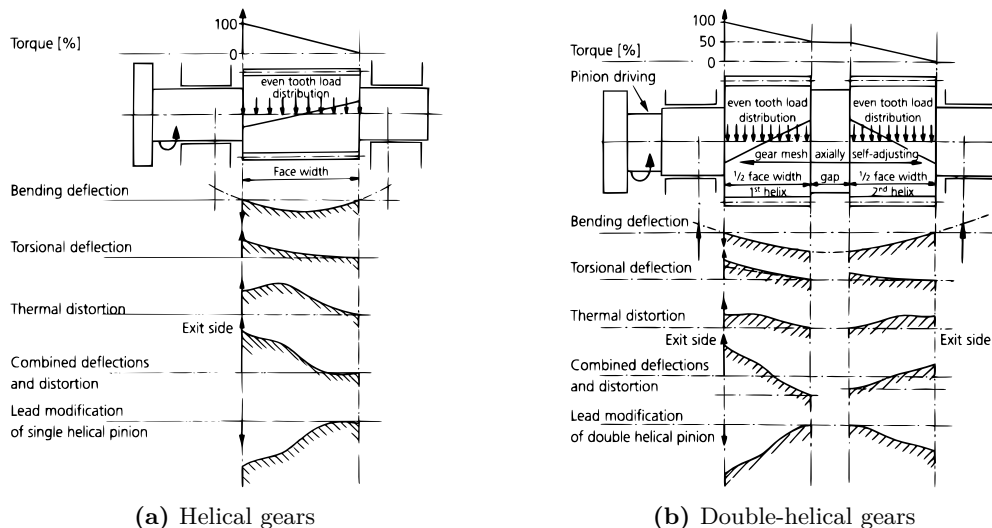


Figure 2.32: Lead modification guidelines to compensate thermo-mechanical deviations [160]

In a more recent paper, J.B. Amendola [8] also suggests adding a deep lead correction in the highest temperature gradient particularly for wide face helical gears at high PLV. Although it may not be the optimum lead correction it eases the stress on the lube oil film as it is squeezed through the mesh in the hottest section of the flank, thereby reducing the tendency of varnished particles adhering to the gear teeth in that regime [8]. It will not however appreciably change the heat gradient or shift the hot section.

Finally, current ANSI/AGMA 6011 [12], API 613 [161] and ISO 13691:2002 [162] standards also indicate that gears with pitch line velocities in excess of 100 m/s are susceptible to thermal distortion and consideration should be given to helix modifications in such cases. According to all standards if the total helix mismatch, including combined bending, torsional deflection and thermal distortion of the tooth and rotor, exceeds 25 μm for through hardened gears, or 15 μm for case or surface hardened gears, then helix modification should be applied to provide a uniform load distribution across the entire face width. However, there is no method currently available to predict the composite effect of mechanical and thermal loads and therefore, gearbox testing at full power is required to determine the shape and amount of modification.

2.4 Critical review of the state of the art

The review of the state of art has revealed that gearbox thermal distortion does affect load distribution, mechanical stresses and transmission error. However, most of the references point towards high speed large size gears from the oil and gas industry, where most of the knowledge is the result of years of field experience devoted to the analysis of bearing patterns [13]. In such cases, the method to predict tooth load distribution and corresponding tooth modifications is strictly empirical [162] and any attempts to correlate temperature distribution to thermal distortion have been deemed useless [13]. Furthermore, very few up-to-date publications are available in the open literature as most of the references are 30 years old (or more) and much of the data still remains unpublished due to proprietary reasons (e.g. [163]). As a consequence of this lack of information, it is not possible to fully understand the thermally induced geometry distortion phenomena and their interactions with mechanical deflections or tooth modifications.

Early research works by Martinaglia in 1973 [21] and more recent ones by Matsumoto in 2001 [20] experimentally showed that uneven temperature distribution across the face width is due to the axial pumping of the oil-air mixture. Such temperature difference causes an increase in root bending stress that may lead to failure [20]. On the other hand, Welch and Boron [18] and Akazawa [121] experimentally observed heavy marking of the tooth root of similar turbo gears. In both cases, the authors explain these phenomena by the teeth expansion in both directions, radial and axial, that cause a mismatch of lead and profile. Preliminary finite element analyses were conducted to predict such temperature mismatch and load increase [121, 151] but several questions remain unanswered. Although the authors do enumerate the different geometry distortion mechanisms, namely tooth expansion, helix mismatch or pitch cylinder barrelling; they do not refer to the order of magnitude of the individual profile or lead deviations and their composite effect when pinion and gear are considered. Moreover, their results only refer to helical gears and the impact of temperature increase on spur gear contact remains unpublished.

In such cases, tooth modifications are applied on the basis of experience [24]. Contrary to mechanical deflections, thermal distortions are not currently predicted, hence, neither compensated for (at least in the design stage). Several research works on temperature distribution of steel cylindrical gears are found in literature (e.g. [133, 164]) but none of them calculates thermal distortion. However in the case of plastic gears, Raghuraman et al. [136] have recently studied the influence of microgeometry on steady-state temperature field and the resulting flank distortion. Although they did not compensate micro-geometry after the thermal expansion, they did show the effects of such modifications in temperature distribution. Therefore, it is expected that the inverse procedure can be applied to correct non-uniformities. Besides, if gear teeth geometry is modified at ambient temperature, considering only predicted elastic deflections, apparently those modifications are no longer valid at operating temperatures. It seems that, tooth modifications should be predicted considering both, load and temperature distributions.

It has also been shown that the temperature dependent properties of plastic gears affect considerably transmission error and load distribution [139]; and profile errors on such gears have also been experimentally confirmed [140]. Moreover, contrary to gears in the oil and gas industry, these studies have been performed in small to medium size gears with pitch diameters close to 100 mm. However, very few results on steel cylindrical gears of this size have been found. Among these, the research work by Hensel et al. [141] stands out as they showed that the harmonics of TE have a significant sensitivity to thermal changes when contact ratios are close to an integer value. Yet, these research works only considered equal temperature for both pinion and gear and the existence of temperature gradients inside the gear itself was neglected. Furthermore, Hensel et al.'s work [141] was based on Kashyap et al.'s [140] who presented two methods to analytically compute geometry distortion: i) module change and ii) profile slope change. However, Henriot [26] showed that gear teeth expansion is affected by both at the same time. At this point it seems that the gear teeth geometry distortion is not clearly understood.

It is also of interest to stress that gear pairs may be subject to different temperatures [23] and thermal gradients within the body [119]. Such temperature differences are the result of operating conditions, gear geometry and lubrication system. Gradients result in thermal stresses that affect the amount of distortion [165] and therefore a thermo-mechanical analysis must be carried out [166]. The computation of temperature distribution in cylindrical gears is usually performed by means of the finite element method [167], the finite difference method [136] or the thermal network method [168]. Although the finite element or finite difference methods provide accurate temperature distributions, the required computational time is high; therefore, such numerical models are usually devoted to the temperature field of one of the gears [167] with auxiliary elements or heat inputs being usually neglected (e.g. shafts or bearings). Additionally, convection coefficients and/or frictional heat flux are usually constant and they are not updated with transient temperatures. On the other hand, thermal network models provide fast and accurate results but the degree of discretization to compute radial and axial temperature distributions is not sufficient. In this sense, the development of a fast and reliable thermal model of the gear pair is desired, as the understanding of temperature distribution and its influencing parameters will allow to predict the amount of thermal distortion and compensate geometry deviations.

For this purpose, heat generated in the gear mesh and the surroundings must be accurately predicted. Different heat sources have been identified at the beginning of this chapter and prediction models have also been introduced. It has been observed that current research efforts are oriented towards a deeper understanding of spin power losses that dominate at high speeds; as the sliding friction losses that rule at low speeds present a significant amount of analytical and empirical solutions [34]. Different friction coefficient models have been presented in Table 2.1 and it has been shown that these models present a strong dependency on experimental conditions, especially the selected lubricants, and therefore they can't be generalized to other oils. Some authors [50] clearly state that even a small difference in friction coefficient can lead to significant errors in the prediction of power losses, and as a consequence, temperature distribution as well. Therefore, it is also of interest to develop a general tool for the prediction of friction coefficient and power losses for different oils.

Finally, it has been observed that thermally-induced geometry distortion effects seem to be limited to high speed gears. The reason for such assumption may be related to the fact that temperature increase is proportional to the square of PLV while mechanical deflections depend on torque [14]. However, if strictly examined, thermal deformation due to frictional heat generated in the gear mesh or the bearings can occur even in low-speed gears. Furthermore, temperature differences between pinion and gear have also been observed at low speeds [28] and therefore, relative pitch errors and profile slope deviations can be influential as well. From a practical point of view, it is usually assumed that thermal distortion does not affect tooth geometry in such cases but an accurate prediction of tooth contact behaviour taking thermal deformations into considerations can provide a significant advance in the calculation of the optimum tooth modifications. What's more, several articles [20, 89, 90] and standards [12, 27] support the idea of improving common loaded tooth contact analysis methods (LTCA) adding a thermal deformation calculation procedure to the conventional work-flow.

Research opportunities

The critical review of the state of art has exposed several research opportunities on the field of thermally induced geometry distortions of cylindrical gears. Some of the most relevant topics are summarized here:

- The quantification of individual sources of thermal distortion: pitch errors, profile and helix slope deviations and flank line form errors.
- The prediction of the total amount of active flank thermal distortion for a given temperature distribution.
- The analysis of the interaction between elastic deflections and thermal distortions on tooth contact parameters.
- The evaluation of the impact of thermal distortion in tooth contact parameters of low speed middle-size steel cylindrical gears.
- The study of teeth modifications to compensate thermal distortions.
- The experimental observation of the effects of thermal distortion on tooth contact parameters, namely: load distribution, transmission error and backlash behaviour.

Additionally, secondary research opportunities have also been identified in the more general context of efficiency and thermal behaviour of cylindrical gear transmissions:

- The development of a simple sliding friction coefficient model for gears based on primary rheological behaviour of the lubricant and flank surface topography parameters.
- The development of a power loss computation procedure for gears that accounts for local fluid film behaviour through instantaneous temperatures and pressures.
- The prediction of local frictional heat flux and heat partition in gears as a function of geometry and operating conditions.
- The development of a fast and reliable model for the prediction of temperature distribution in cylindrical shaft-gear pairs, including heat from bearings and sealings.
- The experimental measurement of thermal gradients in cylindrical gear pairs under variable operating conditions.
- The empirical correlation of mesh power losses with gear pair bulk temperature subject to variable lubricating conditions.

The research opportunities identified herein have been grouped and restated in terms of several thesis objectives in Section 1.3.

*If you talk to a man in a language he understands,
that goes to his head. If you talk to him in his
language, that goes to his heart.*

— Nelson Mandela, 1918 - 2013

3

Gear Kinematics and Load Distribution Modelling

Contents

3.1	Involute teeth geometry description	50
3.1.1	Fundamental law of gearing and conditions of existence	50
3.1.2	Generation and modification of teeth geometry	56
3.2	Kinematic behaviour	63
3.2.1	Determination of kinematic relations	63
3.2.2	No-load transmission error behaviour	68
3.3	Load distribution and transmission error	71
3.3.1	Statement of the problem	71
3.3.2	Thin slice approach for 3D gear contact problems	76
3.3.3	Load capacity	81
3.4	Finite element validation	84
3.4.1	Description of the model and test cases	84
3.4.2	Results and discussion	87
3.5	Conclusions of Chapter 3	91

This chapter lays the foundations of analytical modelling of load distribution and kinematic behaviour of cylindrical gears, which are necessary to understand the heat generation mechanism in the gear mesh. The first section introduces basic concepts of gear teeth geometry from the involute surface generation perspective. Manufacturing processes are briefly described and the fundamental law of gearing is defined. Then, kinematic relations between pinion and gear are established focusing on backlash and tooth separation which affect load distribution and transmission error. Gear teeth behaviour under applied load is discussed next where the different stiffness components are described; and finally, the load distribution problem is stated and the solution method is presented. A FE model will be developed at the end of this chapter to validate analytical results for common spur gear geometries with modifications, results will be discussed and conclusions are withdrawn.

3.1 Involute teeth geometry description

The involute curve is the basis of the most commonly used gear geometry in machinery. Although other types of geometries such as the Wildhaber-Novikov or cycloidal are also present in some sectors such as mechanical clocks, involute gears are the most extended gear type in industry. Among the main advantages of involute teeth it can be highlighted that manufacturing process is largely facilitated with respect to other geometries, carried out by simple straight-sided tools that can be used by several techniques, as shown later in this chapter. Furthermore, the tooth force direction is constant and mesh behaviour is insensitive to centre distance variation which helps gearbox assembly. However, it is often claimed that the main disadvantage of this geometry is that contact surfaces are non-conformal making difficult hydrodynamic lubrication and leading to high pressures that cause undesired failures (e.g. pitting or wear). Moreover, manufacturing process may result in undercut when a small number of teeth is required, which reduces bending load capacity as a consequence. In spite of these criticisms involute gears still represent the main geometry in common transmissions.

3.1.1 Fundamental law of gearing and conditions of existence

The involute of a circle is the curve traced by the free end of a taut string which is unwinding from a fixed circle named “base circle” (see Figure 3.1). At any instant, the direction of the normal to the curve is pointed out by the taut string, and the instantaneous radius of curvature, ρ_y , is the distance between the free end, P_y , and the tangent point to the base circle, T .

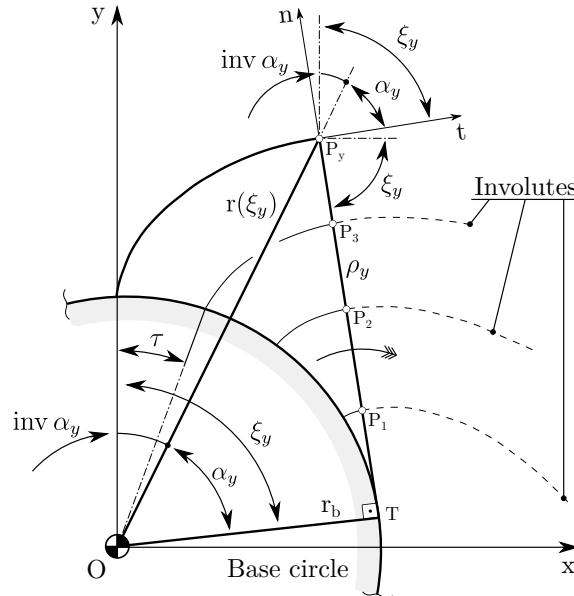


Figure 3.1: Graphical description of involute curve generation

From Figure 3.1 the following mathematical relation results:

$$r_b \cdot \tan(\alpha_y) = r_b \cdot \xi_y = r_b \cdot (\alpha_y + \text{inv } \alpha_y) \quad (3.1)$$

From which the so called “involute function”, $\text{inv } \alpha_y$, is obtained:

$$\text{inv } \alpha_y = \tan(\alpha_y) - \alpha_y \quad (3.2)$$

$$\alpha_y = \arctan(\xi_y) \quad (3.3)$$

In the following, angles α_y and ξ_y will be referred to as “pressure angle” and “roll angle” respectively. The latter can be related to the radial distance of the free end of the taut string following:

$$r_b \cdot \xi_y = \sqrt{r^2 - r_b^2} \rightarrow r(\xi_y) = r_b \cdot \sqrt{1 + \xi_y^2} \quad (3.4)$$

Which gives rise to the parametrical representation of the involute curve:

$$r(\xi_y) = r_b \cdot \sqrt{1 + \xi_y^2} \cdot \begin{cases} \sin[\xi_y - \arctan(\xi_y)] \\ \cos[\xi_y - \arctan(\xi_y)] \end{cases} \quad (3.5)$$

Equation 3.5 will be later used to compute gear teeth geometry by the generating method as well as derived geometrical properties such as curvature radius or normal directions.

Law of gearing

Involute profiles are the result of the rolling motion between the taut string and the base circle shown in Figure 3.1. However, it can also be concluded that the same relative motion is reproduced when the string is the one kept fixed and the base circle rolls over it. If instead of considering a single circle one considers two wheels sharing the same cord, it is possible to foresee that both bodies must rotate at a constant ratio, $i = \omega_1/\omega_2$, to avoid phase difference in common points P_y . For a gear transmission, it is of primary importance to be able to determine the counter-profile of a given involute that allows transmitting such a continuous motion with constant speed ratio. This problem is known as the “fundamental law of gearing”.

Let two imaginary concave-convex involute profiles, with arbitrary base circle centres O_1 and O_2 , meet at any point P_y in space. The motion of this point must follow the common normal direction to prevent flank separation, in this manner, continuous action is achieved. The direction of the common normal is defined by the tangent line to both base circles, therefore, the velocity, v_y , of point P_y along this line is mathematically defined by:

$$v_y = \cos(\alpha_{y,1}) \cdot \omega_1 \cdot r_{y,1} = -\cos(\alpha_{y,2}) \cdot \omega_2 \cdot r_{y,2} \quad (3.6)$$

Setting $\cos(\alpha_y) = r_b/r_y$ in each side of Equation 3.6:

$$v_y = r_{b,1} \cdot \omega_1 = -r_{b,2} \cdot \omega_2 \quad (3.7)$$

Relating Equation 3.7 with the speed ratio, i :

$$i = \frac{\omega_1}{\omega_2} = -\frac{r_{b,2}}{r_{b,1}} = -\frac{r_2}{r_1} \quad (3.8)$$

Where $r_{1,2}$ is the known as the pitch radius which is the distance between the centre of the base circle of each body and the intersecting point between the common tangent line and the line joining centres. This relationship allows determining the counter-profile of any given involute as well as the geometry of the manufacturing tool. In this sense, if each of the points P_y in Figure 3.1 are considered the cutting edges of an imaginary tool, it is possible to see that such tool must have straight sides and the generating process can be regarded as a series of inclined segments which intersect a circular gear blank. The envelope of all the line segments forms the involute tooth profile.

Generating methods

Gear teeth can be manufactured by several methods: machining, casting, rolling, etc. In this work, only generating methods are described where gear teeth geometry is obtained based on the law of gearing presented above. The machining techniques shown in Figure 3.2 share this principle of operation. These methods are the most common gear manufacturing techniques and all of them can be regarded as the rolling-off of a perfectly plastic cylindrical gear blank over an infinitely long rack where the footprint forms the gear tooth profile. This rack is known as “basic rack”.

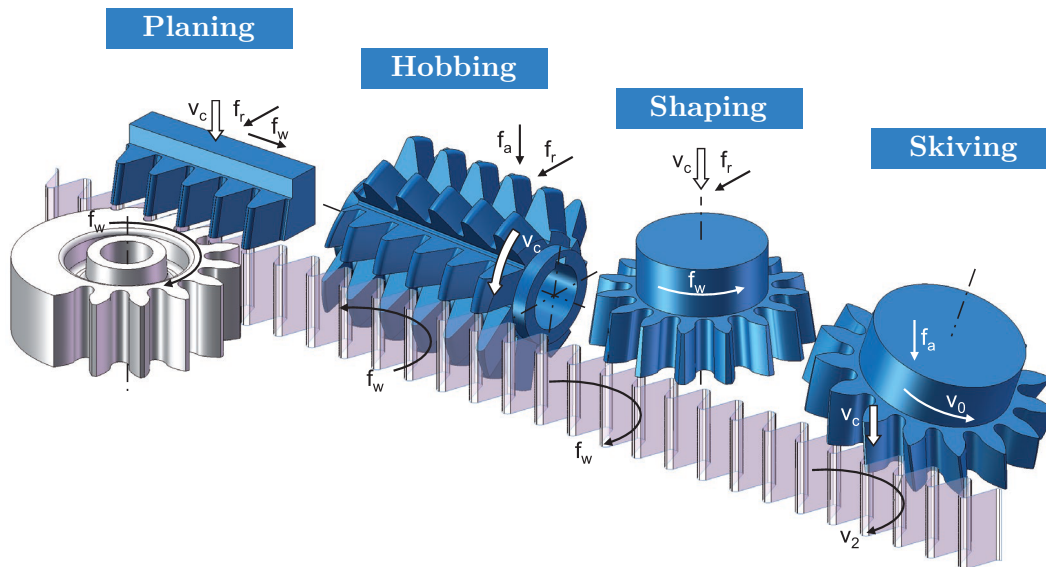


Figure 3.2: Generation processes for gear manufacturing [169]

Each of the methods in Figure 3.2 is characterized by a distinctive relative motion between a trapezoidal-shaped blade (rack, hob, shaper cutter, etc.) and the workpiece. The type of motion combination depends on the technique but all of them are characterized by a cutting movement and a feed motion which generate the same virtual basic profile: the basic rack (grey-colored in Figure 3.2). For instance, the planing method is the combination of a vertical reciprocal cutting motion and a radial feed of the rack, combined with the rotation of the circular gear blank which is followed by a tangential displacement of the rack tool. The motion of the rack-type cutter removes material chips per stroke thus shaping or “generating” the teeth. Similarly, gear shaping process replaces the tangential displacement of the rack by a rotational motion that follows the workpiece. In both cases, the so called “basic rack” is embodied by the cutting face of the tool. Additional processes, tools and motion combinations are shown in Figure 3.2 where gear hobbing stands out for being the most versatile in industry.

Basic rack

Although each of the processes above has its own distinctive features, from a theoretical geometry generation point of view, they all can be represented by the basic rack. The main advantage of such representation is that it is possible to standardize the main dimensions

and geometry proportions. Moreover, a pinion and a gear with the same basic rack mesh together as they have the same pitch. This characteristic is known as “interchangeable property” and allows combining different gear sets regardless of their size. The basic rack is standardized in ISO 53 [170] and the main dimensions are shown in Figure 3.3.

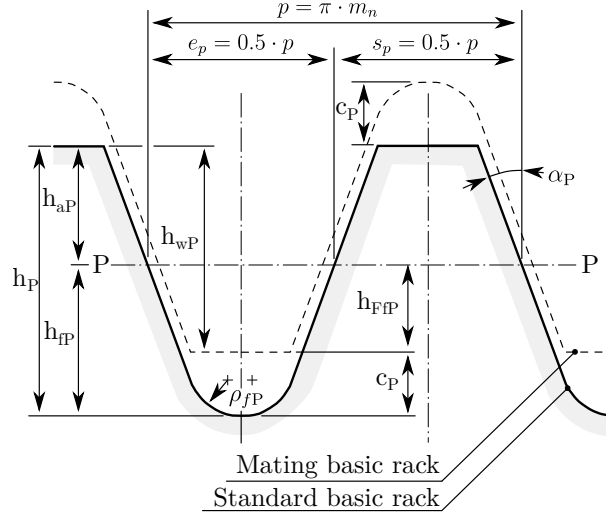


Figure 3.3: Basic rack dimensions according to ISO 53

The standard profile according to ISO 53 is characterized by having a constant pressure angle of $\alpha_P = 20^\circ$. Other quantities are summarized in Table 3.1 where each dimension has been non-dimensionalized dividing by the normal module, m_n , which varies from 1 mm to 50 mm for common industrial applications according to ISO 54 [171].

Table 3.1: Basic rack coefficients for standard profiles according to ISO 53 [170]

	A	B	C	D
h_{aP}/m_n	1	1	1	1
h_{fP}/m_n	1.25	1.25	1.25	1.4
ρ_{fP}/m_n	0.38	0.3	0.25	0.39
c_P/m_n	0.25	0.25	0.25	0.4

When the datum line P-P of the rack cutter in Figure 3.3 is tangent to the pitch circle of the work-piece both are in their nominal positions and the tooth thickness of the basic rack equals the space width of the gear blank as a consequence. In this situation gears are called “without profile shift”. However, the reference line of the basic rack can be positioned within arbitrary bounds which affects teeth radial position and thickness. The concept profile shift or addendum modification refers to the amount by which the position of the rack cutter is shifted relative to the nominal position and it is usually made non dimensional dividing by the normal module. In such case the quantity, x , is called profile shift coefficient. Gears are usually profile shifted to enhance load capacity by increasing tooth thickness, design a given gear ratio at a specified centre distance or enhance sliding conditions to minimize wear. These advantages are achieved with the same basic rack but special rules must be observed to guarantee proper manufacturing and meshing conditions.

Conditions of existence

Pinion and gear must fulfil a certain number of conditions to ensure continuous meshing and avoid interferences during operation or during the cutting process. First, from the manufacturing point of view the following situations must be avoided:

1. When a small number of teeth is required interference between the manufacturing tool and the work-piece produces gear root undercut. The latter should be avoided by selecting a proper profile shift coefficient; otherwise, undercut weakens tooth root bending capacity.
2. On the opposite, if too large addendum modification is designed, zero thickness at the tooth tip result and produce pointed teeth.

Second, from an operating point of view, the following criteria applies to guarantee proper meshing:

1. Similarly to manufacturing, if the tip corner of a gear enters the fillet of its mate interference in operation arises and profiles are damaged. This must be avoided.
2. To ensure a constant output rotational speed contact ratios less than unity must be discarded as it results in intermittent operation.

Finally, although theoretically perfect gears fulfilling these criteria work properly, it is desirable that real gears are provided sufficient backlash allowance to cope with manufacturing and assembly errors, tooth deflections produced by mechanical loads and, in this work, thermally-induced geometry distortions. For this reason, an additional criteria will be added to the preceding.

The conditions stated below are written in terms of the basic rack dimensions, the number of teeth, z , the base radius, r_b , the face width, b , and the profile shift coefficient, x . Furthermore, the guidelines have been generalized for either spur or helical gears by introducing the helix angle, β , and the normal and transverse pressure angles, α_n and α_t respectively, which are related by $\tan(\alpha_n) = \tan(\alpha_t) \cdot \cos(\beta)$.

a) Undercut: In order to avoid gear teeth undercut, the minimum number of teeth must be greater than the following quantity:

$$z \geq z_{min} = \frac{2 \cdot \left[h_{fP} - x - \rho_{fP} \cdot \left(1 - \sin(\alpha_n) \right) \cdot \cos(\beta) \right]}{\sin^2(\alpha_t)} \quad (3.9)$$

According to Equation 3.9 the minimum number of teeth to avoid undercutting basically depends on the profile shift coefficient, x , the helix angle, β and the height of the basic rack dedendum, h_{fP} . For the general case of standard spur gears manufactured with the ISO 53-A basic rack profile without profile shift, the minimum number of teeth is approximately 17. This condition could also be written in terms of minimum profile shift coefficient to avoid undercut for a given number of teeth. In such case we have:

$$x \geq x_{min} = h_{fP} - \rho_{fP} \cdot \left(1 - \sin(\alpha_n) \right) - \frac{z \cdot \sin^2(\alpha_t)}{2 \cdot \cos(\beta)} \quad (3.10)$$

b) Thickness at tooth tip: To avoid pointed teeth during manufacturing, profile shift coefficient should be chosen following:

$$\frac{\pi + 4 \cdot x \cdot \tan(\alpha_n)}{z} + 2 \cdot \left[\tan(\alpha_t) - \alpha_t \right] - \tan\left(\arccos\left(\frac{r_b}{r_a}\right)\right) + \arccos\left(\frac{r_b}{r_a}\right) > 0 \quad (3.11)$$

To ensure a minimum thickness in the tip AGMA standard usually prescribes a limiting value of $s_{c,min} = 0.3 \cdot m_n \cdot r_a^{-1}$, where the tip radius $r_a = 0.5 \cdot m_n \cdot z + x \cdot m_n + h_{aP}$

c) Interference in operation: If the pinion and the gear are not undercut (see Equation 3.9), this requirement is met if:

$$r_{b,1}^2 + \left[(r_{b,1} + r_{b,2}) \cdot \tan(\alpha_{w,t}) - \sqrt{r_{a,2}^2 - r_{b,2}^2} \right]^2 \geq r_{lim}^2 \quad (3.12)$$

$$r_{lim} = m_n \cdot \sqrt{\left[z - h_{aP} + x + \rho_{fP} \cdot (1 - \sin(\alpha_n)) \right]^2 + \left[\frac{\cos(\beta)}{\tan(\alpha_n)} \cdot [h_{aP} - x - \rho_{fP} \cdot (1 - \sin(\alpha_n))] \right]^2} \quad (3.13)$$

Where r_{lim} represents the limit radius resulting from the intersection between the involute profile and the trochoidal path of the tool. Basically, this condition states that if the involute profile of the mating wheel meshes below the limit diameter of the reference gear, interference in operation exists and wedges the gears. In Equation 3.13, parameter $\alpha_{w,t}$ represents the working pressure angle resulting from gears meshing at their mounting centre distance, a_w ,

$$\alpha_{w,t} = \arccos \left[(z_1 + z_2) \cdot \left(\frac{m_n \cdot \cos(\alpha_t)}{2 \cdot a_w \cdot \cos(\beta)} \right) \right] \quad (3.14)$$

d) Continuous motion: In order to ensure continuous action a new teeth must enter the mesh zone before the previous one leaves. This is represented by the contact ratio, ϵ , which is the average number of teeth in contact along the line of action. To ensure this condition the gear contact ratio must be greater than unity which is ensured by:

$$\epsilon = \frac{\sqrt{r_{a,1}^2 - r_{b,1}^2} + \sqrt{r_{a,2}^2 - r_{b,2}^2} - m_n \cdot \frac{z_1 + z_2}{2 \cdot \cos(\beta)} \cdot \cos(\alpha_t) \cdot \tan(\alpha_n)}{\frac{\pi \cdot m_n}{\cos(\beta)} \cdot \cos(\alpha_t)} + b \cdot \frac{\sin(\beta)}{\pi \cdot m_n} \quad (3.15)$$

d) Backlash: From a practical perspective it is not possible to operate with zero backlash due to the combined effect of assembly tolerances, manufacturing allowances and thermal expansion on theoretical mesh behaviour. It is therefore necessary to manufacture teeth with a smaller tooth thickness, which is reached decreasing the design profile shift coefficient, x , by a prescribed machining allowance, q , and the desired tooth thickness tolerance, E_s . The resulting addendum modification coefficient is named “generating profile shift coefficient” and it is denoted by x_E .

$$x_E = x + \frac{E_s}{2 \cdot m_n \cdot \tan(\alpha_n)} + \frac{q}{m_n \cdot \sin(\alpha_n)} \quad (3.16)$$

From pinion and gear generating addendum modifications it is possible to compute the available normal backlash in the mesh, j_{bn} , following:

$$j_{bn} = m_n \cdot [\cos(\alpha_n) \cdot (z_1 + z_2) \cdot (\text{inv } \alpha_{wt} - \text{inv } \alpha_t) - 2 \cdot (x_{E,1} + x_{E,2}) \cdot \sin(\alpha_n)] \quad (3.17)$$

From Equation 3.16 it is concluded that high speed gear units with large backlash allowances to accommodate thermal expansion but with small modules (such as those used in aeronautical or automotive fields), the difference between the design and generating profile shift can be significant which affects tooth thickness and root stresses as a consequence. Therefore, it is of primary importance to keep manufacturing tolerances to a minimum.

3.1.2 Generation and modification of teeth geometry

The generation of gear teeth by rolling the tool over the gear blank is computed based on Padieth's approach [172] where the counterpart of the basic rack is rolled over the pitch diameter, d . Thus, the addendum height of the basic rack in Figure 3.3, becomes the dedendum of its counterpart and the bottom radius of the former is the tip radius of the latter. This way, the addendum of the counterpart generates the gear teeth dedendum. Figure 3.4 shows the reference geometry for the generation process where the subscript 0 is used to differentiate from the same quantities in ISO 53 basic rack.

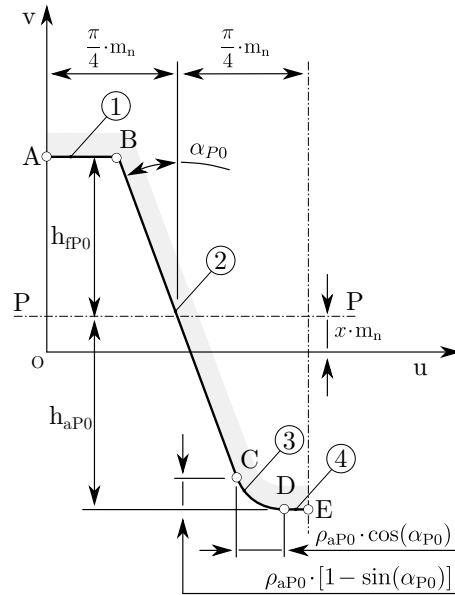


Figure 3.4: Local system of coordinates and main dimensions of basic rack counterpart

The local system of coordinates (u, v) has been attached to the reference line of the tool which is tangent to the pitch circle in the rolling process (see Figure 3.5). However, the datum line P-P of the basic rack counterpart can be shifted with respect to the reference line by the profile shift amount. The latter will allow to vary generated tooth thickness as stated in previous sections. Four different regions are considered, where the intersecting points A to E can be easily determined from the basic rack dimensions. Thus, we have:

1. Region 1 (segment A-B) that generates the tooth tip.
2. Region 2 (segment B-C) producing the tooth flank.
3. Region 3 (rounding C-D) which gives rise to the tooth fillet.
4. Region 4 (segment D-E) that generates the tooth bottom.

Although the basic rack dimensions are standardized, the gear teeth generating process explained next is not limited to the dimensions in Table 3.1, the only limitation is that pinion and gear must be generated with the same basic rack. Table 3.2 summarizes the limits and coordinates of each section of the counterpart in the normal plane which are generalized for arbitrary dimensions:

Table 3.2: Boundaries of regions in basic rack counterpart

Point	Coordinates
A	$A_x = 0$ (3.18)
	$A_y = h_{fP0} + x \cdot m_n$ (3.19)
B	$B_x = \pi \cdot m_n / 4 - h_{fP0} \cdot \tan(\alpha_{P0})$ (3.20)
	$B_y = A_y$ (3.21)
C	$C_x = \pi \cdot m_n / 4 + (h_{aP0} - \rho_{aP0} \cdot [1 - \sin(\alpha_{P0})]) \cdot \tan(\alpha_{P0})$ (3.22)
	$C_y = x \cdot m_n - h_{aP0} + \rho_{aP0} \cdot [1 - \sin(\alpha_{P0})]$ (3.23)
D	$D_x = C_x + \rho_{aP0} \cdot \cos(\alpha_{P0})$ (3.24)
	$D_y = x \cdot m_n - h_{aP0}$ (3.25)
E	$E_x = \pi \cdot m_n / 2$ (3.26)
	$E_y = D_y$ (3.27)

Analytical determination of tooth profile

When the counterpart to the basic rack is continuously rotated an angle ξ_y around the gear blank, the generated tooth profile is obtained from the envelope of all the instantaneous positions of the rack. To this end, the latter must be expressed in the (x, y) system of coordinates first; which is attached to the fixed workpiece as shown in Figure 3.5.

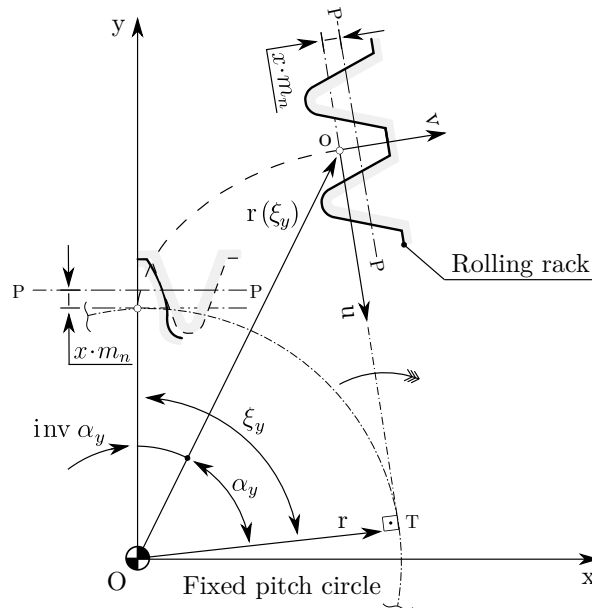


Figure 3.5: Graphical description of tooth profile generation method

For a given roll angle ξ , the location of the origin O of the local system of coordinates (u, v) attached to the tool relative to the fixed system of coordinates (x, y) is calculated from the parametric representation of the involute curve in Equation 3.5. The coordinate transformation between the local and global system of coordinates yields the following parametrical equation:

$$r(\xi) = r \cdot \sqrt{1 + \xi^2} \cdot \begin{Bmatrix} \sin[\xi - \arctan(\xi)] \\ \cos[\xi - \arctan(\xi)] \end{Bmatrix} + u \cdot \begin{Bmatrix} \cos(\xi) \\ -\sin(\xi) \end{Bmatrix} + v \cdot \begin{Bmatrix} \sin(\xi) \\ \cos(\xi) \end{Bmatrix} \quad (3.28)$$

Which describes the basic rack counterpart in the fixed system of coordinates (x, y) at any instant of the tool rotation.

Now, in order to compute the tooth profile, the envelope theorem is applied [172]:

$$\frac{\partial x}{\partial \xi} \cdot \frac{\partial y}{\partial u} - \frac{\partial y}{\partial \xi} \cdot \frac{\partial x}{\partial u} = 0 \quad (3.29)$$

Which yields the following relation between the rotation angle ξ and the local coordinates (u, v) to construct the envelope:

$$\xi = \frac{1}{r} \cdot \left(u + v \cdot \frac{dv}{du} \right) \quad (3.30)$$

Therefore, from the local coordinates of the counterpart rack in Table 3.3, it is possible to determine the full tooth profile applying Equations 3.28 and 3.30.

Table 3.3: Gear teeth generating functions per segment

Region	Boundaries	Functions
1	$A_x < u < B_x$	$v(u) = A_y = B_y$ (3.31)
		$dv/du = 0$ (3.32)
2	$B_x \leq u \leq C_x$	$v(u) = B_y - (u - B_x) \cdot \cot(\alpha_{P0})$ (3.33)
		$dv/du = -\cot(\alpha_{P0})$ (3.34)
3	$C_x < u < D_x$	$v(u) = D_y + \rho_{aP0} - \left[\rho_{aP0}^2 - (u - D_x)^2 \right]^{1/2}$ (3.35)
		$dv/du = (u - D_x) \cdot \left[\rho_{aP0}^2 - (u - D_x)^2 \right]^{-1/2}$ (3.36)
4	$D_x \leq u \leq E_x$	$v(u) = D_y = E_y$ (3.37)
		$dv/du = 0$ (3.38)

The tooth geometry computed this way is represented in the normal plane. To compute profile geometry in the transverse plane at any axial position, z , it is only necessary to twist the tooth an angle $\gamma \cdot z$ where $\gamma = \sin(\beta)/r$. Thus, for a given roll angle, ξ , and axial position, z , the parametrical representation of the curve in the transverse plane is given by:

$$r(\xi, z) = \begin{bmatrix} \cos(\gamma \cdot z) & -\sin(\gamma \cdot z) \\ \sin(\gamma \cdot z) & \cos(\gamma \cdot z) \end{bmatrix} \times \begin{Bmatrix} r_x(\xi) \\ r_y(\xi) \end{Bmatrix} \quad (3.39)$$

Where $r_x(\xi)$ and $r_y(\xi)$ are the x and y components of the parametric representation of the profile in the normal plane computed from Equation 3.28.

Finally, the start and end of each region in the tooth profile is determined by the intersection of the different envelopes. In this sense, in order to determine a unique intersection between the envelope of the flank and the trochoidal path of the tip rounding, an iterative procedure must be used [172] which is specially useful when undercut arises.

Application of tooth modifications

From a theoretical point of view gear teeth profile obtained following generating methods are conjugate and thus they allow homokinetic transmission of rotational motion. However, profile inaccuracies caused by manufacturing or heat treatment methods, positioning errors in the assembly process and/or elastic deflections under load may lead to alterations in the load distribution pattern giving rise to noise and local contact pressure increases that end up in gear teeth failure. In order to avoid such undesired bearing patterns teeth modifications are usually applied which are desired alterations of the tooth face on its normal direction compared to its original involute geometry. Such alterations are applied after the heat treatment process by generating grinding methods (similarly to the machining procedure described earlier) and they are usually in the order of a few dozens of microns in the normal direction to the initial flank. In the following paragraphs, the main types of modifications are described:

a) Profile modifications: They are intended to avoid premature contact as the result of teeth deflections under load making the gear drive operate quietly. Profile modifications enable a gradual entry and exit into and out of the mesh and therefore they reduce dynamic loadings. Transverse profile modifications can be applied to one or both ends of the active profile (known as “tip/root reliefs”) or to the whole profile (“profile crowning” or “profile slope modification”). They are usually defined by the length of roll, the maximum depth of the relief measured in the profile normal direction at the tip/root and the type of modification. Figure 3.6 depicts the main types of profile modifications.

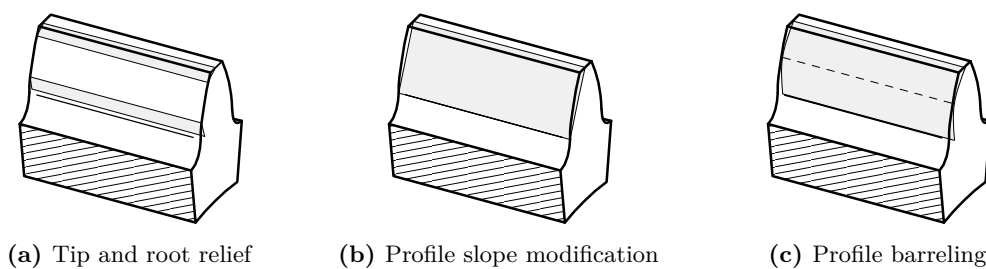


Figure 3.6: Different types of profile modification

b) Flank line modifications: Flank line modifications are intended deviations applied along the axial direction in order to reduce the load concentration caused by elastic deformations of shafts, bearings supports and housing, as well as to accommodate gear assembly misalignments. There are three types of flank line modifications (see Figure 3.7): i) end reliefs, ii) helix angle modifications and iii) flank line crowning. As in the case of profile modifications these can also be applied to the tooth surface partially or totally, and they are defined by the length and depth of the relief over the original surface and they can follow a linear or parabolic equation.

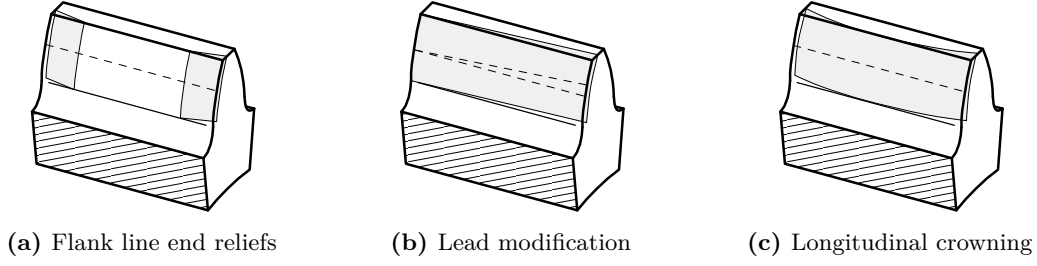


Figure 3.7: Different types of flank line modification

c) Topological modifications: A good contact pattern must ensure that individual lines of contact are as long as possible as they reduce the contact pressure acting on the gear and pinion. Relieving the gear teeth flanks using standard modifications in the profile and longitudinal directions entails changes to the geometry and the maximum length of each line of contact depends to a great extent on the type and amount of end reliefs. This means that profile and flank modifications do not necessarily have a beneficial effect on gear mesh behaviour. To ensure a proper tooth contact when several parameters are involved “topological modifications” can be applied [173]. In this type of modification gear tooth active flank is deviated from the nominal surface point by point using a multi-axis numerical control grinder. These type of modification is not covered in this work but it has been presented here for completeness.

Figure 3.8 graphically summarizes the main characteristics and dimensions of profile modifications. As it can be seen, the generated profile deviates from the theoretical involute by the backlash allowance, $\kappa = \cos(\alpha_n) \cdot E_s/2$, where E_s is the chordal tooth thickness tolerance. The latter has been automatically introduced when the generating profiles shift, x_E , from Equation 3.16, substitutes the design addendum modification, x , in Table 3.2. Therefore, in the following, the term “theoretical profile” will be used for profiles with no-backlash and design addendum modification and the term “generated” will refer to that including manufacturing tolerances and backlash.

Tooth modifications, δ , must be applied in the normal direction to each point in the flank. The following can be achieved by modifying the basic rack counterpart geometry presented in Figure 3.4 for each of the aforementioned modification types and then derivate the appropriate expressions in Tables 3.2 and 3.3. However, this procedure requires a different tool for all possible combinations and the application of longitudinal modifications results costly. Instead, a different approach is proposed. From the parametrical representation of the theoretical active flank with Equation 3.28, normal directions are easily computed and modified geometry, $R(\xi_y)$ results from:

$$R(\xi_y) = r(\xi_y) - \hat{n}(\xi_y) \cdot \delta(\xi_y) \quad (3.40)$$

$$\hat{n}(\xi_y) = \begin{cases} -\cos(\xi_y) \\ \sin(\xi_y) \end{cases} \quad (3.41)$$

Where $\delta(\xi_y)$ is a polynomial expression representing the amount of tip or root relief for each roll angle in the relief region.

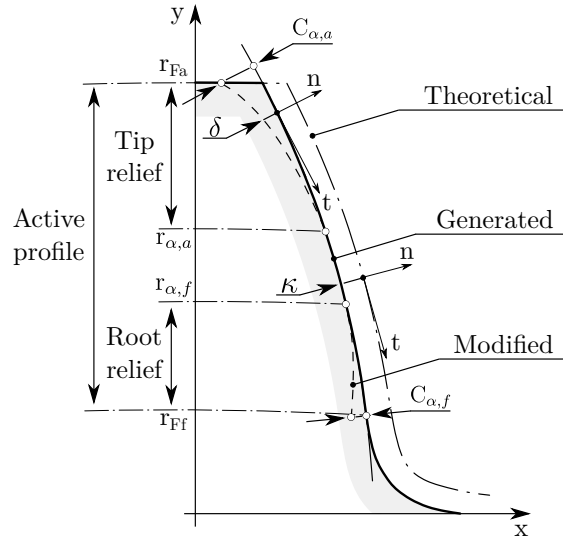


Figure 3.8: Profile modifications relative to theoretical and generated tooth geometry

In order to generalize the procedure for profile and longitudinal modifications, the modification diagram depicted in Figure 3.9 is defined. The horizontal axis, represents the roll angle or the axial position (in brackets) and the vertical axis the total amount of modification.

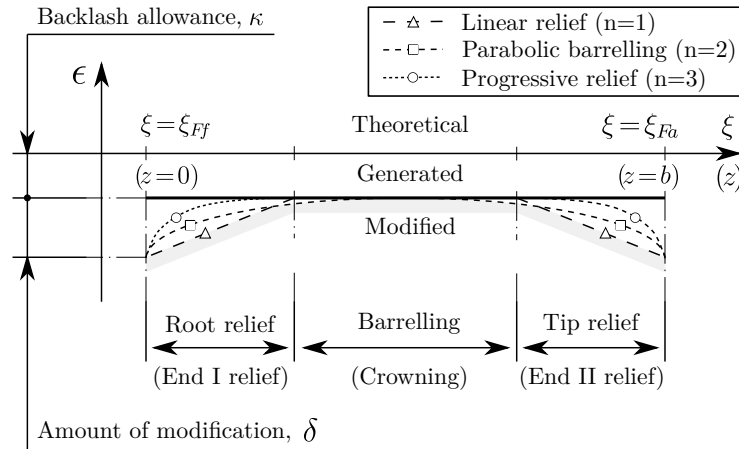


Figure 3.9: Generalized tooth profile and longitudinal modification scheme

From Figure 3.9 it is concluded that the different types of modifications presented at the beginning of this section (linear end reliefs, parabolic barrelling, progressive tip reliefs, etc.) can all be defined with the same type of equation:

$$\delta(\xi) = C_{\alpha} \cdot \left(\frac{\xi - \xi_i}{\xi_o - \xi_i} \right)^n \quad (3.42)$$

$$\delta(z) = C_{\beta} \cdot \left(\frac{z - z_i}{z_o - z_i} \right)^m \quad (3.43)$$

Where $\xi_i(z_i)$ and $\xi_o(z_o)$ are the beginning and end of the relief respectively, $C_{\alpha}(C_{\beta})$ is the amount of modification at the end of the active profile (face) and parameters $n(m)$ regulate

the type of modification: 1 for linear, 2 for parabolic, etc. For instance, for a simple linear tip relief, n is set to 1 and $\xi_o = \xi_{Fa}$ is the roll angle at the tip diameter; the designer only needs to define the amount of modification at the tip C_α and the start roll angle or diameter for modification, $\xi_{\alpha,a}$ or $r_{\alpha,a}$ respectively which are inter-related by Equation 3.5.

One of the main advantages of the method is that it easily allows to stack up different types of modifications as they all follow the same normal direction in Equation 3.41. However, the method is only valid in the flank region as the intersection between the fillet rounding and the root relief is discontinuous giving rise to a notch that does not exist in real generated gears. For accurate geometry modelling basic rack must be modified and envelope must be computed similarly to the procedure explained in Section 3.1.2.

Determination of curvature radius and normal directions

The determination of the curvature radius in the principal directions is a key parameter to compute contact stresses by the Hertz theory. In the case of a theoretically perfect involute profile, the principal radius of curvatures are contained in the base tangent plane. The first principal curvature radius is the distance in the normal direction from the reference point, P_y , to the tangent to the base circle, T , which is the instantaneous centre of rotation (see Figure 3.1) and the second principal curvature radius is infinite if profiles are not modified. Therefore, in theoretically perfect spur gears:

$$\rho_y(\xi_y) = r_b \cdot \tan(\alpha_y) = r_b \cdot \tan[\arctan(\xi_y)] \quad (3.44)$$

However, in presence of profile and/or longitudinal modifications the instantaneous centre of rotation is no longer located in the base cylinder and a different approach is required. From the parametrical representation of the modified profile in Equation 3.40 the principal curvature k in the normal plane at any roll angle, ξ , is computed from [174]:

$$k(\xi) = \frac{\frac{dRx}{d\xi} \cdot \frac{d^2Ry}{d\xi^2} - \frac{dRy}{d\xi} \cdot \frac{d^2Rx}{d\xi^2}}{\left[\left(\frac{dRx}{d\xi} \right)^2 + \left(\frac{dRy}{d\xi} \right)^2 \right]^{3/2}} \quad (3.45)$$

From this equation the local radius of curvature is simply the inverse of the absolute value of curvature, $\rho_y = |k(\xi_y)|^{-1}$. Similarly, the unit normal vector is given by [174]:

$$\hat{n}(\xi) = \frac{1}{\sqrt{\left(\frac{dRx}{d\xi} \right)^2 + \left(\frac{dRy}{d\xi} \right)^2}} \cdot \left\{ \begin{array}{l} -\frac{dRy}{d\xi} \\ \frac{dRx}{d\xi} \end{array} \right\} \quad (3.46)$$

Where the derivative terms are computed from the previous parametrical representations of the flank and the sign convention is given by the product of unit normal vectors $\hat{n} = \hat{k} \times \hat{t}$; with \hat{k} and \hat{t} the unit normals in axial and tangent directions.

In the case of spur gears, the instantaneous contact between meshing teeth is equivalent to two cylinders in contact whose principal radius in the normal plane varies along the line of action but the common contact line remains parallel to the axis of rotation at any instant of time. However, in the case of helical gears, such contact is represented by two cones with the same conicity, equal to the base helix angle, β_b , and the common contact

line is bent an angle $\psi = \arctan(\sin(\alpha_n) \cdot \tan(\beta_b))$ with respect to the tooth trace which is known as ‘inclination angle’ (see Figure 3.10b). As a consequence, not only curvature radius varies along the line of action but also along the axial direction. Following Euler’s transformation [175] the radius of curvature in the rolling direction at any roll angle is:

$$\rho_y(\xi_y)|_{\hat{\eta}} = \rho_y(\xi_y) \cdot \frac{\cos(\psi)}{\cos(\beta_b)} \quad (3.47)$$

Where $\hat{\eta}$ is the rolling direction according to the local system of coordinates in Figure 3.10.

Finally, the second principal radius of curvature can be computed similarly from the base tangent plane representation of the flank. In such case, in Equations 3.45 and 3.46, the x and y axis do not follow the system of coordinates attached to the gear in the normal plane but that fixed to the tooth trace and the line of action respectively. For instance, in case of longitudinally crowned cylindrical gears, the paraboloidal approximation $\delta(z) = z^2/(2 \cdot R)$ leads to the second principal radius of curvature $\rho(z) = b^2/(8 \cdot C_\beta)$ which is useful to compute elliptical contacts based on the Hertzian assumption.

3.2 Kinematic behaviour

The kinematic behaviour of the gear mesh determines power losses and heat flux to a great extent. Therefore, in order to understand friction and thermal behaviour in depth, it is necessary to analyse the geometrical boundaries of the line of action, the kinematic relations between pinion and gear along this path and the different velocity components in the mesh. Moreover, when theoretical gears mesh together, rotational motion is transmitted perfectly but generated gears show a phase difference due to the existence of backlash or modifications. This leads to a relative positioning error that affects load distribution and generated heat as a consequence. In this section, kinematic behaviour and related parameters are described.

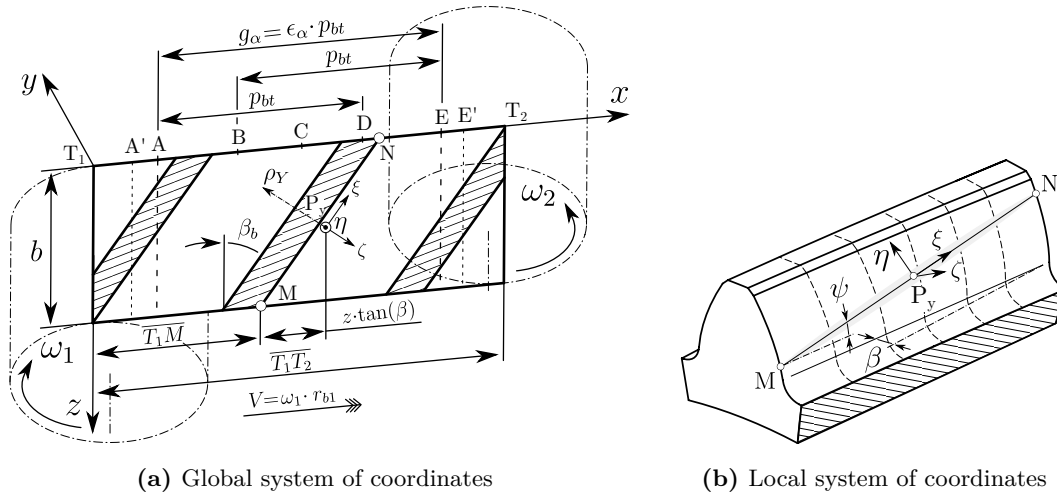
3.2.1 Determination of kinematic relations

Geometrical boundaries of the conjugate action

The conjugate action of a pair of cylindrical gears in mesh has a delimited length and it is comprised between the tangent points to the base cylinders, T_1 and T_2 , from which pinion and gear involute profiles are developed. When the tip of the gear tooth contacts the bottom of the corresponding pinion mate, the start of the active profile is defined (see point A in Figure 3.10a). Similarly, the end of the path of contact is defined by tip of the pinion touching the bottom of the gear (point E). The distance between both ends, A and E, determines the full length of the path of contact, g_α . Figure 3.10 depicts the base tangent plane and the systems of coordinates to be used in the following. The global system of coordinates applies to the load distribution problem while the local system of coordinates will be used for contact analysis.

In the case of theoretical profiles, the total length is calculated from:

$$g_\alpha = \sqrt{r_{a,1}^2 - r_{b,1}^2} + \sqrt{r_{a,2}^2 - r_{b,2}^2} - a_w \cdot \sin(\alpha_{w,t}) \quad (3.48)$$



(a) Global system of coordinates

(b) Local system of coordinates

Figure 3.10: Geometrical boundaries and systems of coordinates within the base tangent plane

Moreover, the line of action is divided by the pitch point in approach and recess paths of contact, g_a and g_f respectively, with $g_\alpha = g_a + g_f$. Thus, we have:

$$g_{a,1} = g_{f,2} = \sqrt{r_{a,1}^2 - r_{b,1}^2} - r_{b,1} \cdot \tan(\alpha_{w,t}) \quad (3.49)$$

$$g_{f,1} = g_{a,2} = \sqrt{r_{a,2}^2 - r_{b,2}^2} - r_{b,2} \cdot \tan(\alpha_{w,t}) \quad (3.50)$$

If the length of the line of action is compared to the transverse base pitch, p_{bt} , it is possible to determine the average number of teeth in contact in the mesh, ϵ_α , which is known as “contact ratio”:

$$\epsilon_\alpha = \frac{g_\alpha}{p_{bt}} = \frac{g_a + g_f}{p_{bt}} = \epsilon_a + \epsilon_f \quad (3.51)$$

Where $p_{bt} = r_b \cdot \tau$ with τ being the angular pitch (see Figure 3.1). From previous equations, it is deduced that the length of the mesh period depends on the tip and base radius as well as on operating parameters such as the centre distance or the working pressure angle. Any significant change to the active flank tip diameter (e.g. by applying chamfers, roundings, etc.) shortens the available length for contact and the contact ratio is reduced as a consequence (see corresponding condition of existence in Equation 3.15).

The contact ratio, indicates the maximum and minimum number of teeth in contact in the mesh and it is possible to derive the regions where single, double or multiple contact exist, calculating the available number of base pitches from the geometrical boundaries. The transition points will be referred to as “characteristic points”. Thus, for a standard contact ratios and considering that the distance to the pitch point is given by $\overline{T_1C} = r_{b,1} \cdot \tan(\alpha_{w,t})$, we have:

$$\overline{T_1E} = \overline{T_1C} + g_{a,1}; \quad (3.52)$$

$$\overline{T_1A} = \overline{T_1C} - g_{f,1}; \quad (3.53)$$

$$\overline{T_1B} = \overline{T_1E} - 1 \cdot p_{bt}; \quad (3.54)$$

$$\overline{T_1D} = \overline{T_1A} + 1 \cdot p_{bt}; \quad (3.55)$$

Sections \overline{AB} and \overline{DE} are double teeth contact regions and section \overline{BD} has a single pair of teeth in contact. In this case $1 < \epsilon_\alpha < 2$ but it is also possible to derive the characteristic points for higher contact ratios following the same procedure.

Transmitted load is shared between the different number of teeth pairs in contact along the line of action: normal load is reduced when multiple teeth pairs are meshing together and increases abruptly in the single tooth region if modifications are not applied. Moreover, the geometrical boundaries, A to E, can be displaced due to the elastic behaviour of the teeth under applied load (points A' and E' in Figure 3.10a), giving rise to an increased length of the path of contact and higher contact ratio. Meshing teeth enter these regions before than expected which gives rise to a premature contact; and if the enlarged length accommodates an additional base pitch, load distribution is changed completely. This behaviour will be further discussed in Section 3.3.

Finally, in the case of helical gears the end of a tooth trace can overlap the beginning of the next and therefore, an overlap length, g_β and an overlap contact ratio, ϵ_β , exist:

$$g_\beta = b \cdot \tan(\beta_b) \quad (3.56)$$

$$\epsilon_\beta = \frac{g_\beta}{p_{bt}} \quad (3.57)$$

The sum of the transverse and overlap contact ratios is known as total contact ratio, $\epsilon_\gamma = \epsilon_\alpha + \epsilon_\beta$. Although several other quantities regarding mesh behaviour and geometrical boundaries can be introduced, the aforementioned parameters are sufficient to understand this document. The reader is referred to ISO 21771 for further information [176].

Mesh phase relations

Mesh phase relations are fundamental to understand the rolling-sliding behaviour of the contact point moving along the base tangent. Furthermore, composite stiffness, affecting load distribution and transmission error, requires the accurate calculation of instantaneous geometry parameters, and hence, it demands relating kinematically pinion and gear during their rotational movement. From the law of gearing in Section 3.1.1 it is possible to relate the geometrical quantities of any tooth in the pinion with the corresponding parameters of its mate in the gear, while the angular pitch, τ , relates the variables of that tooth with those of the preceding and succeeding teeth. From these relations, it is possible to solve the full system of kinematic and geometric equations.

Figure 3.11 shows the main angular quantities and velocity parameters for a reference tooth in the pinion, named “master” in the following. The phase angle, ϕ_y , is selected as the reference parameter to relate teeth angular variables; and the radial distances to the point of contact, $r_{y,1}$ and $r_{y,2}$, will be used to relate pinion and gear.

Assuming an odd number of teeth in the pinion, the master tooth is the one located in the middle (identified by subscript N). For a given angular position of the latter, the phase of the preceding ($N - 1$) and succeeding teeth ($N + 1$) is calculated from the angular pitch, τ , following:

$$\phi_{y,N-1} = \phi_{y,N} - 1 \cdot \tau \quad (3.58)$$

$$\phi_{y,N+1} = \phi_{y,N} + 1 \cdot \tau \quad (3.59)$$

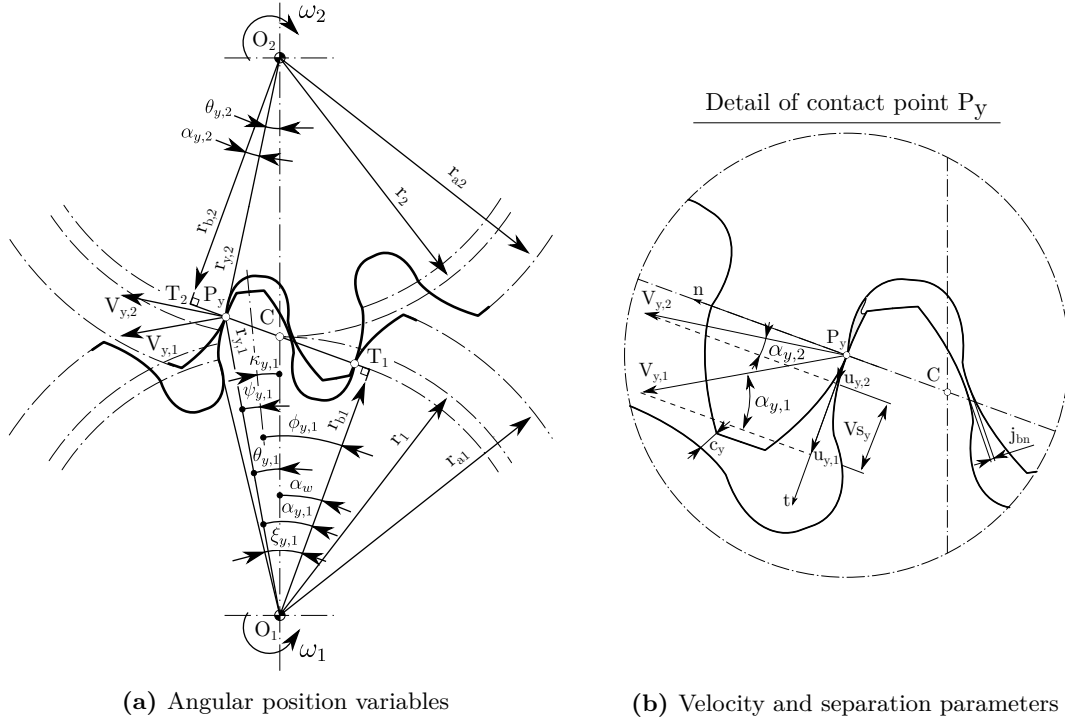


Figure 3.11: Position and velocity parameters in the gear mesh

The same procedure applies for teeth next to the adjacent ones which are separated by several angular pitches from the master tooth. This way, when the latter is located inside the engagement region, the angular position of those teeth close to it is perfectly defined.

On the other hand, from triangle $\triangle O_1 P_y O_2$ it is possible to determine the radius of the contact point P_y from the gear side, $r_{y,2}$. However, two situations must be considered: i) in mesh and ii) out of mesh. The former is easily computed applying the law of cosines but the latter, necessary to identify premature contact when gears are loaded, requires an additional parameter known as “separating distance”, c_y (see Figure 3.11b). For in-mesh condition we have:

$$r_{y,2} = \sqrt{a_w^2 + r_{y,1}^2 - 2 \cdot a_w \cdot r_{y,1} \cdot \cos(\theta_{y,1})} \quad (3.60)$$

Where a_w is the centre distance and $r_{y,1}$ is the distance to the point of contact from the pinion rotation centre which is calculated from the parametrical representation of the tooth in Equation 3.28. Angle $\theta_{y,1}$ is computed from Figure 3.11a and yields:

$$\theta_{y,1} = \kappa_{y,1} + \psi_{y,1} \quad (3.61)$$

$$\kappa_{y,1} = \phi_{y,1} - \alpha_{w,t} \quad (3.62)$$

$$\psi_{y,1} = \frac{\pi + 4 \cdot x \cdot \tan \alpha_n}{2 \cdot z} + \text{inv } \alpha_t - \text{inv } \alpha_{y,1,t} \quad (3.63)$$

Where ψ_y is known as “tooth thickness half angle” [176] and determines the transverse tooth thickness, s_y , and the attack angle, $\alpha_{F,y}$ of the tooth at any angular position, which are necessary to compute tooth stiffness in Section 3.3.2.

$$s_y = 2 \cdot r_y \cdot \psi_y \quad (3.64)$$

$$\alpha_{F,y} = \tan(\alpha_y) - (\psi_y + \text{inv } \alpha_{y,t}) \quad (3.65)$$

In the case of out of mesh condition the following equation applies:

$$r'_{y,2} = \sqrt{\left(\sqrt{r_{y,2}^2 - r_{b,2}^2} - c_y\right)^2 + r_{b,2}^2} \quad (3.66)$$

Separating distance, c_y , is defined as the distance along the line of action between mating flanks when they lie outside the geometrically defined phase of mesh. Thus, when gears are meshing such separation is zero and $r'_{y,2} = r_{y,2}$. A graphical example of this parameter is shown in Figure 3.11b: if the pinion rotates in the clockwise direction the line of action is reversed and the distance between the new flanks, which are still not in touch, is described by parameter c_y . This variable is further discussed in Section 3.2.2.

Consequently, from Equations 3.58, 3.59 and 3.66 the phase of mesh of any tooth of the gear pair can be fully defined from base parameters ϕ_y and r_y and from now on, a tooth is considered to be “potentially in mesh” if its phase angle, ϕ_y , fulfils the condition: $\phi_{A'} \leq \phi_y \leq \phi_{E'}$, where A' and E' are the start and end of the path of contact when load is applied (see Figure 3.10a)

Velocity components and derivative parameters

In spur gears, when the tangential velocity of the contact point, P_y , relative to pinion or gear, is decomposed on the common tangent direction, the relative velocity at which the pinion flank rolls over that of the gear is obtained (and viceversa). The latter is known as rolling velocity, u_y , and from Figure 3.11b it is calculated as:

$$u_{y,1} = V_{y,1} \cdot \sin(\alpha_{y,1}) = (\omega_1 \cdot r_{y,1}) \cdot \sin(\alpha_{y,1}) = \omega_1 \cdot \rho_{y,1} \quad (3.67)$$

$$u_{y,2} = V_{y,2} \cdot \sin(\alpha_{y,2}) = (\omega_2 \cdot r_{y,2}) \cdot \sin(\alpha_{y,2}) = \omega_2 \cdot \rho_{y,2} \quad (3.68)$$

Similarly, in the case of helical gears, the rolling velocity of any point P_y follows the perpendicular direction to the contact line which is inclined with respect to the tooth trace as shown in Figure 3.10b. In the global system of coordinates attached to the base tangent plane we have:

$$u_{y,1}(x, z) = \omega_1 \cdot \left(x + z \cdot \tan(\beta_b)\right) \cdot \cos(\psi) \quad (3.69)$$

$$u_{y,2}(x, z) = \omega_2 \cdot \left(\overline{T_1 T_2} - x - z \cdot \tan(\beta_b)\right) \cdot \cos(\psi) \quad (3.70)$$

Where $x = \overline{T_1 M} = r_{b,1} \cdot \tan(\alpha_{Mt})$ corresponds to the distance between the tangent to the pinion base cylinder and the contact point M located in the tooth end in Figure 3.10b.

From the above equations, it is seen that rolling velocities mainly depend on the local pressure angle and the radial distance, thus, they change during the engagement. Moreover, pinion and gear rolling velocities are not equal which causes sliding of the surfaces. Only at the pitch point C , tangential velocities and local pressure angles are equal and therefore pure rolling exists. The main derivative velocity parameters are summarized below:

$$Vs_y = |u_{y,1} - u_{y,2}| \quad (3.71)$$

$$Vr_y = u_{y,1} + u_{y,2} \quad (3.72)$$

$$Ve_y = \frac{u_{y,1} + u_{y,2}}{2} \quad (3.73)$$

Sliding and rolling velocities, V_{s_y} and V_{r_y} , are directly related to power losses in the line of action while entraining velocity, V_{e_y} , indicates the rate at which the oil film enters the Hertzian contact region. Both parameters are fundamental to understand mesh losses in Chapter 4. From these parameters additional relations can be computed, namely:

$$S = \frac{u_{y,1} - u_{y,2}}{u_{y,1}} \quad (3.74)$$

$$SRR = \frac{2 \cdot (u_{y,1} - u_{y,2})}{u_{y,1} + u_{y,2}} \quad (3.75)$$

Where S is known as slip ratio, and SRR is the slide to roll ratio, which are frequently used to analyse traction behaviour at high speeds.

Figure 3.12 depicts the common kinematic behaviour of a pair of spur gear teeth. As it can be seen, sliding velocity is maximum in the profile ends and zero at the pitch point with a linear slope between both ends. This means that maximum power losses, heat or even wear will occur at the tip/root of the gear. Moreover, rolling velocity is not constant indicating that the gear ratio is other than unity. As a consequence, the slide-to-roll and slip ratios are not symmetric indicating that thermal effects in the lubricant are more prominent towards the root of the pinion, leading to a thinner oil film and a higher probability of flank wear.

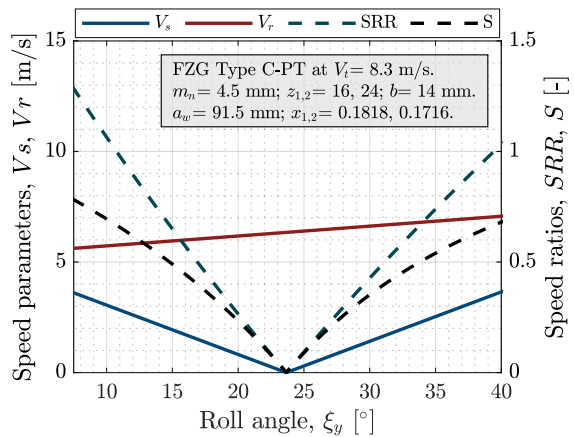


Figure 3.12: Kinematic behaviour of the FZG Type C-PT spur gear set at $V_t = 8.3$ m/s

3.2.2 No-load transmission error behaviour

When theoretically perfect gears mesh together, the ratio of rotational speeds is constant; but manufactured profiles are not free of inaccuracies and profile errors produce a phase difference in the motion. Besides, backlash allowance to accommodate thermal growth or tooth modifications applied to compensate deflections under load, also produce a deviation from the theoretical rigid-body motion. Therefore, in order to fully characterize kinematic behaviour of generated teeth it is necessary to analyse this parameters.

No-load separation

As it has been described in Section 3.2.1 gear teeth motion develops between single and multiple teeth contact regions with abrupt normal load changes in between. However, thanks to the elasticity of gear teeth, engagement shock occurs progressively as teeth contact before expected, thus sharing load gradually. The parameter controlling this behaviour is strictly geometric and it is known as no-load separation. The latter is defined as the additional rotation necessary to contact a tooth held fixed in the mating gear. When the rotation is translated to distance along the line of action separating distance, c_y , as presented in Equation 3.66 is obtained.

Kinematic behaviour of the separating distance was first studied by Richardson [177] who found that the latter depends mainly on the diameter and pressure angle at the tip of pinion and gear, and depending on which one is held fixed, no-load separation is different. A rather complex algorithm was developed with two different equations for the approach and recess paths of contact; and due to the small differences between both, a simple general model was proposed based on the polynomial approximation of the curves. Later, Seager et al. [178] further developed this simplification and studied the effect of geometry parameters, namely pitch and pressure angle, and found that considerable corner contact may occur due to pitch errors. Lin and Wang [179] presented an alternative exact method which was used to analyse dynamic effects and concluded that neglecting this parameter underestimates resonant speeds and overestimates dynamic loads. Finally, in an attempt to simplify the calculation methods presented previously, and trying to minimize error in approximate equations, Munro [180] et al. proposed a new model with a straight-forward procedure with which no-load transmission error could be analysed in depth.

The approximate equation proposed by Munro et al. in [180] is used in this work and it has been developed herein for the case of pinion approach and recess.

$$c_y \Big|_{Rec} = \frac{1}{2} \cdot \left(\frac{1}{\rho_{a,1}} + \frac{1}{\rho_{a,2}} \right) \cdot \left[r_{a,1} \cdot \Delta\theta_{a,1} \cdot \cos \left(\arcsin \left(\frac{r_{b,1}}{r_{a,1}} \right) - \frac{\Delta\theta_{a,1}}{2} \right) \right]^2 \quad (3.76)$$

$$c_y \Big|_{App} = \frac{1}{2 \cdot i} \cdot \left(\frac{1}{\rho_{a,1}} + \frac{1}{\rho_{a,2}} \right) \cdot \left[r_{a,1} \cdot \Delta\theta_{a,1} \cdot \cos \left(\arcsin \left(\frac{r_{b,2}}{r_{a,2}} \right) - \frac{\Delta\theta_{a,1}}{2 \cdot i} \right) \right]^2 \quad (3.77)$$

Where $\Delta\theta_{a,1}$ is the angle of rotation of the driving gear (see Figure 3.11a) measured from the theoretical start or end of the line of action depending on the approach or recess condition. All the rest of the parameters refer to the tip of pinion or gear.

Figure 3.13 depicts the behaviour of the separating distance for a common spur gear set. Separation during engagement is zero but when the start or end of the active profile (known as SAP or EAP respectively) is close, tooth separation increases progressively following a parabolic function of rotation. In reduction units, separation in recess is usually smaller than in approach but both are very similar as observed. It is also interesting to note that even at significant distances from the tip, the separation is very small indicating that premature contact can be expected. For example, at a distance of 1 mm along the line of action from the tip, no-load separation is 50 μm which can be exceeded by mechanical deflections causing corner contact unless tip relief is provided. In this sense, backlash allowance and profile modifications play an important role as they tend to separate theoretical flanks to avoid interference, however, such alterations of the theoretical profile produce a phase difference in the rigid-body motion which will be known as no-load transmission error.

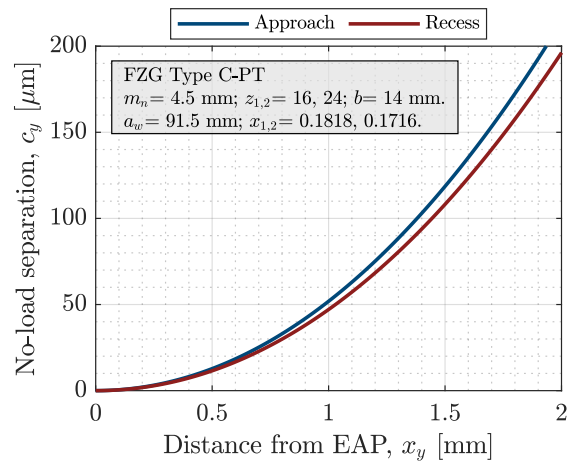


Figure 3.13: Separating distance of the theoretical FZG Type C-PT spur gear set

No-load transmission error

The rigid-body motion of a gear pair is defined by the law of gearing presented in Section 3.1.1. However, any manufacturing error, backlash allowance or intended modification distorts the theoretical continuous motion along the line of action. Introducing the local velocity difference, Δv_y , in Equation 3.7 describing the rigid body motion one obtains:

$$\omega_1 \cdot r_{b,1} + \omega_2 \cdot r_{b,2} + \Delta v_y = 0 \quad (3.78)$$

Where Δv_y can be mathematically related to geometry deviations in the flank normal by:

$$\Delta v_y = \frac{d\Delta x_y}{dt} = \frac{1}{\cos(\beta_b)} \cdot \frac{d\Delta \eta_y}{dt} \quad (3.79)$$

Introducing Equation 3.79 in 3.78 and integrating, local no-load transmission error results:

$$\text{NLTE}_y = -\frac{\Delta \eta_y}{\cos(\beta_b)} = -\frac{\epsilon_{T,y}}{\cos(\beta_b)} \quad (3.80)$$

Where $\epsilon_{T,y} = \max[\epsilon_{y,1}(z) + \epsilon_{y,2}(z) + c_y]$ is the maximum composite deviation among all potential contact points in the contact line considering that normal deviations from the theoretical profile are negative if material is removed from the ideal involute profile (see Figure 3.8). Individual surface deviations, $\epsilon_{y,i}$, defined this way include flank modifications and backlash allowance, which have been defined with parameters δ and κ respectively in Figure 3.8.

In the case of teeth generated with tooth thickness tolerance E_s according to Equation 3.16 the computation of the no-load transmission error yields a constant value equal to half the normal backlash $j_{b,n}$ which is a negative value indicating that the driven gear lags behind its theoretical position. However, if teeth are manufactured including modifications, no-load transmission error along the line of action depends on the sum of pinion and gear local deviations for each position in the mesh. Figure 3.14 graphically describes this situation where the theoretical profiles of the standard FZG Type C-PT gear pair have been modified.

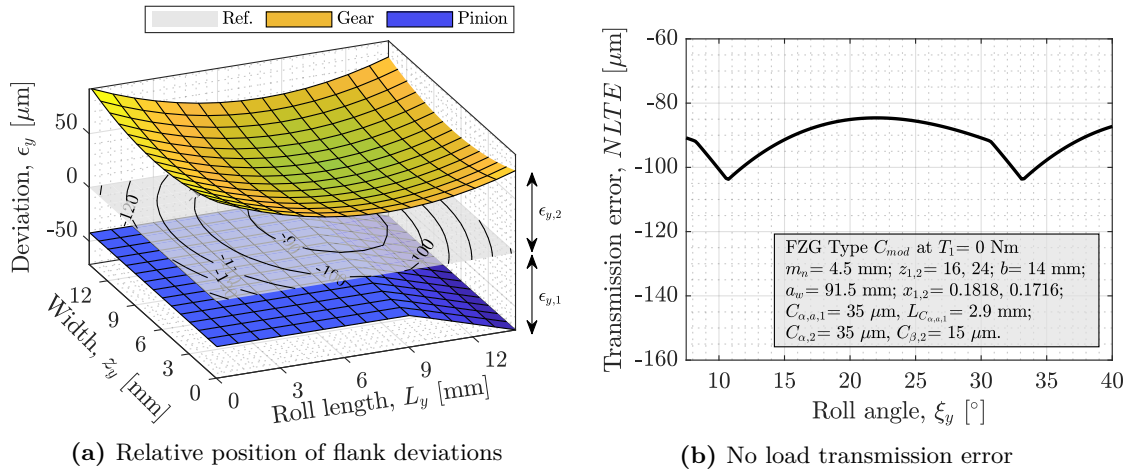


Figure 3.14: Sample calculation of no-load transmission error in modified FZG type C gear

Pinion teeth profile include a linear tip relief while gear flank has been double-crowned in the profile and lead directions. The relative deviations in the normal direction are shown in Figure 3.14a and the grey coloured reference plane shows the contour plot of the composite $\Delta\eta_y$ values which result from the sum of local deviations in pinion and gear. If the latter is computed for each position along the line of action no load transmission error results as depicted by Figure 3.14b. It is observed that the continuous motion is no longer kept and two bumps arise as the result of the profile modifications. In this case, longitudinal crowning does not change transmission error behaviour because the pinion is not modified in the lead direction.

3.3 Load distribution and transmission error

It has been shown in previous sections that gear teeth are subject to a variable number of teeth in contact during the engagement. Geometrical boundaries of multiple teeth contact regions have been shown to be dependent on the contact ratio and the base pitch, but instantaneous load on these regions is not uniformly distributed among all teeth pairs in mesh as one would expect. This is due to the variable stiffness along the line of action and the surface modifications or errors that prevent gear teeth contact. Moreover, the continuous rotational motion defined in the fundamental law of gearing is also interrupted by local loads that induce a phase difference due to elastic deformation of the teeth. The latter must be added to the no-load transmission error explained in Section 3.2.2 and, therefore, the final kinematic behaviour of the gear pair will not be completely defined unless the load distribution problem is solved.

3.3.1 Statement of the problem

Load distribution in cylindrical gears has been analysed by a number of researchers. The early works by Poritsky et al. [181], Weber and Banaschek [182] and Trbojevic [183] reported the influence of teeth bending, twisting and contact stiffness in spur and helical gear load distribution under plane stress or plane strain conditions. Later, Hayashi [184] introduced convective effects in infinite width helical gears and discussed the difficulty of solving the 3D load distribution problem analytically. A numerical integration procedure based on the second kind integral equation of Fredholm was introduced and the solution was experimentally validated. Similarly, Umezawa et al. [185] presented a 3D finite difference based solution and Seager [186] developed the so-called “thin slice” approach including longitudinal convective effects to solve finite width helical gear load distribution problems. Finally, while transmission error was computed separately in Seager’s work, and those of the previous authors, Conry and Seireg [187] introduced the full formulation of the load distribution problem including coupled transmission error computation for the first time.

Successive research works have reinforced the original analytical/numerical solutions and have contributed to the understanding of the load distribution problem. Among others, Schmidt [188] and Plackzek [189] analysed the effects of profile modifications; Vedmar [190], Steward [191] and Kunert [192] introduced hybrid analytical-numerical 3D stiffness models obtained from regression of FEM simulations and analysed the influence of misalignments and profile errors; Neupert [193] and Guilbault [194] developed simplified

finite element and finite strip techniques respectively to accelerate computation and analyse root stress behaviour; Ajmi and Velez [195] introduced dynamic effects and a new longitudinal coupling model; and more recently, Pedrero et al. [196] have presented a new analytical solution technique based on the minimization of the elastic potential energy.

Although there are a number of research works in literature taking advantage of these load distribution models to analyse different phenomena on several types of gear geometries, currently, finite element models have become a popular tool to analyse gear mesh problems [197]. However, the solution time and the required computational capacity of these models is large, the accuracy of the result varies significantly with the type of element and boundary conditions and the method is not suited to contact problems because very fine meshes are required. Thus, analytical-numerical models based on the thin-slice approach are still dominant giving very accurate results (with experimentally proved effectiveness [198]) and efficient solution times.

Governing equations

According to Conry and Seireg [187] the load distribution problem is defined as the simultaneous solution of the set of equations representing the conditions of compatibility of motions, equilibrium of moments and existence of contact for each engagement position. Each of these conditions is mathematically described by:

$$\delta_{T,1} + \delta_{T,2} - \epsilon_T \geq r_{b,i} \cdot \theta_i = \text{TE} \quad (3.81)$$

$$T_i = \frac{r_{b,i}}{\cos(\beta_b)} \cdot \sum_{j=1}^N \int_{z_1}^{z_n} w_j(z) dz \quad (3.82)$$

$$w_j(z) \geq 0 \quad (3.83)$$

Equation 3.81, known as “condition of compatibility”, states that the sum of pinion and gear elastic deformations under load, $\delta_{T,1}$ and $\delta_{T,2}$, minus the initial gap between teeth, ϵ_T , must be greater than or equal to the rigid body rotation. Small deflections are assumed for steel gears, therefore, contact always remains in the base tangent plane (x, z) and the rigid body motion (known as transmission error, TE, in the following) is taken as the product of the base circle radius and the angular displacement of pinion or gear. The “condition of equilibrium”, represented by Equation 3.82, implies that the sum of all moments applied on the gear must equal the input torque, T_i , with N the total number of simultaneous contact lines. Finally, the “condition of contact existence” in Equation 3.83 states that two surfaces must be in contact at a point for a pressure to exist and therefore, loads must be positive or zero. When the load distribution problem is solved for each position in the path of contact, the solution yields the distribution of normal loads along the profile and longitudinal directions as well as the loaded transmission error behaviour.

Neglecting the influence of shaft, bearing or housing deflections under load, common cylindrical gears are affected by several deflection types as shown by the following equation:

$$\delta_{T,i} = \frac{1}{\cos(\beta_b)} \cdot \sum_{j=1}^N \int_{z_1}^{z_n} [C_{b,i} + C_{s,i} + C_{c,i} + C_{t,i} + C_{r,i} + C_{H,i}](z, z') \cdot w_j(z) dz \quad (3.84)$$

Where the individual compliance contributions of the gear, i , are: i) body rotation compliance, C_r , ii) teeth bending, shearing and compressive compliances, C_b , C_s and C_c respectively, iii) gear teeth base tilting compliance, C_t , and iv) contact compliance, C_H . From these terms, that of contact deflection is very localised and therefore, convective effects can be neglected. In other words, it is a function of the local load and cross influences are not considered which allows subtracting this term from the integral. Restating Equation 3.84 yields:

$$\delta_{T,i} = \frac{1}{\cos(\beta_b)} \cdot \sum_{j=1}^N \left[\int_{z_1}^{z_n} C_{T,i}(z, z') \cdot w_j(z) dz + C_{H,i}(z) \cdot w_j(z) \right] \quad (3.85)$$

Where $C_{T,i}(z, z')$ refers to the total compliance influence function for gear, i , including all terms except that of contact. Note that the integral must be evaluated at the instantaneous length of the contact line for tooth j which is variable in the case of helical gears [199].

On the other hand, initial total gap is the sum of pinion and gear backlash allowance, κ , local values of surface modifications, δ , and unloaded separating distance, c_y , for the considered phase of mesh; all of which are negative values if material is removed from the theoretical profile following the local tangential-normal system of coordinates in Figure 3.8. Note that, in the absence of elastic deflections in Equation 3.81, the initial gap, ϵ_T , is equivalent to the no-load transmission error parameter, NLTE, presented in Equation 3.80:

$$\epsilon_T = \frac{1}{\cos(\beta_b)} \cdot [\epsilon_{T,1} + \epsilon_{T,2} + c_y] = \frac{1}{\cos(\beta_b)} \cdot [(\delta_1 + \delta_2) + (\kappa_1 + \kappa_2) + c_y] \quad (3.86)$$

Numerical approximation

The analytical integration of the set of Equations 3.81 to 3.86 is complex [184] and numerical integration is used instead following two point Gauss-Legendre quadrature rule [191, 200]. Hence, the load distribution problem restated numerically reads:

$$\frac{1}{\cos(\beta_b)} \cdot \sum_{j=1}^N \left[\frac{\Delta}{2} \cdot \sum_{k=1}^{2 \cdot m} C_{T,1,2}(z, z_k) \cdot w_j(z_k) + C_{H,1,2}(z_k) \cdot w_j(z_k) \right] - \epsilon_T \geq r_{b,i} \cdot \theta_i \quad (3.87)$$

$$T_i = \frac{r_{b,i}}{\cos(\beta_b)} \cdot \sum_{j=1}^N \left[\frac{\Delta}{2} \cdot \sum_{k=1}^{2 \cdot m} w_j(z_k) \right] \quad (3.88)$$

$$w_j(z_k) \geq 0 \quad (3.89)$$

Where $C_{T,1,2}$ and $C_{H,1,2}$, are equivalent compliance terms which consider pinion and gear composite influence (see Section 3.3.2), Δ is the Gauss interval size, m is the number of gauss intervals and z_k is the axial coordinate of the Gauss query points which are strategically located along the tooth face width for numerical integration.

Figure 3.15 depicts the parameters involved in the numerical integration of a general case with two gauss intervals dividing the potential engagement region in two halves. The interval size Δ is computed dividing the tooth face width, b , by the number of gauss intervals, m . Moreover, in the case of successive two point Gauss integration, each of the intervals has two query points with axial coordinate z_k which can be calculated from:

$$z_k = \frac{\Delta}{2} \cdot (2 \cdot m_k + K - 1) \quad (3.90)$$

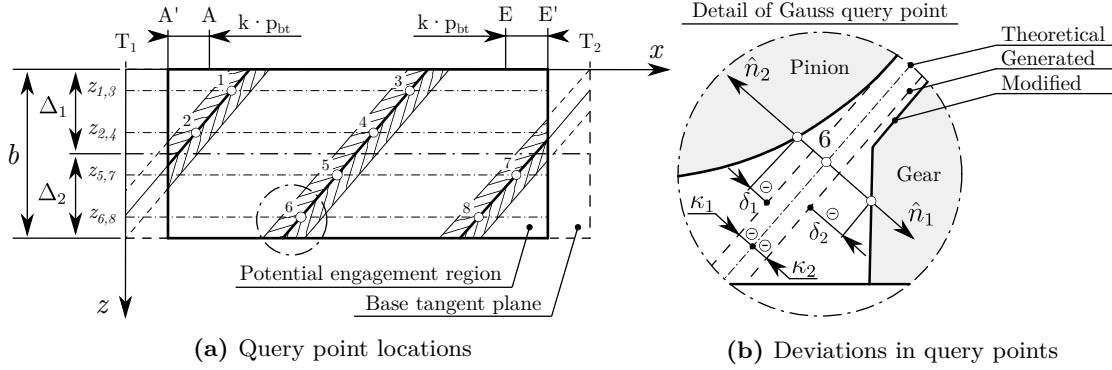


Figure 3.15: Discretization of the base tangent plane for numerical integration

Where m_k is an integer value indicating the gauss interval number with $m_k \in [1, m]$ and $K = \pm 1/\sqrt{3}$ is the quadrature function argument for two point Gauss integration.

As it can be seen in Figure 3.15 the integration points are uniformly distributed along the face width and if higher accuracy is required in the computation, the number of intervals can be increased producing additional query points on each flank. Although a higher number of query points can be used in each interval, Steward [191] pointed out that high order polynomial approximations lead to unstable modelling while repeated two point integration minimizes numerical errors efficiently, thus a maximum of two query points is kept for each interval. Besides, with the aim of detecting premature contact, the region under study has been enlarged by k base pitches with respect to the theoretical bounds (points A to E). This way, and a tooth is assumed to be potentially in mesh if any of its Gauss points is within the new limits $A'E'$. The solution of the system of equations will determine if the incoming or outgoing teeth are effectively in contact or not.

Solution method

Following [187] the compatibility condition can be converted to equality constraint by introducing a slack variable $Y \geq 0$ such that $\delta_{T,1} + \delta_{T,2} - \epsilon_T - r_b \cdot \theta - Y = 0$. Furthermore, multiplying by $2/\Delta$ at both sides of Equation 3.87 and rearranging terms one we obtains the following system of equations in matrix form:

$$\left[[\mathbf{C}_T] + \frac{2}{\Delta} \cdot [\mathbf{C}_H] \right] \cdot \mathbf{w} - \frac{2}{\Delta} \cdot (\epsilon_T + \mathbf{i} \cdot r_{b,i} \cdot \theta_i) - \mathbf{Y} = 0 \quad (3.91)$$

$$\frac{2}{\Delta} \cdot \frac{T_i}{r_{b,i}} = \mathbf{i}^T \cdot \mathbf{w} \quad (3.92)$$

$$\text{Either } w_k = 0 \text{ or } Y_k = 0 \quad (3.93)$$

Where \mathbf{i} is the identity column vector, $\Delta = b/(m \cdot \cos(\beta_b))$ and subscripts i and k refer to the analysed gear and the Gauss query point respectively.

To solve the system of equations, a new method is proposed in this work, which is a different approach compared to similar algorithms presented in [187, 191, 195]. To compute the exact solution efficiently, the system of equations is restated as a Linear Complementarity Problem (LCP) by rewriting Equations 3.91 and 3.92 under the form $\mathbf{Y} = [\mathbf{C}] \cdot \mathbf{w} + \mathbf{q}$ and restating the contact existence condition in Equation 3.93 as $Y_k \cdot w_k = 0$:

$$\begin{Bmatrix} Y_{11} \\ Y_{21} \\ \dots \\ Y_{n1} \\ Y_{(n+1)1} \\ \dots \\ Y_{(N \cdot n + 1)1} \end{Bmatrix} = \begin{bmatrix} C_{T_{11}} + \frac{2}{\Delta} \cdot C_{H_{11}} & C_{T_{12}} & \dots & C_{T_{1n}} & C_{T_{1(n+1)}}^{adj} & \dots & -\frac{2}{\Delta} \\ C_{T_{21}} & C_{T_{22}} + \frac{2}{\Delta} \cdot C_{H_{22}} & \dots & C_{T_{2n}} & C_{T_{2(n+1)}}^{adj} & \dots & -\frac{2}{\Delta} \\ \dots & \dots & \dots & \dots & \dots & \dots & \dots \\ C_{T_{n1}} & C_{T_{n2}} & \dots & C_{T_{nn}} + \frac{2}{\Delta} \cdot C_{H_{nn}} & C_{T_{n(n+1)}}^{adj} & \dots & -\frac{2}{\Delta} \\ C_{T_{(n+1)1}}^{adj} & C_{T_{(n+1)2}}^{adj} & \dots & C_{T_{(n+1)n}}^{adj} & C_{T_{(n+1)(n+1)}} + \frac{2}{\Delta} \cdot C_{H_{(n+1)(n+1)}} & \dots & -\frac{2}{\Delta} \\ \dots & \dots & \dots & \dots & \dots & \dots & \dots \\ 1 & 1 & \dots & 1 & 1 & \dots & 0 \end{bmatrix} \cdot \begin{Bmatrix} w_{11} \\ w_{21} \\ \dots \\ w_{n1} \\ w_{(n+1)1} \\ \dots \\ r_{b,i} \cdot \theta_i \end{Bmatrix} - \frac{2}{\Delta} \begin{Bmatrix} \epsilon_{T_{11}} \\ \epsilon_{T_{21}} \\ \dots \\ \epsilon_{T_{n1}} \\ \epsilon_{T_{(n+1)1}} \\ \dots \\ T_i / r_{b,i} \end{Bmatrix} \quad (3.94)$$

This way, the system of equations can be solved efficiently within a few iterations using Lemke's pivoting algorithm [201], without any need to modify the compliance matrix terms as in [191, 195]. For instance, the solution time for a 33×33 matrix kernel corresponding to 8 Gauss intervals and two teeth in the potential engagement region (total number of 32 Gauss query points) is below 5 msec. The full path of contact is covered in a few seconds where most of the time is spent in the construction of the compliance matrix by addition of the different terms and the inversion of the slice coupling stiffness components.

The terms in the main diagonal of the matrix in Equation 3.94 correspond to the position of load application while the off-diagonal terms represent convective effects. As described by Equation 3.85, contact compliance, C_H , is localized and therefore coupling effects are neglected which means that it only affects the terms in the principal diagonal. However, the total compliance term, C_T , which is the sum of several deflection contributions (i.e. bending, tilting, body rotation, etc.) from pinion and gear, does influence all the rest of the query points. Furthermore, it is to be noted that the distant upper and lower diagonal sub-matrices are off-diagonal coupling terms (denoted by superscript "adj.") which are related to remote deflections of the adjacent teeth due to the rotation of the gear body and tooth base tilting. The latter specially affects load distribution in large diameter gear wheels and in case of pitch errors that cause the next tooth to come into contact before expected. If the master tooth is located in the first positions, the terms affecting the adjacent teeth are located at positions $i, j > n$ with n the number of query points on the same tooth, thus $n = 2 \cdot m$.

Equation 3.94 has been presented in general form and it must be redefined for each position along the contact line. For spur gears of standard proportions, no more than two pairs of teeth are simultaneously in contact and therefore it is only necessary to include the compliance of the preceding and succeeding teeth. However, in high contact ratio spur gears (or helical gears) it is possible for three or more tooth pairs to be simultaneously in mesh which means that the compliance of the next to the adjacent teeth must also be considered. Therefore, the size of the kernel matrix is variable and it is ruled by the number of gauss points in the potential engagement region with size $= N \cdot n + 1 = 2 \cdot N \cdot m + 1$; where N is the number of teeth in potential contact and m is the number of Gauss intervals. For instance, in the case of a spur gear pair with $1 < \epsilon_\alpha < 3$ a minimum set of 5 teeth should be analysed during rotation. If the master tooth (named T3 for being the one in the middle of the set) is located at the beginning of the approach path of contact, there are two teeth preceding it (T4 and T5) and the system of equations should be formulated as follows:

$$\begin{Bmatrix} Y_{T3} \\ Y_{T4} \\ Y_{T5} \\ Y \end{Bmatrix} = \begin{bmatrix} [\mathbf{T3}] & [\text{Adj.}] & [\text{Next}] & -\frac{2}{\Delta} \\ [\text{Adj.}] & [\mathbf{T4}] & [\text{Adj.}] & -\frac{2}{\Delta} \\ [\text{Next}] & [\text{Adj.}] & [\mathbf{T5}] & -\frac{2}{\Delta} \\ 1 & 1 & 1 & 0 \end{bmatrix} \cdot \begin{Bmatrix} w_{T3} \\ w_{T4} \\ w_{T5} \\ r_{b,i} \cdot \theta_i \end{Bmatrix} - \frac{2}{\Delta} \begin{Bmatrix} \epsilon_{T3} \\ \epsilon_{T4} \\ \epsilon_{T5} \\ T_i / r_{b,i} \end{Bmatrix} \quad (3.95)$$

At each phase of mesh, the potential number of teeth in contact must be evaluated, the compliance matrix is redefined and the system of equations is solved for the load vector (which includes transmission error). However, two inconvenients may arise during the solution process. On the one hand, a singular matrix may result when the compliance matrix is inverted. Although a number of reasons may explain this behaviour (e.g. sparse matrix) the problem is usually related to the floating point precision of the machine because compliances have been expressed in SI units which gives rise to very low values in steel gears. To solve this issue variables must be scaled or non-dimensionalized. In this work, length parameters such as, δ , or Δ , are expressed in μm , unit normal loads, w , in $\text{N}/\mu\text{m}$, total compliances in $\mu\text{m}/\text{N}$ and contact compliances in $\mu\text{m}/\text{N}/\mu\text{m}$. On the other hand, contact compliance, C_H , is slightly non-linear and decreases with normal load, therefore, an iterative procedure is required where the initial guess for normal load per unit length can be approximated by $w_k = T_i \cdot \cos(\beta_b)/(2 \cdot r_{b,i} \cdot b)$. Such an iterative procedure may increase computational time; alternatively, it is also possible to linearise contact compliance by using the first term of the Taylor expansion which helps minimize computational cost without great loss of accuracy [202].

3.3.2 Thin slice approach for 3D gear contact problems

The numerical integration procedure described earlier introduces the notion of Gauss query points which are optimal longitudinal locations for the exact integration of a general polynomial function representing line load $w = f(z)$. In the case of two point integration a third order polynomial function is used to fit the latter. As a consequence, tooth deflections, surface deviations and normal loads are only calculated at this reference points and therefore, gear face width can be sliced around them as shown by Figure 3.15 where the length of each section is half the interval size $l = \Delta/2 = b/(2 \cdot m \cdot \cos(\beta_b))$. Hence, the kernel matrix in Equation 3.94 only requires the main compliance terms, $C_{T,nn}$ and $C_{H,nn}$, at the query points plus coupling terms, $C_{T,n(n+1)}$ for the convective effects which relate the deformation of each individual slice to the adjacent ones (see Figure 3.16).

At a particular phase of mesh, total deflection of a single slice is the sum of:

1. Contact deflection of curved flanks pushing against each other.
2. Tooth bending, shearing and compression when subject to a normal load.
3. Tooth foundation tilting due to the reaction moment to the applied load.
4. Gear body rotation or twisting produced by the transmitted torque.
5. Other: gear rim/web deformation, shaft/housing deflections, bearing stiffness, etc.

Neglecting distant deflection terms, total compliance, $C_{T,nn}$, in the principal diagonal of the matrix in Equation 3.94, can be calculated as the equivalent compliance of several springs in series (see Figure 3.16a). Therefore we have:

$$C_{T,nn} = C_{T,1,nn} + C_{T,2,nn} \quad (3.96)$$

$$C_{T,i,nn} = C_{b,i,nn} + C_{s,i,nn} + C_{c,i,nn} + C_{t,i,nn} + C_{r,i,nn} \quad (3.97)$$

Where each of the terms varies along the line of action due to the changing distances from the gear centreline to the point of load application during rotation.

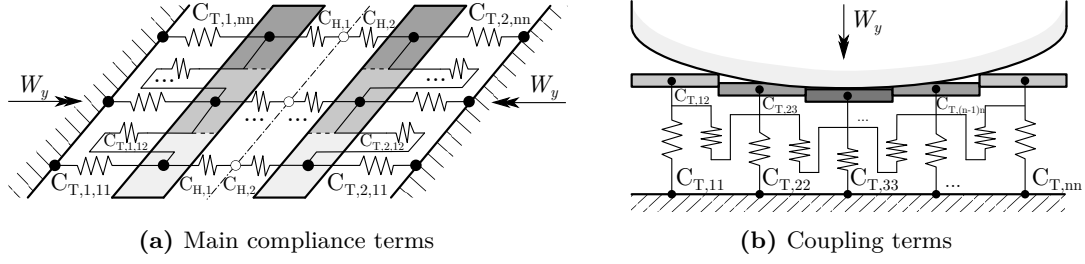


Figure 3.16: Thin slice compliance model representation

Besides, the coupling off-diagonal terms, $C_{T,n(n+1)}$, relate the deflection of an individual slice to the neighbouring ones. Experimental evidence has shown that such convective effects are very important in misaligned gears or when lead modifications are applied [192]. Coupling terms should interrelate the deflection of all query points in a tooth, however, in this model only the deflections of the immediately adjacent slices will be considered as shown in Figure 3.16b. Moreover, slices located at the tooth ends are only connected to the next slice and therefore, a higher deflection results for them which is the expected behaviour.

Tooth bending, shearing and compression compliance

Considering gear teeth as a built-in beam with variable cross section, the bending, shearing and compression compliance terms of a single slice can be computed from the internal energy at each phase of mesh, y . Moving the global system of coordinates to the gear tooth base as shown in Figure 3.17, the different terms are computed following the classical assumptions from material resistance:

$$U_{b,y} = \frac{1}{2} \cdot \int_0^{y_p} \frac{M_{b,y}^2}{\frac{E \cdot l \cdot (2 \cdot x)^3}{12}} dy \quad (3.98)$$

$$U_{s,y} = \frac{1}{2} \cdot \int_0^{y_p} \frac{C \cdot Q_y^2}{G \cdot l \cdot (2 \cdot x)} dy \quad (3.99)$$

$$U_{c,y} = \frac{1}{2} \cdot \int_0^{y_p} \frac{N_y^2}{E \cdot l \cdot (2 \cdot x)} dy \quad (3.100)$$

Where x and y are the half chordal thickness and position of the differential section respectively, l is the slice width, E and G are the Young's modulus and transverse modulus of elasticity respectively and C is the shear correction factor which takes the approximate value 1.2 according to [182]. From Figure 3.17 normal and shearing force, N_y and Q_y , and bending moment, $M_{b,y}$, are computed as:

$$M_{b,y} = W_y \cdot \cos(\alpha_{Fy}) \cdot (y_p - y) \quad (3.101)$$

$$Q_y = W_y \cdot \cos(\alpha_{Fy}) \quad (3.102)$$

$$N_y = W_y \cdot \sin(\alpha_{Fy}) \quad (3.103)$$

where W_y is the local normal load, which is inclined angle, $\alpha_{F,y}$, known as attack angle and already defined in Equation 3.65.

Although the solution presented by reference [182] is very accurate and seems to be sufficient for small diameter gear wheels, it fails when the rotation of the gear body is not negligible with respect to the tilting term. In such cases, the gear body twisting compliance should be added separately. However, Sainsot et al. [203] developed a far more interesting solution which combines body rotation and tooth foundation tilting based on the theory of Muskhelishvili for circular elastic rings. The analytical solution was developed for the same stress distribution assumptions in [182] and a polynomial function fit was found for the terms L^* , M^* , P^* and Q^* in Equation 3.106. In this work, the solution by Sainsot et al. will be used for the combined tilting and rotation compliance C_{tr} . The reader is referred to the original article [203] for detailed information on the analytical solution and numerical approximation.

Furthermore, adjacent teeth deflection terms, C_T^{adj} , in Equation 3.94 are largely due to the rotation of the gear body and they are almost independent of the loading diameter and the axial position of the load [191]. Under this conditions the rotation of the preceding and succeeding teeth is equal and the same twisting compliance term can be used to represent both. Moreover, next-to-adjacent teeth in Equation 3.95 are also affected by the same rotation which allows to fulfil the remaining terms in the matrix. In order to counterbalance the foundation tilting term and compute the remaining body rotation compliance from the previous models, it is possible to use the difference between the deflection calculated by Equation 3.106 according to Sainsot et al. [203] and that calculated by Weber and Banaschek [182]. In this work, this terms are neglected for simplicity.

Longitudinal convective effects

Up to this point the compliance matrix has been fulfilled with the main diagonal terms, $C_{T,nn}$, which correspond to each slice in the model. Therefore, the kernel matrix is non-coupled and the deflection of a single slice does not affect the surrounding ones. If the gear is uniformly loaded along the face width, the deflection of all slices will be nearly the same and the coupling terms do not affect load distribution. However, when rapidly changing loads due to mesh misalignments or tooth modifications act on the gear pair, convective effects are very important to accurately compute load distribution. Therefore, in order to complete the matrix, coupling terms must be added to the off-diagonal positions.

In this work, Börner's method [204] is used, which has been developed from regression of multiple finite element simulations and it has been experimentally validated through several years of automotive field applications [198]. According to Börner the coupling stiffness between two adjacent slices n and $n+1$ is given by:

$$K_{T,n(n+1)} = 2.75 \cdot \left(\frac{m_n}{b} \right)^2 \cdot \frac{K_{T,n} + K_{T,(n+1)}}{2} \quad (3.107)$$

Where m_n is the normal module, b is the tooth face width and the terms $K_{T,i}$ are the stiffness of the linked sections. This terms must be added to the compliance sub-matrix of the teeth under consideration, which is first inverted before the summation and it is later inverted back again before contact compliance terms are introduced. The procedure is mathematically described by Equation 3.108 which is applicable for any sub-matrix representing a tooth N in mesh.

$$[\mathbf{C}_{T,N}] = \left[\begin{array}{cccccc} C_{T,11} & 0 & 0 & \dots & 0 & \\ 0 & C_{T,22} & 0 & \dots & 0 & \\ 0 & 0 & C_{T,33} & \dots & 0 & \\ \dots & \dots & \dots & \dots & \dots & \\ 0 & 0 & 0 & \dots & C_{T,nn} & \end{array} \right]^{-1} + \left[\begin{array}{cccccc} K_{T,12} & -K_{T,12} & 0 & \dots & 0 & \\ -K_{T,12} & K_{T,12} + K_{T,23} & -K_{T,23} & \dots & 0 & \\ 0 & -K_{T,23} & K_{T,23} + K_{T,34} & \dots & 0 & \\ \dots & \dots & \dots & \dots & \dots & \\ 0 & 0 & 0 & \dots & K_{T,(n-1)n} & \end{array} \right]^{-1} \quad (3.108)$$

From this equation it is observed that the bandwidth of the stiffness matrix is reduced to a principal diagonal and two neighbours which accelerates load distribution calculation with respect to other methods including all influence coefficients fulfilling the matrix such as [192].

The inversion of the stiffness matrix as proposed by Equation 3.108 gives rise to the full compliance map representing transverse and longitudinal deflections of any slice when a line load is applied at an arbitrary query point. Figure 3.18 shows such elastic deformations when a torque of 142 Nm is applied to a common FZG type C gear, which is equivalent to a line load of $w = 300$ N/mm. The different contributions to total deflection are depicted in Figure 3.18a. Note that in case of the FZG type C pinion the contribution of the web deformation is very small because the bottom diameter of the teeth is close to that of the supporting shaft, and therefore the size of the bulk gear body is small. Moreover, contrary to the rest of the terms, the difference between a load applied at the tip or at the root of the tooth does not affect the body rotation compliance. However, it is seen that tooth foundation tilting and bending are affected by the position of load and deformations are higher when loads are applied at the tip. Contact compliance term as presented in Section 3.3.2 has been added for completeness. The latter depends on the size of the Hertzian contact half width, material properties and distance to the tooth centreline, t_y , as shown in Figure 3.17; therefore, differences between tip and root are mainly due to local geometry differences.

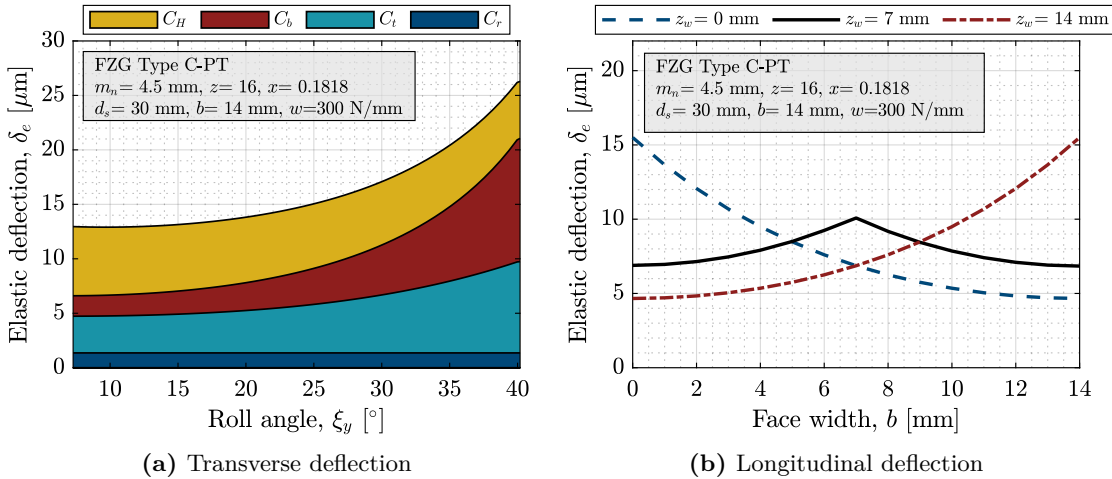


Figure 3.18: Tooth transverse and longitudinal compliance

On the other hand, Figure 3.18b shows the influence of load application position. As expected, maximum deflections are computed at tooth ends because slices at these positions are only linked to a single adjacent section and therefore they only include one coupling term (see Figure 3.16 and Equation 3.108). However, if the load is centered with respect to the full face width, deflections are symmetric. This behaviour is specially useful for load distribution computation in presence of misalignments or when longitudinal modifications are applied.

Teeth contact compliance

Finally, contact compliance, $C_{H,nn}$, must be added to the principal diagonal of the resulting kernel matrix in Equation 3.108. Although several analytical models can be found in literature for this term, in most cases contact deflection is computed from the elastic half-space approach where a 2D Hertzian pressure distribution is applied on a elastic foundation. This type of solution is very extended in load distribution related literature [182, 190, 195] and in this work the approach by Steward [191] is used. The latter is based on Weber and Banaschek's assumptions [182] for the contact of two elastic bodies but it is later corrected for increased compliance near the tooth tip using a semi-empirical correction factor. Hence, Steward's model for composite pinion and gear contact compliance reads:

$$C_{H,nn} = C'_{H,1,nn} + C'_{H,2,nn} \quad (3.109)$$

$$C'_{H,i,nn} = M_{i,y} \cdot C_{H,i,nn} \quad (3.110)$$

$$M_{i,y} = 0.0338 \cdot h_{i,y}^2 - 0.282 \cdot h_{i,y} + 1.627 \iff h_{i,y} < 4.1716 \quad (3.111)$$

$$C_{H,i,nn} = \frac{1}{\pi} \left[\frac{1 - \nu_i^2}{E_i} \cdot \ln \left(\frac{b_{H,y}^2}{4 \cdot t_{i,y}^2} \right) + \frac{\nu_i \cdot (1 + \nu_i)}{E_i} \right] \quad (3.112)$$

Where the correction factor M_y is only applied in the vicinity of the tip and increases contact compliance up to 60 %. The distances to the tooth tip, h_y , and to the tooth centerline, t_y , are calculated from Figure 3.17 following:

$$h_{i,y} = (r_{a,i} - r_{i,y}) \cdot [b_{H,y} \cdot \cos(\alpha_y)]^{-1} \quad (3.113)$$

$$t_{i,y} = r_{b,i} \cdot [\tan(\alpha_y) - \tan(\alpha_{F,y})] \quad (3.114)$$

Finally, $b_{H,y}$, is the Hertzian region half width for line contacts of infinite length, which is a non-linear function of the local normal load, W_y .

$$b_{H,y} = \sqrt{\frac{4}{\pi} \cdot \frac{W_y}{l} \cdot \frac{\rho_{y,1} \cdot \rho_{y,2}}{\rho_{y,1} + \rho_{y,2}} \cdot \left(\frac{1 - \nu_1^2}{E_1} + \frac{1 - \nu_2^2}{E_2} \right)} \quad (3.115)$$

This non-linearity implies that load distribution must be known in advance for accurately computing contact compliance, and therefore an iterative procedure must be used, solving load distribution several times until difference in predicted and computed loads is within a predefined tolerance.

3.3.3 Load capacity

According to the main standards ISO 6336 [11] and AGMA [10] gear teeth are affected by two main failure phenomena: i) root fillet breakage due to excessive teeth bending and ii) pitting failure due to contact pressure overload. Both of them depend on the geometry of gear teeth and instantaneous loads, thus, at any phase of mesh tooth root fillet and contact stress fields must be monitored to avoid exceeding material strength limits. In this section the underlying calculation procedures for both cases are briefly described.

Tooth root bending stress

Essentially, a gear tooth can be seen as a stubby cantilever beam as shown in Figure 3.17. At the base of the beam, there is tensile stress on the loaded side and compressive stress on the opposite side. When gear teeth break, they usually fail by a crack propagation at the base of the tooth on the tensile stress side. The ability of gear teeth to resist such breakage is usually referred to as their flexural strength, σ_F , which can be derived considering traditional material resistance equations. From Figure 3.17 one yields:

$$\sigma_{F0,y} = \frac{M_{b,y} \cdot x_{max}}{I_z} = \frac{[W_y \cdot \cos(\alpha_{Fy}) \cdot y_P] \cdot \left(\frac{s_f}{2}\right)}{\frac{1}{12} \cdot b \cdot s_f^3} \quad (3.116)$$

Where W_y is the local normal load, α_{Fy} is the attack angle, y_P is the bending lever arm, b is gear teeth face width and s_f is the critical section size. AGMA [10] and ISO 6336 [11] standards mainly differ in the way of computing the position of the critical section, which affects not only its size but also the bending lever arm. The former inscribes the largest possible parabola into the gear tooth profile known as ‘‘Lewis parabola’’ while the latter forms a triangle with 30 ° vertex angle between the tooth centreline and the tangent to the fillet radius. The critical section is located at the point at which the parabola or the triangle become tangent to the surface of the gear root fillet. In both standards, shear stresses across the root of the tooth are neglected, while radial stresses are included in AGMA but not in ISO. Furthermore, AGMA assumes that the load is applied at the tip of the gear while ISO considers that it is applied in the vicinity of the pitch point. Such differences, lead to considerable deviations when compared to experimental measurements as shown by recent studies [205]. Although new analytical techniques have been derived lately to compute the exact stress field [206] the methods proposed above are still largely used. In this work the method according to ISO is further developed due to its simplicity to compute the position of the critical section from generated geometry.

In order to take into account different geometry-induced phenomena such as the stress concentration effect in the root fillet or the effect of helix angle, ISO introduces several correction factors, which are derived empirically and multiply Equation 3.116. Thus, for common gears manufactured with the basic rack according to ISO 53 [170] we have:

$$Y_{S,y} = \left(1.2 + 0.13 \cdot \frac{s_f}{y_P}\right) \cdot \left[\frac{s_f}{2 \cdot \rho_f}\right]^{(1.21 + 2.3 \cdot \frac{y_P}{s_f})^{-1}} \quad (3.117)$$

$$Y_\beta = 1 - \epsilon_\beta \cdot \frac{\beta}{120} \quad (3.118)$$

Where Y_S is the stress correction factor accounting for the notch effect in the root fillet which has a radius ρ_f in the critical section and Y_β is the helix angle factor. Furthermore, ISO additionally considers the effect of external factors affecting mesh operation such as the influence of uneven load distributions, dynamic effects or torque variations in the work cycle. However, in this work quasi-static conditions are assumed, no torque variation is expected and local loads are derived from the solution of the load distribution as presented in Section 3.3, thus, the maximum root stress evolution along the line of action can be computed following:

$$\sigma_{F,y}(x, z) = \sigma_{F0,y}(x, z) \cdot Y_{S,y} \cdot Y_\beta = [6 \cdot w_y(x, z) \cdot \cos(\alpha_{Fy}) \cdot y_P \cdot s_f^{-2}] \cdot Y_{S,y} \cdot Y_\beta \quad (3.119)$$

Although root stresses in ISO 6336-3 are presented in a slightly different form and account only for the end point of single tooth contact, the method presented here has been modified to compute bending stresses along the entire line of action and the tooth face width from a given unit normal load distribution $w_y(x, z)$. Equation 3.119 neglects convective effects for the bending moment arm [207] and it has been shown that it largely simplifies the stress field in the fillet region due to a number of reasons cited above, but in this work it is considered sufficient to give an order of magnitude of the maximum stresses in the root fillet.

Tooth flank contact stress

Similarly, tooth flank contact stress evolution along the line of action can be computed from Hertz theory as gear teeth contact is equivalent to two cylinders with variable curvature radius pressing against each other. AGMA [10] and ISO [11] standards are based on the latter and, in the same way as bending stresses, they introduce the impact of non-uniform load distribution, the effect of velocity or variable torques and the influence of specific geometry by means of several correction factors. However, in this work, non-uniformities in load distribution are already considered in the quasi-static load distribution and local geometry parameters for each phase of mesh are also known. Therefore, from Hertz theory for line contacts the instantaneous contact stress can be calculated following:

$$\sigma_{H,y}(x, z) = \sqrt{\frac{w_y(x, z) \cdot \left(\frac{\rho_{y,1} + \rho_{y,2}}{\rho_{y,1} \cdot \rho_{y,2}} \right)}{\pi \cdot \left(\frac{1-\nu_1^2}{E_1} + \frac{1-\nu_2^2}{E_2} \right)}} \quad (3.120)$$

This equation is presented in a slightly different manner in AGMA and ISO standards as correction factors are included to translate the maximum contact stress to the lowest point of pinion double teeth contact and incorporate the effect of contact ratio or the influence of helix angle. However, the general form in Equation 3.120 is preferred as the maximum contact stress position is derived from local conditions.

Finally, Figure 3.19 compares bending and contact stress along the line of action for generated and modified FZG type C-PT gears.

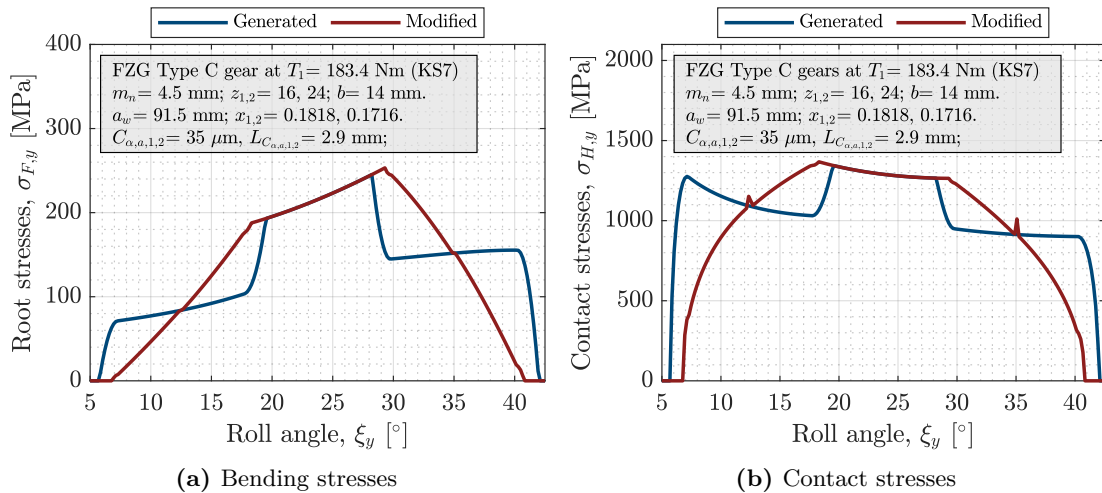


Figure 3.19: Bending and contact stresses for generated and modified FZG type C gear

For a given root geometry, bending stress according to Equation 3.119 is strictly governed by the load distribution. When tip relief is applied to both gears (as in Figure 3.19) there is a smooth transition from double to single tooth contact and therefore loads increase progressively and so does the maximum root stress. However, contact stresses not only depend on local loads, they also depend on instantaneous curvature radius (see Equation 3.120). As a result, when tip relief is applied, an abrupt curvature change is predicted from Equation 3.45 at the start of modifications, which results in contact stress spikes at these positions as shown by Vijayakar [174].

3.4 Finite element validation

In order to validate the analytical load distribution model, a two-dimensional quasi-static finite element model of a gear pair is developed in this section. The objective of this validation is further studying the sensitivity of the analytical model to loaded transmission error behaviour and normal force variation during engagement. Special attention is paid to premature contact phenomena, the increase of mean level and peak to peak TE with torque, contact ratio shift due to large deflections and the influence of random tooth modifications on load distribution reference behaviour. This parameters are representative of the forthcoming thermal distortion phenomena and the analytical model should be capable of accurately describing this features. Additionally, 2D results will be completed with existing 3D data from scientific literature in order to fully validate the model.

3.4.1 Description of the model and test cases

The main characteristics of the reference geometry for the finite element simulation are summarized in Table 3.4.

Table 3.4: Reference spur gear geometry for finite element validation

Parameter	Symbol	Value
Face width	b [mm]	100
Shaft diameter	$ds_{1,2}$ [mm]	80, 80
Normal module	m_n [mm]	4
Number of teeth	$z_{1,2}$ [-]	25, 25
Normal pressure angle	α_n [°]	20
Profile shift coefficient	$x_{1,2}$ [-]	0, 0
Operating centre distance	a_w [mm]	100
Reference tool acc. ISO 53	[-]	C (1.25/1.0/0.25)
Tolerance field acc. DIN 3967	$E_{s,n}$ [mm]	cd25 (-0.11,-0.07)

This reference gear pair has been previously used by several authors [191, 195] and it is characterized by being a symmetrical mesh with equal lengths of approach and recess as well as the same tooth thickness variation along the tooth height (i.e. same manufacturing profile shift coefficients, x_E) ensuring that they have the same bending and foundation stiffness at any point. With this approach, load distribution and transmission error diagrams are symmetrical if no profile modifications are applied and any difference in loaded behaviour can be easily identified from the horizontal and vertical displacements from the reference diagrams.

Finite element mesh and boundary conditions

Pinion and gear are meshed with the methodology proposed by Litvin et al. [208] which is characterized by a higher mesh density in the teeth region with respect to the bulk gear body (see Figure 3.20a). The mesh generation process has been automated and three different regions are distinguished for any gear geometry: i) gear teeth (region 1), ii) root fillet radius (region 2) and iii) gear body (region 3). Additionally, a bias factor has been introduced allowing for a progressive transition of the mesh size from the tooth centreline towards the flank surface. The latter is defined as the ratio of the flank element size to that of the tooth centreline.

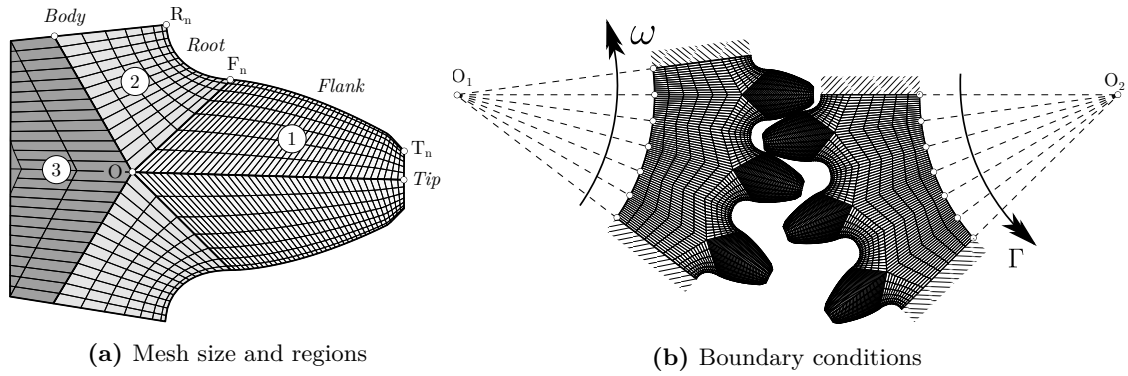


Figure 3.20: Gear pair finite element mesh and boundary conditions

A four-node, iso-parametric, arbitrary quadrilateral element for plane stress applications is used (element type 3 in MSC Marc software). The stiffness of the element is defined by 4 Gaussian integration points and it uses bilinear interpolation functions for deflection computation which is constant along the element. The material properties of the selected case-hardened 16MnCr5 gear steel for the finite element simulation are shown in Table 3.5.

Table 3.5: Material properties of case hardened 16MnCr5 steel for finite element simulation

Parameter	Symbol	Value
Density	ρ [kg/m ³]	7830
Young's modulus	E [GPa]	206
Poisson's coefficient	ν [-]	0.3
Yield strength	R_p [MPa]	695

Furthermore, two different boundary conditions are applied to pinion and gear: on the one hand, the rotational movement is imposed to the pinion with very low angular velocity (1 rpm) to avoid dynamic effects and, on the other hand, resisting torque is applied to the gear; both of which follow the counter-clockwise direction as it can be seen in Figure 3.20b. Moreover, rigid connectors have been defined between the central node located in the axis of rotation and the nodes in the gear-shaft interface. The contact type used for the simulation is of the “node-to-segment” type which does not consider tangential forces because friction coefficient is very low in EHL contacts and therefore frictional effects can be neglected.

In order to minimize the effect of boundary conditions on numerical results a finite element parameter analysis has been carried out before any test case is studied. The results of this preliminary analysis have been published in a conference paper [209] and the simulation parameters for the forthcoming tests have been defined based on its conclusions. It has been found that boundary conditions affect stiffness significantly which modifies the key parameters of transmission error (mean level and peak-to-peak value) and the length of contact under load. It is specially remarkable the influence of the gear body stiffness term and the effect of modelling the full gear with respect to partial models frequently used in literature [208] with a reduced set of teeth (usually 3 or 5). In this work, the full pinion and gear have been modelled and the influence of the gear body up to the shaft diameter has been considered. The number of elements in the flank without re-meshing is 75 which is not sufficient to consider the influence of contact compliance, and therefore contact stresses are neither computed. However, for root bending stress calculation the optimum number of elements in the fillet has been found to be 15. On the other hand, gear tip and bottom only have 8 and 2 elements respectively and the bias factor is set to 8. Finally, the selected time step for simulation is $0.094^\circ/\text{inc}$ in order to accurately describe load distribution and transmission error features. Once the simulation is finished, the result files are post-processed in search of normal load per phase of mesh and the instantaneous rotation angle of the gear.

Test cases

Table 3.6 summarizes the complete set of test cases which have been defined to pursue two different objectives. On the one hand, load distribution and transmission error behaviour under load are studied and on the other, the effect of geometry modifications is analysed.

Table 3.6: Test cases for finite element validation

Parameter	Symbol	Value
Torque levels	T [kNm]	0.625, 1.25, 2.5, 5, 10
Face widths	b [mm]	15, 100
Shaft diameters	ds [mm]	30, 80
Linear tip relief	$C_{\alpha,1}$ [μm]	35
Profile slope mod.	$C_{H\alpha,1}$ [μm]	17.5
Profile barrelling	$C_{\alpha,1}$ [μm]	17.5
Lead crowning	$C_{\beta,1}$ [μm]	30
Mesh misalignment	$f_{\sum\beta,1}$ [μm]	70

In order to study the overall transmission error and load distribution variation with torque five load levels are selected from 625 Nm to 10.000 Nm. Then, a narrow face width of 15 mm is tested for the same load levels, in search of premature contact, contact ratio increase under load and even with the aim of detecting triple contact when large deflections arise. Similarly, the influence of web size will also be analysed as it increases total deflection under load and alters TE mean level and peak to peak value. On a second stage, the influence of random profile modifications is analysed where only the pinion will be modified with tip reliefs, profile slope modifications and profile barrelling. Finally, the numerical validation will be completed with the analysis of the influence of longitudinal modifications and mesh misalignment based on results from literature [195].

3.4.2 Results and discussion

The reference gear pair in Table 3.4 and its narrow counterpart with 15 mm face width have been loaded up to 10 kNm in search of large deflections that produce a significant extension of the path of contact and multiple teeth in mesh. These load levels produce a maximum root stress of 10 times the yield stress in Table 3.5 for the narrow case, which is fictitious but ensures that sufficiently large deformations arise. It will be shown that in such case, the hypothesis of small deflections is no longer kept and the statement of the load distribution problem in section 3.3.1 is not valid which leads to computation errors. Figure 3.21 groups load distribution and transmission error results for both geometries and different torques.

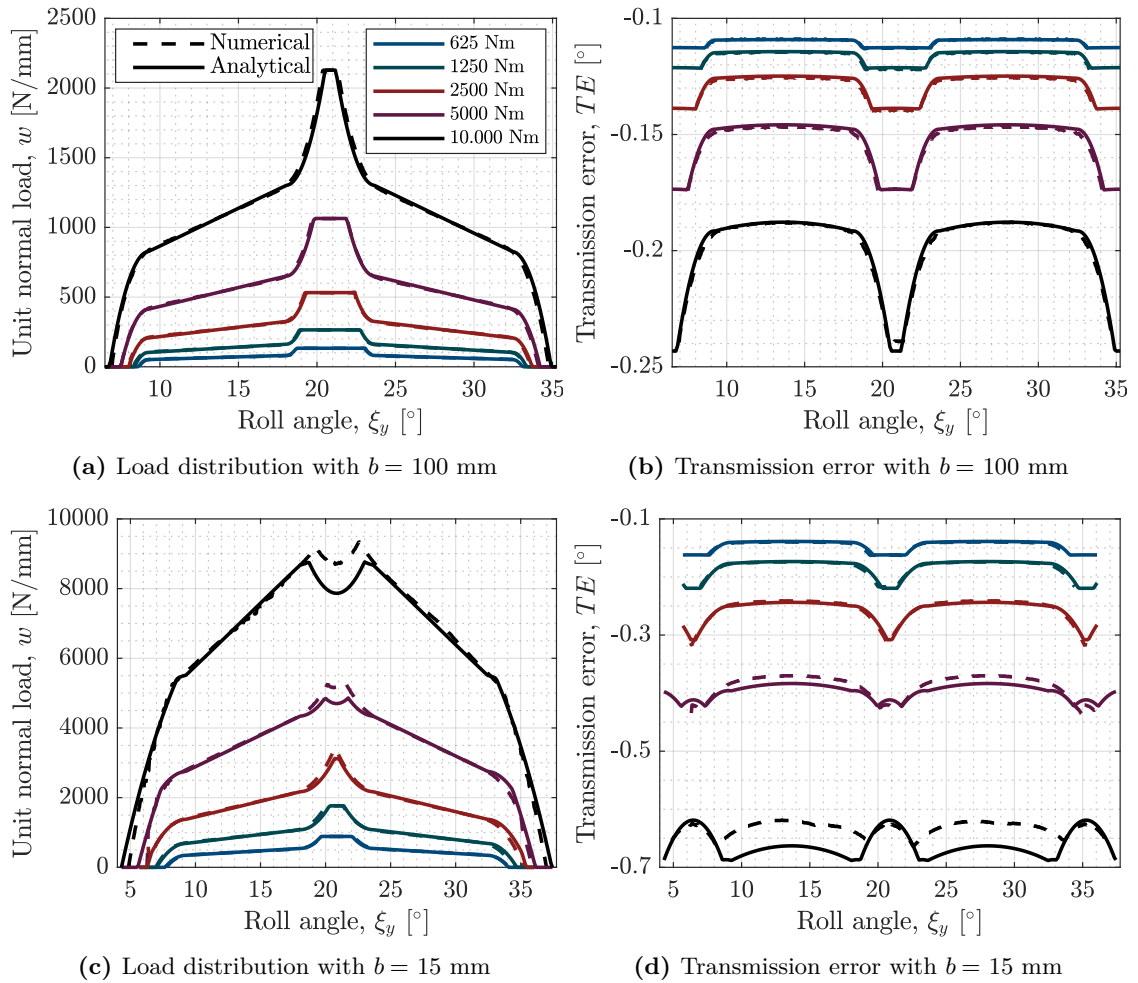


Figure 3.21: Influence of torque and face width on load distribution and transmission error

General loaded behaviour

Overall results in Figure 3.21 show that the analytical model accurately describes load distribution and transmission error behaviour of both gears. Only in the case of the narrow face width subject to the highest load stages the differences become significant in the vicinity of the pitch point where single tooth contact shifts to double as a result of a second tooth pair coming into mesh due to extremely large deformations. The effect of the

separating distance, c_y , on premature contact is depicted in load distribution diagrams. The theoretically abrupt shift from double to single tooth contact is progressively smoothed as load is increased and the analytical model and finite element simulation show the same trend. The length of the line of action is clearly enlarged increasing the contact ratio, and in the case of the narrow face width, contact ratio even shifts to values above 2.

Figure 3.22 shows the influence of load on the latter. In effect, at an approximate torque of 2.5 kNm the deflection of the teeth is large enough to shift the design contact ratio of 1.61 to values above 2 indicating that the minimum number of teeth in contact in the vicinity of the pitch point is 2; which can be observed in the corresponding load distribution diagrams in Figure 3.21c. On the other hand, transmission error behaviour above this load is also altered where the peak-to-peak value and the mean level are distorted due to the effect of multiple teeth contact with increasing errors with load.

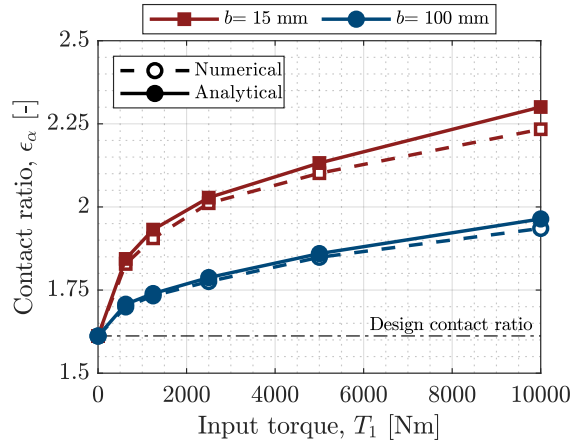


Figure 3.22: Contact ratio increase with load

If the accuracy of the premature contact prediction is measured from the increase of contact ratio, the errors are below 1% for the highest torques on the large face width and below 3% on the narrow face width, showing the same trend in both cases. If attention is paid to the quality of the predicted transmission error mean level and peak to peak values in Figure 3.23, it is found that large face width gears behave similarly to numerical results with errors below 1% for the mean level and 10% for the peak-to-peak at the highest torque. However, in the case of the narrow face width, transmission error mean level and peak-to-peak values are within 5% and 55% accuracy respectively.

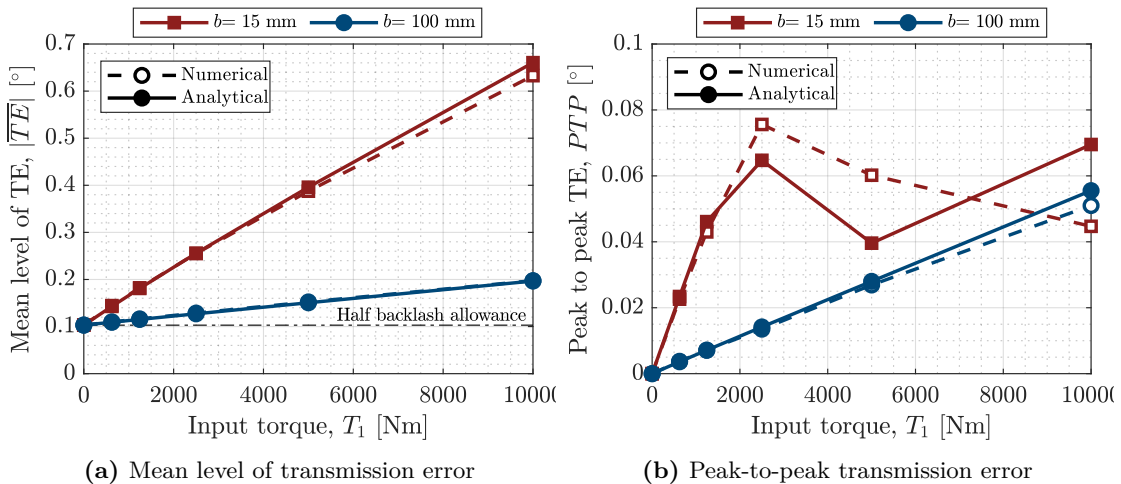


Figure 3.23: Influence of load and face width on mean level and peak-to-peak transmission error

Two reasons explain such differences. On the one hand, the load distribution model is constructed on the assumption that elastic deflections are small enough such that original geometry remains unchanged and contact takes place in the base tangent plane. It is observed in Figure 3.21c that the load distribution diagram for the highest torque is not symmetric in the pitch point, thus, indicating that contact is outside the theoretical line of action. Moreover, if deflections are large, the rigid body motion is no longer the product of the base circle radius and the angular displacement of the pinion, which alters transmission error behaviour. On the other hand, when multiple teeth are in contact, the deflection of a tooth influences the adjacent ones and therefore adjacent teeth compliance terms should be added to the kernel matrix in Equation 3.94. In spite of these differences, the developed load distribution model is accurate enough to capture the characteristic elastic behaviour in normal cases where tooth root bending stresses are below the yield strength of the material.

The influence of web thickness is also analysed and results are shown in Figure 3.24. It is observed that increasing web thickness through a minor shaft diameter extends the length of the line of action with respect to the reference case because higher deflections arise due to the additional body rotation. Transmission error behaviour also supports this trend with increased mean level and higher peak-to-peak values. However, analytical results seem to overestimate deflections which result in slightly different premature contact.

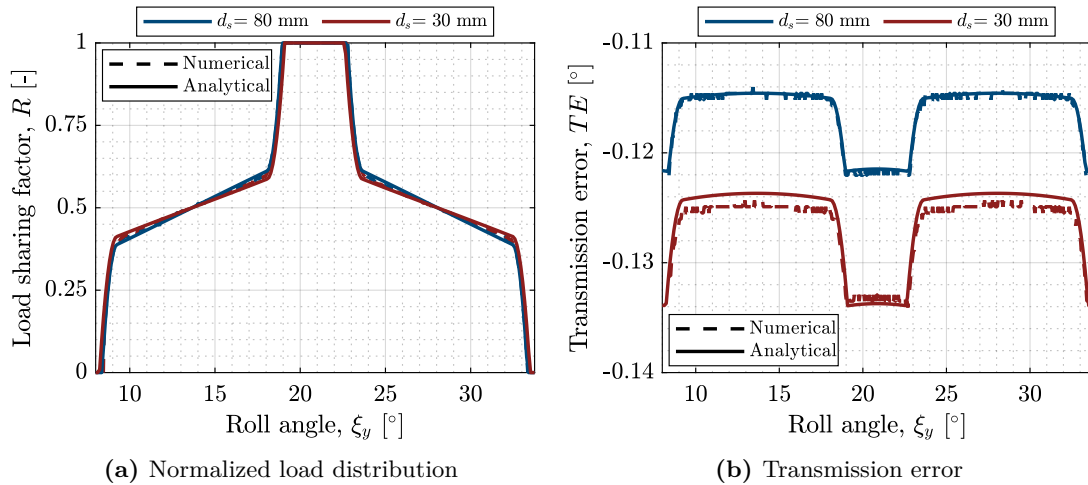


Figure 3.24: Influence of shaft diameter on load distribution and transmission error for large face width gear subject to $T = 1250$ Nm

Moreover, the load share in the double teeth contact region in Figure 3.24a is slightly tilted when web thickness is increased which indicates that additional deflections tend to evenly distribute loads on pinion and gear. Although the results presented here do not include the effect of contact compliance for comparison with the FEM model, a similar trend results when this term is included in the load distribution model, which has recently been confirmed by [210]. On the contrary, the introduction of the adjacent teeth compliance term stiffens the gear mesh, thus reducing deflections and premature contact behaviour and increasing again the slope of the load sharing diagram in the double teeth contact region.

Influence of modifications and misalignments

Tooth modifications are known to significantly alter load distribution and transmission error [198]. In order to validate the model when such intended geometry deviations are applied, random profile and longitudinal modifications have been defined in Table 3.6. Besides, a sufficient number of elements has been introduced in the finite element model to capture such characteristic behaviour.

Figure 3.25 shows the comparison between analytical and numerical solutions for profile modified gears proving the good correlation between both. Analytical results deviate a maximum of 4% with respect to numerical values and follow the overall trend closely. For instance, the 35 μm linear tip relief in the pinion begins at a diameter of 104.5mm, at a midpoint between the pitch and tip diameters. No modification has been applied to the gear thus, the load distribution diagram is not symmetric and there is not a smooth transition between the single and double teeth contact regions. In spite of being a random modification, the analytical model has calculated the same unit normal loads that the finite element model and the beginning and end of each section has been identified properly. In the case of profile slope and profile crowning modifications the results are similar with slight differences of the unit normal load in each section due to errors in compliance terms.

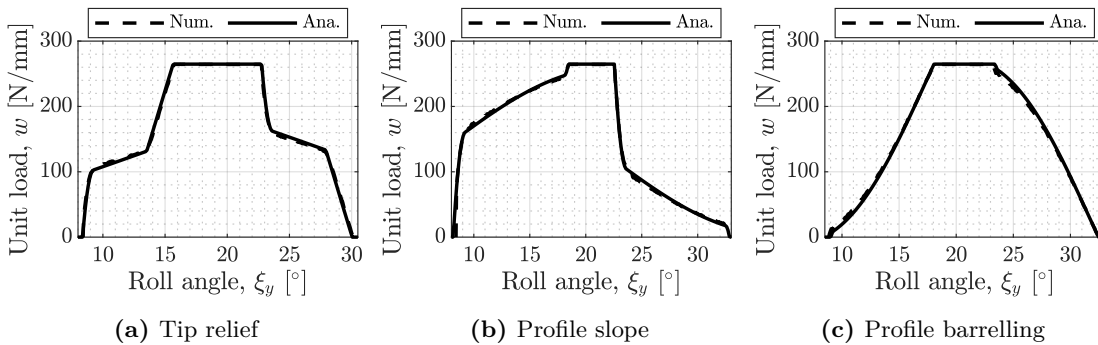


Figure 3.25: Influence of profile modifications applied on pinion

Furthermore, the bi-dimensional finite element model results have been completed with additional 3D FEM data from literature [195]. Two situations are studied: a 30 μm lead crowning and a 70 μm deviation misalignment in the pinion, both characterized by the strong influence of convective effects on load distribution. It is shown in Figure 3.26a that the analytical model computes unit normal loads with a maximum error of 3% at the middle of the face width where maximum loads occur. Moreover, both the numerical and analytical results predict a symmetrical behaviour with zero load at the face ends. Similarly, the start point and slope of the line load in the misalignment case in Figure 3.26b are correctly identified but the maximum loads at the front end is considerably lower. This is because the stiffness matrix bandwidth is 3 and therefore it is not fulfilled with influence coefficients as described previously. Additionally, the correct modelling of edge effects requires mirroring the deflections near the edge as suggested by Jaramillo [211] and in this work the latter is not considered. To deal with this situations Börner [204] suggests adjusting the stiffness matrix proportionally to the number of unloaded sections but this requires an iterative procedure. Alternatively, the decay function proposed by Kunert [192] can be used which fulfils all terms in the compliance matrix including mirroring behaviour.

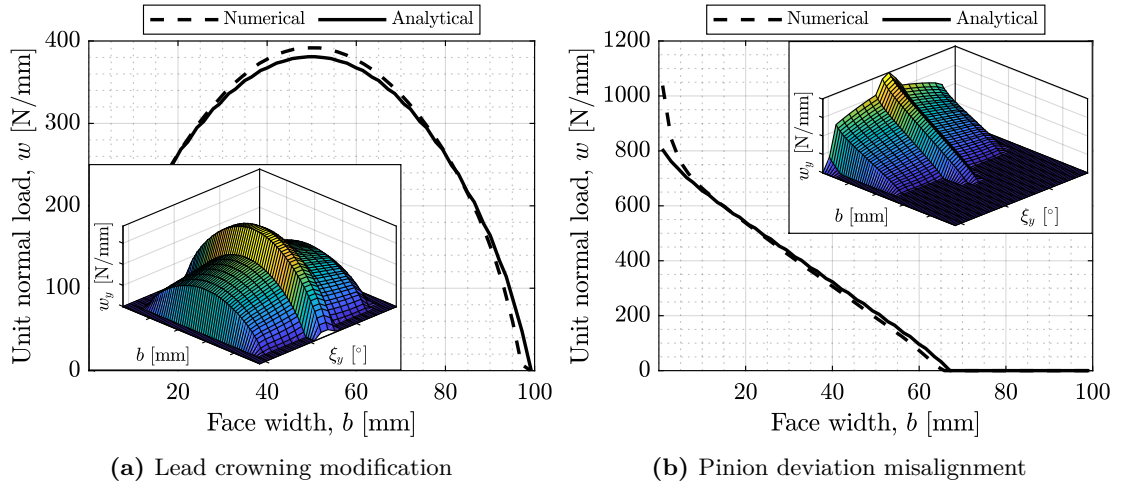


Figure 3.26: Influence of longitudinal modifications and mesh misalignments

3.5 Conclusions of Chapter 3

In this chapter the main concepts and methods for cylindrical gear load distribution and kinematic behaviour modelling have been introduced. It has been shown that accurate load distribution and transmission error predictions can be carried out analytically with minimum computational cost. Furthermore, the parameters presented in this chapter represent the foundations for the next ones, and they will be resumed throughout the work.

In the first section, the main parameters of the involute geometry have been described, the conditions of existence of a gear pair have been defined and the tooth generation procedure by the envelope theorem has been presented. Later, a general method for the profile and lead modification of the teeth has been presented and the corresponding equations for local normal directions and curvature radius have been derived. It has been shown that the profile and lead modifications can be easily grouped without any need for modifying basic rack geometry and tool trajectory.

On a second section, the kinematic behaviour of the cylindrical gear pair has been presented. The geometrical boundaries of theoretical conjugate action have been described and the mesh phase relations among teeth and between pinion and gear have been presented. Then, the main velocity parameters and derived quantities have been presented and it has been shown that kinematic behaviour is closely related to wear or local power losses. Finally, the concept of no-load transmission error has been introduced and it has been proved to be related to the geometrical features of the teeth.

In the third section, the load distribution problem has been stated analytically and later developed numerically following the classical thin-slice approach. A new method for solving the system of equations has been presented based on the restatement of the equations as a Linear Complementarity Problem where Lemke's pivoting algorithm [201] can be used for fast computation. Then, the main compliance terms involved in the solution of load distribution have been derived and convective effects have been introduced following Börner's method [204]. The model has been tested against a finite element model and results have been discussed showing overall good agreement.

*The learning and knowledge that we have,
is, at the most, but little compared with
that of which we are ignorant.*

—Plato, 427 BC - 347 BC

4

Prediction of Friction and Power Losses

Contents

4.1	Introduction	94
4.2	Sliding friction coefficient model	95
4.2.1	Friction coefficient model for full EHL contacts	95
4.2.2	Extension to partial EHL regime	102
4.2.3	Experimental validation	105
4.2.4	Discussion of results	108
4.3	Power loss prediction model	111
4.3.1	Teeth contact thermal behaviour	111
4.3.2	Thermally-coupled power loss prediction model	114
4.3.3	Experimental validation	118
4.3.4	Discussion of results	121
4.4	Conclusions of Chapter 4	122

The following chapter presents the general procedure to predict power losses in the gear mesh, which is the responsible for the heat flowing towards the pinion and gear teeth. First, the method to compute mean power loss from instantaneous values is described. It will be shown that mesh losses depend to a great extent on the instantaneous friction coefficient. Then, a comparison of power loss predictions for common sliding friction coefficient models in literature is presented and the need for a new equation is justified. A new partial elastohydrodynamic friction coefficient model is developed in the second section which is validated with experimental measurements from [212]. It will be shown that accurate predictions can be carried out for different oils from its base rheological properties without additional characterization of their traction behaviour in tribometers. Afterwards, a power loss prediction model is developed and the influence of thermal coupling is discussed. The predicted power losses are compared to numerical and experimental results from [29, 61] and conclusions are withdrawn.

4.1 Introduction

The total heat generated in the gear mesh is the result of the frictional losses along the contact line, P_{VZP} . For a single tooth, the mean value of the power loss along the path of contact is defined by:

$$\bar{P}_{VZP} \Big|_{single} = \frac{1}{g_\alpha} \cdot \int_{z=0}^{z=b} \int_{x=0}^{x=g_\alpha} P_{VZP}(x, z) dx dz \quad (4.1)$$

Where the coordinate system, xyz , is fixed to the base tangent plane as shown in Figure 3.10 with the x axis in the direction of the line of action and the z axis in the direction of the tooth face-width.

Considering that the solution of the load distribution problem yields the real length of the line of action, $g'_\alpha = \epsilon'_\alpha \cdot p_{et}$, and the number of teeth meshing simultaneously, the calculation of the total heat can be generalized in the following manner¹:

$$\bar{P}_{VZP} = \epsilon'_\alpha \cdot \bar{P}_{VZP} \Big|_{single} = \frac{1}{p_{et}} \cdot \int_{z=0}^{z=b} \int_{x=A'}^{x=E'} \left[P_{VZP,s}(x, z) + P_{VZP,r}(x, z) \right] dx dz \quad (4.2)$$

Where the parameters A' and E' denote the real start and end of the line of action and the instantaneous power loss, $P_{VZP}(x, z)$, is calculated from the sum of sliding and rolling power loss terms which depend on the kinematic behaviour of the contact point, the local normal load and the sliding and rolling friction coefficients (see Equation 2.2).

Wimmer [36] showed that most of the friction coefficient models available in literature produce very different results for the same input conditions which give rise to significant deviations, as large as 50% to 100% compared to the experimental measurements. Figure 4.1 shows a comparison of the classical models from Table 2.1 against recent thermal EHL simulations by Ziegltrum et al. [61]. As it can be seen, none of the models follows the finite element results with local friction coefficient differences up to 30% of the simulated result in the best case. Moreover, the model by Benedict and Kelley [46] shows a completely different trend where the sliding friction coefficient at the pitch point tends to infinity, which is contrary to the expected behaviour as pure rolling occurs at this point. Such differences are reproduced later in local power losses (see Figure 4.1b) which result in a deviation of 30% in the predicted mean power loss, therefore, affecting temperature distribution.

¹ From Equation 4.2 it is possible to reach the so-called power loss function by Ohlendorf [36] which is the basis of most empirical friction coefficient models. Neglecting the rolling friction term and considering a constant friction coefficient along the path of contact we have:

$$\bar{P}_{VZP} = \bar{\mu} \cdot \frac{1}{p_{et}} \cdot \int_{z=0}^{z=b} \int_{x=A'}^{x=E'} \left[W(x, z) \cdot Vs(x, z) \right] dx dz \quad (4.3)$$

Multiplying and dividing by the input power, $P_A = F_{bt} \cdot V_{bt}$ results in:

$$\bar{P}_{VZP} = \bar{\mu} \cdot P_A \cdot H_{VL} \quad (4.4)$$

$$H_{VL} = \frac{1}{p_{et}} \int_{z=0}^{z=b} \int_{x=A'}^{x=E'} \left[\frac{W(x, z)}{F_{tb}} \cdot \frac{Vs(x, z)}{V_{tb}} \right] dx dz \quad (4.5)$$

Where the power loss function, H_{VL} , depends exclusively on the instantaneous kinematic and load behaviour of the meshing teeth which can be accurately predicted from gear geometry.

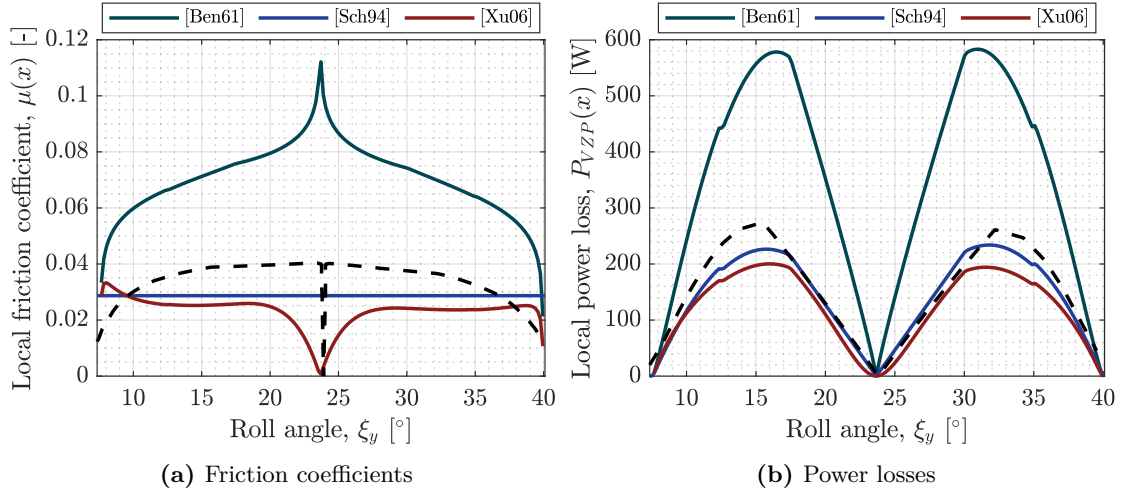


Figure 4.1: Comparison of local friction coefficients and power losses predicted by classical models and thermal EHL simulations by [61] on gear type C_{mod} , KS7, $V_t = 8.3$ m/s and $\Theta_o = 90^\circ\text{C}$

Although, different reasons can explain these deviations, one of the main factors contributing to such errors is the lubricant behaviour. Most friction coefficient equations for gears have been developed for specific lubricants and therefore they cannot be extended to other oils without preliminary characterization of their traction behaviour in FZG tests or tribometer measurements to adjust initial parameters. In this chapter a new friction coefficient model based on rheological properties of the lubricant is proposed and the power loss prediction methodology is updated to account for instantaneous temperature and pressure variations along the path of contact that affect oil film behaviour.

4.2 Sliding friction coefficient model

Gear teeth are non-conformal surfaces subject to a rolling-sliding behaviour along the path of contact; pure rolling only occurs in the pitch point. When subject to torque, teeth deform elastically conforming a small contact region that leads to a high pressure. Additionally, the relative movement of the deformed surfaces drags the oil into the contact region forming a thin hydrodynamic oil film. The sudden change of pressure from the inlet to the outlet of the contact, increases lubricant viscosity and separates surfaces. In such conditions, the non-Newtonian behaviour of the lubricant is beneficial as it avoids asperity contacts, thus reducing friction. This regime is known as elastohydrodynamic lubrication (EHL), which can be separated into full or partial EHL depending on the degree of asperity interaction (see Figure 2.2). In the following, a model for full EHL regime will be developed and then it will be extended to account for mixed lubrication.

4.2.1 Friction coefficient model for full EHL contacts

Theoretical background

For smooth surfaces in line contact sliding friction is the result of the shear stress, τ , of the oil film in the contact region which is subject to high pressure and different rolling speeds of the mating bodies. Figure 4.2 graphically summarizes this situation.

To compute the traction force, it is necessary to know the pressure and film thickness distributions in the contact region which is known as the “EHL problem”. Its mathematical solution requires solving the Reynold’s hydrodynamic equation, together with the film thickness, load balance, elastic deformation and energy equations, considering the non-newtonian behaviour of the lubricant properties which are function of temperature and pressure. If edge effects are neglected, the resulting film thickness and pressure distributions are bi-dimensional and friction force can be computed with Equation 4.6.

$$F = \frac{1}{2} \cdot \int_{-\infty}^{+\infty} h(x) \cdot \frac{\partial p(x)}{\partial x} dx + \int_{-\infty}^{+\infty} \tau(x) \cdot dx \quad (4.6)$$

Where the first term is the rolling friction (already presented in Equation 2.7) and the second term is the sliding friction. The former is only significant with respect to the latter at the low slide to roll ratios occurring near the pitch point and with high viscosity oils. Therefore, it is acceptable to neglect its influence on gear contacts in the full EHL regime.

Several methods have been proposed in the literature review to solve the EHL problem (see Section 2.1.1), all of which require high computational effort. In order to avoid solving the full system of equations, it is possible to assume that the film pressure distribution follows the Hertzian solution for line contacts (see Figure 4.2). In such case the mean traction, $\bar{\tau}$, can be computed from mean values in the contact namely a constant central film thickness over the flattened region, h_c , a mean contact pressure $\bar{p} = \pi/4 \cdot p_H$ and a mean film temperature $\bar{\Theta}_f$, all of which have been obtained under the same Hertzian assumption.

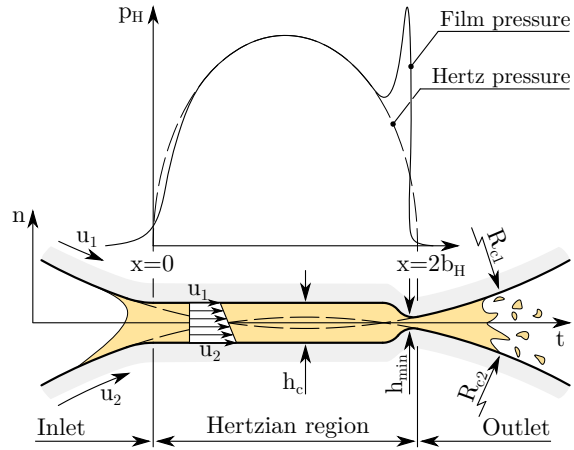


Figure 4.2: Representation of a smooth EHL line contact

Non-Newtonian rheological model

In general, in a rolling-sliding contact traction coefficient $\mu = \bar{\tau}/\bar{p}$, presents a sigmoidal shape when plotted against the slide-to-roll ratio SRR (see Figure 4.3). At low values, the lubricant follows a Newtonian behaviour ($\tau = \eta \cdot \dot{\gamma}$) where the slope is defined by the lubricant viscosity evaluated at the film temperature and pressure. At higher SRR , the curve deviates from the linear trend and non-Newtonian behaviour prevails. In this region, contact pressure increase leads to a maximum traction value followed by a decrease at the highest sliding values. This reduction at high speeds is the result of the temperature rise at the contact inlet that reduces oil viscosity and results in a thinner film thickness. Finally, at the highest shear stress, the lubricant can reach a plastic yield limit known as “limiting shear stress”, τ_L , which levels out the traction curve.

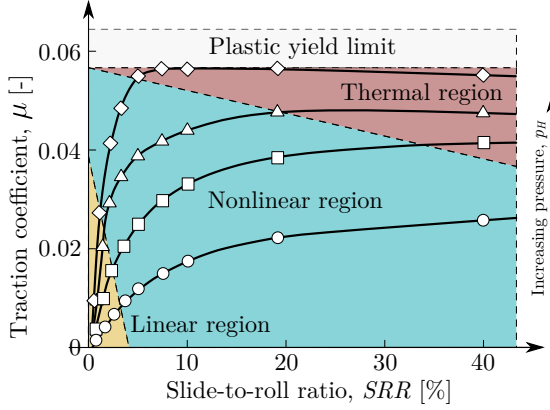


Figure 4.3: Characteristic traction curve of rolling-sliding contacts

Several equations can be found in literature to model lubricant shear stress and Table 4.1 gathers some of the most frequent. Their general behaviour is depicted in Figure 4.4 in non-dimensional terms.

Table 4.1: Common shear stress models in EHL literature

Author	Equation
Ree-Eyring [214]	$\tau = \tau_E \cdot \sinh^{-1} \left(\frac{\eta \cdot \dot{\gamma}}{\tau_E} \right)$ (4.8)
Bair-Winer [215]	$\tau = \tau_L \cdot \left(1 - \exp \left(\frac{-\eta \cdot \dot{\gamma}}{\tau_L} \right) \right)$ (4.9)
Carreau-Yasuda [216]	$\tau = \eta \cdot \dot{\gamma} \cdot \left(1 + \left(\frac{\eta \cdot \dot{\gamma}}{\tau_0} \right)^a \right)^{\frac{(n-1)}{a}}$ (4.10)

As it can be seen the Ree-Eyring [214] and Carreau-Yasuda [216] models result in a very similar behaviour. Only the limiting shear stress model by Bair and Winer [215] captures the levelling of the traction curve when the plastic yield limit is reached. Currently, there is a heated debate on the suitability of each of the models in Table 4.1 to accurately predict non-Newtonian traction [59, 217, 218], where the main arguments are that the Carreau model represents basic rheological behaviour of the lubricant as measured in laboratory tests while the Ree-Eyring approach has been developed from regression analysis of tribometer measurements.

Johnson and Tevaarwerk [213] described this characteristic behaviour of the lubricant with a Maxwell-type visco-elastic model, resulting from the sum of an elastic term, $\dot{\gamma}_e$, and a viscous term, $\dot{\gamma}_v$.

$$\dot{\gamma} = \dot{\gamma}_e + \dot{\gamma}_v = \frac{1}{G} \cdot \frac{d\tau}{dt} + F(\tau) \quad (4.7)$$

Where $\dot{\gamma}$ is the shear rate, G is the elastic shear modulus, $d\tau/dt$ refers to the time derivative of traction and $F(\tau)$ is viscous term which depends on the shear stress model.

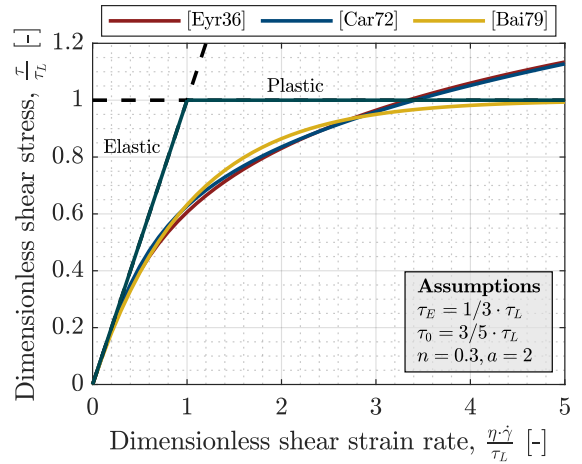


Figure 4.4: Non-dimensional shear stress model comparison

In spite of this discussion, in this work the classical Ree-Eyring equation has been retained as it is the only one with a physical meaning. Thus, Equation 4.7 now reads:

$$\dot{\gamma} = \frac{1}{G} \cdot \frac{d\tau}{dt} + \frac{\tau_E}{\eta} \cdot \sinh\left(\frac{\tau}{\tau_E}\right) \quad (4.11)$$

With η the low shear rate dynamic viscosity of the lubricant and τ the shear stress. In this model, the reference stress, τ_E , is known as the ‘‘Eyring stress’’, which is the threshold value above which the fluid starts to behave in a non-linear manner.

In addition, at the high pressures present in gear contacts, the lubricant may reach the plastic behaviour of Figure 4.4, the so called ‘‘limiting shear stress’’, τ_L , which is proportional to pressure, p , and independent of the shear rate, $\dot{\gamma}$. Incorporating this term in Johnson and Tevaarwerk’s model and solving for shear stress:

$$\tau = \min \left[\tau_E \cdot \sinh^{-1} \left(\frac{\eta}{\tau_E} \cdot \left(\dot{\gamma} - \frac{1}{G} \cdot \frac{d\tau}{dt} \right) \right), \tau_L \right] \quad (4.12)$$

Assumptions

As mentioned in the introductory paragraphs, the average shear stress, $\bar{\tau}$, is computed integrating the local shear stress according to Equation 4.12 over the contact area and then friction coefficient results from $\mu = \bar{\tau}/\bar{p}$, where \bar{p} is the mean contact pressure. However, in this work film pressure is assumed to follow the Hertz solution and the local shear stress is computed from mean conditions in the contact ($\bar{\Theta}_f$ and \bar{p}).

Furthermore, according to Equation 4.12 four fluid properties (τ_E , τ_L , η , G) are required to fully define lubricant behaviour in the concentrated contact, all of which depend on temperature and pressure. Nevertheless, it is possible to reduce the number of parameters needed to compute traction when subject to the following two assumptions:

- **A.1:** The elastic term in Equation 4.12 can be neglected in gear transmissions.
- **A.2:** It is possible to relate τ_E to τ_L through a single base oil dependent coefficient.

According to Evans and Johnson [219], the viscoelastic boundary is ruled by the Deborah number, $D_e = (\eta \cdot V_e)/(G \cdot l)$ where V_e is the entrainment velocity and l the contact width ($l = 2 \cdot b_H$). Writing $d\tau/dt = (V_e/l) \cdot d\tau/d(x/l)$ in Equation 4.12 this non-dimensional number is introduced; if $D_e \ll 1$ elastic effects can be neglected and therefore, the characterization of the elastic shear modulus is no longer necessary. It can be proved that this is the case in most gear transmissions and it is especially suited to automotive and aeronautical applications where lubricant viscosities are low and they usually operate at high input torques and speeds involving high film temperatures. At the contact temperature and pressure of these applications the elastic shear modulus is of the order 10^9 Pa. Considering that the entraining velocity exceeds 1 m/s and the contact width is around 10^{-4} m, the low shear rate dynamic viscosity must exceed 10^5 Pa·s for the elastic effects to become significant.

In order to validate this assumption, a test matrix covering typical steel gear operating conditions has been defined in Table 4.2. Approximately $5 \cdot 10^6$ test cases have been analysed with 6 fully formulated oils from [220]. Only results in the full EHL regime have been retained for the analysis and non-feasible geometries (e.g. tooth interference)

have been discarded. In addition, in order to account for the elastic compliance of the steel flanks the effective elastic shear modulus, G_e , has been computed as defined in [219]. A sample of the results is presented in Figure 4.5 where the variation of the Deborah number along the standardized line of action is shown. A contour plot has been added to the latter to stress the influence of the single and double teeth contact regions.

Table 4.2: Test matrix to identify Deborah number range in gear contacts

Parameter	Units	Value
Gear ratio, u	[-]	1, 1.5, 3
Aspect ratio, b/d	[-]	0.25, 0.5, 1, 2
Normal modules, m_n	[mm]	1, 2, 4, 6
Pinion teeth number, z_1	[-]	25, 50, 75, 100
Normal pressure angle, α_n	[°]	15, 20, 25, 30
Profile shift coefficients, x	[-]	0, 0.1, 0.25, 0.5
Tangential speed, V_t	[m/s]	5, 10, 25, 50
Surface roughness, R_q	[μm]	0.1, 0.2, 0.4, 0.8
Specific line load, F_{bt}/b	[N/mm]	100, 600, 1200, 1800
Contact inlet temperatures, Θ_{in}	[°C]	70, 100, 130, 160
Lubricants [220]	[-]	1 PAO, 2 mineral and 3 ester-based oils

As it can be noticed in Figure 4.5, the Deborah number remains below one in almost every point of the line of action. In the single tooth contact region, sudden pressure increase causes an instantaneous increase in both, viscosity and elastic shear modulus, which shifts the Deborah number. However, the order of magnitude of the ratio η/G is not changed significantly and values remain below one. Furthermore, for any given combination of geometry and operating conditions the lowest values are found in the double teeth contact region where most of the power losses occur due to the high sliding velocities. Therefore, the use of the viscous term in Equation 4.12 seems to be justified to predict power losses in gears.

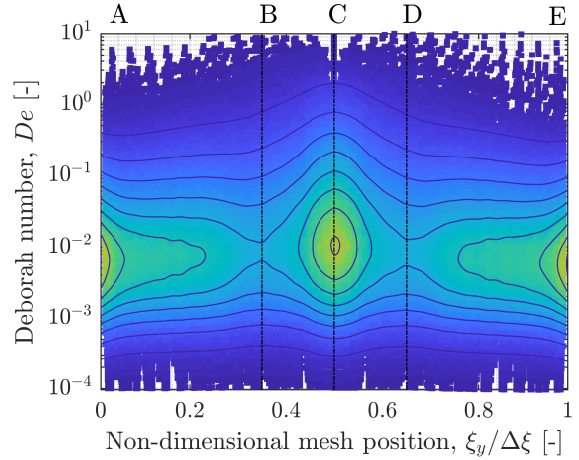


Figure 4.5: Density plot of Deborah number on the path of contact for PAO oil in Table 4.2

A further check of these results is shown in Figure 4.6 where the influence of lubricant viscosity grade and base oil type on Deborah number is analysed. It is of primary interest to know the probability of D_e values falling below unity to justify the assumption. For that purpose, the Kernel density estimation using automatic bandwidth selection method according to [221] has been used. The results indicate that oil type affects Deborah numbers more than viscosity. In Figure 4.6b it is observed that synthetic oils show greater probability of Deborah numbers falling between 10^{-4} and 10^0 . The analysis of the cumulative distribution function shows that poly- α -olefin and ester-based oils have,

respectively, 85% and 94% of the values below 0.1 and if unity is taken as the upper limit, both synthetic base-stocks have 99% of the values below. However, in the case of mineral oils, 86% of the values are below 1.0 and only 56 % is under 0.1. The influence of viscosity is depicted in Figure 4.6a. In general, higher viscosities seem to result in higher probability of values falling outside the boundaries and therefore elastic effects are not negligible.

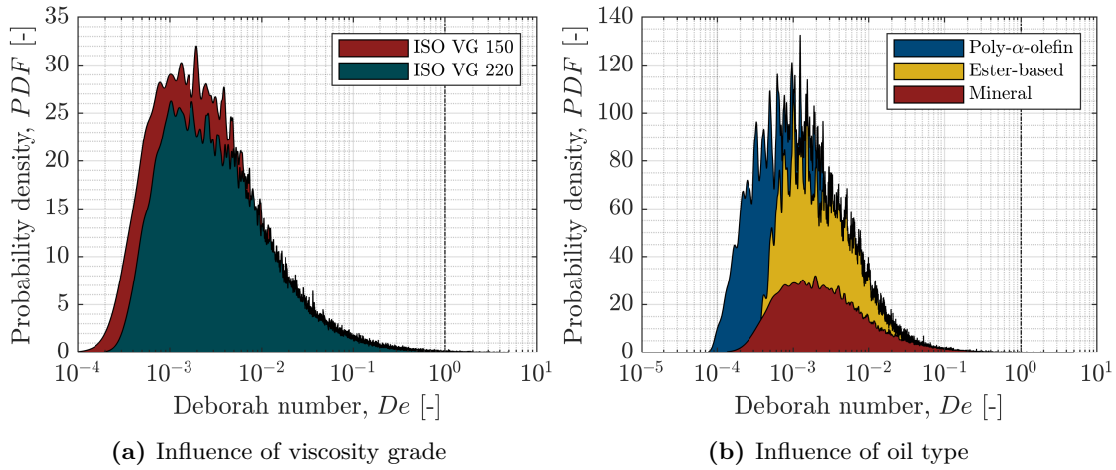


Figure 4.6: Probability density of Deborah numbers below unity in gear operating conditions

In conclusion, considering the low to mid-range viscosities of automotive and aeronautical transmissions and the type of oil, which is mainly synthetic, these results support the initial assumption on the elasticity of gear contacts under full EHL condition. In the following, only viscous behaviour is considered. As far as the assumption on the reference stress is concerned, it is shown next that it is possible to relate the Eyring and limiting stresses with a single oil dependent coefficient.

It is known in the field of tribology, that the main drawback when calculating traction coefficient with the Eyring shear stress model is the fact that the value of the reference stress, τ_E , must be regressed from experimental measurements in tribometers, and consequently, the application of the model without preliminary characterization of the lubricant's traction behaviour becomes difficult. On the contrary, the limiting shear stress can be characterized in laboratory tests using high pressure rheometers. The latter is known to be linearly dependent on pressure $\tau_L = \Lambda \cdot p$, with slope Λ known as the limiting-stress pressure coefficient [222], which is strongly dependent on the base oil type and varies slightly with temperature. Therefore, if a simple relation is found between τ_E and τ_L it is possible to use Equation 4.12 as a prediction model for different lubricants.

Several authors [223, 224] report constant ratios between the reference stress and the limiting shear stress obtained experimentally, while others such as Bair and Winer [225] conclude analytically that $\tau_E \approx 2 \cdot \Lambda / \alpha$ by relating limiting shear stress and Eyring stress models (Equations 4.8 and 4.9). Their results agree well with the experimental values from Johnson and Tevaarwerk [213] and explained the sigmoid shape of the friction curve by the growth of the plastic region within the contact ruled by the limiting shear stress. Similarly, Jacod et al. [226] also found an analytical relationship by applying Eyring and limiting shear stress models to the same traction data such that predicted

values are equal in a wide range of operating conditions and lubricants. Their results were validated with a different set of friction coefficient data and both authors lead to approximately the same solution at the pressure and temperature levels present in EHD contacts (see Figure 4.7) which suggests that the value of τ_E can be related to the piezoviscosity coefficient, α , in such conditions.

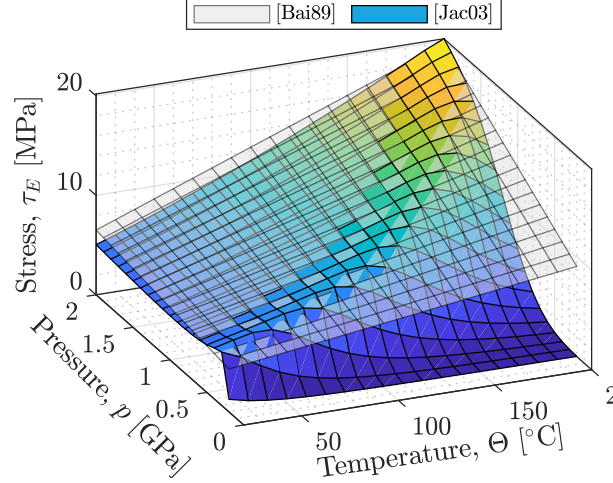


Figure 4.7: Eyring stress predictions by references [225] and [226] as a function of film temperature and pressure: ISO VG 100 mineral oil, $\Lambda=0.047$, $R_e = 10$ mm, $V_e = 5$ m/s and $SRR = 0.1$

It has been found that this conclusion can also be analytically addressed following Eyring's theory of fluid flow [214]. If one recalls the expression by Hirst and Moore [227], shear rate can be written in the following form:

$$\dot{\gamma} = A \cdot k \cdot \Theta \cdot \exp\left(-\frac{E + v_p \cdot p}{k \cdot \Theta}\right) \cdot \sinh\left(\frac{v_\tau \cdot \tau}{2 \cdot k \cdot \Theta}\right) \quad (4.13)$$

Where A is a constant, k is Boltzmann constant ($1.38 \cdot 10^{-23}$ J/K), E is the thermal activation energy for flow and v_p and v_τ are the activation volumes for pressure and shear respectively, both of which are fluid-dependent. Rearranging terms:

$$\dot{\gamma} = \frac{\frac{2 \cdot k \cdot \Theta}{v_\tau}}{\frac{2}{A \cdot v_\tau} \cdot \exp\left(\frac{E}{k \cdot \Theta}\right) \cdot \exp\left(\frac{v_p \cdot p}{k \cdot \Theta}\right)} \cdot \sinh\left(\frac{v_\tau \cdot \tau}{2 \cdot k \cdot \Theta}\right) \quad (4.14)$$

By direct comparison with the viscous term in Equation 4.11,

$$\tau_E = \frac{2 \cdot k \cdot \Theta}{v_\tau} \quad (4.15)$$

$$\eta = \frac{2}{A \cdot v_\tau} \cdot \exp\left(\frac{E}{k \cdot \Theta}\right) \cdot \exp\left(\frac{v_p \cdot p}{k \cdot \Theta}\right) \quad (4.16)$$

The first exponential term in Equation 4.16 is the Andrade equation representing the temperature dependence of viscosity and the second exponential term is the Barus equation where the piezoviscosity coefficient is $\alpha = v_p / (k \cdot \Theta)$. If the latter is related to the reference stress in Equation 4.15:

$$\tau_E = \frac{2 \cdot v_p / v_\tau}{\alpha} \quad (4.17)$$

The resulting mathematical expression is surprisingly similar to that of Bair and Winer [225] where $\tau_E \approx 2 \cdot \Lambda / \alpha$ but in this work it has been obtained from the original Eyring equation [214]. In both cases, the reference stress is inversely proportional to the pressure-viscosity coefficient by some constant related to material properties. Direct comparison of these expressions yields $v_p / v_\tau = \Lambda$, where the ratio v_p / v_τ is usually calculated at high shear stresses and constant shear rate [59]. In such conditions, $\tau \gg \tau_E$, and the expression $\sinh(\frac{\tau \cdot v_\tau}{2 \cdot k \cdot \Theta})$ reduces to $\frac{1}{2} \cdot \exp(\frac{\tau \cdot v_\tau}{2 \cdot k \cdot \Theta})$. As a result, Equation 4.13 turns into:

$$\dot{\gamma} = \frac{1}{2} \cdot A \cdot k \cdot \Theta \cdot \exp\left(\frac{-2 \cdot E - 2 \cdot v_p \cdot p + v_\tau \cdot \tau}{2 \cdot k \cdot \Theta}\right) \quad (4.18)$$

At a constant shear strain rate and taking logarithms at both sides, the following linear relationship with pressure is obtained:

$$\tau = 2 \cdot \frac{v_p}{v_\tau} \cdot p + C \quad (4.19)$$

It is interesting to note that according to Bair and Winer, the limiting shear stress Λ takes the values 0.047 and 0.088 for LVI260 and 5P4E oils respectively [225]; which means that the slope of the plot of mean shear stress against pressure following Equation 4.19 is 0.094 and 0.176 which is in perfect agreement with the values estimated by Hirst and Moore for several fluids in [227].

Final equation

Assuming that the Couette flow dominates in the contact region the strain rate in Equation 4.12 is equal to the velocity gradient, $\dot{\gamma} = V_s / (h_c \cdot \Phi_T)$, where V_s is the sliding speed of the surfaces and h_c is the central film thickness between them corrected for thermal effects with factor Φ_T (see Equation 4.51). If $\tau_E = 2 \cdot \Lambda / \alpha$ is assumed, fluid friction coefficient results in:

$$\mu_f = \min\left[\frac{2 \cdot \Lambda}{\alpha \cdot \bar{p}} \cdot \sinh^{-1}\left(\frac{\eta \cdot \alpha \cdot V_s}{2 \cdot \Lambda \cdot \Phi_T \cdot h_c}\right), \Lambda\right] \quad (4.20)$$

Where viscosity, η , must be evaluated at the mean contact temperature and pressure while the local piezoviscosity coefficient, α , is calculated at Hertz pressure according to [225].

4.2.2 Extension to partial EHL regime

Theoretical background

Tallian [228] suggested that the degree of asperity interaction is governed by the specific film thickness ratio $\lambda = h_c / \sigma$ where h_c is the central EHD film thickness and σ is the composite root mean square roughness of the surfaces. According to Tallian partial EHD exists when $0.5 \div 1 < \lambda < 3 \div 4$. In this regime, normal and tangential loads applied to the contacting bodies are shared between the oil film and the surface asperities according to the following equation:

$$F = F_f + F_s \quad (4.21)$$

Where F is the total load, F_f is the portion of load carried by the elastohydrodynamic film and F_s is the load carried by surface asperities. If Equation 4.21 is stated in terms of traction, τ :

$$\bar{\tau} \cdot A_0 = \tau_s \cdot A_s + \tau_f \cdot A_f \quad (4.22)$$

$$\bar{\tau} = \tau_s \cdot \frac{A_s}{A_0} + \tau_f \cdot \left(1 - \frac{A_s}{A_0}\right) \quad (4.23)$$

$$\bar{\mu} = \frac{1}{\bar{p}} \cdot \left[\tau_s \cdot \frac{A_s}{A_0} + \tau_f \cdot \left(1 - \frac{A_s}{A_0}\right) \right] \quad (4.24)$$

Where $\bar{\mu}$ represents the mean coefficient of friction between the mating surfaces, τ_s and τ_f are the solid and fluid tractions respectively and A_s/A_0 is the ratio of the real contact area (i.e. the summation of the individual contacting spots of radius r_i in Figure 4.8) over the apparent (i.e. Hertzian) contact area. Thus, the ratio A_s/A_0 is defined in the $[0, 1]$ range where 0 represents total separation of the surfaces and 1 is used for full contact.

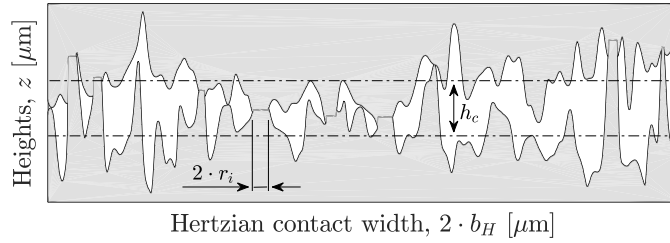


Figure 4.8: Representation of asperities in contact in mixed lubrication

Rewriting $\xi = A_s/A_0$ and introducing solid and fluid friction coefficients, μ_s and μ_f , Equation 4.24 results in the following friction coefficient for partial EHL regimes, which is the basis for most empirical equations available in gear literature [229].

$$\mu = \xi \cdot \mu_s + (1 - \xi) \cdot \mu_f \quad (4.25)$$

Boundary friction coefficient

Contrary to the fluid friction coefficient, that of boundary friction is often assumed constant and independent of the operating conditions [62]. This assumption is strongly supported by several studies: Robbe-Valloire [230] proposed the value 0.08 for a pin-on-disc type contact, Faraon and Shipper [37] reported values close to 0.13 for starved line contacts and recently Masjedi and Khonsary [231] have measured asperity friction coefficients ranging from 0.12 to 0.135 in roller contacts. Although solid friction coefficient is not very sensitive to sliding speed it is slightly dependent on load, temperature and surface roughness [231]. These influencing factors have been included in some partial EHL friction coefficient models for gears [49] but very little variation should be expected with respect to a constant friction coefficient model as concluded by Diab [50].

All these models represent friction coefficient for boundary lubrication in pure sliding contacts. However, gears are subject to a rolling-sliding motion and the mixed EHL sliding friction coefficient model is expected to give zero in the pitch point where pure

rolling occurs. Therefore, the following fit according to Gelinck [232] is used, where the boundary lubrication coefficient is modified in the vicinity of zero slip, s :

$$\mu_s = \mu_{s,\infty} \cdot \frac{2}{\pi} \cdot \operatorname{atan}\left(\frac{\pi}{2} \cdot \frac{s}{s_{eff}}\right) \quad (4.26)$$

In this equation $\mu_{s,\infty}$ represents the boundary friction coefficient under pure sliding ($s = 2$) and s_{eff} is the transition value from the elastic to plastic behaviour of the boundary layer. According to Gelinck [232] the latter takes the approximate value of 0.015 while the former depends on surface structure. In the absence of an initial guess Matsumoto and Morikawa's solid friction coefficient values for typical gear flank topographies can be used [229].

Load sharing function

Finally, in order to extend the range of applicability of the fluid friction coefficient model to the partial EHL regime without increasing computational effort, a simple asperity load sharing model is proposed. Table 4.3 summarizes some of the most relevant equations in gear literature. As it can be seen several functions have been proposed with diverse definitions of the specific film thickness and different domains of application.

Table 4.3: Asperity load sharing functions in gear literature

	Doleschel [49]	Diab [50]	Matsumoto [229]
ξ	$(1 - \frac{\lambda}{2})^2$	$\frac{1}{4} \cdot (1 - \operatorname{erf}(\frac{\lambda}{\sqrt{2}}))$	$\frac{1}{2} \cdot \log_{10}(\frac{1}{\lambda})$
λ	$\frac{\phi_T \cdot h_c}{\frac{Ra_1 + Ra_2}{2}}$	$\frac{\phi_T \cdot h_c}{\sqrt{Rq_1^2 + Rq_2^2}}$	$\frac{h_{min}}{Rz_1 + Rz_2}$
\mathcal{D}	[0, 2]	[0, 3]	[0.01, 1]

Doleschel [49] considered that asperity interactions begin at specific film thickness values below 2 and a second-order polynomial function was used to represent the amount of load carried by asperities. Diab [50] computed the complementary error function to predict the load share parameter and assumed that partial EHL begins at $\lambda \approx 3$. In both cases, specific film thickness was computed using the ratio of the central film thickness (corrected to account for thermal effects) to the combined average or mean square roughness of the surfaces. However, in a recent work Matsumoto [229] considered that load share is governed by the ratio of the minimum film thickness to the sum of the maximum height of asperities which implies that mixed lubrication regime begins long before expected. These load sharing functions have been tested indirectly in twin disc machines through the measurement of the mean friction coefficient but none of them has been compared directly to experimental asperity load sharing results, hence, the accuracy of each function still remains unknown.

According to the extensive experimental work by Schipper [233] friction in a large part of the mixed lubrication regime increases linearly with decreasing $\ln \mathcal{L}$, where $\mathcal{L} = (\eta \cdot Vr) / (\bar{p} \cdot \sigma)$. This parameter is similar to the specific film thickness ratio, λ , but it is specially suited to the analysis of the transition between the full EHL and partial EHL up to the boundary lubrication regime. Based on this number it is possible to set a general Stribeck curve such as that presented in Figure 4.9.

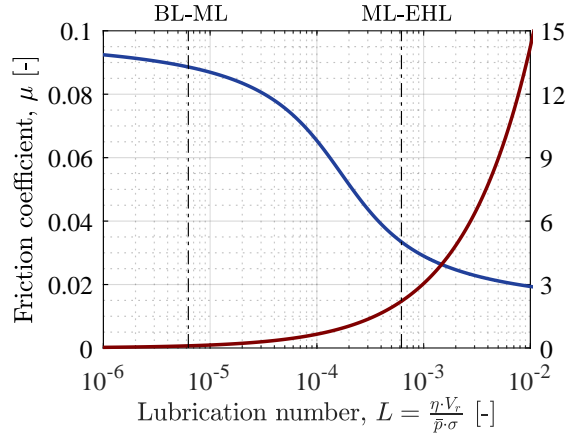


Figure 4.9: Generalized Stribeck curve sample with transitions

It is observed that the onset of partial EHL is close to $\mathcal{L} = 6 \cdot 10^{-4}$ while boundary lubrication regime starts at $\mathcal{L} = 6 \cdot 10^{-6}$. These values correspond to specific film thickness ratios of 2.2 and 0.1 respectively which is consistent to recent experimental research [234]. If the mathematical expressions in Table 4.3 are considered, such behaviour is only ensured by the complementary error function by Diab [50] but the latter must be modified to cope with these limits $\xi(\lambda \approx 2) = 0$ and $\xi(\lambda = 0) = 1$ which results in:

$$\xi = 1 - \operatorname{erf}(\lambda) \quad (4.27)$$

4.2.3 Experimental validation

The fluid friction coefficient model presented in Equation 4.20 has been compared to the experimental results from Mann [212]. Three different base oils ISO VG 100 were tested in a twin-disc machine: i) a naphthenic mineral oil (named N100), ii) a paraffinic mineral oil (M100) and a poly- α -olefin (PAO100). The selected lubricants are known to have very different traction behaviour with the highest friction coefficients for the naphthenic base to the lowest for the poly- α -olefin. None of the selected lubricants included additives and the discs were smoothly polished up to $R_a \approx 0.06 \mu\text{m}$ to avoid asperity interactions so that pure fluid traction could be tested. Table 4.4 outlines basic rheological parameters where the limiting-stress pressure coefficients have been obtained from experimental results in [235].

Table 4.4: Selected lubricant properties from [212] and [235]

	$\nu_k _{40}$ $10^{-6} \left[\frac{\text{m}^2}{\text{s}} \right]$	$\nu_k _{100}$ $10^{-6} \left[\frac{\text{m}^2}{\text{s}} \right]$	$\rho _{15.6}$ $\left[\frac{\text{kg}}{\text{m}^3} \right]$	Λ $10^{-2} [-]$
N100	97.9	8.61	900	5.3
M100	96	10.6	882	4.7
PAO100	94.1	14	840	3.5

In order to model lubricant's dynamic viscosity as a function of temperature and pressure, the so called "modulus equation" is used (see Equation 4.28). The first exponential term describes the temperature dependence of viscosity following the Vogel, Tammann and Fulcher equation and the second exponential term is similar to that of the empirical equation by Paluch [236]. Gold et al. [237] linearised the temperature dependence of parameters A and B and obtained an equation with seven unknown parameters: a_1 , a_2 , b_1 , b_2 , C , D and K which can be obtained numerically from regression of experimental measurements at high pressures.

$$\eta(\Theta, p) = K \cdot \exp\left[\frac{C}{D + \Theta}\right] \cdot \exp\left[\frac{p}{A + B \cdot p}\right] \quad (4.28)$$

$$A(\Theta) = a_1 + a_2 \cdot \Theta \quad (4.29)$$

$$B(\Theta) = b_1 + b_2 \cdot \Theta \quad (4.30)$$

The viscosity-pressure-temperature (VPT) behaviour of the gear oils in Table 4.4 was fitted from Mann's high-pressure falling body viscosimeter measurements [212]. Table 4.5 summarizes the regression coefficients along with the coefficient of determination (R^2) which shows good agreement. A comparison of numerical predictions and experimental measurements is provided in Figure 4.10.

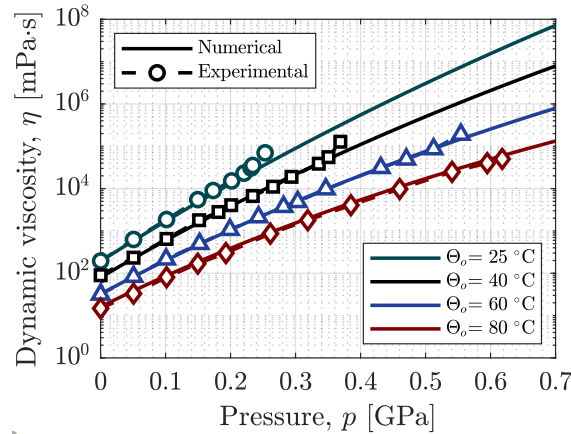


Figure 4.10: Numerical-experimental correlation of the VPT behaviour of M100 oil

The main advantage of the modulus equation over other equations is that the pressure dependence of the viscosity-pressure coefficient, α , is additionally taken into account. A simple analogy of Equation 4.28 with the classical Barus equation yields:

$$\alpha(\Theta, p) = [A + B \cdot p]^{-1} = [a_1 + a_2 \cdot \Theta + (b_1 + b_2 \cdot \Theta) \cdot p]^{-1} \quad (4.31)$$

Table 4.5: Regression coefficients for the selected lubricants

	a_1 $10^7 [\text{Pa}]$	a_2 $10^5 [\frac{\text{Pa}}{\text{K}}]$	b_1 $10^{-3} [-]$	b_2 $10^{-5} [\frac{1}{\text{K}}]$	C $10^3 [\text{K}]$	D $10^2 [\text{K}]$	K $10^{-6} [\text{Pa}\cdot\text{s}]$	R^2 [%]
N100	-7.23	3.48	5.00	-1.83	0.65	-2.06	161.60	99.67
M100	-2.28	2.26	-68.20	27.68	0.89	-1.82	86.86	88.73
PAO100	-5.73	3.90	-39.50	23.54	1.74	-1.16	12.26	99.59

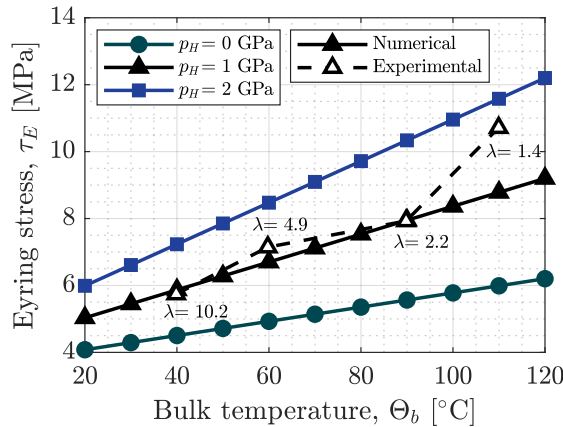


Figure 4.11: Eyring stress as a function of temperature and pressure for M100 oil

If the latter is used to predict the behaviour of the reference stress, τ_E , it can be seen in Figure 4.11 that the numerical predictions are in good agreement with the experimentally measured values from [38] for the M100 oil. These results were obtained by curve-fitting the classical Ree-Eyring non-newtonian model to twin disc traction tests at 8 m/s rolling velocity, 10% slip, 1 GPa Hertz pressure and different oil jet temperatures. Specific film thickness ratio has been included in Figure 4.11 in order to give insight into the lubrication regime in the contact. At full EHL, numerical

predictions follow the experimental results, but at 110 °C $\lambda = 1.4$ and therefore asperity contact may occur giving rise to higher friction coefficients and therefore higher values of the regressed Eyring shear stress.

Mann [212] carried out several traction tests for the different oils at varying rolling velocities from 2 m/s to 16 m/s and slip ratios in the range [0,0.4] at constant Hertz pressure of 1 GPa and oil jet temperature of 60°C. Disc bulk temperatures were measured at different input speeds and slip ratios which allows predicting film thickness accurately. Figure 4.12 shows the numerical predictions for the M100 mineral oil case. The model captures the typical behaviour of the traction tests with a linear region showing Newtonian behaviour at the lowest slip ratios, followed by a non-linear region with a maximum and a thermal region at the highest slip ratios where the heat generated within the contact leads to a reduction of the friction coefficient. As it can be concluded from Figure 4.12 the proposed model correctly captures the friction behaviour at the highest rolling speeds and slip ratios with errors below 10%. This effect is important as most of power losses occur near the tip and root of gears where the slip ratio is highest along the path of contact.

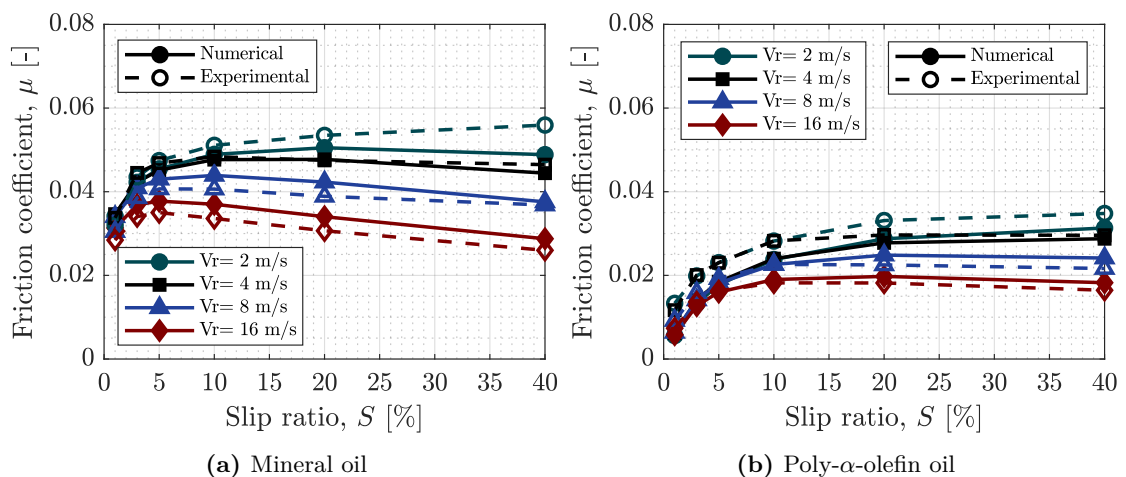


Figure 4.12: Numerical-experimental correlation of traction curves for different oil types

Finally, Figure 4.13a shows the overall performance of the model for each lubricant type with respect to the empirical models in Table 2.1. The lowest friction coefficients are predicted for the poly- α -olefin oil and the highest values correspond to the naphthenic mineral oil which is in agreement with experimental evidence in scientific literature. The predicted values are within $\pm 5 \cdot 10^{-3}$ error which is considerably lower than empirical models shown in Figures 4.13b to 4.13d.

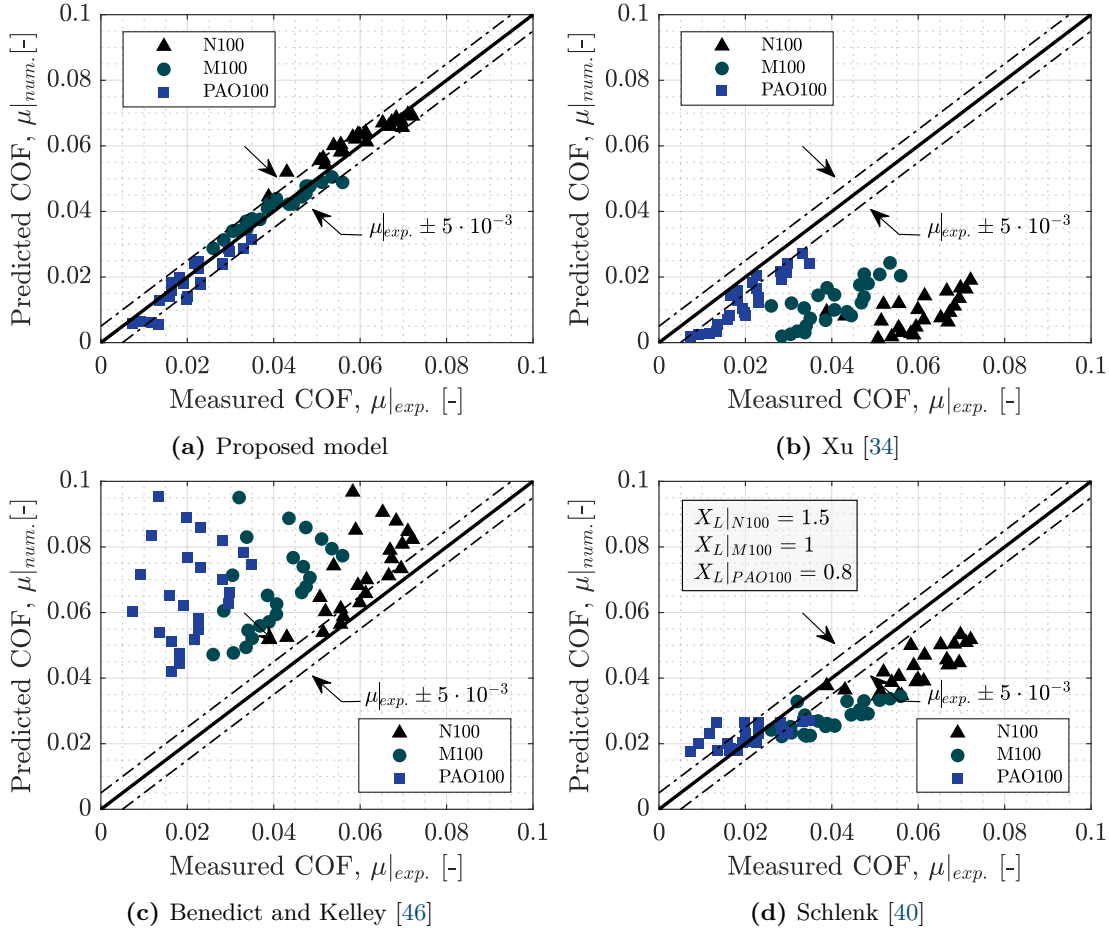


Figure 4.13: Measured and predicted friction coefficients according to proposed model and equations from literature in Table 2.1

4.2.4 Discussion of results

The comparison of the analytical and experimental results presented in this section shows that, in general, accurate predictions of the full EHL friction coefficient can be carried out for any lubricant from its VPT behaviour; at least for low-to-medium viscosities (up to ISO VG 220 in this work), where the elastic behaviour of the lubricant can be neglected. However, it is observed in Figure 4.12b that traction behaviour at low rolling speeds and slip ratios is deviated from the experimental measurements by up to 25%, indicating that the elastic term is not negligible. This is due to the low contact inlet temperatures at these operating conditions. According to Mann [212] the measured disk bulk temperature for the poly- α -olefin oil is approximately 55 °C for these conditions

which leads to higher viscosities than expected and therefore higher probability of elastic behaviour. In the case of the mineral oil this temperature is close to 70 °C, resulting in lower viscosity, and therefore the deviations might not be perceptible.

On the other hand, the model has adopted the classical Ree-Eyring approach which is claimed to underestimate shear thinning phenomena [217]. At high shear rates, shear thinning in the inlet zone leads to lower film thickness and therefore lower friction coefficients, which may explain the slight differences between experimental measurements and numerical predictions. This behaviour is found in mineral oil-polymer blends and some synthetic oils and therefore, in such situations, film thickness may need to be corrected [238]. However, in this case, the selected lubricants are simple fluids, not blended, and shear thinning is not expected. The subject is not clear as the slight differences may also be attributed to the shear heating effect which has been considered through parameter Φ_T . The latter is an empirical coefficient which has been fitted from experimental measurements with different oil types, therefore, results are affected by the regressed coefficients. This behaviour is especially visible at the lowest rolling velocities where the parameter Φ_T is overestimating the inlet shear heating effect as predicted by Hili et al. [239], which results in lower friction coefficients than those measured experimentally.

One of the main drawbacks of the model is the dependency on the accurate modeling of the VPT behaviour of the lubricant, especially that of the local piezo-viscosity coefficient, α , which is the basis of the Eyring stress prediction model. This models can only be developed from high pressure viscometer measurements and this type of rheometer is not commercially available; therefore, very few gear lubricants have been characterized by research centres up to the pressure levels encountered in EHL contacts and lubricant behaviour still tends to be regressed from tribometer measurements [240]. Therefore, only temperature dependent piezoviscosity equations can be used, typically computed from the kinematic viscosity with expressions of the type $\alpha = s \cdot \nu^t$ which are frequent in literature [237]. One could, as an approximation, use two-slope viscosity-pressure models such as that suggested by [34].

Moreover, absolute viscosity requires the description of the lubricant behaviour over the full pressure range of the application, which may vary from 0.1 to 2 GPa. It has been described in literature that viscosity shows a “faster-than-exponential” response at high pressures [241] which may be present at the temperature and pressure levels of gear contacts. This behaviour explains the inflection of the viscosity curves in Figure 4.10 at pressures of 230 MPa, 350 MPa and 510 MPa at 25°C, 40°C and 60°C respectively, which is the responsible for the 88 % coefficient of determination in Table 4.5. If these outliers are ignored in the regression of the Modulus equation, the coefficient of determination increases up to 99.26% for the M100 oil. The inflection pressure is explained by the Free-volume theory [241] and the convenience of using relative models (e.g. Yasutomi) has been analysed. However, the parameters in these models must be regressed from viscosity measurements above and below the pressure inflection and in the case of M100 mineral oil there is not enough information available. Nevertheless, it is known that the inflection pressure increases with increasing temperature and, in the case of the M100 oil, it is not even observed at the highest temperature. If one considers the contact conditions in Mann’s twin disc tests, the pressure inflection will probably not be present in the

analysed test cases and therefore the Modulus equation is sufficiently accurate to describe the piezo-viscosity behaviour. As far as the naphthenic and polyalphaolefin base-stock behaviour is concerned, the reversal of curvature is not observed in the analysed pressure and temperature range; which explains the good agreement of the proposed model.

As far as the Eyring stress behaviour is concerned, it has been shown in Figure 4.11 that the predicted trend closely follows the experimental results by Michaelis for the same oil [38]. However, regressing Eyring stress behaviour from experimental measurements in tribometers can be imprecise if full EHL conditions are not guaranteed. This is might the most probable reason behind the discrepancy at the highest temperature (110 °C). The surface roughness in the experiments by Michaelis was $R_q = 0.1\mu\text{m}$ and the specific film thickness at the contact pressure and temperature results in $\Lambda = 1.4$ indicating that partial EHL regime exists. As a result, friction coefficient value is shifted due to asperity collisions and the regressed Eyring stress is higher. Figure 4.14 explains this situation. A small variation of approximately $2.5 \cdot 10^{-3}$ can lead to an Eyring stress diminution of 2 MPa which is the approximate difference with the theoretical predictions. Similarly, thermal effects could also affect the regressed value, but in this case, the reduction of the film thickness due to this effect has been considered through parameter ϕ_T .

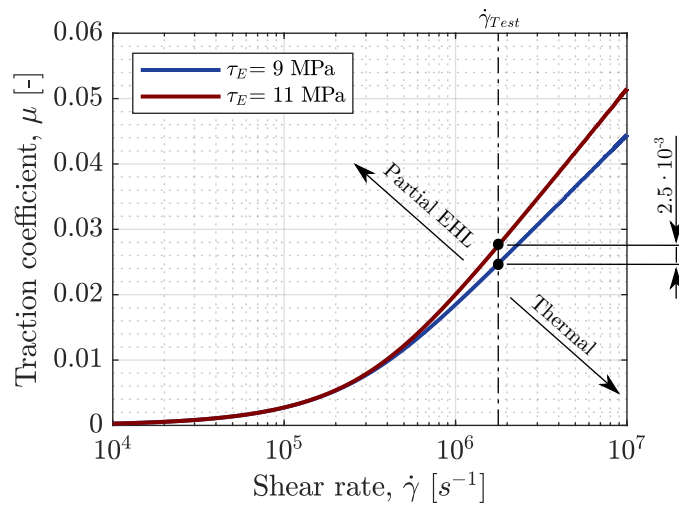


Figure 4.14: Influence of Eyring stress on traction coefficient

4.3 Power loss prediction model

The prediction of power losses with the proposed friction coefficient model requires the accurate calculation of the thermal state of the gear teeth contact in each point along the line of action. It can be seen in Equations 4.20 that local fluid friction coefficient depends on the absolute viscosity, η , and piezo-viscosity coefficient, α , both evaluated at the mean temperature and pressure of the fluid film within the Hertzian contact region. Meanwhile, the central film thickness, h_c , which is also affecting the asperity load sharing ratio in Equation 4.27, must be evaluated at the inlet temperature and ambient pressure, which is dependent on the bulk temperatures of the bodies. Although the physical relation between both is well established and it is frequently used in the field of tribology [242] it has not been adopted by the power loss prediction models in gear literature which still follow the isothermal approach where film thickness and friction coefficient are both calculated at the bulk temperature [243]. This method is accurate in rolling contacts but fails when sliding is present as recent thermal EHL simulations have shown [61]. Therefore it is necessary to fully understand the non-isothermal behaviour of the contact before power losses can be predicted.

4.3.1 Teeth contact thermal behaviour

The temperature at the interface of two smooth surfaces in direct contact subject to a relative sliding motion is known as “conjunction temperature” (contact temperature in the following, Θ_c). According to Jaeger [244] the maximum contact temperature is the result of the sum of the steady-state temperature of the solids (known as bulk temperature, Θ_b) and a transient term known as “flash temperature rise”, $\Delta\Theta_{fl}$, which is dependent on the thermal properties of the mating bodies, the relative sliding velocity and the heat flux. The latter depends on local contact area and power loss through the normal load, W , friction coefficient μ , and sliding velocity, Vs . Thus, it can be concluded that friction is affected by temperature but temperature is also affected by friction, which leads to an iterative procedure to solve the local temperature field. Additionally, in the case of lubricated contacts such as that shown in Figure 4.15, there is a oil film within the Hertzian region and film temperature, Θ_f , is even higher due to the internal heat dissipation, $\Delta\Theta_v$, [64]. Therefore, for any given point along the LOA, oil film and contact inlet temperatures (i.e. the mean bulk temperature of the solids) can be related through the summation of individual contributions (see Equation 4.32). From this relation, it is possible to compute film thickness at the mean inlet conditions and then calculate traction at the mean Hertzian conditions.

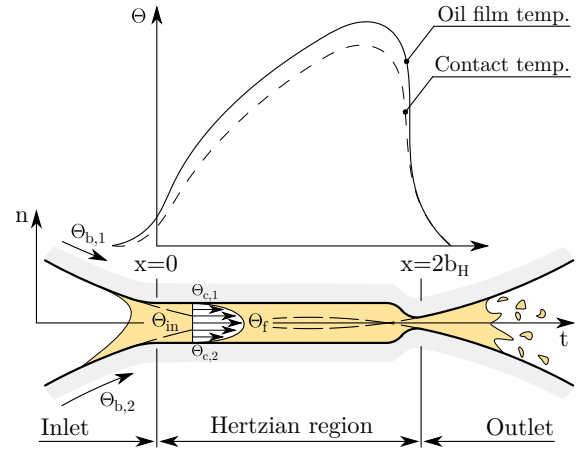


Figure 4.15: Representation of a smooth thermal EHL line contact

Therefore, for any given point along the LOA, oil film and contact inlet temperatures (i.e. the mean bulk temperature of the solids) can be related through the summation of individual contributions (see Equation 4.32). From this relation, it is possible to compute film thickness at the mean inlet conditions and then calculate traction at the mean Hertzian conditions.

$$\Theta_f = \Theta_c + \Delta\Theta_v = \Theta_{in} + \Delta\Theta_{fl} + \Delta\Theta_v \quad (4.32)$$

The instantaneous heat generated in the gear mesh, $Q = P_{VZP,i}$, is divided between pinion and gear and the proportion of the total heat flowing to each of them depends on the magnitude of thermal resistances (see Figure 4.16). In the field of tribology, Archard's "true flash temperature rise" [245] concept is usually applied to calculate mean contact temperature and then compute traction. Flash temperature rise for each body is calculated individually and both are coupled by means of the heat partitioning coefficient, α , according to Jaeger [244]². However, this method assumes that the contact is perfect and the temperature of the mating surfaces is the same, which requires bulk temperatures to be equal. In order to allow for temperature differences between pinion and gear Olver's method [246] is applied here which, contrary to that of Archard's, assumes that both bodies are subject to the same ambient temperature, (i.e. the oil sump) and that film temperature is equal for both bodies. This situation is depicted in the thermal network model of Figure 4.16.

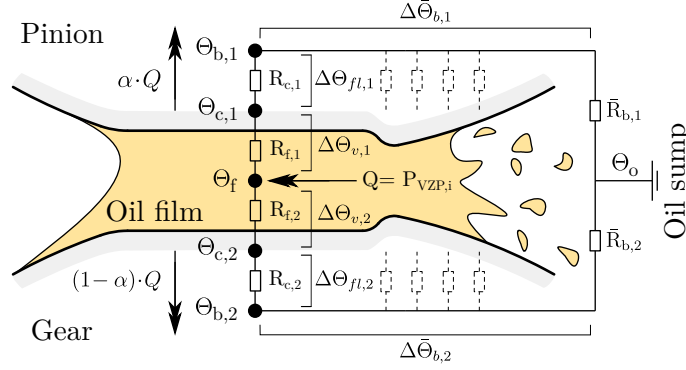


Figure 4.16: Thermal network scheme of the EHL line contact

Olver [246] presented the method for two discs in contact, with constant heat flux and axisymmetric geometry. In this work, the procedure is further developed for the specific case of meshing gears which are characterized by variable instantaneous heat inputs and non uniform geometry. If Equation 4.32 is considered from pinion and gear sides, one has:

$$\Theta_f = \Theta_o + \Delta\bar{\Theta}_{b,1} + \Delta\Theta_{fl,1} + \Delta\Theta_{v,1} = \Theta_o + \Delta\bar{\Theta}_{b,2} + \Delta\Theta_{fl,2} + \Delta\Theta_{v,2} \quad (4.33)$$

From Figure 4.16 it is possible to relate individual temperature increases with the corresponding thermal resistances and heat flux. For the instantaneous film and flash temperature rise terms, resistances are placed in series. However, the pinion and gear bulk temperature rise is the result of the summation of individual heat contributions along the line of action, thus the bulk temperature rise is computed as several resistances placed in parallel. With these conditions, the local film temperature, $\Theta_{f,i}$, is calculated as follows:

$$\Theta_{f,i} = \frac{1}{n} \cdot \sum_{i=1}^{i=n} [Q_i \cdot \alpha_i \cdot R_{b,1,i}] + Q_i \cdot \alpha_i \cdot (R_{c,1,i} + R_{f,1,i}) \quad (4.34)$$

$$\Theta_{f,i} = \frac{1}{n} \cdot \sum_{i=1}^{i=n} [Q_i \cdot (1 - \alpha_i) \cdot R_{b,2,i}] + Q_i \cdot (1 - \alpha_i) \cdot (R_{c,2,i} + R_{f,2,i}) \quad (4.35)$$

Rearranging terms and operating, the local heat partitioning coefficient, α_i , reads:

$$\alpha_i = \frac{\bar{R}_{b,2} + R_{c,2,i} + R_{f,i}}{(\bar{R}_{b,1} + R_{c,1,i}) + (\bar{R}_{b,2} + R_{c,2,i}) + 2 \cdot R_{f,i}} \quad (4.36)$$

Where the pinion and gear bulk resistance terms, $\bar{R}_{b,1}$ and $\bar{R}_{b,2}$, are the mean values of the thermal resistances along the line of action. On the other hand, the film resistance term, $R_{f,i}$, is the same for pinion and gear if half film thickness is considered for each. Assuming that the viscous heat dissipation is uniform across the film, the resistance according to Johnson and Greenwood [247] applies:

$$R_{f,i} = \frac{h_{c,i}}{8 \cdot k_{o,i} \cdot A_i} \quad (4.37)$$

Where A_i is the instantaneous Hertzian contact area, $A_i = 2 \cdot b_{H,i} \cdot l$, and $k_{o,i}$ is the thermal conductivity of the oil at the mean film temperature and pressure of the contact point of interest.

On the other hand, the transient term, $R_{c,i}$, depends on the Peclet number, L , which is a non-dimensional value, $L = (u \cdot b_H)/(2 \cdot \chi_i)$, describing the relative speed at which the heat source moves along the flank surface thus indicating the heat penetration capacity into the solid. Rolling speed in gears is usually high and therefore Peclet numbers are $L \gg 5$. In such case, the local contact thermal resistance is:

$$R_{c,i} = \frac{1.064}{k_i \cdot A_i} \cdot \left(\frac{\chi_i \cdot b_{H,i}}{u_i} \right)^{0.5} \quad (4.38)$$

With χ_i and k_i the thermal diffusivity and conductivity of the material, $b_{H,i}$ the contact half width and u_i the rolling speed of the pinion or gear surface. Corresponding equations for medium and low Peclet numbers can be found in [248].

The mean value of the steady-state thermal resistance, \bar{R}_b , is the most complex term of all as it depends on the specific geometry of the gear, its material and the overall heat transfer coefficient. The full thermal network model developed in Chapter 5 will allow to determine the value of this term for any given geometry, operating condition and immersion depth. Nevertheless, it is possible to compute an approximate value from empirical equations such as that from Terekhov [117] shown in Equation 4.41.

$$\bar{R}_b = \frac{B}{V_t \cdot H \cdot b \cdot c_{p_o} \cdot \rho_o} \cdot R_e^{\Psi_1} \cdot P_r^{\Psi_2} \cdot \left(\frac{H}{r_a} \right)^{\Psi_3} \cdot \left(\frac{V}{V_o} \right)^{\Psi_4} \cdot \left(\frac{h}{r_a} \right)^{\Psi_5} \cdot \left(\frac{h}{b} \right)^{\Psi_6} \quad (4.41)$$

² From Equation 4.36 it is possible to reach Jaeger's expression for the local heat partitioning coefficient, α , which is common in tribology. Following Archard [245] it is assumed that the mean flash temperature increase is the same for both bodies, that is, steady-state and film thermal resistances are neglected. In such conditions, we have:

$$\alpha_i = \frac{R_{c,2,i}}{R_{c,1,i} + R_{c,2,i}} \quad (4.39)$$

Considering high Peclet numbers the contact resistance according to Equation 4.38 applies:

$$\alpha_i = \frac{1.064 \cdot k_i^{-1} \cdot A_i^{-1} \cdot u_{2,i}^{-0.5} \cdot \sqrt{\chi \cdot b_{H,i}}}{1.064 \cdot k_i^{-1} \cdot A_i^{-1} \cdot (u_{1,i}^{-0.5} + u_{2,i}^{-0.5}) \cdot \sqrt{\chi \cdot b_{H,i}}} = \frac{\sqrt{u_{1,i}}}{\sqrt{u_{1,i}} + \sqrt{u_{2,i}}} \quad (4.40)$$

Which depends exclusively on the rolling speeds of the mating surfaces.

Where V_t is the pitch line velocity, H is the immersion depth, b is the face width, cp_o is the specific heat capacity of the oil, ρ_o is the density of the oil, Re is the Reynolds number, Pr is the Prandtl number, r_a is the tip radius, V is the immersed volume of the gear, V_o is the volume of the oil bath and h is the tooth height. Coefficient B depends on rotating sense and it is equal to $0.301 \cdot 10^{-4}$ if the teeth enter the oil bath after the mesh and $0.25 \cdot 10^{-4}$ for the opposite direction. Coefficients Ψ_1 to Ψ_6 are listed in Table 4.6.

Table 4.6: Coefficients for steady-state thermal resistance according to Terekhov [117]

Ψ_1	Ψ_2	Ψ_3	Ψ_4	Ψ_5	Ψ_6
1.15	1.31	-0.2	0.25	2.15	-0.45

Finally, as stated in the introductory paragraph, a mean bulk temperature is required to compute film thickness. Due to differences in rotational speed, size and immersion depths, pinion and gear are usually subject to different steady-state temperatures. According to Stolarsky [249], the mean bulk temperature at the inlet can be calculated from the bulk temperature of the surfaces weighted by the ratio of local rolling speeds. From this value, film temperature can be calculated following Equation 4.32. Summarizing, the final system of equations reads:

$$\bar{\Theta}_{b,1} = \Theta_o + \bar{R}_{b,1} \cdot \bar{P}_{VZP} \quad (4.42)$$

$$\bar{\Theta}_{b,2} = \Theta_o + \bar{R}_{b,2} \cdot \bar{P}_{VZP} \quad (4.43)$$

$$\Theta_{in,i} = \frac{1}{2} \cdot (\bar{\Theta}_{b,1} + \bar{\Theta}_{b,2}) + \frac{1}{2} \cdot \frac{(n_i - 1)}{(n_i + 1)} \cdot (\bar{\Theta}_{b,1} - \bar{\Theta}_{b,2}) \quad (4.44)$$

$$\Theta_{f,i} = \Theta_{in,i} + (R_{c,1,i} + R_{f,i}) \cdot \alpha_i \cdot P_{VZP,i} \quad (4.45)$$

Where n_i depends on material combination and rolling velocities. For steel gears this parameter reduces to $n_i = \sqrt{u_{i,1}/u_{i,2}}$.

4.3.2 Thermally-coupled power loss prediction model

The friction coefficient model presented in the previous section is included in the power loss prediction flowchart shown in Figure 4.17. The model accounts for thermal effects and therefore accurately predicts friction when gears are subject to high speeds or torques that produce a considerable film temperature increase. The additional steps with respect to the isothermal approach are highlighted with broken lines

The process starts with the discretization of the base tangent plane and the contact analysis of the meshing gears (frequently known as LTCA). For each point of the domain, surface velocities u_1 and u_2 and its derivatives (sliding, V_s , rolling, V_r , and entrainment speeds, V_e) are determined from generated geometry and rotational speed. Then, instantaneous load, W , is calculated with the load distribution model presented in Chapter 3, which allows computing local maximum and mean contact pressures, p_H and \bar{p} respectively, as well as the half contact widths, b_H , following Hertz theory for line contacts.

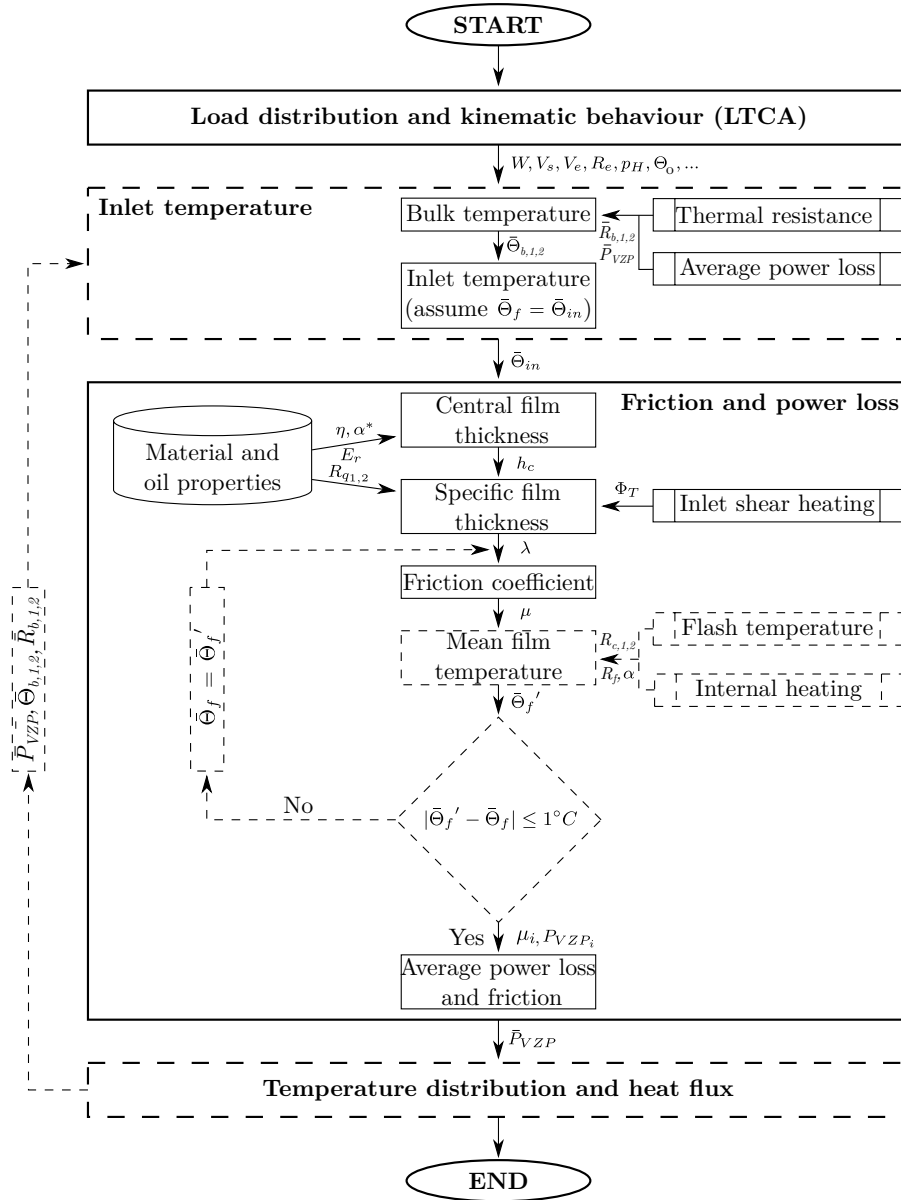


Figure 4.17: Thermally-coupled friction coefficient and power loss prediction flow chart

Once kinematic and load parameters are known, bulk temperatures are estimated with Equations 4.42 and 4.43. The initial guess for the mesh power loss, P_{VZP} , is computed following Ohlendorf’s approach [43] already described in Footnote 1 of the introductory section. Contact inlet temperatures for each position along the line of action are computed with Equation 4.44 and local film temperatures are assumed equal to inlet temperatures in the first loop until an estimate of the instantaneous power loss is obtained after the first iteration.

Then, film thickness is computed at the inlet temperature. Considering that gears operate in the piezo-viscous elastic regime, an appropriate equation is used to predict the latter as it directly affects friction coefficient through the fluid portion and the load sharing function in Equations 4.20 and 4.27 respectively. For this purpose, Hamrock and

Dowson's central film thickness [250] for smooth surfaces is computed, which has been modified to account for surface roughness through parameter γ according to Jonhson et al. [251]. This parameter reduces fluid pressure proportionally to asperity interaction, with $\gamma = (1 - \xi)^{-1}$, where ξ is the load sharing function already defined in Equation 4.27.

$$h_c = 2.69 \cdot R \cdot G^{0.53} \cdot U^{0.67} \cdot Q^{-0.067} \cdot (1 - 0.61 \cdot e^{-0.73 \cdot k}) \quad (4.46)$$

$$G = \frac{\alpha^* \cdot E}{\gamma} \quad (4.47)$$

$$U = \frac{\eta_0 \cdot V_e \cdot \gamma}{E \cdot R} \quad (4.48)$$

$$Q = \frac{W}{E \cdot R^2} \quad (4.49)$$

According to Hertz theory, E is the reduced modulus of elasticity, R is the effective radius of curvature in the entraining direction and $k = \infty$ in the case of line contacts. Attention is to be paid to the value of α^* which is the reciprocal asymptotic isoviscous pressure-viscosity coefficient (see Equation 4.50). This parameter is considered an effective value of α over the pressure range encountered in the contact and it is proved to better characterize the oil film formation in EHL contacts rather than α [252].

$$\alpha^* = \left(\int_0^{pH} \frac{\eta_0}{\eta(p)} dp \right)^{-1} \quad (4.50)$$

At this point, film thickness reduction factor, Φ_T , is also determined following Equation 4.51; and finally specific film thickness is computed from Equation 4.52.

$$\Phi_T = \frac{1 - 13.2 \cdot \frac{pH}{E_r} \cdot L^{0.42}}{1 + 0.213 \cdot (1 + 2.23 \cdot SRR^{0.83}) \cdot L^{0.64}} \quad (4.51)$$

$$\lambda = \frac{\Phi_T \cdot h_c}{\sqrt{Rq_1^2 + Rq_2^2}} \quad (4.52)$$

Where SRR is the slide-to-roll ratio and $L = \eta_0 \cdot \beta \cdot V_e^2 / k$ is the thermal loading parameter, with β and k the temperature-viscosity coefficient and fluid thermal conductivity respectively, both evaluated at the inlet temperature and ambient pressure.

Once the lubrication regime is known, friction coefficient is computed from Equations 4.20, 4.25, 4.26 and 4.27, where lubricant dynamic viscosity, η , is evaluated at the assumed mean film temperature and mean contact pressure, while the local pressure-viscosity coefficient, α , is calculated at Hertz pressure. Finally, instantaneous traction coefficient, μ_i , together with the sliding speed, $V_{s,i}$, and normal load, W_i , is used to predict local power loss $P_{VZP,i}$, and finally film temperature is updated through Equation 4.45.

If the new film temperature is different from that initially estimated, a new temperature field is established and the procedure is repeated until the difference in estimated and calculated film temperatures is less than 1°C. The procedure is repeated for each point in the line of action until the full path of contact is covered. Finally, instantaneous power loss values are integrated over the path of contact according to Equation 4.2 to predict the mean power loss, which is used to update the initial bulk temperature. The thermal network model developed in Chapter 5 will introduce a new step in the procedure allowing to compute the pinion and gear body thermal resistances for any given operating conditions, geometry and immersion depth.

Influence of thermal coupling

As it has been stated in the introductory paragraph, current gear power loss prediction models usually neglect the influence of film temperature increase and the isothermal approach is used with friction being evaluated at the bulk temperature of the bodies [243]. In this section, a thermal coupling method for film thickness and traction has been presented and a comparison of the isothermal and thermal approaches is carried out next.

The numerical procedure described earlier is compared to the recent results by Ziegler et al. [61] who analysed the influence of the non-Newtonian rheological behaviour of different oil types in the friction coefficient and the power loss in gears using finite element-based TEHL simulations. Comparisons are carried out in terms of local friction coefficients and power losses. A single gear set is considered (see Table 4.7) which is characterized by being a modified version of the standard FZG gear type C-PT with a tip relief of $35\mu\text{m}$. The test conditions comprise a constant torque of 183.4 Nm at load stage 7 (producing a maximum contact pressure of 1400 MPa near the lowest point of single tooth contact), a pitch line velocity of 8.3 m/s and a constant bulk temperature of $90\text{ }^\circ\text{C}$. Smooth surfaces are considered for the simulation, thus, only fluid friction coefficient model is compared. Finally, a ISO VG 100 mineral oil is used for this comparison with very similar properties to that presented in Table 4.4.

Table 4.7: Spur gear geometry used in [61]

Parameter	Symbol	FZG C_{mod}
Number of teeth	$z_{1,2}$ [-]	16, 24
Module	m [mm]	4.5
Face width	b [mm]	14
Pressure angle	α_n [°]	20
Profile shift	$x_{1,2}$ [-]	0.182, 0.172
Tip relief	$Ca_{1,2}$ [μm]	35
Loss factor at KS-7	H_{VL} [-]	0.1680
Material	[-]	16MnCr5

First, the film temperature evolution along the line of action is analysed in Figure 4.18. It is seen that computed temperatures are close to those predicted numerically with a maximum error of $6\text{ }^\circ\text{C}$ in the recess path of contact. The average temperature in the thermal result is approximately $115\text{ }^\circ\text{C}$ which is $25\text{ }^\circ\text{C}$ higher than the bulk temperature considered in the isothermal approach. These differences are expected to give rise to substantial deviations in friction coefficient and power losses.

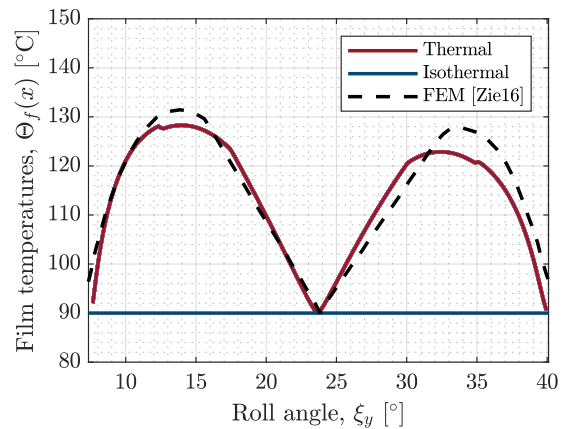


Figure 4.18: Comparison of computed film temperatures and numerical simulations from [61]

Friction and power loss results are presented in Figure 4.19. As it was expected the isothermal approach clearly deviates from the thermal calculation. If friction is evaluated at the bulk temperature, higher viscosities result which overestimate friction coefficient. Furthermore, in this example the isothermal calculation has reached the plastic yield limit levelling out the traction curve. In the absence of such limiting shear stress property it is expected that friction coefficients are even higher and power losses as a consequence. On the other hand, analytically predicted thermal fluid friction coefficients and power losses are very close to the simulated results. Slight differences are seen in the vicinity of tip and root, probably due to the effect of the sliding speed which affects film thickness and traction as a consequence.

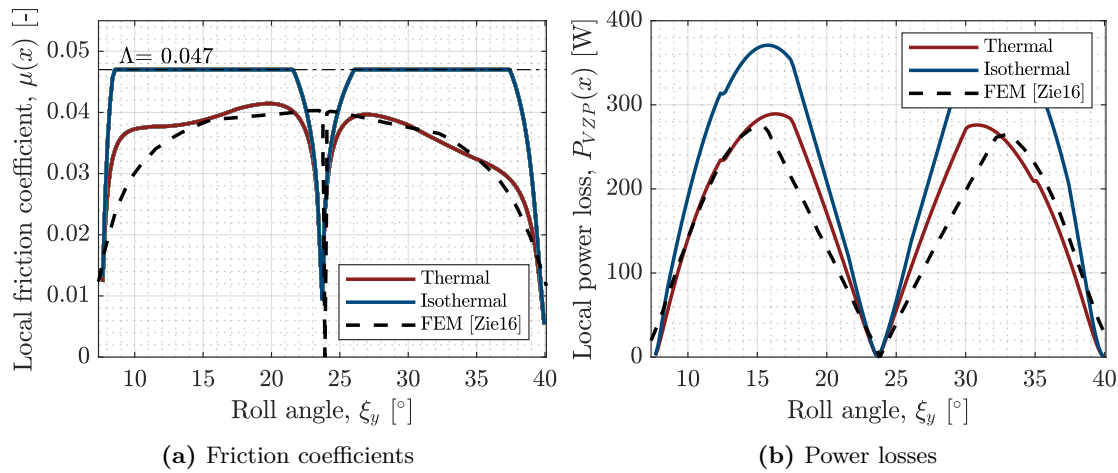


Figure 4.19: Influence of thermal coupling in friction coefficient and power losses along the line of action and comparison with simulation results from [61]

These results can be compared to those computed with classical friction coefficient models in Figure 4.1. It can be concluded that the proposed approach correctly captures the thermal behaviour of the contact and its influence of both friction and power losses.

4.3.3 Experimental validation

Two objectives are pursued in the following section: on the one hand, the thermally-coupled power loss prediction methodology presented in section 4.3.2 is tested for variable conditions in the contact. On the other hand, the influence of the load sharing function for partial EHL lubrication modelling is further analysed and conclusions on its accuracy are withdrawn. For this purpose, the analytical predictions are compared to the experimental results by Hinterstoißer [29] who analysed the influence of operating conditions, oil type and flank surface topography on mean friction coefficient of spur and helical gears in mesh.

The gear set under consideration is the FZG gear type C_{mod} already described in Table 4.7. Three load stages are applied resulting in pinion torques of 94 Nm (KS 5), 183 Nm (KS 7) and 302 Nm (KS 9), and tangential speed is varied from 0.5 m/s to 20 m/s ensuring boundary to full film lubrication in the contact. Moreover, three constant

oil sump temperatures are selected, 60 °C, 90 °C and 120 °C, for two different ISO VG 100 oils: a paraffinic mineral oil (MIN100) and a poly- α -olefin oil (PAO100), both with extreme pressure additives. The rheological parameters of these lubricants are presented in [61], and they have been regressed from the high-pressure viscosity measurements in [31] following the Roelands model. However, the limiting-stress pressure coefficients, Λ , are taken from Table 4.4 as base oils are the same as those presented in Section 4.2.3. Finally, two different finishing processes are selected to analyse the influence of asperity interaction: polishing with $R_a = 0.2 \mu\text{m}$ and axial grinding where $R_a = 0.4 \mu\text{m}$.

Figure 4.20 shows the influence of speed and load on the predicted power losses with respect to the experimental measurements. Analytical predictions follow the measurements closely with the highest power losses at the highest load and speed. The overall agreement is good with average errors below 5% except at the highest tangential speeds where the maximum error reaches 20% for the poly- α -olefin oil at the lowest load stage. It is also observed that PAO100 oil shows lower power losses than MIN100 which is in agreement with scientific literature.

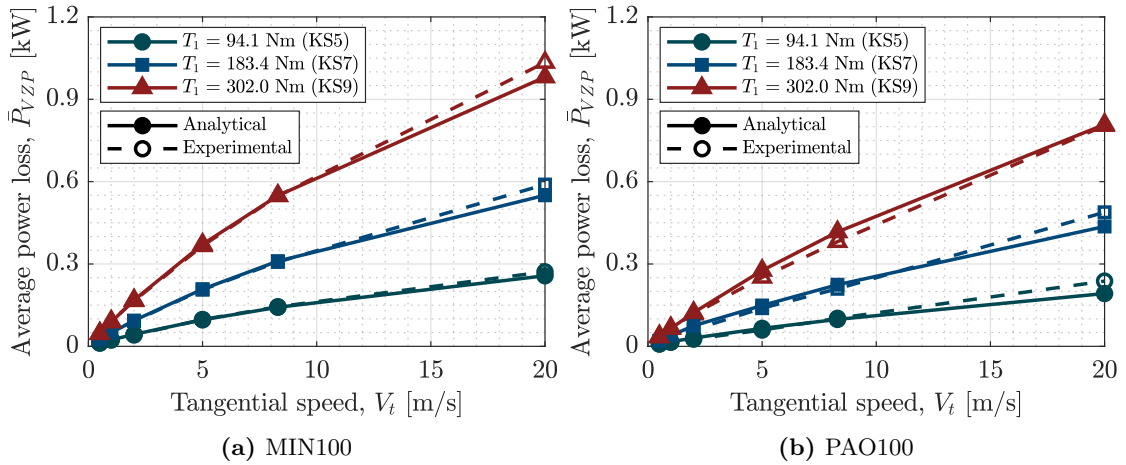


Figure 4.20: Analytical-experimental correlation of power loss predictions as a function of speed and torque for mineral and poly- α -olefin oils at constant temperature $\Theta_o = 90 \text{ }^\circ\text{C}$

Oil sump temperature is maintained constant at 90 °C in Figure 4.20 which leads to partial EHL regime over the full tangential velocity range, except at very low speeds where boundary friction prevails. Even at the lowest load stage and highest speeds, specific film thickness values are around 1.3 and 1.1 at the pitch point for the poly- α -olefin and mineral oils respectively; which indicates that asperity contact exists and therefore boundary friction coefficient is influencing results. In these tests, the values for $\mu_{s,\infty}$ in Equation 4.26 have been set to 0.065 for the mineral base and 0.05 for the PAO, which have been obtained from average friction coefficient values at the lowest speeds (0.5 m/s), and highest torques (KS9) and oil temperatures (120 °C).

In order to analyse the influence of the proposed load sharing function an additional test is provided. Figure 4.21 shows the influence of oil sump temperature and flank surface roughness on power losses at constant torque of 183.4 Nm for the mineral oil. Oil sump temperature increase reduces specific film thickness in the same way as surface roughness.

At the highest oil sump temperature specific film thickness ranges from 0.05 to 0.3 at the pitch point thus indicating a strong influence of boundary friction coefficient value over the full range of tangential speed. On the opposite, at the lowest oil sump temperature λ rises from 0.2 up to 1.4 showing a minor influence of boundary friction value. A similar effect is observed when surface roughness is increased. Specific film thickness in polished surfaces range from 0.15 to 0.85 at 90 °C oil temperature while ground surfaces extend from 0.07 to 0.4. It is observed again that errors arise when specific film thickness is low, indicating that the asperity load sharing model is valid when $\lambda > 0.5$ approximately.

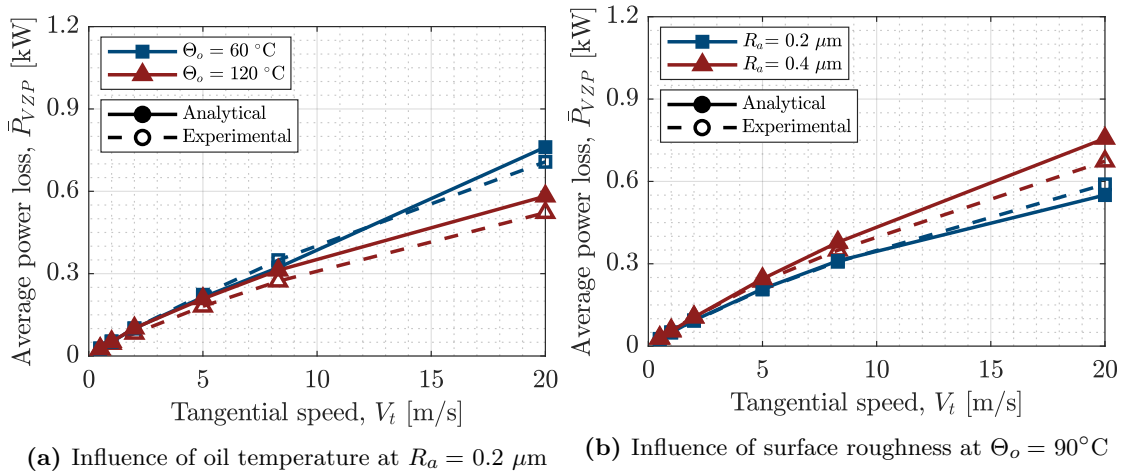


Figure 4.21: Analytical-experimental correlation of power loss predictions as a function of oil temperature and surface roughness for mineral oil at constant torque $T_1 = 183.4 \text{ Nm}$ (KS7)

Finally, Figure 4.22 shows the overall performance of the power loss model. It can be seen that the maximum computed error in the aforementioned conditions is 25% with only 3% of outliers. Moreover, 68% of these results show errors below 10% with respect to the experimental measurements, which is definitely lower than the current models in literature as shown by [36].

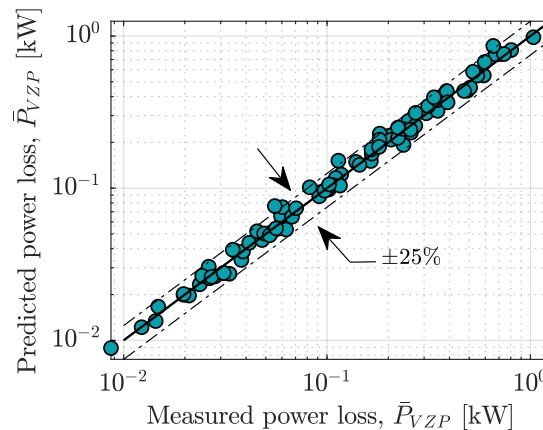


Figure 4.22: Overview of predicted power losses and experimental measurements from [29]

4.3.4 Discussion of results

It is observed in Figure 4.20 that predicted power loss error increases with speed in both lubricants. Maximum error in PAO100 is 20% at 94.1 Nm and 7% in MIN100 at 183Nm. In both cases, predicted power losses are slightly lower than those measured experimentally. However, it must be noted that the methodology proposed above neglects the influence of rolling traction. If the rolling friction force according to [66] is considered, computed errors drop to less than half of these values.

On the other hand, predicted errors for the test cases in Figure 4.21 are 10% at worst, which is acceptable considering the simple asperity load sharing function used. However, it must be noted that the accuracy of the results is strongly dependent on the boundary friction coefficient value. Contrary to the generalized assumption that the value of the solid friction coefficient, $\mu_{s,\infty}$, does not affect friction coefficient [50], it does have a significant influence in partial EHL friction coefficient models based on the load sharing approach. The shaded-error bar in Figure 4.23 stresses the influence of varying $\pm 25\%$ the solid friction coefficient, $\mu_{s,\infty}$. It can be concluded that slight variations of the boundary friction coefficient result in significant deviations of the predicted power losses; specially at the highest tangential speeds where results are influenced by the increased sliding speeds. Recent experimental studies [253, 254] support this affirmation where boundary friction coefficient is affected by the surface structure, running in, lubricant additives or surface coatings; but in the absence of especial features, a value of 0.07 is suggested for common axially ground gears.

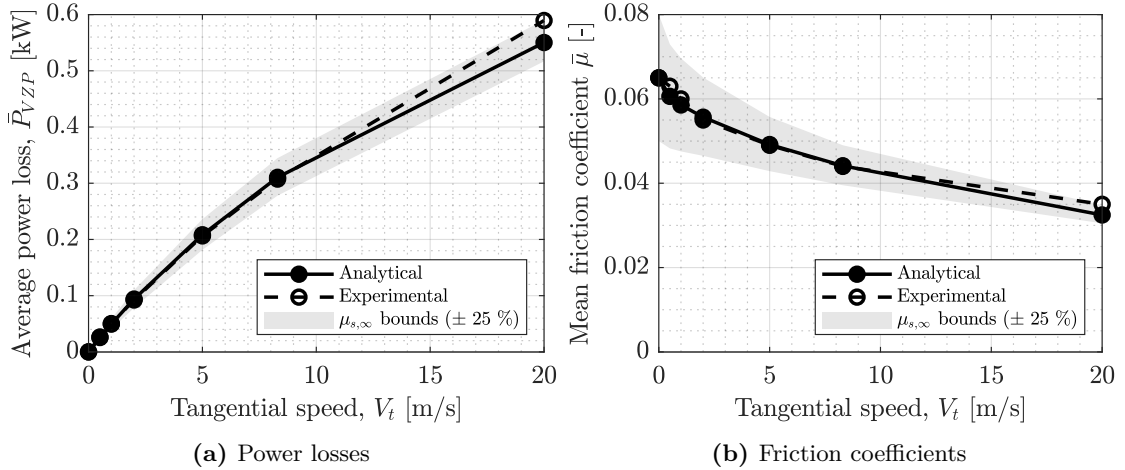


Figure 4.23: Influence of boundary friction coefficient on predicted average power losses and friction coefficients for C_{mod} gears at 183.4 Nm, $\Theta_o = 90^\circ$ C and variable tangential speeds

Finally, as far as the underlying assumptions is concerned (see traction coefficient computed from mean conditions in the Hertzian region and a simple load sharing function used to represent partial EHL), it can be concluded that they seem sufficiently accurate to predict the variation of the friction coefficient with minimum computational effort. The solution time of a heavily loaded and high speed test case is approximately 10 ms with the temperature field solved within 5 to 10 iterations for a tolerance of 1° C in a 64 bit Intel-Core i5 laptop running at 2.4 GHz. The results are in close agreement with the experimental measurements for most of the test cases shown in Figure 4.22.

4.4 Conclusions of Chapter 4

In this chapter, a partial EHL friction coefficient model to predict power losses in cylindrical gears has been proposed. It has been shown that accurate predictions can be carried out for any lubricant from its base rheological properties without preliminary traction measurements to adjust parameters, which is common practice in gear literature [243].

The proposed friction coefficient is based on the Ree-Eyring non-newtonian rheological model where the reference stress value is predicted from the piezoviscosity coefficient, α and the limiting shear stress coefficient, Λ . It has been shown that the elastic term can be neglected for common operating conditions and lubricants and the limiting shear stress behaviour has been incorporated to avoid exceeding the plastic yield limit of the lubricant at high contact pressures.

Moreover, the range of applicability of the friction coefficient model has been extended to cover partial EHL regime using a simple asperity load sharing approach, where the load sharing function, ξ , is described by the complementary error function of the specific film thickness. The influence of the boundary friction coefficient value has been discussed and a reference value of 0.07 has been proposed for ground gears.

Additionally, an iterative thermally-coupled power loss prediction methodology has been described, which allows the prediction of the film and contact inlet mean temperatures necessary to compute traction and film thickness respectively. The latter is computed from Hamrock and Dowson's equation [250] modified to include the influence of fluid pressure reduction due to asperity contact [251]. The thermal coupling condition assumes that pinion and gear share the same film and oil sump temperatures which allows different bulk temperatures of pinion and gear.

Both, the friction coefficient model and power loss prediction methodology have been compared to experimental measurements in twin disc machines [212], FZG gear tests [29] and numerical simulations [61] showing good agreement with different operating conditions and lubricants; with errors below 25% in almost all the considered test cases and less than 10% in approximately 70% of the cases.

*To fight and conquer in all our battles is not
supreme excellence; supreme excellence consists in
breaking the enemy's resistance without fighting.*

— Sun Tzu's *The Art of War*, 5th century BC

5

Thermal Model for Cylindrical Gear Pairs

Contents

5.1	Introduction	124
5.2	Description of the thermal network model	125
5.2.1	Thermal network definition	126
5.3	Heat transfer in meshing gear pairs	132
5.3.1	Heat sources	132
5.3.2	Heat dissipation in dip-lubricated gears	138
5.4	Governing equations and solution method	144
5.4.1	Solution method	145
5.4.2	Thermo-mechanical coupling	147
5.5	Experimental validation	151
5.5.1	Discussion of results	154
5.6	Conclusions of Chapter 5	156

This chapter is focused on objective O.5 in Section 1.3. The computation of thermal distortion in external cylindrical gears requires predicting their steady-state temperature field before hand. With this aim, a novel thermal model is developed in this chapter which simultaneously predicts the temperature distribution of dip lubricated shaft-gear pairs considering variable operating conditions. In the first section, basic concepts of the thermal network concept by Blok [112] are presented, cylindrical gear pair modelling assumptions are discussed and relevant equations are summarized. Then, predicted mesh power losses from Chapter 4 are converted to heat inputs in pinion and gear; additional sources of heat from bearings and seals are also introduced and heat dissipation mechanisms specific to dip lubricated gear pairs are described. The system of equations is set in matrix form and the solution method for steady state and transient problems is presented next. In order to validate the proposed model, analytical predictions are compared to experimental measurements in literature, results are discussed and conclusions are withdrawn at the end of the chapter.

5.1 Introduction

Different procedures have been suggested in literature for the thermal analysis of gear drives. Analytical models [63, 96, 255] calculate gear and oil sump steady-state temperatures from the energy balance between the heat generated in the gearbox (from gear mesh, bearings, seals, etc.) and the heat dissipated through the casing (by conduction, convection and radiation). These models represent the global heat flow in the gearbox and they are used by gear rating standards to guarantee thermal equilibrium [16]. However, they neglect temperature gradients and therefore fail to predict gear temperature distribution accurately; which is the basis for thermal distortion modelling in the next chapter.

When gear temperature distribution is required, finite element models have been extensively used in literature. Patir and Cheng [126], followed by Townsend and Akin [128], developed a model for jet lubricated gears including oil flow rate-dependent convection heat transfer coefficients and variable heat fluxes depending on the operating conditions. This model was later extended to the transient case by El-Bayoumy [127], who represented mesh friction losses as a moving heat source along the tooth profile. In all three cases, it was concluded that appreciable temperature gradients exist in the gear body and the teeth face-width direction depending on the cooling rate, geometry and operating conditions. These findings were later confirmed by Long et al. [131] who performed a sensitivity analysis and highlighted the influence of tooth face width on temperature variations. The most recent thermal finite element studies dig into some of the aspects of the previous models while maintaining the basic assumptions. Wang et al. [256] have recently studied the influence of oil jet convection heat transfer applying CFD calculations; Li et al. [133] has included dynamic effects in the heat flux while Fernandes et al. [167] studied the influence of the gear material on the temperature distribution. Almost all finite element models up to date are restricted to jet lubrication systems and very few studies consider dip lubricated conditions [99, 257] due to the complex oil flow patterns. Although the method has proved to be effective in the accurate prediction of the temperature distribution in gears, the large size of the models leads to time-consuming calculations and the influence of transient temperatures on convection heat transfer coefficients, fluid properties and power losses is neglected.

To compute overall temperature distribution of the gearbox considering previously described issues, the thermal network method [112] is an efficient compromise between accuracy and computational time. Each node of the network represents an isothermal element (i.e. bearings, gears, oil sump, etc.) and the elements are connected by one-dimensional thermal resistances accounting for conduction, free/forced convection and radiation heat transfer. This type of lumped parameter models have been successfully applied to very different mechanical parts and scales, from EHL contact modelling [258] to bearing or sealing temperature distribution [259, 260] where the accuracy of the results is related to the degree of detail of each component's volume discretization. Manin [137], Changenet [125] and more recently Geiger [120], applied this procedure to predict dip-lubricated gearbox temperatures including thermal gradients between components and heat fluxes coming from bearings, seals and oil churning. However, in these models the degree of discretization of each gear does not allow to assess the radial and longitudinal temperature distributions with sufficient accuracy. Although temperature differences between pinion and gear can be computed, thermal gradients inside each of them are still neglected [125].

To solve this problem, the thermal network model presented in this chapter is further developed with respect to previous works [120, 125, 137]. Pinion and gear volume discretization is extended to account for radial and axial temperature gradients while maintaining a reduced number of nodes with respect to finite element models. Furthermore, the influence of immersion depth, temperature-dependent convection heat transfer coefficients and heat inputs from the gear mesh, bearings and spin power loss sources are considered too.

5.2 Description of the thermal network model

The proposed model is based on the differential control volume concept used to derive the general form of the heat diffusion equation [261]. In the case of spur and helical gear pairs, their geometry can be discretized as a series of cylindrical control volumes of isotropic material, with the same thermal properties in the three directions. Applying the conservation of energy to a single differential control volume (depicted in Figure 5.1), the following three dimensional heat conduction equation can be obtained:

$$\frac{1}{r} \cdot \frac{\partial}{\partial r} \left(r \cdot \frac{\partial \Theta}{\partial r} \right) + \frac{1}{r^2} \cdot \frac{\partial^2 \Theta}{\partial \phi^2} + \frac{\partial^2 \Theta}{\partial z^2} + \frac{\dot{q}}{k} = \frac{1}{\chi} \cdot \frac{\partial \Theta}{\partial t} \quad (5.1)$$

where k and χ are the thermal conductivity and diffusivity of the material respectively.

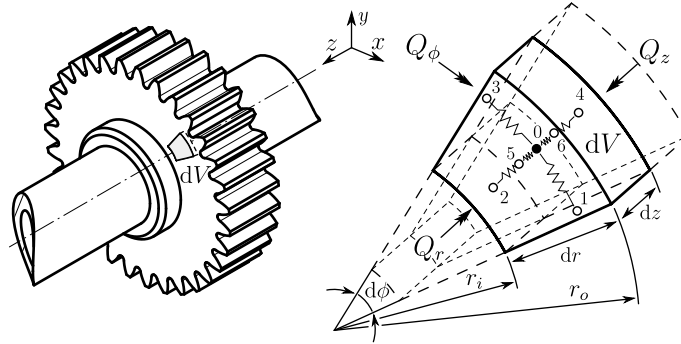


Figure 5.1: Cylindrical control volume and corresponding thermal resistance simplification

The solution to Equation 5.1 for a single cylindrical volume can be computed analytically for common boundary conditions [262], however, gears often include several cylindrical interconnected regions with different diameters (shaft, hub, web, etc.) which are subject to variable heat inputs and convection heat transfer coefficients. In such cases, numerical solutions with different meshes are required (e.g. [136, 167]) but in this work, the thermal network concept by Blok [112] is used instead.

Equation 5.1 is further simplified neglecting circumferential heat flow because it is assumed that the gear rotation period is much shorter than the time necessary for any circumferential temperature change [137]. Furthermore, considering that thermally-induced geometry distortions should be computed in the steady-state regime, a two-dimensional heat diffusion equation is obtained, where the terms on the left hand side correspond to radial and longitudinal heat conduction respectively:

$$\frac{1}{r} \cdot \frac{\partial}{\partial r} \left(r \cdot \frac{\partial \Theta}{\partial r} \right) + \frac{\partial^2 \Theta}{\partial z^2} = -\frac{\dot{q}}{k} \quad (5.2)$$

If there is no internal heat generation, \dot{q} , it is possible to compute the temperature at the boundary surfaces of the control volume (surfaces 1 to 6 in Figure 5.1) considering one dimensional radial and longitudinal heat conduction separately. In such case, Equation 5.2 leads to:

$$\frac{\partial}{\partial r} \left(r \cdot \frac{\partial \Theta}{\partial r} \right) = 0 \rightarrow \Theta(r) = A \cdot \ln(r) + B \quad (5.3)$$

$$\frac{\partial^2 \Theta}{\partial z^2} = 0 \rightarrow \Theta(z) = C \cdot z + D \quad (5.4)$$

where the coefficients A , B , C and D can be calculated from the temperatures of the outer surfaces of the control volume in Figure 5.1; that is, surfaces 2 and 4 for radial conduction and surfaces 5 and 6 for longitudinal heat diffusion. Finally, the heat flux between surfaces is computed from Fourier's law considering the temperature gradient between surfaces in both directions ($\Delta\Theta_r$ and $\Delta\Theta_z$).

$$Q_r = \left[-k \cdot \frac{d\Theta(r)}{dr} \right] \cdot S_r = \frac{2 \cdot \pi \cdot k \cdot \Delta z}{\ln(r_o/r_i)} \cdot \Delta\Theta_r \quad (5.5)$$

$$Q_z = \left[-k \cdot \frac{d\Theta(z)}{dz} \right] \cdot S_z = \frac{\pi \cdot k \cdot (r_o^2 - r_i^2)}{\Delta z} \cdot \Delta\Theta_l \quad (5.6)$$

with S_r and S_z the cross sectional area for heat conduction in each direction.

The radial and longitudinal heat flows, Q_r and Q_z respectively, from Equations 5.5 and 5.6 can be generalized as $Q = G \cdot \Delta\Theta$ where G is the thermal conductance between nodes, which depends exclusively on the size of the control volume (inner radius, r_i , outer radius, r_o , and length, Δz) and its thermal conductivity, k . The conductive thermal resistance, R , being the inverse of the conductance, G , we have:

$$R_r = \frac{\ln(r_o/r_i)}{2 \cdot \pi \cdot k \cdot \Delta z} \quad (5.7)$$

$$R_z = \frac{\Delta z}{\pi \cdot k \cdot (r_o^2 - r_i^2)} \quad (5.8)$$

Therefore, it is possible to model the gear-shaft system as a series of small interconnected regions where the thermal resistances are ruled by the dimensions in each direction. A sample resistance simplification of the control volume concept is shown in Figure 5.1 where the central node represents the mass of the region and the outer nodes act as connectors with adjacent volumes.

5.2.1 Thermal network definition

The thermal network model developed in this chapter is based on the "thin-slice" approach used in the computation of load distribution in Chapter 3. If the circumferential temperature gradients are neglected as described previously, the resulting temperature distribution is bi-dimensional following the radial and longitudinal directions. Thus, gears can be sliced in the face-width direction; and similarly to the gear body and teeth stiffness modelling in Figure 3.16, it is possible to develop the corresponding thermal resistance representation.

Gear-shaft assembly modelling

On the one hand, gear body and shafts are discretized axially and radially as shown in Figure 5.2. Each annular cell within the solid is composed of a single mass node (black dots) and four surface nodes (white dots), two in the radial direction and two in the longitudinal one. Thermal resistances of conduction, convection and radiation are used to connect surface nodes in the gear-shaft assembly to the surrounding fluids. For clarity, surface nodes have been suppressed in the main view but a sample of their connections is shown in detail E. Similarly, heat transfer resistances with the surrounding fluids are only depicted on the left hand side of the figure but the same heat transfer relations apply on the right side.

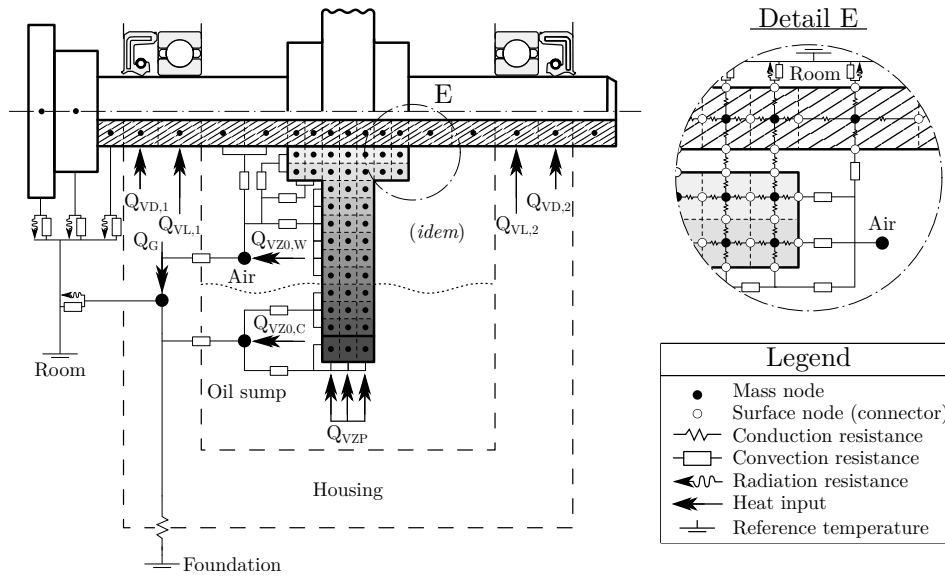


Figure 5.2: Thermal network of the shaft-gear assembly

On the other hand, housing, oil sump and air inside the gearbox, are all represented through individual mass nodes connected to the gear-shaft system by means of convection resistances as shown in Figure 5.2. Oil sump and housing nodes account for the oil and housing volumes respectively and similarly, the influence of the air inside the housing is accounted for by subtracting the oil and gear pair volumes to the total casing's internal volume.

Mass nodes in the annular regions of the gear-shaft assembly are located in the centre of the cell at the mean radius, \bar{r} , and represent the total mass of a single isothermal cylindrical volume with heat capacity $m \cdot c_p$. The total mass, m , of any annular cell belonging to the shaft or the gear is calculated with Equation 5.9.

$$m = \rho \cdot V = \rho \cdot [\pi \cdot (r_o^2 - r_i^2) \cdot \Delta z] \quad (5.9)$$

where ρ is the density of the material, r_o and r_i are the outer and inner radius respectively and Δz is the width of the individual volume. In the case of helical gears, the width of the volumes inside the teeth and body is $\Delta z' = \Delta z / \cos(\beta_b)$ as nodes are located in the direction of the helix in the base tangent plane.

These nodes are connected to surface nodes located in the boundaries of the cell by means of radial and longitudinal thermal resistances derived from Equations 5.7 and 5.8. Adjacent cells share some of these surface nodes and therefore the equivalent radial or longitudinal resistance between consecutive mass nodes is the sum of the resistances in series as shown by Equations 5.10 and 5.11.

$$R'_r = \sum_{j=1}^n R_{r,j} = \sum_{j=1}^n \frac{\ln(r_{o,j}/r_{i,j})}{2 \cdot \pi \cdot k_j \cdot \Delta z_j} \quad (5.10)$$

$$R'_z = \sum_{j=1}^n R_{z,j} = \sum_{j=1}^n \frac{\Delta z_j}{\pi \cdot k_j \cdot (r_{o,j}^2 - r_{i,j}^2)} \quad (5.11)$$

Furthermore, surface nodes are also used to connect the gear to the surrounding parts or fluids by means of conduction, convection or radiation resistances. In this sense, when two solids are connected to each other, such as the gear-shaft assembly, the temperature at the interface is known to drop as a result of the fitting imperfections caused by geometrical errors (e.g. cylindricity, flatness, etc.). Such imperfections cause the total contact surface to be reduced while a fluid (oil or air) fills the gaps. To model this temperature drop Changenet [263] proposed the use of contact resistances whose values are calculated as:

$$R_p = \frac{C}{S} \cdot \left(\frac{k_1 + k_2}{2 \cdot k_1 \cdot k_2} \right) \quad (5.12)$$

where $k_{1,2}$ is the thermal conductivity of the materials, S is the apparent contact area and C is a constant value depending on the contact pressure and surface roughness. In this model, the gear-shaft assembly shown in detail E in Figure 5.2 is assumed to be press-fitted and therefore contact resistance is neglected. However, for the contact resistance between the housing (cast iron) and the foundation (steel) in Figure 5.3, a mean value of $4.5 \cdot 10^{-3}$ m is adopted according to [263].

In order to compute the most accurate temperature distribution within the gears, shafts are also included in the model; as heat inputs from nearby bearings or seals may alter the resulting temperature distribution. However, only the portion inside the gearbox is sufficiently discretized while the influence of the outer portion of the shaft and couplings in contact with room air is simplified by defining an equivalent shaft with effective cylinder diameter, d' , of length l' , according to Equations 5.13 and 5.14 from ISO 14179 standard [15]. Such equivalent cylinders are used to compute convection and radiation heat transfer with ambient air and their effective heat capacity represents the influence of the outer portion in transient calculations. Similarly to the rest of the shaft, these nodes are also connected to the thermal network by means of longitudinal resistances.

$$d' = \frac{1}{l'} \cdot \sum_{j=1}^n d_j \cdot l_j \quad (5.13)$$

$$l' = \sum_{j=1}^n l_j \quad (5.14)$$

with d_j and l_j the diameter and length of the n different cylindrical sections that comprise the shaft and/or the couplings located outside the gearbox.

Gear pair and housing modelling

The thermal network model shown in Figure 5.2 can be readily solved if appropriate boundary conditions are set and the solution yields the radial and longitudinal temperature distribution of a single gear. However, it is possible to solve pinion and gear thermal state at the same time by connecting both networks in the gear mesh as shown in Figure 5.3. For this purpose a special form of thermal resistance is required, known as constriction resistance, which is explained later in this section.

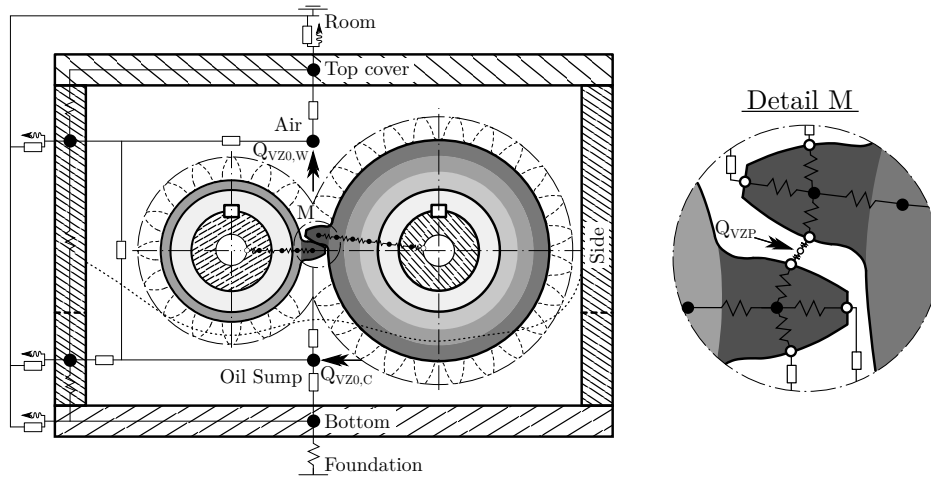


Figure 5.3: Thermal network of the gear pair and housing

Moreover, external casing exchanges heat by natural convection and radiation with room air but also by forced convection with oil and air inside the gearbox. If a single mass node is used to represent the housing, as in Figure 5.2, its temperature will be fundamentally ruled by that of the room and the foundation which are considered constant in this work. As a consequence, oil sump and air temperature will be influenced by the latter. To improve accuracy without increasing the number of nodes in excess, external housing can be subdivided in different regions depending on the dominant internal heat dissipation mechanism.

Although the oil flow pattern inside the gearbox is very complex, two distinct regions are considered when the gears are at rest: the part fully submerged in the oil bath and the one in contact with interior air (see Figure 5.3). At the same time, each of these regions comprises horizontal and vertical plates, therefore, four volumes are defined: i) the flat horizontal plate submerged in the oil bath, ii) the immersed vertical part of the casing, iii) the rest of the vertical part in contact with the interior air and iv) the horizontal top cover plate. Each of them is described with a mass node representing its heat capacity as shown in Figure 5.3 and all of them are connected to the ambient by means of natural convection and radiation resistances. A further description of the heat transfer mechanisms related to the housing is provided later in this section.

By following this procedure, which is characterized by using a coarse discretization for the housing and the internal fluids and a finer one for the gear pair, global and local temperature distributions can be predicted without dramatically increasing computational effort as shown by Manin [137]. With approximately 200 mass nodes per gear-shaft assembly, it is possible to obtain a sufficiently accurate description of the temperature distribution which is far less than the mesh size required by finite element models.

Gear teeth modelling

It has been shown in previous sections that the gear-shaft assembly can be modelled as a series of interconnected annular volumes. However, gear teeth cannot be considered a full annulus where the heat flow expands uniformly in the radial direction as gear teeth and spaces coexist in the same annular region. In addition, gear teeth are subject to non-axisymmetrical conditions due to differences in the heat flux on each flank (heat input from the gear mesh on one side and convection heat transfer by centrifugal fling-off on the other) and therefore circumferential heat flux can no-longer be neglected. Although several of the previous works [125, 137, 264, 265] do assume that gear teeth can be treated as an annular region, in this work a different approach is proposed.

Considering that in most gear applications the size of the teeth is small with respect to the gear body (usually $d/h > 10$), temperature gradients inside the tooth are minimal and a single bulk temperature can be assumed instead. In other words, gear teeth are represented with a single mass node located in the pitch diameter and in the centre of the tooth (see detail M in Figure 5.3). Its mass represents the total mass of the teeth and it is connected to the gear body and the tooth tip by means of planar-wall conduction resistances with value $R = L/(k \cdot A)$ where L correspond to the tooth addendum or dedendum height, k is the thermal conductivity and $A = z \cdot s_c \cdot l$ is the average surface for conduction heat transfer in the tooth height direction; which is now proportional to the number of teeth and the individual cross section ($\approx s_c \cdot l$). In the same way, mass node representing gear teeth is connected to the left and right flanks by means of the same type of thermal resistances but this time, the length in the lateral direction is half the chordal tooth thickness and the average available cross section for heat transfer is $A = z_{1,2} \cdot A_{1,2}$ where pinion and gear flank surface is computed following Geiger's approximate equations [120]:

$$A_1 = \frac{\pi \cdot d_{w,1} \cdot l \cdot \epsilon_\alpha}{\cos(\beta_b)} \cdot \left[\sin(\alpha_{wt}) + \frac{\pi \cdot \cos(\alpha_{wt})}{z_1} \cdot (\epsilon_a - \epsilon_f) \right] \quad (5.15)$$

$$A_2 = \frac{\pi \cdot d_{w,2} \cdot l \cdot \epsilon_\alpha}{[1 + 0.11 \cdot (u - 1)^2] \cdot \cos(\beta_b)} \cdot \left[\sin(\alpha_{wt}) + \frac{\pi \cdot \cos(\alpha_{wt})}{z_2} \cdot (\epsilon_f - \epsilon_a) \right] \quad (5.16)$$

with $d_{w1,2}$ and α_{wt} being the working pitch diameters and pressure angle respectively, ϵ_α the transverse contact ratio (with ϵ_1 and ϵ_2 the corresponding ratios for approach and recess paths of contact), β_b the base helix angle, l the tooth slice thickness and u the gear ratio.

Pinion and gear are meshed independently following the procedure described at the beginning of this section, but instead of solving each one separately, they are connected at the gear mesh by means of a special form of contact resistances commonly referred to as "constriction resistances" [266]; which have already been presented in Equation 4.38. As explained earlier in Chapter 4, the existence of a constriction of the heat flux in the Hertzian contact area due to its small size makes the contact temperature to be higher than that of the immediate flank subsurface and due to the differences in rolling speed of the surfaces, a variable heat flux towards the pinion and the gear is produced [244] (see Equation 4.40). Furthermore, the mean film temperature, which is common for both gears and allows traction coefficient to be evaluated independently of film thickness, is even higher due to the existence of an additional resistance produced by the latter (see Equation 4.37). In order to account for both effects, average thermal resistances

of constriction are computed, which automatically rule the heat partition between the bodies depending on the number of teeth and the rolling speed. Thus, the mesh node in detail M in Figure 5.3 is connected to the pinion and gear flanks by means of average contact and film thermal resistances placed in series following Equation 5.17:

$$\bar{R}'_{s,i} = \frac{1}{z_i} \cdot \bar{R}_{s,i} = \frac{1}{z_i} \cdot [\bar{R}_{c,i} + \bar{R}_{f,i}] = \frac{1}{z_i \cdot g_\alpha} \cdot \int_0^{g_\alpha} \frac{1}{A} \cdot \left[\frac{1.064}{k} \cdot \left(\frac{\chi \cdot b_H}{u_i} \right)^{0.5} + \frac{h_c}{8 \cdot k_o} \right] dx \quad (5.17)$$

where g_α is the length of the path of contact, k and χ are the thermal conductivity and diffusivity of the gear material respectively, k_o is the thermal conductivity of the lubricant, b_H is the instantaneous contact half width, $A = 2 \cdot b_H \cdot l$ is the Hertzian contact area and h_c is the central film thickness. It can be easily noticed that the differences in the average constriction resistance values on the side of the pinion and that of the gear are ruled by the rolling speed term, u_i , and the number of teeth, z_i , because the rest of the parameters are common to both gears along the path of contact. Moreover, at very high loads, the influence of the film resistance is negligible as the film thickness is approaching zero and therefore contact resistance term prevails.

Figure 5.4 depicts the behaviour of the instantaneous constriction resistances on FZG type C gear pair which result from the sum of the contact and film terms as presented in Equations 4.37 and 4.38. As expected, maximum values are located towards the start and end of the active profile where the ratio of the rolling speed to the contact half width is largest. On the contrary, when unit load increases in the single tooth contact region, the contact area increases as well and reduces the resistance in both gears which take the same value in the pitch point where rolling velocities are equal. Furthermore, it is observed that due to the geometry of gear type C with almost balanced specific sliding, the average thermal resistances are very similar; thus, the average heat flux towards each body will be approximately equal and only the difference in the number of teeth between pinion and gear will ensure that the former receives a larger amount of heat per revolution than the latter (see z_i in denominator of Equation 5.17). The influence of thermal resistance on heat partition will be further discussed in section 5.3.1.

Similarly to the rest of the gear body, gear teeth are also connected to the oil sump node by means of convection resistances accounting for centrifugal fling-off on the flanks and forced convection on the tooth tip and front/rear faces. Furthermore, in long face width gears, longitudinal gradients exist because the ends of the teeth are subject to enhanced convection heat transfer due to additional contact with the oil sump. Therefore, tooth face width is sliced in the longitudinal direction in the same way as the gear body. The thermal connection between each of the slices of the reference tooth and the corresponding ones in the gear body, ensures the continuity of the heat flux from the gear mesh towards the gear body and shaft and viceversa.

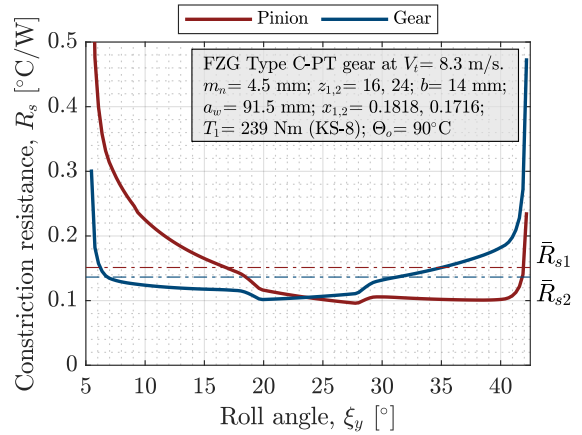


Figure 5.4: Constriction resistance behaviour along the path of contact in FZG type C gears

5.3 Heat transfer in meshing gear pairs

Up to this point thermal network nodal discretization has been described and the different types of heat conduction resistances have been outlined. In order to solve for the temperature distribution, heat inputs and heat dissipation mechanisms must also be identified. In this work, common dip-lubricated gear pairs are considered which are usually supported by rolling element bearings and hermetically sealed by lip type sealings preventing oil leaks from the housing. Therefore, the main heat sources are those relative to the power loss contributions of these machine elements, together with the mesh heating itself, and the relevant heat dissipation mechanisms are related to the oil/air mixture flows inside the gearbox.

5.3.1 Heat sources

Following the classification in section 2.1.1 of the literature review, two sources of heat are considered in the proposed model: i) load dependent power losses from the gear mesh and rolling element bearings and ii) spin losses coming from lip sealings, oil churning and air windage. Gear mesh, bearing and lip sealing power losses are introduced in specific surface nodes in the thermal network model as shown in Figures 5.2 and 5.3; while, churning and windage losses are directly input to the mass nodes representing oil sump and interior air volumes. The calculation method, order of magnitude and heat application procedure of gear related power losses is discussed in the following paragraphs, while those affecting lip sealing and bearings have been gathered in Appendix A.

Spin power losses

Tables 2.3 and 2.4 in the literature review have already presented some of the available models for the prediction of no-load losses in gears. In this work, churning losses are computed following the empirical model by Changenet [73] while windage is predicted using Diab's model [81].

a) Oil churning: Changenet's model for the prediction of oil churning losses has been extensively tested on different gear geometries, lubricants and operating conditions. Furthermore, the original model [73] has been successively improved to account for the influence of enclosures [267], oil aeration [268] or flow regimes [77]. According to the latter, churning power losses are computed as:

$$P_{VZ0,C} = \frac{1}{2} \cdot \rho_o \cdot \omega^3 \cdot r^3 \cdot S_m \cdot C_m \quad (5.18)$$

where ρ_o is the oil density, ω is the rotating speed, r is the pitch radius, S_m is the submerged area of the gear and C_m is the dimensionless drag torque.

The immersed surface of the gear, S_m , is the sum of the lateral surfaces of the disc and that of teeth and can be approximated following [77]:

$$S_m = r^2 \cdot [2 \cdot \theta - \sin(2 \cdot \theta)] + d \cdot b \cdot \theta + \frac{2 \cdot z \cdot h \cdot b \cdot \theta}{\pi \cdot \cos(\alpha_n) \cdot \cos(\beta)} \quad (5.19)$$

with d the pitch diameter, b the face width, z the number of teeth, h the tooth height and α_n and β are the normal pressure angle and helix angle respectively. Finally, variable θ is half the chord angle defined by the stationary oil level on a partially submerged gear, which can be computed from the ratio of the immersion depth, H , to the pitch radius, r , following $\cos(\theta) = 1 - H/r$.

The dimensionless churning torque, C_m is defined using the theorem of Vaschy-Buckingham of dimensional analysis where the coefficients of each dimensionless group are adjusted based on experimental evidence. To separate the different flow regimes two parameters are used in this work:

$$\gamma = \omega^2 \cdot (r \cdot b \cdot m_n)^{1/3} \quad (5.20)$$

$$\text{Re}_c = \frac{\omega \cdot r \cdot b}{\nu_k} \quad (5.21)$$

Parameter γ represents the influence of the projection of lubricant by centrifugal acceleration while parameter Re_c is known as the critical Reynolds number which separates low and high speed fluid behaviour. The combination of these parameters yields the following four flow regimes which also depend on the Froude number, $\text{Fr} = \omega^2 \cdot r/g$, with g the acceleration of gravity.

- For $\text{Re}_c < 4000$:

$$\gamma < 750 \text{ m/s}^2 \rightarrow C_m = 1.366 \cdot \left(\frac{H}{d}\right)^{0.45} \cdot \left(\frac{V_o}{d^3}\right)^{0.1} \cdot \left(\frac{b}{r}\right)^{0.21} \cdot \text{Fr}^{-0.6} \cdot \text{Re}_c^{-0.21} \quad (5.22)$$

$$\gamma > 1250 \text{ m/s}^2 \rightarrow C_m = 20.797 \cdot \left(\frac{H}{d}\right)^{0.1} \cdot \left(\frac{V_o}{d^3}\right)^{-0.35} \cdot \left(\frac{b}{d}\right)^{0.85} \cdot \text{Fr}^{-0.88} \cdot \text{Re}_c^{-0.21} \quad (5.23)$$

- For $\text{Re}_c > 4000$:

$$\gamma < 750 \text{ m/s}^2 \rightarrow C_m = 0.239 \cdot \left(\frac{H}{d}\right)^{0.45} \cdot \left(\frac{V_o}{d^3}\right)^{0.1} \cdot \left(\frac{b}{r}\right)^{0.21} \cdot \text{Fr}^{-0.6} \quad (5.24)$$

$$\gamma > 1250 \text{ m/s}^2 \rightarrow C_m = 3.644 \cdot \left(\frac{H}{d}\right)^{0.1} \cdot \left(\frac{V_o}{d^3}\right)^{-0.35} \cdot \left(\frac{b}{d}\right)^{0.85} \cdot \text{Fr}^{-0.88} \quad (5.25)$$

where all variables have already been defined except V_o which is the oil volume inside the casing. In both regimes, linear interpolation between the different equations is used for the transition zone $750 < \gamma < 1250$.

These equations predict churning power losses for a single gear and therefore in case of gear pairs, the individual contributions of pinion and wheel must be added. Moreover, if pinion rotates in counter-clockwise direction (towards the gear), a swelling effect occurs resulting in an additional power loss which can be computed following reference [73]. Finally, the total power loss of pinion and gear rotating in the oil sump is input to the mass node representing the oil sump as shown in Figures 5.2 and 5.3.

Figure 5.5a depicts the general behaviour of the churning power loss for variable speeds and oil temperatures. Note that at rotational speeds between 2000 and 3000 rpm a drop in the predicted power loss occurs due to the change in the flow regime. For low speeds the influence of the viscous forces prevails but at the highest speeds centrifugal effects dominate which is a familiar behaviour in fluid dynamics [269]. Besides at high speeds, the critical Reynolds number term disappears from the previous equations indicating that the influence of the lubricant viscosity is negligible. As a result, the predicted power loss at different temperatures is the same. What's more, if pinion and gear churning power losses are compared, it is observed that size plays a significant role with higher power losses for the largest wheel, which is explained by Equation 5.18 where the influence of the pitch radius is cubed.

b) Windage: Diab [81] developed two different approaches for the computation of windage power losses. On the one hand, an analytical model based on fluid flow analysis of the gear sides and teeth was proposed and, on the other, an empirical model based on dimensional analysis was developed, similarly to churning power loss model by Changenet [73]. In this work, the second approach is used where power loss is computed as:

$$P_{VZ0,W} = \frac{1}{2} \cdot \rho_a \cdot \omega^3 \cdot r^5 \cdot C_t \quad (5.26)$$

with ρ_a the density of air, ω the rotational speed, r the pitch radius and C_t the dimensionless windage drag coefficient which is expressed in terms of the several groups of parameters following the Vaschy-Buckingham theorem in dimensional analysis. Diab [81] defined the churning torque as:

$$C_t = 60 \cdot \text{Re}^{-0.25} \cdot \left(\frac{b}{r}\right)^{0.8} \cdot z^{-0.4} \cdot \left[\left(\frac{h_1}{r}\right)^{0.56} + \left(\frac{h_2}{r}\right)^{0.56} \right] \quad (5.27)$$

where z is the number of teeth, b is the tooth face width and $\text{Re} = \omega \cdot r^2 / \nu_k$ is the Reynolds number with ν_k the viscosity of air. Parameter $h_{1,2}$ depends on the presence of deflectors or flanges on the sides of the gear; and if these are neglected, similarly to churning losses, $h_{1,2} = 0.5^{1/0.56} \cdot r$ which yields a unit value for the last term inside the brackets. For further information on this term the reader is referred to [81].

Although the analytical method developed by Diab gives a deeper insight into the influence of gear geometry and flow behaviour, Equation 5.27 is sufficient to predict power losses. Similarly to churning losses, the individual contributions of pinion and gear are added and the total power loss is input to the mass node representing the air volume inside the gearbox (see Figures 5.2 and 5.3).

Predicted trend with rotating speed has been depicted in Figure 5.5b. Compared to churning losses, the influence of gear size is highlighted as power losses are proportional to the fifth power of the pitch radius in Equation 5.26; as a consequence, large gears are expected to result in high power losses. Moreover, Equation 5.27 shows that gear geometry does play a significant role through the number of teeth and tooth face width and very recent experimental research [270] confirms results provided by this model. Finally, it is observed that air temperature's effect is small as its influence is delimited to the Reynolds number where the kinematic viscosity is altered.

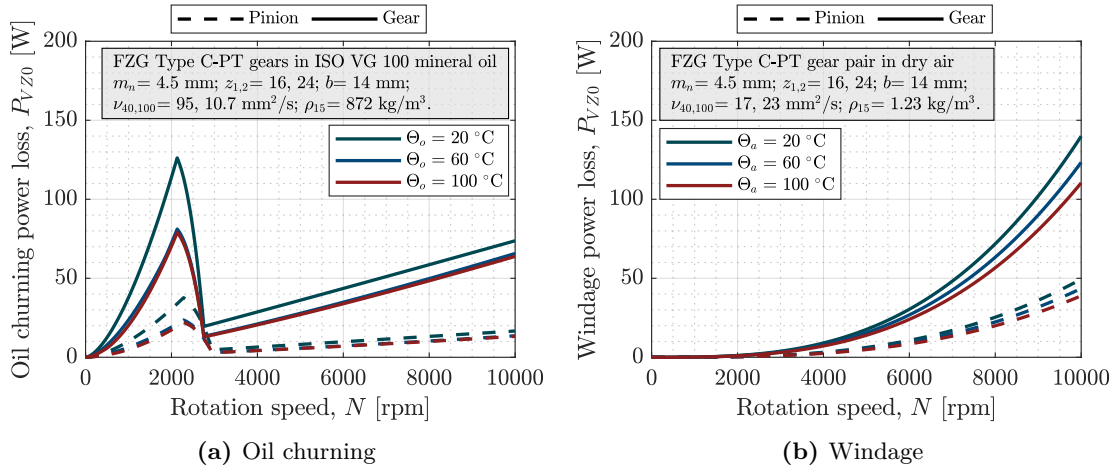


Figure 5.5: Heat generated by FZG Type C-PT pinion and gear due to oil churning and windage

Load-dependent power losses

It has already been shown in Figure 2.1 that load-dependent losses are the dominant terms at low to medium tangential speeds and no-load losses start to dominate at the highest speeds. However, spin power loss terms have been proved to be largely dependent on size and therefore, bearing and gear mesh load dependent losses are still important terms in small and middle size gears.

A gear mesh power loss model has already been introduced in Chapter 4 and the influence of speed, torque and temperature have also been discussed in Section 4.3.3 (see Figures 4.20 and 4.21 summarizing their effects). Contrary to other heat sources such as those from bearings or sealings where heat is introduced in surface nodes located just below them, in the case of the mesh power losses the proposed thermal network model allows introducing longitudinal heat distributions resulting from non-uniform bearing patterns (i.e. face crowning, misalignments, etc.). For this purpose, computed three dimensional power loss, $P_{VZP}(x, z)$, following Equation 2.1 is averaged along the contact path for each axial position, z , yielding the longitudinal mesh heat flux, $Q_{VZP}(z)$.

$$Q_{VZP}(z) = \frac{1}{p_{et}} \cdot \int_0^{g_\alpha} P_{VZP}(x, z) dx \quad \forall z; z \in [0, b]. \quad (5.28)$$

Figure 5.6 shows examples of longitudinal heat fluxes computed following Equation 5.28 for face crowned and misaligned FZG type C-PT gears. As expected, uneven load distributions produce normal load increase affecting sliding friction force and local power losses. For longitudinally crowned gears, highest loads are located in the middle of the face width and in the case of misaligned ones, unit load increase is displaced towards the tooth end. If attention is paid to the 3D power loss distribution details in these figures it is observed that largest values are located in the tooth tip and root where highest sliding occurs. This indicates that local temperature increases are expected in these regions, however, due to the characteristics of the proposed thermal lumped parameter model, such local effects are not visible and a single average bulk temperature is computed instead for each gear slice.

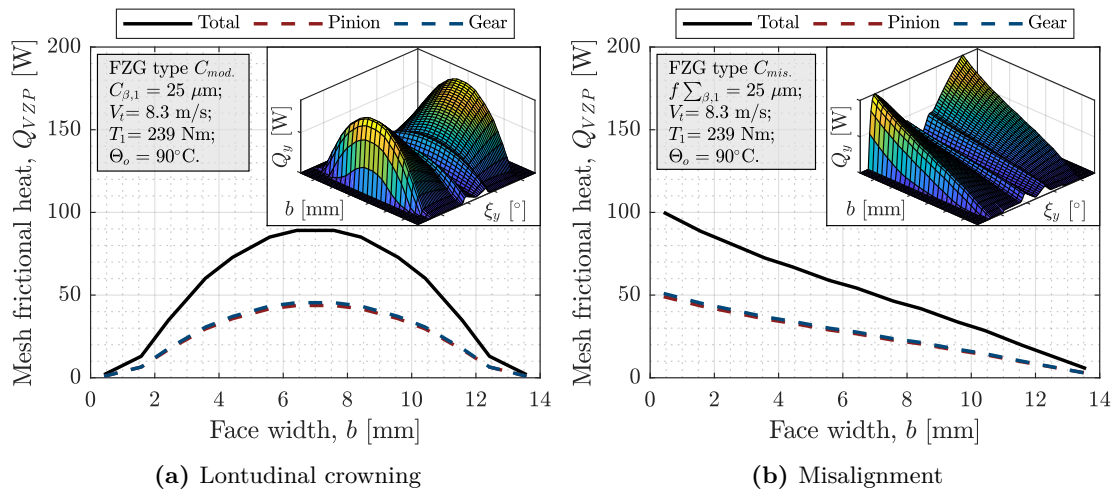


Figure 5.6: Influence of non-uniform load distribution on longitudinal mesh frictional heat

Heat flux computed this way is introduced in the mesh nodes located in different axial positions along the tooth face width. Figure 5.7 depicts the longitudinal discretization of pinion and gear teeth along with the mesh heat input procedure. The average value of the heat flux for each individual slice is computed and introduced in the corresponding mesh node. The latter is connected to surface nodes of pinion and gear teeth by means of constriction resistances computed following Equation 5.17 which automatically rule heat partition towards the pinion and gear (see Figure 5.6 for distribution). Finally, gear teeth are connected to the oil sump mass node, or that of interior air, by means of convection resistances which depend on the relative immersion depth as explained later in Section 5.3.2. As a consequence, pinion and gear steady-state teeth temperature distributions will depend on the relation between heat input pattern, teeth geometry and the amount of heat transferred to the oil sump by convection.

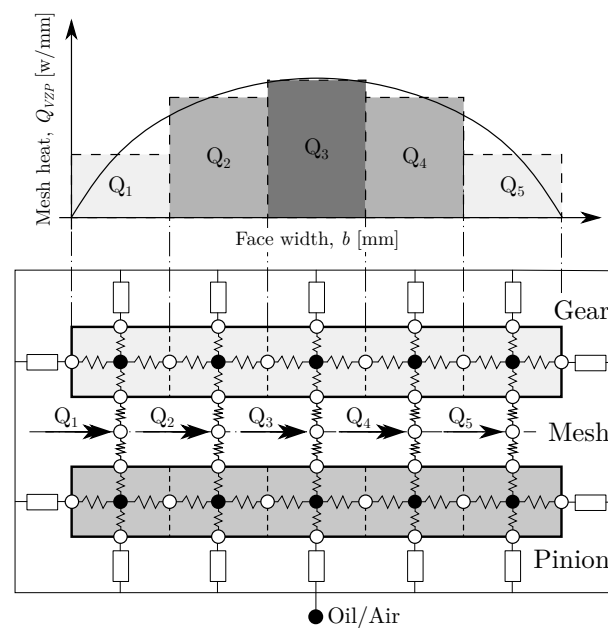


Figure 5.7: Longitudinal discretization of gear teeth for variable axial heat input modelling

Heat partitioning

It has already been shown that due to the variation of the rolling speed of the mating flanks along the line of action, there is a difference in the heat flux entering pinion and gear and local heat partition coefficient, α_y has been proved to be dependent on the relation of transient and steady-state thermal resistances in Equation 4.36. As shown by Jaeger [244], the main influencing factor is the specific sliding along the tooth profile and therefore, tooth geometry plays an important role. For instance, in the case of FZG gear type C in Figure 5.6 approximately 49% percent of the heat flows towards the pinion while 51% goes to the gear because profile shift coefficients have been selected in such a way that specific sliding is balanced. However, if FZG gear type A used for scuffing tests [23] is used instead, almost 64% of the heat flows towards the pinion and 36% goes to the gear.

Figure 5.8 shows an example of the variation of local heat partitioning coefficient along the line of action and its effect on local and average heat flux. As expected, the largest instantaneous values are located in the tooth tip and root where highest sliding occurs.

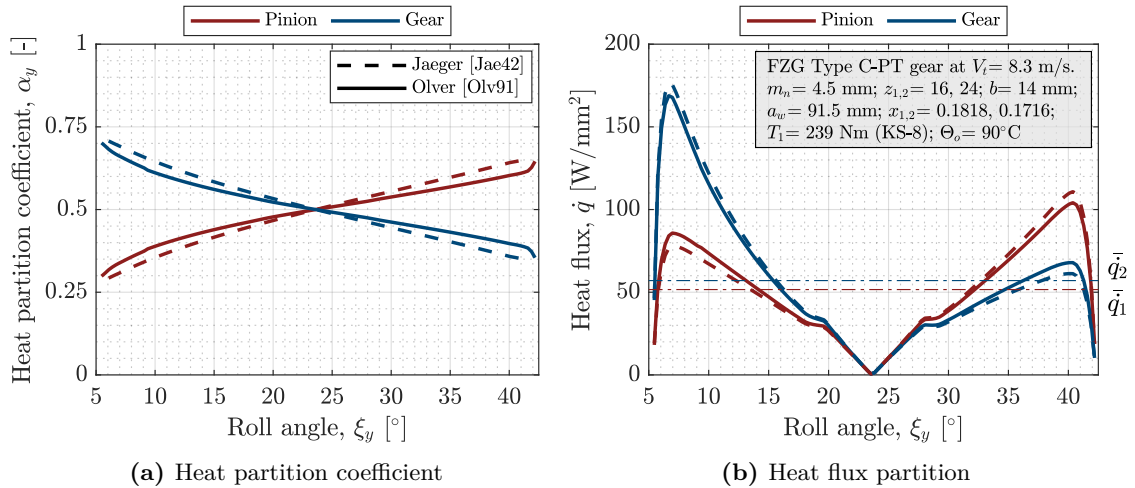


Figure 5.8: Heat partitioning coefficient effect in FZG type C gear pair heat flux

If Jaeger's approach [244] is compared to that of Olver [246] which is used in this thesis, very little variation is observed for the considered case. Contrary to Jaeger's heat partitioning coefficient which exclusively depends on tooth geometry, Olver's also depends on operating conditions; through the steady-state and film resistance terms in Equation 4.36. From the observation of the latter, it can be easily deduced that the film resistance term does not affect heat partitioning when the ratio of the film thickness to the Hertzian contact area is negligible, that is, when high loads are applied. Therefore, in such conditions, both models give the same results if steady-state resistances are not considered. In any case it has been observed that Olver's method affects heat partitioning coefficient less than 10% for a variety of conditions with respect to Jaeger's approach.

Furthermore, it is also interesting to remark that the difference between the average heat flowing towards pinion and gear in Figure 5.8b is small and therefore no apparent gear ratio effect is considered. It is known that due to the difference in rotational speeds, pinion receives more heat per rotation of the gear and therefore constriction resistances must somehow include the influence of the number of teeth to account for this effect

because a single tooth has been used to represent the thermal behaviour of all teeth. Therefore, average thermal resistance in Equation 5.17 has been modified dividing by the number of teeth, which is equivalent to considering z resistances connected in parallel.

Finally, in order to consider the heat partitioning effect in the rest of the power loss sources, a constant coefficient is used following recommendations from in Table 5.1.

Table 5.1: Heat partition coefficients in thermal network model

Source	Mesh	Air	Oil	Shaft	Housing
Lip sealings, P_{VD}	0	0	0.5	0.4	0.1
Bearings, P_{VL}	0	0	0.5	0.25	0.25
Gears, P_{VZP}	1	0	0	0	0
Windage, $P_{VZ0,W}$	0	1	0	0	0
Churning, $P_{VZ0,C}$	0	0	1	0	0

This way, heat applied to any of the nodes in Figures 5.2 and 5.3, represented by variables $Q_{VZP,VL,VD,\dots}$ are computed as the product of the constant coefficient presented in Table 5.1 and the corresponding power loss source. In the case of the gear mesh, windage and oil churning, all heat is directly applied to the corresponding node. On the contrary, in the case of bearings and lip sealings, heat is distributed among the surrounding elements, namely: shaft, oil sump and housing.

5.3.2 Heat dissipation in dip-lubricated gears

Heat transfer in common dip-lubricated gearboxes can be classified in two different mechanisms. Assuming that no external air fan or internal cooling circuit exists, we have: i) composite radiation and natural convection of the gearbox with room air and ii) forced convection with the oil sump and interior air. The former depends on the geometry and size of the casing, its temperature distribution and the properties of air in the surrounding environment. Meanwhile, the latter is far more complex as it heavily depends on the internal fluid behaviour, the immersion depth, the temperature of oil and air, the rotating speed, etc. Recent SPH and CFD simulations and high speed experimental recordings from Hartoni [271] and Liu [71] have shown that the velocity profile of the fluids and oil fraction in air correlate to churning losses and similarly, one would expect to affect forced convection heat transfer as well. As a consequence, a simplified approach is required to deal with the latter in the proposed thermal network model.

Figure 5.9 depicts the overall fluid flows inside the gearbox reproduced from the numerical/experimental findings in [71, 271] and affecting internal forced convection. Natural convection heat transfer outside the gearbox is also shown for completeness.

On the one hand, it is remarked that the heat transfer with the oil sump and the oil-air mixture inside the gearbox is primarily ruled by the relative immersion depth. Oil level determines the amount of lateral surface of the gear and shafts that exchanges heat by forced convection. Two characteristic regions are observed in each gear-shaft assembly: i) a region rotating in the oil sump which is continuously in contact with the lubricant and ii) a non-immersed surface in contact with interior air. Furthermore, the so-called ‘‘interior air’’ is a mixture of splashed oil and air and therefore the mixture properties are dependent on the fraction of oil in air.

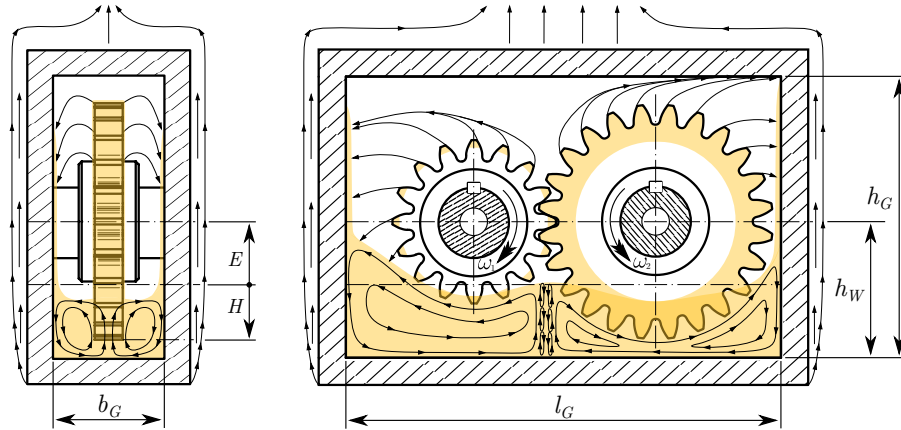


Figure 5.9: Oil and air flow patterns around dip lubricated gear pair and housing

If, on the contrary, attention is paid to the housing, oil level determines three different regions: i) a fully immersed domain where the velocity of the fluid is related to the tangential speed of the meshing gears, ii) a volume of oil/air mixture outside the sump partially in contact with the housing and iii) a stream of oil flowing down the walls of the casing under the action of gravity due to lubricant being thrown off the gears. Each of these regions of the gears, shafts and housing has a different convection resistance but all of them can be computed from Equation 5.29 where A is the heat exchange surface, k is the thermal conductivity of the fluid, L is the characteristic dimension and Nu is the Nusselt number.

$$R_h = (A \cdot h)^{-1} = L \cdot (A \cdot k \cdot Nu)^{-1} \quad (5.29)$$

On the other hand, the outer surfaces of the gearbox exchange heat with the room by natural convection and radiation. If the casing is considered a set of several vertical and horizontal plates as in Figure 5.3, natural convection coefficients, h , can be easily correlated to empirical equations in scientific literature [272] and radiation heat transfer can be simplified following the Stefan-Boltzmann law [261]. Therefore, both mechanisms can be combined in a single thermal resistance by considering them as resistances in parallel (see Figures 5.2 and 5.3).

Forced convection with oil/air mixture

Following the graphical description of internal fluid flows in Figure 5.9, it is expected that the separation between regions in contact with oil and those in contact with air to be diffuse; as it is defined by a dynamic oil level that depends on a number of factors such as oil splashing, volumetric expansion at increasing lubricant temperature, oil aeration, etc. Therefore, for the sake of simplicity, both regions are assumed to be separated by the stationary oil level which defines a gear height in contact with oil, H , and the corresponding height in contact with air, E , such that $r_a = E + H$, with r_a the tip radius of the gear (see Figure 5.9).

Volumes in contact with the lubricant in Figure 5.2 are connected to the mass node representing the oil sump by forced convection thermal resistances, and those in contact with air are connected to the air node in the same way. Equation 5.29 being identical for

both, and the characteristic dimensions and affected areas very similar for regions nearby, the main difference in the amount of heat evacuated from these surfaces is imposed by the Nusselt number, Nu , representing fluid behaviour, through the Reynolds, Re , and Prandtl, Pr , numbers in Equations 5.33 to 5.46.

$$Re = \frac{U \cdot L}{\nu_k} \quad (5.30)$$

$$Pr = \frac{c_p \cdot \eta}{k} \quad (5.31)$$

where ν_k , c_p , η and k are the kinematic viscosity, specific heat, absolute viscosity and thermal conductivity of the fluid (oil or air) respectively; all of which are evaluated at the mean boundary layer temperature, $\bar{\Theta}_f = 0.5 \cdot (\Theta_s + \Theta_o)$, which depends on the surface and oil temperatures. The velocity term, U , represents the relative velocity of the fluid and it is the product of the rotational speed and the mean radius in case of cylindrical/annular regions. For other regions, such as the bottom plate of the housing, the reference velocity must be defined.

Furthermore, if an oil-air mixture is considered outside the sump, the thermophysical properties must include the effect of oil volume fraction in air. To solve this issue, the mixing approach for steam-water systems presented by Idsinga [273] is used, assuming that the oil-air mixture is a homogeneous two-phase fluid inside the gearbox. On the one hand, absolute viscosity, thermal conductivity and density can be directly calculated with Equation 5.32, where ζ is the property to be evaluated, and ξ is the oil-air ratio. On the other hand, heat capacity and kinematic viscosity are affected by the specific volume.

The latter being very different in magnitude for oil and air, any small change in oil fraction in air will completely alter the thermophysical behaviour of the mixture. Figure 5.10 depicts this situation where it is observed that a change as small as 1% in volume fraction completely modifies kinematic viscosity and specific heat of the mixture.

$$\zeta' = \zeta_a + \xi \cdot (\zeta_o - \zeta_a) \quad (5.32)$$

a) Forced convection in the gear-shaft assembly: Forced convection heat transfer in the gear-shaft assembly depends on the affected area, the characteristic length and the Nusselt number in each of the considered regions. In cylindrical/annular surfaces in contact with oil or air, the area to be used in Equation 5.29 is the total area and the characteristic length is the mean diameter. However, in the gear tooth region (depicted in detail in Figure 5.3), the lateral and tooth tip convection heat transfer surface is the sum of the corresponding areas of all teeth and the characteristic lengths are the transverse tooth thickness and the tooth height respectively.

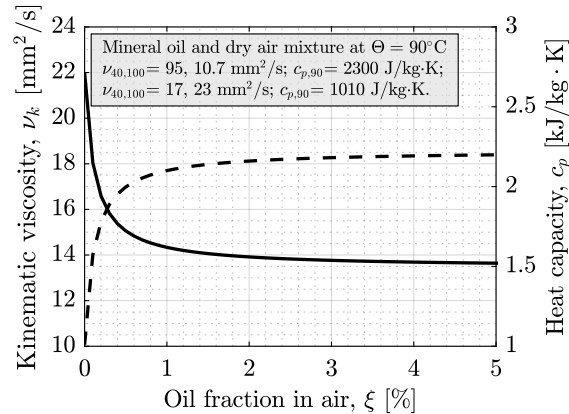


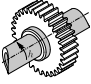

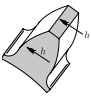
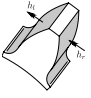
Figure 5.10: Oil-air mixture properties as a function of the fraction of oil in air

Finally, the Nusselt number, Nu , for each region in Figure 5.2 and 5.3 is determined by considering an equivalent geometry as follows:

- Cylindrical surfaces of the shaft and gear hub exchange heat by tangential flow, thus, both can be considered equivalent to shafts rotating in a fluid.
- Lateral surfaces of the gear and tooth ends exchange heat with the oil/air by circumferential flow and therefore they are equivalent to a disc rotating in a fluid.
- Tooth tip and bottom exchange heat with the oil/air by parallel flow and they can be modelled as a fluid flow over an horizontal flat plate.
- Flanks exchange heat by pressure and suction when they enter the oil sump and therefore, they can be assimilated to a perpendicular flow on a vertical flat plate.

Table 5.2 summarizes the forced convection correlations to be applied on each region based on equivalent geometries and flow regime. For intermediate values of the Reynolds number, Re , linear interpolation of the equations is used.

Table 5.2: Forced convection heat transfer correlations for rotating gears and shafts

Region	Description	Ref.	Convection correlation	
	Cylindrical surfaces	[274]	$10^3 < Re < 10^5 \rightarrow Nu = 0.133 \cdot Re^{2/3} \cdot Pr^{1/3}$	(5.33)
	Lateral surfaces	[275]	$Re < 2.5 \cdot 10^5 \rightarrow Nu = 0.4 \cdot Re^{1/2} \cdot Pr^{1/3}$	(5.34)
			$Re > 3.2 \cdot 10^5 \rightarrow Nu = 0.238 \cdot Re^{4/5} \cdot Pr^{3/5}$	(5.35)
	Tooth tip and ends	[120]	$Re < 5 \cdot 10^5 \rightarrow Nu = 0.664 \cdot Re^{1/2} \cdot Pr^{1/3}$	(5.36)
			$Re > 5 \cdot 10^5 \rightarrow Nu = 0.037 \cdot (Re^{4/5} - 23100) \cdot Pr^{1/3}$	(5.37)
	Left/right flanks	[276]	$1 \cdot 10^4 < Re < 5 \cdot 10^4 \rightarrow Nu_l = 0.592 \cdot Re^{1/2} \cdot Pr^{1/3}$	(5.38)
			$7 \cdot 10^3 < Re < 8 \cdot 10^4 \rightarrow Nu_r = 0.17 \cdot Re^{2/3} \cdot Pr^{1/3}$	(5.39)

Moreover, as described in the literature review in Section 2.1.2, one of the most important heat transfer mechanisms in meshing gears is that produced by centrifugal fling off when teeth exit the oil sump. This phenomena is not shown in Table 5.2 as the calculation does not yield a Nusselt number but the corresponding thermal resistance between each flank and the oil sump. Following Changenet [263] the equivalent fling-off resistance including the influence of all teeth is:

$$R_f = \frac{2 \cdot \pi}{b \cdot z \cdot h \cdot C \cdot \sqrt{k_o \cdot \rho_o \cdot c_{p,o} \cdot \omega \cdot \theta}} \quad (5.40)$$

$$C = 0.257 + \frac{0.885}{\left[1 + \exp\left(\frac{\psi - 0.776}{0.109}\right) \right]^{0.119}} \quad (5.41)$$

$$\psi = \left(\frac{r \cdot \chi \cdot \theta^2}{\nu_k \cdot h} \right)^{1/4} \quad (5.42)$$

where all parameters have been already introduced except angle θ which is the available angle for the projection of oil outside the sump. This angle increases with decreasing oil level and therefore, convection resistance due to normal flow in Table 5.2 is proportionally reduced. Both mechanisms interact on gear teeth as thermal resistances in parallel.

b) Forced convection in the housing: Internal surfaces of the housing, such as the bottom plate, the vertical sides or the top cover, exchange heat by forced convection with interior oil and air due to the rotation of the gears. Similarly to the gear-shaft assembly, the affected area in each of the convection resistances in Figure 5.3 is the surface directly in contact with the fluid, this way, the bottom plate and the lower parts of the side plates are connected to the oil sump node, while the portion of the casing outside the sump is connected to the air node. Housing geometry being simplified as an assembly of horizontal and vertical flat plates, the affected area to be used in Equation 5.29 is easy to calculate as it only depends on the length, width and height of the plates in Figure 5.9. Meanwhile, the characteristic length, L , and mean velocity of the fluid, U , are not easy to define as they depend on the flow pattern inside the casing which has been proved to be complex [271]. Therefore, the following criteria is established based on the simplified fluid behaviour depicted in Figure 5.9.

Table 5.3: Characteristic lengths and mean fluid velocities in housing plates

Part	L	U
Horizontal top cover	l_G	V_t
Horizontal bottom plate	l_G	V_t
Vertical immersed side wall	$h_W - E$	V_t
Vertical non-immersed side wall	$h_G - h_W + E$	V_m
Vertical immersed front/rear plates	l_G	V_t
Vertical non-immersed front/rear plates	l_G	V_m

Parameters l_G , h_G , h_W and E in Table 5.3 are reference dimensions in Figure 5.9, V_t is the tangential velocity at the pitch radius and V_m is the average velocity of the fluid relative to the walls. Note that the side-walls and front/rear plates of the casing outside the sump in Figure 5.9, are subject to an oil stream flowing down the walls due to the latter being thrown off the gears by centrifugal effects, thus, the average stream velocity depends on the action of gravity and the height relative to the oil sump. According to Changenet [263] the mean velocity of the fluid in this plates, V_m , can be calculated as:

$$V_m = \frac{1}{h} \cdot \int_0^h V(y) dy = \frac{1}{h} \cdot \int_0^h g \cdot \sqrt{\frac{2 \cdot y}{g}} dy = \sqrt{\frac{8 \cdot g \cdot h}{9}} \approx 2.95 \cdot \sqrt{h_G - h_W + E} \quad (5.43)$$

which depends on the casing height and the oil level relative to the shaft position.

Finally, the Nusselt number in all internal surfaces is defined following correlations 5.45 and 5.46 as fluid is assumed to flow parallel to each of the plates, without any distinction between vertical and horizontal ones. Only average velocity differences must be considered on the Reynolds number following recommendations from Table 5.3.

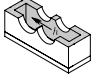
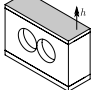
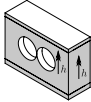
Natural convection with room

Outer surfaces of the housing exchange heat with the surrounding environment by natural convection, therefore, casing plates are also connected to the room node by means of thermal resistances accounting for this effect (see Figure 5.3). Equation 5.29 is also applied here, where the heat transfer area is the total area of the vertical or horizontal plates, and the characteristic dimension is the height or length of the plates respectively. Nusselt number correlations for the different regions are presented in Table 5.4 and it is observed that, contrary to forced convection in the internal surfaces, fluid behaviour is no longer ruled by the Reynolds number but that of Rayleigh, Ra, following:

$$\text{Ra} = \frac{g \cdot \beta \cdot L^3 \cdot \Delta\Theta}{\nu_k^2} \cdot \text{Pr} \quad (5.44)$$

where all parameters are known except β which is the fluid volume expansion coefficient.

Table 5.4: Forced and natural convection heat transfer correlations for housing plates

Region	Description	Ref.	Convection correlation
	Inner surfaces	[120]	$\text{Re} < 5 \cdot 10^5 \rightarrow \text{Nu} = 0.664 \cdot \text{Re}^{1/2} \cdot \text{Pr}^{1/3}$ (5.45)
			$\text{Re} > 5 \cdot 10^5 \rightarrow \text{Nu} = 0.037 \cdot (\text{Re}^{4/5} - 23100) \cdot \text{Pr}^{1/3}$ (5.46)
	Horizontal plates	[261]	$10^4 < \text{Ra} < 10^7 \rightarrow \text{Nu} = 0.54 \cdot \text{Ra}^{1/4}$ (5.47)
			$10^7 < \text{Ra} < 10^{11} \rightarrow \text{Nu} = 0.15 \cdot \text{Ra}^{1/3}$ (5.48)
	Vertical plates	[272]	$\text{Ra} < 10^9 \rightarrow \text{Nu} = 0.68 + \frac{0.67 \cdot \text{Ra}^{1/4}}{[1 + (0.492/\text{Pr})^{9/16}]^{4/9}}$ (5.49)
			$\text{Ra} > 10^9 \rightarrow \text{Nu} = \left[0.825 + \frac{0.387 \cdot \text{Ra}^{1/6}}{[1 + (0.492/\text{Pr})^{9/16}]^{8/27}} \right]^2$ (5.50)

Radiation with ambient

Finally, natural convection resistance with room is usually followed by a radiation term in parallel (see Figures 5.2 and 5.3) which is determined from the Stefan-Boltzmann law [261]. According to the latter, the heat transfer from any surface at temperature Θ_i , to a much larger environment at constant temperature Θ_j , is given by:

$$Q_{i,j} = \sigma \cdot \epsilon_i \cdot A_i \cdot (\Theta_i^4 - \Theta_j^4) \rightarrow Q_{i,j} = [\sigma \cdot \epsilon_i \cdot A_i \cdot (\Theta_i^2 + \Theta_j^2) \cdot (\Theta_i + \Theta_j)] \cdot \Delta\Theta \quad (5.51)$$

with $\sigma = 5.67 \cdot 10^{-8} \text{ W/m}^2 \cdot \text{K}^4$ the Stefan-Boltzmann constant, ϵ_i the surface emissivity and A_i the available heat exchange surface. From the term in brackets on the right hand side of Equation 5.51, the thermal resistance for radiation is obtained:

$$R_{rd} = \frac{1}{\sigma \cdot \epsilon \cdot A \cdot (\Theta_i^2 + \Theta_j^2) \cdot (\Theta_i + \Theta_j)} \quad (5.52)$$

where the surface emissivity depends on topography, coatings and degree of oxidation. In the absence of reference values, tabulated approximations for gearboxes can found in [16].

At this point it is also remembered that, similarly to housing radiation with ambient, composite forced convection and radiation effect also influences the external equivalent shaft-coupling described in the first section of this chapter in Equations 5.13 and 5.14.

5.4 Governing equations and solution method

The thermal network model has already proved to be accurate in thermal analysis of complex gear systems [125] with several gear pairs, bearings, etc. However, in all previous works, gears are usually represented by a single bulk temperature and very few works discuss the existence of radial and longitudinal thermal gradients [137]. The thermal network model developed herein accounts for such temperature distribution in the gear body but may be inaccurate in the gear teeth region where thermal gradients have been neglected and a single mass node has been used to represent the thermal state of all teeth.

The convenience of this assumption must be analysed before computing temperature distribution such that the degree of discretization can be set before hand. For this purpose the Biot number, Bi , behaviour is investigated; which is a dimensionless parameter giving a measure of the temperature drop inside the solids [261]. The latter is defined as the ratio of the internal resistance of the solid to heat conduction to the external resistance to heat convection (see Equation 5.53). Therefore, the assumption that small temperature gradients exist within the gear tooth will be valid when the amount of heat evacuated through the external surfaces is larger than the heat conducted inside the solid, in other words, when the Biot number is smaller than one.

$$Bi = \frac{R_{cond.}}{R_{conv.}} = \frac{h \cdot L}{k} \quad (5.53)$$

with h the overall heat convection coefficient, k the thermal conductivity and L the characteristic length which is defined here as the ratio of the total volume to the external surface area, $L = V/A$.

Figure 5.11 shows the influence of rotation speed and tooth size on the Biot number. The amount of heat evacuated through the external surface (i.e. overall convection coefficient h in Equation 5.53) increases with speed and therefore the Biot number increases as well. Meanwhile, tooth size affects characteristic lengths. It is observed that this parameter remains below one in all cases, but it is also remarked that the proposed assumption is specially adequate for small module gear teeth as the Biot number remains close to 0.1 which is the accepted critical value in scientific literature [261]. Moreover, face width also affects this parameter thus indicating that the number of slices in the face width direction must be defined with care. In this work, axial discretization criteria is set to one slice per millimetre face width, while radial discretization can vary depending on relative immersion depth and gear size. With this mesh, the approximate number of control volumes per gear-shaft assembly is 200 which gives a total amount of less than 500 mass nodes for the complete gearbox.

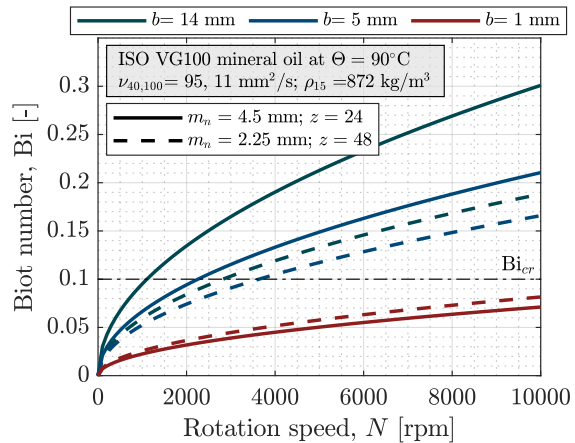


Figure 5.11: Biot number as a function of speed, tooth module and face width

5.4.1 Solution method

The solution of the thermal lumped parameter model is given by the system of equations assembled in matrix form in Equation 5.54 in which $[\mathbf{C}]$, is the thermal capacity matrix, $[\mathbf{K}]$ is the conductivity matrix (where $K_{i,j} = R_{i,j}^{-1}$), \mathbf{Q} is the heat input vector, Θ , is the temperature vector, t denotes time and the superimposed dot indicates time differentiation.

$$[\mathbf{C}(\Theta, t)] \cdot \dot{\Theta} + [\mathbf{K}(\Theta, t)] \cdot \Theta = \mathbf{Q}(t) \quad (5.54)$$

Therefore, the initial value problem for Equation 5.54 consists of finding $\Theta = f(t)$, the temperature vector at any instant $t < t_{end}$ and subject to the initial condition $\Theta(0) = \Theta_0$ with Θ_0 the vector of imposed initial temperatures.

If Equation 5.54 is developed and restated numerically for each node we have:

$$m_i \cdot c_{pi} \cdot \frac{d\Theta_i}{dt} + \sum_{\substack{j=1 \\ j \neq i}}^n \frac{\Theta_i - \Theta_j}{R_T(i, j)} = Q_i \quad (5.55)$$

where m_i is the mass of the considered node, c_{pi} is the heat capacity, $d\Theta_i/dt$ is the time derivative of temperature, $\Theta_{i,j}$ is the temperature of two connected nodes i and j from n total number of nodes, $R_T(i, j)$ is the equivalent thermal resistance between both and Q_i is the heat input on node i .

Parameter $C_i = m_i \cdot c_{pi}$ is the heat capacity of mass nodes, that is the amount of heat required by the latter to increase its temperature one degree. Thus, the term $C_i \cdot d\Theta_i/dt$ on the left of Equation 5.55 is the thermal inertia and represents the time required by each control volume to reach a steady-state thermal condition. As a consequence, mass nodes only affect the transient calculation and steady-state condition can be computed by neglecting the term on the left. Both conditions further are described below.

Steady-state calculation

On the one hand, steady-state regime can be computed from Equation 5.55 neglecting thermal inertia or by simply applying the conservation of energy to each control volume.

$$Q_i = \sum_{\substack{j=1 \\ j \neq i}}^n \frac{\Theta_i - \Theta_j}{R_T(i, j)} = \Theta_i \cdot \sum_{\substack{j=1 \\ j \neq i}}^n \frac{1}{R_T(i, j)} - \sum_{\substack{j=1 \\ j \neq i}}^n \frac{\Theta_j}{R_T(i, j)} \quad (5.56)$$

Following Chagnenet [263] this equation can be rewritten in the following form:

$$Q_i = \sum_{j=1}^n K_T(i, j) \cdot \Theta_j \quad (5.57)$$

$$\text{if } i \neq j \longrightarrow K_T(i, j) = -\frac{1}{R_T(i, j)} \quad (5.58)$$

$$\text{if } i = j \longrightarrow K_T(i, i) = \sum_{\substack{k=1 \\ k \neq i}}^n \frac{1}{R_T(i, k)} \quad (5.59)$$

which leads to a matrix expression of the type $\mathbf{Q} = [\mathbf{K}] \cdot \Theta$ shown in Equation 5.60 that can be readily solved by direct numerical procedures such as LU decomposition [277].

Note that the principal diagonal terms in Equation 5.60, represent the sum of all resistances connected to the considered node while the non-diagonal terms are coupling terms between different nodes, which is very similar to the compliance matrix representation in Equation 3.94. Logically, if two nodes are not interconnected the conductance between them is zero. Besides, the heat input vector considers all power loss sources, $P_{V,i}$, explained in Section 5.3.1 and multiplied by the heat partitioning coefficients, α_i from Table 5.1, such that $Q_i = \alpha_i \cdot P_{V,i}$. In the rest of the nodes the total amount of applied heat is zero.

$$\begin{pmatrix} Q_1 \\ Q_2 \\ \dots \\ Q_n \end{pmatrix} = \begin{bmatrix} \sum_{i \neq 1}^n \frac{1}{R_T(1,i)} & -\frac{1}{R_T(1,2)} & \dots & -\frac{1}{R_T(1,n)} \\ -\frac{1}{R_T(1,2)} & \sum_{i \neq 2}^n \frac{1}{R_T(2,i)} & \dots & -\frac{1}{R_T(2,n)} \\ \dots & \dots & \dots & \dots \\ -\frac{1}{R_T(1,n)} & -\frac{1}{R_T(2,n)} & \dots & \sum_{i \neq n}^n \frac{1}{R_T(n,i)} \end{bmatrix} \cdot \begin{pmatrix} \Theta_1 \\ \Theta_2 \\ \dots \\ \Theta_n \end{pmatrix} \quad (5.60)$$

Transient calculation

On the other hand, transient regime is computed from Equation 5.55 after restatement following Equations 5.57 to 5.59 which yields the discrete solution:

$$m_i \cdot cp_i \cdot \frac{d\Theta_i}{dt} + \sum_{j=1}^n K_T(i,j) \cdot \Theta_j = Q_i \quad (5.61)$$

Similarly, if the latter is restated in matrix form we have:

$$\frac{d\Theta}{dt} = \left[\frac{\mathbf{1}}{\mathbf{C}} \right] \cdot (\mathbf{Q} - [\mathbf{K}_T] \cdot \Theta) \quad (5.62)$$

Note that Equation 5.62 represents a set of non-linear ordinary differential equations (ODE), because conductances, $[\mathbf{K}_T]$, and heat inputs, \mathbf{Q} , are dependent on instantaneous temperatures, Θ . To solve this ODE system Picard's iteration algorithm [278] is used which has been found suitable to deal with the non-linearities arising from fluid properties, convection coefficients and radiation.

Boundary conditions

To solve the system of equations, two types of boundary conditions can be set: fixed temperatures and fixed heat fluxes. Room and gearbox foundation temperatures in Figures 5.2 and 5.3 are assumed constant and equal to 20°C and 40°C respectively. Although it is possible to analyse the influence of foundation resistance by considering it as a rectangular fin as shown in [264] very little variation is expected in internal heat distribution and therefore, it is simplified by considering it as a constant temperature which is justified by its large external surface area exchanging heat with room air. As far as constant heat inputs is concerned, no fixed heat flux is imposed at all, as all power loss sources are non-linear and depend on oil and air temperatures. Finally, for transient calculations, it is assumed that all initial temperatures are equal to room temperature which is taken as 20°C in this work.

5.4.2 Thermo-mechanical coupling

It has been shown earlier in this chapter that heat sources and convection heat transfer coefficients are non linear as they depend on oil and air temperatures. Furthermore, fluid heat capacities are also affected by density change and if gear material property variations are considered as well, the system of equations is fully non-linear thus requiring iterative procedures to solve it. However, if only steel gears are considered, thermophysical property variations can be neglected as maximum bulk temperatures are below tempering temperatures in almost all cases. As a consequence, conduction resistances and heat capacities in steel nodes are linear terms as they only depend on geometry, while those related to fluid nodes are non-linear. Figure 5.12 shows the computation flowchart for steady-state and transient regimes considering both terms.

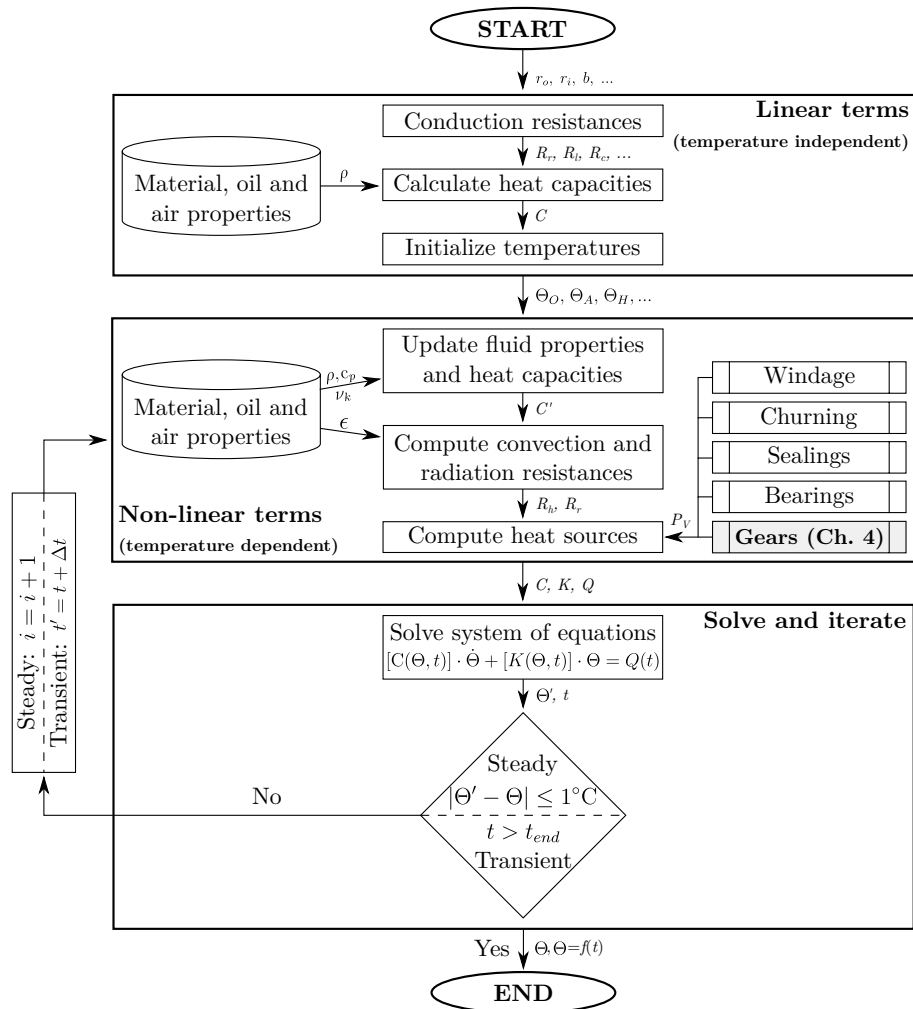


Figure 5.12: Thermo-mechanical temperature distribution prediction flowchart

At the beginning, gear geometry is discretized and geometrical parameters of each control volume are input to the algorithm, such that conduction resistances and heat capacities (linear terms) are calculated first. Then, initial temperatures are set and non-linear terms are estimated. Oil viscosity is updated following the Vogel, Tammann and Fulcher model which has already been presented in the first term of Equation 4.28, while other parameters such as density, thermal conductivity or heat capacity can be computed for a number of fluids following reference [279]. Similarly dry air property variations with temperature are gathered in [280] and if an oil air-mixture is considered instead, Equation 5.32 is to be used. Next, convection heat transfer resistances are computed from the Nusselt number, which depends on the boundary layer temperature and, similarly, radiation resistances are calculated from the temperature of the housing and that of room. On the other hand, heat sources are calculated from operating conditions and fluid temperatures following models presented in Section 5.3.1 while gear mesh power loss is specifically computed from the model developed in Chapter 4. Finally, steady-state or transient solutions are calculated with Equations 5.57 or 5.61 respectively and the process is repeated until steady-state convergence is achieved or maximum computing time is reached in transient cases.

Interpretation of results

Temperature distributions from the solution of Equation 5.54 applied to the thermal network model developed in this chapter, are mainly located in the longitudinal plane of each gear, which is defined by the reference tooth symmetry axis. Therefore, final thermal state can be shown as a series of contour plots where $\Theta_i = f(x_i, 0, z_i)$. An example of the result for the reference gear pair FZG type C-PT is shown in Figure 5.13.

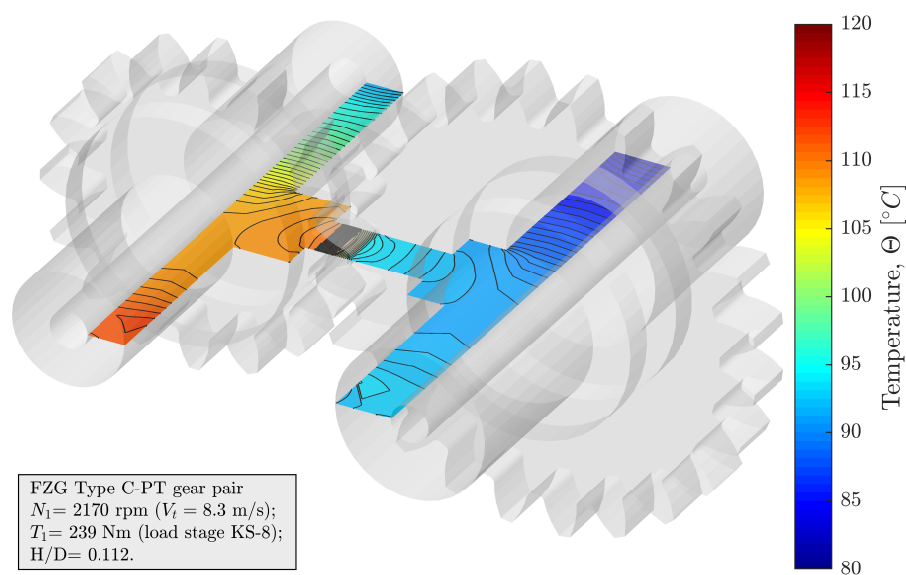


Figure 5.13: Computed two-dimensional steady-state temperature distribution of FZG type C-PT gear pair at $V_t = 8.3$ m/s, $T_1 = 239$ Nm and relative immersion depth $H/D = 0.112$

As expected, overall pinion temperature is larger than that of the gear; with maximum values located in the pitch cylinders and near the front bearings in both cases. In the standard FZG test rig, these bearings are roller type, reference NJ406, which have been proved to give large power losses with respect to the deep-groove ball bearings reference 6306 located in the back (see Figure A.1). Rotational speed of pinion shaft being higher than that of the gear, resulting power losses are significantly larger in the former and, as a consequence, temperature in the shaft portion just below the inner ring of such bearings is increased. Contrarily, it is interesting to remark that minimum temperatures are located in the rear end of each shaft which is the region close to the equivalent external coupling in Figure 5.2. Convection heat transfer in this region is increased due to the presence of the latter and temperature is lower as a consequence.

Furthermore, in the standard FZG test rig, bearings are located close to the gear ends and therefore heat generated by bearings and sealings is conducted towards the pinion and gear. Similarly, enhanced heat dissipation on the rear shaft ends affects to both gears as well, and as a consequence of these effects, overall temperature profile of pinion and gear is altered. This behaviour is observed in Figure 5.14 where the isotherms are slightly distorted towards the lower ends of the gears close to bearing supports.

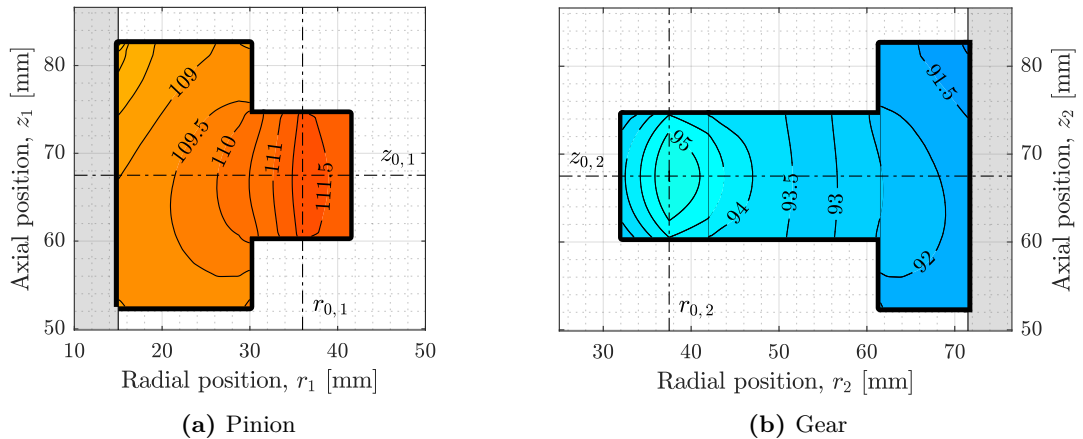


Figure 5.14: Detail of predicted pinion and gear steady-state temperature distributions in the longitudinal plane at $V_t = 8.3$ m/s, $T_1 = 239$ Nm and relative immersion depth $H/D = 0.112$

If attention is paid to bulk temperatures in Figure 5.14, it is clearly visible that pinion temperature increase is higher than that of the gear by approximately 15°C for the considered operating conditions. Moreover, temperature is proportional to radial and axial position and follows an approximately polynomial trend in both directions, with the maximum value located in the pitch cylinder and the minimum value in the shaft. Besides, it is also concluded from this figure that the tooth tip of both gears has a lower temperature than the pitch cylinder due to the increased convection heat transfer in this region. These trends are consistent with FEM results by Patir and Cheng [126].

Such temperature distributions are of interest for thermal distortion modelling in the next chapter and therefore, attention is paid to them by defining two reference positions in Figure 5.14, one for each direction, with names r_0 and z_0 respectively. The former is tangent to the working pitch cylinder while the latter is defined by the orthogonal plane in the middle of the face width.

Temperature distributions for both directions are shown in Figure 5.15, where pinion and gear temperatures are gathered in the same diagrams to reveal the shape and amount of thermal gradients. On the one hand, it is observed in Figure 5.15a that there is a clear temperature difference between pinion and gear produced by the low immersion depth, which is $H/D = 0.112$ in this case. Such oil sump level applied to the FZG type C-PT gear pair, only lubricates the gear while pinion is not in contact with oil any more. As a consequence, pinion heat dissipation is poor and temperature is higher than its mating gear. Besides, both wheels have a radial thermal gradient of approximately 3°C in the pinion and 4°C in the gear, following a polynomial trend as previously described.

Moreover, it has been found that in most cases, radial temperature distribution can be modelled by a power law function of order n , which takes the values 1.47 and 1.37 for the pinion and gear respectively in Figure 5.15a. This trend is repeated in almost all combinations of speed and torque and in some cases, specially when oil level is high, the order of the power law function can even be below unity. Furthermore, radial temperature differences of large gears have also been analysed and it has been found that temperature gradient between teeth and shaft can reach 20°C to 25°C while large gear ratios lead to temperature differences between pinion and gear of as much as 30°C .

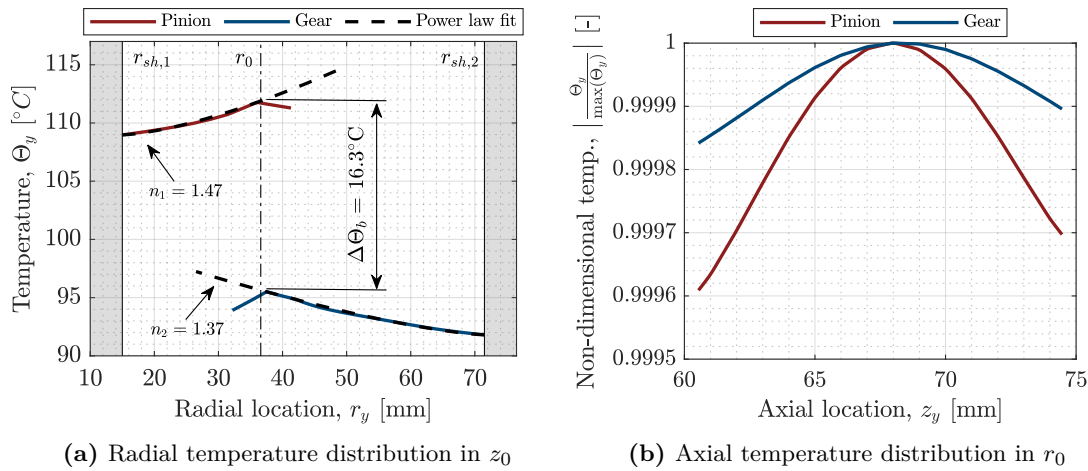


Figure 5.15: Radial and axial temperature distributions in the reference sections of FZG type C-PT at $V_t = 8.3$ m/s, $T_1 = 239$ Nm and relative immersion depth $H/D = 0.112$

On the other hand, longitudinal temperature distribution usually follows a parabolic trend [126], provided that load distribution is uniform (i.e. without mesh misalignment). In dip lubricated systems, convection heat transfer coefficients and submerged surface areas of both gear ends are equal, which leads to a symmetric longitudinal temperature profile. However, in the current case shown in Figure 5.15b, nearby bearings and sealings slightly distort such temperature distribution leading to a non-symmetric temperature profile. The size of the pinion being reduced with respect to the gear, the degree of distortion of the axial temperature distribution due to nearby bearings and sealings is larger in the pinion than in the gear. For the narrow FZG type C-PT gears shown in Figure 5.15b, the temperature of the ends is approximately 0.05°C less than the centre of the gear which is negligible. However, additional test cases have been analysed and, similarly to Long et al. [131], it has been found that longitudinal thermal gradient largely depends on the face width as heat tends to concentrate in the middle of the flank.

Finally, if pinion and gear thermal behaviour are compared to that of surrounding oil and air, it is observed in Figure 5.16 that bulk temperature of gears is clearly higher than the temperature of oil and air by approximately 20°C to 40°C which is consistent with scientific literature [281]. Moreover, heat capacity of air being much lower than that of oil, the former needs more time to stabilize. Gears and oil, have almost reached their steady-state condition after one hour but air still requires more time (see Figure 5.16). After two hours, close to the steady state condition, fluid temperatures are very similar while pinion and gear are still clearly different.

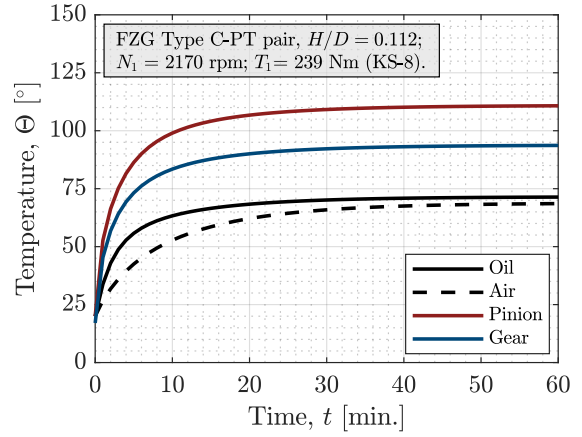


Figure 5.16: Computed transient temperatures of FZG type C-PT gear pair, oil sump and interior air at $V_t = 8.3$ m/s, $T_1 = 239$ Nm and $H/D = 0.112$

5.5 Experimental validation

Thermal network model results in this chapter have been compared to the experimental temperature measurements by Otto [28] who analysed the influence of speed, torque and relative immersion depth on pinion and gear bulk temperatures. Reference gear FZG type C-PT was used by Otto which is the original, non-modified counterpart of gear type C_{mod} already used in the previous and following chapters and described in Table 4.7. The gear oil used in his experiments is the FVA3-A oil [282] whose properties are very similar to the mineral oil M100 in Table 4.4. Although extreme pressure additives (6.5% Anglamol 99 from Lubrizol) have been incorporated to prevent scuffing damage at the highest temperatures, the pressure-temperature-viscosity behaviour can be assumed equal [31] and therefore, sliding friction coefficient model presented in Chapter 4 is still applicable.

Although the full experimental work by Otto [28] also analyses additional parameters such as the influence of rotating direction, gear type and lubrication system, only variables shown in Table 5.5 are considered in the following numerical-experimental comparisons.

Table 5.5: Test conditions in Otto's experiments [28]

Parameter	Symbol	Value
Relative immersion	H/D [%]	50, 29.8, 23, 16.3, 11.2, 7
Torque	T [Nm]	94, 239, 372
Tangential speed	V_t [m/s]	8.3, 20
Oil temperature	Θ_o [°C]	90 ± 3

Oil temperature is kept constant at $90 \pm 3^\circ\text{C}$ and several immersion depths are selected, measured relative to the gear. Furthermore, low and high tangential speed conditions are analysed, which correspond to 2170 rpm and 5220 rpm rotational speed at the pinion shafts. Similarly, three torque levels are applied: KS-5, KS-8 and KS-10 stages; producing 0.92 GPa, 1.47 GPa and 1.83 GPa maximum contact pressure respectively.

Gear geometry is detailed in reference [28] but the thermal network model also requires housing and shaft dimensions as well as oil/air volumes. Unless otherwise stated, housing geometry refers to the standard FZG test rig and therefore, main dimensions can be found in scientific literature [30, 271]. Oil/air volume necessary to compute heat capacities are computed from dimensions in Figure 5.9 with:

$$V_o = b_G \cdot l_G \cdot (h_W - E) \quad (5.63)$$

$$V_a = V_{Tot} - V_o = (b_G \cdot l_G \cdot h_G) - V_o \quad (5.64)$$

where the static oil level relative to shaft centreline, E , depends on relative immersion depth, H/D , following $E = D \cdot (1/2 - H/D)$ with D the tip diameter of the gear.

First, predicted power losses are compared to experimentally measured values in Figure 5.17. It is observed that the model captures the influence of load and speed on power losses with higher losses at the highest input powers. Meanwhile, immersion depth indirectly affects the latter by means of the bulk temperature.

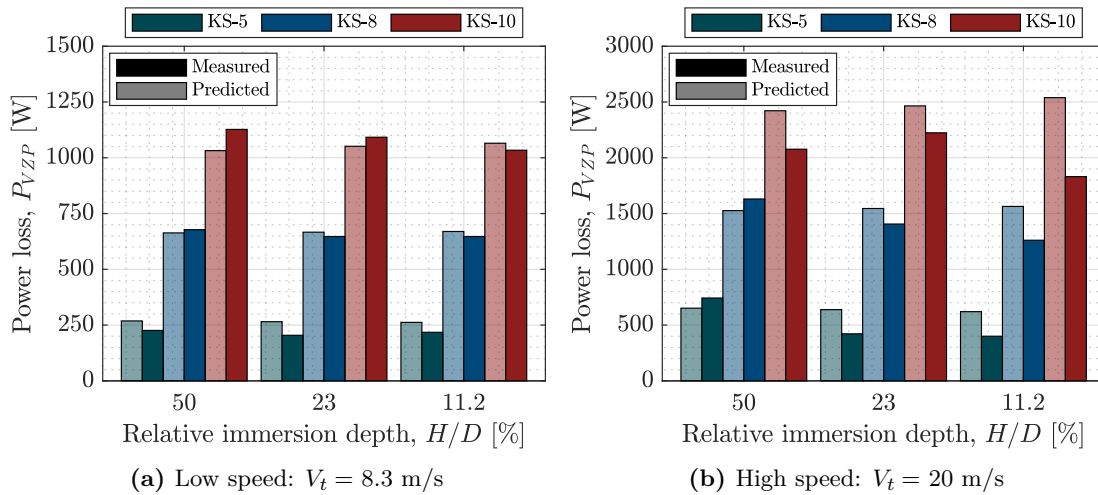


Figure 5.17: Predicted and measured power loss comparison for different operating conditions in Otto's experiments [28]

At the lowest tangential speed, predicted power loss is close to the measured values with 4% average error and a maximum of 25% at load stage KS-5 and 23% immersion depth. These values are in agreement with the proposed power loss model in Chapter 4. However, at high speeds, deviations are increased with an average error of 13% and a maximum error of 40% at stage KS-10 and 11.2% immersion depth. Besides, it is observed that in both speed levels, experimentally measured power losses decrease with immersion depth; which is contrary to the expected behaviour as immersion depth only affects to spin power losses and mesh frictional losses are only influenced by torque, speed and bulk temperature. If the latter increases with decreasing oil level, it is expected that friction coefficient increases as well giving rise to higher losses. Meanwhile, predicted power losses are almost constant with immersion depth thus indicating that average friction coefficient is not affected by the corresponding temperature increase and therefore, its value along the line of action is in the partial EHL regime and close to the boundary friction value.

Temperature predictions and experimental measurements for the conditions in Table 5.5 are gathered in Figure 5.18. Low speed results are shown in the first row (subfigures a and b) and those related to high speed in the second (subfigures c and d) with pinion temperatures on the left and those of the gear on the right. In all cases, experimentally measured bulk temperatures are referred to the centre of the tooth, aligned with the tooth symmetry axis and located 6 mm below the tooth tip [28], while numerical predictions are obtained at the pitch diameter as shown in Figure 5.3.

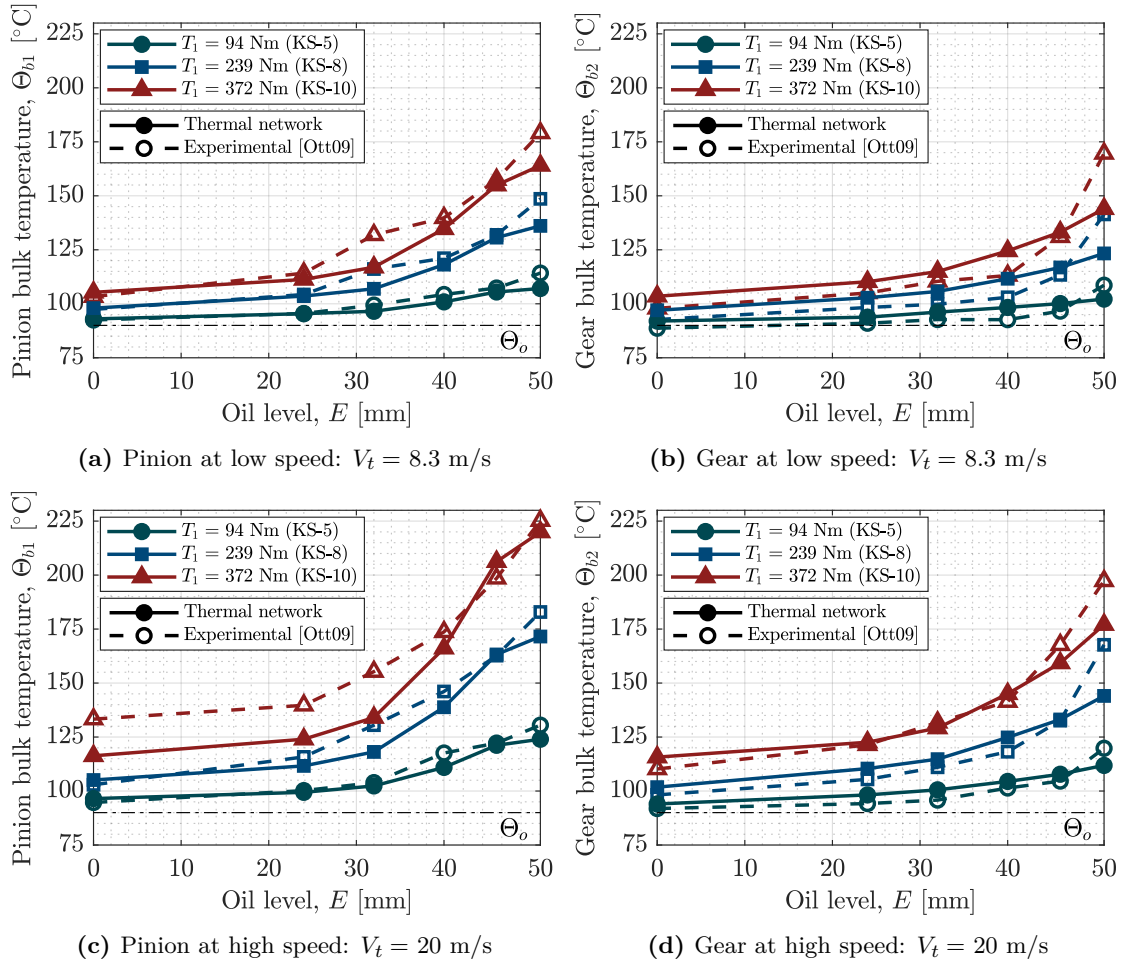


Figure 5.18: Comparison of temperature measurements from [28] and thermal network predictions for variable speeds, torques and immersion depths on FZG type C-PT gear pair

In general, temperature increases with decreasing oil level, with the highest bulk temperatures at the highest speeds and torque levels. Immersion depth affects temperature increase because the available submerged surface area for forced convection heat transfer is reduced; while torque and speed influence temperature increase by means of the mesh power loss which depends both parameters as shown in Equation 2.2. Furthermore, pinion temperature is always higher than that of the gear which is the expected behaviour, as described previously in this chapter. In general terms, the predicted numerical trend is correct with immersion depth and input power, with a maximum error of 25°C in the gear at low speed, highest torque and lowest oil level.

Moreover, there is a significant deviation in the pinion thermal behaviour at high speed and high torque, as experimental values deviate from previous trends at high immersion depth. In this sense, it is interesting to remark that the difference between pinion and gear temperatures at the highest immersion depth ($H/D = 0.5$) is minimal as heat is continuously dissipated by the oil sump, and therefore both values are almost equal. This behaviour has also been confirmed with a different data set by Geiger [120] in the same gear type and test rig; therefore such temperature increase of the pinion in Figure 5.18c is not easily explained. In any case, temperature differences between pinion and gear start to be noticeable from 32 mm oil level onward in all cases; which corresponds to approximately 23% relative immersion depth.

5.5.1 Discussion of results

Comparison of numerical results and experimental measurements in Figure 5.18 has shown that the model captures the overall thermal behaviour with operating conditions. Figure 5.19 shows an general view of the correlation between numerically predicted bulk temperatures of pinion and gear and experimental measurements. A maximum deviation of 15% has been found which is equivalent to 25°C located at the lowest immersion depth in the gear. Meanwhile, 70% of the predicted values have errors below 5°C , which is satisfactory. Experimental uncertainty has not been provided by Otto [28] and therefore, it is not possible to assess the accuracy of the proposed model with confidence.

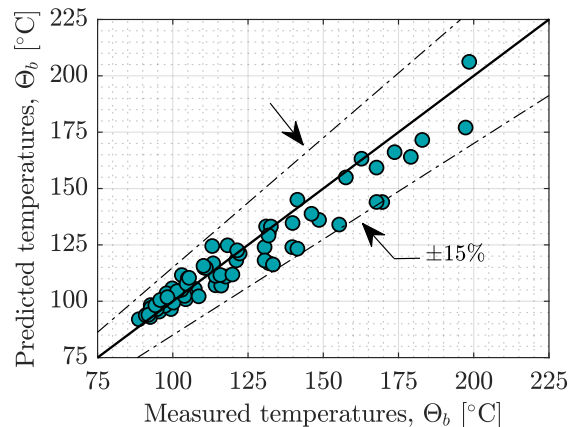


Figure 5.19: Overview of predicted and measured bulk temperatures of pinion and gear

It has been shown in Figure 5.17 that experimental power loss measurements decrease with oil level, but this behaviour is not consistent with scientific literature as friction coefficient has been proved to increase due to lubricant starvation in the contact [37]. Figure 5.20 compares analytically predicted power losses, specific film thickness and average friction coefficient with experimental measurements at constant torque and both tangential velocities. In both cases, specific film thickness values indicate that gear mesh operates in the partial EHL regime with average friction coefficients increasing with the reduction of oil level. At low speed the overall agreement is excellent but at high speed condition significant deviations arise. Experimentally measured values decrease with the immersion depth indicating that friction coefficient is considerably reduced with temperature because speed and torque remain constant. This effect may be due to the influence of lubricant additives but such a decrease is improbable and the effect may rather be attributed to experimental uncertainty. FZG power loss measurement procedure requires subtracting experimentally measured spin losses and numerically predicted bearing losses under load to the total power loss [41] and therefore, mesh frictional losses may be distorted by errors in the predicted bearing behaviour in the high speed condition.

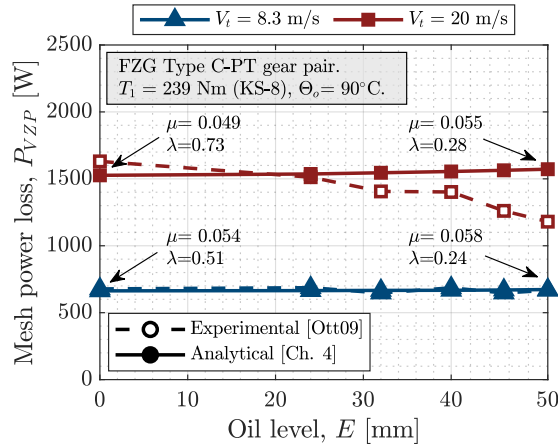


Figure 5.20: Power losses as a function of oil level and operating speed at constant torque

On the other hand, it has also been shown that at the high speed high torque condition, pinion temperature is unusually high and the initial value deviates from the experimental trend even if the oil level is maximum (see Figure 5.18c). Close analysis of experimental results of pinion types A and C in Otto's experiments [28] has revealed that the former has a lower temperature than the latter at the highest immersion depth which is also difficult to explain as the heat partitioning coefficient of gear type A is considerably higher than that of gear type C (previously explained in section 5.3.1). If the number of teeth, module and face width of both gear sets is the same, and so are the operating conditions, temperature of gear type C at $H/D = 0.5$ should be lower than that of gear type A.

If these outliers are not considered, deviations in the rest of the cases may be due to differences in heat transfer conditions. The composite effect of several variables may explain such discrepancies. For instance, literature review has shown that the definition of local forced convection coefficients in dip lubricated systems is difficult [100] and constant average values are used instead for each of the different sections of the gear (e.g. flanks, tip, shaft). Moreover, it is well known that the empirical equations used in the determination of the average Nusselt numbers in Tables 5.2 and 5.4 have errors of $\pm 15\%$ [261] and, as a consequence, the amount of dissipated heat is also affected. It has been observed that introducing these effects on the model modify bulk temperatures by 2°C to 5°C over the whole range of immersion depths and conditions.

Similarly, the dynamic oil level produced by oil sump volume expansion, aeration and lubricant splashing can affect heat transfer coefficients and temperature distribution as a consequence. LePrince [283] already showed that temperature increase of the lubricant rises up to 15% the relative immersion depth which affects churning power losses and, in the same way, it may affect convection heat transfer. Figure 5.21 depicts the influence of a such a dynamic oil level on bulk temperatures where it is observed that increasing or decreasing the oil level by this amount clearly changes numerically predicted values approaching measurements. It is interesting to remark that this variation of immersion depth affects pinion temperatures more than those of the gear due to its smaller size. Moreover, if lubricant level is minimum and neither lubricates pinion nor gear, temperatures reach almost the same value in both gears which is very similar to the condition where immersion depth is maximum and both gears are well lubricated.

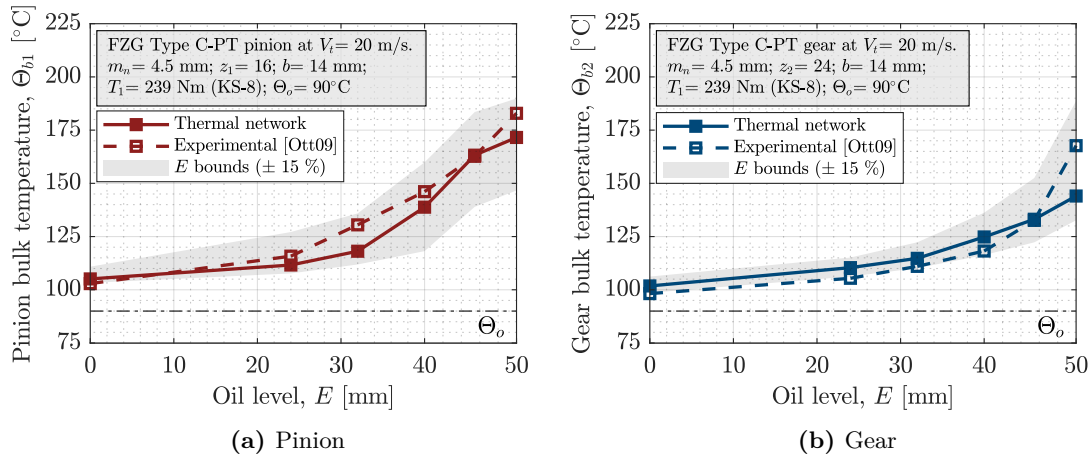


Figure 5.21: Influence of dynamic oil level on tooth temperatures

If oil sump level is assumed to vary with dynamic conditions, it is possible to assume as well that interior air is affected by dispersed oil droplets. A 1% oil volume fraction has been considered in the oil-air mixture inside the casing, whose thermophysical properties have been modelled following Equation 5.32. In all cases, the temperature increase at low immersion depths is considerably reduced due to the increase of the Reynold's number through the reduced kinematic viscosity. Nusselt numbers increase with the latter and so does the total amount of heat dissipated by forced convection; as a consequence, temperatures are reduced in all cases. Therefore, oil-air mixture helps reduce increased temperatures similarly to jet lubrication conditions [126].

Finally, the influence of boundary conditions has also been analysed. In this thesis, room and foundation temperatures have been assumed constant and equal to 20°C and 40°C respectively. The former has been varied $\pm 5^\circ\text{C}$ and the latter has been increased up to 60°C . Although gearbox plate temperatures have been modified by approximately 5°C in the worst case, gear pair temperature distribution has been affected little by a maximum of 0.3°C , because the oil sump temperature is set constant and equal to 90°C in Otto's experiments [28] and therefore the latter has a greater influence on pinion and gear bulk temperatures than the temperature outside the casing. Meanwhile the variation of the lubricant temperature by $\pm 3^\circ\text{C}$ does affect pinion and gear bulk temperatures in approximately the same amount. In this sense, it is interesting to see that if the oil temperature is not imposed, pinion and gear reach 112°C and 96°C respectively in the low speed condition at $E = 46$ mm and 236 Nm torque shown in Figure 5.15; which is clearly reduced with respect to the constant oil sump temperature case of Figure 5.21.

5.6 Conclusions of Chapter 5

In this chapter a novel thermal model of the gear pair has been developed based on the thermal network concept by Blok [112]. Compared to similar models in scientific literature (e.g. [125]) the model proposed herein accounts for radial and longitudinal temperature distributions of both, pinion and gear, which are necessary to compute gear teeth thermal distortion in the next chapter.

In the first section, theoretical background has been presented and thermal lumped parameter simplification of the general three dimensional heat conduction equation has been obtained. Radial and axial thermal resistances for conduction within cylindrical volumes have been calculated and the gear-shaft system has been discretized following the “thin-slice” approach, where each slice is thermally coupled to adjacent ones similarly to the load distribution model in Chapter 3. Furthermore, individual nodes have been incorporated to model the oil sump, interior air and housing and a single tooth has been used to represent the thermal-state of all teeth.

In the next section, heat sources in gearboxes have been identified and spin and load power loss terms have been analysed individually. It has been shown that the former starts to dominate at high tangential velocities while the latter is significant over the full range of rotating speeds. Moreover, the influence of heat partitioning on gear mesh has been analysed and mesh frictional heat input on the thermal network has been described. For other heat sources a constant coefficient has been adopted. Then, heat transfer mechanisms by convection have been introduced and corresponding thermal resistances have been determined. It has been shown that forced convection heat transfer inside the gearbox depends on the complex oil flows of the sump and a simplified approach to deal with it has been proposed. Natural and forced convection correlations for each region of the thermal network have been gathered and radiation resistances have been defined.

The solution method has been presented next. Steady-state and transient calculations have been described, boundary conditions have been set and a thermo-mechanical calculation flowchart has been defined to deal with the non-linearities of heat sources and convection heat transfer resistances. It has been shown that resulting radial temperature distribution of pinion and gear can be modelled by a power law function while longitudinal temperature distribution is of parabolic shape in dip lubricated systems, provided that load distribution is uniform and no additional heat source is nearby. These results are consistent with evidences from scientific literature [126] and they can be used to model thermally-induced gear geometry distortion in the next chapter.

Finally, numerical results have been compared to experimental values from [28] for dip lubricated gear pairs with variable rotating speeds, torques and immersion depths. Although numerical trends are similar to experimental results, deviations arise in some conditions which seem to be ruled by forced convection heat transfer conditions resulting from the complex oil flow patterns inside the gearbox.

Mistakes are, after all, the foundations of truth, and if a man does not know what a thing is, it is at least an increase in knowledge if he knows what it is not.

— Carl Jung, 1875 - 1961

6

Thermal Distortion

Contents

6.1	Introduction	160
6.2	Thermally-induced geometry distortion	160
6.2.1	Profile distortion	161
6.2.2	Helix distortion	168
6.3	Thermal effects on mesh behaviour	172
6.3.1	No-load transmission error and backlash	173
6.3.2	Thermo-mechanical behaviour	177
6.4	Case study	184
6.4.1	Results	185
6.4.2	Compensation of thermal distortion	188
6.5	Design recommendations	190
6.5.1	Tooth modification guidelines	193
6.6	Conclusions of Chapter 6	195

This chapter describes the prediction of gear teeth thermally-induced geometry distortion and the effects of deviations on mechanical behaviour. First, analytical modelling of gear teeth thermal deformation is presented. The influence of basic gear geometry parameters, temperature increase and thermal gradient are analysed and resulting geometry distortion is classified in terms of pitch, profile and lead deviations following current practice in ISO 1328-1 [284] gear standard. Then, the impact of thermally-induced deviations on mesh behaviour is studied; the influence of composite pinion and gear distortions on backlash and no-load transmission error is computed and uneven load distribution and relative stress behaviour are analysed. In the next section, the thermo-mechanical behaviour of an helical gear test case is fully described, teeth modifications to enhance contact performance are proposed and results are compared with the initial geometry. Finally, design guidelines to deal with thermal effects are summarized at the end of the chapter and conclusions are withdrawn.

6.1 Introduction

It has been shown in Chapter 5 that the overall gear pair temperature is far from being constant. Gear geometry, operating conditions and immersion depth affect radial and longitudinal temperature distribution and therefore, thermally-induced uneven dilatation exists. Furthermore, pinion and gear are usually subject to different temperatures if gear ratio is other than unity; as a consequence, the degree of expansion is also different. In such conditions, theoretically perfect mesh of pinion and gear is distorted and, similarly to manufacturing errors, contact behaviour under load is expected to be altered.

6.2 Thermally-induced geometry distortion

From Equations 3.4 and 3.5 it is possible to prove that the involute property is lost when thermal gradients exist. We designate by $R(\xi_y)$ the parametric representation of the distorted involute flank which is the result of the sum of the original involute, $r(\xi_y)$, and the local thermal deformation, $u(\xi_y)$. Neglecting the influence of thermal stresses we have:

$$|R(\xi_y)| = |r(\xi_y)| + |u(\xi_y)| \quad (6.1)$$

$$|u(\xi_y)| = \alpha_L \cdot \Delta\Theta(r_y) \cdot |r(\xi_y)| \quad (6.2)$$

Where the radial temperature distribution can also be represented parametrically as a function of the roll angle because $r_y = f(\xi_y)$ and therefore $\Delta\Theta(r_y) = \Delta\Theta(\xi_y)$. If the distorted geometry $R(\xi_y)$ is still involute after thermal deformation, there must be a constant base radius, R_b , that complies with Equation 3.5 in the following way:

$$R(\xi_y) = |R(\xi_y)| \cdot \begin{cases} \sin[\xi_y - \arctan(\xi_y)] \\ \cos[\xi_y - \arctan(\xi_y)] \end{cases} \quad (6.3)$$

$$|R(\xi_y)| = |r(\xi_y)| \cdot [1 + \alpha_L \cdot \Delta\Theta(\xi_y)] = r_b \cdot \sqrt{1 + \xi_y^2} \cdot [1 + \alpha_L \cdot \Delta\Theta(\xi_y)] = R_b \cdot \sqrt{1 + \xi_y^2} \quad (6.4)$$

From Equation 6.4 one yields $R_b = r_b \cdot [1 + \alpha_L \cdot \Delta\Theta(\xi_y)]$ which leads to the conclusion that, unless temperature increase is constant, there is not a single solution for the base circle radius and therefore flank geometry is no longer involute.

The effects of thermally-induced geometry distortion have been depicted in Figure 6.1, where a perfect involute including profile modifications is subject to an overall temperature increase that affects the designed profile. From this figure, and further analysis of Equations 6.3 and 6.4, several conclusions can be inferred. On the one hand, it is seen that for the case of small teeth where the roll angle difference between the start and end of the active profile is small, temperature gradients can be neglected and therefore, it can be assumed that temperature increase is constant which leads to a new involute with slightly larger base circle diameter. As a consequence, base pitch is increased and pressure angle is reduced giving rise to a new involute with different properties if compared to that originally designed. Moreover, if pinion and gear have different temperatures (e.g. in case of gear ratio other than unity), a pitch mismatch will result and therefore mechanical performance will be affected. In case of modified profiles designed to enhance contact behaviour under load, (see detail in Figure 6.1),

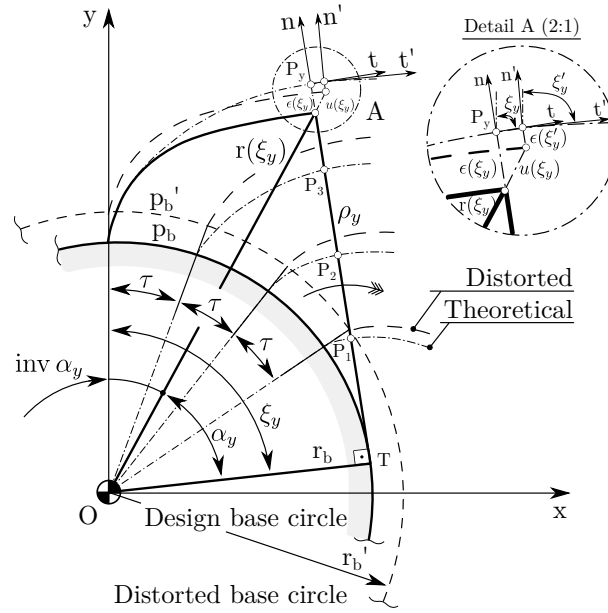


Figure 6.1: Schematic representation of thermally-induced involute geometry distortion

temperature increase will distort the latter as the modified geometry with allowance $\epsilon(\xi_y)$ at the desired design roll angle, ξ_y , is moved to a new position, ξ_y' , with a different allowance, $\epsilon(\xi_y')$. As a consequence, load distribution and transmission error behaviour will no longer be the one predicted in the design stage at the operating load.

On the other hand, if tooth depth is bigger and temperature differences are no more negligible, additional form deviations overlap to the change of pressure angle and pitch, thus altering predicted mechanical response significantly. Furthermore, in large face width gears, longitudinal temperature differences will produce variable degrees of thermal distortion along the tooth trace and therefore, local profile slope and form deviations arise in the active flank. In the case of helical gears, helix angle errors will produce a contact line mismatch that will tend to increase loads towards one of the face ends, thus increasing the probability of gear failure.

All these phenomena interact in pinion and gear and the composite effect is currently far from predictable [8]. Individually, geometry is affected by two factors: i) radial thermal deformations distorting the transverse profile and ii) helix angle mismatch due to axial expansion. Both terms are studied separately in the following sections and analytical methods are proposed to compute thermal deformations from a given temperature distribution. Finally, mesh behaviour under combined thermo-mechanical loads will be studied with the aid of the load distribution model developed in Chapter 3.

6.2.1 Profile distortion

Thermal expansion of a thin gear slice subject to a radial temperature distribution is assumed to be approximately equal to that of a hollow disc where the radial and circumferential stresses and relative displacements are ruled exclusively by the radial

position. According to Hetnarsky and Slami [165], for plane stress conditions we have:

$$u(r_y) = (1 + \nu) \cdot \frac{\alpha_L}{r_y} \cdot \int_{r_{sh}}^{r_a} [\Delta\Theta(r_y) \cdot r_y] dr + C_1 \cdot r_y + \frac{C_2}{r_y} \quad (6.5)$$

$$\sigma_{rr}(r_y) = -\frac{E \cdot \alpha_L}{r_y^2} \int_{r_{sh}}^{r_a} [\Delta\Theta(r_y) \cdot r_y] dr + \frac{E \cdot C_1}{1 - \nu} - \frac{E \cdot C_2}{(1 + \nu) \cdot r_y^2} \quad (6.6)$$

$$\sigma_{\phi\phi}(r_y) = \frac{E \cdot \alpha_L}{r_y^2} \cdot \int_{r_{sh}}^{r_a} [\Delta\Theta(r_y) \cdot r_y] dr - E \cdot \alpha_L \cdot \Delta\Theta(r_y) + \frac{E \cdot C_1}{1 - \nu} + \frac{E \cdot C_2}{(1 + \nu) \cdot r_y^2} \quad (6.7)$$

Where E , α_L and ν are material's elasticity modulus, thermal expansion coefficient and Poisson's ratio respectively, $\Delta\Theta(r_y) = \Theta(r_y) - \Theta_0$ is the temperature increase at the radial distance r_y ; and C_1 , C_2 are constants dependent on boundary conditions. For free thermal expansion of a hollow disc with inner radius equal to the shaft radius, r_{sh} , and outer radius equal to tooth tip radius, r_a , both constants are determined applying the boundary conditions $\sigma_{rr}(r_y = r_{sh}) = 0$ and $\sigma_{rr}(r_y = r_a) = 0$.

Since the temperature distribution must be integrated to obtain local thermal deformations, $u(r_y)$, a power law temperature variation between the shaft (subscript "sh") and the tooth tip (subscript "a") is assumed following:

$$\Theta(r_y) = (\Theta_a - \Theta_{sh}) \cdot \left(\frac{r_y - r_{sh}}{r_a - r_{sh}} \right)^n + \Theta_{sh} \quad (6.8)$$

The radial temperature distribution of each gear slice resulting from the thermal model is regressed under the form of Equation 6.8 and in such conditions, the integral, $\Theta(r_y)^*$, in Equations 6.5 to 6.7 can be solved analytically leading to:

$$\Theta(r_y)^* = \frac{\Theta_a}{(r_a - r_{sh})^n} \cdot \left[\frac{(r_y - r_{sh})^{(n+1)} \cdot (n \cdot r_y + r_y + r_{sh})}{(n+1) \cdot (n+2)} \right] - \frac{\Theta_0}{2} \cdot (r_y^2 - r_{sh}^2) \quad (6.9)$$

This solution is applicable to any power law radial temperature distribution and contrarily to the mechanical model presented in Chapter 3 no longitudinal coupling is considered, that is, the influence of thermal stresses in the axial direction is neglected.

Applying the boundary conditions for free thermal expansion, constants C_1 and C_2 can be solved; which can be used together with Equations 6.5 and 6.9 to compute the radial displacement, $u(r_y)$, of any point in the flank. Thus, we have:

$$C_1 = \frac{(1 - \nu) \cdot \alpha_L}{r_a^2 - r_{sh}^2} \cdot \Theta(r_y)^* \quad (6.10)$$

$$C_2 = \frac{(1 + \nu) \cdot \alpha_L \cdot r_{sh}^2}{r_a^2 - r_{sh}^2} \cdot \Theta(r_y)^* \quad (6.11)$$

Although the method has been developed for hollow discs, it can be easily extended to solid ones by setting $r_{sh} = 0$ and considering that at the centre of the solid disc displacements are zero and radial and circumferential stresses have the same value. Moreover, an additional interesting solution is derived from previous Equations that allows analysing the influence of thermal stresses on the induced geometry distortion. By setting $\sigma_{rr} = \sigma_{\phi\phi} = 0$ over the whole range of radial positions, r_y , constants C_1 and C_2 resolve into:

$$C_1 = \frac{(1 - \nu) \cdot \alpha_L}{2} \cdot \Delta\Theta(r_y) \quad (6.12)$$

$$C_2 = \frac{(1 + \nu) \cdot \alpha_L}{2} \cdot [r_y^2 \cdot \Delta\Theta(r_y) - 2 \cdot \Theta(r_y)^*] \quad (6.13)$$

Substituting the latter in Equation 6.5, the displacement of any point in the flank without considering thermal stresses is obtained:

$$u(r_y) = \alpha_L \cdot \Delta\Theta(r_y) \cdot r_y \quad (6.14)$$

Which leads to the classical solution for constant temperature increase $u(r_y) = \alpha_L \cdot \Delta\Theta \cdot r_y$.

Finally, the general parametrical representation of a spur gear involute profile with composite design modifications and thermally-distorted geometry, $R(\xi_y)$, is computed from:

$$R(\xi_y) = \left[r_b \cdot \sqrt{1 + \xi_y^2} + u(\xi_y) \right] \cdot \begin{cases} \sin[\xi_y - \arctan(\xi_y)] \\ \cos[\xi_y - \arctan(\xi_y)] \end{cases} - \hat{n}(\xi_y) \cdot \delta(\xi_y) \quad (6.15)$$

To calculate thermally-induced profile errors with respect to the theoretical involute, normal deviations, $\epsilon'(\xi_y)$, are computed similarly to intended modifications following:

$$R(\xi_y) = r(\xi_y) - \hat{n}(\xi_y) \cdot \epsilon'(\xi_y) \quad (6.16)$$

Furthermore, at a sufficiently large distance away from the base circle and assuming that local thermal deformation in steel gears is small, this equation approximates to:

$$\epsilon'(\xi_y) \approx \delta(\xi_y) + u(\xi_y) \cdot \sin[(\arctan(\xi_y))] = \delta(\xi_y) + u(\xi_y) \cdot \sin(\alpha_{yt}) \quad (6.17)$$

Which is used as thermally-induced separation in Equation 3.86 to solve load distribution and transmission error under thermo-mechanical loads.

Figure 6.2 shows a sample of the degree of distortion of FZG Type C_{mod} pinion and gear from Table 4.7 subject to different temperatures.

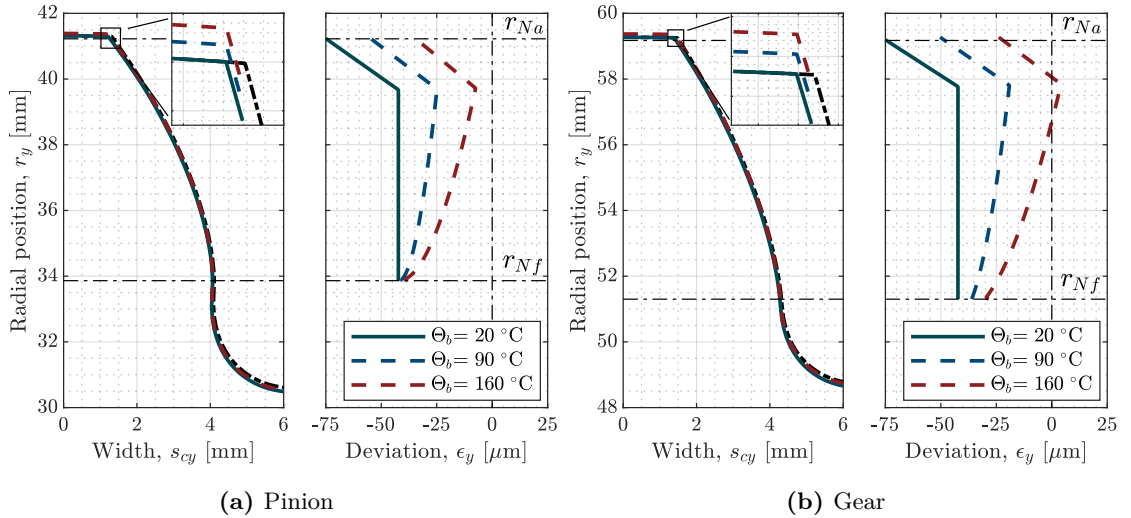


Figure 6.2: Thermally-induced flank distortion at constant temperature in FZG type C_{mod} gears

Both wheels have been designed with DIN 3967-*cd25* tolerance field [156] which results in a mean manufacturing allowance of 42 μm . The initial separation at ambient temperature is the sum of the latter and the linear tip relief, however, as temperature is increased, thermal deviations reduce the available backlash and approximate to the theoretical profile. If sufficient allowance is not provided both gears will exceed the position of the theoretical involute at high temperatures and gears may jam.

Moreover, it is observed in Figure 6.2 that the initial vertical line representing the involute profile is bent progressively indicating that pressure angle deviations arise with temperature change. If the amount of slope deviation is different in pinion and gear, contact conditions may differ from those calculated at the design stage.

The accuracy of the disc approximation applied to gear geometries has been validated with the aid of finite element simulations where a radial temperature distribution following Equation 6.8 has been applied to different spur gear geometries, gradient types and temperature levels. Results show that sufficient accuracy is obtained with maximum errors of 5% between analytical predictions and numerical results at the highest temperatures and steepest gradients. These differences are mainly located towards the root of the tooth because thermal stress concentrations arise in this region. The procedure and results are summarized in Appendix B.

In order to understand the effect of each variable on the total amount of profile deviation, a parameter analysis has been carried out and results are shown in Figure 6.3.

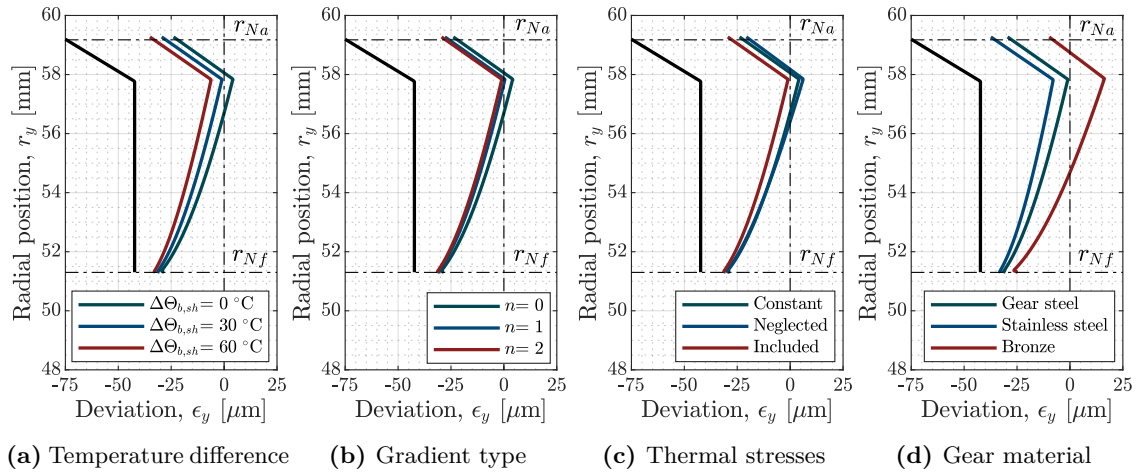


Figure 6.3: Influence of parameters on FZG type C_{mod} gear thermally-induced flank distortion

First, the temperature difference between teeth and shaft is studied for the case of the maximum teeth temperature of $\Theta_b = 160$ °C. Thermal model simulations from Chapter 5 have shown that the temperature distribution between both is approximately parabolic with a maximum temperature difference of 20 °C to 30 °C depending on the gear geometry, rotational speed and oil level. It is seen in Figure 6.3a that such a temperature profile, can result in a reduction of up to 5 μm per 30 °C difference with respect to the constant temperature case. The effect of the gradient type in Figure 6.3b is similar. Analysed temperature distributions usually follow a parabolic trend ($n=2$) and the difference with respect to the constant temperature case ($n=0$) is approximately 5 μm with the linear profile following closely. Furthermore, under such temperature distribution the effect of thermal stresses is called into question and results for the latter are depicted in Figure 6.3c. It is seen that a difference of up to 7 μm exists if thermal stresses are neglected at the maximum bulk temperature of $\Theta_b = 160$ °C and temperature difference of 30 °C with the shaft. However, for common operating temperature distributions in steel gears, the influence of the thermal gradient is not very relevant and it may be neglected. This assumption will lead to considerable simplifications in the prediction of tooth modifications to compensate for thermal distortions.

Finally, material properties are studied in Figure 6.3d. As expected, metallic gears with large linear expansion coefficient, α_L , such as bronze, experience the largest deformations but for common steel gears the differences are within the $\pm 3 \mu\text{m}$ tolerance. In this sense, even larger distortions should be expected in polymer gears, not only due to the increased thermal expansion coefficient but also for the low thermal conductivity that tends to localize the highest temperatures in the tooth region giving rise to significant gradients and producing higher distortion levels. In this work, only steel gears are analysed.

In the following sections, geometry distortion is broken down in individual terms as suggested by ISO 1328-1 standard [284] where pitch deviations, f_{pt} , coexist with profile and lead errors, named F_α and F_β respectively; which are produced by the superposition of slope deviations, f_H , and form alterations, f_f .

Pitch deviations

As it can be seen in Figure 6.4, thermal distortion produces a diameter expansion and as a consequence, tooth-to-tooth arc distance is increased for a given angular pitch, τ .

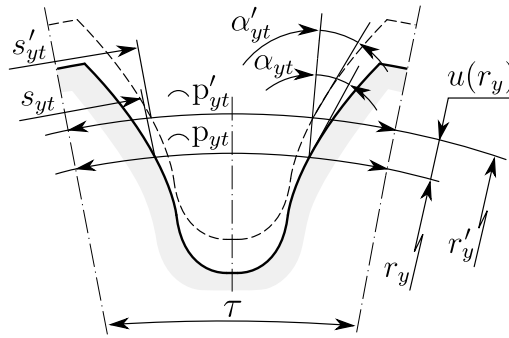


Figure 6.4: Thermally-induced pitch and pressure angle deviations

The difference between the design pitch in the transverse plane, p_{yt} , and the real one, p'_{yt} in the vicinity of the reference diameter is referred to as single pitch deviation, f_{pt} , by ISO 1328-1 standard [284]. Thus, it is calculated as:

$$f_{pt} = p'_{yt} - p_{yt} = \tau \cdot (r'_y - r_y) = \frac{2 \cdot \pi}{z} \cdot u(r_y) \quad (6.18)$$

Pitch errors are known to affect mesh behaviour [25] and maximum manufacturing deviations are limited by ISO 1328-1 standard [284] as a function of reference diameter, module and accuracy grade. Figure 6.5 depicts the influence of temperature on this parameter for different modules and number of teeth relative to the limitations of the standard. The maximum allowable deviation corresponds to the largest module or number of teeth while the minimum values are those of the smallest. In both cases, radial temperature gradients are parabolic with values increasing proportionally to bulk temperature up to a maximum difference of $30 \text{ }^\circ\text{C}$ with the shaft.

It is observed that at common operating bulk temperatures (usually above $80 \text{ }^\circ\text{C}$), pitch distortion exceeds ISO 1328-1 standard limitations for the reference accuracy grade of 5. Moreover, depending on the module, pitch deviation doubles and even triples design limitations. This is explained by the size of the reference diameter which is ruled

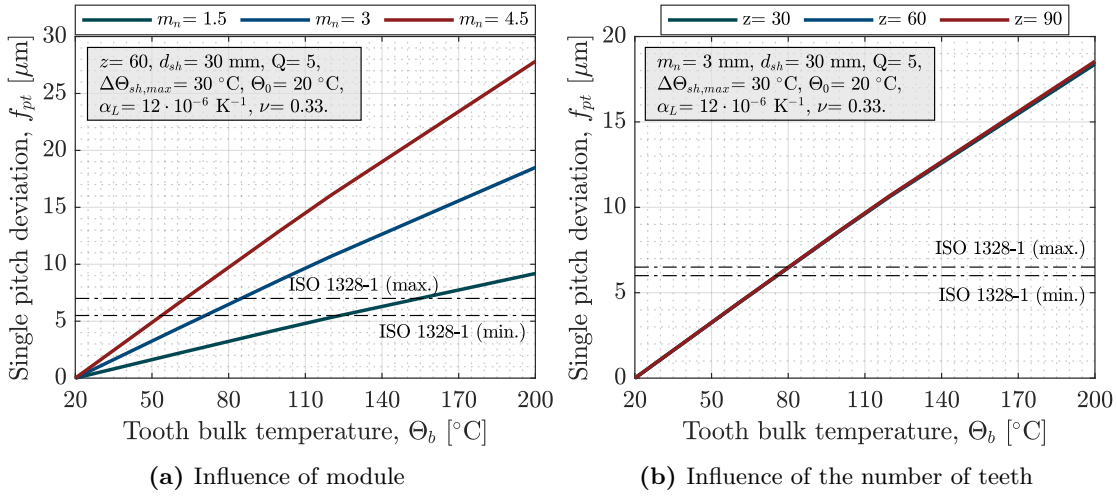


Figure 6.5: Influence of temperature, normal module and number of teeth on pitch deviations

by the module at a fixed number of teeth, that is, fixed angular pitch. Big diameters distort more and therefore, they easily exceed the maximum allowed value. On the contrary, for a given module, the increase in the number of teeth in Figure 6.5b does not affect as much because angular pitch decreases and diameter increases, both in the same proportion, and therefore they cancel each other. Furthermore, it is remarked that the slope of the curves is almost linear which is explained by temperature gradient between teeth and shaft which is rather small.

At this point, it is to be noted that ISO 1328-1 standard limitations are not designed for uniform pitch deviations resulting from temperature increase, but for variable pitch errors in the circumferential direction which arise as the result of the manufacturing process inaccuracies. Therefore, ISO 1328-1 standard allowances should be reinterpreted for thermally-induced deviations and they should rather be applied to relative pitch errors resulting from temperature differences between pinion and gear. According to Figure 6.5, the latter might be in the order of 5 μ for a maximum temperature gradient of 30 $^{\circ}\text{C}$ and the largest module. If this value is compared to the maximum allowance it is still acceptable.

Finally, it is interesting to compare the influence of gear teeth accuracy grade with the pitch deviations relative to the ISO 1328-1 recommendations. Figure 6.6 summarizes the latter and it shows that gears manufactured with high accuracy are more sensitive to temperature increase as they can exceed design limits at low temperatures. At this high quality levels thermally-induced geometry distortions should be evaluated together with manufacturing errors as total pitch deviations resulting from the addition of both effects can lead to uneven load distribution and malfunctioning of the gear mesh.

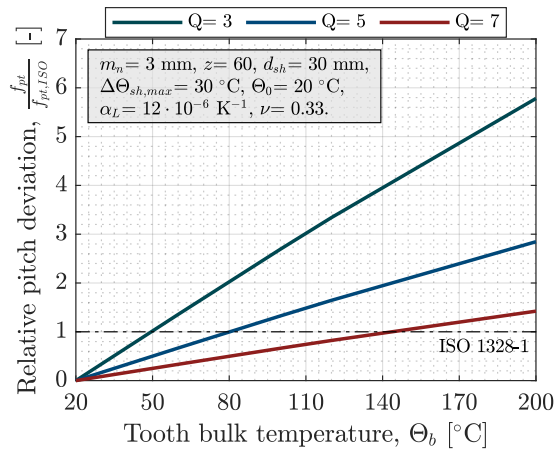


Figure 6.6: Influence of temperature and accuracy grade on relative pitch deviations

Total profile deviations

According to ISO 1328-1 standard [284], total profile deviation in the transverse plane is the perpendicular distance between to design traces enclosing the real profile over the evaluation length; which is equal to 92% of the total active length measured from the end of the active profile (characteristic point E). Total deviation, F_α is the result of the superposition of two different errors: i) profile slope deviations, $f_{H\alpha}$, and ii) profile form errors, $f_{f\alpha}$. In the case of thermally-induced geometry distortions, the former is the consequence of the overall diameter growth due to temperature increase (see Figure 6.4) and the latter is the result of thermal gradients altering the involute profile locally.

Figure 6.7 depicts the influence of basic design parameters on thermally-induced total deviation. In all cases, gear teeth bulk temperature and thermal gradients inside the gear body are increased progressively with maximum teeth temperatures of 200 °C and thermal gradients up to 30 °C between teeth and shaft with a parabolic trend. The length of the active profile for the evaluation of total errors is computed considering that the gear is mated with a rack as suggested by ISO 1328-1 standard [284] and the position and slope of the mean profile trace is found by the least squares method.

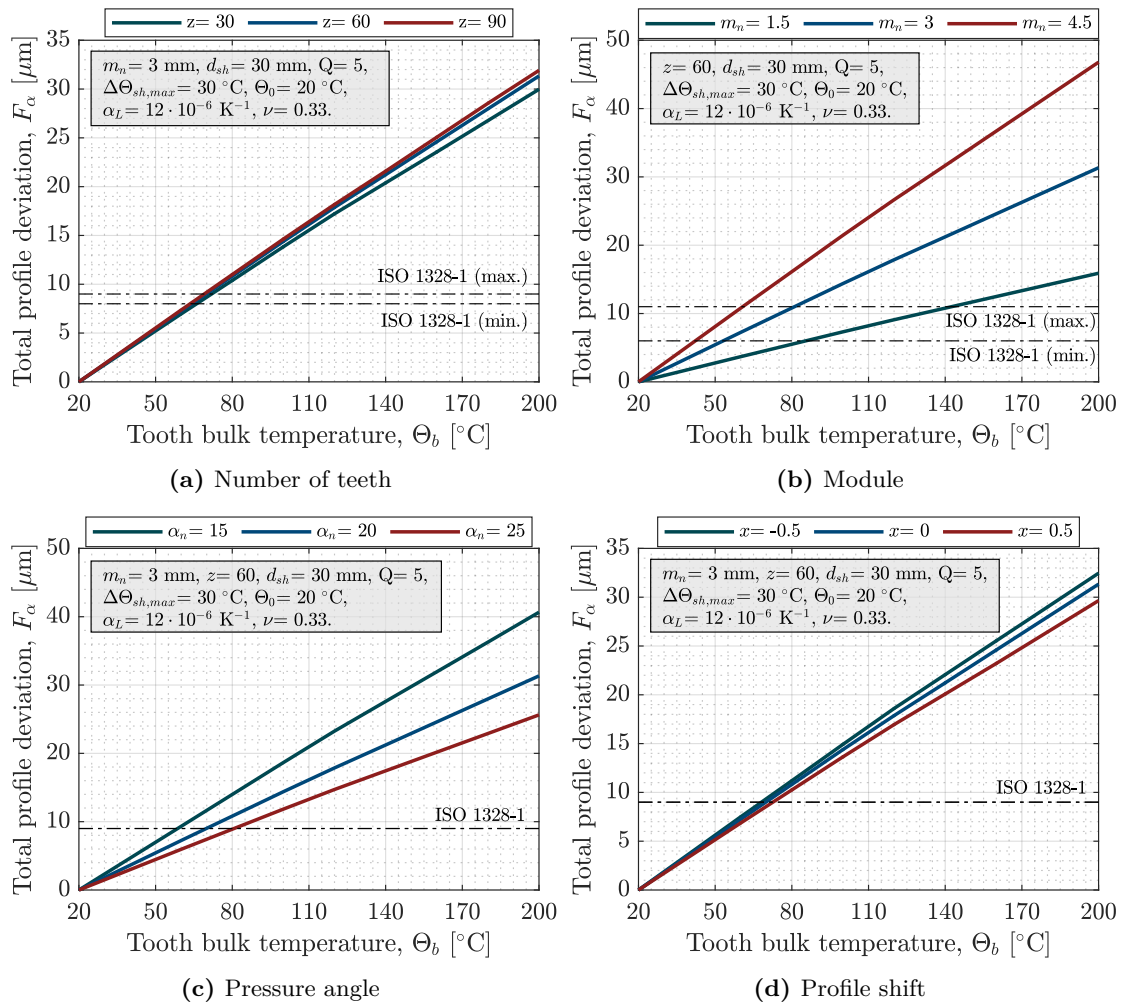


Figure 6.7: Total profile deviations as a function of initial design parameters

Under the aforementioned thermal conditions, temperature rise produces a significant increase of the total deviation which exceeds ISO 1328-1 design limitations at medium temperatures (approximately 80 °C) similarly to pitch deviations. In all cases an almost linear trend with temperature rise is maintained similarly to pitch deviations.

The influence of normal module and pressure angle stands out over the rest, as they produce a larger variation of total deviation with temperature rise, both approaching 20 μm to 30 μm at common operating temperatures. On the one hand, higher normal module indicates larger diameters, hence, higher distortions, but also increased profile evaluation lengths; as a consequence, total profile deviation between the start and end of the active profile is bigger. On the other hand, pressure angle decrease produces an increase in total profile deviation for a fixed module and number of teeth. This is explained by the relation between the base circle diameter increase and profile inclination, which are interrelated by $\Delta d_b \approx -\Delta\alpha_y \cdot d_b \cdot \tan(\alpha_n)$ [159]. From this equation, it is deduced that base circle diameter expansion leads to a different inclination error depending on the design pressure angle, which is reflected in the total profile deviation in Figure 6.7c.

In the analysed variable range, total profile deviation, F_α , is affected mostly by profile slope deviations, $f_{H\alpha}$. The latter is calculated as the perpendicular distance between two design traces that intersect the mean profile trace of the distorted flank. It happens that, in all analysed test cases, the perpendicular distances yielding the total profile error and the slope deviation is almost identical. It has been found that, approximately 99.5 % of the distortion is due to the change in profile slope. Only in the case of very large modules ($m_n \gg 4.5$ mm) and/or abrupt thermal gradients ($n \gg 2$) profile form errors, $f_{f\alpha}$, might become significant.

Profile slope errors are explained by the increase in base circle diameter (see Figure 6.6) which necessarily decreases pressure angle, to cope with the equation $d_b = m_n \cdot z \cdot \cos(\alpha_n)$ at a fixed module and number of teeth. This conclusion has also been addressed by several authors [24, 26, 159], and more recently, Kashyap [140] has measured experimentally the influence of temperature on plastic gear profile slope deviations confirming this trend. Therefore, in order to avoid pressure angle mismatch between pinion and gear subject to different temperatures, profile slope modifications should be applied to correct the expected uneven load distribution and transmission error patterns.

Finally it is interesting to remark in Figures 6.2 and 6.3 that single pitch error and total profile deviation can be interrelated provided that form errors are neglected. In such conditions, profile diagram plotted against the roll angle is a linear curve and pitch errors calculated in the reference diameter can be translated into profile slope errors and vice-versa. This relation allows to predict pinion and gear individual modifications to enhance contact behaviour under thermo-mechanical loads (equations in section 6.5).

6.2.2 Helix distortion

Thermal expansion is three-dimensional and therefore it is not limited to the radial direction in the transverse plane as assumed in section 6.2.1; it also affects the longitudinal direction and, as a consequence, helix angle is distorted in helical gears. Moreover, due to the temperature concentration in the centre of the face width, dilatation is not uniform along the tooth trace which gives rise to pitch cylinder barrelling [18].

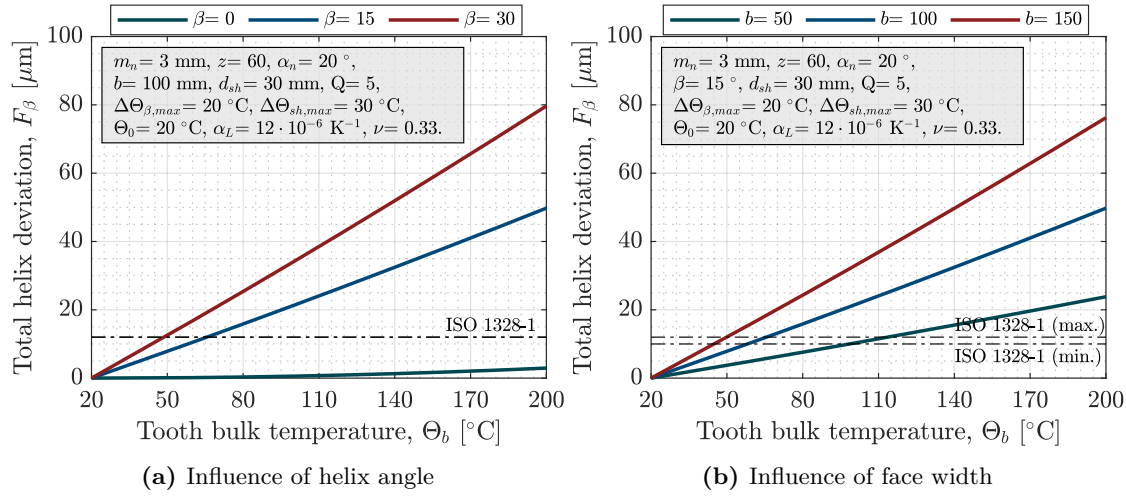


Figure 6.9: Influence of temperature, helix angle and face width on total helix deviations

Additionally, in order to analyse the effect of temperature concentration in the centre of the face width a longitudinal parabolic temperature gradient is simulated, with a maximum difference of 20°C between the tooth centre and the face ends for a reference face width of 100 mm .

Two parameters are studied in Figure 6.9, the influence of face width and that of helix angle. In general, it is observed that the amount of total deviation exceeds ISO 1328-1 standard limitations; moreover, the values double and nearly triple those of total profile deviations, F_α , indicating that thermally induced helix slope errors can be harmful. Helix angle and face width increase have both the same proportional effect on total helix deviations, which is explained by Equation 6.22 indicating that most of the total helix distortion is due to slope deviation, $f_{H\beta}$. This is additionally supported by results at helix angle $\beta = 0^\circ$ where the slightly increasing values are due to form deviations resulting from longitudinal temperature gradient. If the same amount of form error is overlapped in the rest of the cases it is concluded that total deviations are mainly due to slope errors.

On the other hand, the steep slope of the curves points out that temperature differences between pinion and gear will lead to a significant helix mismatch and therefore specific load will be increased towards one of the face ends. For instance, it is seen in Figure 6.9b that in case of a medium helix angle ($\beta = 15^\circ$) but sufficiently large face width, a temperature difference between pinion and gear of 20°C leads to an helix mismatch of $10 \mu\text{m}$ which is enough to produce a noticeable increase in tooth root stress and accelerate breakage.

As described earlier, form deviations are not the main cause of thermal distortion, but its values are higher than the corresponding ones in the profile direction where it was shown to be negligible; thus, their effect is further studied. Thermal model simulations show that if mesh is aligned, temperature distribution in the longitudinal direction is symmetric, that is, front and back ends are subject to the same temperature and maximum value is located in the middle of the face width (if no axial oil pumping action is considered). Temperature profile is approximately parabolic and therefore a parabolic crowning would result from the uneven expansion in the base tangent plane. Figure 6.10 depicts the cumulative distortion of the design helix subject to a slope deviation and form deviation.

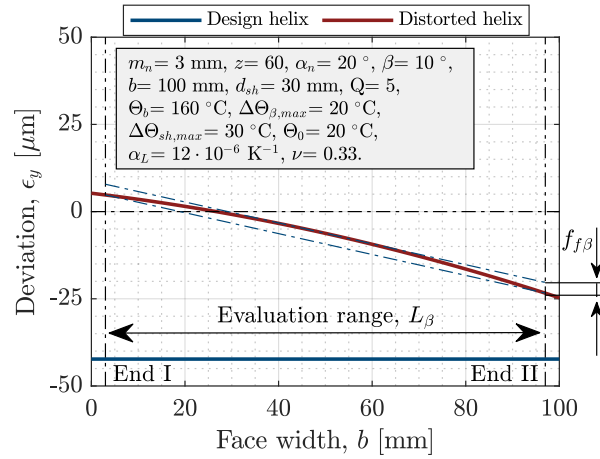


Figure 6.10: Definition of helix form deviation according to ISO 1328-1

According to ISO 1328-1 standard [284] the evaluation range in the longitudinal direction is equal to the length of tooth trace shortened by 5% of the face width at each end, and the mean helix is found by the least squares method. Under this conditions form deviation is defined as the distance between two duplicates of the mean helix which are tangent to the distorted profile on each side (see parameter $f_{f\beta}$ in Figure 6.10). If the variation of this parameter is analysed as a function of temperature, helix angle and face width, it is observed that values are in the order of a few microns for common operating temperatures and they do not exceed manufacturing limitations, even at the highest temperatures.

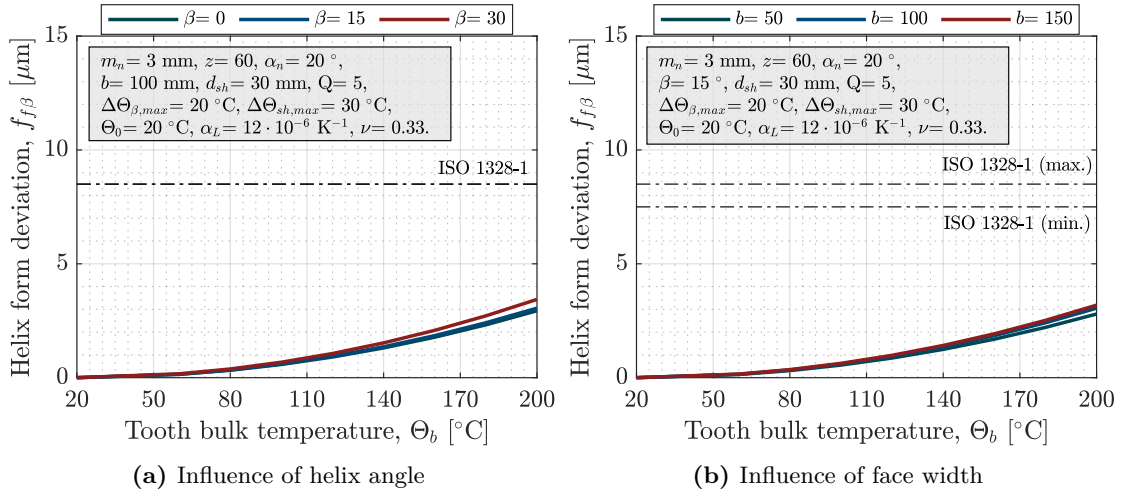


Figure 6.11: Influence of temperature, helix angle and face width on helix form deviations

Moreover, from the observation of Figure 6.9 it is concluded that the amount of form deviation, $f_{f\beta}$, is directly related to the maximum temperature difference along the tooth trace and it does not depend on the size of the face width, which is consistent with results in Figure 6.11b. However, face width does affect the curvature radius of the thermally induced longitudinal crowning and therefore contact conditions under load are expected to be modified.

If thermally induced crowning is modelled as a parabolic curve $\Delta\epsilon(z_y) = A \cdot z_y^2 + B \cdot z_y + C$ resulting from the parabolic temperature distribution, local curvature is calculated as:

$$k(z_y) = \frac{|f''(z_y)|}{\left(1 + [f'(z_y)]^2\right)^{\frac{3}{2}}} = \frac{2 \cdot A}{\left(1 + [2 \cdot A \cdot z_y + B]^2\right)^{\frac{3}{2}}} \quad (6.23)$$

Moving the system of coordinates to the point of maximum distortion in the middle of the face width, we have $A = 4 \cdot [u_{max} \cdot \sin(\alpha_{yn})] \cdot b^{-2}$, $B = 0$ and $C = 0$. Therefore, curvature radius, $R = 1/k$, at the centre of the face width ($z_y = 0$) and in the base tangent plane is:

$$R(z_y = 0) = \frac{1}{2 \cdot A} = \frac{b^2}{8 \cdot u_{max} \cdot \sin(\alpha_{yn})} = \frac{b^2}{8 \cdot r_y \cdot \alpha_L \cdot \Delta\Theta_{\beta,max} \cdot \sin(\alpha_{yn})} \quad (6.24)$$

Where r_y is the radial distance, b is the face width, α_{yn} is the local normal pressure angle, α_L is the thermal expansion coefficient and $\Delta\Theta_{\beta,max}$ is the maximum temperature difference along the face width relative to tooth ends. For any other axial position, inverse of Equation 6.23 applies.

Tooth trace crowning is usually beneficial as it tends to minimize the effects of mesh misalignments by concentrating load towards the centre of the face width. However, gear mesh between a crowned pinion and wheel with two principal curvatures in the profile and longitudinal directions is no longer a line contact and therefore, Hertz's contact stress equations in Section 3.3.3 should be modified to account for elliptical bearing patterns. An increase in contact pressure is expected if crowned geometry is considered but if one analyses the order of magnitude of thermally-induced barrelling, it is not expected to produce significant alterations of the initial contact stress. On the contrary, the amount of helix slope deviations is far from negligible and it can be detrimental, thus lead modifications should be applied in pinion and gear to avoid undesired load concentrations at tooth edges.

6.3 Thermal effects on mesh behaviour

As it has been described previously thermal distortion produces a diameter growth and therefore basic mesh parameters are affected along with the profile and helix geometries themselves. Among others, the position of the start/end of the active profile is shifted, separating distance, normal backlash and root clearance are reduced and composite parameters such as reduced curvature radius are altered. Therefore, in order to better understand mesh behaviour under the effect of thermally-induced distortions, the parameter analysis in the following section will be separated in no-load terms and load-related variables.

For this purpose FZG type C-PT gear pair will be used. The modified version has already been presented in Table 4.7, but no relief will be applied in this section unless otherwise stated. The geometry is characterized by being a reduction spur gear pair with narrow face width, therefore, longitudinal gradients can be neglected and only radial temperature distribution is considered. Three torque levels according to ISO 14635 [285] are selected: i) low (KS-5= 94.1 Nm), ii) medium (KS-7= 183.4 Nm) and ii) high (KS-9= 302 Nm). Overall temperature levels and gradients are set according to the thermal simulation results which have been experimentally measured by [28]. Finally, initial gear geometry and temperature will be slightly varied to show the effect of specific distributions on mesh behaviour (e.g. large face width with longitudinal gradient).

6.3.1 No-load transmission error and backlash

Figure 6.12 shows the effect of diameter growth on clearance decrease. A radial expansion of the pinion is translated into a normal backlash decrease which affects gear positioning during rotation. This way, no-load transmission error behaviour and that of backlash are closely related, and therefore, the latter should be analysed first.

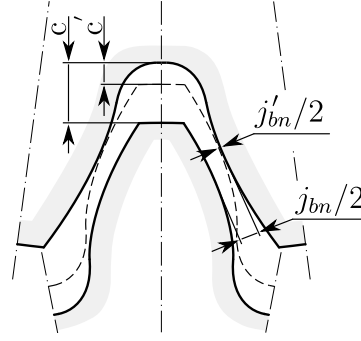


Figure 6.12: Thermally-induced clearance decrease

Moreover, if thermally-induced normal backlash decrease exceeds initially manufactured clearance as computed by Equation 3.17, mesh jamming will occur. To avoid this situation, the latter must be greater than the former in all the potential meshing points in the base tangent plane. This condition can be stated as follows:

$$|\epsilon_1 + \epsilon_2| > |\Delta\epsilon_1 + \Delta\epsilon_2| - \Delta\epsilon_H = \Delta j_{bn} \quad (6.25)$$

Where the initial clearances in the normal direction, $\epsilon_{1,2}$, of pinion and gear are the sum of manufacturing allowances, $\kappa_{1,2}$, and design modifications, $\delta_{1,2}$ (as shown in Figure 3.9), thermally-induced deflections, $\Delta\epsilon_{1,2}$, are calculated following Equation 6.19 and the term $\Delta\epsilon_H$ accounts for the backlash increasing effect of housing expansion which can be computed from:

$$\Delta\epsilon_H = u_H \cdot \sin(\alpha_{wt}) \cdot \cos(\beta_b) \quad (6.26)$$

Therefore, for each point, $P_y(r_y, z_y)$, in the meshing plane the following condition must be satisfied to avoid gear jamming.

$$\frac{1}{\cos(\beta_b)} \cdot \underbrace{[\epsilon_1 + \epsilon_2]}_{\text{Initial allowance}} > \underbrace{[u_1 \cdot \sin(\alpha_{yt,1}) + u_2 \cdot \sin(\alpha_{yt,2})]}_{\text{Radial dilatation}} \pm \underbrace{[\Delta_{x,1} - \Delta_{x,2}]}_{\text{Axial growth}} - \underbrace{u_H \cdot \sin(\alpha_{wt})}_{\text{Housing expansion}} \quad (6.27)$$

Where $u_{1,2}$ represent the radial expansion of each gear slice calculated with Equation 6.5, $\Delta_{x1,2}$, reflects the influence of the overall longitudinal dilatation computed following Equation 6.22 and $u_H = a_w \cdot \alpha_H \cdot \Delta\Theta_H$ is the centre distance thermal growth due to the temperature increase of the housing. Note that the left hand side of Equation 6.27 is similar to the no-load transmission error as defined in Section 3.2.2. Therefore, NLTE can also be used to detect gear jamming by identifying the conditions that produce NLTE=0 in any point of the line of action. Both parameters, backlash and NLTE will be analysed in the following sections.

Backlash behaviour

Figure 6.13 shows the influence of temperature increase, gradients and tolerance field on backlash behaviour in the working pitch circle and relative to the initial manufacturing allowance. The influence on the reduction of backlash of elastic deformations, individual geometry deviations or centre distance tolerances is not considered and only the effect of temperature increase is depicted. In case of standard manufacturing allowances for mechanical applications (see tolerance field for DIN3967-*cd25* [156]) it is observed that tooth bulk temperature increase affects backlash reduction strongly, at an approximate rate of 25% reduction per 50°C increase.

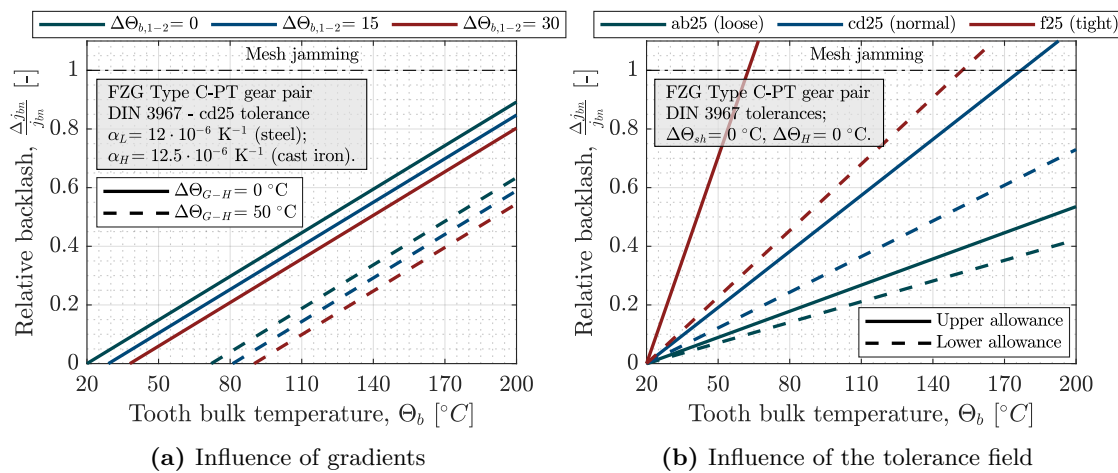


Figure 6.13: Influence of temperature and manufacturing allowances on mesh jamming probability

Temperature differences between pinion and gear shift the initial curve slightly, approximately 5% per 15°C difference, while gradients with the housing affect more severely, 25% per 50°C. Therefore, for standard tolerances, if the composite effect of pinion, gear and housing is considered, it is unlikely that mesh jamming will occur, even at the highest temperatures. However, for tight allowances (see Figure 6.13b) the probability of mesh jamming is increased exponentially. According to Niemann [33] tolerance field *f25* is suited to machine tool applications and *ab25* to turbo gears. The former might collapse with small temperature variations as the slope of the curve is very steep, while the latter is designed to avoid such situations because it only reaches half the initial allowance at the maximum bulk temperature. If the effect of housing and temperature differences between pinion and gear are considered as in Figure 6.13a mesh jamming probability is delayed. Furthermore, the additional influence of load tends to increase backlash, therefore, the same result would be expected and mesh jamming probability would be reduced. As a consequence, one would expect jamming to occur under conditions of tight backlash, small elastic deflections and high temperatures so that the influence of thermal distortion prevails over mechanical loads.

In general, it is concluded that applications where high positioning and temperature requirements exist, might suffer from mesh jamming, and therefore special attention needs to be paid. Moreover, it is also observed that if pinion, gear and housing temperatures can be predicted with accuracy, initial design backlash can be reduced considerably, which favours the reduction of the overall transmission error between pinion and gear.

No-load transmission error

As it has been described previously, temperature increase produces a backlash decrease and this has a definite impact on transmission error mean level. Moreover, thermally-induced geometry errors predicted in section 6.2.1 are also observable through this parameter. Figure 6.14, shows the relation between temperature increase, gradients and relative profile errors on no-load transmission error of FZG type C-PT gear pair.

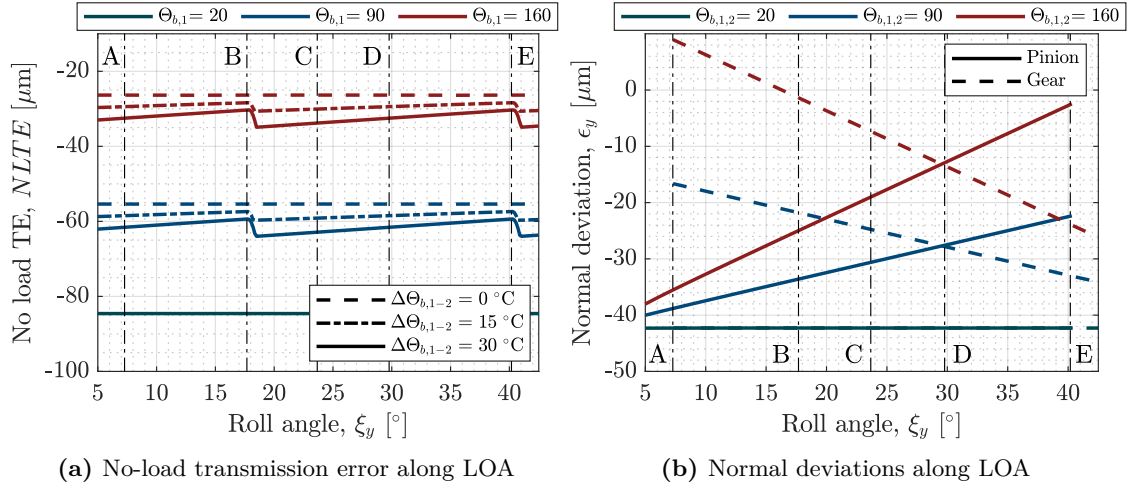


Figure 6.14: Influence of bulk temperature increase and gradients on no-load transmission error and normal deviations along the line of action

For equal pinion and gear temperatures in Figure 6.14a the mean level of transmission error is shifted by an amount equal to the backlash decrease, $\Delta_{jbn} = \Delta\epsilon_1 + \Delta\epsilon_2$, as calculated by the right hand side of Equation 6.27 in the working pitch circle. However, when temperature gradients exist between pinion and gear, the amount is reduced slightly and profile deviations start to be noticeable showing a change in pressure angle with an approximate step of $5 \mu\text{m}$ from double to single teeth contact regions. This is due to the profile slope difference resulting from uneven thermal expansion which is explained by Figure 6.14b. When bulk temperatures of pinion and gear are constant, total profile deviations are strictly due to a change in pressure angle which is translated into a linear curve when plotted against the roll angle. At the same temperature, the slope of the curve is equal for pinion and gear and therefore they compensate each other resulting in a constant transmission error in Figure 6.14a. On the contrary, when a temperature gradient exists between both, a relative slope deviation arises which gives rise to a non-uniform transmission error along the line of action. Similarly, any kind of thermal gradient within the gear body will reduce the total thermal deformation as well and the total shift in transmission error mean level will be reduced as a consequence. The described behaviour will be overlapped on the loaded transmission error diagram as shown in the next section.

This relation between temperature, profile slope, backlash and NLTE can be demonstrated analytically. For constant temperature increase we have:

$$\Delta\epsilon(\xi_y) \approx u(\xi_y) \cdot \sin(\alpha_{yt}) = [r_b \cdot \sqrt{1 + \xi_y^2} \cdot \Delta\Theta_b \cdot \alpha_L] \cdot \sin[\arctan(\xi_y)] \quad (6.28)$$

Applying inverse trigonometric relations: $\sin[\arctan(\xi_y)] = \xi_y \cdot (1 + \xi_y^2)^{-1/2}$. Therefore, Equation 6.28 can be rewritten as:

$$\Delta\epsilon(\xi_y) \approx \Delta\Theta_b \cdot \alpha_L \cdot r_b \cdot \xi_y = \alpha_L \cdot \Delta\Theta_b \cdot \rho_y = \alpha_L \cdot \Delta\Theta_b \cdot \overline{T_n P_y} \quad (6.29)$$

Equation 6.29 shows the described linear behaviour with the roll angle and computing backlash decrease along the line of action for equal pinion and gear temperatures we have:

$$\Delta_{jbn} = \Delta\epsilon_1 + \Delta\epsilon_2 = \alpha_L \cdot \Delta\Theta_b \cdot \overline{T_1 P_y} + \alpha_L \cdot \Delta\Theta_b \cdot [\overline{T_1 T_2} - \overline{T_1 P_y}] = \alpha_L \cdot \Delta\Theta_b \cdot \overline{T_1 T_2} \quad (6.30)$$

Which is constant for a given gear pair with the same material and equal temperatures, thus proving that under these conditions NLTE diagram is only shifted with respect to the initial behaviour. If housing expansion as computed by Equation 6.26 is considered together with this relation the amount of total backlash change is reduced maintaining the constant trend along the line of action.

Premature contact

The change of profile and helix slopes, together with the increase of tip diameter and pitch, also affects the position of characteristic points along the line of action (points A to E) and similarly to load-induced contact path increase, the real start/end of the active profile may also be shifted. These parameters are also geometry-dependent in the same way as NLTE behaviour, and therefore, they are analysed in this section.

The real length of the path of contact is ruled by tooth stiffness and separating distance (see section 3.2.2) and thermally-induced geometry distortions are expected to affect the latter. Therefore, the influence of temperature increase on premature contact should be studied. Figure 6.15a shows the overall behaviour of separating distance. Bulk temperatures are constant and there is no difference between pinion and gear; this way, thermal deformations are maximum and premature contact effects are more visible. To simplify the analysis, all thermal expansion effects have been modelled as if gears were generated with an increased module similarly to Kashyap [140].

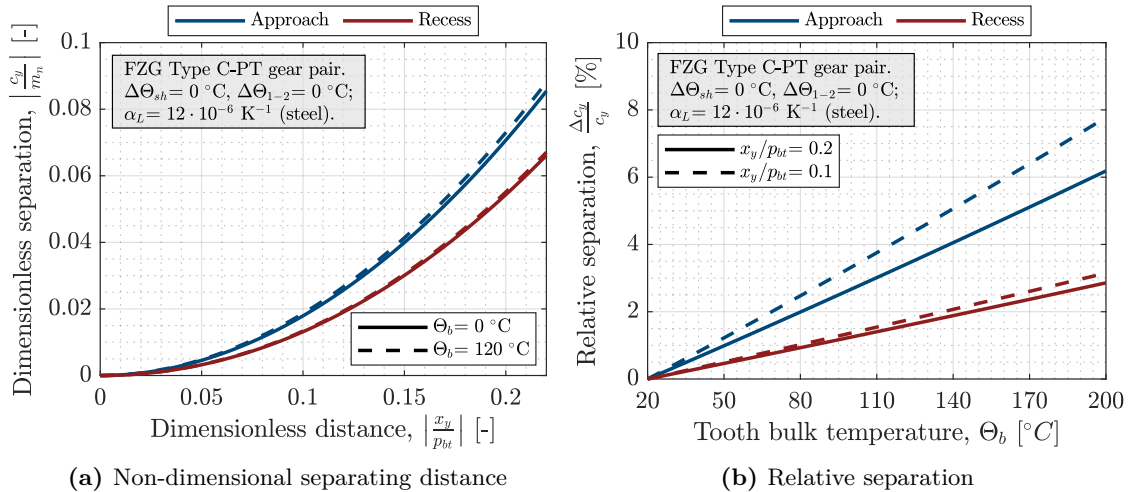


Figure 6.15: Influence of temperature on separating distance

It is observed in Figure 6.15a that approach and recess separating distances are almost unaffected by temperature increase, hence, no significant alteration of premature contact is expected. If the separation behaviour with respect to ambient temperature is analysed in Figure 6.15b a 2% to 4% increase is observed in recess and approach paths of contact respectively. Besides, it is to be noted that the effect of temperature at very small distances ($x_y/p_{bt} = 0.1$) is more pronounced in approach than in recess. This is explained by the pitch error induced by temperature increase which is reflected in the new module. When approach separating distance is calculated, the gear is assumed held stationary and the pinion virtually rotates until contact occurs. Thus, when thermally-induced pitch growth exists, the pinion needs further rotation to reach contact thus increasing separating distance in the line of action. In the recess calculation, the inverse situation exists, pinion is assumed stationary and gear rotates. The radius of the latter being bigger than that of the former the rotation needed to overcome pitch growth is reduced. As a consequence, separating distance in approach is more sensitive to temperature than in recess. In any case, the order of magnitude of the thermally-induced separation is very small compared to the initial geometry and premature contact phenomena is not expected to be altered significantly. This situation will be validated in load distribution diagrams in section 6.3.2.

6.3.2 Thermo-mechanical behaviour

The composite effect of thermally induced geometry deviations and load is studied next. As it has been described earlier, temperature increase mainly affects profile and helix angles giving rise to a slope mismatch when pinion and gear are subject to different temperatures. Therefore, FZG type C-PT spur gears are only affected by pressure angle deviations and the influence of the latter on load distribution, transmission error and stress behaviour is analysed in this section. The analytical results shown in the following have been validated with a finite element model and both have been recently published in two conference papers [286, 287].

Load distribution

Figure 6.16 shows the influence of bulk temperature and gradients between pinion and gear on the load distribution diagram. As expected, constant and equal temperature for both gears give rise to the same pressure angle error and compensate each other producing the same diagram. However, when thermal gradients exist between pinion and gear the amount of deviation is different and uneven load distribution arises. For the considered gear pair, unit load is reduced approximately 10 N/mm per 15 °C temperature difference in Figure 6.16b. As no thermal gradient exists between tooth tip and shaft, only profile slope error arises and therefore the lines in the double teeth contact region are perfectly parallel. In any case, it has been shown that common operating temperature distributions have small gradients, hence, form deviations are negligible.

Moreover, small differences in premature contact are observed in Figure 6.16a. Increasing temperatures produce larger pitches as shown in the previous section; but they also increase deviations along the profile, with maximum values found at the tip. As a consequence, teeth come into contact before expected. It will be shown later in this chapter that both effects, pitch errors and profile slope deviations are related.

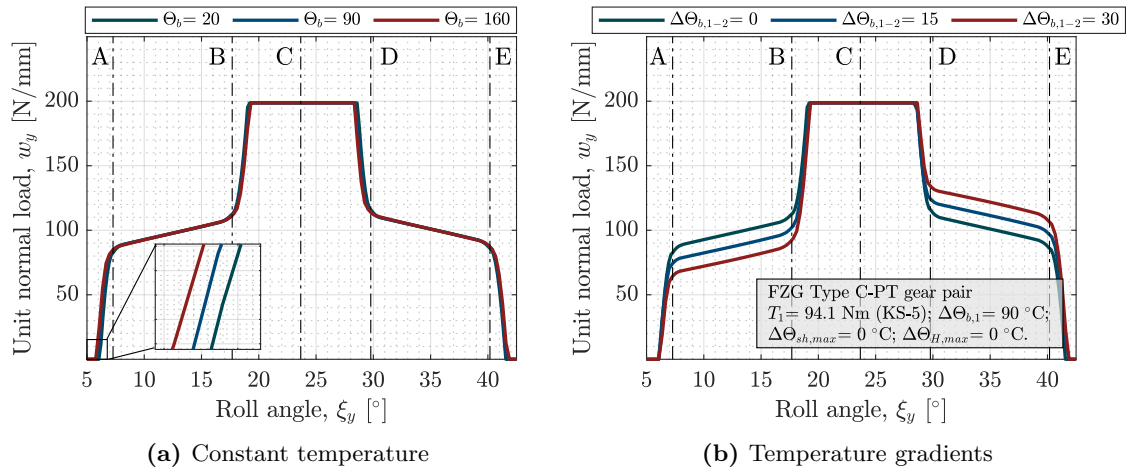


Figure 6.16: Influence of bulk temperature and gradients on load distribution at constant torque

Figure 6.17 shows the influence of temperature on the relative increase of the contact length with respect to the influence of load. It can be concluded that the thermal effect implies approximately 2 % increase for the maximum bulk temperature while the lowest torque level (KS-5) implies 8 % increase. Note that the order of magnitude of this effect is very close to that of the no-load separating distance (see Figure 6.15b) indicating that both are inter-related.

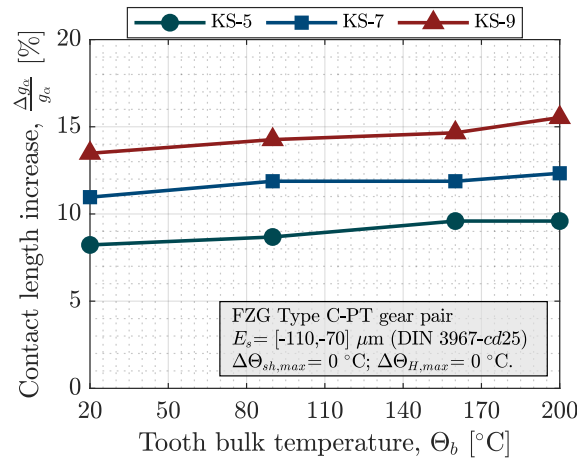


Figure 6.17: Influence of temperature and load on relative contact length increase

In order to analyse the influence of thermally-induced barrelling, the narrow face width of FZG type C-PT gear pair is modified to introduce longitudinal gradients. Face width is doubled and temperature difference between tooth ends and centre is 10°C for pinion and gear which are subject to constant bulk temperatures of 60 °C and 90 °C respectively. The effects of this temperature field on 3D load distribution are depicted in Figure 6.18a. As expected, it is observed that the barrelling effect tends to concentrate load in the middle of the face width. If longitudinal temperature gradients are small, thermally-induced crowning is not significant and can even be beneficial to compensate mesh misalignment. However, in case of large longitudinal thermal gradients contact stresses may be affected by excessive crowning and accelerate tooth failure.

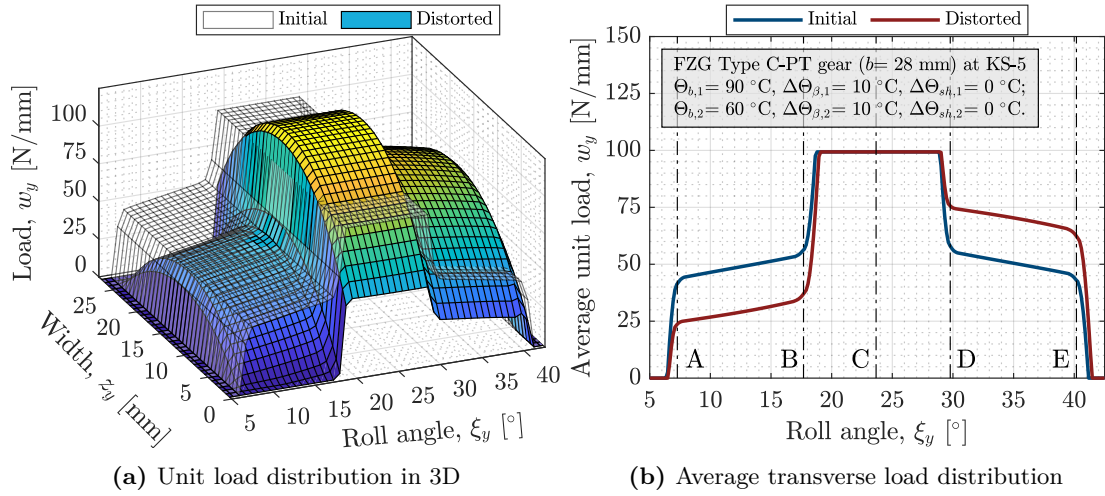


Figure 6.18: Influence of longitudinal thermal gradient on load distribution at constant torque

If the average unit loads along the line of action are analysed in Figure 6.18b, it is observed that the difference in normal load between the initial and distorted diagrams is approximately $20 \mu\text{m}$ which is the corresponding value for a 30 °C temperature difference between pinion and gear as shown previously. However, apparently, the effect of thermal distortion is more visible in Figure 6.18b than in the preceding Figure 6.16b. This is explained by the increased face width which leads to a reduction of the maximum unit load to half the original value in Figure 6.16a while the difference between initial and distorted profiles in the double teeth contact region remains equal; as a result, the visual effect is enhanced. This leads to the conclusion that when elastic and thermal deformations coexist the influence of thermal distortion is dominant at low loads while the elastic deflections prevail at high torques. The relation between both deformations defines the shape of the load distribution diagram.

Furthermore, the temperature distribution described in Figure 6.18 leads to an approximate crowning of $1.5 \mu\text{m}$ for the pinion and $2.2 \mu\text{m}$ for the gear which is not significant if considered individually but leads to a composite crowning of $3.7 \mu\text{m}$ altering load distribution diagram. These values are somewhat higher than the form deviations predicted at $\beta = 0$ in Figure 6.11. This is due to the fact that bulk temperatures in the current case are assumed constant for each thin slice and therefore radial expansion is not affected by thermal stresses, thus, producing maximum deformations. On the contrary, thermal distortion simulations in Figure 6.11 are dependent on radial gradients that lead to thermal stresses limiting the amount of deformation. This behaviour is further described by Figure 6.19 where both situations are compared in the longitudinal and transverse planes. If gradients in the profile direction are neglected, thermal crowning effect dominates longitudinal load distribution increasing unit load by 22% at the tooth centre while decreasing it approximately 50% at tooth ends. This behaviour is overlapped to profile distortions in the transverse load distribution shown in Figure 6.19b leading to a considerable change of the load share in the double teeth contact region of the recess path of contact. However, if profile and longitudinal thermal gradients coexist, deformations are reduced and unit load in the centre increases only 8% with respect to the

initial state. The composite effect of profile and longitudinal gradients in the transverse direction reduces non-uniformities. Thus, the accurate prediction of three-dimensional load distribution requires including this effect on computed deviations.

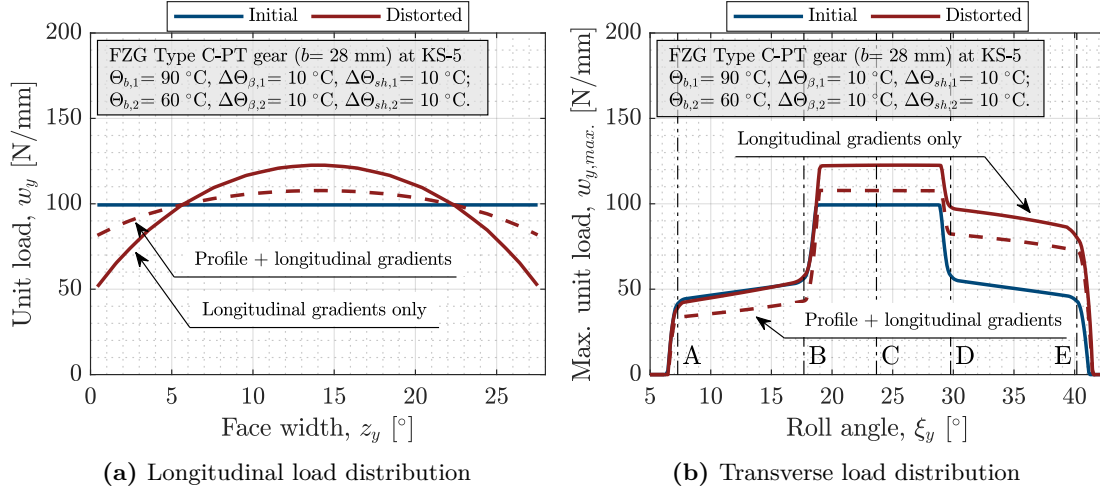


Figure 6.19: Influence of composite longitudinal and radial thermal gradients on load distribution

In general, it is concluded that unit load along the face width of spur gears is ruled by the thermally-induced barrelling effect resulting from thermal gradients and load share in the transverse direction is affected by profile slope mismatch due to temperature differences between pinion and gear. Furthermore, in helical gears, the helix slope deviation is overlapped and load distribution can be affected even more. This situation will be analysed in the test case in section 6.4.

Transmission error

It has been shown previously that NLTE is mainly influenced by backlash decrease, therefore, behaviour under load will be affected accordingly and previously described uneven load distribution features will be reflected in the TE diagram as shown in Figure 6.20.

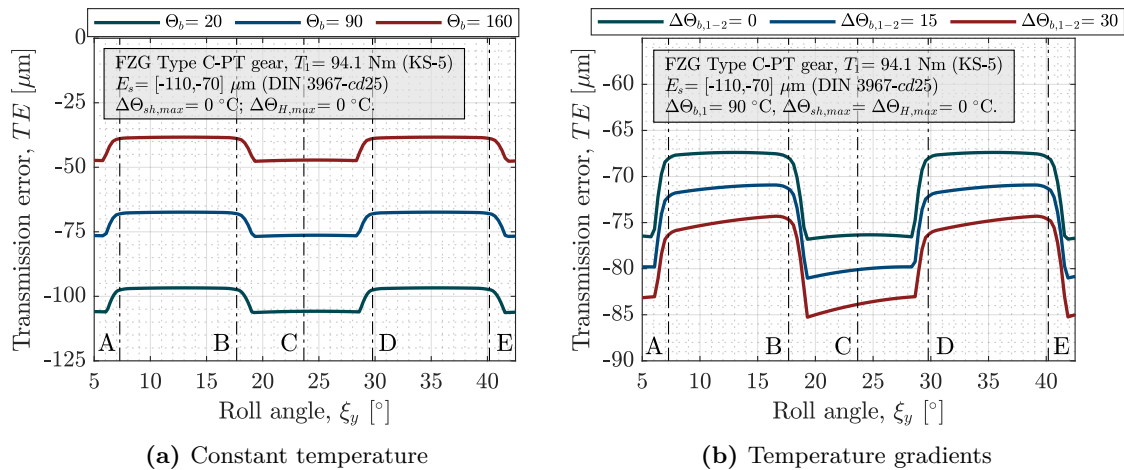


Figure 6.20: Influence of bulk temperature increase and gradients on TE at constant torque

In this case, pinion and gear temperatures are assumed constant, thus no form error effect is perceived and slope deviations prevail. It is observed in sub-figure 6.20a that TE mean level is reduced proportionally to temperature increase and the amount is exactly equal to the reduction of backlash calculated by Equation 6.27 and depicted in Figure 6.14a. No temperature difference exists between pinion and gear, therefore, pressure angle errors are equal and they compensate each other. However, when temperature differences between pinion and gear arise (see Figure 6.20b) it is observed that curves are bent slightly due to the relative profile slope deviation. This behaviour has also been described in Section 6.3.1.

Figure 6.20b also indicates that temperature differences produce uneven expansions and the change in mean level of transmission error is reduced relative to the equal temperature case. The amount of reduction is 3 μm to 4 μm for the considered gear geometry. Moreover, peak to peak transmission error also seems to be affected by such temperature differences by approximately 1 μm per 15 $^{\circ}\text{C}$ difference. In order to further analyse both parameters the composite behaviour of temperature and load is compared in Figure 6.21.

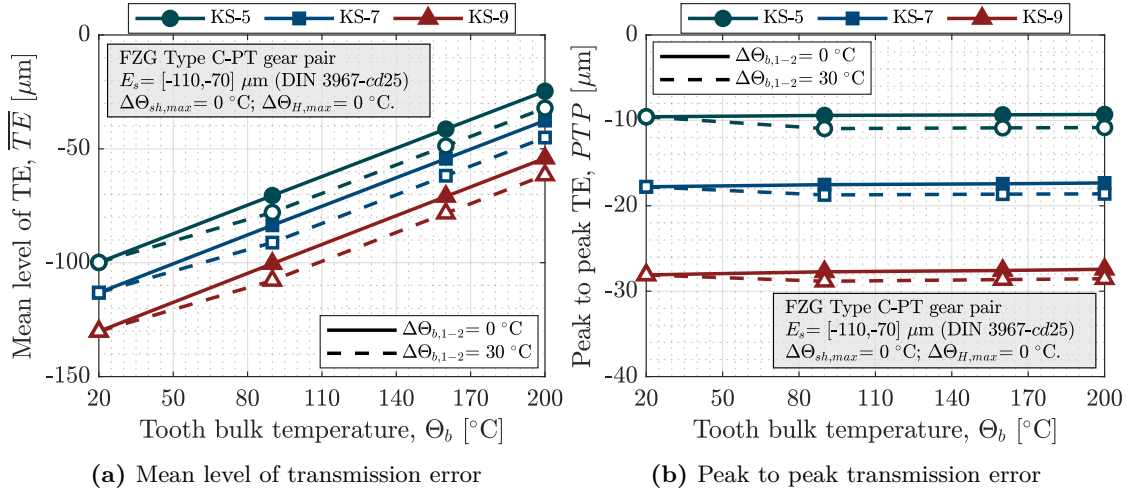


Figure 6.21: Influence of temperature and load on mean level and peak to peak TE

As expected, the mean level is increased proportionally to temperature increase and the existence of temperature differences reduces the total amount of backlash change. If the influence of load is compared to that of temperature it is observed that the latter has a bigger impact on the mean level. Contrarily, the influence of load on peak to peak transmission error is prevailing. An approximate torque increase of 100 Nm (from KS-5 to KS-7) increases peak to peak value 8 μm while a 100 $^{\circ}\text{C}$ overall temperature increase affects less than 0.5 μm . Temperature gradients increase such difference with approximately 1.5 μm for 30 $^{\circ}\text{C}$ temperature difference between pinion and gear at the lowest torque. This amount is decreased to approximately half its value at the highest torque stage indicating that the effects of thermal distortion are more visible at the lowest torques, when thermally-induced deformations are bigger in magnitude than elastic deflections.

Finally, if the influence of longitudinal gradients is analysed in Figure 6.22 it is observed that the mean level decreases about 3 μm relative to the profile distortion case due to the effect of thermally-induced crowning, while peak to peak value remains almost constant. If radial gradients are considered as well, the total amount of form deviation is expected to be reduced due to the effect of thermal stresses and therefore the change in transmission error will not be as significant.

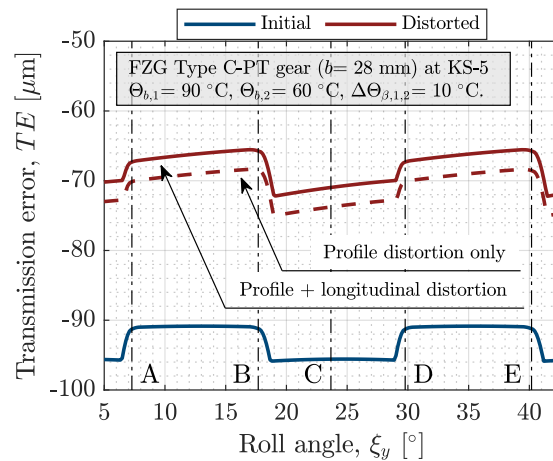


Figure 6.22: Influence of longitudinal temperature gradient on TE at constant torque

Bending and contact stresses

The variation of unit load along the line of action due to temperature differences affects bending and contact stresses and therefore these parameters must be analysed as well as they can lead to a premature failure of the gear pair.

Equations 3.119 and 3.120 have shown that the stress field depends on unit load and geometry. In the case of bending stresses root fillet geometry is not altered significantly relative to ambient temperature and therefore root fillet maximum stress is only influenced by changes in unit load. However, in the case of contact stress, and specially when longitudinal temperature gradients exist, composite radius of curvature varies with temperature difference and therefore tooth contact is no longer a line contact but an elliptical one. Thermally-induced crowning not only concentrates load in the middle of the face width but it also changes contact pressure through geometry distortion. Therefore, thermal effects affect bending and contact stresses differently. Figure 6.23 shows the impact of thermally-induced uneven load distribution on the stress field. The influence of temperature differences is depicted only, as equal temperature increase does not affect unit load.

It has been shown that thermally-induced profile slope deviation mismatch increases unit load in the double teeth contact region in recess path of contact. Therefore, bending stress in this region is more affected than in the approach path of contact due to the existence of larger distances from the tip to the critical section. The relative bending stress increase with respect to the equal temperature case is 20 MPa in the recess path of contact and the reduction in the approach region is 10 MPa for the lowest load (KS-5). In case of the highest load stage (KS-9), the same stress differences are computed as the amount of thermal deformation is equal for the same temperature distribution. On the other hand, contact stresses in Figure 6.23b are mainly affected by changes in unit load; the influence of composite radius of curvature variation being negligible as very small differences are observed. The contact stress difference in the double teeth contact regions in the approach and recess paths of contact is approximately 75 MPa which represents 8% of the maximum contact pressure.

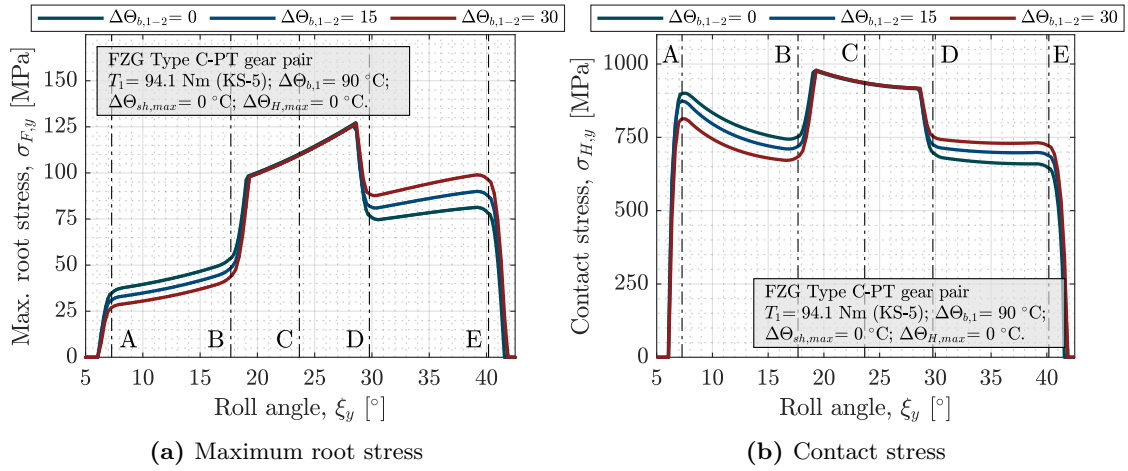


Figure 6.23: Influence of temperature difference on stresses at constant torque

Both diagrams in Figure 6.23, show maximum values of bending and contact stresses unaffected as unit load in the single tooth contact region remains constant for the considered load stage. However, when the influence of longitudinal thermal gradients is considered in large face width gears, unit loads are no more constant and maximum contact and bending stress values are altered. Figure 6.24 depicts this situation for the gear slice in the middle of the face width which is subject to the greatest load. Maximum bending and contact stress values are increased 15 % and 25% respectively for the case of longitudinal gradients only. For the same increase in unit load the bigger increase of contact stresses is explained by the application of the elliptical Hertzian stress formulation according to Appendix C. Longitudinal curvature radius as calculated by Equation 6.23 is considered and leads to an additional increase of 10% with respect to bending stresses. However, if the effect of radial temperature distribution is taken into account in combination with longitudinal gradients, thermal deformations are reduced and maximum stresses values too, which is observed in the dashed lines in Figure 6.24b.

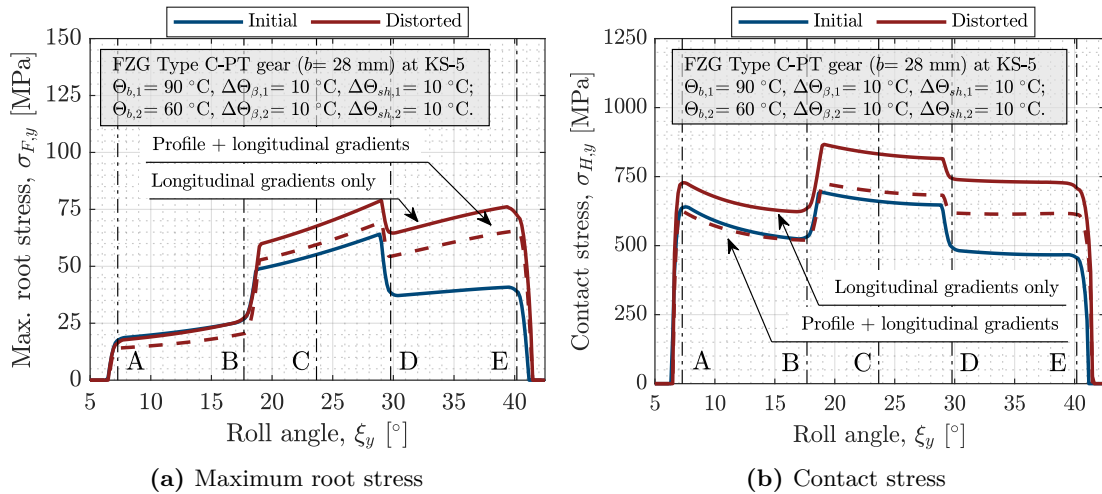


Figure 6.24: Influence of longitudinal thermal gradients on stress distribution at constant torque

6.4 Case study

In this section a test case is defined to analyse the full thermo-mechanical behaviour of a electric vehicle transmission with helical gear stages. The reference geometry is selected from [265] as it is considered a representative gearbox complying with the future trends in the field [5].

Current EV gearboxes are characterized by having a single reduction ratio with two or three helical gear stages, nominal power is approximately 50 kW and maximum motor speeds are in the order of 14.000 rpm [4]. However, future trends point towards higher traction motor speeds while maintaining gearbox design [2] and the selected gearbox is one of such examples. It is part of a EV transmission prototype designed to run at a maximum motor output speed of 45.000 rpm [265] with two possible architectures characterized by having two and three gear stages respectively and reduction ratios from 32 to 34. Thus, considering the low number of stages, the transmission ratio of each pair is high.

Table 6.1 summarizes the main geometrical characteristics of the selected helical gear pair. The latter corresponds to the output shaft in the two-stage architecture with approximate centre distance of 150 mm. The reduction ratio is 5.7, with transverse contact ratio $\epsilon_\alpha = 1.399$ and overlap ratio, $\epsilon_\beta = 1.125$ [265]. Profile shift coefficients have been assumed to balance specific sliding as no information is available on this parameter. Moreover, pinion and gear are tip relieved and the length of the linear modification corresponds to 15% of the active length of the profile. The amount of modification has been selected so as to ensure smooth meshing at the reference test condition.

Table 6.1: EV helical gear stage sample from reference [265] for thermal distortion case study

Parameter	Symbol	Value
Number of teeth	$z_{1,2}$ [-]	14, 80
Normal module	m_n [mm]	3
Pressure angle	α_n [°]	20
Helix angle	β [°]	20
Face width	$b_{1,2}$ [mm]	36, 31
Shaft diameter	$d_{sh,1,2}$ [mm]	25, 38
Profile shift coefficient*	$x_{1,2}$ [-]	0.427, -0.444
Linear tip relief*	Ca/LCa [$\mu\text{m}/\text{mm}$]	10/1.95
Quality acc. ISO 1328	Q [-]	7
Reference tool acc. ISO 53**	[-]	C (1.25/1.0/0.25)
Tolerance field acc. DIN 3967***	E_s [μm]	$d26$ (-44, -94), (-80, -160)
Material and treatment	[-]	16MnCr5 (case-hardened)
Surface roughness	Ra [μm]	0.6 (ground)

* Values estimated from additional data in [265]

** Assumption of the author

*** Niemann's recommendation for automotive applications [33]

Both gears are supported by single row tapered roller bearings on each end and the whole system is dip lubricated. According to reference [265] the immersion depth is defined relative to the gear in the high-speed stage and it is set to a value of 25% of its radius. This value corresponds to approximately 65 mm below the shaft centreline, indicating that the pinion in Table 6.1 is not immersed in oil and the relative immersion depth in the gear is approximately 50 %.

Finally, the gear unit is subject to the 90 km/h road condition as defined in [265]. Motor speed for the latter is 28.000 rpm at nominal power of 50 kW. This conditions are translated into approximately 5000 rpm input speed and 100 Nm torque in the pinion of the considered gear stage in Table 6.1. The gearbox is lubricated with a common automotive gearbox lubricant ISO VG 46 with a maximum allowed temperature of 100°C with continuous cooling. For further details on any other characteristic of the selected test case the reader is referred to reference [265].

6.4.1 Results

If one takes into account gear geometry and operating conditions it is observed that the composite effect can be detrimental from the thermal point of view. Pinion is not immersed in the oil bath and high gear ratios and input speeds result in a large number of tooth engagements per second giving rise to a large amount of heat being generated, thus temperature differences arise and may affect mesh behaviour.

Figure 6.25 shows the resulting temperature distribution for the helical gear pair in Table 6.1 subject to 5000 rpm input speed and 100 Nm input torque. Steady-state temperatures have been calculated with the thermal model in Chapter 5 with power losses predicted following the methodology in Chapter 4. Viscosity-pressure-temperature behaviour of the lubricant is modelled following ISO VG 46 automatic transmission fluid parameters from [237] which has similar properties to the that used in reference [265].

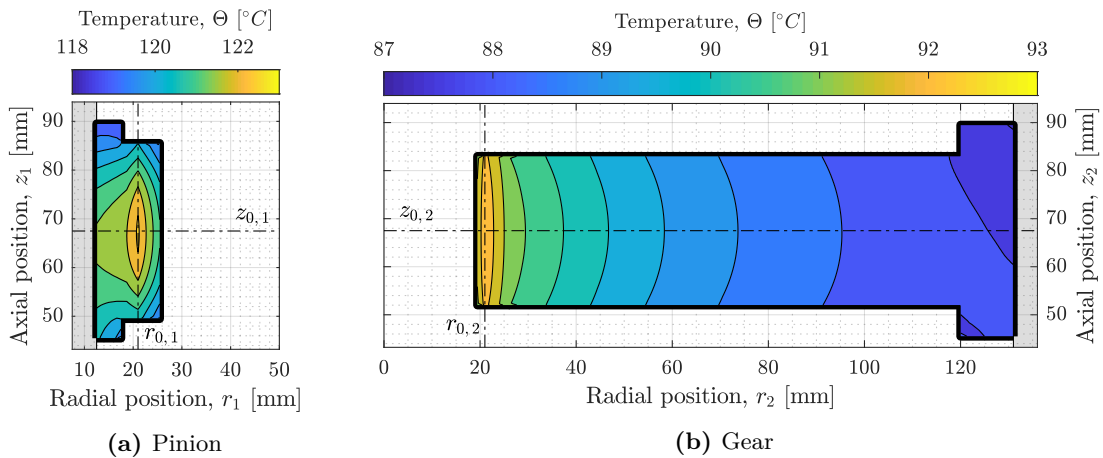


Figure 6.25: Temperature distribution of pinion and gear in case study

Steady state temperature in the pinion is 30°C higher in average than that of the gear because rotational speed is almost six times higher in the former, while the heat exchange surface is significantly reduced. Therefore, temperature differences arise as expected and relative profile and helix slope distortions exist as well. Moreover, the size of the pinion being much smaller than that of the gear, the overall temperature of the former is almost with rather small radial gradients. However, due to the high rotational speed heat is concentrated in the middle of the face width and therefore longitudinal gradients exist. Maximum temperature difference along the tooth trace is 3°C in the pinion and 1.5°C in the gear, thus, a very small thermally-induced crowning may appear in combination with helix and profile slope deviations. Meanwhile, due to the bigger size of the gear, a 6°C radial gradient exists between the shaft and the tooth tip.

From predicted steady-state temperature distribution, thermally-induced normal deviation of each individual thin slice is calculated following Equation 6.19 and the latter has been used to solve the thermo-mechanical load distribution problem according to the model presented in Chapter 3. Figure 6.26 summarizes both results.

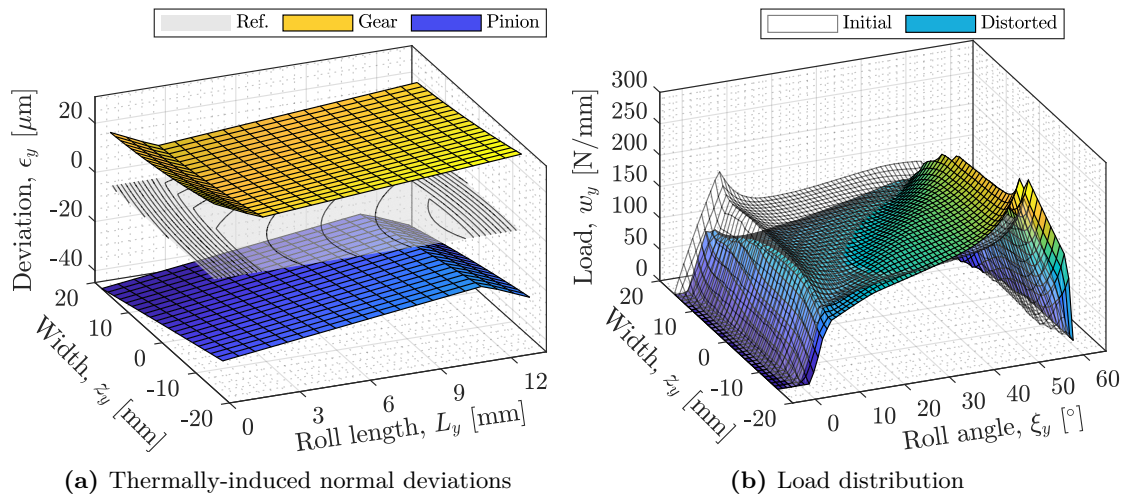


Figure 6.26: Helical gear thermally-induced deviations and corresponding behaviour under load

On the one hand, the inclined surfaces in Figure 6.26a indicate that profile and helix slope deviations are the main cause of thermal distortion in the test case. The grey surface in the middle shows the position of the theoretical involute flank and the relative normal distances between the distorted pinion and gear flanks are shown as iso-curves. The values of the iso-curves decrease with the length of roll and face width, thus pointing out that contact will occur first in the recess path of contact and towards the front tooth end, where the sum of normal deviations is minimum. Moreover, these curves also show a slight crowning which may tend to balance uneven load distribution.

On the other hand, the influence of these deviations on load distribution is reproduced in Figure 6.26b where distorted load distribution is compared to the initial diagram. The overall behaviour of load distribution is consistent with deviations in Figure 6.26a. Maximum unit load increase is located towards one of the ends in the recess path of contact while it is decreased on the opposite corner of the diagram. This effect will have a definite impact on root bending stress distribution as the maximum load increase is located towards the tip region where the bending lever arm is increased. Moreover, a small crowning effect is also observable in the start of the active profile and if attention is paid to the latter, it is noticed that the diagram is slightly displaced towards the left because normal deviations are maximum in this region and therefore an additional rotation is required to start contact, in other words, premature contact is delayed. All these effects are interrelated and they can be explained by the thermally-distorted surfaces in Figure 6.26a.

Bending stress behaviour is analysed next. Non-uniformities in load distribution are reflected back in stress behaviour with the additional influence of the relative position of the load with respect to the critical section. The composite effect of both parameters is depicted in Figure 6.27 for pinion and gear. In both cases distorted stress diagram exceeds initially calculated values. The projected curves in planes XZ and YZ in Figures

6.27a and 6.27c are planar cuts in the position of maximum stress showing a considerable increase of the latter with respect to the same position in the initial diagram, yielding a 46% increase for the pinion and 22% for the gear. Furthermore, Figures 6.27b and 6.27d indicate that the position of maximum stress is moved towards one of the ends because load is increased on one edge and reduced on the opposite. Such an increase in root bending stress should be considered for fatigue life calculations because in this type of applications high speeds in pinion further accelerates tooth breakage.

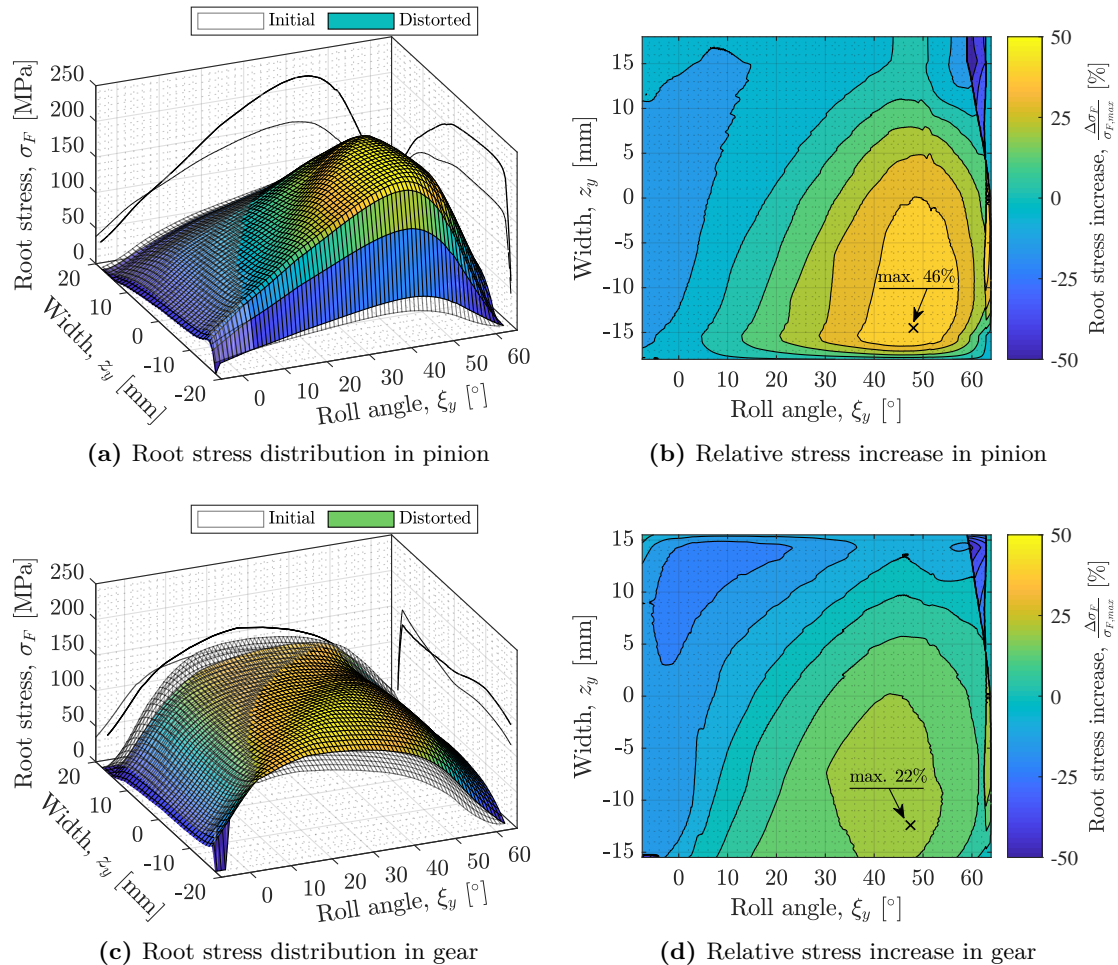


Figure 6.27: Thermally-induced root stress distribution and relative increase in pinion and gear

As far as contact stress behaviour is referred, it is observed in Figure 6.28 that contact pressure increases proportionally to load distribution and the effect of thermally-induced crowning is very small, even negligible. This is explained by the small longitudinal thermal gradients arising in the thermal simulation (see Figure 6.25) plus the effect of the radial gradients that limit the amount of thermal distortion and reduce thermally-induced crowning. On the one hand, pinion is affected by a 3°C maximum longitudinal temperature difference but the size of the pinion is small and therefore the amount of barrelling is also reduced. On the other hand, the gear is bigger but it is subject to a 1.5°C gradient in the face width direction which is rather small and also limits the amount of barrelling. As a consequence, composite effect of thermally-induced crowning is not noticeable (see Figure 6.26a).

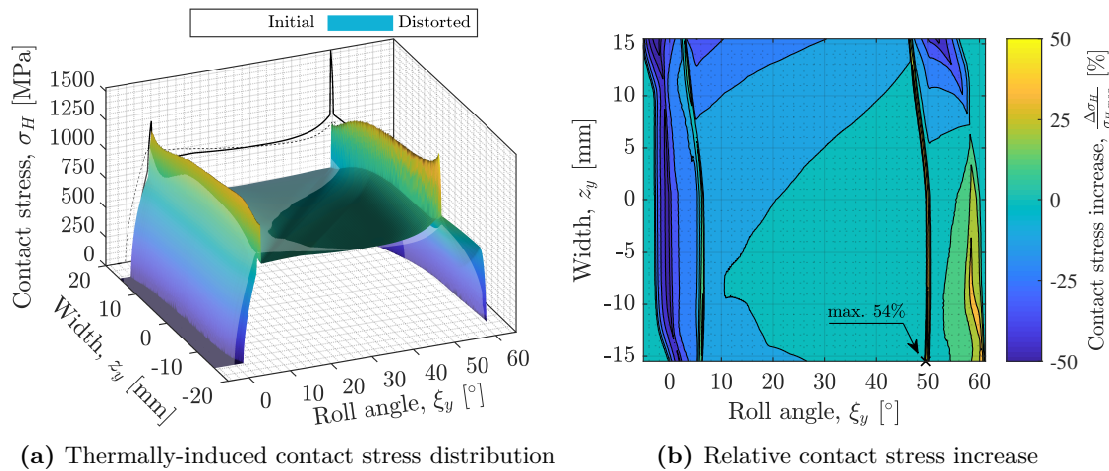


Figure 6.28: Thermally-induced contact stress distribution and relative increase

Besides, it is also observed in Figure 6.28b that the location of the maximum contact stress is shifted towards the tooth end in the recess path of contact, due to the uneven load distribution produced by temperature differences between pinion and gear. The maximum contact stress increase is 54% relative to the initial solution but it must be noted that such an increase is due to the existence of a tip relief causing contact pressures to increase suddenly. The influence of linear tip relief on contact pressure is revealed by the curved parallel lines in Figure 6.28b. Apart from the effect of the modification, maximum contact stress increase is approximately 40% and it is located at the end of the contact path where unit loads are increased (see Figure 6.26b). In the mid-region, the change in contact stress is $\pm 10\%$ on average.

6.4.2 Compensation of thermal distortion

In order to avoid stress increasing effects of thermal distortion it is possible to compensate the geometry at ambient temperature by applying tooth modifications in the design stage. For this purpose, operating temperature distribution for a given torque, speed and oil level, must be predicted using the thermal model developed in Chapter 5 and induced deformations are computed from Equations 6.5, 6.19 and 6.22. Then, normal deviation diagrams such as the one presented in Figure 6.26a can be used to determine the type and amount of modification.

For the test case under study, two types of modifications should be applied as concluded from the observation of Figure 6.26a: i) profile slope correction and ii) helix slope modification. The specific amount for the former is computed calculating the average normal distance along the helix direction between the initial profile and the distorted one at the tip. Similarly, the amount of helix modification is computed calculating the mean distance between the initial and distorted profiles at the tooth end. The average values for profile slope modifications are $17\mu\text{m}$ and $14\mu\text{m}$ for pinion and gear respectively; while helix slope modifications are $15\mu\text{m}$ and $9\mu\text{m}$. It is interesting to remark that due to the composite influence of radial and longitudinal temperature gradients the amount of crowning is very low, approximately $0.2\mu\text{m}$ in the pinion and $0.4\mu\text{m}$ in the gear, thus, no modification is applied to compensate the small barrelling effect.

Figure 6.29 summarizes the effects of tooth corrections on transverse and longitudinal load distribution. Three different axial positions have been depicted in Figure 6.29a: the transverse section in the middle of the face width and both tooth ends. Unit load in the face ends is balanced when modifications are applied, however, it is observed that it is slightly reduced with respect to the initial geometry while it is increased in the middle of the face width. This effect is the result of the thermally induced crowning not being corrected which concentrates load in the centre of the face width and relieves both ends, thus resulting beneficial. The same conclusion can be addressed if attention is paid to the longitudinal load distribution in Figure 6.29b. Thermally distorted geometry leads to non-uniform distributions by reducing unit load in one of the ends due to helix slope errors. If no barrelling effect existed, load decreased on End II would increase that of End I, however, thermally-induced crowning tends to balance this behaviour. Moreover, after applying slope modifications, the remaining thermally-induced barrelling effect still concentrates load in the centre relieving the ends. The amount of crowning being very small longitudinal load distribution is not severely affected.

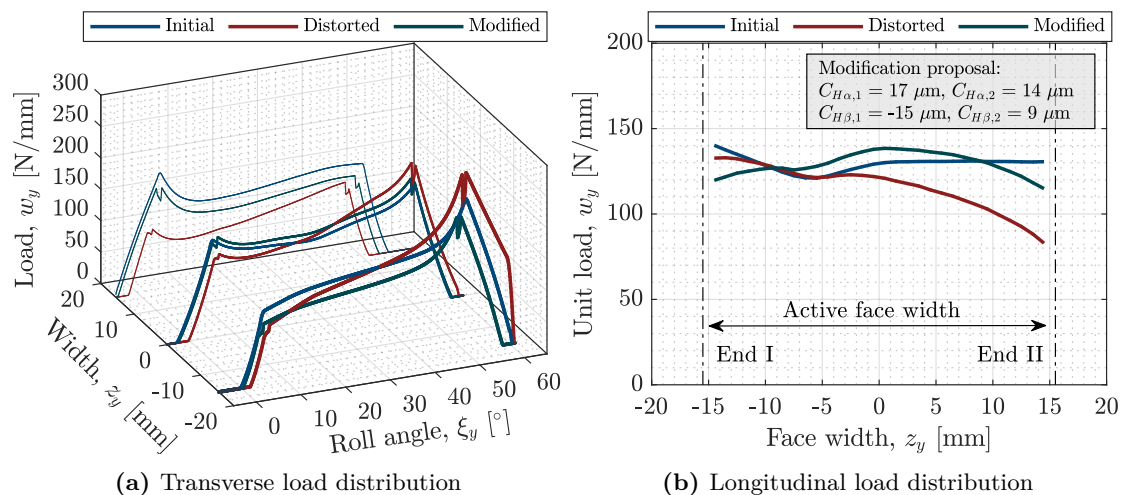


Figure 6.29: Compensated load distribution relative to initially designed and thermally distorted

On the other hand, transmission error comparison for the initial, distorted and compensated geometries is shown in Figure 6.30. The mean level of TE is clearly reduced in Figure 6.30a due to the reduction of backlash which is the expected behaviour. Meanwhile, transmission error in compensated geometry is close to the initially designed one and the only difference between both is the thermally-induced crowning effect which has not been corrected. The differences between the three curves can be better analysed if the backlash reduction term is removed from the diagram (see Figure 6.30b). The difference in mean level and peak to peak value between the initial curve and the distorted one is due to the effect of uneven load distribution. Peak to peak TE has increased approximately $0.2 \mu\text{m}$ and the overall shape of the curve has changed significantly due to the effect of relative profile slope deviation, which produces a increasing slope similarly to spur gears (see Figure 6.20b). Finally, TE mean level in modified geometry is close to the initial curve and peak to peak values have been reduced by approximately $0.2 \mu\text{m}$ due to the thermally-induced barrelling effect which seems to be beneficial from the NVH point of view.

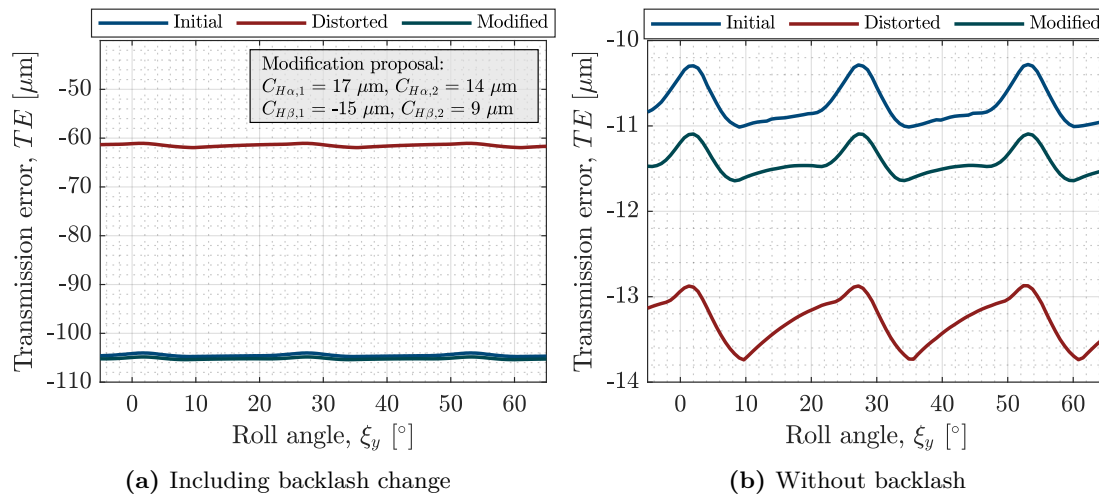


Figure 6.30: Influence of distorted and compensated geometries on loaded transmission error

6.5 Design recommendations

It has been shown in previous sections that thermal distortion effects are multiple. From a geometrical point of view, temperature increase enlarges reference diameters and reduces local pressure angles and helix slope, which affects pitch deviations and backlash as well. The way that such geometrical defects combine and interact in pinion and gear determines mesh behaviour; as a consequence, load distribution and transmission error diagrams are distorted accordingly with respect to those computed at ambient temperature. Therefore, it is of interest to give an overview of thermal distortion effects and corresponding modification proposals to enhance contact behaviour under combined thermo-mechanical loads.

Table 6.2 summarizes the influence of each temperature distribution parameter on composite geometry deviations and corresponding gear mesh parameters. Temperature variables are located in columns and affected mesh parameters in rows. The former are represented by: i) equal temperature increase, ii) temperature differences between pinion and gear, iii) radial thermal gradients, iv) longitudinal gradients and v) housing expansion. Meanwhile, geometry deviations are classified according to ISO 1328-1 standard [284] terms and mesh-related variables are grouped into those affecting backlash, transmission error, load distribution or stress behaviour.

The upward or downward-pointing arrows in Table 6.2 indicate increasing or decreasing composite effect and the large, small or negligible influence boundaries are expressed in terms of length of the line of action, with values 5 μm and 1 μm for geometry deviation variables. This way, temperature parameters affecting more than the upper boundary indicate considerable influence while those values less than the lower limit are negligible. In case of mesh-related parameters these boundaries are expressed in terms of percent change and correspond to 10% and 5% respectively. The effect of each temperature parameter on geometry and contact behaviour relative to these limits is summarized next.

Table 6.2: Summary of the influence of temperature distribution parameters on geometry, mesh behaviour, load distribution, transmission error and stresses

	$\Delta\theta_{b_1} = \Delta\theta_{b_2}$	$\Delta\theta_{b_1} \neq \Delta\theta_{b_2}$	$\Delta\theta_{sh} \neq \Delta\theta_b$	$\Delta\theta_\beta \neq \Delta\theta_b$	$\Delta\theta_H \neq 0$	
Geometry	Δf_{pt}	-	↑↑	↑	≈	-
	$\Delta f_{H\alpha}$	-	↓↓	↓	-	-
	$\Delta f_{f\alpha}$	-	-	≈	-	-
	$\Delta f_{H\beta}$	-	↓↓	-	-	-
	$\Delta f_{f\beta}$	-	-	-	↑	-
Mesh	Δj_{bn}	↓↓	↓↓	↓	-	↑↑
	Δc_y	≈	-	-	-	≈
TE	ΔTE	↓↓	↓↓	↓	↓	↑↑
	PTP	-	↑	≈	↑	-
Stress Load	$K_{H\alpha}$	-	↑↑	↑	↑	-
	$K_{H\beta}$	-	↑↑	↑↑	↑↑	-
	σ_F	-	↑↑	↑	↑	-
	σ_H	-	↑↑	↑	↑↑	-

* Legend: ↑↑/↓↓: large increasing or decreasing effect respectively, ↑/↓: small increasing or decreasing effect, ≈: approximately equal, negligible influence, -: does not affect, no influence.

a) Equal temperature increase ($\Delta\theta_{b_1} = \Delta\theta_{b_2}$) produces an overall gear expansion, thus, increasing the reference circle diameter and transverse pitch by the same amount, while profile slope and helix angle are decreased in the same proportion. No form errors exist because there are no thermal gradients. Thus, the only parameter affected by temperature is backlash which is decreased in a constant proportion (proved in Equation 6.30). Moreover, same pitch and slope errors produce no change in load distribution (nor stresses) and the influence of premature contact is negligible. The only significant effect is shown in transmission error where the mean level is increased with respect to that calculated at ambient temperature due to backlash decrease (see Figures 6.16a and 6.20a). As a consequence, no special counter-measures need to be taken; and if tight backlash allowances are to be used, attention should be paid to gear jamming probability by checking Equation 6.27 carefully (see Figure 6.13b).

b) Temperature differences between pinion and gear ($\Delta\theta_{b_1} \neq \Delta\theta_{b_2}$) mainly produce a relative slope deviation, both in profile and longitudinal directions, while relative pitch errors arise accordingly. These effects can be inter-related as shown later in this section. No form errors exist because temperatures are constant in each gear. Similarly to the preceding situation backlash is reduced, but in this case, the individual contribution to total backlash decrease is different with one of the gears expanding less than the other. Moreover, the influence of temperature differences on transmission error is not merely due to backlash decrease and corresponding diagrams present a different look with curves bent increasingly with temperature due to the no-load transmission error term (compare Figures 6.14a and 6.20b). Peak to peak values are slightly modified due to relative profile deviations and mean level reduction is smaller with respect to the equal temperature case. On the other hand, relative slope errors produce uneven load distribution and stress behaviour diagrams as local normal loads are affected by non-uniform deviations in the

base tangent plane. Thermally-induced relative profile deviations produce increasing loads in the double teeth contact region in the recess path of contact, and composite longitudinal deviations overload one of the ends in helical gears. The combination of both effects tends to increase contact and bending stress considerably towards one of the ends accelerating tooth failure. To overcome this situation, lead and profile need to be modified following guidelines in section 6.5.1. According to results in Figures 6.7 and 6.9, special attention is to be paid to gear designs with modules above 3mm, low pressure angles (less than 20°), helix slopes above 20° and large face-widths (more than 50 mm). Any combination of these parameters and sufficiently large temperature differences may require further thermo-mechanical analysis (e.g. turbo gears, marine gears, etc.).

c) Temperature gradients in the profile direction ($\Delta\Theta_{sh} \neq \Delta\Theta_b$) reduce the total amount of deformation due to the existence of thermal stresses 6.3. Two reasons may produce such behaviour: i) large temperature differences between teeth and shaft and ii) gradient type. The latter is usually parabolic and it is not very affected by operating conditions, therefore any factor contributing to temperature differences between teeth and shaft may reduce the total amount of deviation which is beneficial, as profile slope errors (and pitch deviations) are reduced with respect to the constant temperature case. Radial gradients result in form deviations but these are negligible as the size of the teeth with respect to that of the body is usually small and therefore teeth are usually subject to an almost constant temperature. Furthermore, in case of large face widths with longitudinal temperature differences, radial gradients reduce the amount of thermally-induced crowning and unit loads and stresses are reduced too as a consequence (see Figure 6.24). This effect seems to be beneficial as it controls the amount of distortion. Therefore, no special requirements are needed in thermal situations characterized by small radial gradients.

d) Temperature gradients in the lead direction ($\Delta\Theta_\beta \neq \Delta\Theta_b$) produce a barrelling of the pitch cylinder that concentrates load in the middle of the face width as shown in Figure 6.18. The amount of form deviation depends on the pitch diameter and maximum temperature difference; with curvature radius calculated following Equation 6.24. Large face width gears are prone to significant temperature differences along the face width, but they are usually followed by a large diameter with radial gradients as well, which limit total deformation as previously stated. The final amount of thermally-induced crowning largely depends on the size of the gear and the specific temperature distribution. This effect can be considered beneficial to compensate mesh misalignments provided that maximum temperature is located in the middle of the face-width. However, in cases of large temperature differences and/or non-symmetric distributions, such as the one produced by axial oil pumping in turbo-gears, this effect can be detrimental as it concentrates load towards the exit side. In such cases special counter-measures are needed [8].

e) Centre distance expansion ($\Delta\Theta_H \neq 0$) is influenced by the overall temperature increase of the housing which is inevitable due to the heat generated in the transmission. The main effect is the increase of backlash which helps reduce mesh jamming probability (see Figure 6.13a). If front and back faces of the housing are subject to temperature differences mesh misalignment may occur due to uneven expansion.

6.5.1 Tooth modification guidelines

As it can be concluded from the preceding summary the main detrimental effects of thermal distortion are due to the existence of relative profile and helix slope deviations along with the increase of local loads due to thermally-induced crowning. Pitch deviations, separating distance change and backlash decrease are collateral geometry effects and they can be predicted from the preceding ones, while loaded behaviour depends on the composite effect of pinion and gear geometry distortion plus torque.

In order to determine simple design rules to deal with thermal deformations it will be assumed that the influence of gradients is negligible; thus pinion and gear temperatures are considered constant. Under such conditions, thermal distortion in the profile direction is exclusively due to pressure angle variation as shown in Figure 6.31.

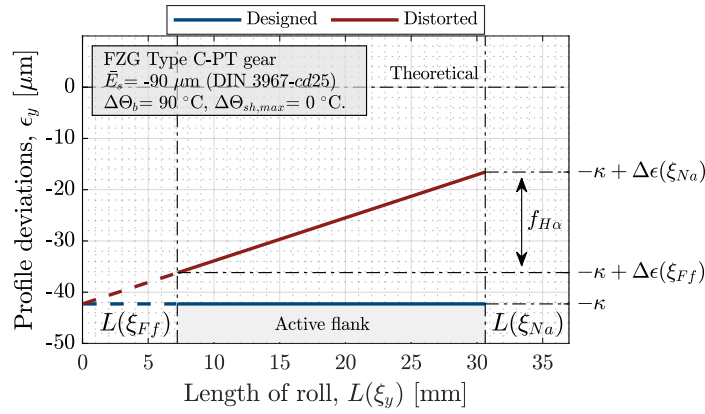


Figure 6.31: Derivation of profile slope error for tooth modification

Transverse pressure angle modification proposal, $C_{H\alpha}$, should compensate for the amount of profile slope deviation at the tip; relative to the form diameter which starts at roll angle ξ_{Ff} . Thus, $C_{H\alpha} = -f_{H\alpha}$, and applying Equation 6.29 we have:

$$C_{H\alpha,i} = \Delta\epsilon(\xi_{Na,i}) - \Delta\epsilon(\xi_{Ff,i}) = \alpha_{L,i} \cdot \Delta\Theta_{b,i} \cdot r_{b,i} \cdot (\xi_{Na,i} - \xi_{Ff,i}) \quad (6.31)$$

Where ξ_{Na} and ξ_{Ff} are the roll angles at the active tip and root form diameters respectively.

Similarly, according to Figure 6.8, suggested flank line modification should compensate for the helix slope deviation according to the relation $C_{H\beta} = -f_{H\beta}$. Therefore from Equation 6.22 helix slope modification is computed as:

$$C_{H\beta,i} = b_{F,i} \cdot \alpha_{L,i} \cdot \Delta\Theta_{b,i} \cdot \tan(\beta_b) \quad (6.32)$$

Where $b_{F,i}$ is the usable tooth face width which is reduced by end chamfers.

Figure 6.32 depicts the amount of recommended tooth profile and helix slope modifications as a function of temperature computed using Equations 6.31 and 6.32 for the helical gear pair in the case study in section 6.4. For average pinion and gear bulk temperatures of 120°C and 90°C respectively, recommended profile and helix slope modifications are 17 μm and 15 μm for the pinion and 14 μm and 9 μm for the gear; which are in perfect agreement with the proposed modifications in section 6.4.2. Furthermore, to facilitate practical application, it is possible to compute the relative profile and helix slope modifications and apply them to the pinion following common practice in gear manufacturing. This procedure yields 3 μm and 6 μm for profile and helix slope modifications respectively.

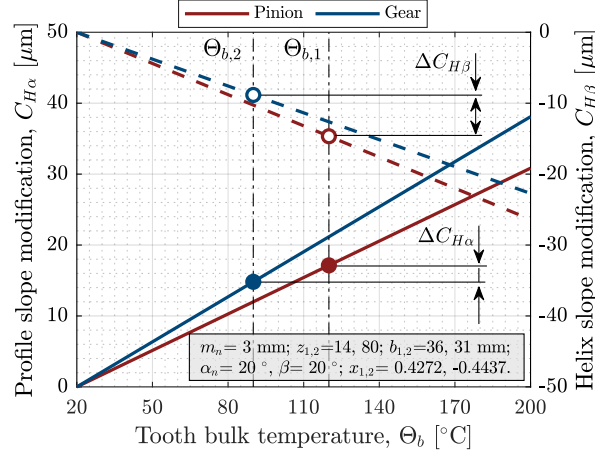


Figure 6.32: Profile and helix slope modification proposal for the helical gear pair in case study

Note that increased temperature “adds” material to the active flank at the tip (see Figure 6.31), hence, according to ISO 21771 [176] sign convention, such slope deviations are negative and therefore, profile modifications applied at ambient temperature must be positive values by removing material to compensate thermal effects. In case of flank line modifications, if we assume that pinion is subject to the highest temperature, thermally-induced helix slope deviations are positive in the pinion and negative in the gear, thus, flank line modifications are negative and positive respectively. To simplify the graphical description in Figure 6.32, the latter has been depicted as a negative value.

As far as the thermally-induced barrelling term is concerned, this is not easy to compensate at ambient temperature because it requires a negative parabolic crowing. Thus, it is only recommended to watch contact pressure levels closely by following the formulation presented in Appendix C and the longitudinal curvature radius computed by Equation 6.24. This situation is only detrimental in cases of significant gradients and narrow face widths leading to small radius of curvature and high contact pressures.

Similarly, to avoid the probability of mesh jamming, it is interesting to define tooth thickness allowances, E_s , according to thermally induced backlash decrease. As a close approximation of the mean value along the line of action, it is possible to calculate the latter on the working pitch circles of the fixed end in the base tangent plane where Equation 6.27 reduces to:

$$\frac{1}{2} \cdot |E_{s,1} + E_{s,2}| \cdot \cos(\alpha_n) > [u_1(r_{w,1}) + u_2(r_{w,2}) - u_H(a_w)] \cdot \sin(\alpha_{wt}) \cdot \cos(\beta_b) \quad (6.33)$$

As in previous simplifications, temperature of pinion, gear and housing are assumed constant and each can be manufactured with a different material thus:

$$u_i(r_{w,i}) = r_{w,i} \cdot \alpha_{L,i} \cdot \Delta\Theta_{b,i} \quad (6.34)$$

$$u_H(a_w) = a_w \cdot \alpha_H \cdot \Delta\Theta_H \quad (6.35)$$

Where, r_w and a_w are the working pitch radius and centre distance. Note that if pinion and gear are subject to the same temperature increase, the right hand side in Equation 6.33 is equivalent to that presented in DIN 3967 standard [156].

Finally, the derivation of pitch errors as a function of profile slope deviations is described for completeness. From Figure 6.31 one can easily see that pitch errors and backlash decrease are closely related to slope deviations. Applying similar triangles, distortion at the pitch point (characteristic point C) is:

$$\frac{\Delta\epsilon(\xi_C)}{r_b \cdot \xi_C} = \frac{\Delta\epsilon(\xi_{Na})}{r_b \cdot \xi_{Na}} \quad (6.36)$$

Relating this result to Equation 6.18 single pitch deviations are computed as:

$$f_{pt} = \tau \cdot u(r_C) = \tau \cdot \frac{\Delta\epsilon(\xi_C)}{\sin(\alpha_t)} = \frac{\tau}{\cos(\alpha_t)} \cdot \frac{\Delta\epsilon(\xi_{Na})}{\xi_{Na}} \quad (6.37)$$

Where $\Delta\epsilon(\xi_{Na})$ is calculated from Equation 6.29. Therefore, one can model thermally induced pitch errors as slope deviations and vice-versa, which is consistent with the results by Kashyap [140] in plastic gears.

6.6 Conclusions of Chapter 6

In this chapter, a thermally-induced geometry distortion model for spur and helical gears has been developed and the effects of such deviations on loaded behaviour have been tested. The model is based on the classical thin slice approach used in the computation of load distribution and it assumes that thermal expansion of each point in the involute is mainly radial, thus dependent on the transverse temperature distribution and thermal stresses of the considered slice. Meanwhile, the influence of longitudinal temperature distribution is neglected which implies that there is no axial coupling between slices. Thermal growth is computed following the disc approximation and deformations are assumed to be small in steel gears, as a consequence, the contact point still lies in the base tangent plane which allows solving the load distribution problem as usual by introducing local normal deviations as initial separations.

In the first section, the type and amount of deviation has been analysed following classification in ISO 1328 standard [284]. It has been shown that profile and helix slope deviations are the main causes of thermal distortion; and for a given temperature distribution, the amount of profile slope error is mainly affected by normal module and pressure angle while helix deviations depend on face width and helix angle. Form alterations have been shown to be negligible in the transverse plane and rather small in the longitudinal direction, however, if the composite effect of pinion and gear helix form deviations is considered, crowning effects may be noticeable in loaded behaviour. Pitch deviations have also been analysed and it has been proved to be significantly increased with respect to the limitations of the standard, however, if pinion and gear are subject to the same temperature increase, no relative pitch deviation exists and therefore no change in load distribution is expected.

The influence of temperature increase on mesh behaviour has been analysed next. The relationship between changes in unloaded transmission error and backlash has been discussed and the latter has been found to be one of the most important parameters in NLTE behaviour together with relative profile slope differences. Then, geometry deviation effects on load distribution have been studied. Premature contact increase has been found

to be negligible relative to the influence of torque and uneven load distributions have been found to be dependent on temperature differences between pinion and gear. Moreover, longitudinal thermal gradients produce a barrelling of the pitch cylinder giving rise to load concentrations in the middle of the face width, but the composite effect of radial and longitudinal gradients tends to reduce the amount of form deviation and load concentration effect as well. The influence of uneven load distribution in transmission error and stress field has been studied showing that thermal effects on root stresses are prominent at the lowest line loads while contact pressure is mainly affected by the barrelling effect.

Finally, a practical test case has been defined where an EV gearbox helical gear stage has been analysed. It has been shown that maximum stress increases up to 46% as a consequence of the composite effect of pinion and gear thermal distortion. Tooth modifications to compensate thermally-induced deviations have been proposed and corresponding reduction on load distribution and transmission error have been reported. At the end of the chapter, thermal distortion effects have been summarized and design recommendations to deal with thermal distortion effects have been proposed.

No amount of experimentation can ever prove me right;
a single experiment can prove me wrong.

— Albert Einstein, 1879 - 1955

7

Experimental Study

Contents

7.1	Back-to-back gear test bench design	198
7.2	Experimental methodology	202
7.2.1	Test specimens	202
7.2.2	Working conditions	204
7.2.3	Experimental setup and procedure	204
7.2.4	Transmission error measurement	206
7.3	Results	210
7.3.1	Backlash tests	210
7.3.2	Loaded transmission error measurements	212
7.3.3	Loaded and thermally affected transmission error tests	213
7.4	Discussion	215
7.5	Conclusions of Chapter 7	217

This chapter meets the demands of objective O.6 in Section 1.3. First, the development of a custom back-to-back test rig is described and supported gear geometries, operating conditions and sensor characteristics are presented. Next, thermo-mechanical tests to be carried out are discussed, test specimen characteristics are gathered and working conditions are set up. In this section, transmission error measurement procedure is described; from the acquisition of raw data, as measured by position encoders, until the characteristic shape of TE diagram is obtained, together with reference values such as the mean level or the peak to peak value. Quasi-static mechanical tests will be carried out first in order to validate TE behaviour under load; and the influence of temperature will be analysed next by heating up the system in a controlled manner. Finally, measurements are compared to analytical predictions, results are discussed and conclusions are withdrawn. To the authors knowledge, no previous experimental evidence of the effect of temperature on quasi-static transmission error exist and therefore, results presented in this chapter are novel.

7.1 Back-to-back gear test bench design

In order to validate the thermo-mechanical behaviour of external cylindrical gears in mesh, a back-to-back test rig has been designed based on the standard FZG machine architecture [285]. The main differences between the test bench designed at Mondragon University and those commercially available are the speed and torque limitations which have been increased to analyse high power density transmissions.

Description

The designed test rig, shown in Figure 7.1, is composed of two equivalent gearboxes (known as “test” and “drive”) with inverse gear ratios which are connected by two shafts, one of them being split in two parts. A load clutch is inserted in the split section of the shaft and a lever arm allows to load the system by rotating one of the ends of the clutch while the other is held fixed. Then, a set of eight bolts is tightened to couple both ends of the clutch and the lever arm is removed letting both gearboxes subject to a prescribed torque. The amount of torque is determined placing a different number of specific weight discs pulling the lever arm and the exact value can be measured in a torque transducer located inside the loop. Finally, the traction motor rotates the main shaft which is connected to the split one by means of the test and drive gearboxes, thus closing the mechanical loop. This way, the torque necessary to rotate the system is equal to the torque loss inside the loop which allows reducing the traction motor size while maintaining a high torque inside the loop.

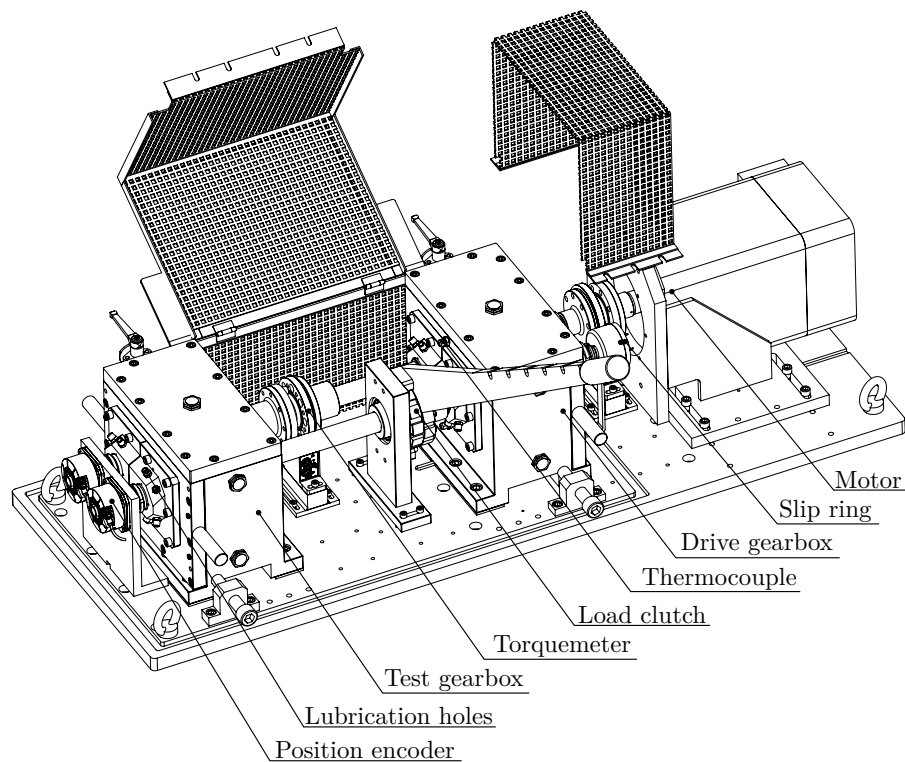


Figure 7.1: Designed back-to-back test rig for external cylindrical gears

The test gear set is located inside the test gearbox in the front and an identical gear pair is assembled in the drive gearbox in the back. Pinion and gear are mounted in such a way that the rotational speed of each shaft is the same from the perspective of the test gearbox or the drive one. However, the lubrication characteristics (oil type, viscosity, etc.) of each transmission is not required to be the same; this way, two different lubricants or lubrication conditions can be compared within the same test rig. Furthermore, several gear failure phenomena can be analysed with this architecture (pitting, scuffing, wear, etc.) and if both gearboxes are identical and an additional torque-meter is placed in the output of the traction motor, mesh efficiency measurements can be carried out as well; by measuring the total torque loss of the system and subtracting the corresponding torque loss of bearings, seals and that produced by oil drag.

Design characteristics

As it can be noticed, this type of architecture is very versatile, but it has not been designed to support the high tangential speeds present in EV transmissions. Motor speeds in common FZG test rigs are usually around 3000 rpm producing a maximum of 10 m/s circumferential speed in standard FZG gear type C geometry, and speed increasing units are used to reach 5000 rpm resulting in approximately 20 m/s [28]. Tangential velocities in EV transmissions are in the order of 50 m/s and such speed levels require special bearing types and lubrication systems. Moreover, in order to analyse helical gears the bearing type must be replaced due to the thrust force produced by the helix angle. Therefore, the basic FZG design has been modified to cope with these requirements and additional enhanced characteristics have been provided together with the new speed limitations:

- Operating centre distance: $a_w = 110$ mm
- Face width: $b \leq 50$ mm (up to 75 mm with special gear design)
- Gear ratio: $u \leq 2$
- Helix angle: $\beta \leq 30^\circ$
- Tangential speed: $V_t \leq 60$ m/s
- Torque inside loop: $T \leq 1000$ Nm
- Nominal motor speed and torque: $N = 6000$ rpm, $T = 136$ Nm
- Maximum motor speed and torque (1h): $N_{\max.} = 10000$ rpm, $T_{\max.} = 60$ Nm

To achieve these traction speed and torque characteristics a liquid-cooled squirrel-cage induction AC motor for EV vehicles has been selected (reference 1PV5135-4WS14-Z from Siemens) with built-in temperature sensors and position encoders. Moreover, in order to maximize tangential speeds, centre distance has been increased to allow for larger diameter and gear ratios with respect to the standard FZG test rig. Shaft diameters have also been modified from 30 mm to 40 mm and maximum torque inside the loop now reaches 1000 Nm. Front bearing supports are type NU208-E-XL-TVP2 separable cylindrical roller bearings from INA-FAG and those in the back are reference 3308-DA-MA double row angular contact ball bearings with split inner ring. The thermally safe reference speed for both bearings is 7500 rpm and the mechanical limiting speed reaches 10900 rpm. Besides, the rotary shaft seal material must be designed to support high peripheral shaft speeds and temperatures, as a consequence, common elastomer seals are not valid. In the proposed design, Trelleborg's Turcon Varilip[®] PDR [288] rotary shaft seals are used with a maximum surface speed of 100 m/s and very low torque loss (≈ 0.12 Nm).

When the test rig is subject to high speeds, considerable heating of the bearings arises and a continuous cooling system is required. An independent lubrication circuit has been designed such that the oil from the bearings is physically separated from the gear oil sump by means of a specially designed housing. An ISO VG 46 oil is pumped into each of the bearing supports through the lubrication pipes in Figure 7.2 at 1 l/min oil flow rate. In order to avoid overflowing the bearings, an additional suction pump has been installed which is driven by a servomotor and balances the oil level inside the individual supports by controlling the oil level in the tank with a digital level and a PLC.

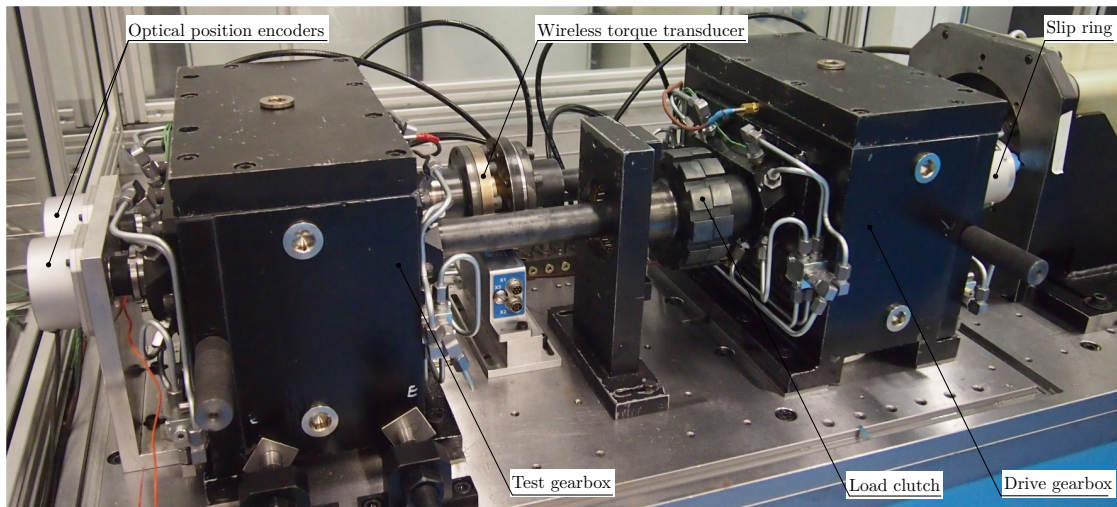
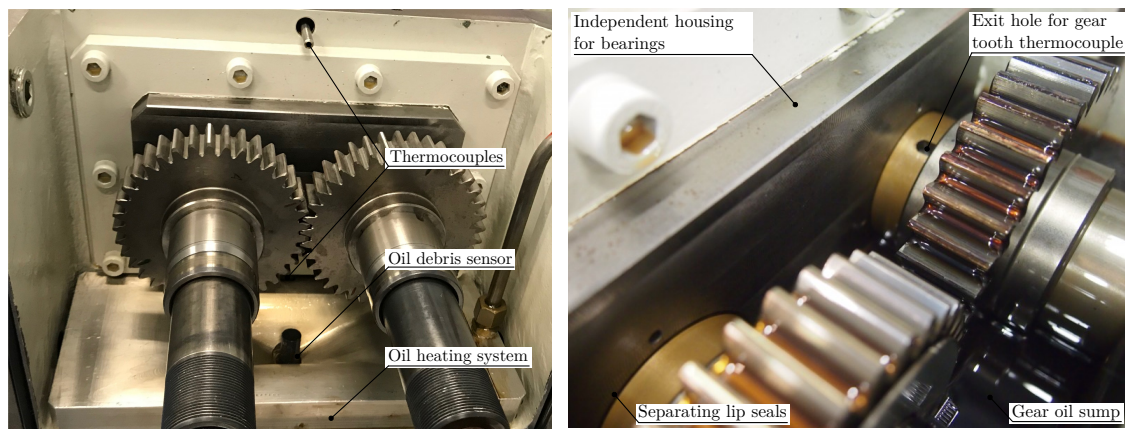


Figure 7.2: Overall view of designed test rig

On the other hand, gears inside the gearbox are dip lubricated and the relative immersion depth can be adjusted easily. If necessary, oil is heated by means of high power density thermoelectric resistances located inside a sealed aluminium plate submerged in the oil bath (see Figure 7.3a). A thermocouple immersed in the oil sump measures the temperature of the lubricant which is then heated by means the thermal resistances connected to a PID temperature controller.



(a) Oil sump heating system

(b) Oil level

Figure 7.3: Oil sump heating system and oil level inside gearbox

Sensing

The test rig includes several sensors to measure temperature, torque, speed, transmission error and oil condition. Several T-type thermocouples measure the temperature of different parts and a National Instruments chassis with thermocouple modules synchronizes all temperature signals. For instance, outer ring of bearings, housing, oil sump and oil-air mixture inside each gearbox are monitored. Temperature of gear teeth centre and several radial locations are measured too and the rotating thermocouple signals are transmitted by means of a pair of slip rings reference 1988-2BR-FAG180 from Fabricast. Figure 7.4 shows a 0.5 mm diameter thermocouple assembled in 3 mm module gear teeth with a thin metal sheet pressing it against the tooth end to avoid loss of contact.



Figure 7.4: Thermocouple inserted in small module tooth

Meanwhile, two wireless torque transducers with double range (1:5) up to 1 kNm from Kistler with rotor and stator Ki-Torq 4550A and 4541A respectively, measure torque in the loop and system friction torque. These torquemeters also include speed measurement capabilities allowing to measure instantaneous total power loss. Moreover, each gearbox includes a Gill 4212 oil debris sensor (located in the middle of the oil heater in Figure 7.3a) monitoring wear rate and allowing for tooth failure detection by tracking small and large particles.

The measurement of transmission error is carried out with the aid of a pair of high resolution optical angle encoders from Heidenhain reference RCN 2510 and a EIB 741 interpolation unit. These encoders have been selected because they are considered a good compromise between compact size, ease of installation, speed limitations and system accuracy. A picture of their assembly is presented in Figure 7.5. Pinion and gear shafts are hollow and a shaft extension coaxial within ± 0.02 mm tolerance is used to mount both encoders at the shafts ends, which are later locked by means of a ring nut.

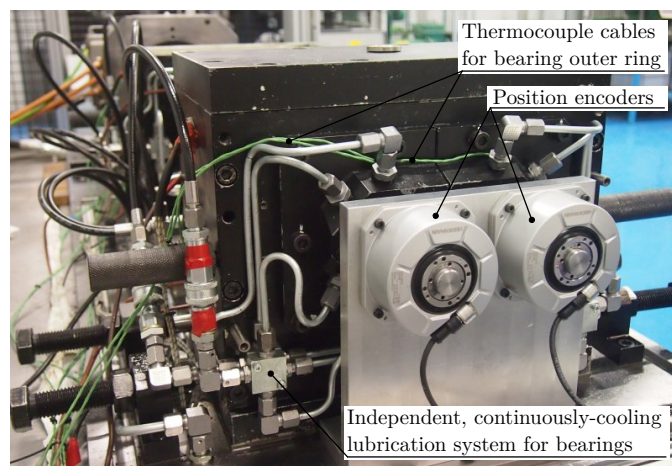


Figure 7.5: Position encoder assembly and independent bearing lubrication system

The overall characteristics of the position encoders are gathered in Table 7.1. Their accuracy is ± 2.5 second of arc which is equivalent to $\pm 0.6 \mu\text{m}$ in terms of length of the line of action for a 100 mm base diameter gear. Similarly, the position error per signal period is $\pm 0.07 \mu\text{m}$ for the same specimen.

Table 7.1: Heidenhain RCN 2510 optical encoder characteristics

Parameter	Units	Value
System accuracy	["]	± 2.5
Position error per signal period	["]	± 0.3
Signal periods per revolution	[-]	16384
Position values per revolution	[-]	268435456 (28 bits)
Clock frequency	[MHz]	16
Permissible speed	[rpm]	3000
Maximum temperature	[°C]	50

These optical encoders are single-turn absolute-type encoders and they operate using the photoelectric imaging principle [289] which is a non-contacting optical scanning method. The exact angular position value is read immediately from a graduated disk at any time, even after several tests and conditions, provided that the encoder is not disassembled in between measurements. Therefore, it is possible to manually align the zero degree reference of the encoder with a given tooth during the installation so that the angular position of any other tooth is located unambiguously in different tests. This characteristic allows to track the influence of composite manufacturing deviations or tooth defaults of a specific mesh cycle on the corresponding transmission error diagram. However, to obtain transmission error as a function of time, it is necessary to convert the single-turn absolute values to continuous incremental signals following the procedure described in Appendix D.

Finally, encoders mounted on the input and output shaft of the test gearbox are connected to the EIB 741 evaluation unit via EnDat 2.2 interface. Angular positions of both shafts are synchronized with the internal clock signal and up to 250 000 position values can be recorded per channel which is enough for off-line TE measurements. The EIB application software controls the different measurement options, allows programming triggers and processes the measured values which can be exported to a .csv file for further analysis.

7.2 Experimental methodology

The test rig described above has been specially designed to research on gear efficiency and thermal behaviour at high tangential speeds; and similarly to the standard FZG test bench, common gear failure modes such as pitting, scuffing or wear can be analysed as well. In this work, thermal distortion is studied by means of the analysis of the transmission error behaviour under quasi-static conditions.

7.2.1 Test specimens

In this work, two spur gear sets are selected from several available gear geometries. Both gear sets are characterized by having a common 3 mm module, 25 mm face width and 20° pressure angle while gear ratios are different as shown in Figure 7.6 (specimen A is a 1:1 transmission while set B is 2:1). Additional information can be found in Table 7.2.

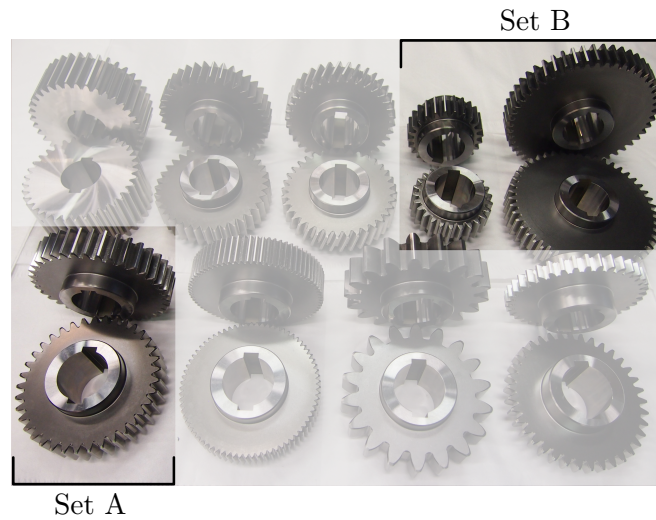


Figure 7.6: Spur gear sets A and B for quasi-static transmission error measurements

Note that the number of teeth is non-hunting and therefore each tooth will contact the same mate in the gear every time so that the composite manufacturing pitch and profile deviations will be constant for each mesh cycle. This allows to clearly identify thermal distortion effects as variable composite tooth errors are not expected. Finally, both geometries have been manufactured with the same reference profile, material, quality and tooth thickness tolerance; the only difference being the profile shift coefficient which have been selected to balance specific sliding on each gear set. As a consequence, pinion and gear teeth geometry in set A are identical and those of set B are different due to dissimilar addendum modifications. Profile diagrams and corresponding manufacturing deviations are presented in Appendix E.

Table 7.2: Spur gear sets A and B for experimental measurements

Parameter	Symbol	Set A	Set B
Normal module	m_n [mm]	3	
Normal pressure angle	α_n [°]	20	
Number of teeth	$z_{1,2}$ [-]	37, 37	25, 50
Profile shift coefficient	$x_{1,2}$ [-]	-0.1608, -0.1608	-0.0234, -0.7337
Effective face width	b [mm]	25	
Shaft diameter	d_{sh} [mm]	40	
Tip rounding	h_k [mm]	0.6	
Tolerance field acc. DIN 3967	E_s [μm]	cd25	
Quality acc. ISO 1328	Q [-]	5	
Reference tool acc. ISO 53	[-]	A (1.25/1.0/0.38)	
Contact ratio (approach, recess)	ϵ_α (ϵ_a, ϵ_f) [-]	1.48 (0.74, 0.74)	1.63 (0.95, 0.67)
Material and treatment	[-]	17NiCrMo6, case-hardened	
Surface hardness	[-]	58-62 HRC	
Flank roughness (ground)	Ra (Rz) [μm]	0.4 (2)	

7.2.2 Working conditions

The test program considers two steps: mechanical tests are carried out first and thermo-mechanical behaviour is analysed next. The former is used as a reference to analyse the effects of temperature increase on the quasi-static transmission error. Table 7.3 shows the working conditions for each of the gear sets.

Table 7.3: Operating conditions for experimental transmission error tests

Parameter	Symbol	Value
Input speed	N_1 [rpm]	60
Input torque	T_1 [Nm]	50, 100, 200, 400, 600
Immersion depth	H/R [-]	0.5
Oil temperature	Θ_o [°C]	50, 75, 100, 125, 150

Tests will be completed at 1 Hz constant rotational speed which is considered sufficiently low to avoid introducing dynamic effects according to Munro [290]. Lower speeds can be achieved by the traction motor, however, at the highest temperatures and torques, mesh friction affects speed control and stick-slip phenomena shows up producing an intermittent TE pattern. Therefore, in order to avoid changing the preset speed in between tests, a common 60 rpm reference is used for mechanical and thermo-mechanical tests. Nevertheless, in order to guarantee quasi-static behaviour, a preliminary dynamic study will be carried out and transmission error repeatability measurements will be completed.

Besides, the test program comprises five torque levels, from 50 Nm to 600 Nm. Reference torque of 200 Nm corresponds to an approximate unit load of 150 N/mm in gear set A which is the lower limit of application of ISO 6336 standard [11] and the maximum torque of 600 Nm leads to the pitting and bending stress limits in sets A and B respectively; thus, torque levels have been selected such that low and high unit loads are considered in combination with thermal effects.

Finally, quasi-static thermo-mechanical tests are completed by progressively heating the oil sump up to 150°C while rotating the gear pair at the same speed and prescribed torque; until the steady-state temperature in gear teeth is reached in both gears for each temperature stage. FVA3 paraffinic mineral oil will be used in the tests whose properties are well characterized by several reports [31, 282] and it has already been presented in Chapter 4. The relative immersion depth will be kept constant just below the gear hub as shown in Figure 7.3b.

7.2.3 Experimental setup and procedure

The experimental setup for the thermo-mechanical tests is depicted in Figure 7.7. Three main acquisition systems stand out: i) a Kistler Ki-Torq wireless torque transducer, ii) a National Instruments compact DAQ chassis with thermocouple modules and iii) a Heidenhain EIB interpolating unit for position encoders. A personal computer centralizes all acquisition systems and includes the corresponding measurement software along with the interface to the PLC and PID controllers for the traction motor speed and oil bath temperature control respectively. After each test, transmission error calculation is completed off-line by means of an automated Matlab script.

the lowest load stage to the highest one. A minimum of three repetitions are carried out in mechanical tests each of them comprising several torque levels and three different individual measurements. Although no significant temperature increase is expected in these tests due to their short duration, temperature is measured continuously in several parts such as gears, bearings, oil sump, housing and room.

The test program continues with the thermo-mechanical tests. The general procedure is kept but this time oil sump temperature is increased progressively in each load stage. Once torque value is preset, traction motor is rotated at constant speed and oil sump is heated with thermal resistances. Oil temperature is measured with a thermocouple immersed in the oil sump which sends instantaneous measurements to the PID controller and the acquisition system. The temperature of the oil bath, gear and housing is monitored in real time and when steady-state condition is reached in all of them, angular position measurements are conducted following the procedure of the mechanical tests, with the same number of individual measurements. Temperature is increased afterwards and when the next steady-state thermal stage is reached, measurements are completed in the same way. When the maximum temperature level for the considered load stage is attained, the measurements are finished until the whole system is cooled down. Then, next load stage is prescribed and the process is repeated. When all combinations of load and temperature are finished the process starts again with a new repetition until three full repetitions are completed.

Finally, when all tests in set A are finished, set B is tested following the same procedure. In between, additional tests such as no-load transmission error tests and backlash measurements are performed.

7.2.4 Transmission error measurement

Transmission error has been defined in Chapter 3 as the variation of the output rotational motion of the driven wheel for constant rotational speed in the driver one. Therefore TE is a relative magnitude relating angular positions of pinion and gear, requiring a common zero reference position and continuous incremental measurements. Considering that the RCN 2510 is a single-turn absolute encoder, measured values must be corrected. The method to compute transmission error from absolute values is described in Appendix D.

Fast Fourier Transform and high-pass filtering

In order to analyse transmission error behaviour correctly, the influence of gear eccentricity is filtered while maintaining the mean level and peak to peak values. To this aim, a Fast Fourier Transform (FFT) is carried out followed by a high-pass filtering of the signal. The main steps in the procedure are depicted in Figure 7.8.

First, the original signal is detrended by an amount equal to the mean level, so that the sinusoidal curve is located on the abscissa as in Figure 7.8a. If the FFT is performed with the original signal, a big amplitude arises at 0 Hz masking small amplitudes of interest hence the offset must be removed. However, it is important to keep the mean value of TE as it depends on the initial position of the gear, the applied load and the available backlash. Thus, for the same initial position, it is expected to be affected by torque and temperature and therefore, this value is preserved until filtered TE curve is reconstructed.

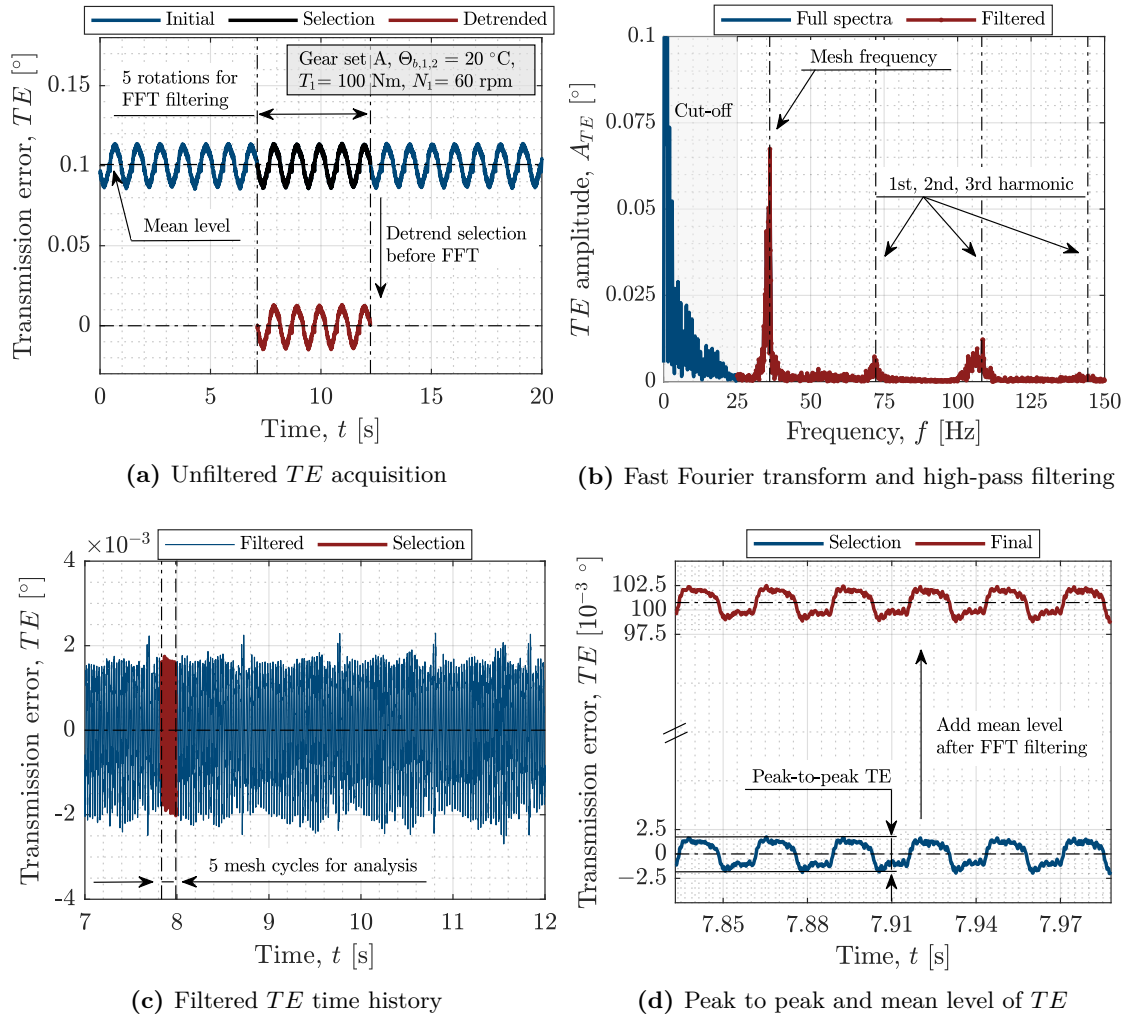


Figure 7.8: TE measurement process in gear set A at 60 rpm and 100 Nm torque

Fast Fourier Transform is computed in Figure 7.8b. Mesh frequency corresponds to the number of teeth multiplied by the shaft rotation frequency in Hertz, $f_m = z \cdot f_s$. In these tests the latter is 1 Hz thus, mesh frequency is equal to the number of teeth. Subsequent harmonics are located and N integer times the mesh frequency, f_m . Gear eccentricities to be filtered are low frequency terms (below mesh frequency), therefore the high-pass filter must keep frequencies above the desired cut-off value ($f_c \approx \frac{1}{2} \cdot f_m$ here). Once the original signal has been filtered, it can be reconstructed by computing the inverse transform (see Figure 7.8c) and finally initial offset is added to keep the mean level as shown in Figure 7.8d.

Repeatability tests

In order to analyse the degree of repeatability of loaded TE tests, the procedure described in [291] is followed, where the amplitude of the signal at the mesh frequency and subsequent harmonics are measured for different repetitions. It has been observed that these parameters differ significantly for each load stage. Moreover, the location of the maximum at the mesh frequency is slightly shifted with respect to 1 Hz reference. These errors are probably due to small speed variations induced by the traction motor control at 60 rpm along with torque fluctuations caused by assembly misalignments and eccentricities.

Figure 7.9 summarizes the transmission error amplitude variation at mesh frequency for both geometries subject to different torques. Similar behaviour of the harmonics has been observed but they are not displayed here for simplicity. It is observed in this figure that the amplitude fluctuation is considerable for each load stage and therefore, contrary to procedure described in reference [291], it is not possible to extract reliable information of the thermo-mechanical tests relying exclusively on amplitude at mesh frequency and subsequent harmonics. To solve this issue additional Fourier transforms and filtering

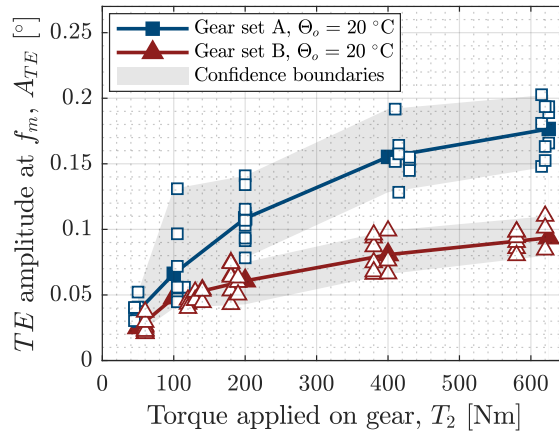


Figure 7.9: FFT amplitude repeatability at mesh frequency as a function of torque

needs to be carried out followed by individual analysis of each test. However, this procedure is time consuming and may lead to loss of information if relevant frequencies are ignored.

Moreover, it has been observed that the disassembly and assembly of the same gear set during contact pattern check and correction procedure yields different unfiltered TE diagrams. A beating effect distorting the signal, similar to that described in reference [292], has been found in some cases typically repeating itself once per revolution. The origin of this effect has been identified in the torque variations due to misalignments between the test and drive gearboxes which are rigidly connected by shafts without flexible couplings. After the inverse Fourier transform is performed, a periodic TE peak is still observed in such cases (see Figure 7.8c) which can be filtered out following the procedure described in [292].

In view of these mechanical issues, the following approach has been adopted in this thesis. The full signal is analysed (with a minimum of 20 full rotations) and only low frequencies are filtered out, those corresponding to gear eccentricities. The cut-off frequency, is set to 20 Hz in gear set A and 10 Hz in gear Set B. All the rest of frequencies above the cut-off value are used for reconstruction. Then, a reliable and distant region from the beating effect is selected for comparison. In order to simplify the analysis a finite number of mesh cycles is selected (usually five). Mean level is extracted from the unfiltered TE diagram and peak to peak value is calculated directly from the filtered graph corresponding to the selected number of mesh cycles. The latter is computed as the difference between the mean maximum TE and mean minimum TE of the selected five mesh cycles. In all tests, the same five mesh cycles are selected for analysis, those just before the angular position of 270° relative to the zero reference identified by the position of the keyseat in the pinion.

In order to investigate the repeatability of this procedure, the transmission error under load of both gear sets is analysed. Two torque levels are studied at constant 60 rpm rotational speed: 100 Nm and 200 Nm, both relative to the driven gear. The measurement is conducted for approximately 30 seconds, then stopped and restarted after a minute pause. Three different repetitions are measured at the same constant torque. The pause is limited to a minute to avoid temperature increases affecting the mean level.

Figure 7.10 depicts the repeatability of the selected mesh cycles in both gear sets under this conditions. Ordinate axis represents the raw mean level of transmission error after reconstruction of the Fourier transform, which follows the procedure described in Appendix D. As it can be seen, the results are within approximately $5 \cdot 10^{-4}$ degree tolerance in both gear sets which corresponds to the order of magnitude of the accuracy of the encoder.

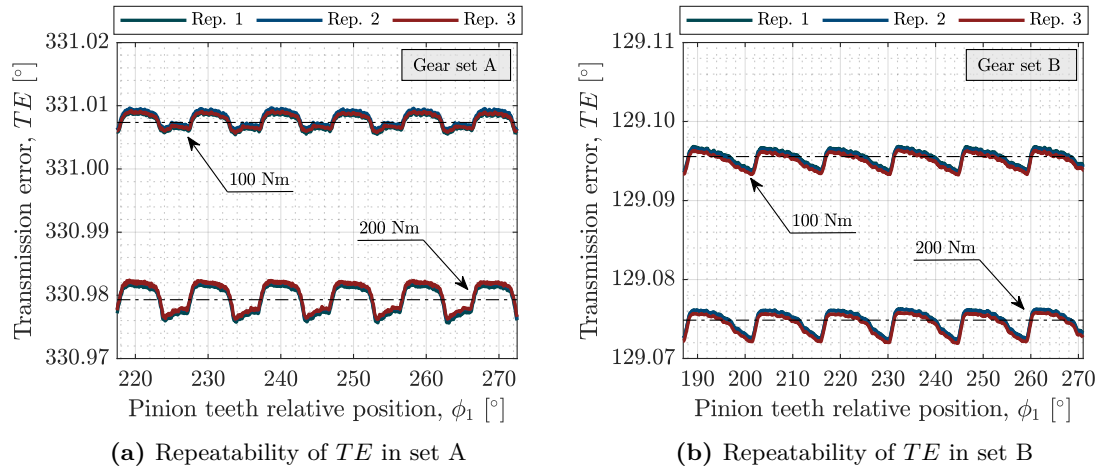


Figure 7.10: Repeatability of transmission error in gear sets A and B

In view of the good repeatability of the mean level and peak to peak parameters it is possible to analyse their behaviour under combined torque and temperature, provided that no dynamic effects distorts the results.

Dynamic effects

According to Munro [290] no dynamic effect should be expected at 60 rpm rotational speed. Nevertheless, this assumption is validated through an preliminary test where rotational speed of gear set B is varied from 0 to 500 rpm at constant reference torque of 200 Nm. Figure 7.11 summarizes TE mean level and peak to peak results as a function of speed.

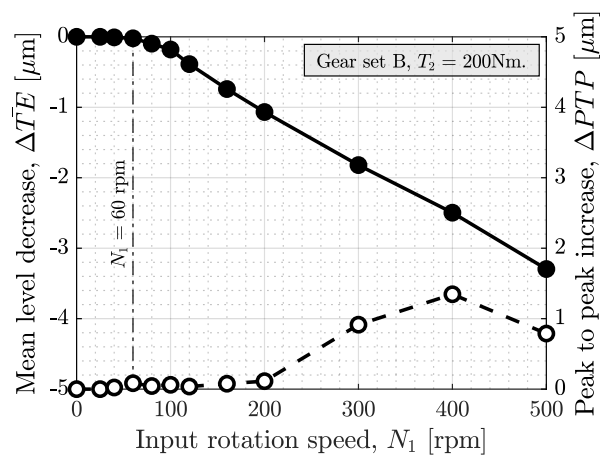


Figure 7.11: TE mean level and peak to peak behaviour with increasing rotational speed

It is observed in Figure 7.11 that mean level decrease starts at approximately 80 rpm while peak to peak differences become noticeable from 200 rpm on. In both cases, the change is very small, below the accuracy of the encoder. Thus, if the limitations of the latter are considered, the speed limit to avoid dynamic effects is set in 160 rpm producing a mean level decrease of 0.7 μm , just above the resolution of the encoder. Thus, constant test speed of 60 rpm is sufficient to analyse quasi-static transmission error and it can be doubled if necessary, specially in high temperature high torque conditions where the traction motor may show a stick-slip motion pattern.

7.3 Results

In the following section experimental results are summarized. Three types of measurements are shown: i) no-load transmission error tests at different temperatures (backlash tests), ii) loaded TE tests at room temperature and iii) thermo-mechanical tests. In all cases, mean level of transmission error and peak to peak values are analysed following the procedure described in the Section 7.2.4.

7.3.1 Backlash tests

Torque applied by the lever arm produces teeth deflection making the driven gear lag behind its theoretical position, thus resulting in a negative transmission error [293]. If backlash exists, an additional negative separation exists because the pinion needs to rotate an amount equal to the angular backlash before contact with the driven gear occurs. Furthermore, it has been shown in Chapter 6 that if temperature is increased, backlash is reduced and the negative angular position of the gear is shifted towards positive values. Thus, the effect of torque and that of temperature coexist as they must be combined within the same diagram for correct assessment of transmission error behaviour. Therefore, in order to analyse thermo-mechanical loaded transmission error, a common mean level reference for both gear types needs to be set before hand.

Up to this point it has been shown that the mean level of raw transmission error measurements is located in an arbitrary position between 0° and 360° relative to the driven gear's encoder zero angular position (see axis y in Figure 7.10). If no torque is applied, this position theoretically corresponds to the unloaded contact between pinion and gear flanks, once backlash angle is overcome and gear eccentricity effects are filtered out. If rotation direction is changed, the sinusoidal diagram is shifted by an amount equal to the backlash angle until the opposite flanks meet each other. Therefore, following Fish [292], the reference position is defined by the average of mean levels corresponding to clockwise and counter-clockwise rotations under no load. In this position, pinion teeth are located in the middle of the space width with half backlash angle on each side (if no manufacturing errors exist). The latter can be used as the zero transmission error position so that the start of loaded behaviour takes place once half normal backlash is overcome. Hence, in the following diagrams half normal backlash position, $j_{bn}/2$, will be highlighted as the reference position indicating the start of tooth deflections at room temperature.

Backlash tests are preliminary measurements to characterize the amount of available clearance at increasing oil sump temperatures. These tests are carried out before thermo-mechanical ones and they are used to validate the influence of temperature on backlash so that a correlation between this parameter and the mean level behaviour can be established in future experiments. The driven gear position is fixed with the load clutch support while the pinion is rotated in clockwise and counter-clockwise directions until contact of the flanks occurs and loop torque signal is increased in the torque transducer. Several repetitions are completed in three different angular positions and constant oil sump temperature. The graphical representation of the measurements of both encoders shows the amount of available backlash and the mean value among the different measurements is used for comparison with the design backlash.

Figure 7.12 depicts the influence of temperature on total normal backlash, j_{bn} , relative to the design value. Analytical predictions effectively meet the design value at ambient temperature while increasing the oil temperature reduces the amount of available backlash linearly; which is the expected behaviour if pinion and gear temperatures are assumed to be constant and equal to that of the oil sump. Meanwhile, experimental measurements follow the analytical prediction provided that the influence of the housing expansion is suppressed. Note that gear dilatation tends to reduce backlash while centre distance expansion increases it. Hence, if the effect of the latter is not eliminated from the raw experimental measurement, it is not possible to analyse the influence of the gear expansion term.

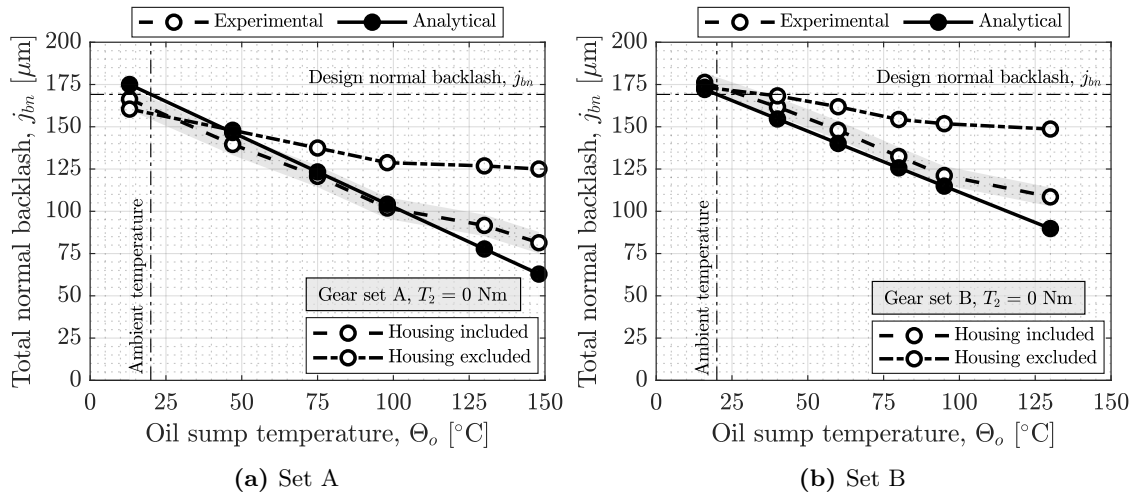


Figure 7.12: Influence of temperature on backlash reduction

Both gear sets show the same trend with temperature with analytical predictions following closely at least up to 100°C temperature. However, it is to be noted that the experimental measurement slightly deviate from the analytical predictions due to several reasons. On the one hand, housing and gear manufacturing and assembly tolerances affect this correlation and on the other hand, theoretical linear thermal expansion coefficient for steel may deviate up to $\pm 5 \cdot 10^{-7} \text{ K}^{-1}$ from its real value. Moreover, temperature differences may exist between the preset oil sump temperature and that of pinion and gear. Although manufacturing tolerances of the housing and thermal expansion coefficient deviations have been considered in the shaded error bar, the temperature differences are difficult to control as it will be shown later in this section, specially at the highest temperatures where the largest deviations arise.

7.3.2 Loaded transmission error measurements

Figure 7.13 summarizes loaded transmission error results for both gear sets. The overall behaviour is depicted in subfigures 7.13a and 7.13b, while the summary of mean level and peak to peak trend with torque can be found in Figures 7.13c to 7.13f. Analytical predictions have been included in these pictures to highlight the expected behaviour.

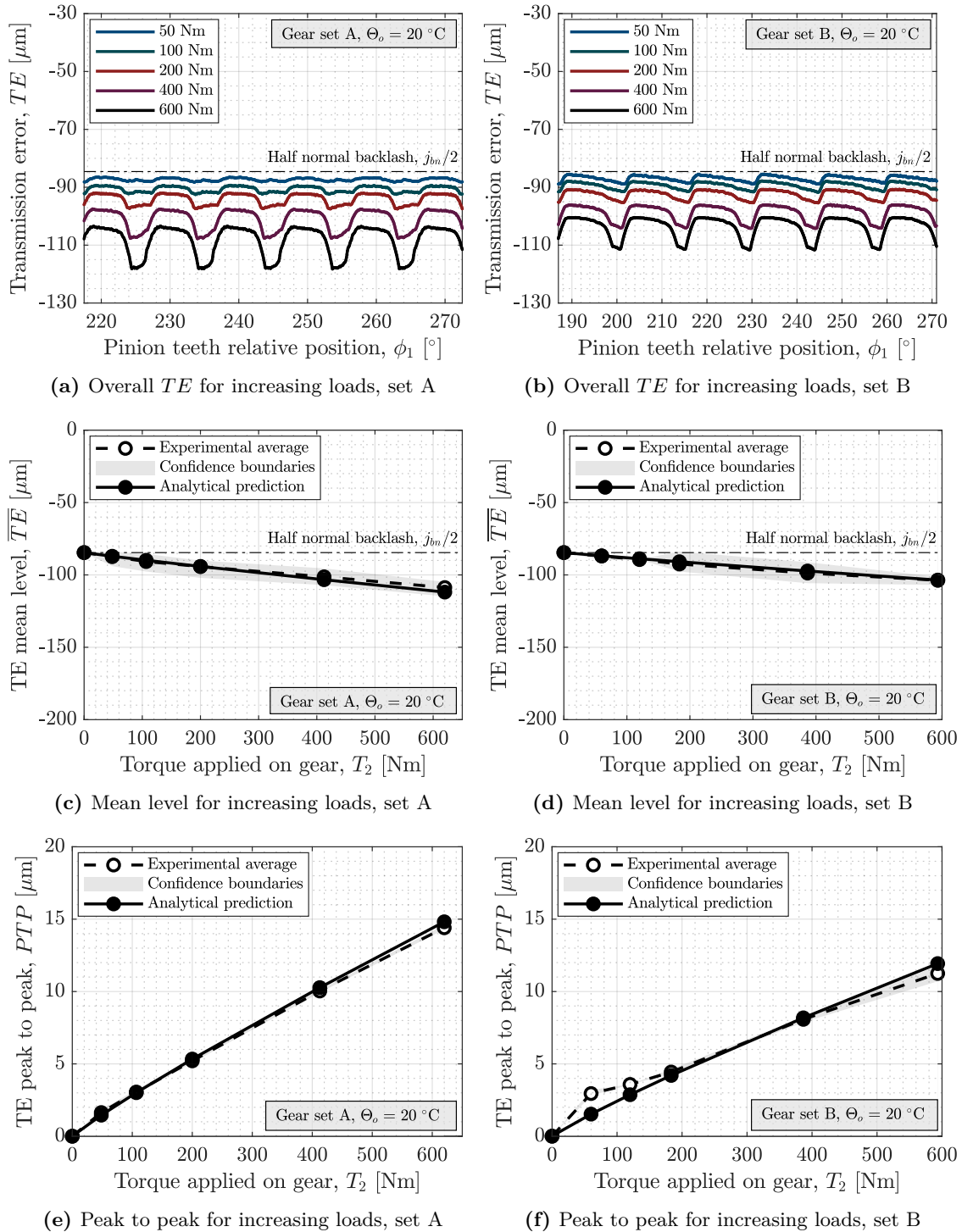


Figure 7.13: Experimental loaded TE results for gear sets A and B

If attention is paid to the TE diagrams in Figures 7.13a and 7.13b, it is observed that load tends to increase both, transmission error mean level and peak to peak values; therefore, the gear is increasingly delayed with respect to its theoretical position. Reference position corresponding to half normal backlash and coincident with the no-load transmission error term is highlighted in all diagrams such that increasing separation from this position indicates that the backlash gap increases with load. Moreover, it is also remarked that peak to peak values increase with torque while the premature contact effect tends to contract the region of single tooth contact at higher loads. These characteristics are coincident with the expected features at increasing loads already described in Chapter 3.

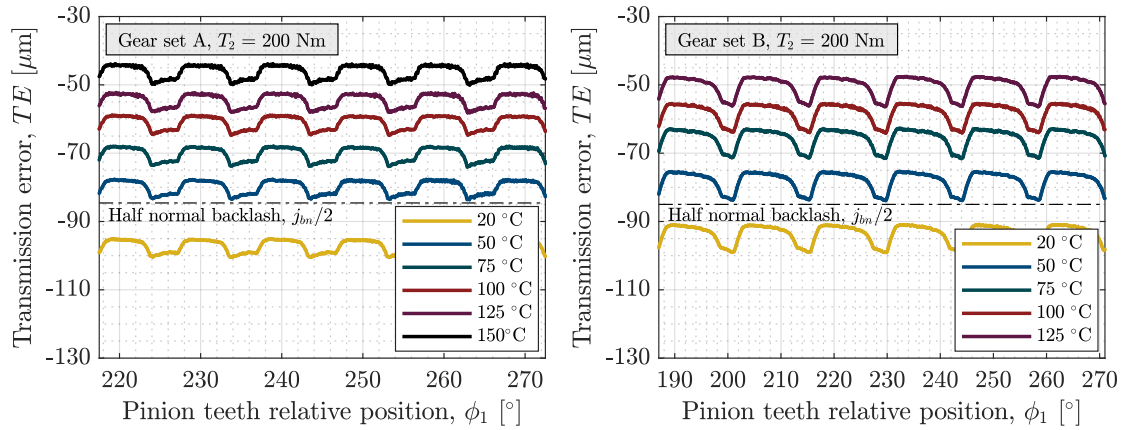
However, it must be stressed at this point that the experimental values need to be corrected to be comparable to analytical values as the torsional compliance of the key and the shaft have not been considered in the analytical model presented in Chapter 3. This issue has already been pointed out by Munro [293] and it mainly affects to the mean level; also known as DC component of transmission error by this author. Key and shaft sizes being equal for both gear sets, the correction factor is constant and takes the value 0.15 in these tests. The agreement between analytical and experimental TE mean level is excellent after this modification. As far as the peak to peak TE behaviour is concerned, analytical predictions closely follow experimental results in both gear sets, except at low loads in set B where the experimental values seem to deviate from the overall trend.

7.3.3 Loaded and thermally affected TE tests

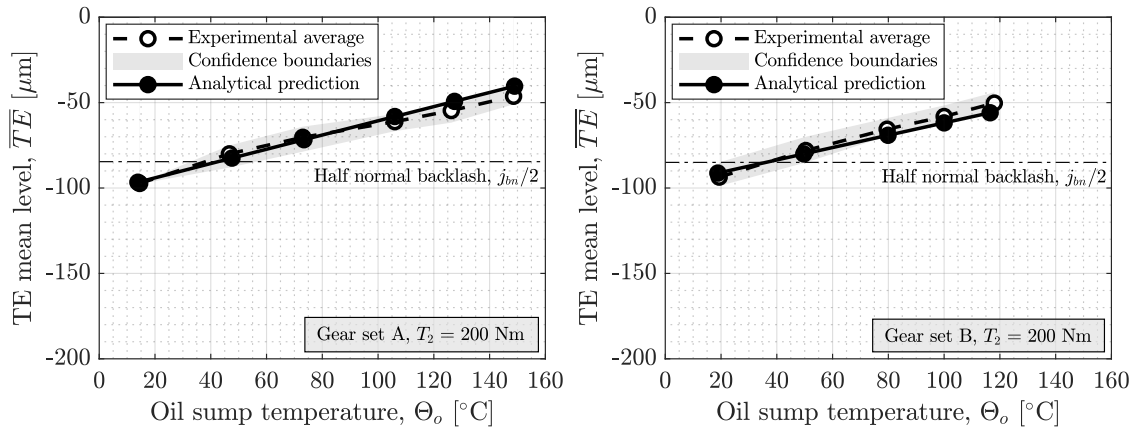
Figure 7.14 shows the influence of increasing temperature at constant torque in both gear sets. The lever arm loads the gear pair at 200 Nm (corresponding to the driven gear) and the set is rotated at constant speed of 60 rpm (measured in the driving pinion). The oil sump is heated to the prescribed temperature and transmission error measurements are completed once steady-state temperature is reached in the thermocouple located in the tooth of the drive transmission gear.

Transmission error diagrams in Figures 7.14a and 7.14b show that temperature increase shifts the initial curve at ambient temperature towards positive values, thus reducing the backlash gap which is the expected behaviour. The overall shape of TE remains unchanged and no additional features are observed at first sight; therefore, no apparent peak to peak change is noticed. If these figures are compared to the corresponding ones in the loaded TE measurements it is observed that the effect of temperature increase on mean level is greater than that of load which is confirmed by the slope of the curve in Figures 7.14c and 7.14d. Moreover, if the mean level behaviour in these figures is compared to that of backlash in Figure 7.12 it is observed that the shift in mean level perfectly correlates to backlash change due to temperature which is one of the conclusions addressed in Chapter 6. Again, slight deviations between analytical predictions and experimental results arise at the highest temperatures due to the influence of temperature differences between components.

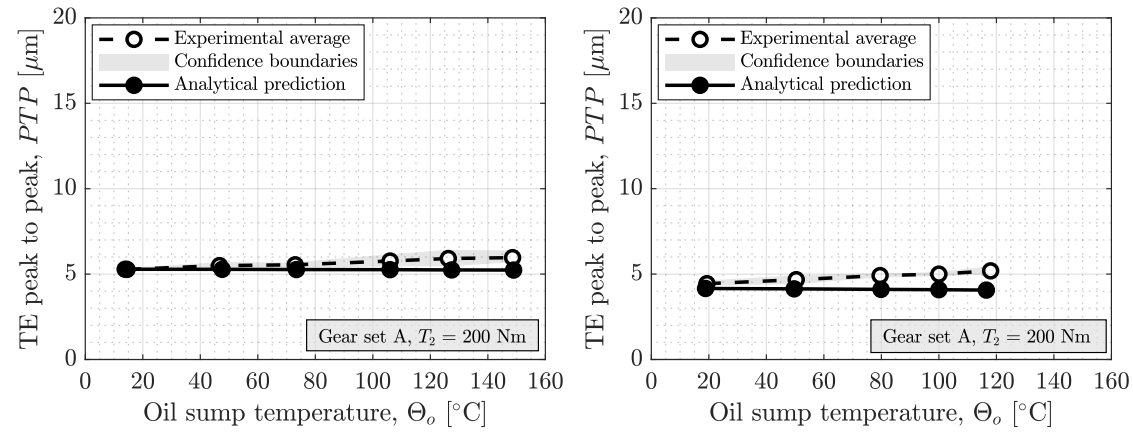
It is interesting to remark that if pinion and gear temperatures are constant and equal to that of the oil sump, the analytical model does not predict any significant change in peak to peak transmission error behaviour. However, experimental results in Figures 7.14e and 7.14f show increasing peak to peak values with temperature, which indicates that temperature differences must exist, specially at the highest temperatures. This trend is reproduced in all combinations of temperatures and torques as shown later in Figure 7.15.



(a) Overall TE for increasing temperatures, set A (b) Overall TE for increasing temperatures, set B



(c) Mean level for increasing temperatures, set A (d) Mean level for increasing temperatures, set B



(e) Peak to peak for increasing temperatures, set A (f) Peak to peak for increasing temperatures, set B

Figure 7.14: Experimental thermal TE results for gear sets A and B at 200 Nm torque

Figure 7.15 gathers all thermomechanical results in gear sets A and B. All torque and temperature combinations repeat the mean level and peak to peak patterns already described in preceding figures. Increasing torque decreases TE mean level (stretches available backlash gap) while increasing temperature increases it (contracts available backlash gap); the influence of temperature on the latter being more prominent.

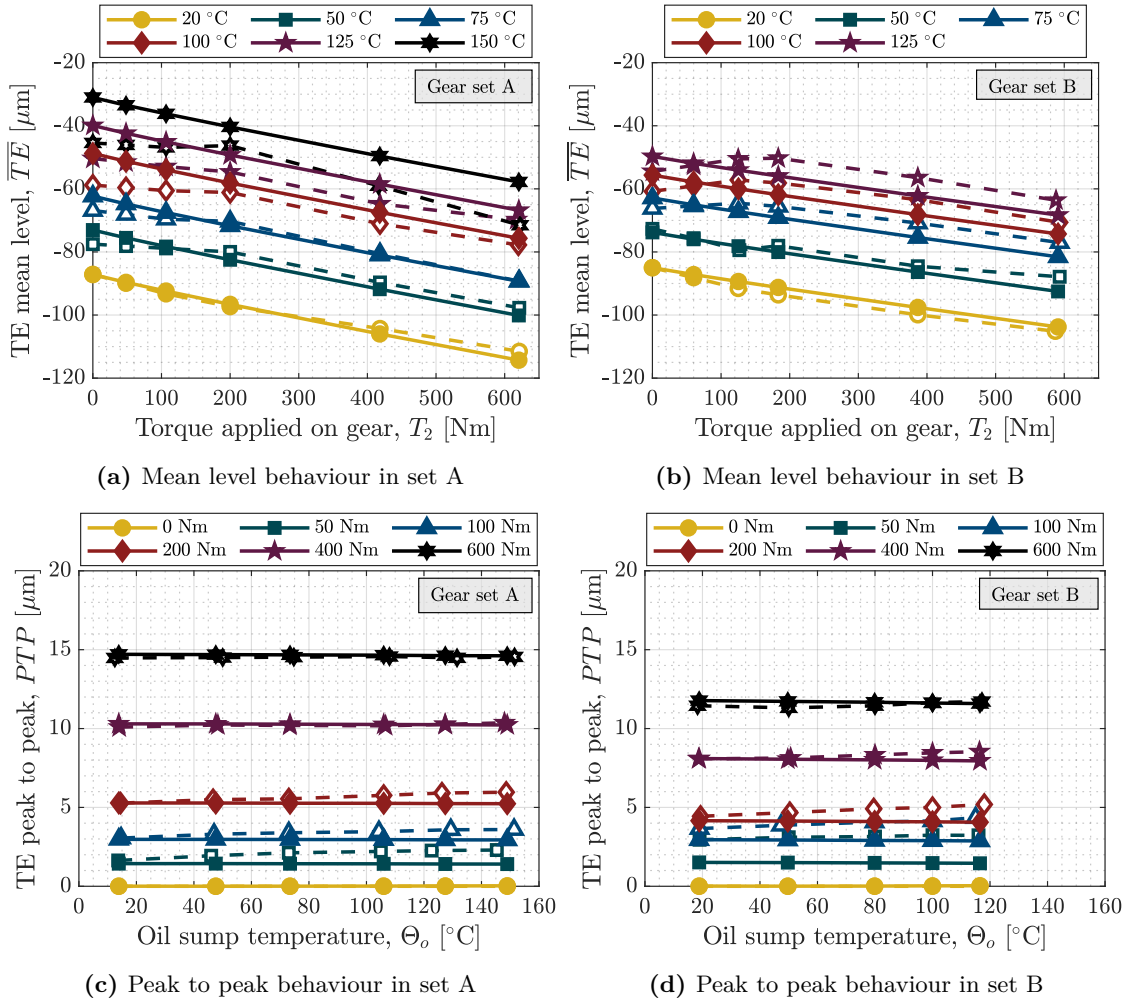


Figure 7.15: Summary of experimental and analytical transmission error mean level and peak to peak results for variable temperatures and torques for both gear sets

Mean level analytical predictions are consistent with conclusions in Chapter 6 and closely follow the experimental trend, at least up to 100°C oil sump temperature for all torque levels. Meanwhile, analytical peak to peak values remain almost constant for each load stage but experimental results slightly increase with temperature. Furthermore, it is interesting to note that the effect of temperature on experimentally measured peak to peak seems to be more pronounced at low torques which is consistent with analytical predictions made in Section 6.3.2. Such differences in mean level and peak to peak arising at the highest temperatures may be explained by existing temperature gradients between components which has already been shown to affect TE in Figure 6.21.

7.4 Discussion

Comparison of analytical results and experimental measurements has shown that accurate predictions of thermo-mechanical TE behaviour can be made when the temperature distribution is known. In this sense, measurements point out that at high temperatures (above 100°C) thermal gradients may exist which explains that experimental results deviate from the analytical trends. Thus, the influence of temperature distribution is discussed here.

Figure 7.16 summarizes the measured mean temperatures and corresponding deviations of different parts of the gearbox for each oil sump temperature stage. At oil bath temperatures below 100°C , the steady state sump temperature is almost equal to the preset value. Furthermore, no significant temperature differences exist between the oil sump and the gear teeth and the standard deviation is quite small, approximately $\pm 3^{\circ}\text{C}$. Thus, the PID control accurately maintains the oil sump temperature at the prescribed value. However, at higher temperatures, the standard deviation increases significantly indicating that the PID control hardly maintains oil sump temperature. Moreover, gear tooth temperature is higher than that of the oil bath probably due to oil film thickness decrease in the contact zone. As a consequence, friction coefficient in the mesh takes the boundary friction coefficient value and progressively heats gear teeth above the oil bath temperature due to surface sliding.

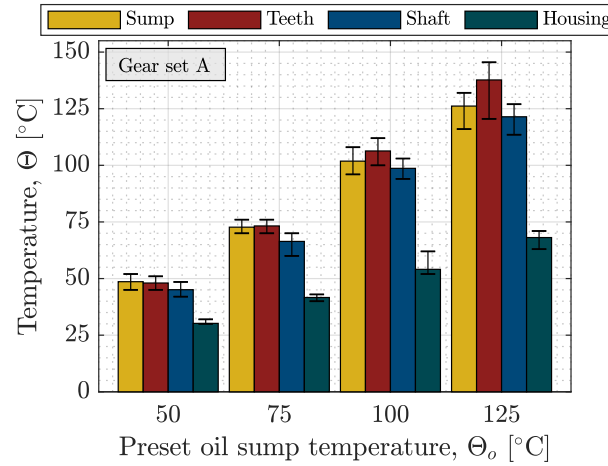


Figure 7.16: Gearbox temperature distribution relative to preset temperature in PID

In cases where the tooth temperature is higher than that of the oil, the available backlash should be reduced more than expected. Therefore, experimentally measured mean level of transmission error in Figure 7.15a should overcome the predicted value, but this is not the case. It is to be noted in Figure 7.16 that at high temperatures not only thermal gradients arise between the oil sump and the gear teeth but also between the teeth and the shaft. Consequently, radial thermal gradients prevent maximum tooth deformations and corresponding backlash reduction. The final transmission error value depends on the exact temperature distribution for each case. Thus, the initial assumption on the temperature of the gear being constant and equal to that of the oil bath is not true at the highest temperature levels.

Moreover, the existence of thermal gradients also explains the increasing peak to peak TE with temperature. Analytical predictions discussed in Section 6.3.2 showed that an approximate temperature difference between pinion and gear of 30°C produced a peak to peak increase of about $1.5\ \mu\text{m}$. The maximum increase for the reference torque is approximately $0.7\ \mu\text{m}$ for gear set A and $1\ \mu\text{m}$ for set B. Therefore, temperature differences between pinion and gear must be close to 15°C and 20°C respectively.

Figure 7.17 shows the influence of an increasing temperature difference on both gear sets. As expected, peak to peak transmission error computed including temperature differences approaches the experimental result. However, it is not probable that such a significant thermal gradient exist between pinion and gear, especially on gear set A. Temperature distributions presented in Chapter 2 have shown that thermal gradients depend on rotation speed, gear ratio and lubrication conditions; therefore, if the immersion depth is high, gear ratio is equal to one and speed is low, pinion and gear temperatures are expected to be equal and constant.

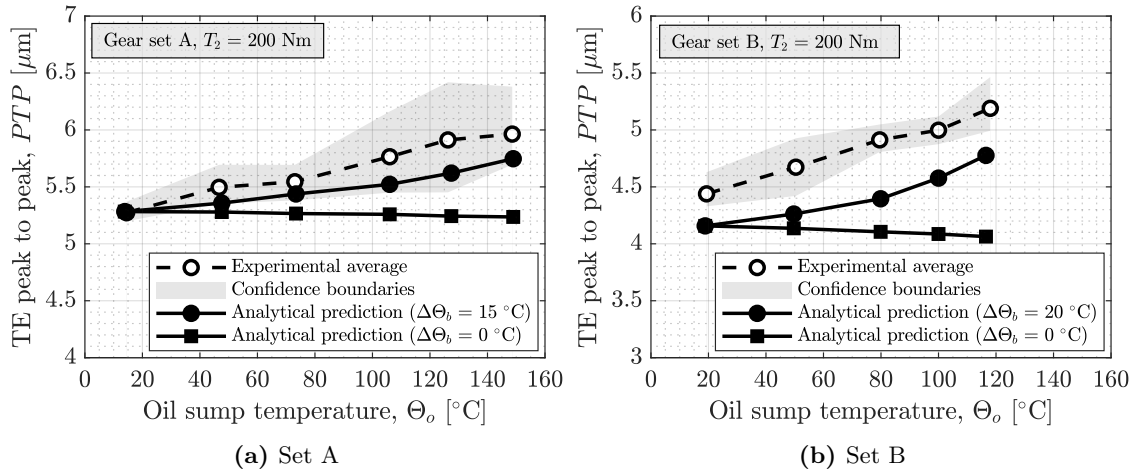


Figure 7.17: Influence of temperature differences on peak to peak transmission error

Currently it is not possible to measure transmission error and pinion and gear temperatures at the same time as encoders and slip rings must be mounted on the same shafts. The measured tooth temperature values correspond to the driven gear in the drive gearbox. Test and drive gearboxes being equal, temperatures measured on one side can be extrapolated to the other. The problem is that only temperatures of one gear can be measured in the drive gearbox and therefore it is not possible to validate such temperature differences unless individual thermal and TE tests are carried out under the same operating conditions. This study will be left for future work.

7.5 Conclusions of Chapter 7

In this chapter an experimental study of thermo-mechanical quasi-static transmission error behaviour has been presented. Scientific literature review in Chapter 2 has shown that no experimental evidence on the composite effect of temperature and torque on quasi-static transmission error exists up to date. Although some authors (e.g. [292]) already pointed out that temperature influences mean level of transmission error and thus affects positioning accuracy, no previous reference to peak to peak behaviour has been found and comparison to torque effects have not been performed. Overall results show that the effect of temperature and torque coexist in TE diagrams. Both parameters have a significant role in the mean level of transmission error while the influence of torque on peak to peak is prominent relative to that of temperature. Although the correlation between the change of mean level and that of backlash for increasing temperatures is clear, peak to peak variation due to temperature is not obvious.

In the first section of this chapter the design characteristics of a new back-to-back gear test rig developed during this thesis have been presented. The test bench is based on the standard FZG machine but enhanced characteristics to study thermal behaviour of high speed gear transmissions have been introduced. Then, experimental methodology has been described, geometrical characteristics of two test specimens have been presented and operating conditions for the tests have been defined.

The experimental setup and measurement procedure have been described next. It has been shown that due to the nature of the optical encoders, single-turn absolute angular position measurements need to be converted to continuous incremental signals before transmission error is computed. Fast Fourier Transform and high pass filtering procedures have been described and repeatability tests have been carried out. It has been shown that due to manufacturing and assembly errors, the amplitude at mesh frequency and subsequent harmonics can not be used to determine the influence of torque and temperature on transmission error due to lack of repeatability; as a consequence, a different approach has been proposed.

Finally, quasi-static thermo-mechanical transmission error measurement results have been presented. Tests have been carried out at low rotational speed, constant torque and constant oil sump temperatures such that pinion and gear teeth temperature is assumed equal to that of the oil bath. It has been shown that temperature increase reduces the amount of available backlash and therefore mean level of transmission error is affected. Both parameters have been shown to be correlated as proved analytically in the Chapter 6. Transmission error behaviour under load and temperature have been analysed next. Analytical results closely follow the experimental measurements and mean level of TE and peak to peak values have been compared. Although, results under load are far more accurate than those of temperature, the predicted trend is correct in all cases. It has been shown that existing errors are probably due to thermal gradients arising at the highest oil sump temperature which are difficult to control. Although such temperature differences explain the discrepancies of the measured mean level and peak to peak TE , further experimental study is required before definite conclusions are withdrawn.

*Reasoning draws a conclusion, but does not
make the conclusion certain, unless the mind
discovers it by the path of experience.*

— Roger Bacon’s *Opus Majus*, 1267

8

Conclusions and Future Work

Contents

8.1 Concluding remarks	220
8.2 Recommendations for future work	222
8.3 Scientific contributions	223

This chapter summarizes the principal contributions of the thesis. At this point, it is fundamental to recall the main objective of this work which has been stated as: “To predict, evaluate and correct uneven mechanical behaviour of spur and helical gears due to thermally-induced flank geometry distortion”. To this aim, it has been necessary to quantify frictional heating from the gear mesh which is one of the primary heat sources affecting gear bulk temperature. A new friction coefficient model for cylindrical gears has been proposed and a power loss prediction methodology has been defined. Then, a thermal model of meshing gear pairs has been developed to compute steady-state temperature distribution. The latter has been coupled to the power loss prediction algorithm such that predicted temperatures are used to recalculate mesh frictional heating with greater accuracy. Once steady-state condition is reached, radial and longitudinal temperature distributions have been analysed and a thermal expansion model has been proposed. The understanding of the type and amount of thermal distortion, along with its effects on loaded behaviour, have allowed to correct tooth geometry and compensate undesired contact behaviour. The present research work concludes with an experimental study validating some of the analytical predictions. Overall results indicate that thermal distortion does play an important role on mechanical behaviour and it should be considered in tooth contact analysis, specially in high-speed and high gear ratio applications. In the following, the main conclusions relative to each of the initial objectives are gathered, other tasks carried out during the thesis are outlined and recommendations for future work are highlighted.

8.1 Concluding remarks

In the present thesis a complete analytical thermo-mechanical approach for the prediction and compensation of thermally-induced geometry distortion is proposed. Several tasks have been covered in the chapters of the thesis, each of them meeting the requirements of one of the six specific objectives stated in Section 1.3, namely: geometry generation and tooth contact analysis, mesh heat prediction, temperature distribution calculation, thermal expansion modelling, distorted tooth geometry modification and experimental observation of thermal distortion effects on mesh behaviour. Individual conclusions are outlined here.

O.1) Load distribution and kinematic behaviour modelling. An analytical load distribution and transmission error computation model based on the classical thin-slice approach and including convective effects has been proposed in Chapter 3. Following Conry and Seireg's definition of the load distribution problem [187], the system of equations has been restated numerically as a Linear Complementarity Problem (LCP) where Lemke's pivoting algorithm [201] has been used to obtain the exact solution. Analytical results computed with this novel procedure, have been compared to finite element simulations showing very good agreement; except at the highest torques where large teeth deflections produce a significant increase of the contact ratio under load thus involving adjacent teeth compliance. This model is used in the Chapter 4 to predict load dependent instantaneous friction coefficients and heat flux in the base tangent plane (stated as objective 2).

O.2) Frictional heat flux prediction. Literature review in Chapter 2 has shown that most of the available sliding friction coefficient models require empirical lubricant-specific coefficients and therefore they cannot be used with different oils without prior characterization in tribometers. To solve this issue, a new EHL friction coefficient model has been proposed in Chapter 4 based on primary rheological parameters of the lubricant. The Ree-Eyring non-Newtonian model [59] is used in this work where the reference stress is predicted from piezo-viscosity and limiting shear stress coefficients. Furthermore, the range of applicability of the model has been extended to cover partial EHL regime; by using a simple asperity load sharing equation described by the complementary error function of the specific film thickness. Moreover, an original thermally-coupled power loss prediction method has also been proposed in this chapter, which accounts for tooth temperature distribution and separates skin temperatures (necessary to compute oil film thickness) from film temperature (required to compute traction). Both, the friction coefficient model and the power loss prediction method, have been compared to experimental results from literature using different oils. Errors below 25% were obtained in all the considered test cases and less than 10% in 70% of them, which is acceptable considering the number of assumptions involved in pursuit of simplicity. This heat estimation is used in Chapter 5 to compute temperature distribution in cylindrical gear pairs (objective 3).

O.3) Temperature distribution calculation. A thermal lumped parameter model of dip lubricated gear pairs has been developed in Chapter 5. The new model is characterized by computing simultaneously the temperature distribution of shafts, pinion and gear in the radial and longitudinal directions with minimum computational effort with respect to finite element models. For this purpose, gear body and shaft are discretized in

cylindrical volumes while gear teeth are assumed to be subject to a constant temperature; as thermal gradients are negligible due to its small size with respect to the rest of the body. Moreover, heat inputs from bearings, sealings, oil churning and windage have been quantified and the influence of variable immersion depths on local convection heat transfer coefficients has been considered. Resulting temperature distributions show a power law type behaviour in the radial direction and parabolic type in the longitudinal one, with up to 20°C difference between tooth centre and shaft and 10°C gradient along the face width in large gears. The proposed model has been compared to experimental results from Otto [28] and, although discrepancies have been found, the overall trend with immersion depth is predicted. Further refinement of the model is required to increase accuracy at the lowest immersion depths but the proposed model is used to calculate thermal distortion in the next chapter (objective 4).

O.4) Thermal distortion modelling. A novel thermally-induced geometry distortion model for spur and helical gears has been developed in Chapter 6 and the effects of flank deviations on loaded behaviour have been analysed. The thermal distortion model is based on the thin-slice approach used in the computation of load distribution and assumes that the expansion of each point in the involute is mainly radial, thus dependent on the transverse temperature distribution of each slice. Thermal growth is computed following the disc approximation and considering the effect of thermal stresses due to power law-type temperature distributions previously observed in Chapter 5. It has been shown that profile and helix slope deviations are the main causes of thermal distortion while form errors are negligible; except when large longitudinal thermal gradients exist which produce a barrelling of the pitch cylinder. Furthermore, it has been found that thermal stresses limit the amount of total deviation and loaded behaviour is only affected when significant temperature differences between pinion and gear exist ($> 10^\circ\text{C}$); which is consistent with experimental observations in scientific literature [24]. Finally, an helical gear stage from an EV application has been fully analysed from geometry distortion to loaded behaviour. The numerical results point out that uneven load distribution due to the composite effect of profile and helix slope deviations affect root and contact stresses with a 46% increase in the maximum bending stress in the pinion and a 54% in the maximum contact stress. Transmission error behaviour is also affected; both in the overall behaviour and peak-to-peak values. The identification of the main parameters influencing thermally-induced geometry distortion and its effects on mesh behaviour, leads to the definition of tooth geometry compensation methods (objective 5).

O.5) Tooth geometry compensation. The type and amount of flank deviation have also been analysed in Chapter 6 following the classification and limitations defined by ISO 1328 standard [284]. It has been observed that, for a given temperature distribution, the amount of profile slope error is mainly affected by normal module and pressure angle while lead deviations depend on face width and helix angle. Besides, it has been proven that pitch deviations and backlash are geometrically related to slope deviations. Although the former significantly increases with temperature, no relative pitch deviation exists if pinion and gear are subject to the same temperature increase, and therefore, no load

distribution alteration is expected. Meanwhile, thermal effects on backlash should only be considered in applications with high positioning accuracy requirements or in case of tight manufacturing allowances where gear jamming may occur. Design recommendations have been gathered at the end of Chapter 6 and simple tooth modification guidelines have been established assuming that gear temperature is constant. It has been shown for the first time that it is possible to compensate thermally-induced geometry distortion at the design stage provided that temperature differences between pinion and gear are known.

O.6) Experimental observation of thermal distortion effects. The present thesis concludes with an experimental study on thermo-mechanical quasi-static transmission error behaviour of spur gears (objective 6). For this purpose, a back-to-back gear test rig has been designed, manufactured and assembled during the thesis; with enhanced characteristics with respect to the standard FZG machine to study thermal behaviour of cylindrical gears. Two different sets of spur gears have been analysed and it has been shown that the effects of temperature and torque coexist in TE behaviour. Temperature increase reduces the amount of available backlash and therefore rises the mean level of transmission error, while torque increase affects in the opposite way, by descending the TE diagram. The influence of temperature on mean level is prominent with respect to that of torque; on the contrary, peak to peak TE is clearly affected by load while temperature effect is almost negligible. Both observations agree well with predicted analytical trends from Chapter 6 but further experimental investigation is required to validate other results such as the influence of temperature differences between pinion and gear on tooth root strain.

8.2 Recommendations for future work

This PhD dissertation has provided a fundamental understanding of heat generation sources in cylindrical gears, parameters affecting temperature distribution and resulting thermally-induced geometry distortion effects. The analytical and experimental observations made during the development of each of the objectives presented in Section 1.3 has led to the definition of the following directions for future work.

- **O.1:** Literature review has shown that double helical gears are subject to complex thermo-mechanical interactions. It is desirable to extend the load distribution model to include such gears specially focusing on edge effect modelling and accurate contact pressure distribution calculation (i.e. Boussinesq-Cerruti type solution).
- **O.2:** Friction coefficient model has been developed in the full EHL regime and partial EHL regime behaviour has been largely simplified. To keep an engineering perspective avoiding extensive numerical calculations, a master curve for asperity-load sharing modelling is desired, either empirical or numerical, similarly to [294].
- **O.3:** The thermal model has been developed for dip-lubricated gear pairs and extension to jet lubricated systems is necessary to analyse axial oil pumping effects. The latter can be modelled as an advection heat transfer along the tooth face width yielding a non-symmetrical temperature distribution and contact pattern.

- **O.4:** Thermal distortion model has been developed following a power law type temperature distribution and temperature deviations near the tooth tip or in the axial directions have been neglected. A different approach is required to include the latter and quantify the influence of local thermal gradients on computed deviations.
- **O.5:** Tooth modification guidelines have been provided, assuming that if no thermal gradient exist form deviations are negligible and slope errors prevail. However, helical gears subject to longitudinal temperature gradients are frequent and form deviations do exist. It is necessary to further analyse compensation techniques for such cases.
- **O.6:** Transmission error and backlash behaviour in spur gears subject to load and temperature has been analysed and extension to helical gears is expected. Moreover, measurement of tooth root strain misbehaviour relative to temperature differences between pinion and gear is desired; as it is an indicator of uneven load distribution.

8.3 Scientific contributions

The work presented in this thesis has been published in different scientific conferences and journals, which are grouped below into the different objectives defined in Chapter 1.

On load distribution [O.1]:

1. A. Iñurritegui, A. Arana, M. Hernandez, J. Elizegi, I. Ulacia, J. Larrañaga. “Modelizado bidimensional de engranajes cilíndricos por elementos finitos”. In: *Proceedings of the XXII Congreso Nacional de Ingeniería Mecánica*, 2018.

On friction and power losses [O.2]:

2. A. Arana, J. Larrañaga, I. Ulacia. “Partial EHL friction coefficient model to predict power losses in cylindrical gears”. In: *Proceedings of the Institution of Mechanical Engineers, Part J: Journal of Engineering Tribology* 233.2 (2018), pp. 303-316.
3. A. Arana, J. Larrañaga, I. Ulacia. “Analysis of the influence of lubricant type on friction coefficient of cylindrical gears”. In: *Proceedings of the 6th Lubrication, Maintenance and Tribology Conference*, 2018.
4. A. Arana, J. Larrañaga, I. Ulacia. “Gear mesh power loss prediction under mixed lubrication regimes at high speeds”. In: *Proceedings of the 5th Lubrication, Maintenance and Tribology Conference*, 2016.
5. A. Arana, I. Ulacia, J. Larrañaga, M. Izquierdo, I. Eraña. “Análisis numérico de modelos de predicción de eficiencia de engranajes cilíndricos rectos”. In: *Proceedings of the XX Congreso Nacional de Ingeniería Mecánica*, 2014.
6. A. Arana, I. Ulacia, J. Larrañaga, M. Izquierdo, I. Eraña. “Experimental spur gear efficiency evaluation including bearing and lubrication losses”. Oral presentation. In: *International Gear Conference*, 2014.

On temperature distribution [O.3]:

7. A. Arana, J. Larrañaga, I. Ulacia. “Prediction of gear bulk temperature rise in dip lubricated gears”. In: *Proceedings of the Balkan Association on Power Transmission Conference*, 2016.
8. A. Arana, I. Ulacia, J. Larrañaga. “Modelo térmico transitorio de engranajes cilíndricos en condiciones de lubricación mixta”. In: *Proceedings of the XXI Congreso Nacional de Ingeniería Mecánica*, 2016.
9. A. Arana, I. Ulacia, J. Larrañaga. “Metodología de cálculo térmico de transmisiones a engranajes”. In: *XX Congreso de Máquina Herramienta y Tecnologías de Fabricación*, 2015.

On thermal distortion [O.4, O.5]:

10. A. Arana, A. Iñurritegui, J. Larrañaga, I. Ulacia. “Influence of thermal distortion on load distribution, transmission error and premature contact”. In: *Proceedings of the International Gear Conference*, 2018. Vol. 1, pp. 446-459.
11. J. Larrañaga, I. Ulacia, A. Iñurritegui, A. Arana, J. German, J. Elizegi. “Influence of thermal distortion on spur gear tooth contact”. In: *Proceedings of the AGMA Fall Technical Meeting*, 18FTM07, 2018.

Other contributions made during the thesis:

12. I. Ulacia, J. Larrañaga, A. Arana, A. Iñurritegui, J. Elizegi. “Fatigue life prediction of spherical gear couplings”. In: *Proceedings of the AGMA Fall Technical Meeting*, 18FTM14, 2018.
13. I. Ulacia, J. Larrañaga, A. Arana, J. Elizegi J.A. Esnaola. “Predicción de vida a fatiga de acoplamientos dentados abombados con elevadas desalineaciones”. In: *Revista Iberoamericana de Ingeniería Mecánica* 22.2 (2018), pp. 91-101.
14. I. Ulacia, A. Arana, J. Maskariano, J. Larrañaga. “Analysis of fatigue and wear in crowned spline couplings”. In: *Proceedings of the 10th International Symposium on Machine and Industrial Design in Mechanical Engineering*, 2018.
15. I. Ulacia, A. Arana, J. Maskariano, J. Larrañaga. “Analysis of wear in crowned spline couplings”. In: *Proceedings of the 6th Lubrication, Maintenance and Tribology Conference*, 2018.
16. J. Larrañaga, A. Arana, I. Ulacia, J.A. Esnaola. “Misalignment effect on contact and stress pattern of spline couplings”. In: *Proceedings of the Balkan Association on Power Transmission Conference*, 2016.

Appendices

*A gem cannot be polished without friction,
nor a man perfected without trials.*

— Lucius Annaeus Seneca, 5 BC - 65 AD



Bearing and Sealing Power Loss Models

To enhance the readability of the document, bearing and lip sealing power loss models to be used within Chapter 5 are gathered in this appendix. The most common models in scientific literature are presented: that of SKF [295] for bearing power losses and the model by Freudenberg [296] for lip sealings.

Lip sealings

Shaft sealing losses are difficult to characterize as complex microscopic polymer-shaft friction mechanisms occur in the contact zone [297]. Generally speaking, power losses are computed from the torque loss in the rotating shaft following Equation A.1:

$$P_{VD} = T_{VD} \cdot \omega = \frac{1}{2} \cdot d_{sh} \cdot \mu \cdot W \cdot \omega = \frac{\pi}{2} \cdot d_{sh}^2 \cdot \mu \cdot p \cdot b \cdot \omega \quad (\text{A.1})$$

The problem with the proposed approach is computing the friction coefficient in the contact zone, μ , the contact pressure, p , and the width of the contact area, b , due to the large deflections occurring in the contact zone due to polymer elasticity and micro-scale asperity interactions. To solve this issue, manufacturer Freudenberg Simrit [296] derived the following empirical equation based on a large number of measurements:

$$P_{VD} = 7.69 \cdot 10^{-6} \cdot d_{sh}^2 \cdot N \quad (\text{A.2})$$

However, this equation does not consider the influence of lubricant temperature, Θ_o , which tends to reduce friction coefficient and thus, power losses. Linke [298] further developed this equation to account for oil kinematic viscosity, ν_k , at its operating temperature; yielding the same results for the SAE 20 oil at 100°C, which is the reference oil in the derivation of Equation A.2. The model derived by Linke reads:

$$P_{VD} = [145 - 1.6 \cdot \Theta_o + 350 \cdot \log(\log(\nu_{k,40} + 0.8))] \cdot 10^{-7} \cdot d_{sh}^2 \cdot N \quad (\text{A.3})$$

Figure A.1a at the end of Appendix A depicts the general behaviour of Equation A.3 with the main variables. Note that the influence of oil temperature is considerable increasing or decreasing power losses approximately 1% per degree at 4000 rpm. Furthermore, shaft diameter effect is also highlighted as power losses depend on the square of the latter. For the considered diameters, lip sealing losses are larger than those produced by oil churning and windage in Figure 5.5 thus contributing to shaft heating and altering the gear temperature distribution if it is nearby.

Bearings

Two different types of bearing power loss models are frequent in scientific literature: i) the classical Avrid Palmgren empirical model [299] and ii) the SKF computational model [295]. The former is the basis of current thermal rating standards [16] and determines the rolling bearing friction torque as the sum of a load dependent term and a no-load one, both of which are evaluated through experimental measurements of different bearing types and sizes. The latter, analytically extends this approach by considering that the total friction torque is the sum of four different physical sources of torque loss, namely: rolling, sliding, oil drag and sealings. Recent experimental evidence [29] shows that appreciable differences exist between both models and therefore, the SKF model is preferred in this work where total bearing power loss is computed from:

$$P_{VL} = T_{VL} \cdot \omega \quad (\text{A.4})$$

$$T_{VL} = T_{VL0} + T_{VLP} = [T_{drag} + T_{seal}] + [T_{rr} + T_{sl}] \quad (\text{A.5})$$

with the no-load term, T_{VL0} , corresponding to the sum of torque losses produced by sealings, T_{seal} , and oil drag, T_{drag} ; while the loaded term depends on rolling and sliding friction torques, T_{rr} and T_{sl} respectively.

On the one hand, drag losses due to oil agitation can be predicted following Equations A.6 and A.7 for ball bearings and roller bearings respectively.

$$T_{drag} = N^2 \cdot d_m^3 \cdot \left[0.4 \cdot V_M \cdot K_{ball} \cdot d_m^2 + 1.093 \cdot 10^{-7} \cdot \left(\frac{N \cdot d_m^2 \cdot f_t}{\nu_k} \right)^{-1.379} \cdot R_s \right] \quad (\text{A.6})$$

$$T_{drag} = N^2 \cdot d_m^3 \cdot \left[4 \cdot V_M \cdot K_{roll} \cdot C_W \cdot B \cdot d_m + 1.093 \cdot 10^{-7} \cdot \left(\frac{N \cdot d_m^2 \cdot f_t}{\nu_k} \right)^{-1.379} \cdot R_s \right] \quad (\text{A.7})$$

with d_m being the bearing mean diameter, ν_k the kinematic viscosity of oil at the operating temperature and N the rotational speed in rpm. The rest of the parameters: V_M , $K_{ball,roll}$, C_W , B , f_t and R_s are dependent on the geometry of the bearing, its size and the operating conditions. The reader is referred to SKF catalogue [295] for additional information on them.

On the other hand, if bearings contain contact seals, frictional torque is estimated with:

$$T_{seal} = K_{S1} \cdot d_s^\beta + K_{S2} \quad (\text{A.8})$$

where d_s is the seal counterface diameter and β and $K_{S1,2}$ are exponents and constants depending on the bearing type and size.

Figure A.1b depicts the predicted trend for no-load losses in deep groove ball bearing type 6306 and cylindrical roller bearing reference NJ406. The former is usually the rear bearing support in each shaft of the FZG back to back test rig while the latter is commonly the front bearing. These bearings do not include sealings and therefore, curves only represent drag losses. Note that drag moment is higher in roller element bearings with almost three times higher power losses at the highest speed. This behaviour is explained by the geometry of the rollers which creates more drag than perfect spherical balls, however, it is also highlighted that the mean diameter of reference NJ406 is larger than that of 6306 and therefore, composite drag and size effect is shown in the figure. Furthermore, it is also interesting to remark that the influence of oil viscosity is negligible at mid to high temperatures, therefore, low viscosity oils are desired to minimize bearing spin losses.

Meanwhile, load-dependent rolling friction term is computed following:

$$T_{rr} = \phi_{sh} \cdot \phi_{rs} \cdot G_{rr} \cdot (\nu_k \cdot N)^{0.6} \quad (\text{A.9})$$

where ν_k is the kinematic viscosity of the lubricant at operating temperature, N is the rotational speed in rpm and G_{rr} is a variable dependent on bearing type, size and loads. Parameters ϕ_{sh} and ϕ_{rs} are factors accounting for the inlet shear heating effect in the contact area and the starvation of lubricant at high speeds respectively.

$$\phi_{sh} = \frac{1}{1 + 1.84 \cdot 10^{-9} \cdot (N \cdot d_m)^{1.28} \cdot \nu_k^{0.64}} \quad (\text{A.10})$$

$$\phi_{rs} = \frac{1}{e^{\left[K_{rs} \cdot \nu_k \cdot N \cdot (d+D) \cdot \sqrt{\frac{K_z}{2 \cdot (D-d)}} \right]}} \quad (\text{A.11})$$

with D , d and d_m the outer, inner and mean diameters respectively and K_{rs} and K_z constants depending on lubrication method and gear geometry. Note that the inlet shear heating effect has already been introduced in Equation 4.51 for the gear mesh, which accounts for the influence of the oil film thickness reduction at high speeds.

Finally, the sliding friction torque is calculated using:

$$T_{sl} = G_{sl} \cdot \mu_{sl} \quad (\text{A.12})$$

where G_{sl} depends on bearing type, size and loads and μ_{sl} is the sliding friction coefficient which is also based on a asperity load sharing approach similarly to Equation 4.25 in gears.

$$\mu_{sl} = \phi_{bl} \cdot \mu_{bl} + (1 - \phi_{bl}) \cdot \mu_{EHL} \quad (\text{A.13})$$

$$\phi_{bl} = \frac{1}{e^{[2.6 \cdot 10^{-8} \cdot (\nu_k \cdot N)^{1.4} \cdot d_m]}} \quad (\text{A.14})$$

with μ_{bl} and μ_{EHL} the boundary lubrication and the elastohydrodynamic lubrication friction coefficients respectively. SKF model recommends, $\mu_{bl} \approx 0.15$ for mineral oils and $\mu_{EHL} = 0.05$ for ball bearings and $\mu_{EHL} = 0.02$ for roller bearings. These values are already known to be dependent on the lubricant type, rheological properties, surface roughness and contact conditions, however, no analytical method is proposed in [295] to compute these parameters and experimental values are used instead.

Figures A.1c and A.1d summarize the loaded behaviour of ball and roller bearing references 6306 and NJ406 respectively for different radial loads, speeds and oil temperatures. It is observed that the influence of oil temperature in Figure A.1c is important if compared to no-load power loss terms. At low temperatures the viscosity is high and additional effort is required to shear the lubricant in the contact zone thus increasing friction coefficient and power losses. As temperature is increased, viscosity is reduced and friction and power losses decrease as a consequence. The effect of load is depicted in Figure A.1d, increasing loads produce larger rolling and sliding torque losses through the G_{rr} and G_{sl} terms in Equations A.9 and A.12. However, load is known to affect on EHL friction coefficient value as well but SKF model does not allow to introduce this effect. If the influence of bearing type is analysed, roller bearings also produce a larger power loss similarly to spin losses.

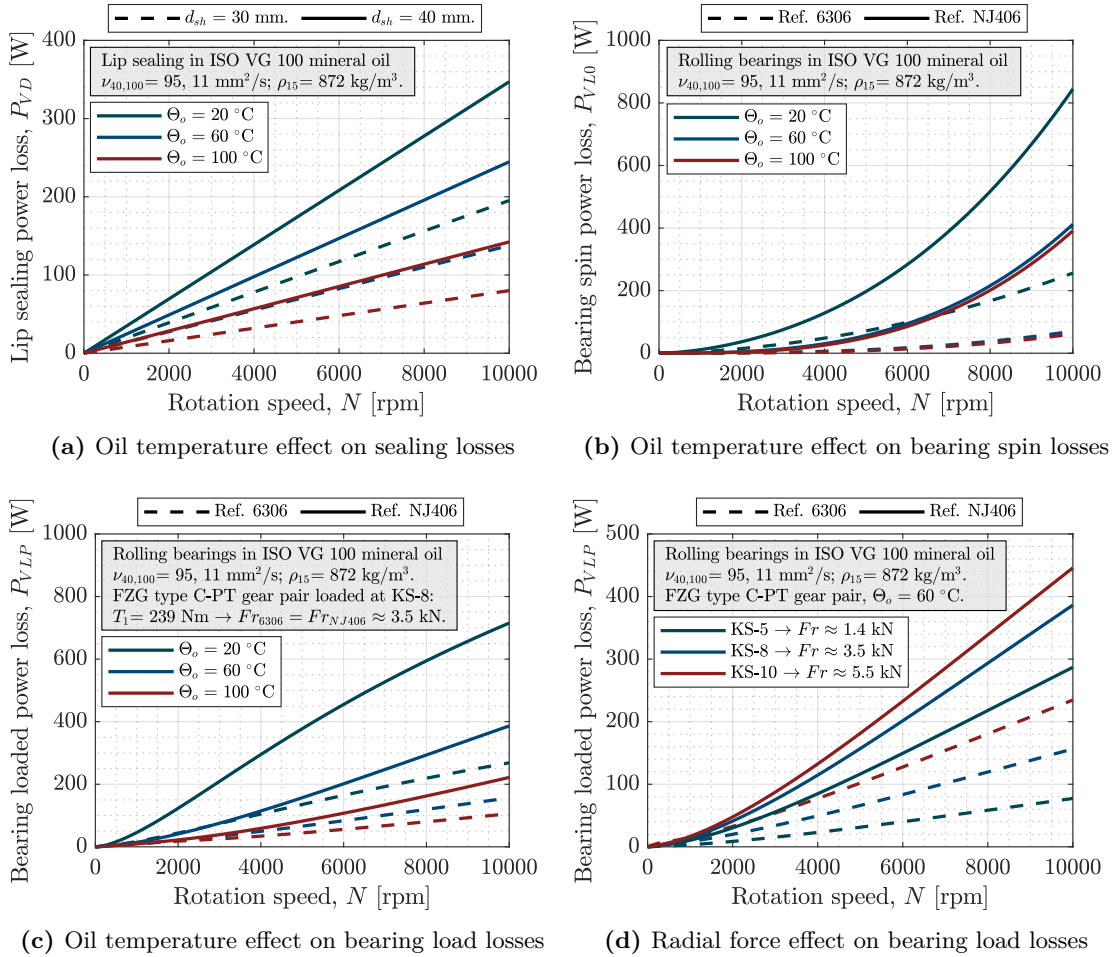


Figure A.1: Influence of speed, load and temperature on lip sealing and bearing power losses

*We may have all come on different ships,
but we're in the same boat now.*

— Martin Luther King, 1929 - 1968

B

Analytical - Numerical Distortion Comparison

Thermally-induced geometry distortion in external cylindrical gears has been modelled following analytical solutions for disc expansion under the plane stress condition (see Section 6.2.1). The main underlying assumptions for such simplification are that temperature distribution in each gear slice is fundamentally radial and no circumferential thermal gradient exists in the steady-state regime. The size of gear teeth being relatively small with respect to that of the gear body, and if tooth thermal gradients are neglected, local displacements in the involute profile are mainly due to the gear body expansion. Therefore, the whole gear can be approximated as a disc subject to a radial temperature distribution. In order to validate this approach, analytical distortions computed with Equations 6.5 and 6.17 are compared to those obtained with a finite element model where spur gears are subject to power law type temperature distribution.

Two different geometries have been meshed following the procedure and element type presented in Section 3.4.1, but in this case, only a single gear has been considered. The power law temperature distribution follows Equation 6.8, no rotation has been applied and the displacement boundary conditions have been defined such that the local horizontal and vertical axis of the gear have been left free for expansion, while the displacements in the orthogonal directions are restrained (see Figure B.1). Only deformations of the active profile are analysed and the influence of thermal stress is closely observed. Table B.1 summarizes basic geometrical parameters of the considered test cases.

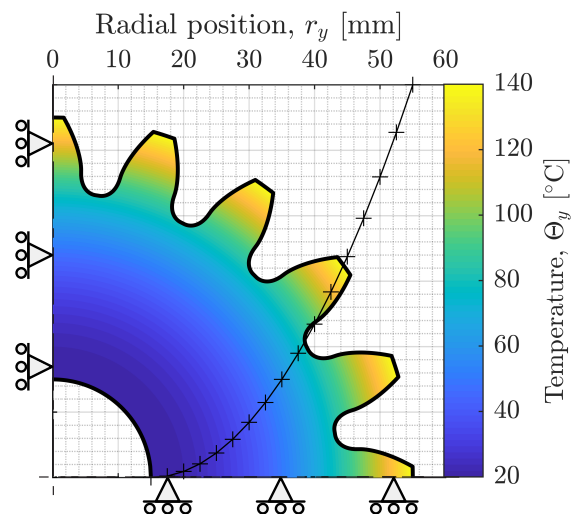


Figure B.1: FE modelling of gear expansion subject to a parabolic radial thermal gradient

In order to analyse the influence of tooth size relative to that of the gear body, two different modules are proposed in Table B.1 with the number of teeth updated accordingly to yield the same pitch diameter. Furthermore, temperature distributions are exaggerated to analyse the influence of thermal stresses on flank deviations; with gradients following a linear, parabolic or hyperbolic trend and temperature differences between the shaft and the tooth tip ranging from 20°C to 200°C.

Table B.1: Spur gear geometries for finite element simulation of thermal distortion

Parameter	Symbol	Value
Normal module	m_n [mm]	1.25 / 5
Number of teeth	z [-]	80 / 20
Profile shift coeff.	x_E [-]	-0.0989/ -0.0247
Pressure angle	α_n [°]	20
Shaft diameter	d_{sh} [mm]	30
Reference tool acc. ISO 53	[-]	A (1.25/1.0/0.38)
Thermal expansion coeff.	α_L [K ⁻¹]	$12 \cdot 10^{-6}$
Modulus of elasticity	E [GPa]	206
Poisson's ratio	ν [-]	0.3

Figure B.2 shows a sample thermal distortion of the smallest module gear subject to a 100°C tip temperature increase of parabolic shape. Analytical results follow those obtained numerically and the influence of thermal stresses is also depicted. Note that the shaft is subject to ambient temperature while the tooth tip temperature is considerably increased with respect to the latter, hence, thermal gradients are important and thermal stress influence on the total amount of deformation is significant. This behaviour is repeated in all the considered test cases and it becomes more visible with increasing temperature differences between tip and shaft.

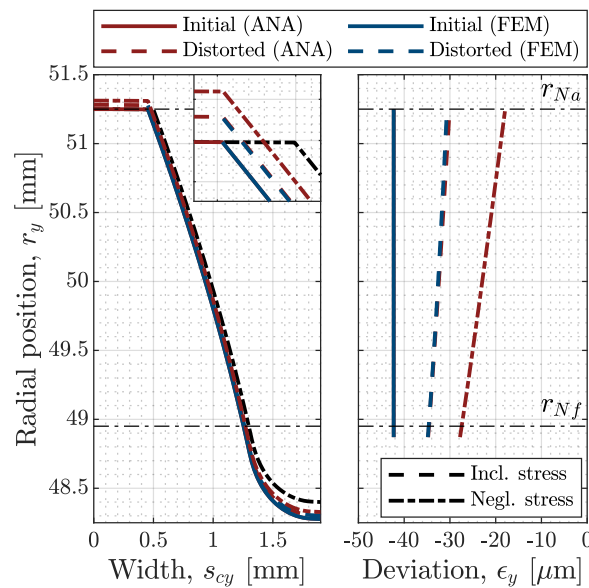


Figure B.2: Influence of thermal stresses on analytical predictions and comparison to numerical results for the case of small module gear subject to a 100°C parabolic temperature increase at tip

The overall performance of the analytical thermal distortion model with respect to the finite element simulations is summarized in Figure B.3. The acceptance criteria for the so called “disc approximation” has been defined as maximum errors not exceeding 5% of the result computed numerically in every point in the profile direction. It can be observed that this limiting situation is achieved at the largest module subject to high temperature differences between tip and shaft. Therefore, the initial assumption concerning the aspect ratio between tooth and gear body seems to be limited to tooth heights less than 10% of the pitch diameter. In case of smaller modules, analytically computed thermal deformation is predicted with sufficient accuracy.

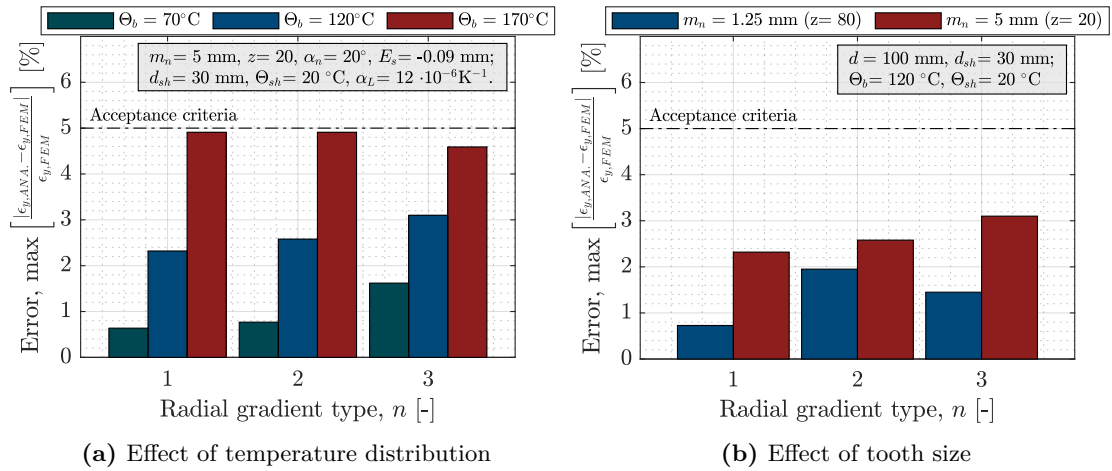


Figure B.3: Influence of thermal gradient and tooth size on computed distortion error

Moreover, if one considers that maximum bulk temperature must not exceed the tempering temperature (approximately 170°C for case carburized steels), it can be assumed that the disc approximation is satisfactory up to 5 mm module as shown in Figure B.3a. Nevertheless it must be emphasised that the imposed thermal gradients are very step as shaft temperature is assumed to be equal to the ambient temperature. In a real situation, differences between the shaft and the tooth reach a maximum of 20°C to 30°C as shown by [119] and therefore, the effect of thermal stresses is reduced. Hence, the disc approximation for gear thermal distortion modelling is considered sufficiently accurate for common operating conditions.

Life was always a matter of waiting for the right moment to act.

— Paulo Coelho's *Veronika Decides to Die*, 1998

C

Hertz Theory for Elliptical Contacts

When two non-conformal elastic bodies with different radii of curvature in the principal directions are pushing against each other, the contact region is elliptical. This situation is found in spur or helical gears when one or both of the wheels are longitudinally crowned and, in such case, classical Hertz theory for line contacts must be modified to account for the radius in the face-width direction. Figure C.1 depicts the general case of two ellipsoids in contact, with parallel orthogonal planes where the common rolling direction is defined by x axis, which is perpendicular to the semi-minor axis, b_H of the contact ellipse. In the case of spur gears, this direction is tangent to the involute profiles of pinion and gear and it is contained in the transverse plane along with one of the principal radius of curvature; while the other, is parallel to the tooth trace. However, in the case of helical gears, Euler's theorem must be applied to find the principal radius of curvature in the common rolling direction which is inclined an angle, ψ , with respect to the tooth trace. For this purpose the following transformation must be applied to the curvatures in the profile and lead directions and the new radii of curvature are obtained from the inverse of the latter [175]:

$$k_{x',i} = k_{x,i} \cdot \cos^2(\psi) + k_{y,i} \cdot \sin^2(\psi) \quad (\text{C.1})$$

$$k_{y',i} = k_{x,i} \cdot \sin^2(\psi) + k_{y,i} \cdot \cos^2(\psi) \quad (\text{C.2})$$

From these values, reduced curvature radius can be predicted and finally, Hertzian contact parameters for elliptical regions are computed following the formulation in Table C.1.

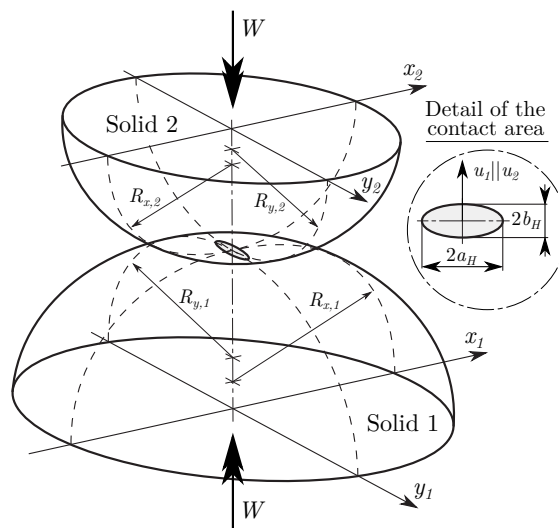


Figure C.1: Schematic representation of non-conformal solids in contact (adapted from [248])

Table C.1: Summary of Hertzian parameters for elliptical contacts

Parameter	Equation
Reduced radius	$\frac{1}{R'} = \frac{1}{R_x} + \frac{1}{R_y} = \left(\frac{1}{R_{x,1}} + \frac{1}{R_{x,2}} \right) + \left(\frac{1}{R_{y,1}} + \frac{1}{R_{y,2}} \right)$ (C.3)
Reduced elasticity	$\frac{1}{E'} = \frac{1}{2} \cdot \left(\frac{1-\nu_1^2}{E_1} + \frac{1-\nu_2^2}{E_2} \right)$ (C.4)
Mean pressure	$p_m = \frac{W}{\pi \cdot a_H \cdot b_H}$ (C.5)
Maximum pressure	$p_H = \frac{3}{2} \cdot p_m$ (C.6)
Semi-major axis	$a_H = \alpha \cdot \left(\frac{3 \cdot W \cdot R'}{E'} \right)^{\frac{1}{3}}$ (C.7)
Semi-minor axis	$b_H = \beta \cdot \left(\frac{3 \cdot W \cdot R'}{E'} \right)^{\frac{1}{3}}$ (C.8)
Normal approach	$\delta = \gamma \cdot \left(\frac{9 \cdot W^2}{8 \cdot R' \cdot E'^2} \right)^{\frac{1}{3}}$ (C.9)

The dimensionless parameters, α , β and γ are computed following Moes equations [300]:

$$\alpha \approx \kappa^{\frac{1}{3}} \cdot \left[\frac{2}{\pi} \cdot \mathbf{E}(m) \right]^{\frac{1}{3}} \quad (\text{C.10})$$

$$\beta \approx \kappa^{\frac{-2}{3}} \cdot \left[\frac{2}{\pi} \cdot \mathbf{E}(m) \right]^{\frac{1}{3}} \quad (\text{C.11})$$

$$\gamma \approx \kappa^{\frac{2}{3}} \cdot \left[\frac{2}{\pi} \cdot \mathbf{E}(m) \right]^{\frac{-1}{3}} \cdot \left[\frac{2}{\pi} \cdot \mathbf{K}(m) \right] \quad (\text{C.12})$$

where the elliptical integrals, $\mathbf{E}(m)$ and $\mathbf{K}(m)$, are calculated from the analytical solutions by Reussner [301], which yield maximum errors less than one percent provided that $\kappa > 0$.

$$\mathbf{E}(m) \approx \frac{\pi}{2} \cdot (1-m) \cdot \left[1 + \frac{2 \cdot m}{\pi \cdot (1-m)} - \frac{1}{8} \cdot \ln(1-m) \right] \quad (\text{C.13})$$

$$\mathbf{K}(m) \approx \frac{\pi}{2} \cdot (1-m) \cdot \left[1 + \frac{2 \cdot m}{\pi \cdot (1-m)} \cdot \ln \left(\frac{4}{\sqrt{1-m}} \right) - \frac{3}{8} \cdot \ln(1-m) \right] \quad (\text{C.14})$$

In these equations parameter $m = 1 - \kappa^2$ and the ellipticity ratio is defined as $\kappa = b_H/a_H$ which can be approximated from the ratio of reduced curvatures $\lambda = R_x/R_y$ following:

$$\kappa \approx \left[1 + \sqrt{\frac{\ln(16/\lambda)}{2 \cdot \lambda}} - \sqrt{\ln(4) + 0.16 \cdot \ln(\lambda)} \right]^{-1} \iff 0 < \lambda \leq 1 \quad (\text{C.15})$$

*If you do not change direction, you
may end up where you are heading.*

— Lao Tse, 601 BC - 531 BC

D

Absolute to Incremental Angle Conversion Method

Heidenhain RCN 2510 optical encoders are single-turn absolute-type encoders. Thus, angular positions of pinion and gear directly obtained from the EIB 741 evaluation unit are given in angular units relative to a common time sample and not a common angular zero position. The starting positions $\theta_1(t=0)$ and $\theta_2(t=0)$ are different and values change from 359° to 0° periodically, as each shaft's rotation exceeds the zero angular position of the corresponding encoder. Therefore, absolute values need to be converted to incremental before computing transmission error. If one considers that the number of position values per revolution is constant for these encoders (see Table 7.1), it is possible to compute continuous incremental positions if a common reference is set. Figure D.1 summarizes the computation algorithm for this and the procedure is briefly described herein.

The sense of rotation is determined first by analysing the values of the angular positions of pinion and gear: increasing values indicate counter-clockwise rotation (positive rotation) while decreasing values are related to clockwise direction (negative). The reference position for the former is 0° and that for the latter is 360° . The index of the angular positions closest to the reference of the pinion are identified and all measurements up to this index are deleted in pinion and gear. The first position in the angular position array of the pinion now corresponds to a value close to 0° or 360° . If the gear ratio is other than unit, several gear positions exist for the same pinion references. In order to avoid considering different positions in each test, the closest value to 0° in the gear is selected always and results up to this index are deleted in pinion and gear so that the same reference position is used always.

In a second step, absolute measurements are converted to incremental values by computing time and position differences and adding them to the initial references. Time reference is 0 seconds and position reference is the first angular position in the preceding arrays. A rotation counter is also included for completeness. Pinion and gear relative position arrays are fulfilled and initial positions are corrected at the end, such that the first value of the pinion array is always 0° .

Finally, transmission error is computed as a function of time and the mean value is also calculated as it is used to perform Fast Fourier Transform (FFT) and filtering signals.

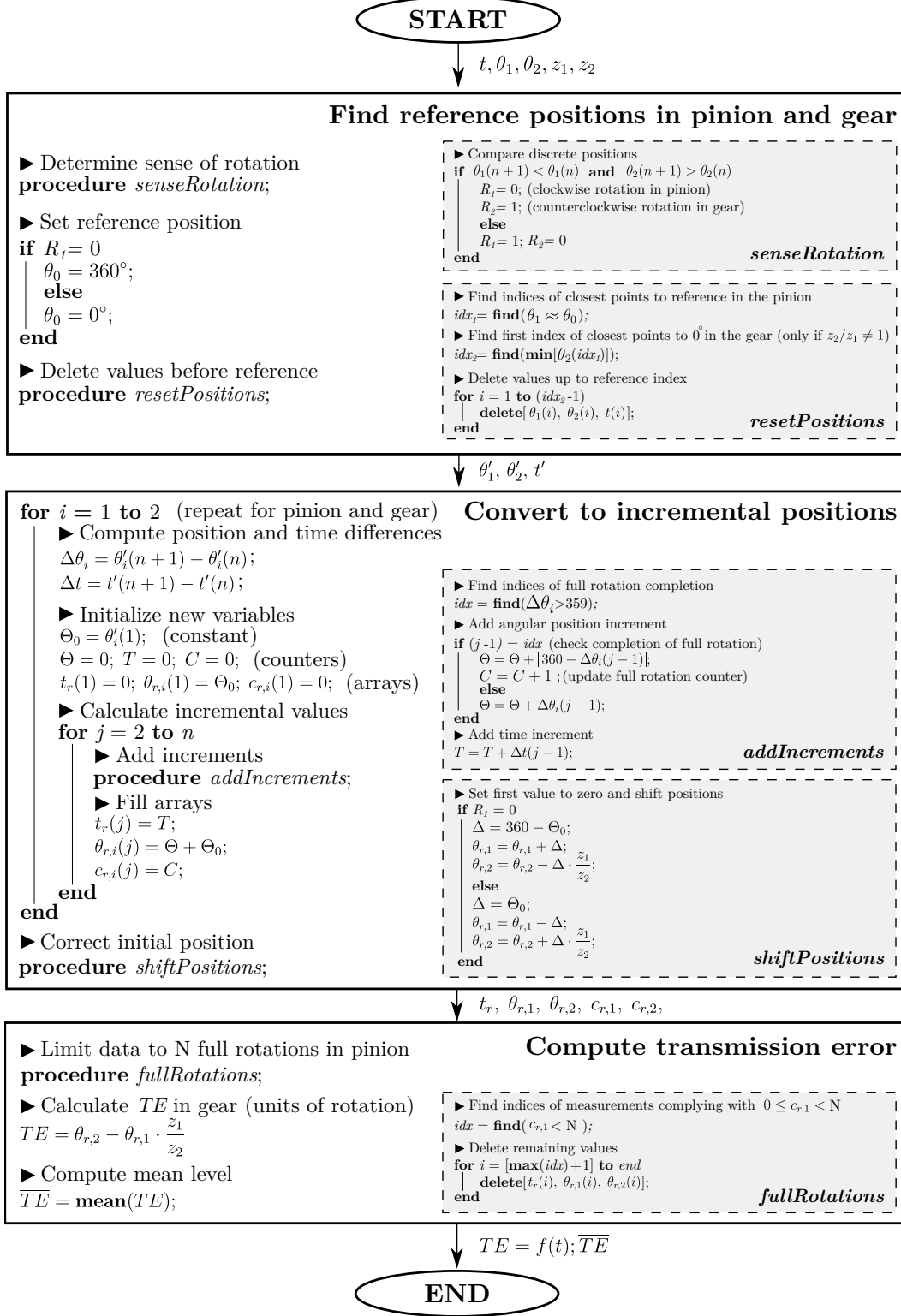


Figure D.1: Experimental transmission error measurement algorithm for absolute encoders

*All we have to decide is what to do with the time
that is given to us.*

— J.R.R. Tolkien's *The Lord of the Rings*, 1954

E

Manufactured Gear Inspection Data

In the following pages manufacturing drawings and inspection data of the gear sets used in the experimental study in Chapter 7 are shown and Table E.1 below gathers complementary information.

Table E.1: Additional data for spur gear sets A and B used in experimental measurements

Parameter	Symbol	Set A	Set B
Working pitch diameters	$d_{1,2}$ [mm]	110, 110	73.33, 146.67
Tip diameter	$d_{a1,2}$ [mm]	116.04, 116.04	80.86, 151.60
Root diameter	$d_{f1,2}$ [mm]	102.54, 102.54	67.36, 138.10
Base diameter	$d_{b1,2}$ [mm]	104.31, 104.31	70.48, 140.95
Active tip diameter	$d_{Na1,2}$ [mm]	114.82, 114.82	79.66, 150.40
Active root diameter	$d_{Nf1,2}$ [mm]	106.57, 106.57	70.98, 142.93
Tip clearance	$c_{1,2}$ [mm]	0.847, 0.847	0.695, 0.655
Generating profile shift coeff.	$x_{E1,2}$ [-]	-0.202, -0.202	-0.065, -0.789
Transverse base pitch	$p_{bt1,2}$ [mm]	8.86, 8.86	8.86, 8.86
Length of the path of contact	g_{α} [mm]	13.06	14.34
Chordal tooth thickness	$s_{c1,2}$ [mm]	4.27, 4.27	4.66, 3.11
Tooth height	h [mm]	6.75	6.75
Normal backlash	j_{bn} [mm]	0.1695	0.1970
Backlash angle	φ_j [°]	0.1859	0.3209

E.1 Pinion and gear type A

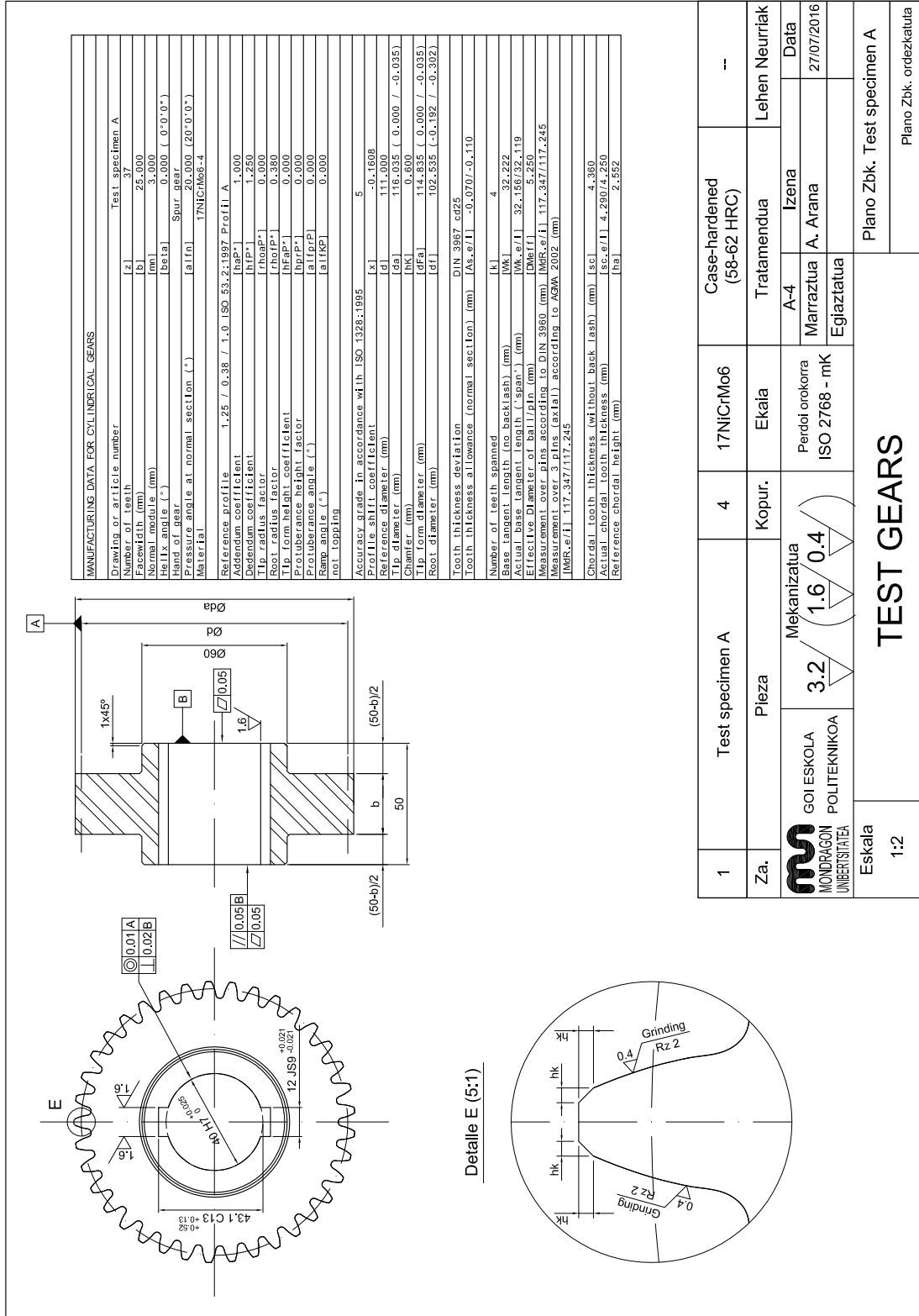


Figure E.1: Drawing of pinion and gear type A for manufacturing

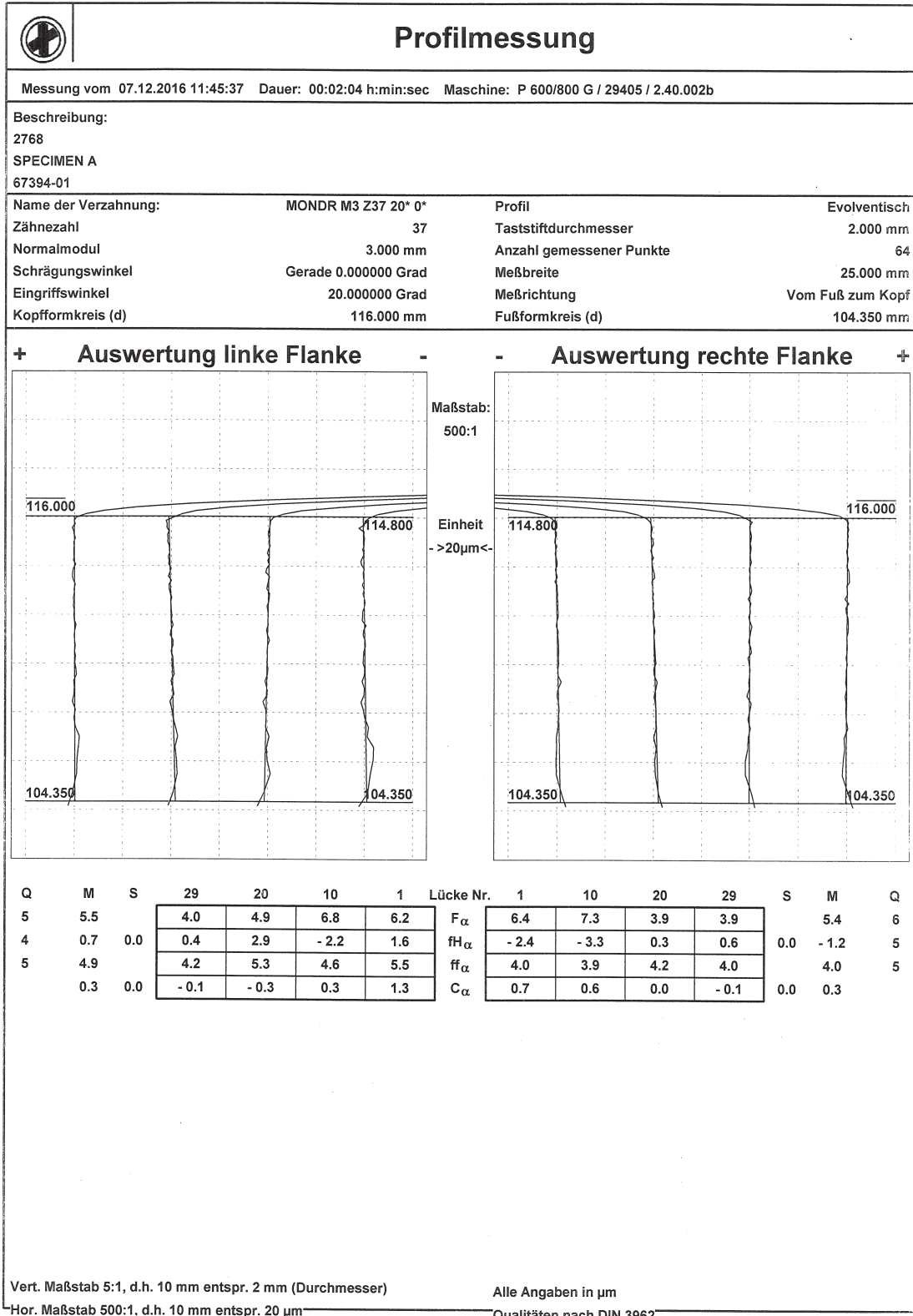


Figure E.2: Pinion and gear type A profile measurements

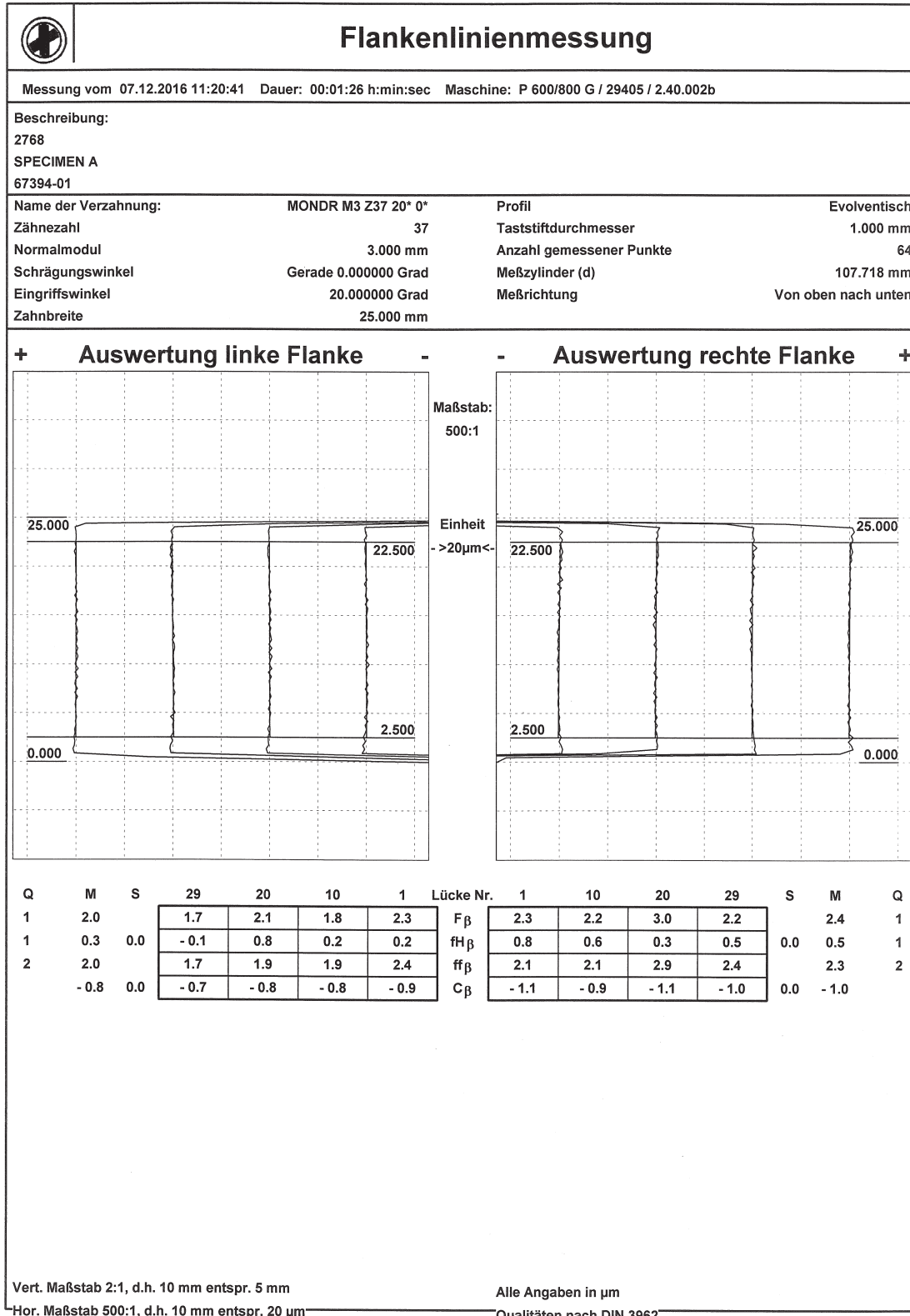


Figure E.3: Pinion and gear type A flank line measurements

E.2 Pinion type B

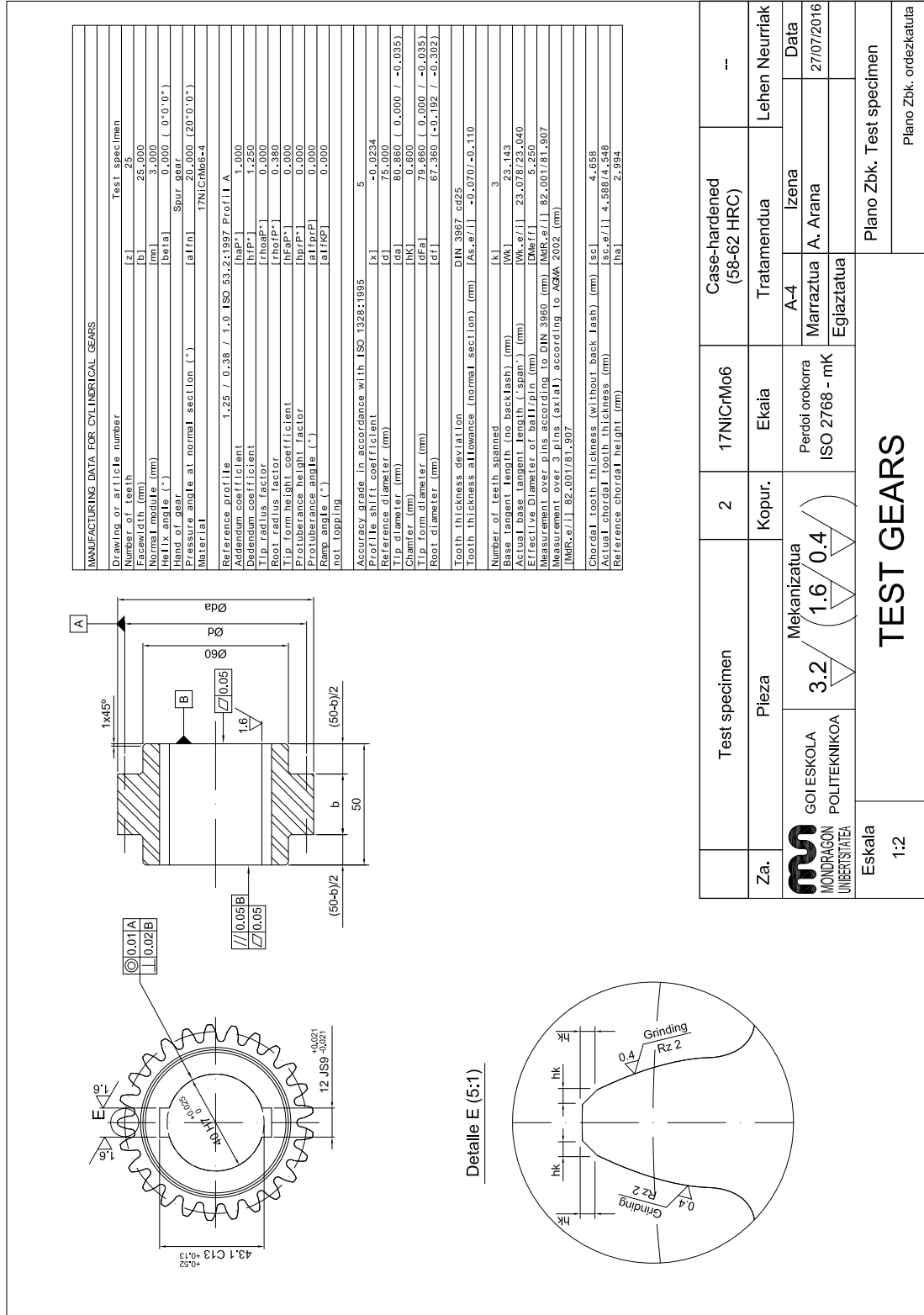


Figure E.4: Drawing of pinion type B for manufacturing

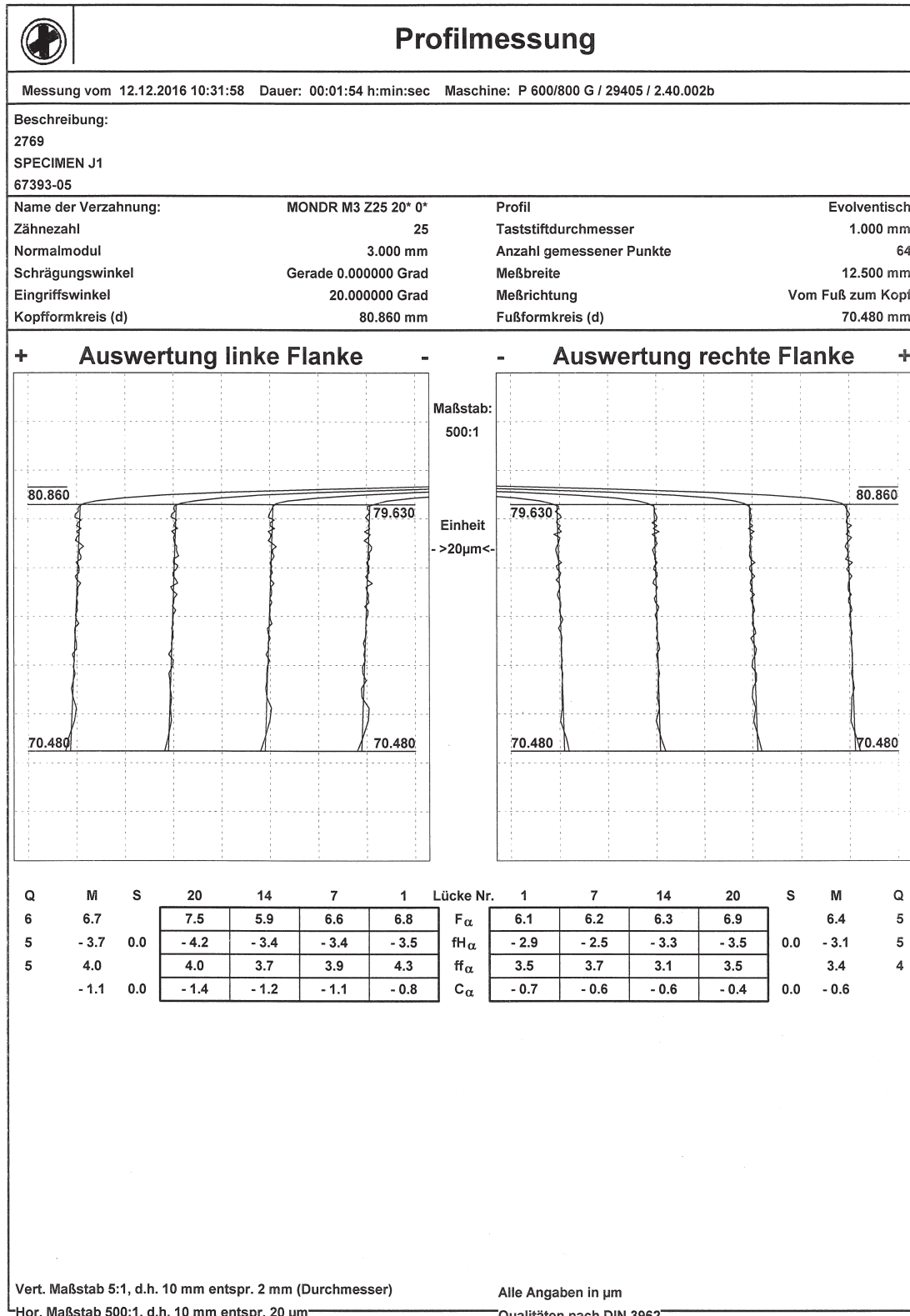


Figure E.5: Pinion type B profile measurements

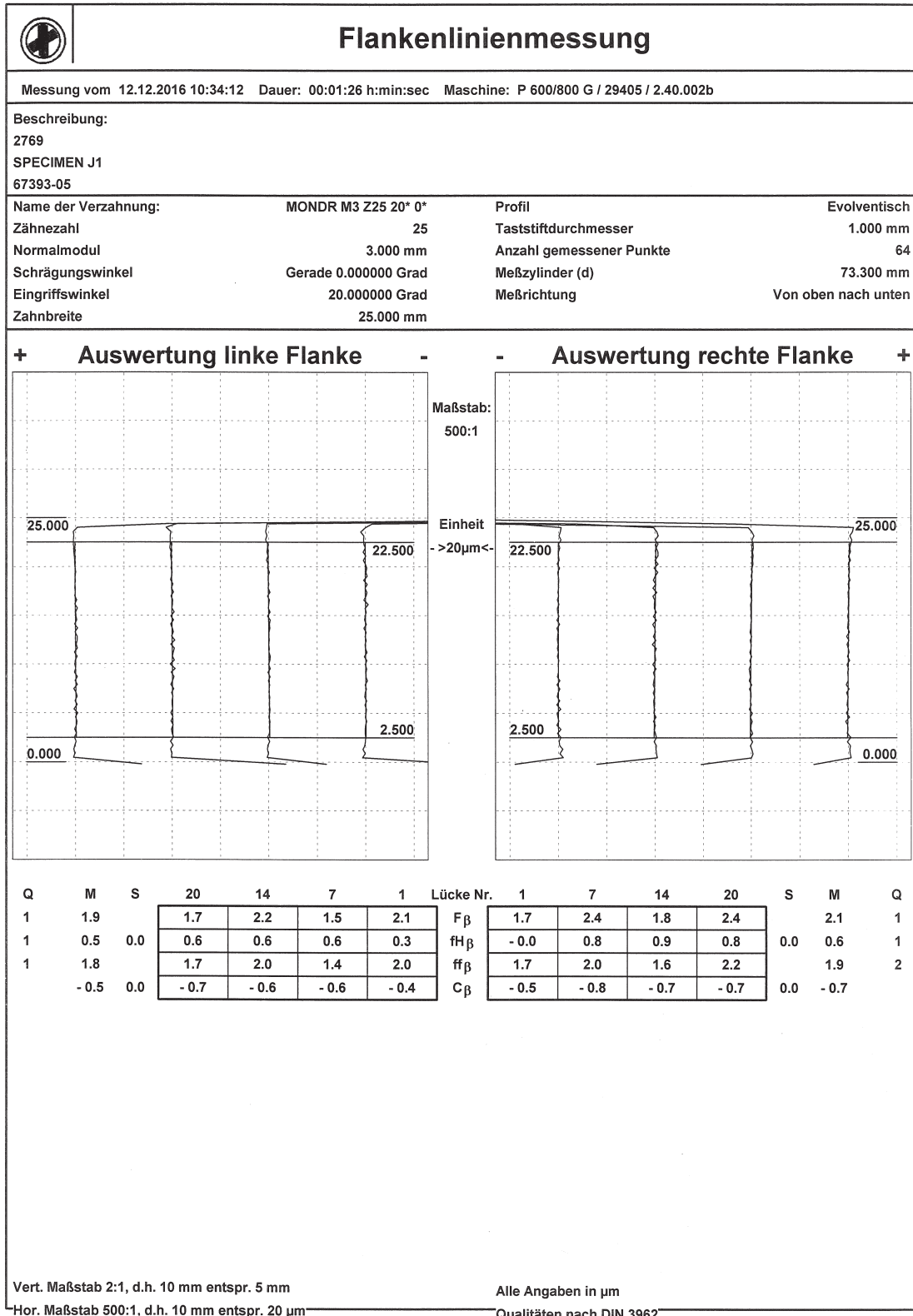


Figure E.6: Pinion type B flank line measurements

E.3 Gear type B

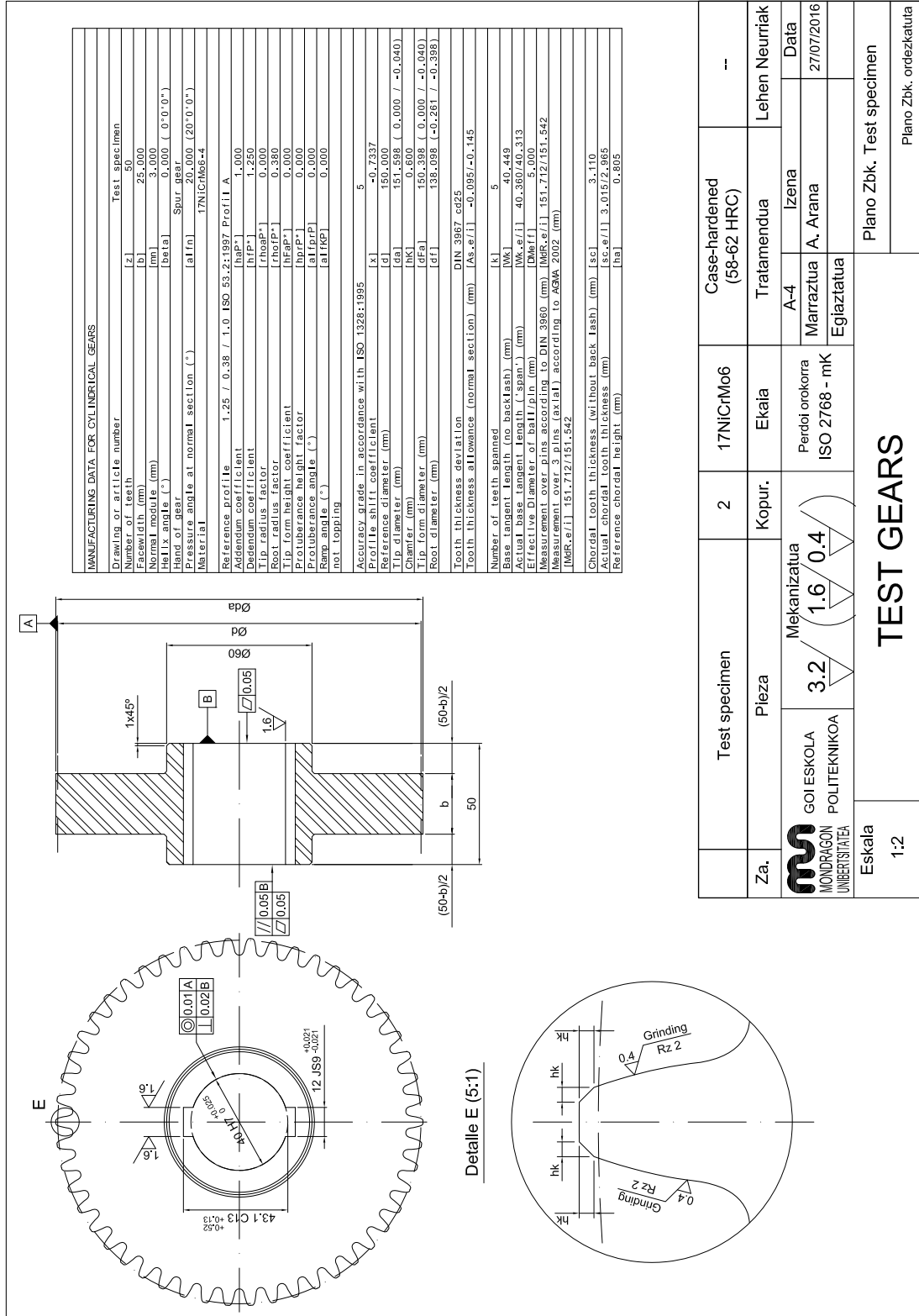


Figure E.7: Drawing of gear type B for manufacturing

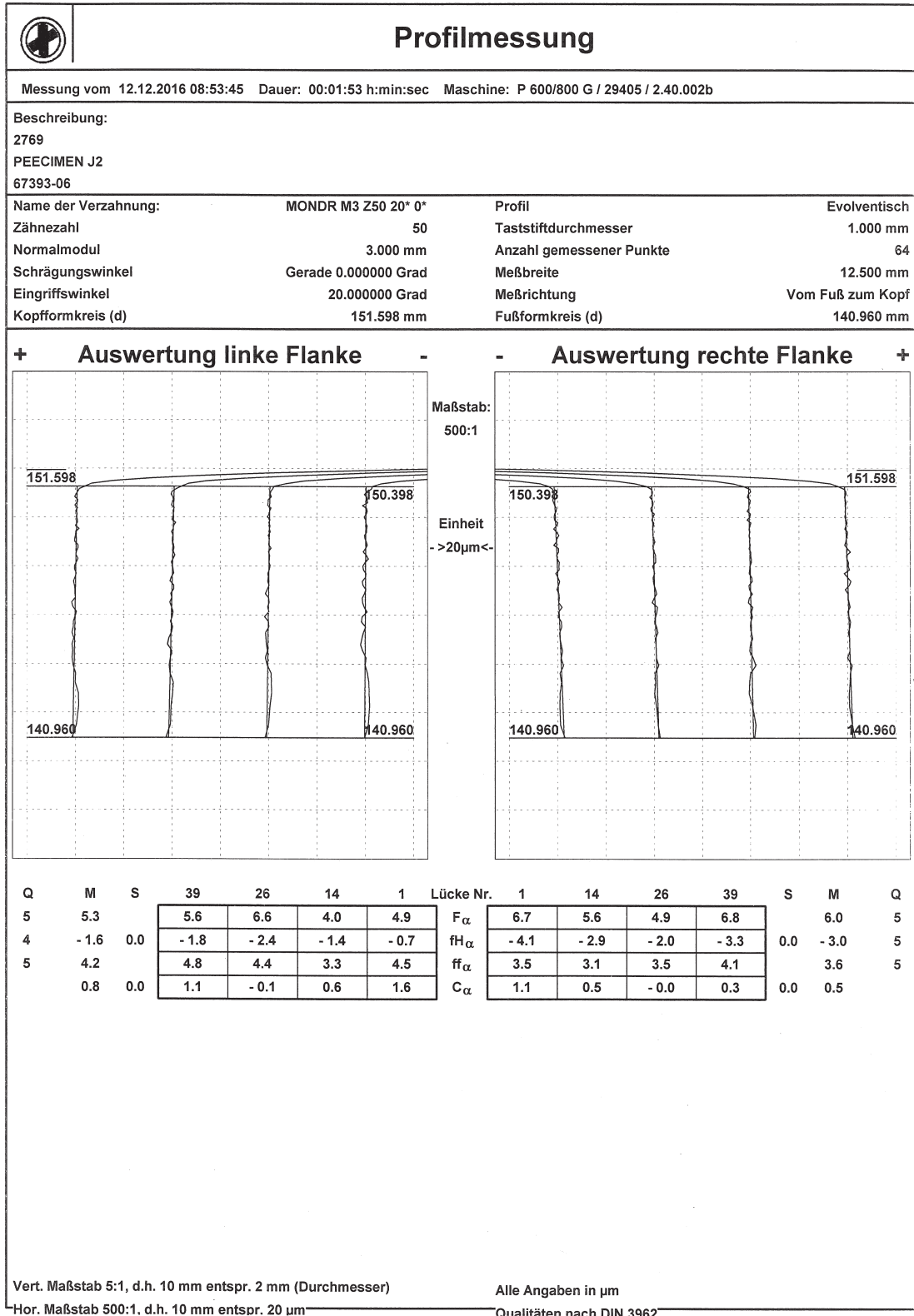


Figure E.8: Gear type B profile measurements

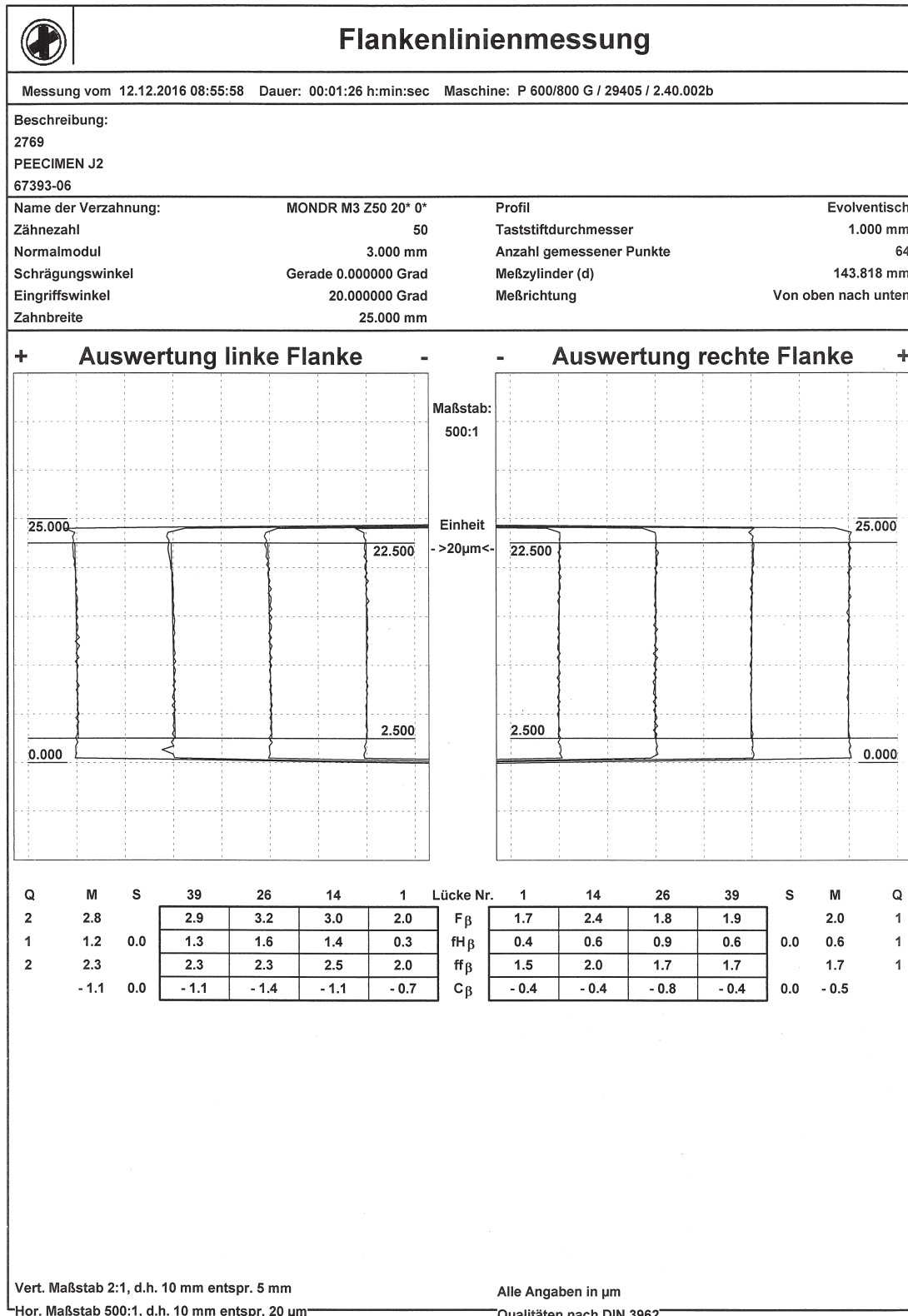


Figure E.9: Gear type B flank line measurements

You cannot hope to build a better world
without improving the individuals.

— Marie Curie, 1867 – 1934

References

- [1] F.J. Joachim, J. Börner and N. Kurz. “Power Losses in Transmissions, Axles, and Steering Systems”. In: *Encyclopedia of Lubricants and Lubrication*. Ed. by T. Mang. Springer-Verlag Berlin Heidelberg, 2014, pp. 1398–1411.
- [2] U.S. Department of Energy’s Vehicle Technologies Office. *Annual Merit Review*. Online. 2018. URL: www.energy.gov/eere/vehicles/vehicle-technologies-office.
- [3] DRIVE partnership (Research, Innovation for Vehicle efficiency and Energy sustainability). *Electrical and Electronics Technical Team Roadmap*. Technical report 2017/10. U.S. Department of Energy’s Vehicle Technologies Office, 2017.
- [4] C.W. Ayers. *Traction Drive and Gearing Design Comparisons for Multiple Manufacturers and Models*. Technical report 2013/482. Oak Ridge National Laboratory, 2013.
- [5] P. Gwinner et al. “Innovative High-speed Powertrain Concept for Highly Efficient Electric Vehicles”. In: *Automobiltechnische Zeitschrift (ATZ) Worldwide* 119.3 (2017), pp. 66–71.
- [6] Forschungsvereinigung Antriebstechnik. *Speed4E projekt: Hyper-Hochdrehzahl für den elektrifizierten automobilen Antriebsstrang zur Erzielung maximaler Reichweiten*. Online. 2018. URL: www.speed4e.de.
- [7] C.W. Ayers. “Electric Motor Architecture Research and Development”. In: *U.S. DOE Hydrogen and Fuel Cells Program and Vehicle Technologies Program Annual Merit Review and Peer Evaluation Meeting*. 2013.
- [8] J.B. Amendola, J.B. Amendola III and D. Yatzook. “Longitudinal Tooth Contact Pattern Shift”. In: *Proceedings of the AGMA Fall Technical Meeting*. 11FTM18. 2011.
- [9] R.F. Handschuh and C.J. Kilmain. *Preliminary investigation of the thermal behavior of high-speed helical gear trains*. Technical report 2002-211336. National Aeronautics and Space Administration, 2002.
- [10] *ANSI/AGMA 2101-D04: Fundamental Rating Factors and Calculation Methods for Involute Spur and Helical Gear Teeth (Metric Edition of ANSI/AGMA 2001-D04)*. Standard. American Gear Manufacturers Association, 2010.
- [11] *ISO 6336-1: 2006: Calculation of load capacity of spur and helical gears - Part 1: Basic principles, introduction and general influence factors*. Standard. International Organization for Standardization, 2006.
- [12] *ANSI/AGMA 6011-J14: Specification for High Speed Helical Gear Units*. Standard. American Gear Manufacturers Association, 2014.
- [13] J.B. Amendola. *Lead correction derivation method for high capacity Turbo-Gears with high pitch line velocities for both single and double helical gears*. Technical report. ARTEC Machine Systems, 2008.
- [14] S.P. Radzevich. *Dudley’s Handbook of Practical Gear Design and Manufacture*. 2nd Edition. Taylor and Francis, 2012.
- [15] *AGMA/ISO 14179: Gear Reducers - Thermal Capacity Based on ISO/TR 14179-1*. Standard. American Gear Manufacturers Association, 2004.
- [16] *ISO/TR 14179-1: 2001: Thermal capacity – Part 1: Rating gear drives with thermal equilibrium at 95°C sump temperature*. Standard. International Organization for Standardization, 2001.

- [17] B.R. Höhn and K. Michaelis. “Influence of oil temperature on gear failures”. In: *Tribology International* 37.2 (2004), pp. 103–109.
- [18] W.P. Welch and J.F. Boron. “Thermal Instability in High Speed Gearing”. In: *Journal of the American Society for Naval Engineers* 72.3 (1960), pp. 471–486.
- [19] J.B. Amendola. “Single Vs. Double Helical Gears”. In: *Turbomachinery Magazine* (Oct. 2006).
- [20] S. Matsumoto, Y. Tozaki and M. Fukutomi. “Temperature distribution in teeth and blanks of ultra high-speed gears (1st report, measurement of temperature distribution in teeth and blanks)”. In: *JSME International Journal, Series C: Mechanical Systems, Machine Elements and Manufacturing* 44.1 (2001), pp. 203–209.
- [21] L. Martinaglia. “Thermal behavior of high-speed gears and tooth correction for such gears”. In: *Mechanism and Machine Theory* 8.3 (1973), pp. 293–303.
- [22] W. Nägeli. *Gear Tothing*. Technical report. Maag Gear-Wheel Company, 1987.
- [23] B.R. Höhn, K. Michaelis and H.P. Otto. “Influence of immersion depth of dip lubricated gears on power loss, bulk temperature and scuffing load carrying capacity”. In: *International Journal of Mechanics and Materials in Design* 4.2 (2008), pp. 145–56.
- [24] H. Sigg. “Profile and longitudinal corrections on involute gears”. In: *Proceedings of the AGMA Fall Technical Meeting*. 109.16. 1965.
- [25] A. Fuentes-Aznar, S. Eisele and I. González-Pérez. “Computerized simulation of manufacturing errors in cylindrical spur gears and their compensation through flank modifications”. In: *Advanced Gear Engineering*. Ed. by V. Goldfarb, E. Trubachev and N. Barmina. Vol. 51. Mechanisms and Machine Science. Springer, 2018, pp. 1–25.
- [26] G. Henriot. *Traité théorique et pratique des engrenages*. 6th Edition. Dunod, 1979.
- [27] *AGMA 927-A01: Load Distribution Factors - Analytical Methods for Cylindrical Gears*. Standard. American Gear Manufacturers Association, 2000.
- [28] H.P. Otto. “Flank Load Carrying Capacity and Power Loss Reduction by Minimised Lubrication”. PhD thesis. Technische Universität München, 2009.
- [29] M. Hinterstoißer. “Zur Optimierung des Wirkungsgrades von Stirnradgetrieben”. PhD thesis. Technische Universität München, 2014.
- [30] C. Prakash del Valle. “Modelo térmico de una máquina FZG de pruebas de engranajes”. MA thesis. Universidad Politécnica de Madrid, 2014.
- [31] Institut für Tribologie und Energiewandlungsmaschinen. *Thermophysikalische Eigenschaften (Schmierstoffe) - Bestimmung und Modellierung der thermophysikalischen Eigenschaften von Schmier- und Kraftstoffen unter hohen Drücken*. Technical report 1002. Forschungsvereinigung Antriebstechnik, 2013.
- [32] *DIN 51354, Teils 1 und 2: FZG-Zahnrad-Verspannungs-Prüfmaschine*. Standard. Deutsches Institut für Normung, 1990.
- [33] G. Niemann and H. Winter. *Maschinenelemente. Band 2: Getriebe allgemein, Zahnradgetriebe-Grundlagen, Stirnradgetriebe*. 2nd Edition. Springer-Verlag Berlin Heidelberg, 2003.
- [34] H. Xu et al. “Prediction of Mechanical Efficiency of Parallel-Axis Gear Pairs”. In: *Journal of Mechanical Design* 129.1 (2006), pp. 58–68.
- [35] S. Wu and H.S. Cheng. “A Friction Model of Partial-EHL Contacts and its Application to Power Loss in Spur Gears”. In: *Tribology Transactions* 34.3 (1991), pp. 398–407.
- [36] A.J. Wimmer. “Lastverluste von Stirnradverzahnungen - Konstruktive Einflüsse, Wirkungsgradmaximierung, Tribologie”. PhD thesis. Technische Universität München, 2005.
- [37] I.C. Faraon and D.J. Schipper. “Stribeck Curve for Starved Line Contacts”. In: *ASME Journal of Tribology* 129 (2007), pp. 181–187.

- [38] K. Michaelis. “Die Integraltemperatur zur Beurteilung der Freßtragfähigkeit von Stirnradgetrieben”. PhD thesis. Technische Universität München, 1987.
- [39] M. Yoshizaki et al. “Study on frictional loss of spur gears (concerning the influence of tooth form, load, tooth surface roughness, and lubricating oil)”. In: *Tribology Transactions* 34.1 (1991), pp. 138–146.
- [40] L. Schlenk. “Untersuchungen zur Freßtragfähigkeit von Großzahnradern”. PhD thesis. Technische Universität München, 1994.
- [41] C.M.C.G. Fernandes et al. “Gearbox power loss. Part II: Friction losses in gears”. In: *Tribology International* 88 (2015), pp. 309–316.
- [42] M. Andersson, M. Sosa and U. Olofsson. “The effect of running-in on the efficiency of superfinished gears”. In: *Tribology International* 93 (2016), pp. 71–77.
- [43] H. Ohlendorf. “Verlustleistung und Erwärmung von Stirnrädern”. PhD thesis. Technische Universität München, 1958.
- [44] J.I. Pedrero, M. Pleguezuelos and M. Muñoz. “Simplified calculation method for the efficiency of involute spur gears”. In: *Proceedings of the ASME International Design Engineering Technical Conferences and Computers and Information in Engineering Conference*. Vol. 6. DETC2009-87179. 2009, pp. 131–138.
- [45] P. Velez and F. Ville. “An Analytical Approach to Tooth Friction Losses in Spur and Helical Gears-Influence of Profile Modifications”. In: *Journal of Mechanical Design* 131.10 (2009).
- [46] G.H. Benedict and B.W. Kelley. “Instantaneous Coefficients of Gear Tooth Friction”. In: *ASLE Transactions* 4.1 (1961), pp. 59–70.
- [47] J.P. O’Donoghue and A. Cameron. “Friction and Temperature in Rolling Sliding Contacts”. In: *ASLE Transactions* 9.2 (1966), pp. 186–194.
- [48] Y.N. Drozdov and Y.A. Gavrikov. “Friction and scoring under the conditions of simultaneous rolling and sliding of bodies”. In: *Wear* 11.4 (1968), pp. 291–302.
- [49] A. Doleschel. “Wirkungsgradberechnung von Zahnradgetrieben in Abhängigkeit vom Schmierstoff”. PhD thesis. Technische Universität München, 2003.
- [50] Y. Diab, F. Ville and P. Velez. “Prediction of Power Losses Due to Tooth Friction in Gears”. In: *Tribology Transactions* 49.2 (2006), pp. 260–270.
- [51] Y. Xi et al. “Traction formula for rolling-sliding contacts in consideration of roughness under low slide to roll ratios”. In: *Tribology International* 104 (2016), pp. 263–271.
- [52] F. Ville et al. “On the two-disc machine: A polyvalent and powerful tool to study fundamental and industrial problems related to elastohydrodynamic lubrication”. In: *Tribology Research: From Model Experiment to Industrial Problem*. Ed. by G. Dalmaz et al. Vol. 39. Tribology Series. Elsevier, 2001, pp. 393–402.
- [53] B.R. Höhn, K. Michaelis and A. Doleschel. “Frictional behaviour of synthetic gear lubricants”. In: *Tribology Research: From Model Experiment to Industrial Problem*. Ed. by G. Dalmaz et al. Vol. 39. Tribology Series. Elsevier, 2001, pp. 759–768.
- [54] M.J.D. Castro and J.H.O. Seabra. “Coefficient of friction in mixed film lubrication: Gears versus twin-discs”. In: *Proceedings of the Institution of Mechanical Engineers, Part J: Journal of Engineering Tribology* 221.3 (2007), pp. 399–411.
- [55] K.P. Oh and S.M. Rohde. “Numerical Solution of the Point Contact Problem Using the Finite Element Method”. In: *International Journal of Numerical Methods in Engineering* 1 (1977), pp. 1507–1518.
- [56] H.A. Okamura. “A contribution to the numerical analysis of isothermal elastohydrodynamic lubrication”. In: *Proceedings of the 9th Leeds-Lyon Symposium on Tribology*. 1982, pp. 313–320.

- [57] P.R. Goglia, T.F. Conry and C. Cusano. “The Effects of Surface Irregularities on the EHL of Sliding Line Contacts. Part I- Single Irregularities”. In: *Journal of Tribology* 106.1 (1984), pp. 104–112.
- [58] T. Lubrecht. “The numerical solution of the elastohydrodynamically lubricated line and point contact problem using multigrid techniques”. PhD thesis. University of Twente, 1987.
- [59] H. Spikes and Z. Jie. “History, Origins and Prediction of Elastohydrodynamic Friction”. In: *Tribology Letters* 56.1 (2014), pp. 1–25.
- [60] L. Bobach et al. “Thermal elastohydrodynamic simulation of involute spur gears incorporating mixed friction”. In: *Tribology International* 48 (2012), pp. 191–206.
- [61] A. Ziegler, T. Lohner and K. Stahl. “TEHL simulation on the influence of lubricants on load-dependent gear losses”. In: *Tribology International* 113 (2016), pp. 252–261.
- [62] S. Li and A. Kahraman. “A Method to Derive Friction and Rolling Power Loss Formulae for Mixed Elastohydrodynamic Lubrication”. In: *Journal of Advanced Mechanical Design, Systems, and Manufacturing* 5.4 (2011), pp. 252–63.
- [63] B.R. Höhn, K. Michaelis and T. Vollmer. “Thermal rating of gear drives: balance between power loss and heat dissipation”. In: *Proceedings of the AGMA Fall Technical Meeting*. 96FTMS. 1996.
- [64] A.W. Crook. “The lubrication of rollers”. In: *Philosophical Transactions of the Royal Society of London A: Mathematical, Physical and Engineering Sciences* 250.981 (1958), pp. 387–409.
- [65] N.E. Anderson and S.H. Loewenthal. *Spur-gear-system efficiency at part and full load*. Technical report 1980-1622. National Aeronautics and Space Administration, 1980.
- [66] P.G. Goksem and R.A. Hargreaves. “The Effect of Viscous Shear Heating on Both Film Thickness and Rolling Traction in an EHL Line Contact - Part I: Fully Flooded Conditions”. In: *Journal of Tribology* 100.3 (1978), pp. 346–352.
- [67] Y. Michlin and V. Myunster. “Determination of power losses in gear transmissions with rolling and sliding friction incorporated”. In: *Mechanism and Machine Theory* 37.2 (2002), pp. 167–174.
- [68] J.F. Archard and K.P. Baglin. “Nondimensional Presentation of Frictional Traction in Elastohydrodynamic Lubrication—Part I: Fully Flooded Conditions”. In: *Journal of Lubrication Technology* 97.3 (1975), pp. 398–410.
- [69] S. Matsumoto et al. “Evaluation Method of Power Loss in High-Speed Gears”. In: *Proceedings of the JSLE International Tribology Conference*. 1985, pp. 1165–1170.
- [70] S. Seetharaman. “An investigation of load-independent power losses of gear systems”. PhD thesis. Ohio State University, 2009.
- [71] H. Liu et al. “Detailed Investigations on the Oil Flow in Dip-Lubricated Gearboxes by the Finite Volume CFD Method”. In: *Lubricants* 6.2 (2018).
- [72] A.S. Terekhov. “Hydraulic losses in gearboxes with oil immersion”. In: *Vestnik Mashinostroeniya* 55.5 (1975), pp. 13–17.
- [73] C. Chagnenet and P. Velex. “A model for the prediction of churning losses in geared transmissions - preliminary results”. In: *Journal of Mechanical Design* 129.1 (2006), pp. 128–133.
- [74] E. Lauster and M. Boos. “Zum Wärmehaushalt Mechanischer Schaltgetriebe für Nutzfahrzeuge”. In: *VDI-Berichte* 488 (1983), pp. 45–55.
- [75] R.J. Boness. “Churning losses of discs and gears running partially submerged in oil”. In: *Proceedings of the ASME International Power Transmission and Gearing Conference*. Vol. 1. 1989, pp. 355–359.

- [76] P. Luke and A.V. Olver. “A study of churning losses in dip-lubricated spur gears”. In: *Proceedings of the Institution of Mechanical Engineers, Part G: Journal of Aerospace Engineering* 213.5 (1999), pp. 337–346.
- [77] C. Changenet et al. “A note on flow regimes and churning loss modeling”. In: *Journal of Mechanical Design* 133.12 (2011), p. 121009.
- [78] C. Gorla et al. “Hydraulic losses of a gearbox: CFD analysis and experiments”. In: *Tribology International* 66.0 (2013), pp. 337–344.
- [79] R.F. Handschuh and M.J. Hurrell. *Initial Experiments of High-Speed Drive System Windage Losses*. Technical report 2011-216925. National Aeronautics and Space Administration, 2011.
- [80] P.H. Dawson. “Windage Loss in Larger High-Speed Gears”. In: *Proceedings of the Institution of Mechanical Engineers, Part A: Journal of Power and Energy* 198.1 (1984), pp. 51–59.
- [81] Y. Diab et al. “Windage losses in high speed gears: Preliminary experimental and theoretical results”. In: *Proceedings of the ASME International Design Engineering Technical Conferences and Computers and Information in Engineering Conference*. Vol. 4. DETC2003/PTG-48115. 2003, pp. 941–947.
- [82] D.W. Dudley and D.P. Townsend. *Dudley’s gear handbook*. McGraw-Hill, 1991.
- [83] M.J. Hill et al. “CFD Analysis of Gear Windage Losses: Validation and Parametric Aerodynamic Studies”. In: *Journal of Fluids Engineering* 133.3 (2011), p. 10.
- [84] S. Pallas et al. “Application and validation of a simplified numerical approach for the estimation of windage power losses in spur gears”. In: *Computers & Fluids* 84 (2013), pp. 39–45.
- [85] Y. Marchesse et al. “Investigations on CFD simulation for predicting windage power losses generated by helical gears”. In: *Proceedings of the STLE Annual Meeting and Exhibition*. 2014.
- [86] R.F. Handschuh and C.J. Kilmain. *Experimental Study of the Influence of Speed and Load on Thermal Behavior of High-Speed Helical Gear Trains*. Technical report 2005-213632. National Aeronautics and Space Administration, 2005.
- [87] H. Mizutani, Y. Isikawa and D.P. Townsend. *Effects of lubrication on the performance of high speed spur gears*. Technical report 1989-101969. National Aeronautics and Space Administration, 1989.
- [88] Y. Ariura et al. “The Lubricant Churning Loss in Spur Gear Systems”. In: *Bulletin of the Japan Society of Mechanical Engineers* 16.95 (1973), pp. 881–892.
- [89] Y. Diab et al. “Experimental and Numerical Investigations on the Air-Pumping Phenomenon in High-Speed Spur and Helical Gears”. In: *Proceedings of the Institution of Mechanical Engineers, Part C: Journal of Mechanical Engineering Science* 219.8 (2005), pp. 785–800.
- [90] C. Milian et al. “A model of the pumping action between the teeth of high-speed spur and helical gears”. In: *Gear Technology Magazine* (May 2004), pp. 50–54.
- [91] F. Concli and C. Gorla. “Analysis of the oil squeezing power losses of a spur gear pair by mean of CFD simulations”. In: *Proceedings of the ASME 11th Biennial Conference on Engineering Systems Design and Analysis*. Vol. 2. ESDA2012-82591. 2012, pp. 177–184.
- [92] H. Winter and K. Michaelis. “Untersuchungen zum Wärmehaushalt von Getrieben”. In: *Antriebstechnik* 20.3 (1981), pp. 70–74.
- [93] G. Funck. “Wärmeabführung bei Getrieben unter quasistationären Betriebsbedingungen”. PhD thesis. Technische Universität München, 1985.
- [94] A.E. Phillips. “The Development of a Practical Thermal Rating Method for Enclosed Gear Drives”. In: *Proceedings of the AGMA Fall Technical Meeting*. 96FTM9. 1996.

- [95] H. Winter, K. Michaelis and Funck G. “Wärmeabführung bei Getrieben unter Quasistationären Betriebsbedingungen. Teil II: Untersuchungen zur Wärmeabführung über Stahlfundamente und Übertragung der Prüfstandsergebnisse auf die Praxis”. In: *Antriebstechnik* 26.6 (1987), pp. 49–55.
- [96] H. Winter and K. Michaelis. “Investigations on the thermal balance of gear drives”. In: *Proceedings of the 5th World Congress on Theory of Machines and Mechanisms*. 1979, pp. 354–358.
- [97] G. Lössl. “Berechnen und auswerten des Wärmeübergangs an Wellen und Wellenzapfen”. In: *Maschinenmarkt* 85.36 (1979).
- [98] Y. Terauchi et al. “On the Heat Balance of Gear Equipment : On a Method for Predicting the Bulk Temperature Rise of Gears and Temperature Rise of Oil with Dip Cooling”. In: *JSME International Journal. Ser. 3, Vibration, control engineering, engineering for industry* 34.1 (1991), pp. 97–105.
- [99] D. Joule, S. Hinduja and J.N. Ashton. “Thermal Analysis of a Spur Gearbox Part 1: Steady State Finite Element Analysis”. In: *Proceedings of the Institution of Mechanical Engineers , Part C: Journal of Mechanical Engineering Science* 202.4 (1988), pp. 245–256.
- [100] M. Yazdani et al. “Prediction of the thermo-fluids of gearbox systems”. In: *International Journal of Heat and Mass Transfer* 81 (2015), pp. 337–346.
- [101] A. Christodoulis. “Prediction of Power Losses in an Automotive Gearbox Incorporating a Thermally Coupled Lubrication Model”. PhD thesis. Imperial College London, 2017.
- [102] G.J.J. Van Heijningen. “Fling-off cooling of gear teeth”. In: *Tribology International* 17.1 (1984), pp. 11–18.
- [103] A. DeWinter and H. Blok. “Fling-off cooling of gear teeth”. In: *Journal of Engineering for Industry* 96.1 (1974), pp. 60–70.
- [104] H. Blok. “Transmission de chaleur par projection centrifuge d’huile”. In: *Société d’Etudes de l’Industrie de l’Engrenage* 59 (1970), pp. 14–23.
- [105] L.S. Akin and J.J. Mross. “Theory for the Effect of Windage on the Lubricant Flow in the Tooth Spaces of Spur Gears”. In: *Journal of Manufacturing Science and Engineering* 97.4 (1975), pp. 1266–1272.
- [106] Y. Terauchi, K. Nagamura and C. Wu. “On Heat Balance of Gear Meshing Apparatus: Experimental and Analytical Heat Transfer Coefficient on Tooth Faces”. In: *JSME International Journal. Ser. 3, Vibration, control engineering, engineering for industry* 32.3 (1989), pp. 467–474.
- [107] M.J. Pechersky and M.J. Wittbrodt. “An analysis of fluid flow between meshing spur gear teeth”. In: *Proceedings of the ASME International Power Transmission and Gearing Conference*. 1989.
- [108] H. Houjoh et al. “Pressure Measurement of Ambient Air in the Root Space of Helical Gears for the Purpose of Understanding Fluid Flow to Improve Lubrication Efficiency”. In: *Proceedings of the ASME International Design Engineering Technical Conferences and Computers and Information in Engineering Conference*. Vol. 4. DETC2003/PTG-48117. 2003, pp. 957–964.
- [109] H. Houjoh and K. Umezawa. “The Sound Radiated from Gears : On the Existence of Aerodynamic Sound”. In: *JSME International Journal* 30.259 (1987), pp. 153–160.
- [110] Y. Terauchi and Y. Miyao. “On the Measurement of Temperature Flashes on Spur Gear Teeth : 1st Report, The Case of Meshing with a Pair of Ground Standard Gears”. In: *Bulletin of the Japan Society of Mechanical Engineers* 7.26 (1964), pp. 444–451.
- [111] G. Niemann and G. Lechner. “The measurement of surface temperatures on gear teeth”. In: *ASME Journal of Basic Engineering* 87.3 (1965), pp. 641–651.

- [112] H. Blok. *The Postulate about the Constancy of Scoring Temperature*. Special publication 237. National Aeronautics and Space Administration, 1970.
- [113] Y. Terauchi and H. Mori. “Comparison of theories and experimental results for surface temperature of spur gear teeth”. In: *Journal of Manufacturing Science and Engineering* 96.1 (1974), pp. 41–50.
- [114] *AGMA 925-A03: Effect of Lubrication on Gear Surface Distress*. Standard. 2013.
- [115] G. Deng et al. “Initial temperature evaluation for flash temperature index of gear tooth”. In: *Journal of tribology* 117.3 (1995), pp. 476–481.
- [116] P. Oster. “Beanspruchung der Zahnflanken unter Bedingungen der Elastohydrodynamik”. PhD thesis. Technische Universität München, 1982.
- [117] A.S. Terekhov. “Basic Problems of Heat Calculation of Gear Reducers”. In: *Proceedings of the JSME International Conference on Motion and Power Transmissions*. 1991, pp. 490–495.
- [118] G. Knauer. “Zur Grubchentragefähigkeit einatzgearteter Zahnraeder - Einfluß von Werkstoff, Schmierstoff und Betriebstemperatur”. PhD thesis. Technische Universität München, 1988.
- [119] J. Greiner. “Untersuchungen zur Schmierung und Kühlung einspritzgeschmierter Stirnradgetriebe”. PhD thesis. Universität Stuttgart, 1990.
- [120] J.S. Geiger. “Wirkungsgrad und Wärmehaushalt von Zahnradgetrieben bei Instationären Betriebszuständen”. PhD thesis. Technische Universität München, 2014.
- [121] M. Akazawa, T. Tejima and T. Narita. “Full Scale Test of High Speed, High Powered Gear Unit- Helical Gears of 25,000 PS at 200 m/s PLV”. In: *Proceedings of the ASME International Power Transmissions and Gearing Conference*. 80-C2/DET-4. 1980.
- [122] J. Wang. “Design Technologies of High-Speed Gear Transmission”. In: *Proceedings of the AGMA Fall Technical Meeting*. 01FTM10. 2001.
- [123] R.F. Handschuh et al. “Double Helical Gear Performance Results in High Speed Gear Trains”. In: *Proceedings of the AHS 65th Annual Forum and Technology Display*. E-16947. 2009.
- [124] M. Taburdagitan and M. Akkok. “Determination of surface temperature rise with thermo-elastic analysis of spur gears”. In: *Wear* 261 (2006), pp. 656–665.
- [125] C. Changenet, X. Oviedo-Marlot and P. Velex. “Power loss predictions in geared transmissions using thermal networks-applications to a six-speed manual gearbox”. In: *ASME Journal of Mechanical Design* 128.3 (2006), pp. 618–625.
- [126] N. Patir and H.S. Cheng. “Prediction of the Bulk Temperature in Spur Gears Based on Finite Element Temperature Analysis”. In: *ASLE Transactions* 22.1 (1979), pp. 25–36.
- [127] L.E. El-Bayoumy, L.S. Akin and D.P. Townsend. “An investigation of the transient thermal analysis of spur gears”. In: *ASME Journal of Mechanical Design* 107.4 (1985), pp. 541–548.
- [128] D.P. Townsend and L.S. Akin. “Analytical and experimental spur gear tooth temperature as affected by operating variables”. In: *ASME Journal of Mechanical Design* 103.1 (1981), pp. 219–226.
- [129] R. Grekoussis and J. Retzepis. “Stationäres Temperaturfeld von Stirnrädern”. In: *Antriebstechnik* 29.3 (1990). Thermal analysis, pp. 67–70.
- [130] A. Mihailidis and V. Bakolas. “FEM-determination of the stationary temperature field of spur gears”. In: *Proceedings of the 2nd Balkan Conference on Tribology*. Vol. 96. 1996, pp. 537–546.
- [131] H. Long et al. “Operating temperatures of oil-lubricated medium-speed gears: Numerical models and experimental results”. In: *Proceedings of the Institution of Mechanical Engineers, Part G: Journal of Aerospace Engineering* 217.2 (2003), pp. 87–106.

- [132] B. Luo and W. Li. “Influence factors on bulk temperature field of gear”. In: *Proceedings of the Institution of Mechanical Engineers, Part J: Journal of Engineering Tribology* 231.8 (2017), pp. 953–964.
- [133] W. Li and J. Tian. “Unsteady-state temperature field and sensitivity analysis of gear transmission”. In: *Tribology International* 116 (2017), pp. 229–243.
- [134] W. Li, P. Zhai and L. Ding. “Analysis of thermal characteristic of spur/helical gear transmission”. In: *Journal of Thermal Science and Engineering Applications* 11.2 (2019).
- [135] W. Li et al. “Thermal analysis of helical gear transmission system considering machining and installation error”. In: *International Journal of Mechanical Sciences* 149 (2018), pp. 1–17.
- [136] N. Raghuraman, D. Houser and Z.H. Wright. “Numerical Thermal 3D Modeling of Plastic Gearing”. In: *Gear Solutions Magazine* (Dec. 2017).
- [137] L. Manin and D. Play. “Thermal behavior of power gearing transmission, numerical prediction and influence of design parameters”. In: *Journal of Tribology* 121.4 (1999), pp. 693–702.
- [138] S. Koshigoe et al. *A Computer Program for the Computation of Running Gear Temperatures Using Green's Function*. Technical report 1996-107241. National Aeronautics and Space Administration, 1996.
- [139] J. Wang. “Numerical and experimental analysis of spur gears in mesh”. PhD thesis. Curtin University of Technology, 2003.
- [140] S. Kashyap et al. “Methods of describing plastic gear geometry after a temperature change with application to the prediction of gear load distribution”. In: *Proceedings of the ASME International Design Engineering Technical Conferences and Computers and Information in Engineering Conference*. Vol. 8. DETC2011-47501. 2011, pp. 497–505.
- [141] E. Hensel et al. “Thermal Influences on Gear Micro Geometry and Acoustic Excitation”. In: *Romax Technology European User Forum*. 2015.
- [142] B. Luo and W. Li. “Experimental study on thermal dynamic characteristics of gear transmission system”. In: *Measurement* 136 (2019), pp. 154–162.
- [143] G. Li et al. “Quantitative analysis on the non-similarity of thermal deformation of the gear”. In: *Proceedings of the 4th International Symposium on Precision Mechanical Measurements*. Vol. 7130. 2008.
- [144] Y. Zhang, Y.T. Fei and S.L. Liu. “Thermal deformation of helical gears”. In: *Proceedings of the 6th. International Symposium on Precision Engineering Measurement and Instrumentation*. Vol. 7544. 2010.
- [145] H.X. Wang, K. Li and F. Qin. “Analyzing the Influence of Temperature on the Involute Gear Profile with ANSYS”. In: *Advanced Materials Research* 411 (2012), pp. 174–178.
- [146] Y. Shi et al. “Study on the Contact Properties for Involute Cylindrical Gear Based on Thermal Analysis”. In: *Applied Mechanics and Materials* 339 (2013), pp. 510–514.
- [147] Y.N. Wang, Z.L. Sun and M.A. Yin. “Considering Thermal Deformation in Gear Transmission Error Calculation”. In: *Applied Mechanics and Materials* 281 (2013), pp. 211–215.
- [148] Y. Zhang et al. “Thermal influence on precise gear transmission”. In: *Proceedings of the 8th. International Symposium on Precision Engineering Measurement and Instrumentation*. Vol. 8759. 2013.
- [149] Y.M. Hu, F.J. Zhang and Y.M. Shao. “On Strain of Gear Meshing Thermo-Mechanical Coupling”. In: *Key Engineering Materials* 572 (2014), pp. 359–362.
- [150] H. Wang et al. “Calculation of static transmission errors associated with thermo-elastic coupling contacts of spur gears”. In: *Vibroengineering Procedia* 20 (2018), pp. 237–241.

- [151] Y. Tozaki, S. Matsumoto and M. Fukutomi. “Temperature distribution in teeth and blanks of ultra-high-speed gears (2nd report, calculation of temperature distribution in teeth and blanks)”. In: *JSME International Journal, Series C: Mechanical Systems, Machine Elements and Manufacturing* 44.1 (2001), pp. 210–216.
- [152] K. Hayashi and T. Sayama. “Load Distribution in Marine Reduction Gears”. In: *Bulletin of the Japan Society of Mechanical Engineers* 5.18 (1962), pp. 351–359.
- [153] C. Wang, H.Y. Cui and Q.P. Zhang. “The derivation of transformation matrix before and after thermal distortion for modification”. In: *Proceedings of the Institution of Mechanical Engineers, Part C: Journal of Mechanical Engineering Science* 229.9 (2015), pp. 1686–1692.
- [154] Y. Wang et al. “Thermomechanical coupled contact analysis of alternating meshing gear teeth surfaces for marine power rear transmission system considering thermal expansion deformation”. In: *Advances in Mechanical Engineering* 10.1 (2018).
- [155] R.W. Howells, J.J. Sciarra and G. Shek. “Thermal and structural analysis of helicopter transmission housings using NASTRAN”. In: *Proceedings of the 5th NASTRAN User’s Experiences Conference*. 1976.
- [156] *DIN 3967: Backlash, Tooth Thickness Allowances, Tooth Thickness Tolerances*. Standard. Deutsches Institut für Normung, 1978.
- [157] Y. Terauchi, M. Fujii and Y. Oubatake. “Dynamic Behavior of Straight Bevel Gears: 3rd report, on the effect of preloading on bearing”. In: *Bulletin of the Japan Society of Mechanical Engineers* 25.206 (1982), pp. 1329–1335.
- [158] T. Eldridge et al. “Axial alignment and thermal growth effects on turbomachinery trains with double-helical gearing”. In: *Proceedings of the 34th Turbomachinery Symposium*. 2005, pp. 93–104.
- [159] MAAG Gear-Wheel company LTD. *MAAG Gear book*. 1963.
- [160] J.B. Amendola. *A General Discussion on Gear Configurations*. Technical report. ARTEC Machine Systems, 2013.
- [161] *API 613: Special Purpose Gear Units for Petroleum, Chemical and Gas Industry Services*. Standard. American Petroleum Institute, 2003.
- [162] *ISO 13691: 2002: Petroleum and natural gas industries– High-speed special-purpose gear units*. Standard. International Organization for Standardization, 2002.
- [163] R. Höhn, K. Michaelis and M. Heizenröther. “Untersuchung Thermisch Bedingter Verformungen auf die Lastverteilung bei Zahnrädern”. (Unpublished).
- [164] Y. Shi, Y. Yao and J. Fei. “Analysis of bulk temperature field and flash temperature for locomotive traction gear”. In: *Applied Thermal Engineering* 99 (2016), pp. 528–36.
- [165] R.B. Hetnarski and M.R. Eslami. “Thermal Stresses – Advanced Theory and Applications”. In: *Solid Mechanics and Its Applications*. Vol. 158. Springer, 2009.
- [166] Y. Wang et al. “Thermomechanical coupled contact analysis of alternating meshing gear teeth surfaces for marine power rear transmission system considering thermal expansion deformation”. In: *Advances in Mechanical Engineering* 10.1 (2018), pp. 1–12.
- [167] C.M.C.G. Fernandes et al. “Finite element method model to predict bulk and flash temperatures on polymer gears”. In: *Tribology International* 120 (2018), pp. 255–268.
- [168] C. Changenet, F. Ville and P. Velex. “Thermal behavior of a high-speed gear unit”. In: *Gear Technology Magazine* (Jan. 2016).
- [169] F. Klocke and C. Brecher. *Zahnrad- und Getriebetechnik. Auslegung – Herstellung – Untersuchung – Simulation*. Carl Hanser Verlag München, 2017.
- [170] *ISO 53: 1998: Cylindrical gears for general and heavy engineering — Standard basic rack tooth profile*. Standard. International Organization for Standardization, 1998.

- [171] *ISO 54: 1996: Cylindrical gears for general engineering and for heavy engineering — Modules*. Standard. International Organization for Standardization, 1996.
- [172] R. Padieth. “Exakte Ermittlung der Zahnform”. In: *Antriebstechnik* 17.10 (1978), pp. 434–436.
- [173] J. Harianto and D.R. Houser. “A methodology for obtaining optimum gear tooth microtopographies for noise and stress minimization over a broad operating torque range”. In: *Proceedings of the ASME International Design Engineering Technical Conferences and Computers and Information in Engineering Conference*. Vol. 7. DETC2007-34655. 2007, pp. 289–303.
- [174] M. Vijayakar. “Edge effects in gear tooth contact”. In: *Proceedings of the 7th International Power Transmission and Gearing Conference*. Vol. 88. 1996, pp. 205–212.
- [175] F.L. Litvin and A. Fuentes. *Gear Geometry and Applied Theory*. 2nd Edition. Cambridge University Press, 2004.
- [176] *ISO 21771: 2007: Gears — Cylindrical involute gears and gear pairs — Concepts and geometry*. Standard. International Organization for Standardization, 2007.
- [177] H.H. Richardson. “Static and dynamic load, stress, and deflection cycles in spur-gear systems”. PhD thesis. Massachusetts Institute of Technology, 1958.
- [178] D.L. Seager. “Separation of Gear Teeth in Approach and Recess, and the Likelihood of Corner Contact”. In: *ASLE Transactions* 19.2 (1976), pp. 164–170.
- [179] H.H. Lin et al. “Effect of Extended Tooth Contact on the Modeling of Spur Gear Transmissions”. In: *Proceedings of the 29th Joint Propulsion Conference and Exhibit*. 1993.
- [180] R.G. Munro, L. Morrish and D. Palmer. “Gear transmission error outside the normal path of contact due to corner and top contact”. In: *Proc. of the Institution of Mechanical Engineers, Part C: Journal of Mechanical Engineering Science* 213.4 (1999), pp. 389–400.
- [181] H. Poritsky, A.D. Sutton and A. Pernick. “Distribution of Tooth Loading Along a Pinion”. In: *Journal of Applied Mechanics* 67.12 (1945), pp. 78–86.
- [182] C. Weber and K. Banaschek. “Formänderung und Profilrücknahme bei gerad- und schrägverzahnten Rädern”. In: *Schriftenreihe Antriebstechnik* (1953).
- [183] M.D. Trobojevic. “Load Distribution on Helical Gear Teeth”. In: *The Engineer* 204.5298 (1957), pp. 187–190.
- [184] K. Hayashi. “Load Distribution on the Contact Line of Helical Gear Teeth : Part 1 Fundamental Concept”. In: *Bulletin of the Japan Society of Mechanical Engineers* 6.22 (1963), pp. 336–343.
- [185] K. Umezawa, J. Ishikawa and K. Hayashi. “Deflections due to a Concentrated Load on a Cantilever Thick Plate of Finite Length for Gears”. In: *Bulletin of the Japan Society of Mechanical Engineers* 12.53 (1969), pp. 1204–1211.
- [186] D.L. Seager. “Tooth Loading and Static Behavior of Helical Gears”. In: *ASLE Transactions* 13.1 (1970), pp. 66–77.
- [187] T.F. Conry and A. Seireg. “A Mathematical Programming Technique for the Evaluation of Load Distribution and Optimal Modifications for Gear Systems”. In: *ASME Journal of Engineering for Industry* 94 (1973), pp. 1115–1122.
- [188] G.R. Schmidt. “Berechnung der Walzpressung Schragverzahnter Stirnräder unter Berücksichtigung der Lastverteilung”. PhD thesis. Technische Universität München, 1973.
- [189] T. Placzek. “Lastverteilung und Flankenkorrektur in gerad- und schrägverzahnten Stirnradstufen”. PhD thesis. Technische Universität München, 1988.
- [190] L. Vedmar. “On the Design of External Involute Helical Gears”. PhD thesis. Lund Technical University, 1981.

- [191] J.H. Steward. “The Compliance of Solid, Wide-Faced Spur Gears”. In: *Journal of Mechanical Design* 112.4 (1990), pp. 590–595.
- [192] J. Kunert. “Experimentell gestützte Untersuchungen zum Verformungs-und Spannungsverhalten an außenverzahnten Stirnrädern für eine verbesserte Beanspruchungsanalyse”. PhD thesis. Technische Universität Dresden, 1999.
- [193] B. Neupert. “Berechnung der Zahnkräfte, Pressungen und Spannungen von Stirn- und Kegelradgetrieben”. PhD thesis. Rheinisch-Westfälische Technische Hochschule Aachen, 1983.
- [194] R. Guilbault, C. Gosselin and L. Cloutier. “Express Model for Load Sharing and Stress Analysis in Helical Gears”. In: *ASME Journal of Mechanical Design* 127.6 (2004), pp. 1161–1172.
- [195] M. Ajmi and P. Velex. “A model for simulating the quasi-static and dynamic behaviour of solid wide-faced spur and helical gears”. In: *Mechanism and Machine Theory* 40.2 (2005), pp. 173–190.
- [196] J.I. Pedrero et al. “Load distribution model along the line of contact for involute external gears”. In: *Mechanism and Machine Theory* 45.5 (2010), pp. 780–794.
- [197] I. González-Pérez and A. Fuentes-Aznar. “Implementation of a Finite Element Model for Gear Stress Analysis Based on Tie-Surface Constraints and Its Validation Through the Hertz’s Theory”. In: *ASME Journal of Mechanical Design* 140.2 (2018).
- [198] J. Börner. “Efficient simulation of gear manufacturing and tooth contact analysis for evaluating noise excitation”. In: *Proceedings of the International Gear Conference*. 2018, pp. 906–917.
- [199] M. Maatar and P. Velex. “Analytical expression for the time-varying contact length in perfect cylindrical gears: Some possible applications in gear dynamics”. In: *ASME Journal of Mechanical Design* 118.4 (1996), pp. 586–589.
- [200] C.D. Haddad. “The Elastic Analysis of Load Distribution in Wide-faced Helical Gears”. PhD thesis. University of Newcastle upon Tyne, 1991.
- [201] J.E. Lloyd. “Fast Implementation of Lemke’s Algorithm for Rigid Body Contact Simulation”. In: *Proceedings of the IEEE International Conference on Robotics and Automation*. 2005.
- [202] D. Petersen. “Auswirkung der Lastverteilung auf die Zahnfußstragfähigkeit von hoch überdeckenden Stirnradpaarungen”. PhD thesis. Technische Universität Carolo-Wilhelmina zu Braunschweig, 1989.
- [203] P. Sainsot, P. Velex and O. Duverger. “Contribution of gear body to tooth deflections—a new bidimensional analytical formula”. In: *ASME Journal of Mechanical Design* 126.4 (2004), pp. 748–752.
- [204] J. Börner, N. Kurz and F. Joachim. “Effective Analysis of Gears with the Program LVR (Stiffness Method)”. In: *Proceedings of the VDI International Conference on Gears*. 2002, pp. 721–736.
- [205] T.J. Lisle, B.A. Shaw and R.C. Frazer. “External spur gear root bending stress: A comparison of ISO 6336: 2006, AGMA 2101-D04, ANSYS finite element analysis and strain gauge techniques”. In: *Mechanism and Machine Theory* 111 (2017), pp. 1–9.
- [206] D. Krüger. “Auslegungsgrenzen, Grübchen-und Zahnfußstragfähigkeit asymmetrischer Stirnradverzahnungen”. PhD thesis. Technische Universität Chemnitz, 2017.
- [207] T. Paucker, M. Otto and K. Stahl. “A precise prediction of the tooth root stresses for involute external gears with any fillet geometry under consideration of the exact meshing position”. In: *Proceedings of the International Gear Conference*. 2018.
- [208] F.L. Litvin et al. “Modified involute helical gears: computerized design, simulation of meshing and stress analysis”. In: *Computer Methods in Applied Mechanics and Engineering* 192 (2003), pp. 3619–3655.

- [209] A. Iñurritegui et al. “Modelizado bidimensional de engranajes cilíndricos por elementos finitos”. In: *Proceedings of the XXII Congreso Nacional de Ingeniería Mecánica*. 2018.
- [210] M.B. Sánchez, M. Pleguezuelos and J.I. Pedrero. “Approximate equations for the meshing stiffness and the load sharing ratio of spur gears including hertzian effects”. In: *Mechanism and Machine Theory* 109 (2017), pp. 231–249.
- [211] T.J. Jaramillo. “Deflections and Moments Due to a Concentrated Load on a Cantilever Plate of Infinite Length”. In: *Journal of Applied Mechanics* 17.72 (1950).
- [212] U. Mann. “Schmierfilmbildung in Elastohydrodynamischen Kontakten”. PhD thesis. Technische Universität München, 1995.
- [213] K.L. Johnson and J.L. Tevaarwerk. “Shear behaviour of elastohydrodynamic oil films”. In: *Proceedings of the Royal Society of London, Series A (Mathematical and Physical Sciences)* 356.1685 (1977), pp. 215–36.
- [214] H. Eyring. “Viscosity, Plasticity and Diffusion as Examples of Absolute Reaction Rates”. In: *The Journal of Chemical Physics* 4.4 (1936), pp. 283–291.
- [215] S. Bair and W.O. Winer. “A rheological model for elastohydrodynamic contacts based on primary laboratory data”. In: *ASME Journal of Lubrication Technology* 101.3 (1979), pp. 258–65.
- [216] P.J. Carreau. “Rheological Equations from Molecular Network Theories”. In: *Transactions of the Society of Rheology* 16.1 (1972), pp. 99–127.
- [217] S. Bair et al. “Comment on "History, Origins and Prediction of Elastohydrodynamic Friction" by Spikes and Jie in Tribology Letters”. In: *Tribology Letters* 58.16 (2015), pp. 1–8.
- [218] H. Spikes and Z. Jie. “Reply to the comment by Scott Bair et al. on "History, Origins and Prediction of Elastohydrodynamic Friction" by Spikes and Jie in Tribology Letters”. In: *Tribology Letters* 58.17 (2015), pp. 1–6.
- [219] C.R. Evans and K.L. Johnson. “Regimes of traction in elastohydrodynamic lubrication”. In: *Proceedings of the Institution of Mechanical Engineers. Part C. Mechanical engineering science* 200.5 (1986), pp. 313–324.
- [220] J.A. Brandão et al. “Traction curves and rheological parameters of fully formulated gear oils”. In: *Proceedings of the Institution of Mechanical Engineers, Part J: Journal of Engineering Tribology* (2011).
- [221] Z.I. Botev, J.F. Grotowski and D.P. Kroese. “Kernel density estimation via diffusion”. In: *The Annals of Statistics* 38.5 (2010), pp. 2916–2957.
- [222] M. Björling et al. “Towards the true prediction of EHL friction”. In: *Tribology International* 66 (2013), pp. 19–26.
- [223] K.J. Sharif et al. “Comparison of non-Newtonian EHL models in high sliding applications”. In: *Tribology Research: From Model Experiment to Industrial Problem*. Ed. by G. Dalmaz et al. Vol. 39. Tribology Series. Elsevier, 2001, pp. 787–796.
- [224] M. Bercea, V. Paleu and I. Bercea. “Lubricant Oils Additivated with Polymers in EHD Contacts: Part 1. Rheological Behaviour”. In: *Lubrication Science* 17.1 (2004), pp. 1–24.
- [225] S. Bair and W.O. Winer. “High Shear Stress Rheology of Liquid Lubricants at Pressures of 2 to 200 MPa”. In: *ASME Journal of Tribology* 112.2 (1989), pp. 245–252.
- [226] B. Jacod, C.H. Venner and P.M. Lugt. “Extension of the Friction Mastercurve to Limiting Shear Stress Models”. In: *ASME Journal of Tribology* 125.4 (2003), pp. 739–46.
- [227] W. Hirst and A.J. Moore. “Elastohydrodynamic Lubrication at High Pressures. II. Non-Newtonian Behaviour”. In: *Proceedings of the Royal Society of London, Series A (Mathematical and Physical Sciences)* 365 (1979), pp. 537–565.

- [228] T.E. Tallian. “The theory of partial elastohydrodynamic contacts”. In: *Wear* 21.1 (1972), pp. 49–101.
- [229] S. Matsumoto and K. Morikawa. “The new estimation formula of coefficient of friction in rolling-sliding contact surface under mixed lubrication condition for the power loss reduction of power transmission gears”. In: *Proceedings of the International Gear Conference*. 2014, pp. 1078–1088.
- [230] F. Robbe-Valloire et al. “Theoretical prediction and experimental results for mixed lubrication between parallel surfaces”. In: *Boundary and Mixed Lubrication*. Ed. by D. Dowson et al. Vol. 40. Tribology Series. Elsevier, 2002, pp. 129–137.
- [231] M. Masjedi and M.M. Khonsari. “Theoretical and experimental investigation of traction coefficient in line-contact EHL of rough surfaces”. In: *Tribology International* 70 (2014), pp. 179–189.
- [232] E. Gelinck. “Mixed Lubrication of Line Contacts”. PhD thesis. University of Twente, 1999.
- [233] J. Schipper. “Transitions in the lubrication of concentrated contacts”. PhD thesis. University of Twente, 1988.
- [234] A. Clarke et al. “An investigation into mixed lubrication conditions using electrical contact resistance techniques”. In: *Tribology International* 93 (2016), pp. 709–16.
- [235] E. Höglund. “Influence of lubricant properties on elastohydrodynamic lubrication”. In: *Wear* 232.2 (1999), pp. 176–184.
- [236] S. Bair. “Choosing pressure-viscosity relations”. In: *High Temperatures - High Pressures* 44.6 (2015), pp. 415–428.
- [237] P.W. Gold et al. “Viscosity-Pressure-Temperature Behaviour of Mineral and Synthetic Oils”. In: *Journal of Synthetic Lubrication* 18.1 (2001), pp. 51–79.
- [238] G.E. Morales-Espejel and A.W. Wemekamp. “Ertel-Grubin methods in elastohydrodynamic lubrication- a review”. In: *Proceedings of the Institution of Mechanical Engineers, Part J: Journal of Engineering Tribology* 222.1 (2008), pp. 15–34.
- [239] J. Hili et al. “Experimental Investigation of Elastohydrodynamic (EHD) Film Thickness Behavior at High Speeds”. In: *Tribology Transactions* 53.5 (2010), pp. 658–666.
- [240] M. Hammami et al. “Axle Gear Oils: Tribological Characterization Under Full Film Lubrication”. In: *Tribology International* 106 (2016), pp. 109–122.
- [241] S. Bair and P. Kottke. “Pressure-viscosity relationships for elastohydrodynamics”. In: *Tribology Transactions* 46.3 (2003), pp. 289–295.
- [242] P.M. Lugt and G.E. Morales-Espejel. “A Review of Elasto-Hydrodynamic Lubrication Theory”. In: *Tribology Transactions* 54.3 (2011), pp. 470–496.
- [243] T. Jurkschat, T. Lohner and K. Stahl. “Improved calculation of load-dependent gear losses by consideration of so far disregarded influences”. In: *Proc. of the Institution of Mechanical Engineers, Part J: Journal of Engineering Tribology* (2018).
- [244] J.C. Jaeger. “Moving sources of heat and the temperature at sliding contact”. In: *Proceedings of the Royal Society* 76 (1942), pp. 205–224.
- [245] J.F. Archard. “The temperature of rubbing surfaces”. In: *Wear* 2.6 (1959), pp. 438–455.
- [246] A.V. Olver. “Testing Transmission Lubricants: The Importance of Thermal Response”. In: *Proceedings of the Institution of Mechanical Engineers, Part G: Journal of Aerospace Engineering* 205.1 (1991), pp. 35–44.
- [247] K.L. Johnson and J.A. Greenwood. “Thermal analysis of an Eyring fluid in elastohydrodynamic traction”. In: *Wear* 61.2 (1980), pp. 353–374.
- [248] G.W. Stachowiak and A.W. Batchelor. *Engineering Tribology*. 4th Edition. Butterworth-Heinemann, 2014.

- [249] T. Stolarski. *Tribology in Machine Design*. Butterworth-Heinemann, 1990.
- [250] B.J Hamrock and D. Dowson. “Isothermal Elastohydrodynamic Lubrication of Point Contacts: Part III - Fully Flooded Results”. In: *Journal of Tribology* 99.2 (1977), pp. 264–275.
- [251] K.L. Johnson, J.A. Greenwood and S.Y. Poon. “A simple theory of asperity contact in elastohydrodynamic lubrication”. In: *Wear* 19.1 (1972), pp. 91–108.
- [252] H. van Leeuwen. “The determination of the pressure - viscosity coefficient of a lubricant through an accurate film thickness formula and accurate film thickness measurements”. In: *Proceedings of the Institution of Mechanical Engineers, Part J: Journal of Engineering Tribology* 223.8 (2009), pp. 1143–1163.
- [253] K. Bobzin et al. “Friction reduction of highly-loaded rolling-sliding contacts by surface modifications under elasto-hydrodynamic lubrication”. In: *Wear* 328-329 (2015), pp. 217–28.
- [254] T. Lohner et al. “On the running-in behavior of lubricated line contacts”. In: *Proceedings of the Institution of Mechanical Engineers, Part J: Journal of Engineering Tribology* 231.4 (2015), pp. 441–452.
- [255] Y. Terauchi et al. “On Heat Balance of Gear Equipment : 2nd Report. On a Method for Predicting Bulk Temperature Rise of Gears and Temperature Rise of Oil with Dip-cooling”. In: *Transactions of the Japan Society of Mechanical Engineers Series C* 55.514 (1989), pp. 1438–1445.
- [256] Y. Wang et al. “Convection heat transfer and temperature analysis of oil jet lubricated spur gears”. In: *Industrial Lubrication and Tribology* 68.6 (2016), pp. 624–31.
- [257] A.I. Christodoulis et al. “The Efficiency of a Simple Spur Gearbox - A Thermally Coupled Lubrication Model”. In: *Proceedings of the AGMA Fall Technical Meeting*. 14FTM08. 2014.
- [258] S. Wang, C. Cusano and T.F. Conry. “Thermal analysis of elastohydrodynamic lubrication of line contacts using the Ree-Eyring fluid model”. In: *Journal of Tribology* 113.2 (1991), pp. 232–244.
- [259] F. Pouly et al. “Power Loss Predictions in High-Speed Rolling Element Bearings Using Thermal Networks”. In: *Tribology Transactions* 53.6 (2010), pp. 957–967.
- [260] D. Frölich, B. Magyar and B. Sauer. “Semi-analytical model for the contact temperature calculation in radial shaft seals”. In: *Proceedings of the STLE Annual Meeting*. Vol. 2. 2014, pp. 756–760.
- [261] T.L. Bergman et al. *Introduction to Heat Transfer*. Wiley, 2011.
- [262] S.R. Nekoo. “Exact Solution for Heat Conduction Problem of a Sector of a Hollow Cylinder”. In: *American Journal of Mechanical Engineering* 1.2 (2013), pp. 50–57.
- [263] C. Changenet. “Modélisation du comportement thermique des transmissions par engrenages”. PhD thesis. Institut National des Sciences Appliquées de Lyon, 2006.
- [264] J. Durand de Gevigney et al. “Thermal modelling of a back-to-back gearbox test machine: Application to the FZG test rig”. In: *Proceedings of the Institution of Mechanical Engineers, Part J: Journal of Engineering Tribology* 226.6 (2012), pp. 501–515.
- [265] A. Neurouth. “Etude de la performance énergétique d’une transmission de puissance haute vitesse”. PhD thesis. Institut National des Sciences Appliquées de Lyon, 2016.
- [266] N. Laraqi. “Influence de la vitesse de glissement sur la résistance thermique de constriction”. In: *Revue générale de thermique* 34.408 (1995), pp. 735–741.
- [267] C. Changenet and P. Velex. “Housing Influence on Churning Losses in Geared Transmissions”. In: *ASME Journal of Mechanical Design* 130.6 (2008).
- [268] G. LePrince et al. “Influence of Aerated Lubricants on Gear Churning Losses—An Engineering Model”. In: *Tribology Transactions* 54.6 (2011), pp. 929–938.

- [269] P. Albers. “A study to oil churning losses in a gearbox”. MA thesis. Ecole Catholique d’Arts et Metiers de Lyon, 2004.
- [270] M. Ruzek et al. “On windage losses in high-speed pinion-gear pairs”. In: *Mechanism and Machine Theory* 132 (2019), pp. 123–132.
- [271] E.A. Hartono. “Study of fluid flow inside the gearbox”. MA thesis. Chalmers University of Technology, 2014.
- [272] S.W. Churchill and H.S.H. Chu. “Correlating equations for laminar and turbulent free convection from a vertical plate”. In: *International Journal of Heat and Mass Transfer* 18.11 (1975), pp. 1323–1329.
- [273] W. Idsinga, N. Todreas and R. Bowring. “An assessment of two-phase pressure drop correlations for steam-water systems”. In: *International Journal of Multiphase Flow* 3.5 (1977), pp. 401–413.
- [274] K.M. Becker. “Measurements of convective heat transfer from a horizontal cylinder rotating in a tank of water”. In: *International Journal of Heat and Mass Transfer* 6.12 (1963), pp. 1053–1062.
- [275] E.C. Cobb and O.A. Saunders. “Heat transfer from a rotating disk”. In: *Proceedings of the Royal Society of London A: Mathematical, Physical and Engineering Sciences* 236.1206 (1956), pp. 343–351.
- [276] E. M. Sparrow, J.P. Abraham and J.C.K. Tong. “Archival correlations for average heat transfer coefficients for non-circular and circular cylinders and for spheres in cross-flow”. In: *International Journal of Heat and Mass Transfer* 47 (2004), pp. 5285–5296.
- [277] J. Kiusalaas. *Numerical Methods in Engineering with Matlab*. Cambridge University Press, 2005.
- [278] W.A. Robin. “Solving differential equations using modified Picard iteration”. In: *International Journal of Mathematical Education in Science and Technology* 41.5 (2010), pp. 649–665.
- [279] D. Bartel. *Simulation von Tribosystemen: Grundlagen und Anwendungen*. Vieweg Teubner Verlag, 2010.
- [280] F.J. McQuillan, J.R. Culham and M.M. Yovanovich. *Properties of dry air at one atmosphere*. Technical report UW/MHTL 8406, G-01. University of Waterloo, 1984.
- [281] A.V. Olver. “Gear lubrication- A review”. In: *Proceedings of the Institution of Mechanical Engineers, Part J: Journal of Engineering Tribology* 216.5 (2002), pp. 255–267.
- [282] E.M. Laukotka. *Datensammlung Referenzöle*. Technical report 660. Forschungsvereinigung Antriebstechnik, 2007.
- [283] G. Leprince. “Pertes mécaniques par frottement et lubrification dans une boîte de vitesses”. PhD thesis. Institut National des Sciences Appliquées de Lyon, 2011.
- [284] *ISO 1328-1: 1995: Cylindrical Gears — ISO system of accuracy — Part 1: Definitions and allowable values of deviations relevant to corresponding flanks of gear teeth*. Standard. International Organization for Standardization, 1997.
- [285] *ISO 14635-1: 2000: Gears — FZG test procedures — Part 1: FZG test method A/8.3/90 for relative scuffing load-carrying capacity of oils*. Standard. International Organization for Standardization, 2000.
- [286] A. Arana et al. “Influence of thermal distortion on load distribution, transmission error and premature contact”. In: *Proceedings of the International Gear Conference*. 2018, pp. 446–459.
- [287] J. Larrañaga et al. “Influence of Thermal Distortion on Spur Gear Tooth Contact”. In: *Proceedings of the AGMA Fall Technical Meeting*. 18FTM07. 2018.
- [288] Trelleborg. *Turcon Varilip PDR*. Catalogue. 2008.

- [289] Heidenhain GmbH. *Angle Encoders With Integral Bearing*. Catalogue. 2015.
- [290] R.G. Munro, D. Palmer and L. Morrish. “An experimental method to measure gear tooth stiffness throughout and beyond the path of contact”. In: *Proceedings of the Institution of Mechanical Engineers, Part C: Journal of Mechanical Engineering Science* 215.7 (2001), pp. 793–803.
- [291] Z. Wright. “Loaded Transmission Error Measurement System for Spur and Helical Gears”. PhD thesis. The Ohio State University, 2009.
- [292] M.A. Fish. “Transmission Errors in Precision Worm Gear Drives”. PhD thesis. University of Huddersfield, 1998.
- [293] R.G. Munro. “The DC component of gear transmission error”. In: *Proceedings of the ASME International Power Transmission and Gearing Conference*. Vol. 1. 1989, pp. 467–470.
- [294] M. Masjedi and M.M. Khonsari. “Film Thickness and Asperity Load Formulas for Line-Contact Elastohydrodynamic Lubrication With Provision for Surface Roughness”. In: *ASME Journal of Tribology* 134.1 (2012).
- [295] SKF. *Rolling bearings*. Catalogue. 2018.
- [296] Freudenberg. *Simrit: Radialwellendichtringe*. Catalogue. 1976.
- [297] T. Engelke. “Einfluss der Elastomer-Schmierstoff-Kombination auf das Betriebsverhalten von Radialwellendichtringen”. PhD thesis. Leibnitz Universität Hannover, 2011.
- [298] H. Linke. *Stirnradverzahnung. Berechnung - Werkstoffe - Fertigung*. 2nd Edition. Hanser, 2010.
- [299] A. Palmgren. *Ball and roller bearing engineering*. SKF Industries, 1959.
- [300] H. Moes. *Lubrication and Beyond*. University of Twente, 2000.
- [301] H. Reusner. “Druckflächenbelastung und Oberflächenverschiebung im Wälzkontakt von Rotationskörpern”. PhD thesis. Fakultät für Maschinenbau der Universität Karlsruhe, 1977.

